OCTOBER 2022

AJNR

VOLUME 43 • PP 1377–1547

AJNR

AMERICAN JOURNAL OF NEURORADIOLOGY

OCTOBER 2022
VOLUME 43
NUMBER 10
WWW.AJNR.ORG

THE JOURNAL OF DIAGNOSTIC AND INTERVENTIONAL NEURORADIOLOGY

Cellular density in adult glioma
Surgical or endovascular treatment of MCA aneurysms
Adaptive language mapping paradigms
Neuroimaging definition of the Dandy-Walker phenotype

Official Journal ASNR • ASFNR • ASHNR • ASPNR • ASSR

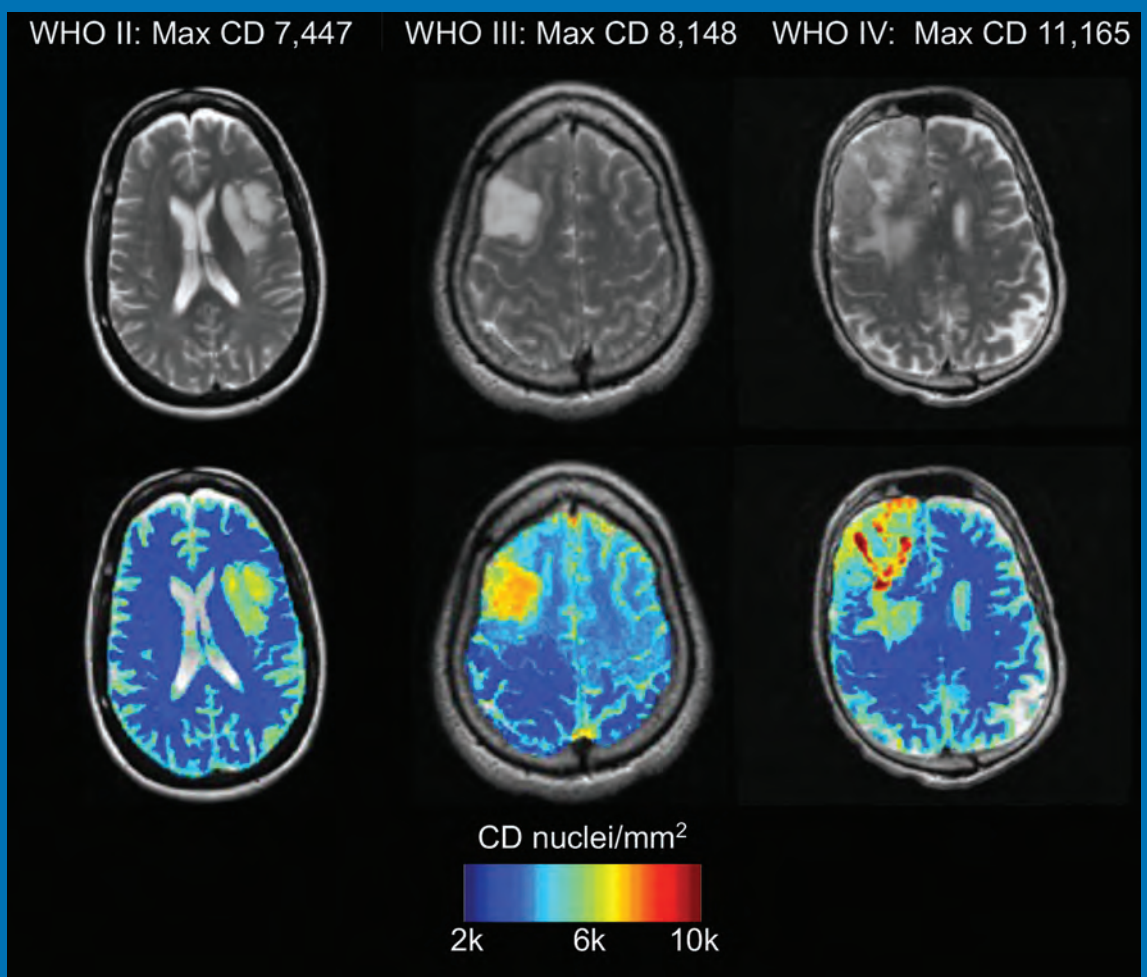

Introducing FRED™ X™

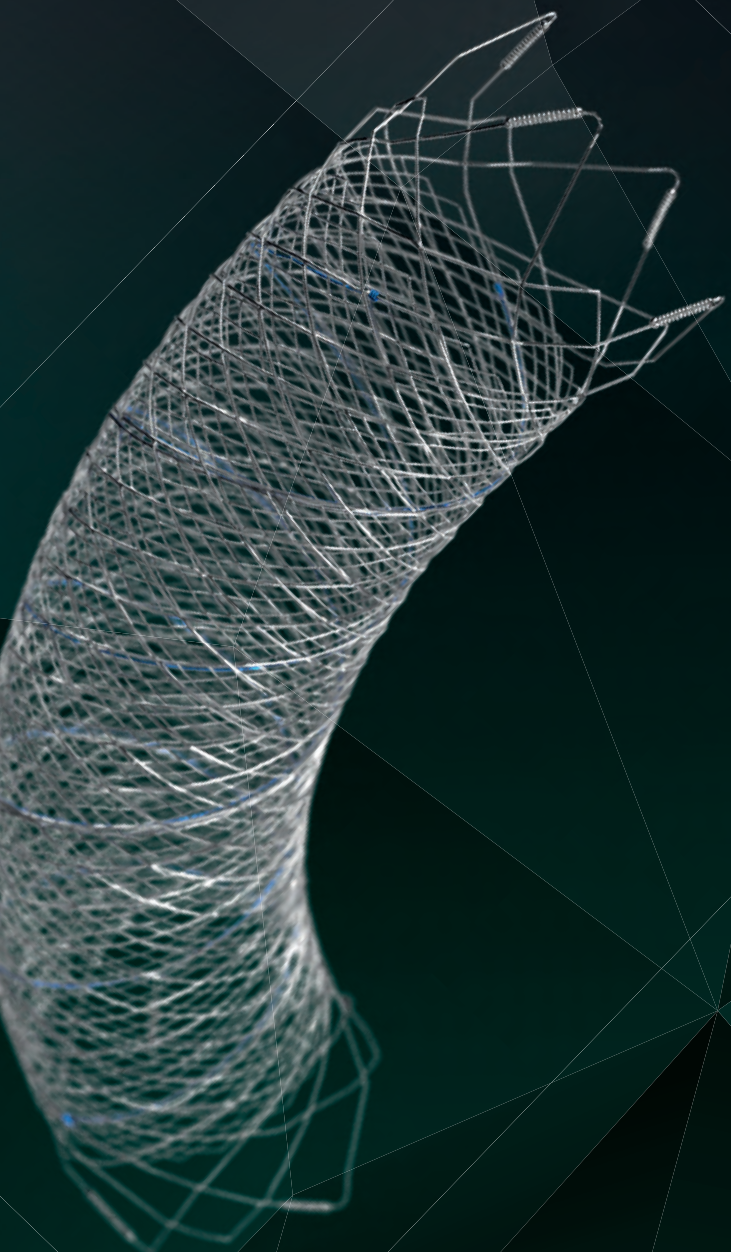

THE NEXT ADVANCEMENT

IN FLOW DIVERSION TECHNOLOGY

The FRED™ X Flow Diverter features the same precise placement and immediate opening of the FRED™ Device, now with X Technology. X Technology is a covalently bonded, nanoscale surface treatment, designed to:

- ***Reduce material thrombogenicity[1]***
- ***Maintain natural vessel healing response[2,3,4]***
- ***Improve device deliverability and resheathing[1]***

The only FDA PMA approved portfolio with a 0.021″ delivery system for smaller device sizes, and no distal lead wire.

MicroVention™ TERUMO

For more information, contact your local MicroVention sales representative or visit our website. ***www.microvention.com***

* Data is derived from in vivo and ex vitro testing and may not be representative of clinical performance.

1. Data on file
2. Tanaka M et al. Design of biocompatible and biodegradable polymers based on intermediate water concept. Polymer Journal. 2015;47:114-121.
3. Tanaka M et al. Blood compatible aspects of poly(2-methoxyethylacrylate) (PMEA) – relationship between protein adsorption and platelet adhesion on PMEA surface. Biomaterials. 2000;21:1471-1481.
4. Schiel L et al. X Coating™: A new biopassive polymer coating. Canadian Perfusion Canadienne. June 2001;11(2):9.

Indications for Use: The FRED X System is indicated for use in the internal carotid artery from the petrous segment to the terminus for the endovascular treatment of adult patients (22 years of age or older) with wide-necked (neck width 4 mm or dome-to-neck ratio < 2) saccular or fusiform intracranial aneurysms arising from a parent vessel with a diameter 2.0 mm and 5.0 mm.

Rx Only: Federal (United States) law restricts this device to sale by or on the order of a physician.

WEB™ 17

Aneurysm Embolization System

LOWER PROFILE

NEW SIZES

MORE ACCESS OPTIONS

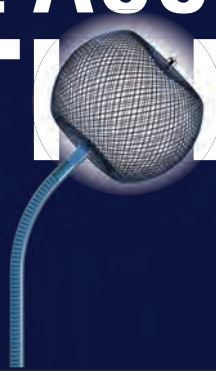

INDICATIONS FOR USE:
The WEB Aneurysm Embolization System is intended for the endovascular embolization of ruptured and unruptured intracranial aneurysms and other neurovascular abnormalities such as arteriovenous fistulae (AVF). The WEB Aneurysm Embolization System is also intended for vascular occlusion of blood vessels within the neurovascular system to permanently obstruct blood flow to an aneurysm or other vascular malformation

POTENTIAL COMPLICATIONS:
Potential complications include but are not limited to the following: hematoma at the site of entry, aneurysm rupture, emboli, vessel perforation, parent artery occlusion, hemorrhage, ischemia, vasospasm, clot formation, device migration or misplacement, premature or difficult device detachment, non-detachment, incomplete aneurysm filling, revascularization, post-embolization syndrome, and neurological deficits including stroke and death. For complete indications, potential complications, warnings, precautions, and instructions, see instructions for use (IFU provided with the device).

VIA 21, 27, 33 - The VIA Microcatheter is intended for the introduction of interventional devices (such as the WEB device/stents/flow diverters) and infusion of diagnostic agents (such as contrast media) into the neuro, peripheral, and coronary vasculature.

VIA 17,17 Preshaped - The VIA Microcatheter is intended for the introduction of interventional devices (such as the WEB device/stents/flow diverters) and infusion of diagnostic agents (such as contrast media) into the neuro, peripheral, and coronary vasculature.

The VIA Microcatheter is contraindicated for use with liquid embolic materials, such as n-butyl 2-cyanoacrylate or ethylene vinyl alcohol & DMSO (dimethyl sulfoxide).

The device should only be used by physicians who have undergone training in all aspects of the WEB Aneurysm Embolization System procedure as prescribed by the manufacturer.

RX Only: Federal law restricts this device to sale by or on the order of a physician.

For healthcare professional intended use only.

MicroVention™
TERUMO

MicroVention Worldwide Innovaton Center — PH +1.714.247.8000

35 Enterprise
Aliso Viejo, CA 92656 USA
MicroVention UK Limited — PH +44 (0) 191 258 6777
MicroVention Europe, S.A.R.L. — PH +33 (1) 39 21 77 46
MicroVention Deutschland GmbH — PH +49 211 210 798-0
Website — microvention.com

CE 0297

multihance®
(gadobenate dimeglumine)
injection, 529 mg/mL

What does seeing better with MultiHance® mean?[1-4*]

MultiHance® demonstrated superiority in both qualitative and quantitative enhancement of brain lesions compared with Dotarem® at 0.1 mmol/kg dose.[1†]

- The 0.1 mmol/kg dose of MultiHance demonstrated consistently better visualization for all readers for all visualization endpoints vs non-contrast MRI.
- 3 blinded and independent readers reported superiority ($P<0.002$) of 0.1-mmol/kg MultiHance for all endpoints in Arm 1.
- 3 blinded independent readers also reported the mean percentage signal enhancement of lesions on the TISE images was significantly ($P<.0006$) higher for MultiHance compared with Dotarem in patients given 0.1-mmol/kg doses of both agents. Similar results were obtained for determination of LBR. LBR findings on TIGRE images were similar.

The individuals who appear are for illustrative purposes. All persons depicted are models and not real patients.
Please see Brief Summary of Prescribing Information including Boxed Warning on adjacent page.

*MRI imaging of the CNS in adult and pediatric patients to visualize lesions with abnormal BBB or abnormal vascularity of the brain, spine and associated tissues or to evaluate adults with known or suspected renal or aorto-ilio-femoral occlusive vascular disease.

†Multicenter, multinational, double-blind randomized, intraindividual crossover study design of 177 patients with known or suspected brain tumors. Each patient received 0.1-mmol/kg doses of MultiHance and Dotarem in two identical MR imaging examinations. For Arm 1, the contrast agents for patients were administered by IV using manual bolus injection (n=83) or power a power injector (n=13). The agents were administered at 0.1mmol/kg of body weight, corresponding to 0.2 mL/kg for MultiHance and for Dotarem. For Arm 2, Administration of agents were IV using manual bolus injection (n=83) or power a power injector (n=24). The agents were administered 0.05 mmol/kg of body weight, corresponding to 0.1 mL/kg for MultiHance and at 0.1mmol/kg of body weight, corresponding to 0.2 mL/kg for Dotarem. All injections were followed by a saline flush of up to 30 mL. The interval between the 2 MR imaging examinations was >48 hours to avoid carryover effects but <14 days to minimize the chance of disease progression. All images were evaluated by 3 blinded, independent experienced radiologists who were unaffiliated with the study centers. Each reader evaluated the patient images separately and independently. Images were evaluated qualitatively for diagnostic and quality and scored for: 1) lesion border delineation, 2) disease extent, 3) visualization of lesion internal morphology, and 4) lesion contrast enhancement compared with surrounding normal tissue. All assessments used a 3-point scales from 1 (examination 1 better) through 0 (examinations equal) to 1 (examination 2 better).

Dotarem® (Gadoterate) is a registered trademark of Guebert, Aulnay-sous-Bois, France. **Reference:** Vaneckova M, Herman M, Smith MP, et al. The benefits of high relaxivity for brain tumor imaging: results of a multicenter intraindividual crossover comparison of gadobenate dimeglumine with gadoterate meglumine (The BENEFIT Study). *AJNR Am J Neuroradiol.* 2015 Sep;36(9):1589–1598.

MultiHance® (gadobenate dimeglumine) injection, 529 mg/mL and
MultiHance® Multipack™ (gadobenate dimeglumine) injection, 529 mg/mL

Indications and Usage:
MultiHance® (gadobenate dimeglumine) injection, 529 mg/mL is a gadolinium-based contrast agent indicated for intravenous use in:

- Magnetic resonance imaging (MRI) of the central nervous system (CNS) in adults and pediatric patients (including term neonates) to visualize lesions with abnormal blood-brain barrier or abnormal vascularity of the brain, spine, and associated tissues and
- Magnetic resonance angiography (MRA) to evaluate adults with known or suspected renal or aorto-ilio-femoral occlusive vascular disease

IMPORTANT SAFETY INFORMATION:

WARNING: NEPHROGENIC SYSTEMIC FIBROSIS

Gadolinium-based contrast agents (GBCAs) increase the risk for NSF among patients with impaired elimination of the drugs. Avoid use of GBCAs in these patients unless the diagnostic information is essential and not available with non-contrasted MRI or other modalities. NSF may result in fatal or debilitating systemic fibrosis affecting the skin, muscle and internal organs.

- **The risk for NSF appears highest among patients with:**
  - **chronic, severe kidney disease (GFR <30 mL/min/1.73m^2), or**
  - **acute kidney injury.**
- **Screen patients for acute kidney injury and other conditions that may reduce renal function. For patients at risk for chronically reduced renal function (e.g. age >60 years, hypertension or diabetes), estimate the glomerular filtration rate (GFR) through laboratory testing.**
- **For patients at highest risk for NSF, do not exceed the recommended MultiHance dose and allow a sufficient period of time for elimination of the drug from the body prior to re-administration.**

CONTRAINDICATIONS
MultiHance is contraindicated in patients with known allergic or hypersensitivity reactions to gadolinium-based contrast agents.

WARNINGS AND PRECAUTIONS
Nephrogenic Systemic Fibrosis: NSF has occurred in patients with impaired elimination of GBCAs. Higher than recommended dosing or repeated dosing appears to increase risk.
Hypersensitivity Reactions: Anaphylactic and anaphylactoid reactions have been reported, involving cardiovascular, respiratory, and/or cutaneous manifestations. Some patients experienced circulatory collapse and died. In most cases, initial symptoms occurred within minutes of MultiHance administration and resolved with prompt emergency treatment. Consider the risk for hypersensitivity reactions, especially in patients with a history of hypersensitivity reactions or a history of asthma or other allergic disorders.
Gadolinium Retention: Gadolinium is retained for months or years in several organs. The highest concentrations have been identified in the bone, followed by brain, skin, kidney, liver, and spleen. At equivalent doses, retention varies among the linear agents. Retention is lowest and similar among the macrocyclic GBCAs. Consequences of gadolinium retention in the brain have not been established, but they have been established in the skin and other organs in patients with impaired renal function. Minimize repetitive GBCA imaging studies, particularly closely spaced studies when possible.
Acute Renal Failure: In patients with renal insufficiency, acute renal failure requiring dialysis or worsening renal function have occurred with the use of GBCAs. The risk of renal failure may increase with increasing dose of the contrast agent. Screen all patients for renal dysfunction by obtaining a history and/or laboratory tests.
Extravasation and Injection Site Reactions: Extravasation of MultiHance may lead to injection site reactions, characterized by local pain or burning sensation, swelling, blistering, and necrosis. Exercise caution to avoid local extravasation during intravenous administration of MultiHance.
Cardiac Arrhythmias: Cardiac arrhythmias have been observed in patients receiving MultiHance in clinical trials. Assess patients for underlying conditions

or medications that predispose to arrhythmias. The effects on QTc by MultiHance dose, other drugs, and medical conditions were not systematically studied.
Interference with Visualization of Certain Lesions: Certain lesions seen on non-contrast images may not be seen on contrast images. Exercise caution when interpreting contrast MR images in the absence of companion non-contrast MR images.

ADVERSE REACTIONS
The most commonly reported adverse reactions are nausea (1.3%) and headache (1.2%).

USE IN SPECIFIC POPULATIONS
Pregnancy: GBCAs cross the human placenta and result in fetal exposure and gadolinium retention. Use only if imaging is essential during pregnancy and cannot be delayed.
Lactation: There is no information on the effects of the drug on the breastfed infant or the effects of the drug on milk production. However, limited literature reports that breastfeeding after MultiHance administration to the mother would result in the infant receiving an oral dose of 0.001%-0.04% of the maternal dose.
Pediatric Use: MultiHance is approved for intravenous use for MRI of the CNS to visualize lesions with abnormal blood brain barrier or abnormal vascularity of the brain, spine, and associated tissues in pediatric patients from birth, including term neonates, to less than 17 years of age. Adverse reactions in pediatric patients were similar to those reported in adults. No dose adjustment according to age is necessary in pediatric patients two years of age and older. For pediatric patients, less than 2 years of age, the recommended dosage range is 0.1 to 0.2 mL/kg. The safety of MultiHance has not been established in preterm neonates.

You are encouraged to report negative side effects of prescription drugs to the FDA. Visit www.fda.gov/medwatch or call 1-800-FDA-1088.

Please see full Prescribing Information and Patient Medication Guide for additional important safety information for/regarding MultiHance (gadobenate dimeglumine) injection, 529 mg/mL at https://imaging.bracco.com/sites/braccoimaging.com/files/technica_sheet_pdf/us-en-2019-01-16-spc-medication-guide-multihance.pdf

MultiHance is manufactured for Bracco Diagnostics Inc. by BIPSO GmbH – 78224 Singen (Germany) and by Patheon Italia S.p.A., Ferentino, Italy.

References: 1. Vaneckova M, Herman M, Smith MP, et al. The benefits of high relaxivity for brain tumor imaging: results of a multicenter intraindividual crossover comparison of gadobenate dimeglumine with gadoterate meglumine (The BENEFIT Study). *AJNR Am J Neuroradiol.* 2015 Sep;36(9):1589–1598. **2.** Seidl Z, Vymazal J, Mechi M, et al. Does higher gadolinium concentration play a role in the morphologic assessment of brain tumors? Results of a multicenter intraindividual crossover comparison of gadobutrol versus gadobenate dimeglumine (the MERIT Study). *AJNR Am J Neuroradiol.* 2012 Jun-Jul;33(6):1050–1058. **3.** Maravilla KR, Maldjian JA, Schmalfuss IM, et al. Contrast enhancement of central nervous system lesions: multicenter intraindividual crossover comparative study of two MR contrast agents. *Radiology.* 2006 Aug;240(2):389–400. **4.** Rowley HA, Scialfa G, Gao PY, et al. Contrast-enhanced MR imaging of brain lesions: a large-scale intraindividual crossover comparison of gadobenate dimeglumine versus gadodiamide. *AJNR Am J Neuroradiol.* 2008 Jul;29(9):1684–1691.

Bracco Diagnostics Inc.
259 Prospect Plains Road, Building H
Monroe Township, NJ 08831 USA
Phone: 609-514-2200
Toll Free: 1-877-272-2269 (U.S. only)
Fax: 609-514-2446

BRACCO

Bracco Diagnostics

multihance®
(gadobenate dimeglumine)
injection, 529 mg/mL

Rx ONLY
Please see full prescribing information.
A brief summary follows.

WARNING: NEPHROGENIC SYSTEMIC FIBROSIS

Gadolinium-based contrast agents (GBCAs) increase the risk for NSF among patients with impaired elimination of the drugs.

Avoid use of GBCAs in these patients unless the diagnostic information is essential and not available with non-contrasted MRI or other modalities. NSF may result in fatal or debilitating systemic fibrosis affecting the skin, muscle and internal organs.

- The risk for NSF appears highest among patients with:
  - chronic, severe kidney disease (GFR <30 mL/min/1.73m2), or
  - acute kidney injury.
- Screen patients for acute kidney injury and other conditions that may reduce renal function. For patients at risk for chronically reduced renal function (e.g. age > 60 years, hypertension or diabetes), estimate the glomerular filtration rate (GFR) through laboratory testing.
- For patients at highest risk for NSF, do not exceed the recommended MultiHance dose and allow a sufficient period of time for elimination of the drug from the body prior to re-administration. [see ***Warnings and Precautions (5.1)***]

1 INDICATIONS AND USAGE

1.1 MRI of the Central Nervous System (CNS)

MultiHance is indicated for intravenous use in magnetic resonance imaging (MRI) of the central nervous system (CNS) in adults and pediatric patients (including term neonates), to visualize lesions with abnormal blood-brain barrier or abnormal vascularity of the brain, spine, and associated tissues.

1.2 MRA of Renal and Aorto-ilio-femoral Vessels

MultiHance is indicated for use in magnetic resonance angiography (MRA) to evaluate adults with known or suspected renal or aorto-ilio-femoral occlusive vascular disease.

4 CONTRAINDICATIONS MultiHance is contraindicated in patients with known allergic or hypersensitivity reactions to gadolinium-based contrast agents [see ***Warnings and Precautions (5.2)]***.

5 WARNINGS AND PRECAUTIONS

5.1 Nephrogenic Systemic Fibrosis (NSF) Gadolinium-based contrast agents (GBCAs) increase the risk for nephrogenic systemic fibrosis (NSF) among patients with impaired elimination of the drugs. Avoid use of GBCAs among these patients unless the diagnostic information is essential and not available with non-contrast enhanced MRI or other modalities. The GBCA-associated NSF risk appears highest for patients with chronic, severe kidney disease (GFR <30 mL/min/1.73m^2) as well as patients with acute kidney injury. The risk appears lower for patients with chronic, moderate kidney disease (GFR 30-59 mL/min/1.73m^2) and little, if any, for patients with chronic, mild kidney disease (GFR 60-89 mL/min/1.73m^2). NSF may result in fatal or debilitating fibrosis affecting the skin, muscle and internal organs. Report any diagnosis of NSF following MultiHance administration to Bracco Diagnostics (1-800-257-5181) or FDA (1-800-FDA-1088 or www.fda.gov/medwatch).

Screen patients for acute kidney injury and other conditions that may reduce renal function.

Features of acute kidney injury consist of rapid (over hours to days) and usually reversible decrease in kidney function, commonly in the setting of surgery, severe infection, injury or drug-induced kidney toxicity. Serum creatinine levels and estimated GFR may not reliably assess renal function in the setting of acute kidney injury. For patients at risk for chronically reduced renal function (e.g., age > 60 years, diabetes mellitus or chronic hypertension), estimate the GFR through laboratory testing.

Among the factors that may increase the risk for NSF are repeated or higher than recommended doses of a GBCA and the degree of renal impairment at the time of exposure. Record the specific GBCA and the dose administered to a patient. For patients at highest risk for NSF, do not exceed the recommended MultiHance dose and allow a sufficient period of time for elimination of the drug prior to re-administration. For patients receiving hemodialysis, physicians may consider the prompt initiation of hemodialysis following the administration of a GBCA in order to enhance the contrast agent's elimination. The usefulness of hemodialysis in the prevention of NSF is unknown [see ***Dosage and Administration (2) and Clinical Pharmacology (12)***].

5.2 Hypersensitivity Reactions Anaphylactic and anaphylactoid reactions have been reported, involving cardiovascular, respiratory, and/or cutaneous manifestations. Some patients experienced circulatory collapse and died. In most cases, initial symptoms occurred within minutes of MultiHance administration and resolved with prompt emergency treatment. Prior to MultiHance administration, ensure the availability of personnel trained and medications to treat hypersensitivity reactions. If such a reaction occurs stop MultiHance and immediately begin appropriate therapy. Additionally, consider the risk for hypersensitivity reactions, especially in patients with a history of hypersensitivity reactions or a history of asthma or other allergic disorders. Observe patients for signs and symptoms of a hypersensitivity reaction during and for up to 2 hours after MultiHance administration.

5.3 Gadolinium Retention Gadolinium is retained for months or years in several organs. The highest concentrations (nanomoles per gram of tissue) have been identified in the bone, followed by other organs (e.g. brain, skin, kidney, liver, and spleen. The duration of retention also varies by tissue and is longest in bone. Linear GBCAs cause more retention than macrocyclic GBCAs. At equivalent doses, gadolinium retention varies among the linear agents with Omniscan (gadodiamide) and Optimark (gadoversetamide) causing greater retention than other linear agents [Eovist (gadoxetate disodium), Magnevist (gadopentetate dimeglumine), MultiHance (gadobenate dimeglumine)]. Retention is lowest and similar among the macrocyclic GBCAs [Dotarem gadoterate meglumine), Gadavist (gadobutrol), ProHance (gadoteridol)].

Consequences of gadolinium retention in the brain have not been established. Pathologic and clinical consequences of GBCA administration and retention in skin and other organs have been established in patients with impaired renal function [see ***Warnings and Precautions (5.1)***]. There are rare reports of pathologic skin changes in patients with normal renal function. Adverse events involving multiple organ systems have been reported in patients with normal renal function without an established causal link to gadolinium retention [see ***Adverse Reactions (6.2)***]. While clinical consequences of gadolinium retention have not been established in patients with normal renal function, certain patients might be at higher risk. These include patients requiring multiple lifetime doses, pregnant and pediatric patients, and patients with inflammatory conditions. Consider the retention characteristics of the agent when choosing a GBCA for these patients. Minimize repetitive GBCA imaging studies, particularly closely spaced studies when possible.

5.4 Acute Renal Failure In patients with renal insufficiency, acute renal failure requiring dialysis or worsening renal function have occurred with the use of gadolinium-based contrast agents. The risk of renal failure may increase with increasing dose of the contrast agent. Screen all patients for renal dysfunction by obtaining a history and/or laboratory tests. Consider follow-up renal function assessments for patients with a history of renal dysfunction.

5.5 Extravasation and Injection Site Reactions Extravasation of MultiHance may lead to injection site reactions, characterized by local pain or burning sensation, swelling, blistering, and necrosis. In animal experiments, local reactions including eschar and necrosis were noted even on Day 8 post perivenous injection of MultiHance. Exercise caution to avoid local extravasation during intravenous administration of MultiHance. If extravasation occurs, evaluate and treat as necessary if local reactions develop.

5.6 Cardiac Arrhythmias Cardiac arrhythmias have been observed in patients receiving MultiHance in clinical trials [see ***Adverse Reactions (6.1)***]. Assess patients for underlying conditions or medications that predispose to arrhythmias.

A double-blind, placebo-controlled, 24-hour post dose continuous monitoring, crossover study in 47 subjects evaluated the effect of 0.2 mmol/kg MultiHance on ECG intervals, including QTc. The average changes in QTc values compared with placebo were minimal (<5 msec). QTc prolongation between 30 and 60 msec were noted in 20 subjects who received MultiHance vs. 11 subjects who received placebo. Prolongations ≥ 61 msec were noted in 6 subjects who received MultiHance and in 3 subjects who received placebo. None of these subjects had associated malignant arrhythmias. The effects on QTc by MultiHance dose, other drugs, and medical conditions were not systematically studied.

5.7 Interference with Visualization of Certain Lesions Certain lesions seen on non-contrast images may not be seen on contrast-images. Exercise caution when interpreting contrast MR images in the absence of companion non-contrast MR images.

6 ADVERSE REACTIONS

The following adverse reactions are discussed in greater detail in other sections of the label:

- Nephrogenic systemic fibrosis [see ***Warnings and Precautions (5.1)***]
- Hypersensitivity reactions [see ***Warnings and Precautions (5.2)***]

6.1 Clinical Trials Experience

Because clinical trials are conducted under widely varying conditions, adverse reaction rates observed in the clinical trials of a drug cannot be directly compared to rates in the clinical trials of another drug and may not reflect the rates observed in practice.

Adult In clinical trials with MultiHance, a total of 4967 adult subjects (137 healthy volunteers and 4830 patients) received MultiHance at doses ranging from 0.005 to 0.4 mmol/kg. There were 2838 (57%) men and 2129 (43%) women with a mean age of 56.5 years (range 18 to 93 years). A total of 4403 (89%) subjects were Caucasian, 134 (3%) Black, 275 (6%) Asian, 40 (1%) Hispanic, 70 (1%) in other racial groups, and for 45 (1%) subjects, race was not reported.

The most commonly reported adverse reactions in adult subjects who received MultiHance were nausea (1.3%) and headache (1.2%). Most adverse reactions were mild to moderate in intensity. One subject experienced a serious anaphylactoid reaction with laryngeal spasm and dyspnea [see ***Warnings and Precautions (5.2)***]. Serious adverse reactions consisting of convulsions, pulmonary edema, acute necrotizing pancreatitis, and anaphylactoid reactions were reported in 0.1% of subjects in clinical trials.

Adverse reactions that occurred in at least 0.5% of 4967 adult subjects who received MultiHance are listed below (Table 2), in decreasing order of occurrence within each system.

TABLE 2: ADVERSE REACTIONS REPORTED IN ≥ 0.5% OF ADULT SUBJECTS WHO RECEIVED MULTIHANCE IN CLINICAL TRIALS

Number of subjects dosed	4967
Number of subjects with any adverse reaction	517 (10.4%)
Gastrointestinal Disorders	
Nausea	67 (1.3%)
General Disorders and Administration Site Disorders	
Injection Site Reaction	54 (1.1%)
Feeling Hot	49 (1.0%)
Nervous System Disorders	
Headache	60 (1.2%)
Dysgeusia	33 (0.7%)
Paresthesia	24 (0.5%)
Dizziness	24 (0.5%)

The following adverse reactions occurred in less than 0.5% of the 4967 adult subjects who received MultiHance. Serious adverse reactions described above are not repeated below.

Blood and Lymphatic System Disorders: Basophilia; **Cardiac Disorders:** Atrioventricular block first degree; **Eye Disorders:** Eye pruritus, eye swelling, ocular hyperemia, visual disturbance; **Gastrointestinal Disorders:** Abdominal pain or discomfort, diarrhea, dry mouth, lip swelling, paraesthesia oral, tongue edema, vomiting; **General Disorders and Administration Site Conditions:** Chest pain or discomfort, chills, malaise; **Immune System Disorders:** Hypersensitivity; **Investigations:** Nonspecific changes in laboratory tests (including hematology, blood chemistry, liver enzymes and urinalysis), blood pressure and electrocardiogram parameters (including PR, QRS and QT intervals and ST-T segment changes). **Musculoskeletal and Connective Tissue Disorders:** Myalgia; **Nervous System Disorders:** Parosmia, tremor; **Respiratory, Thoracic and Mediastinal Disorders:** Dyspnea, laryngospasm, nasal congestion, sneezing, wheezing; **Skin and Subcutaneous Tissue Disorders:** Hyperhidrosis, pruritus, rash, swelling face, urticaria.

Pediatric In clinical trials of MultiHance in MRI of the CNS, 217 pediatric subjects received MultiHance at a dose of 0.1 mmol/kg. A total of 112 (52%) subjects were male and the overall mean age was 8.3 years (range 4 days to 17 years). A total of 168 (77%) subjects were Caucasian, 12 (6%) Black, 12 (6%) Asian, 24 (11%), Hispanic, and 1 (<1%) in other racial groups.

Adverse reactions were reported for 14 (6.5%) of the subjects. The frequency and the nature of the adverse reactions were similar to those seen in the adult patients. The most commonly reported adverse reactions were vomiting (1.4%), pyrexia (0.9%), and hyperhidrosis (0.9%). No subject died during study participation. A serious adverse reaction of worsening of vomiting was reported for one (0.5%) patient with a brain tumor (glioma) for which a causal relationship to MultiHance could not be excluded.

Pediatric Patients In clinical trials of MultiHance in MRI of the CNS, 307 pediatric subjects received MultiHance at a dose of 0.1 mmol/kg. A total of 160 (52%) subjects were male and the overall mean age was 6.0 years (range, 2 days to 17 years). A total of 211 (69%) subjects were Caucasian, 24 (8%) Black, 15 (5%) Asian, 39 (13%), Hispanic, 2 (<1%) in other racial groups, and for 16 (5%), race was not reported. Adverse reactions were reported for 14 (4.6%) of the subjects. The frequency and the nature of the adverse reactions were similar to those seen in the adult patients. The most commonly reported adverse reactions were vomiting (1.0%), pyrexia (0.7%), and hyperhidrosis (0.7%). No subject died during study participation.

6.2 Post-marketing Experience

The following adverse reactions have been identified during post approval use of MultiHance. Because these reactions are reported voluntarily from a population of uncertain size, it is not always possible to reliably estimate their frequency or establish a causal relationship to drug exposure.

Immune System Disorders: Anaphylactic, anaphylactoid and hypersensitivity reactions manifested with various degrees of severity up to anaphylactic shock, loss of consciousness and death. The reactions generally involved signs or symptoms of respiratory, cardiovascular, and/or mucocutaneous abnormalities.

General Disorders and Administration Site Conditions: Extravasation of MultiHance may lead to injection site reactions, characterized by local pain or burning sensation, swelling, blistering, and necrosis [***see Warnings and Precautions (5.4)***]. Adverse events with variable onset and duration have been reported after GBCA administration [***see Warnings and Precautions (5.3)***]. These include fatigue, asthenia, pain syndromes, and heterogeneous clusters of symptoms in the neurological, cutaneous, and musculoskeletal systems. **Skin:** Gadolinium associated plaques.

7 DRUG INTERACTIONS

7.1 Transporter-Based Drug-Drug Interactions MultiHance and other drugs may compete for the canalicular multispecific organic anion transporter (MOAT also referred to as MRP2 or ABCC2). Therefore MultiHance may prolong the systemic exposure of drugs such as cisplatin, anthracyclines (e.g. doxorubicin, daunorubicin), vinca alkaloids (e.g. vincristine), methotrexate, etoposide, tamoxifen, and paclitaxel. In particular, consider the potential for prolonged drug exposure in patients with decreased MOAT activity (e.g. Dubin Johnson syndrome).

8 USE IN SPECIFIC POPULATIONS

8.1 Pregnancy Risk Summary GBCAs cross the placenta and result in fetal exposure and gadolinium retention. The human data on the association between GBCAs and adverse fetal outcomes are limited and inconclusive (see Data). In animal reproduction studies, gadobenate dimeglumine has been shown to be teratogenic in rabbits following repeated intravenous administration during organogenesis at doses up to 6 times the recommended human dose. There were no adverse developmental effects observed in rats with intravenous administration of gadobenate dimeglumine during organogenesis at doses up to three times the recommended human dose (see Data). Because of the potential risks of gadolinium to the fetus, use MultiHance only if imaging is essential during pregnancy and cannot be delayed. The estimated background risk of major birth defects and miscarriage for the indicated population is unknown. All pregnancies have a background risk of birth defect, loss, or other adverse outcomes. In the U.S. general population, the estimated background risk of major birth defects and miscarriage in clinically recognized pregnancies is 2 to 4% and is 15 to 20%, respectively. Data *Human Data* Contrast enhancement is visualized in the human placenta and fetal tissues after maternal GBCA administration. Cohort studies and case reports on exposure to GBCAs during pregnancy have not reported a clear association between GBCAs and adverse effects in the exposed neonates. However, a retrospective cohort study, comparing pregnant women who had a GBCA MRI to pregnant women who did not have an MRI, reported a higher occurrence of stillbirths and neonatal deaths in the group receiving GBCA MRI. Limitations of this study include a lack of comparison with non-contrast MRI and lack of information about the maternal indication for MRI. Overall, these data preclude a reliable evaluation of the potential risk of adverse fetal outcomes with the use of GBCAs in pregnancy. *Animal Data* Gadolinium Retention GBCAs administered to pregnant non-human primates (0.1 mmol/kg on gestational days 85 and 135) result in measurable gadolinium concentration in the offspring in bone, brain, skin, liver, kidney, and spleen for at least 7 months. GBCAs administered to pregnant mice (2 mmol/kg daily on gestational days 16 through 19) result in measurable gadolinium concentrations in the pups in bone, brain, kidney, liver, blood, muscle, and spleen at one month postnatal age.

Reproductive Toxicology Gadobenate dimeglumine has been shown to be teratogenic in rabbits when administered intravenously at 2 mmol/kg/day (6 times the recommended human dose based on bodysurface area) during organogenesis (day 6 to 18) inducing microphthalmia/small eye and/or focal retinal fold in 3 fetuses from 3 separate litters. In addition, MultiHance intravenously administered at 3 mmol/kg/day (10 times the recommended human dose based on body surface area) has been shown to increase intrauterine deaths in rabbits. There was no evidence that MultiHance induced teratogenic effects in rats at doses up to 2 mmol/kg/day (3 times the recommended human dose based on body surface area), however, rat dams exhibited no systemic toxicity at this dose. There were no adverse effects on the birth, survival, growth, development and fertility of the F1 generation at doses up to 2 mmol/kg in a rat peri- and post-natal (Segment III) study.

10 OVERDOSAGE

Clinical consequences of overdosage with MultiHance have not been reported. Treatment of an overdosage should be directed toward support of vital functions and prompt institution of symptomatic therapy. In a Phase 1 clinical study, doses up to 0.4 mmol/kg were administered to patients. MultiHance has been shown to be dialyzable [see ***Clinical Pharmacology (12.3)***].

12 CLINICAL PHARMACOLOGY

12.1 Mechanism of Action Gadobenate dimeglumine is a paramagnetic agent and, as such, develops a magnetic moment when placed in a magnetic field. The large magnetic moment produced by the paramagnetic agent results in a large local magnetic field, which can enhance the relaxation rates of water protons in its vicinity leading to an increase of signal intensity (brightness) of tissue.

In magnetic resonance imaging (MRI), visualization of normal and pathological tissue depends in part on variations in the radiofrequency signal intensity that occur with 1) differences in proton density; 2) differences of the spin-lattice or longitudinal relaxation times (T1); and 3) differences in the spin-spin or transverse relaxation time (T2). When placed in a magnetic field, gadobenate dimeglumine decreases the T1 and T2 relaxation time in target tissues. At recommended doses, the effect is observed with greatest sensitivity in the T1-weighted sequences.

12.2 Pharmacodynamics Unlike other tested paramagnetic contrast agents (See Table 3), MultiHance demonstrates weak and transient interactions with serum proteins that causes slowing in the molecular tumbling dynamics, resulting in strong increases in relaxivity in solutions containing serum proteins. The improved relaxation effect can contribute to increased contrast-to-noise ratio and lesion-to-brain ratio, which may improve visualization.

TABLE 3: RELAXIVITY (mM^{-1}s^{-1}) OF GADOLINIUM CHELATES

	Human plasma	
	r_1	r_2
Gadobenate	9.7[1]	12.5[1]
Gadopentetate	4.9[1]	6.3[1]
Gadodiamide	5.4[2]	---
Gadoteridol	5.4[2]	---

r_1 and r_2 relaxivities indicate the efficiency in shortening T1 and T2 relaxation times, respectively.
[1] In heparinized human plasma, at 39°C.
[2] In citrated human plasma, at 37°C.
--- Not available

Disruption of the blood-brain barrier or abnormal vascularity allows enhancement by MultiHance of lesions such as neoplasms, abscesses, and infarcts. Uptake of MultiHance into hepatocytes has been demonstrated.

12.3 Pharmacokinetics Three single-dose intravenous studies were conducted in 32 healthy male subjects to assess the pharmacokinetics of gadobenate dimeglumine. The doses administered in these studies ranged from 0.005 to 0.4 mmol/kg. Upon injection, the meglumine salt is completely dissociated from the gadobenate dimeglumine complex. Thus, the pharmacokinetics is based on the assay of gadobenate ion, the MRI contrast effective ion in gadobenate dimeglumine. Data for plasma concentration and area under the curve demonstrated linear dependence on the administered dose. The pharmacokinetics of gadobenate ion following intravenous administration can be best described using a two-compartment model.

Distribution Gadobenate ion has a rapid distribution half-life (reported as mean ± SD) of 0.084 ± 0.012 to 0.605 ± 0.072 hours. Volume of distribution of the central compartment ranged from 0.074 ± 0.017 to 0.158 ± 0.038 L/kg, and estimates of volume of distribution by area ranged from 0.170 ± 0.016 to 0.282 ± 0.079 L/kg. These latter estimates are approximately equivalent to the average volume of extracellular body water in man. *In vitro* studies showed no appreciable binding of gadobenate ion to human serum proteins.

Elimination Gadobenate ion is eliminated predominately via the kidneys, with 78% to 96% of an administered dose recovered in the urine. Total plasma clearance and renal clearance estimates of gadobenate ion were similar, ranging from 0.093 ± 0.010 to 0.133 ± 0.270 L/hr/kg and 0.082 ± 0.007 to 0.104 ± 0.039 L/hr/kg, respectively. The clearance is similar to that of substances that are subject to glomerular filtration. The mean elimination half-life ranged from 1.17 ± 0.26 to 2.02 ± 0.60 hours. A small percentage of the administered dose (0.6% to 4%) is eliminated via the biliary route and recovered in feces.

Metabolism There was no detectable biotransformation of gadobenate ion. Dissociation of gadobenate ion *in vivo* has been shown to be minimal, with less than 1% of the free chelating agent being recovered alone in feces.

Pharmacokinetics in Special Populations

Renal Impairment: A single intravenous dose of 0.2 mmol/kg of MultiHance was administered to 20 subjects with impaired renal function (6 men and 3 women with moderate renal impairment [urine creatinine clearance >30 to <60 mL/min] and 5 men and 6 women with severe renal impairment [urine creatinine clearance >10 to <30 mL/min]). Mean estimates of the elimination half-life were 6.1 ± 3.0 and 9.5 ± 3.1 hours for the moderate and severe renal impairment groups, respectively as compared with 1.0 to 2.0 hours in healthy volunteers.

Hemodialysis: A single intravenous dose of 0.2 mmol/kg of MultiHance was administered to 11 subjects (5 males and 6 females) with end-stage renal disease requiring hemodialysis to determine the pharmacokinetics and dialyzability of gadobenate. Approximately 72% of the dose was recovered by hemodialysis over a 4-hour period. The mean elimination half-life on dialysis was 1.21 ± 0.29 hours as compared with 42.4 ± 24.4 hours when off dialysis.

Hepatic Impairment: A single intravenous dose of 0.1 mmol/kg of MultiHance was administered to 11 subjects (8 males and 3 females) with impaired liver function (Class B or C modified Child-Pugh Classification). Hepatic impairment had little effect on the pharmacokinetics of MultiHance with the parameters being similar to those calculated for healthy subjects.

Gender, Age, Race: A multiple regression analysis performed using pooled data from several pharmacokinetic studies found no significant effect of sex upon the pharmacokinetics of gadobenate. Clearance appeared to decrease slightly with increasing age. Since variations due to age appeared marginal, dosage adjustment for geriatric population is not recommended. Pharmacokinetic differences due to race have not been systematically studied.

Pediatric: A population pharmacokinetic analysis incorporated data from 25 healthy subjects (14 males and 11 females) and 15 subjects undergoing MR imaging of the central nervous system (7 males and 8 females) betweenages of 2 and 16 years. The subjects received a single intravenous dose of 0.1 mmol/kg of MultiHance. The geometric mean Cmax was 62.3 µg/mL (n=16) in children 2 to 5 years of age, and 64.2 µg/mL (n=24) in children older than 5 years. The geometric mean AUC 0-∞ was 77.9 µg·h/mL in children 2-5 years of age (n=16) and 82.6 µg·h/mL in children older than 5 years (n=24). The geometric mean half-life was 1.2 hours in children 2 to 5 years of age and 0.93 hours in children older than 5 years. There was no significant gender-related difference in the pharmacokinetic parameters in the pediatric patients. Over 80% of the dose was recovered in urine after 24 hours. Pharmacokinetic simulations indicate similar AUC and Cmax values for MultiHance in pediatric subjects less than 2 years when compared to those reported for adults; no age-based dose adjustment is necessary forthis pediatric population.

17 PATIENT COUNSELING INFORMATION

17.1 Nephrogenic Systemic Fibrosis Instruct patients to inform their physician if they:

• have a history of kidney and/or liver disease, or • have recently received a GBCA.

GBCAs increase the risk for NSF among patients with impaired elimination of the drugs. To counsel patients at risk for NSF: • Describe the clinical manifestations of NSF • Describe procedures to screen for the detection of renal impairment.

Instruct the patients to contact their physician if they develop signs or symptoms of NSF following MultiHance administration, such as burning, itching, swelling, scaling, hardening and tightening of the skin; red or dark patches on the skin; stiffness in joints with trouble moving, bending or straightening the arms, hands, legs or feet; pain in the hip bones or ribs; or muscle weakness.

17.2 Common Adverse Reactions

Inform patients that they may experience:

• reactions along the venous injection site, such as mild and transient burning or pain or feeling of warmth or coldness at the injection site • side effects of feeling hot, nausea, and headache.

17.3 General Precautions

Instruct patients scheduled to receive MultiHance to inform their physician if they:

• are pregnant or breast feeding • have a history of renal disease, heart disease, seizure, asthma or allergic respiratory diseases • are taking any medications • have any allergies to any of the ingredients of MultiHance.

Rx only US Patent No. 4,916,246 Manufactured for Bracco Diagnostics Inc. Monroe Township, NJ 08831 By Patheon Italia S.p.A. - 03013 Ferentino (Italy) Revised October 2018 18-061418B

AJNR
AMERICAN JOURNAL OF NEURORADIOLOGY

CALL FOR AJNR EDITORIAL FELLOWSHIP CANDIDATES

2023 Candidate Information and Requirements

ASNR and AJNR are pleased once again to join efforts with other imaging-related journals that have training programs on editorial aspects of publishing for trainees or junior staff (<5 years on staff), including Radiology (Olmsted fellowship), AJR (Figley and Rogers fellowships), JACR (Bruce J. Hillman fellowship), and Radiologia.

GOALS

- Increase interest in editorial and publication-related activities in younger individuals.
- Increase understanding and participation in the AJNR review process.
- Incorporate into AJNR's Editorial Board younger individuals who have previous experience in the review and publication process.
- Fill a specific need in neuroradiology not offered by other similar fellowships.
- Increase the relationship between "new" generation of neuroradiologists and more established individuals.
- Increase visibility of AJNR among younger neuroradiologists.

ACTIVITIES OF THE FELLOWSHIP

- Serve as Editorial Fellow for one year. This individual will be listed on the masthead as such.
- Review at least one manuscript per month for 12 months. Evaluate all review articles submitted to AJNR.
- Learn how electronic manuscript review systems work.
- Be involved in the final decision of selected manuscripts together with the Editor-in-Chief.
- Participate in all monthly Senior Editor telephone conference calls.
- Participate in 2 virtual meetings of the Editorial Board.
- Evaluate progress and adjust program to specific needs in annual meeting or telephone conference with the Editor-in-Chief.
- Embark on an editorial scientific or bibliometric project that will lead to the submission of an article to AJNR or another appropriate journal as determined by the Editor-in-Chief. This project will be presented by the Editorial Fellow at the ASNR annual meeting. The Foundation of the ASNR will provide $2000 funding for this activity.
- Recruit trainees as reviewers as determined by the Editor-in-Chief.
- Serve as Guest Editor for an issue of AJNR's News Digest with a timely topic.

QUALIFICATIONS

- Be a fellow in neuroradiology from North America, including Canada (this may be extended to include other countries).
- Be a junior faculty neuroradiology member (< 5 years) in either an academic or private environment.
- Be an "in-training" or member of ASNR in any other category.

APPLICATION

- Include a short letter of intent with statement of goals and desired research project. CV must be included.
- Include a letter of recommendation from the Division Chief or fellowship program director. A statement of protected time to perform the functions outlined is desirable.
- Applications will be evaluated by AJNR's Senior Editors prior to the ASNR annual meeting. The name of the selected individual will be announced at the meeting.
- Applications should be received by March 1, 2023 and sent to Ms. Karen Halm, AJNR Managing Editor, electronically at khalm@asnr.org.

The Go-To Job Site for Neuroradiology Employers and Job Seekers

For Job Seekers

- Access to an expanded network of jobs via the National Healthcare Career Network
- Confidential resume posting
- Professional online profile

For Employers

- Employer resources to help you recruit top talent
- Multiple pricing options, including free Fellowship listings
- Resume search

Start here: careers.asnr.org

AJNR go green

AJNR urges American Society of Neuroradiology members to reduce their environmental footprint by voluntarily suspending their print subscription.

The savings in paper, printing, transportation, and postage directly fund new electronic enhancements and expanded content.

The digital edition of *AJNR* presents the print version in its entirety, along with extra features including:

- **Publication Preview**
- **Case Collection**
- **Podcasts**
- **The *AJNR* News Digest**
- **The *AJNR* Blog**

It also reaches subscribers much faster than print. An electronic table of contents will be sent directly to your mailbox to notify you as soon as it publishes.

Readers can search, reference, and bookmark current and archived content 24 hours a day on www.ajnr.org.

ASNR members who wish to opt out of print can do so by using the AJNR Go Green link on the *AJNR* Website (http://www.ajnr.org/content/subscriber-help-and-services). Just type your name in the email form to stop print and spare our ecosystem.

AJNR

AMERICAN JOURNAL OF NEURORADIOLOGY

OCTOBER 2022
VOLUME 43
NUMBER 10
WWW.AJNR.ORG

Publication Preview at www.ajnr.org features articles released in advance of print. Visit www.ajnrblog.org to comment on AJNR content and chat with colleagues and AJNR's News Digest at http://ajnrdigest.org to read the stories behind the latest research in neuroimaging.

AJNR (Am J Neuroradiol ISSN 0195–6108) is a journal published monthly, owned and published by the American Society of Neuroradiology (ASNR), 820 Jorie Boulevard, Oak Brook, IL 60523. Annual dues for the ASNR include approximately 21% for a journal subscription. The journal is printed by Intellicor Communications, 330 Eden Road, Lancaster, PA 17601; Periodicals postage paid at Oak Brook, IL and additional mailing offices. Printed in the U.S.A. POSTMASTER: Please send address changes to American Journal of Neuroradiology, P.O. Box 3000, Denville, NJ 07834, U.S.A. Subscription rates: nonmember $430 ($505 foreign) print and online, $320 online only; institutions $495 ($565 foreign) print and basic online, $980 ($1050 foreign) print and extended online, $380 online only (basic), $825 online only (extended); single copies are $35 each ($40 foreign). Indexed by PubMed/MEDLINE, BIOSIS Previews, Current Contents (Clinical Medicine and Life Sciences), EMBASE, Google Scholar, HighWire Press, Q-Sensei, RefSeek, Science Citation Index, SCI Expanded, ReadCube, and Semantic Scholar.

ONLINE FEATURES

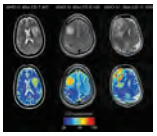

From Gates et al, in this issue: Image-based estimation of glioma cellularity is a promising biomarker for predicting survival, approaching the prognostic power of World Health Organization grading.

BOOK REVIEWS *R.M. Quencer, Section Editor*

Please visit www.ajnrblog.org to read and comment on Book Reviews.

Indicates Editor's Choices selection
Indicates Fellows' Journal Club selection
Indicates open access to non-subscribers at www.ajnr.org
Indicates article with supplemental online data
Indicates article with supplemental online video
Evidence-Based Medicine Level 1
Evidence-Based Medicine Level 2

AJNR

AMERICAN JOURNAL OF NEURORADIOLOGY

Publication Preview at www.ajnr.org features articles released in advance of print. Visit www.ajnrblog.org to comment on AJNR content and chat with colleagues and AJNR's News Digest at http://ajnrdigest.org to read the stories behind the latest research in neuroimaging.

OCTOBER 2022 • VOLUME 43 • NUMBER 10 • WWW.AJNR.ORG

Title: David H. Koch Cancer Center. The David H. Koch Cancer Center is a multiple award-winning structure with many cutting-edge features. Located on the upper east side of Manhattan overlooking the East River. It's blocked modularization promotes visual integration with surrounding structures. Its light-toned terra cotta skin is motivated by a desire to emit a visual positivity and hopefulness, though one could perhaps be forgiven for wondering if every person coping with cancer has these feelings on approach. The facade also has important functional elements, including panels, fins, and windows of varying yet balanced depths and sizes. The interplay of these elements responds to the changing sunlight throughout the day to provide balanced interior lighting without harsh glare. The center's interior lighting system is also modulated throughout the day in correlation with ambient daylight, to create warm and welcoming, yet varying atmospheres, and synchronize with the staffs' circadian rhythms.

Manfred Hauben, MD, MPH, Pfizer Inc and NYU Langone Health, New York City

Application of 7T MRS to High-Grade Gliomas

L. McCarthy, G. Verma, G. Hangel, A. Neal, B.A. Moffat, J.P. Stockmann, O.C. Andronesi, P. Balchandani, and C.G. Hadjipanayis

ABSTRACT

SUMMARY: MRS, including single-voxel spectroscopy and MR spectroscopic imaging, captures metabolites in high-grade gliomas. Emerging evidence indicates that 7T MRS may be more sensitive to aberrant metabolic activity than lower-field strength MRS. However, the literature on the use of 7T MRS to visualize high-grade gliomas has not been summarized. We aimed to identify metabolic information provided by 7T MRS, optimal spectroscopic sequences, and areas for improvement in and new applications for 7T MRS. Literature was found on PubMed using "high-grade glioma," "malignant glioma," "glioblastoma," "anaplastic astrocytoma," "7T," "MR spectroscopy," and "MR spectroscopic imaging." 7T MRS offers higher SNR, modestly improved spatial resolution, and better resolution of overlapping resonances. 7T MRS also yields reduced Cramér-Rao lower bound values. These features help to quantify D-2-hydroxyglutarate in *isocitrate dehydrogenase 1* and *2* gliomas and to isolate variable glutamate, increased glutamine, and increased glycine with higher sensitivity and specificity. 7T MRS may better characterize tumor infiltration and treatment effect in high-grade gliomas, though further study is necessary. 7T MRS will benefit from increased sample size; reductions in field inhomogeneity, specific absorption rate, and acquisition time; and advanced editing techniques. These findings suggest that 7T MRS may advance understanding of high-grade glioma metabolism, with reduced Cramér-Rao lower bound values and better measurement of smaller metabolite signals. Nevertheless, 7T is not widely used clinically, and technical improvements are necessary. 7T MRS isolates metabolites that may be valuable therapeutic targets in high-grade gliomas, potentially resulting in wider ranging neuro-oncologic applications.

ABBREVIATIONS: CRLB = Cramér-Rao lower bound; 2D L-COSY = 2D localized correlated spectroscopy; FID = free induction decay; GABA = gamma-aminobutyric acid; GBM = glioblastoma; Gln = glutamine; Glu = glutamate; Gly = glycine; GPC = glycerophosphocholine; GSH = glutathione; 2HG = D-2-hydroxyglutarate; HGG = high-grade glioma; Lac = lactate; LGG = low-grade glioma; MRSI = MR spectroscopic imaging; PC = phosphocholine; PRESS = point-resolved spectroscopy sequence; RF = radiofrequency; SVS = single-voxel spectroscopy; SAR = specific absorption rate; SASSI = Semi-Adiabatic Spectral-spatial Spectroscopic Imaging; tCho = total choline; WHO = World Health Organization

High-grade gliomas (HGGs) are the most lethal and common types of adult brain cancer, including both World Health Organization (WHO) grade III astrocytomas and grade IV glioblastomas (GBMs).[1] With >10,000 new cases every year in the United States, GBM accounts for 60% of primary adult brain tumors.[2] Even with surgical resection, chemotherapy, and radiation, GBM is associated with a median survival time of 15 months.[3] In light of the deadliness and prevalence of HGGs, considerable research has been devoted to uncovering their metabolic profiles, detected by noninvasive MRS techniques such as single-voxel spectroscopy (SVS) and multiple-voxel MR spectroscopic imaging (MRSI).[4,5] Unless otherwise stated, MRS in this document always refers to ^{1}H-MRS. In this article, we will primarily concentrate on MRS and MRSI but will also occasionally refer to additional imaging methods that can be performed with clinical MR imaging scanners or widely available MR imaging technology and can complement spectroscopic imaging.

MRS characterizes each metabolite on the basis of its unique set of chemical shifts and has been shown to capture up to 17 metabolites, including but not limited to Cho, Cr, glutamate (Glu), glutamine (Gln), lactate (Lac), lipids, mIns, and NAA (Fig 1).[6] It can also detect additional metabolites more associated

Received November 3, 2021; accepted after revision February 11, 2022.

From the Department of Neurosurgery (L.M., C.G.H.), Icahn School of Medicine at Mount Sinai, Mount Sinai Health System, New York, New York; BioMedical Engineering and Imaging Institute (G.V., P.B.), Icahn School of Medicine at Mount Sinai, New York, New York; Department of Neurosurgery (G.H.) and High-field MR Center (G.H.), Department of Biomedical Imaging and Image-Guided Therapy, Medical University of Vienna, Vienna, Austria; Department of Medicine (A.N.), Royal Melbourne Hospital, University of Melbourne, Melbourne, Australia; Department of Neurology (A.N.), Royal Melbourne Hospital, Melbourne, Australia; The Melbourne Brain Centre Imaging Unit (B.A.M.), Department of Radiology, University of Melbourne, Melbourne, Australia; A. A. Martinos Center for Biomedical Imaging (J.P.S., O.C.A.), Massachusetts General Hospital, Charlestown, Massachusetts; and Harvard Medical School (J.P.S., O.C.A.), Boston, Massachusetts.

Priti Balchandani and Constantinos G. Hadjipanayis are co-senior authors.

This article was funded by a National Institutes of Health grant, R01CA202911.

Please address correspondence to Lily McCarthy, MD, Department of Neurosurgery, Icahn School of Medicine at Mount Sinai, Mount Sinai Health System, 1468 Madison Ave, New York, NY 10029; e-mail: lily.mccarthy@icahn.mssm.edu

http://dx.doi.org/10.3174/ajnr.A7502

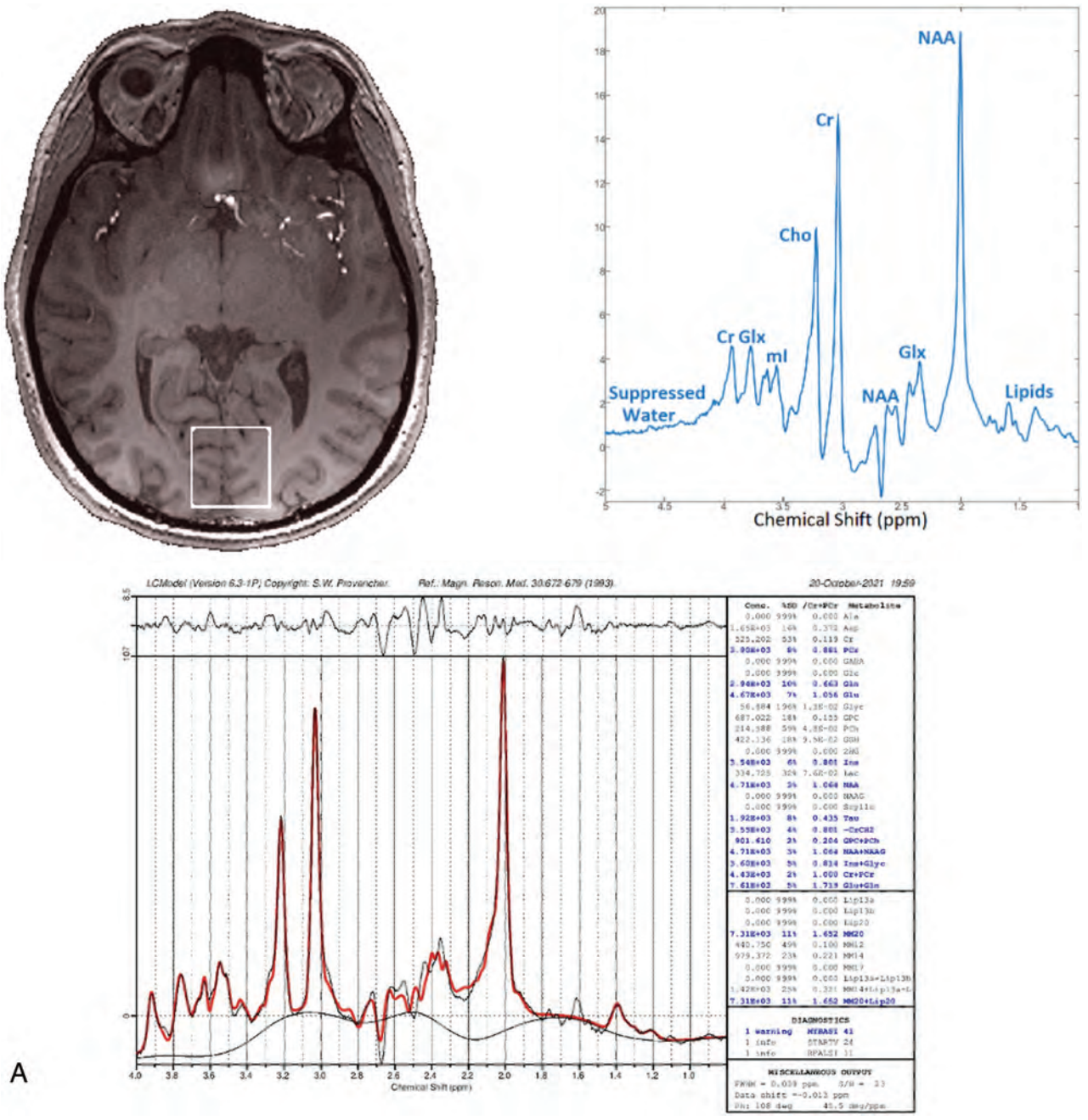

FIG 1. *A*, An MR spectrum generated at 7T from the occipital lobe (predominantly gray matter) of a healthy volunteer is shown (TR/TE = 2000/30.5 ms; number of averages = 32). The real part appears in blue and includes metabolite labels. The same image processed with LCModel is shown below and contains quantified metabolite values. Instead of capturing the increased resolution attainable at higher field strengths, these data are intended to primarily show a very clear spectrum from a normal brain. This was a 3 × 3 × 3 SVS acquisition in 1 minute obtained using an SASSI sequence. In contrast, note a single-voxel ^{1}H-MRS spectrum (TR/TE = 3000/23 ms; number of averages = 8) from a patient with a grade III astrocytoma located in the left parietal region and having an *IDH*-mutant genotype showing various metabolites (*B*). The patient was scanned on a 7T whole-body MR imaging scanner equipped with a single transmit/32-channel receiver array head coil. Tissue infiltrated with gliomas such as the astrocytoma in *B* results in spectra with different metabolic characteristics than the normal tissue in *A*. Lip indicates lipids. The material from *B* was obtained with permission and in collaboration with Sanjeev Chawla in the Department of Radiology at the Perelman School of Medicine at the University of Pennsylvania.

with gliomas such as glycine (Gly) and D-2-hydroxyglutarate (2HG), an oncometabolite produced in mutant *isocitrate dehydrogenase 1* and *2* (*IDH1* and *IDH2*) tumors.[7-9] Most studies on these metabolites have involved MRS at 1.5T and 3T.[10-12] Although 3T MRS has value, it is limited in several ways.[13] One shortcoming is its limited ability to quantify metabolites with overlapping peaks.[14] Another is its low spatial resolution, which detracts from tumor characterization.[15] These drawbacks have prompted more focus on higher-field-strength MR imaging systems.[16]

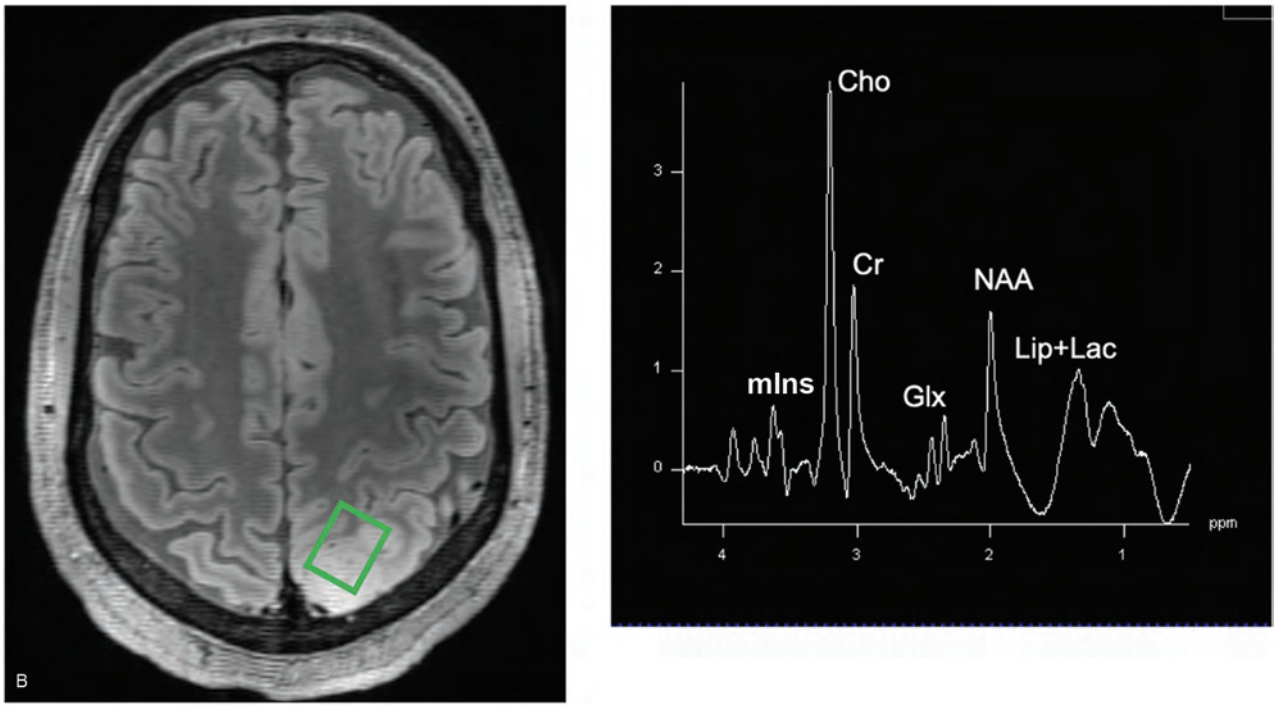

FIG 1. *B*, Continued.

A potential alternative is ultra-high-field 7T MR imaging used in conjunction with MRS.[17] With substantially increased SNR and moderately improved spatial resolution, 7T has received US FDA and Conformité Européenne mark approval for clinical use.[18] Comparisons of spectroscopy at lower field strengths such as 1.5T and 3T versus higher field strengths such as 7T to date have indicated that 7T is associated with substantial gains in SNR and more limited increases in spatial resolution,[19] better spectral separation and therefore additional tumor-specific metabolite information,[20] superior quantification of metabolites with small signals such as Gln,[21] and reduced Cramér-Rao lower bound (CRLB) values.[22-25] CRLB is a measure of the precision of an estimate, similar to an SD, which is used particularly with LCModel (http://www.lcmodel.com/). Despite evidence that these advantages of 7T may address the pitfalls of 3T MRS, its clinical usefulness has not yet been sufficiently explored.[26,27] We aimed to investigate its utility by examining the literature published on 7T MRS in patients with HGGs. Most review articles published to date on ultra-high-field MR neuroimaging have had fairly broad scopes, highlighting techniques besides spectroscopy[16,17,28,29] and/or neurologic disorders other than gliomas.[15,26,30] A more targeted review of the use of 7T MRS to detect metabolites in HGGs is important to describe the current state of the field and provide clinical insight into new areas of investigation. In this article, we highlight the capacity of 7T to distinguish metabolic biomarkers. We also evaluate different protocols to determine optimal spectroscopy sequences. Finally, we turn to questions that remain unanswered. Given that the application of higher-field-strength MRS to glioma-related oncometabolism is still in its early stages, the full potential of this technique has yet to be realized.

Use of 7T MRSI to Aid in the Detection of Metabolic Markers

Resolution of Overlapping Resonances. 7T MRS is more sensitive to individual metabolites in HGGs.[31] These include amino acids such as aspartate and lysine, which may be more difficult to visualize with MRS at conventional field strengths.[31] At higher field strengths, MRS benefits from increased spectral separation. This helps to resolve overlapping resonances that occur at lower field strengths, making metabolic peaks, particularly those of coupled compounds, better separated and easier to quantify. By moderately reducing spectral overlap with better signal and chemical shift dispersion, 7T MRS may resolve specific metabolites more effectively than 3T on the basis of data from comparative studies on the 2 field strengths.[21,23,25,32] Among these metabolites are Glu and Gln. Several studies comparing 3T versus 7T have found that improvements with 7T are particularly noticeable for Glu and Gln, which can be harder to individually measure at 3T due to substantial spectral overlap.[22,33] The more precise quantification of these 2 metabolites has been primarily attributed to improved SNR and chemical shift dispersion at 7T.[22] Compared with 3T, 7T also improves detection of 2HG, discriminating between 2HG and other metabolites that overlap on conventional 1D spectra, including Glu, Gln, and gamma-aminobutyric acid (GABA).[33]

A specific technique that has proved capable of detecting coupled metabolites and resolving overlapping resonances is 2D localized correlated spectroscopy (L-COSY) SVS, which separates and resolves metabolite signals along 2 different frequency dimensions.[34] Although it is still largely in early exploratory stages, this technique has the potential to resolve complex resonances and separate phosphocholine (PC) from glycerophosphocholine (GPC),

Lac from lipids, and Glu from Gln at 7T.[34] 2D L-COSY sequences at 7T result in clear identification and quantification of cross-peaks from metabolites such as GABA, Glu, Gln, glutathione (GSH), isoleucine, lysine, and compounds with Cho with increased separation compared with the same sequences at 1.5 or 3T.[35-37] In 1 study directly comparing one such 2D L-COSY sequence at 3T versus 7T (with the same scan times and voxel sizes at both field strengths), spectra generated at 7T had better signal quality than those at 3T.[37] Cross-peaks to aspartate, GABA, GPC/PC, isoleucine, Lac, and mIns + Cho were readily apparent in 7T spectra but were weak or absent from 3T spectra.[37]

Providing greater spectral dispersion than traditional 1D spectroscopy, 2D L-COSY SVS has emerged as the higher-sensitivity technique.[38] By indirectly recording T1 evolution, 2D L-COSY incorporates a second spectral dimension, detecting the transfer of coherence through cross-peaks between J-coupled metabolites. Metabolites with resonances that would ordinarily manifest as co-resonant with other metabolites become easier to separate. Nevertheless, 2D L-COSY also involves long acquisition times and sparse postprocessing support.[38] Thus, shortening acquisition times and refining postprocessing techniques are vital. One group addressed these issues by constructing a nonuniformly weighted sampling scheme that reduced acquisition time by 25% and still preserved the same SNR, detecting diverse metabolites including GABA, Glu, Gln, GSH, Cho, and PC. These improvements, involving advanced spectral editing in 2D, make 7T MRS more clinically feasible by increasing the reliability of metabolic quantification.[37]

Separating peaks is crucial because it improves differentiation of individual metabolites, which have concentrations that are very small (typically expressed in mmol/l^{-1} or μmol/g^{-1} of examined tissue) and, therefore, difficult to detect.[39] In spectroscopy, the strongest element of the signal is from water and is around 10,000-fold greater than the strongest metabolite signal from NAA.[39] This separation of peaks is also possible at 3T, albeit with higher uncertainty. In addition, the resolution improvement due to this increased chemical shift dispersion at 7T may be diminished by the broadening of linewidths that occur at higher field strengths.[39,40] However, optimized shimming and smaller voxel size can at least partially compensate for broader linewidths and still maintain some of the enhanced resolution associated with 7T.[37,41-43] Future work will further probe the capacity of 7T to separate metabolic peaks and will focus on other important factors such as uncertainty estimates and the amount of covariance.

Enhanced Characterization of Metabolic Pathways in Mutant *IDH* Gliomas. The spectral quality of 7T may shed light on mutant *IDH1* and *IDH2* gliomas that produce the characteristic metabolite 2HG. The 2 mutant *IDH1* and *IDH2* enzymes participate in a reduction of α-ketoglutarate instead of the typical oxidation reaction, producing 2HG.[44] Thus, α-ketoglutarate indicates an *IDH*-mutant profile. At higher field strengths such as 7T, which result in better spectral separation and more exact metabolic readings, 2HG forms a conspicuous signal even after a brief period of data acquisition.[45] The improved spatial resolution, SNR, and spectral separation account for the sensitivity of 7T to this metabolite. 7T SVS has been shown to quantify 2HG with a high degree of specificity, making it easier to see whether this metabolite is present and ascertain the *IDH* status.[27,33,34] One study detected 2HG in all 12 patients with *IDH*-mutant and/or radiography-suggested gliomas under investigation, with the mean concentration of 2HG measured at 3.1 (SD, 1.7) mM and a mean CRLB of 5% (SD, 2%).[46] In one of these patients with an *IDH1*-mutated oligoastrocytoma, the 2HG was estimated to be 6.2 mM, with high precision (CRLB = 2%).[46] Four patients had tumors with lower 2HG concentrations ($<$2 mM), which were still acquired with acceptable precision (CRLB $\leq$7%).[46] Another recent study with 7T SVS estimated 2HG to be within the range of 2.3–3.3 mM in tumors of patients with mutant *IDH* gliomas.[45] Thus, 2HG is an indicator of tumor profile and evolution.[46] 7T SVS has also revealed associations between 2HG and mIns, glucose, and taurine.[47]

Although not every spectroscopy sequence readily quantifies 2HG, the ease with which certain 7T MRS sequences single out this oncometabolite might provide more insight into survival prospects. Optimizing MRS measurements of 2HG at 7T is, therefore, critical. The optimal TE of the point-resolved spectroscopy sequence (PRESS) at 7T was shown to be 78 ms (TE_1 = 58 ms, TE_2 = 20 ms) by Ganji et al,[46] who used density-matrix simulations and phantom validation to enhance signal selectivity for 2HG. Notably, this PRESS TE was superior to short-TE MRS, allowing clearer differentiation between 2HG and other metabolites including Glu, Gln, and GABA.[46] Quantifying 2HG is more difficult at lower field strengths because this oncometabolite often overlaps with Glu, Gln, GABA, and NAA.[48] However, it is still possible to quantify 2HG at 3T if specific strategies are used.[49,50] These include using the optimal PRESS TE of 97 ms established by Choi et al.[51,52] Other potentially useful approaches at 3T involve spectral editing and the 2D correlation method[53] and hyperpolarized ^{13}C MRS.[54] Another strategy for 3D imaging of 2HG at 3T involves echo-planar spectroscopic imaging with dual-readout alternated gradients, which 1 recent study used to generate images of 2HG with a high level of precision (CRLB, $<$10%).[55]

Nevertheless, 2HG substantially benefits from the greater SNR and spectral separation attainable at 7T, as supported by the results from a study by Ganji et al[46] that involved output results from LCModel. Serving as a prior knowledge-based spectral fitting model of complete spectra instead of singular peaks, LCModel evaluates an in vivo spectrum as a linear combination of in vitro spectra from individual metabolite solutions.[56] LCModel, thereby, enables the resolution of spectra that are virtually identical in 1 frequency area, provided that they have distinct signals at other points in the spectrum. In this study, although mean estimates of 2HG and total choline (tCho) were not meaningfully different at 7T and 3T, the mean 2HG CRLB was markedly lower at 7T (5%) than at 3T (8%) due to the higher SNR and spectral resolution associated with higher field strengths.[46] In addition, the mutual dependence of 2HG and GABA signal estimation was much smaller at 7T than at 3T.[46] At 7T, 2HG and GABA signals had substantial opposite polarity and apparent narrowing.[46] Thus, this improved signal separation may permit more facile discrimination of 2HG.[46] This long TE of 78 ms, which is specific to 2HG, can be expanded to 2D MRS at 7T with appropriate modifications. For example, 1 study performed prescription of a VOI based on the 7T 2HG-optimized

PRESS sequence before echo-planar spectroscopic imaging with dual-readout alternated gradients.[45] Thus, the same TE parameters can be applied in different spectroscopic contexts at higher field strengths.

Beyond measuring 2HG, 7T SVS has proved capable of detecting minute differences between *IDH1* and *IDH2*. Mutant *IDH2* gliomas have higher 2HG than *IDH1* gliomas, with more elevated 2HG:Cho and 2HG:Cr in *IDH2* gliomas than in *IDH1* gliomas detected in 2 recent 7T SVS studies.[27,47] In 1 recent 7T SVS study, mutant *IDH2* gliomas also had higher mIns and Cho compared with *IDH1*-mutant gliomas.[47] Thus, 7T MRS may strengthen visualization of metabolic differences between mutant *IDH1* and *IDH2* gliomas.[47] These findings may lead to precision medicine tailored to patients' *IDH* statuses.[47] Distinguishing *IDH*-mutant and *IDH* wild-type tumors is important because mutant *IDH1* and *IDH2* gliomas have better prognoses.[57] A prospective analysis found that patients with grade II, III, and IV *IDH*-mutant gliomas survived longer than those who had *IDH* wild-type.[51,52] Other studies have found similarly robust associations between the presence of *IDH* mutations and increased survival.[58-60]A potential explanation may be that *IDH* responds better to targeted treatment.[57,61] Thus, *IDH* mutations have prognostic value, predicting more favorable responses to radiation and chemotherapy.[57,61] The fact that these mutations are common in grade II and III gliomas and in secondary GBM makes them even more appealing.

The potential advantages of using 7T MRS to spot this oncometabolite extend beyond survival time to treatment. Several inhibitors of mutant *IDH* have already been engineered.[62] 7T MRS may complement this therapeutic targeting by zeroing in on *IDH*-mutant gliomas and further differentiating between *IDH1* and *IDH2* mutants.[27,47] These 2 enzymes have unique characteristics that can be independently targeted by different drugs with distinct mechanisms. These include their location in cells, with *IDH1* typically found in the cytosol, and *IDH2*, in the mitochondrial matrix.[63] 7T MRS could, therefore, help gauge whether a patient has an *IDH*-mutant glioma and, if so, whether the glioma is *IDH1* or *IDH2*, dictating the most appropriate therapy.[27,47] Application of this technique would, in turn, direct novel molecular therapies that impede *IDH*-mutant tumors and thereby prolong survival.[64,65] During the past year, *IDH* has gained increasing recognition as an important tumor marker in the WHO's 2021 Classification of Tumors, which called for grouping all *IDH*-mutant diffuse astrocytic tumors into 1 category based on *IDH* status (astrocytoma, *IDH*-mutant) and subsequently grading them as CNS WHO grade II, III, or IV.[66] Given that *IDH* has therefore become even more central in defining gliomas, using techniques such as 7T MRS to better visualize this oncometabolite, a potential personalized biomarker,[47] may be worthwhile. Most important, immunohistochemical and molecular pathologic analyses of resected tissue acquired through surgery remain the criterion standard for the diagnosis of *IDH*-mutant gliomas.[27] However, there is growing interest in noninvasive approaches, including imaging, as a complement to conventional invasive techniques.[67-69] To that end, it is worth considering whether 7T MRS might be one such noninvasive tool that can be used to gather additional information about *IDH*-mutant brain tumors, which may inform tumor diagnoses, survival predictions, and treatment strategies.[47] Specifically, noninvasive quantification of 2HG levels with MRS may be used to track targeted therapy and guide decisions about possible changes in therapy when necessary.[34] To that end, MRS may have added value when used in conjunction with traditional immunohistochemistry following biopsy or surgery.[34]

Broadening of Possible Therapeutic Targets: Glu, Gln, and Gly. 7T MRS enhances visualization of other metabolites that may serve as therapeutic targets. Glu has been implicated in HGG metabolism and can be identified with 7T MRS, which is capable of isolating Glu from Gln so that these 2 metabolites can be evaluated separately (Fig 2).[70] Separating Glu from Gln is often challenging at 3T with combined Glu and Gln denoted as Glx, but it is easier at 7T, which can differentiate the 2 metabolites, albeit with variable spatial resolution quality.[31] Distinguishing Glu from Gln allows deeper insight into metabolic pathways in gliomas and is particularly clinically relevant given the growing evidence for the influence of glutamatergic synapses on tumor progression.[71] Glioma cells have been shown to secrete Glu, precipitating a rise in excitotoxic, extracellular Glu and promoting malignant growth.[72] Thus, Glu plays a critical-but-complex role in tumors that 7T MRS may help to better characterize.

In a recent study evaluating 23 HGGs with 7T MRSI, increased Glu was found in *IDH* wild-type tumors, while decreased Glu was found in *IDH*-mutant tumors[70] Although additional studies with larger sample sizes and low-grade gliomas (LGGs) are necessary to validate these preliminary findings, this trend suggests that Glu could be a potential marker for the absence of *IDH* mutations.[70] Another 7T MRSI study found that the ratio of Glu/total Cr was substantially decreased in grade II gliomas compared with normal-appearing white and gray matter.[31] Widespread reductions in Glu were also observed in 9 grade II, III, and IV gliomas in a separate study involving 7T MRSI.[73] Considering its role in glioma proliferation and survival as both a metabolic intermediate and the primary excitatory neurotransmitter in the brain, Glu is ripe for targeted interventions.[74] Yet despite the essential part Glu plays in tumorigenic processes, few other studies have used 7T MRS to investigate the spatial profile of Glu in patients with gliomas or to rigorously evaluate whether 7T MRS might be able to identify differences in Glu levels in different grades of gliomas.[70] Observing how Glu varies in larger subject populations could refine the differential diagnoses of LGGs and HGGs.

Gln is likewise altered in gliomas.[75] Changes in Gln are more appreciable at higher field strengths.[73] Increased Gln has been detected in a range of gliomas.[31,70,73] Serving as a substitute for glucose in the tricarboxylic acid cycle, a regulator of oncogene expression and a suppressor of apoptosis, Gln may be an imaging marker for tumor cells, helping to distinguish gliomas from other neurologic disorders.[76] A recent study with 7T MRSI discovered elevated Gln in HGGs, including oligodendrogliomas, diffuse and anaplastic astrocytomas, and GBMs.[73] In a patients with a grade IV GBM, increased Gln overlapped with contrast-enhanced T1WI regions, decreased NAA, and widely reduced metabolic activity in the center of the tumor. Widespread increases in Gln were also observed in a similar 7T MRSI study, further

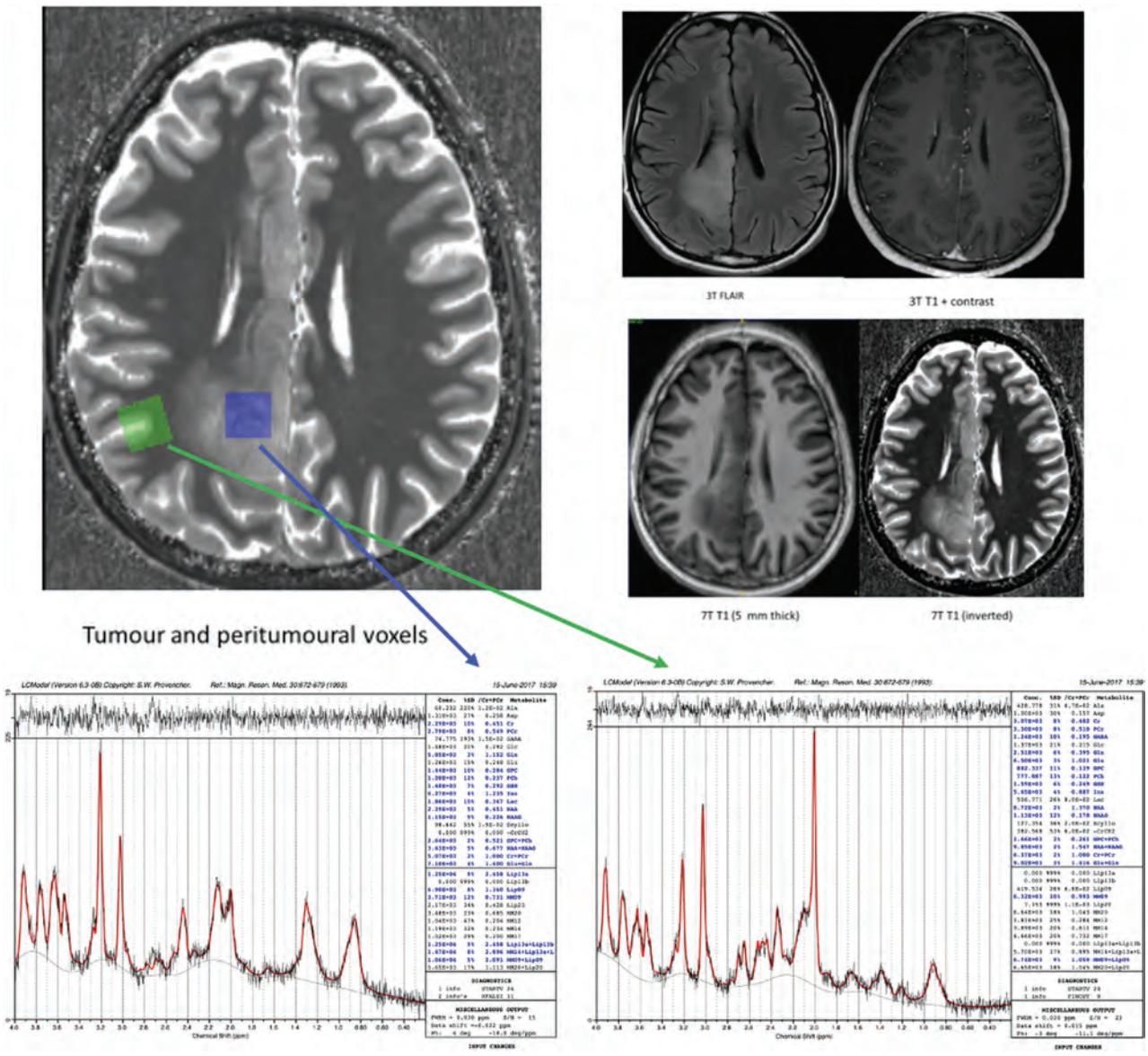

FIG 2. 3T/7T MR imaging data, 7T SVS data, and LCModels from a patient with diffuse glioma are presented (TR/TE for the 7T SVS data = 8500/6 ms), with tumor data on the left (*blue arrow*) and peritumoral data on the right (*green arrow*) for each patient. Inspection of the MRS metabolic profiles shows that the peritumoral region has a relatively normal profile except for a highly elevated Glu concentration compared with both Gln and Cr. This is in contrast to the tumoral region, where there is a complete reversal of this profile with Gln and Cho being elevated compared with Glu, NAA, and Cr. These data provide further evidence of the dysregulation of the Glu-Gln shuffle, serving as a source of seizures in patients with gliomas. This material was obtained with permission and in collaboration with Andrew Neal and Bradford A. Moffatt at the Melbourne Brain Centre Imaging Unit (MBCIU), the University of Melbourne node of the Australian National Imaging Facility.

supporting the centrality of Gln in tumor metabolism and homeostasis.[31] Other 7T studies have also yielded results suggesting that Gln might be a potential tumor biomarker, with one reporting that Gln was almost 100% higher in tumor tissue.[71,77]

Gln is present in several different HGGs and could, therefore, be a target for antineoplastic drugs used to treat many patients with gliomas.[78] In the first step of glutaminolysis, glutaminase catalyzes the deamidation of Gln to Glu, which then serves as a substrate in the tricarboxylic acid cycle or contributes to GSH synthesis (Fig 3).[79] Glutaminase inhibitors, which prevent the conversion of Gln to Glu and thereby decrease tumorigenesis, have the potential to treat HGGs with high Gln levels.[80] Increased Gln could, therefore, be an indicator of treatment with glutaminase inhibitors. 7T MRS could confirm the status of Gln as a biomarker for HGGs, resulting in more targeted therapies that attack Gln pathways.[81] Suppressing these pathways might be effective because Gln supports the growth of highly proliferative cells, especially those in HGGs. Gln contributes to anaplerotic reactions that sustain glycolysis and give malignant tissue an advantage over normal tissue.[81] Gln also provides building blocks for nucleotide synthesis and for the vital antioxidant GSH, both of which make gliomas more resistant to radiation and chemotherapy.[82] Glutaminase inhibitors that exploit the addiction of the cancer cells to Gln would curtail the development of HGGs. In the past few

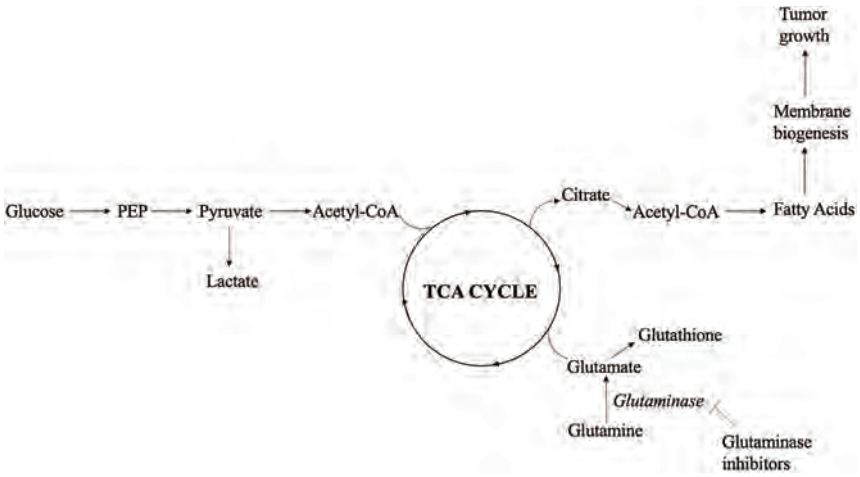

FIG 3. Major glutamine pathways in HGGs are featured. Gln undergoes a deamidation to Glu, which subsequently promotes tumorigenic growth either as a substrate in the tricarboxylic acid (TCA) cycle or as a precursor to GSH. The deamidation reaction is catalyzed by glutaminase. This enzyme is the target of glutaminase inhibitors, which may be useful therapeutic agents for patients with gliomas that involve high levels of glutamine detected by 7T MRS. PEP indicates phosphoenolpyruvate.

years, CB-839 has been the primary glutaminase inhibitor under investigation for the treatment of multiple cancers in clinical trials, most of which have been Phase I and II.[83-85] A recent pharmacometabolic analysis showed that CB-839 effectively inhibited glutaminase activity and curtailed the growth of glioma stemlike cells with high target specificity.[79] These glioma stemlike cells lead to drug resistance and tumor recurrence in GBM.[79] Given that it quantifies levels of Gln so precisely, 7T MRS could reshape glioma treatment, tipping the balance toward more personalized treatments with these glutaminase inhibitors.[81]

Nonetheless, at present, there are very few published 7T MRS studies investigating the significance or clinical utility of Gln measurements in HGGs. As previously discussed, Gln has long been an established precursor of both Glu and GSH and is known to contribute to the cellular energy process and lipid synthesis, suppress apoptosis, and potentially protect cancer cells from radiation therapy.[31,77] In view of its major role in tumor metabolism, biosynthesis, and homeostasis, it would certainly be worth investigating whether the abundant Gln detected in HGGs via 7T MRS may be clinically relevant, serving as a biomarker or therapeutic target.[70,73] More rigorous evaluation of Gln at 7T and even at lower field strengths will provide further insight into how quantification of this metabolite might aid in the management of these tumors.

Gly has long been suspected of being an imaging biomarker for brain tumors, with increased Gly in HGGs including GBMs.[86-88] One of the major challenges to date has been separating Gly from mIns. The differentiation between mIns and Gly has been accomplished at 3T with a long-TE in other individuals with other disorders, including alcohol use disorder[89] and nonketotic hyperglycemia.[90] Nonetheless, studies with spectroscopy at 1.5T and 3T have not separated Gly from mIns in HGGs. Although it is still difficult to differentiate these 2 metabolites on the basis of their chemical shifts even at higher field strengths, there is emerging evidence that 7T MRSI may be better equipped to isolate Gly[70] (Fig 4). Gly may aid in tumor proliferation by serving as an intermediary in nucleotide and Glu synthesis and could, therefore, be a promising metabolic metric.[91] In a recent study on 3T MRSI, every tumor with increased Gly had postcontrast enhancement, a high cell proliferation rate (MIB-1), and shorter survival.[91] The correlation between Gly and MIB-1 indicates that HGGs may remodel Gly metabolism to sustain rapid cell proliferation. These findings support the clinical importance of Gly, with higher levels of Gly correlating with poorer clinical outcomes in patients with HGGs.

Gly could help clinicians differentiate glioma grades, adapt treatment plans accordingly, and predict survival time on the basis of the levels of Gly visualized with 7T MRS.[91] Predicting survival is especially important for HGGs, given that patients with grades III and IV gliomas have worse chances of survival than those with LGGs.[92] However, while several studies have used lower field strength MRS to probe the prognosticative power of Gly, few have explored whether 7T MRS might further validate Gly as an index of HGG aggressiveness. Given that it may be more able to separate out Gly than spectroscopy at lower field strengths, 7T MRS might be able to address questions about whether this metabolite can indeed mark the progression from low- to high-grade disease and from posttreatment to recurrent disease, fully establishing Gly as a biomarker and improving patient care.[91]

Optimization of 7T MRS Sequences

Because 7T MRS is still novel, there is not a criterion standard MRS pulse sequence. The fact that different sequences capture distinct metabolites depending on the clinical context has made it challenging to reach a consensus. A quandary still unresolved is the ideal TE. Transitioning to longer TEs enables differentiation of 2HG from adjacent GABA and Glu.[46] Nevertheless, short-echo 3D MRSI also differentiates Glu and Gln.[93] Future studies will elucidate the optimal TE length. Nonetheless, there are still common threads among successful protocols. Balancing spatial resolution and measurement time is crucial, as is optimizing the SNR. Rapid concentric ring trajectory encoding was recently shown to shorten TRs and enhance SNR efficiency.[77] Dual-readout alternate gradients used in echo-planar MRSI at 7T have also been found to have similar effects on SNR efficiency, resulting in high-resolution imaging of metabolites such as 2HG.[45] The TE for any given acquisition will depend on the precise variables of interest for a particular patient, and >1 acquisition with different TEs may be required, as is often the case for clinical spectroscopy. Thus, these may be additional strategies to consider.

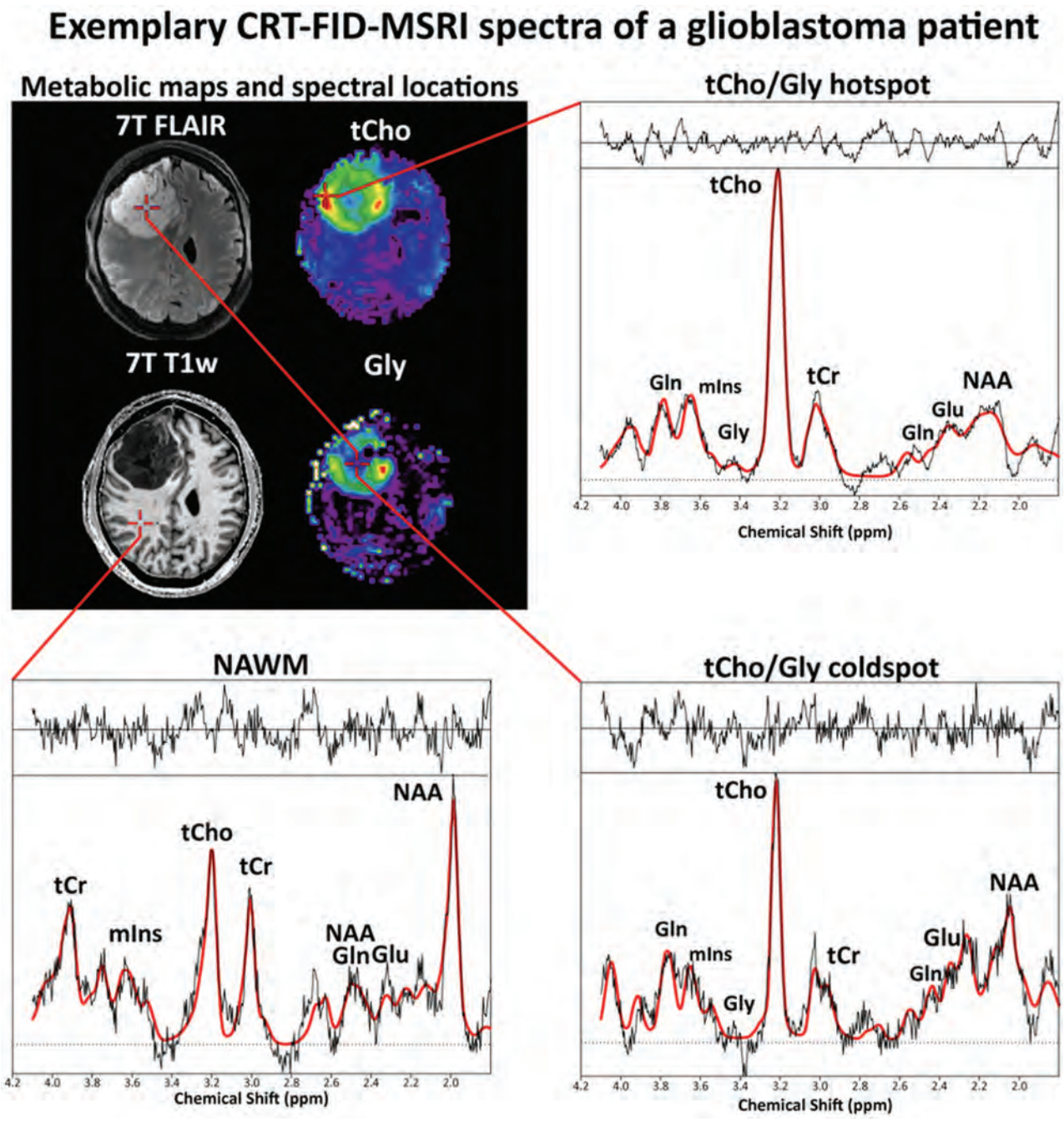

FIG 4. Exemplary 7T concentric ring trajectory FID-MRSI spectra of a patient with GBM. This method uses FID acquisition combined with concentric ring trajectories, bringing together multiple potential benefits: high resolution and acceleration while maintaining sufficient SNR, low SAR, B_1 insensitivity, no selection box, and detection of J-coupled metabolites with 7T spectral separation. This measurement was acquired in 15 minutes with a nominal isotropic resolution of 3.4 mm, covering the cerebrum. Well-defined metabolic peaks are observed at 3 points: a tCho and Gly hotspot, a tCho and Gly cold spot, and normal-appearing white matter (NAWM). It is noticeable that even in the tumor tCho cold spot, tCho concentrations are higher than in NAWM but about 50% lower than in the tCho hotspot. Two of the metabolites that appear in these plots (Gly and Gln) have emerged as promising therapeutic targets and may serve as imaging biomarkers for patients with HGG. This material was obtained with permission from Gilbert Hangel at the High-field MR Center at the Medical University of Vienna. T1w indicates T1WI; tCr, total Cr.

Techniques to augment SNR allow improved resolution and smaller voxel volumes, which consequently enable better spatial localization of differences among individual gliomas.[73] These could, in turn, help define tumor margins, enhancing visualization of metabolic abnormalities. A method to improve the SNR is to use high-channel-count radiofrequency (RF) receive array coils, which have been shown to provide better SNR than volume coils, especially near the cortical surface.[94] Furthermore, new coil technology can improve spectral linewidth by incorporating B_0 shim capabilities in the form of spherical harmonic shim insert coils or local multicoil shim arrays.[41,42] In 1 realization of the local multicoil shimming approach known as the AC/DC coil,

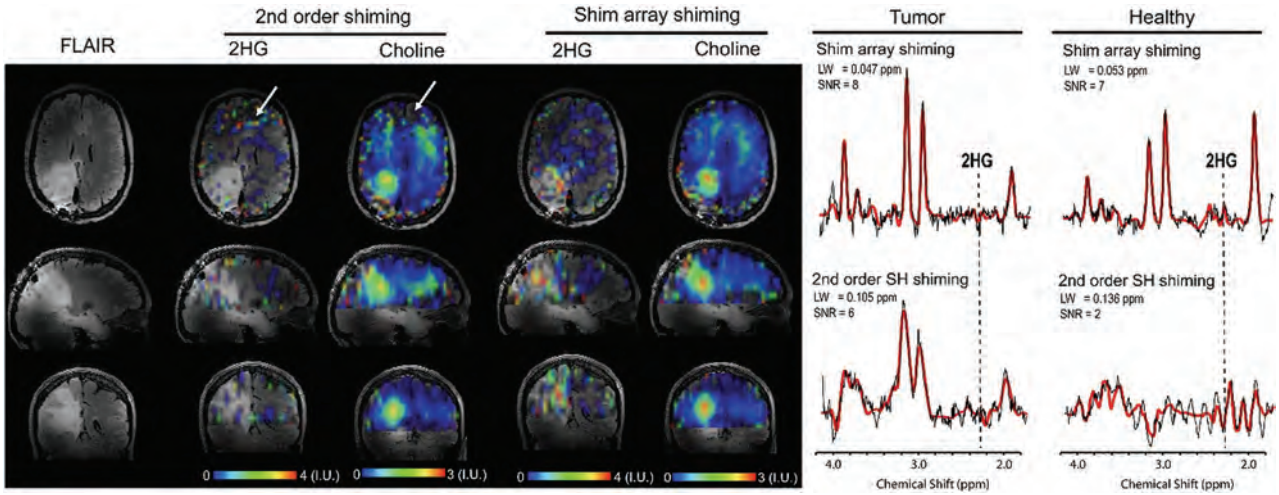

FIG 5. 7T MRSI with standard second order shimming and higher order shimming with an AC/DC shim array was used to visualize Cho and 2HG in an *IDH1* astrocytoma. A metabolic hallmark of *IDH1* and *IDH2* gliomas, 2HG generates a particularly strong signal at 7T, which may make it easier to diagnose patients with *IDH*-mutant profiles. The SNR of 2HG is lower in this example because this patient was treated with an operation and radiochemotherapy, which decrease 2HG levels. The primary clinical objective in this study was to determine whether there were residual mutant *IDH* tumor cells posttreatment. The *white arrows* indicate the frontal area where there are missing voxels in the Cho metabolic map and falsely increased values in the 2HG map due to a larger spectral linewidth obtained with second order shimming. The tumor has a higher contrast-to-noise ratio in the 2HG and Cho maps obtained with the AC/DC shim array. Examples of spectra are shown from tumor and healthy brain in the frontal region (corresponding to the *white arrows*). The position of the 2HG peak at 2.25 ppm is indicated in all spectra. For the adiabatic spin-echo excitation with TE = 78 ms, a negative peak should be obtained for 2HG, which is clearly visible in the tumor spectrum with AC/DC shim but not apparent in the tumor spectrum with standard second order shimming (2SH) shim. In particular, the frontal spectrum obtained with the 2SH shim is completely destroyed by the B_0 inhomogeneity, while metabolite peaks are clearly visible with the AC/DC shim. 2HG is falsely fit in the frontal healthy spectrum with the 2SH shim due to negative spectral artifacts that appear at the 2.25-ppm 2HG peak position. The *dashed vertical line* indicates the location of the main 2HG peak at 2.25 ppm, which should be negative at 7T and TE = 78 ms. All the voxels in the MRSI were fit to create a metabolic map. A spectrum from the frontal voxel was chosen to show a false-positive fit of 2HG in healthy brain when the spectral quality is not adequate. Frontal brain regions are difficult to shim with standard methods, and the AC/DC coil can improve B_0 homogeneity due to additional B_0 shimming. Frontal loops in AC/DC are very close to frontal brain areas and create complex B_0 field patterns to shim out the susceptibility induced by air tissue around the frontal sinus. The second order shimming was obtained with the manufacture's software. This material was obtained with permission from and in collaboration with Jason P. Stockmann and Ovidiu C. Andronesi at the A. A. Martinos Center for Biomedical Imaging, Massachusetts General Hospital and Harvard Medical School. LW indicates linewidth.

independent DC currents are driven in RF receive loops to provide many *dfs* for high-spatial-order B_0 shimming of the brain. This tool was recently shown to improve metabolite linewidth and refine quantification, allowing more brain coverage and the detection of 2HG at higher resolution (Fig 5).[43]

Transceiver arrays also address the increased B_1 inhomogeneity and RF power deposition typical of 7T MRS. These 2 issues, along with acute chemical shift localization (CSL) errors, can result in image artifacts and reduced spatial coverage.[95] Chemical shift localization errors are the spatial shifts in the excited volume for metabolites that resonate at varied frequencies.[95] In 1 study, using an 8-channel transceiver array minimized these problems, harnessing the power of 7T to visualize metabolites such as Glu.[93] Another way to mitigate B_1 inhomogeneity involves adiabatic pulses, a special class of RF pulses that can be integrated into existing MR imaging pulse sequence structures to provide more B_1-insensitive excitation and refocusing of magnetization.[96] However, while these adiabatic pulses yield a more uniform B_1 profile, they also result in more RF deposition, which may have clinical implications if measures are not taken to remain below the specific absorption rate (SAR) safety limits set by the FDA and the International Electrotechnical Commission.[95,97]

Considering that SAR, a quantitative measure of RF power deposition, also increases with field strength, conducting spectroscopy at 7T poses unique problems.[98] Balancing the increased RF power associated with higher field strengths and concerns about patient safety has limited the clinical translation of 7T MRS so far. Nevertheless, a recent study demonstrated that using an adiabatic Shinnar Le-Roux algorithm helps generate a fully adiabatic envelope and a more homogeneous distribution of RF, bypassing some of these obstacles.[95] The pulses obtained with these adiabatic 180° RF pulses, part of a Semi-Adiabatic Spectral-spatial Spectroscopic Imaging (SASSI) pulse sequence, quantified major metabolites while alleviating B_1 heterogeneity, staying within the range of prescribed RF limits and attaining an SNR similar to that in the leading adiabatic alternative, semi-LASER, with just a third of the SAR.[95] The increased B_1 insensitivity and reduced chemical shift localization errors suggest that SASSI might be even more powerful than the aforementioned semi-LASER. Incorporating pulse sequences such as SASSI, which has a more uniform B_1 profile and lower SAR, might, therefore, be warranted. Another approach might be to use a free induction decay (FID) acquisition, which bypasses high SAR pulses altogether. This acquisition strategy minimizes SAR by avoiding multipulse schemes, reducing T2*-decay

even below short-TE approaches, and limiting the signal evolution of J-coupled metabolites such as Gln, Glu, mIns, and taurine.[70]

Both susceptibility artifacts and B_0 inhomogeneity, directly proportionate to field strength, also detract from 7T MRS and skew the geometry and intensity of images. The variations between voxels appear as spectral shifts for metabolite peaks, making frequency-selective pulses that depend on specific spectral bands less accurate and methods for suppressing water and lipid signals more complicated.[99,100] As a result, metabolic peaks widen, peak overlap increases, and SNR decreases. The best way to avoid these obstacles is to use strong referencing schemes, sophisticated B_0 shimming approaches such as dynamic multicoil shimming, and reduced voxel volumes, all of which help to increase SNR and spectral separation.[30,101]

The incorporation of techniques such as compressed sensing might also benefit 7T MRS. Dependent on nonuniform *k*-space undersampling and the assumption of spatial and/or spectral sparsity, compressed sensing MR imaging was first combined with ^{1}H-MRSI in 2009 in vitro[102] and in 2012 in vivo.[102,103] Compressed sensing ^{1}H-MRSI has been used for brain imaging in conjunction with PRESS,[103] semi-LASER prelocalization,[104] and section-selective ^{1}H-FID-MRSI.[105] There are several challenges associated with combining compressed sensing with ^{1}H-MRSI. Large water and lipid nuisance signals can prevent reconstruction algorithms from sensing lower-intensity metabolite peaks due to misadjusted thresholding.[106] The fact that ^{1}H spectra, including MRS with a short-TE, are not sparse can also complicate acceleration along the spectral dimension.[106] However, if these obstacles can be overcome, the application of compressed sensing to MRS has the potential to improve spatial resolution with only minimal increases in acquisition time. Most work to date has involved compressed sensing in spectroscopy at lower field strengths such as 3T, and very few studies have used compressed sensing at higher field strengths such as 7T in investigations of the human brain. However, a very recent study used an effective acquisition-reconstruction scheme involving a ^{1}H-FID-MRSI sequence, a short-TR acquisition, compressed sensing acceleration, and low-rank modeling with total generalized variation constraint for metabolic imaging in 2 and 3 dimensions at 7T in 5 healthy subjects, ultimately generating images with distributions that were highly specific to individual metabolites.[107] Given the high sensitivity and short acquisition time achieved by this group, expanding the use of compressed sensing in 7T MRS would be worthwhile, taking advantage of the additional SNR and other potentials of this higher field strength.

Expanding Horizons: Improved Detection of Infiltrated Tissue and Treatment Effect

Infiltrated Tissue. As a result of its sensitivity to metabolites ranging from Glu to 2HG, MRS offers another way to localize diffuse glioma infiltration that can complement structural information provided by conventional MR imaging.[108,109] A metabolite detected by MRS that has emerged as a strong indicator of the range of tumor infiltration is Cho (Fig 6).[110] The boundaries of both HGGs and LGGs as delineated by MRSI on the basis of Cho-containing compounds correlate with histopathologic analyses, further validating the capacity of spectroscopy to assess the degree of tumor infiltration.[110] Thus, mapping Cho with MRS may help demarcate tumors in treatment planning. More extensive infiltration would be a signal for more aggressive surgical resection or radiation therapy to prevent recurrence.[111] Modifying radiation therapy to account for infiltrated tissue could improve patient outcomes. Increasing high-dose radiation therapy boost volumes, for instance, could decrease the likelihood of recurrence and increase survival rates.[112]

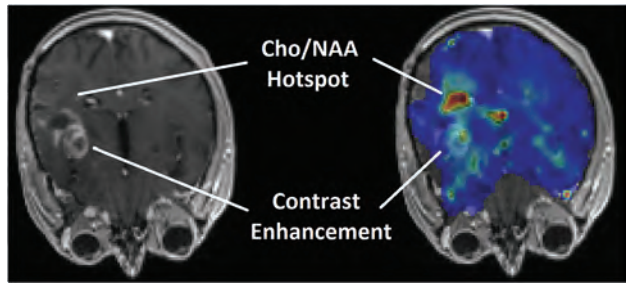

FIG 6. T1-weighted contrast-enhanced MR imaging (*left*) of a patient with a glioma subsequently diagnosed with recurrent tumor (true progression) and the same image with a superimposed map of the Cho/NAA ratio (*right*) acquired using echo-planar spectroscopic imaging. The map shows a hotspot of the elevated Cho/NAA ratio in a region that does not show contrast uptake on postcontrast T1 MR imaging (red depicts Cho/NAA > 1).

MRS could, therefore, help to improve HGG treatment strategies by capturing tumor expansion via metabolic mapping. The limited spatial resolution and spectral sensitivity of MRS at lower field strengths has, heretofore, impeded the usefulness of this technique in detecting tumor infiltration. Given that 7T MRS allows higher spatial resolution, increased SNR, and improved spectral separation, with the highest in-plane resolution published at 7T involving an MRSI ultra-high-resolution sequence with a 128 × 128 matrix and a nominal voxel volume of 1.7 × 1.7 × 8 mm^3, the question emerges: Might performing spectroscopic imaging at higher field strengths address these concerns and refine approaches to diagnosing and treating HGGs?.[113] Future work will clarify whether 7T MRS might provide even more insight into infiltration than spectroscopy at lower field strengths.[114-116]

Treatment Effect. MRS may also strengthen visualization of pseudoprogression, a treatment effect described by the Response Assessment in Neuro-Oncology criteria, in which chemoradiotherapy-induced lesions imitate tumor progression but ultimately stabilize or improve with time.[117-119] Seen in 20% of patients who have undergone treatment, these alterations are produced by temozolomide, which has become the standard of care for GBM.[120] Although they closely resemble more malignant pathology, these changes do not reflect actual tumor growth.[121] In contrast to tumor cells, most of these modifications are asymptomatic.[120] In fact, many even resolve months after patients have finished temozolomide.[122-123] While these lesions are not clinically worrisome, they have complicated neuroradiologic studies.[124] This treatment-related change is radiographically similar to tumorigenic growth.[125] Both exhibit nearly identical contrast-enhancement patterns on conventional MR imaging, which does not differentiate pseudoprogression from progressive disease.[126]

The dearth of imaging parameters that reliably identify these lesions complicates decisions about how to best manage patient care because the approaches to dealing with pseudoprogression versus

Comparison of 3T versus 7T MRS in visualization of metabolic markers in HGGs[a]

	3T	7T
SNR	Lower (–)	Higher (+)
Spatial resolution	Lower (–)	Higher (+)
Resolution of overlapping resonances (ie, PC vs GPC, Lac vs lipids, 2HG vs Glu, Gln, GABA, possibly Glu vs Gln)	Poorer (–)	Better (+)
Range of metabolites	Narrower (–)	Wider (+)
Uncertainty values of metabolite concentrations	Greater (–)	Smaller (+)
Differentiation of *IDH1/IDH2* gliomas vs wild-type gliomas	Less specific (–)	More specific (+)
B_0 inhomogeneity	Lower (+)	Higher (–)
B_1 inhomogeneity	Lower (+)	Higher (–)
RF power deposition (SAR)	Lower (+)	Higher (–)
CSL errors	Less frequent (+)	More frequent (–)
Susceptibility artifacts	Less frequent (+)	More frequent (–)
T1 relaxation time	Shorter (+)	Longer (–)
T2 relaxation time	Longer (+)	Shorter (–)
RF transmit body coils	More accessible (+)	Inaccessible (–)
Metal hardware (ie, titanium plates placed during craniotomies)	Safe (+)	Contraindicated (–)

Note:—CSL indicates chemical shift localization errors; (+), positive features; (–), negative features.
[a]The assets and drawbacks of 7T MRS compared with 3T MRS are delineated.

true progression are radically different.[127] Whereas patients in the latter group require further treatment for persistent tumorigenic activity, those in the former group have a better chance at spontaneous recovery.[128] To prevent patients with pseudoprogression from undergoing avoidable surgery or chemotherapy, seeking noninvasive ways to distinguish pseudoprogression from true progression is essential.[129-130] Using techniques such as MRS is a possible solution.[131] The metabolic details contained within spectroscopic images may help distinguish largely innocuous disease from recurrent glioma, ushering in tailored treatment strategies.[132] Although differentiating pseudoprogression and true tumor progression is still difficult even with MRS, this technique has shown the potential to reveal differences in the spectroscopic features of malignant tissue and treatment effect–damaged tissue.[121,127,133,134] Whereas recurring tumors often have increased Cho due to higher cell membrane turnover, therapy-associated lesions frequently have slightly decreased NAA and substantially decreased lipid-Lac peaks.[121,127,135,136]

In a recent meta-analysis of advanced MR imaging techniques, SVS had the highest diagnostic accuracy, reliably discerning treatment-related changes in patients with HGG.[137] Specific parameters in SVS may be highly sensitive to metabolic differences.[138] These include the ratios of Cho/Cr and Cho/NAA, with higher values in recurring tumors.[139-141] A study with 2D chemical shift imaging SVS at 1.5T found that these ratios were 97% accurate in distinguishing pseudoprogression and tumor advancement.[142] Another study with 3T SVS involving the same 2 Cho metrics reported a similarly high level of accuracy, with 94.1% sensitivity and 100% specificity.[143] As encouraging as findings such as these are, the differential diagnostic utility of MRS continues to be hampered. A long-standing roadblock has been the metabolic overlap between tissue treated with temozolomide and tissue containing actively growing malignant glioma cells on spectroscopy at 1.5T and 3T.[121] Moreover, there is not yet any definitive agreement as to which spectroscopic parameters and threshold levels can best differentiate pseudoprogression from true progression.[118] Both types of lesions also have similar metabolic fingerprints, including low NAA and high Cho, Lac, and lipids.[121]

The high similarity demands more nuanced spectroscopy that can disentangle the 2 on the basis of subtle discrepancies.[144] Once again, 7T MRS surfaces as a prime candidate, well poised to sort out problematic overlap and pinpoint minute metabolic differences. Potential metabolic candidates include Glu, Gln, and Gly. Yet despite all these attributes, no studies have analyzed the diagnostic accuracy of 7T MRS in distinguishing pseudoprogression. In view of its sensitivity and specificity, there is no doubt that this system would be worth exploring. If 7T MRS does provide greater sensitivity to these metabolic variations in proportion to the expectedly higher SNR, then such a discovery would take analyses of treatment effects and therapeutic tactics in new directions.[145] With 7T MRS, differentiation between pseudoprogression and authentic progression might finally become a reality, improving predictions about prognoses and directing calls about therapy.[146]

3T versus 7T: Qualitative and Quantitative Differences

A summary of the qualitative strengths and weaknesses of 3T and 7T is included (Table). In terms of quantitative metrics, as discussed throughout this review, one of the major benefits of 7T is higher SNR, which increases substantially and possibly even supralinearly[147] with B_0, resulting in modestly enhanced spatial resolution and contrast.[26] Coil design can further elevate SNR at higher fields, leading to a 2- to 6-fold increase under certain conditions.[26,148] A study investigating SVS at 3T and 7T using 32-channel head coils found that mean SNR values at 7T were substantially higher than at 3T (135 [SD, 28], 116 [SD, 33], and 138 [SD, 29] versus 83 [SD, 12], 97 [SD, 7], and 83 [SD, 5]) in brain regions under examination (the anterior cingulate cortex, centrum semiovale, and dorsolateral prefrontal cortex).[22] Another

study that also compared 3T and 7T recorded a 1.7-fold increase in the average SNR per unit of time at 7T, providing further support for the improved sensitivity at higher field strengths.[23]

Studies involving 7T have reported increases in linewidths of metabolites such as NAA, Cr, and Cho when measured in hertz but decreases when measured in parts per million.[19] Thus, linewidths increase less than proportionally to field strength and are, therefore, higher in absolute terms in hertz but lower in relative terms in parts per million. Although the short-T2 relaxation times and susceptibility effects at high field contribute to an increased linewidth,[32] the spectral resolution could remain increased at 7T with optimized shimming methods and smaller voxel volumes.[37] Thus, proper compensation with techniques such as shimming is important to minimize broader linewidths that occur at higher field strengths, which can exacerbate spectral overlap and complicate the separation of metabolites, including Glu and Gln.[149]

The increased SNR associated with 7T MRS may be particularly helpful in the detection of Glu and Gln.[149] These 2 metabolites can be reliably differentiated from one another with sophisticated techniques in multiple areas of the brain even at 3T.[149] However, especially at such lower field strengths, Glu and Gln are frequently grouped together as a sum Glx (Glu + Gln), recorded in spectroscopic VOIs in neurologic regions with low SNR and broad linewidths.[149] Combining these 2 metabolites into 1 discrete peak makes discriminating between them very challenging at 3T, particularly in certain areas of the brain.[149] In contrast, at higher field strengths such as 7T, separating Glu from Gln is more achievable due to the potential for higher SNR and greater spectral separation.[24]

CRLBs have been shown to decrease as B_0 increases for many metabolites under investigation in several studies, contributed by both the increased SNR and spectral resolution.[19,150] 7T resulted in higher measurement precision for aspartate (average CRLB 27% at 3T versus 15% at 7T), Glu (average CRLB 5% at 3T versus 3% at 7T), and Gln (average CRLB 19% at 3T versus 9% at 7T) in the 32-channel head coil study.[22] Nevertheless, these differences in measurement precision were less appreciable for larger signals in the spectrum, with CRLBs for 3T and 7T very similar for metabolites including total NAA, total CR, tCho, and mIns and Gly.[22] The benefits provided by 7T in terms of measurement precision (as quantified via CRLBs) may, therefore, vary depending on the specific metabolite of interest. However, there is growing evidence that 7T correlates with decreased CRLBs relative to 3T. Other studies have likewise discovered that Glu has a lower CRLB at 7T than at 3T, including one that involved 7T short-TE MRSI.[25] Another study found that the CRLB averaged over 18 total metabolites was significantly lower (35% lower) at 7T than at 3T ($P < .015$).[23] The CRLBs of Gln, τ, and Glx were the most visibly reduced by 7T.[23] In addition, 7T measured Lac with CRLB <20% (final mean Lac concentration = 0.7 [SD, 0.1] mmol/kg, mean CRLB = 9% [SD, 1.6%], which was a distinct improvement compared with 3T.[23] Yet another study similarly reported lower CRLB ($P < .001$) at 7T versus 3T for Glx in parts of the brain such as the thalamus and pons.[24] At 7T, CRLBs of total NAA, total Cr, and mIns were also lower than at 3T.[24]

Given that 7T MRS has not yet been fully integrated in a clinical setting, there are not yet many statistics of clinical assessment, including tumor grading, available. Thus, comparing 7T with 3T in this area is difficult. Although studies have assigned grades II, III, and IV to lesions via histopathologic analysis before imaging with 7T and 3T,[25] very few have conducted rigorous comparisons of tumor grading at these 2 field strengths and assessed correlations between 7T MRS imaging results and tumor grading. Most studies have concentrated on the capacity of 3T MRS to assess tumor grade.[151-157] One study found that Cho/Cr and combined Lipid-Lac/Cr ratios were helpful in differentiating LGGs from HGGs, with diagnostic accuracy higher (85.7% versus 82.9%) at short-TE or combined short-TE and long-TE than at intermediate-TE only.[152] Another similarly reported that Cho/Cr, in conjunction with other imaging parameters, was an effective marker for distinguishing LGGs and HGGs with 87.0% sensitivity and 88.9% specificity.[153] The usefulness of Cho/Cr in stratifying gliomas of different grades has been documented in several other 3T studies.[155,156] Maximum Cho also proved in 1 study to yield even higher diagnostic accuracy (82.5% versus 72.1% accuracy) than Cho/Cr.[155] In addition, Cho/NAA may ???????? in the differentiation of gliomas, with higher absolute values of Cho/NAA in HGGs than in LGGs seen in 1 study, which combined Cho/NAA with structural MR to achieve 86% sensitivity and 80% specificity.[157]

As the use of 7T MRS becomes more widespread in clinical contexts, similar appraisals of its ability to determine differences between gliomas and aid in the grading process should be undertaken. Although further study is warranted, the use of 7T MRS for tumor grading may have several potential benefits. Given the technical assets of spectroscopy at higher field strengths, including reduced CRLBs and modest improvements in spatial resolution, 7T MRS could further isolate Cho/Cr and Cho/NAA and could provide more information about other metabolites in different HGGs, thereby making the process of differentiating tumor grades less challenging. In particular, elevated Cho, reduced NAA, and levels of lipids and Lacs have been shown to correlate with higher tumor grade and aggressiveness.[158] There are emerging signs that 7T may have a higher capacity than lower field strengths with poorer signals to reveal these kinds of differences in metabolite levels in cancerous-versus-normal tissue and in different gliomas, which may result in more refined detection and classification of tumors.[20,31] However, additional investigations involving spectroscopy and tumor grading are necessary to confirm whether 7T is indeed superior to 3T in this regard.

Future Clinical Directions

More sensitive than conventional MRS to metabolic markers at lower fields, 7T MRS can detect and differentiate among HGGs, revealing different metabolic characteristics (Fig 7). The abnormal metabolic activity visualized by 7T MRS may advance disease etiology, diagnostic approaches, and therapeutic interventions.[112] Nevertheless, 7T MRS of HGGs is still in its infancy. The lack of spectroscopic imaging studies with 7T indicates that advances must still be made.[93] One of the most common problems in every report reviewed is the small sample size. Future studies will include larger groups of patients. Broadening the patient population will increase the statistical power and expand the 7T MRS database.[70] Increasing the sample size will also provide

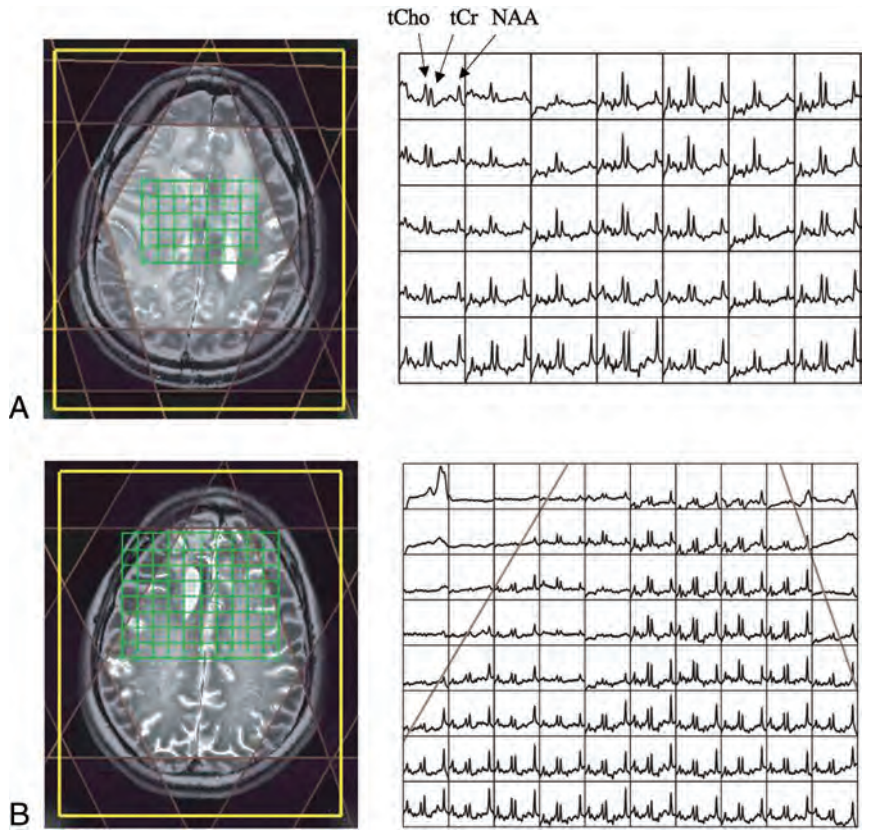

FIG 7. 7T MRSI can capture gliomas in different stages, such as the recurrent grade II oligodendroglioma (progression) in the newly diagnosed, presymptomatic patient in *A* and the recurrent grade II oligodendroglioma (stable) in a treated patient in *B*. These spectra were acquired at 7T and show differences between progressing and nonprogressing tumors. The progressing tumor in the upper figure shows lower NAA in tumor regions and higher relative Cho, whereas the stable tumor in the lower figure demonstrates higher NAA with fewer metabolic abnormalities. NAA is on the right, and tCho and total Cr are in peaks just left of the center as labeled. Spectra data were processed after phasing/frequency corrections and coil combination (with baseline, no quantification). The metabolite range is from ~1.8 to 4.2 ppm. This material was obtained with permission and in collaboration with Yan Li and Peder Larson in the Department of Radiology and Biomedical Imaging at the University of California, San Francisco. tCr indicates total Cr.

information about metabolic heterogeneity in diverse HGGs.[34] Furthermore, deeper insight into tumor microenvironments will elucidate metabolic signatures of various gliomas.[159]

Although there is growing literature on the safety of surgical implants at higher field strengths,[160-163] there are not yet any definitive guidelines for imaging patients with nonmagnetic standard titanium plates placed during HGG resections, which has limited the clinical integration of 7T MRS thus far.[164] It is important to perform additional testing and develop explicit guidance on whether surgical implants are safe at higher fields.[165] The increased use of 7T MRS to scan patients in this category would allow longitudinal evaluations of patients with HGG at different phases of treatment, including postoperative follow-ups during radiation therapy, which have largely been confined to lower field strengths but ought to be expanded more widely to higher field strengths.

Ascertaining absolute metabolite concentrations would make metabolic information more accurate.[166] Measuring T1 and T2 values is one of the only ways to acquire these concentrations.[28] Ratios are derived using Cr peaks, which often vary depending on tissue type, making precise measurements difficult. Unsuppressed water-reference scans provide another way to more accurately quantify concentrations that is superior to ratios because they account for the relaxation times of both metabolites and of water voxels.[55,167-170] Additional standardized markers of tumor aggressiveness would also be useful.[171] Intracellular pH, energy metabolism, and total Cho may indicate more aggressive behavior in gliomas but must be verified.[28] Other metabolites may also warrant further investigation. These include GSH, challenging even for 7T MRS to quantify. There have been a few reports of increased GSH compared with total Cr in HGGs, but there are less data supporting this trend.[31] Given that this metabolite protects cells from free radicals, GSH might be a meaningful therapeutic target.[172,173] Increasing the affinity of 7T MRS for GSH might, therefore, be worthwhile. Most important, GSH and other metabolites including GABA can be visualized at 3T with spectral editing techniques such as MEGA-PRESS.[174] These editing techniques can provide better results at 7T because the increased spectral dispersion allows greatly reduced contamination from coedited macromolecules due to the bandwidth of the editing pulses. High-field acquisitions not only offer higher SNR but also address the problem of overlapping metabolites, better defining low-concentration metabolites such as GSH.[31,175] Future studies should explore integrating MEGA-PRESS into 7T MRS to better visualize GSH.

Another metabolite for which further study may be of benefit is Lac. Although its significance in HGGs and other brain tumors is still not entirely clear, Lac reflects anaerobic glycolysis, which may be a sign of neoplastic growth.[176,177] Increased glycolysis and perfusion in tumor tissue lead to elevated Lac, with higher levels corresponding with increased aggressiveness.[178,179] Imaging Lac in HGGs via techniques such as MRS is crucial because this metabolite may be a biomarker of more aggressive tumors, with increased Lac correlating particularly strongly with grade IV gliomas.[180] Although there have been several studies using lower-field-strength MRS to detect increased Lac, there is still very little 7T MRS literature on Lac in human subjects.[27,34,181] Further investigation is warranted to determine whether 7T provides better visualization of Lac, which could serve as a lens into malignant activity, helping clinicians determine glioma grades, identify the best approaches to treatment, and monitor tumors across time.

Larger signal loss from T2 relaxation resulting in diminished SNR has also been registered at 7T, which necessitates approaches such as stimulated echo acquisition mode sequences with ultrashort TEs and longer TRs, which are optimal for tissues with unknown metabolic relaxation rates.[33,182] Although 7T MRS can resolve many overlapping resonances and has even been shown to separate Glu from Gln, further work is necessary to differentiate metabolites such as these 2 while maintaining high spatial resolution and SNR.[31] Moreover, 7T MRSI often fails to localize lipids in necrotic regions.[31] Future studies will correct these deficiencies and capitalize on the power of 7T to distinguish abnormal metabolites.

CONCLUSIONS

We summarized the literature on 7T MRS and affirmed its usefulness in measuring metabolites. 7T MRS can achieve superior SNR and spectral separation and modestly improved spatial resolution and can also resolve overlapping resonances and isolate specific metabolites such as Glu, Gln, and Gly, which may be valuable therapeutic targets, improving patient outcomes. 7T MRS can also result in reduced CRLB values and improved quantification of small signals compared with 3T MRS. The increased spatial resolution, SNR, and spectral separation of 7T MRS may also enhance the detection of infiltrated tissue and treatment effect. We then underscored the hallmarks of effective 7T spectroscopy sequences that maximize SNR and spatial resolution and minimize B_0 and B_1 inhomogeneity, RF, and acquisition time.

We conclude with some of the failings of 7T MRS. These include safety concerns, the lack of data on other promising metabolites such as GSH and Lac, and the absence of absolute metabolite concentrations and established indices of aggressiveness. These flaws will be addressed as knowledge of glioma pathology and imaging technology continues to evolve.

ACKNOWLEDGMENTS

We thank Drs Peder Larson, Yan Li, Sanjeev Chawla, and Suyash Mohan for helpful correspondence and images for figures.

Disclosure forms provided by the authors are available with the full text and PDF of this article at www.ajnr.org.

REFERENCES

1. Server A, Josefsen R, Kulle B, et al. **Proton magnetic resonance spectroscopy in the distinction of high-grade cerebral gliomas from single metastatic brain tumors.** *Acta Radiol* 2010;51:316–25 CrossRef Medline
2. Wilson TA, Karajannis MA, Harter DH. **Glioblastoma multiforme: state of the art and future therapeutics.** *Surg Neurol Int* 2014;5:64 CrossRef Medline
3. Wolf KJ, Chen J, Coombes J, et al. **Dissecting and rebuilding the glioblastoma microenvironment with engineered materials.** *Nat Rev Mater* 2019;4:651–68 CrossRef Medline
4. Hou LC, Veeravagu A, Hsu AR, et al. **Recurrent glioblastoma multiforme: a review of natural history and management options.** *Neurosurg Focus* 2006;20:E5 CrossRef Medline
5. Zhu H, Barker PB. **MRS and spectroscopic imaging of the brain.** *Methods Mol Biol* 2011;711:203–26 CrossRef Medline
6. Tkác I, Andersen P, Adriany G, et al., **In vivo 1H NMRS of the human brain at 7 T.** *Magn Reson Med* 2001;46:451–56 CrossRef
7. Horská A, Barker PB. **Imaging of brain tumors: MRS and metabolic imaging.** *Neuroimaging Clin N Am* 2010;20:293–310 CrossRef Medline
8. Dang L, White DW, Gross S, et al. **Cancer-associated IDH1 mutations produce 2-hydroxyglutarate.** *Nature* 2009;462:739–44 CrossRef Medline
9. Maudsley AA, Andronesi OC, Barker PB, et al. **Advanced magnetic resonance spectroscopic neuroimaging: experts' consensus recommendations.** *NMR Biomed* 2021;34:e4309 CrossRef Medline
10. Ricci R, Bacci A, Tugnoli V, et al. **Metabolic findings on 3T 1H-MRS in peritumoral brain edema.** *AJNR Am J Neuroradiol* 2007;28:1287–91 CrossRef Medline
11. Bertolino N, Marchionni C, Ghielmetti F, et al. **Accuracy of 2-hydroxyglutarate quantification by short-echo proton-MRS at 3 T: a phantom study.** *Phys Med* 2014;30:702–07 CrossRef Medline
12. Cuccarini V, Antelmi L, Pollo B, et al. **In vivo 2-hydroxyglutarate-proton magnetic resonance spectroscopy (3 T, PRESS technique) in treatment-naïve suspect lower-grade gliomas: feasibility and accuracy in a clinical setting.** *Neurol Sci* 2020;41:347–55 CrossRef Medline
13. Kousi E, Tsougos I, Tsolaki E, et al. **Spectroscopic evaluation of glioma grading at 3T: the combined role of short and long TE.** *ScientificWorldJournal* 2012;2012:546171 CrossRef Medline
14. Laino ME, Young R, Beal K, et al. **Magnetic resonance spectroscopic imaging in gliomas: clinical diagnosis and radiotherapy planning.** *BJR Open* 2020;2:20190026 CrossRef Medline
15. Rutland JW, Delman BN, Gill CM, et al. **Emerging use of ultra-high-field 7T MRI in the study of intracranial vascularity: state of the field and future directions.** *AJNR Am J Neuroradiol* 2020;41:2–9 CrossRef Medline
16. Morrison MA, Lupo JM. **7-T magnetic resonance imaging in the management of brain tumors.** *Magn Reson Imaging Clin N Am* 2021;29:83–102 CrossRef Medline
17. Lohmann P, Werner J-M, Shah N, et al. **Combined amino acid positron emission tomography and advanced magnetic resonance imaging in glioma patients.** *Cancers (Basel)* 2019;11:153 CrossRef Medline
18. Hoff MN, McKinney A, Shellock FG, et al. **Safety considerations of 7-T MRI in clinical practice.** *Radiology* 2019;292:509–18 CrossRef Medline
19. Otazo R, Mueller B, Ugurbil K, et al. **Signal-to-noise ratio and spectral linewidth improvements between 1.5 and 7 Tesla in proton echo-planar spectroscopic imaging.** *Magn Reson Med* 2006;56:1200–10 CrossRef Medline
20. Barrett TF, Sarkiss CA, Dyvorne HA, et al. **Application of ultrahigh field magnetic resonance imaging in the treatment of brain tumors: a meta-analysis.** *World Neurosurg* 2016;86:450–65 CrossRef Medline
21. Stephenson MC. **Applications of multi-nuclear magnetic resonance spectroscopy at 7T.** *World J Radiol* 2011;3:105–13 CrossRef Medline
22. Pradhan S, Bonekamp S, Gillen JS, et al. **Comparison of single voxel brain MRS at 3T and 7T using 32-channel head coils.** *Magn Reson Imaging* 2015;33:1013–18 CrossRef Medline
23. Mekle R, Mlynárik V, Gambarota G, et al. **MRS of the human brain with enhanced signal intensity at ultrashort echo times on a clinical platform at 3T and 7T.** *Magn Reson Med* 2009;61:1279–85 CrossRef Medline
24. Younis S, Hougaard A, Christensen CE, et al. **Feasibility of glutamate and GABA detection in pons and thalamus at 3T and 7T by proton magnetic resonance spectroscopy.** *Front Neurosci* 2020;14:559314 CrossRef Medline
25. Li Y, Lafontaine M, Chang S, et al. **Comparison between short and long echo time magnetic resonance spectroscopic imaging at 3T and 7T for evaluating brain metabolites in patients with glioma.** *ACS Chem Neurosci* 2018;9:130–37 CrossRef Medline
26. Trattnig S, Springer E, Bogner W, et al. **Key clinical benefits of neuroimaging at 7T.** *Neuroimage* 2018;168:477–89 CrossRef Medline

27. Emir UE, Larkin SJ, de Pennington N, et al. **Noninvasive quantification of 2-hydroxyglutarate in human gliomas with IDH1 and IDH2 mutations.** *Cancer Res* 2016;76:43–49 CrossRef Medline
28. Lupo JM, Li Y, Hess CP, et al. **Advances in ultra-high field MRI for the clinical management of patients with brain tumors.** *Curr Opin Neurol* 2011;24:605–15 CrossRef Medline
29. Wei RL, Wei XT. **Advanced diagnosis of glioma by using emerging magnetic resonance sequences.** *Front Oncol* 2021;11:694498 CrossRef Medline
30. Balchandani P, Naidich TP. **Ultra-high-field MR neuroimaging.** *AJNR Am J Neuroradiol* 2015;36:1204–15 CrossRef Medline
31. Li Y, Larson P, Chen AP, et al. **Short-echo three-dimensional H-1 MR spectroscopic imaging of patients with glioma at 7 Tesla for characterization of differences in metabolite levels.** *J Magn Reson Imaging* 2015;41:1332–41 CrossRef Medline
32. Tkác I, Oz G, Adriany G, et al. **In vivo 1H NMRS of the human brain at high magnetic fields: metabolite quantification at 4T vs. 7T.** *Magn Reson Med* 2009;62:868–79 CrossRef Medline
33. Berrington A, et al. **A comparison of 2-hydroxyglutarate detection at 3 and 7 T with long-TE semi-LASER.** *NMR Biomed* 2018;31 CrossRef Medline
34. Verma G, Mohan S, Nasrallah MP, et al. **Non-invasive detection of 2-hydroxyglutarate in IDH-mutated gliomas using two-dimensional localized correlation spectroscopy (2D L-COSY) at 7 Tesla.** *J Transl Med* 2016;14:274 CrossRef Medline
35. Thomas MA, Hattori N, Umeda M, et al. **Evaluation of two-dimensional L-COSY and JPRESS using a 3 T MRI scanner: from phantoms to human brain in vivo.** *NMR Biomed* 2003;16:245–51 CrossRef Medline
36. Binesh N, Yue K, Fairbanks L, et al. **Reproducibility of localized 2D correlated MR spectroscopy.** *Magn Reson Med* 2002;48:942–48 CrossRef Medline
37. Verma G, Hariharan H, Nagarajan R, et al. **Implementation of two-dimensional L-COSY at 7 Tesla: an investigation of reproducibility in human brain.** *J Magn Reson Imaging* 2014;40:1319–27 CrossRef Medline
38. van Dijken BR, van Laar PJ, Holtman GA, et al. **Diagnostic accuracy of magnetic resonance imaging techniques for treatment response evaluation in patients with high-grade glioma, a systematic review and meta-analysis.** *Eur Radiol* 2017;27:4129–44 CrossRef Medline
39. Kochalska K, Łazorczyk A, Pankowska A, et al. **General technical remarks on (1)HMRS translational research in 7T.** *Pol J Radiol* 2019;84:e190–97 CrossRef Medline
40. McKay J, Tkácõ I. **Quantitative in vivo neurochemical profiling in humans: where are we now?** *Int J Epidemiol* 2016;45:1339–50 CrossRef Medline
41. Pan JW, Lo KM, Hetherington HP. **Role of very high order and degree B0 shimming for spectroscopic imaging of the human brain at 7 Tesla.** *Magn Reson Med* 2012;68:1007–17 CrossRef Medline
42. Juchem C, Nixon TW, McIntyre S, et al. **Dynamic multi-coil shimming of the human brain at 7 T.** *J Magn Reson* 2011;212:280–88 CrossRef Medline
43. Esmaeili M, Stockmann J, Strasser B, et al. **An integrated RF-receive/B(0)-shim array coil boosts performance of whole-brain MR spectroscopic imaging at 7 T.** *Sci Rep* 2020;10:15029 CrossRef Medline
44. Andronesi OC, Arrillaga-Romany IC, Ly KI, et al. **Pharmacodynamics of mutant-IDH1 inhibitors in glioma patients probed by in vivo 3D MRS imaging of 2-hydroxyglutarate.** *Nat Commun* 2018;9:1474 CrossRef Medline
45. An Z, Tiwari V, Ganji SK, et al. **Echo-planar spectroscopic imaging with dual-readout alternated gradients (DRAG-EPSI) at 7 T: application for 2-hydroxyglutarate imaging in glioma patients.** *Magn Reson Med* 2018;79:1851–61 CrossRef Medline
46. Ganji SK, An Z, Tiwari V, et al. **In vivo detection of 2-hydroxyglutarate in brain tumors by optimized point-resolved spectroscopy (PRESS) at 7T.** *Magn Reson Med* 2017;77:936–44 CrossRef Medline
47. Shen X, Voets N, Larkin S, et al. **A noninvasive comparison study between human gliomas with IDH1 and IDH2 mutations by MR spectroscopy.** *Metabolites* 2019;9:35 CrossRef Medline
48. Cohen AL, Holmen SL, Colman H. **IDH1 and IDH2 mutations in gliomas.** *Curr Neurol Neurosci Rep* 2013;13:345 CrossRef Medline
49. Sanson M, Marie Y, Paris S, et al. **Isocitrate dehydrogenase 1 codon 132 mutation is an important prognostic biomarker in gliomas.** *J Clin Oncol* 2009;27:4150–54 CrossRef Medline
50. Karpel-Massler G, Nguyen TT, Shang E, et al. **Novel IDH1-targeted glioma therapies.** *CNS Drugs* 2019;33:1155–66 CrossRef Medline
51. Choi C, Ganji SK, DeBerardinis RJ, et al. **2-hydroxyglutarate detection by magnetic resonance spectroscopy in IDH-mutated patients with gliomas.** *Nat Med* 2012;18:624–29 CrossRef Medline
52. Choi C, Ganji S, Hulsey K, et al. **A comparative study of short- and long-TE ^{1}H MRS at 3T for in vivo detection of 2-hydroxyglutarate in brain tumors.** *NMR Biomed* 2013;26:1242–50 CrossRef Medline
53. SongTao Q, Lei Y, Si G, et al. **IDH mutations predict longer survival and response to temozolomide in secondary glioblastoma.** *Cancer Sci* 2012;103:269–73 CrossRef Medline
54. Buckner JC, Shaw EG, Pugh SL, et al. **Radiation plus procarbazine, CCNU, and vincristine in low-grade glioma.** *N Engl J Med* 2016;374:1344–55 CrossRef Medline
55. Kim H, Kim S, Lee HH, et al. **In-vivo proton magnetic resonance spectroscopy of 2-hydroxyglutarate in isocitrate dehydrogenase-mutated gliomas: a technical review for neuroradiologists.** *Korean J Radiol* 2016;17:620–32 CrossRef Medline
56. Shim H. Spectroscopic MRI for brain tumor imaging, molecular imaging. In: Ross B, Gambhir S, eds. *Molecular Imaging*. Elsevier; 2021:1077–90
57. Suh CH, Kim HS, Jung SC, et al. **2-Hydroxyglutarate MRS for prediction of isocitrate dehydrogenase mutant glioma: a systemic review and meta-analysis using individual patient data.** *Neuro Oncol* 2018;20:1573–83 CrossRef Medline
58. Andronesi OC, Kim GS, Gerstner E, et al. **Detection of 2-hydroxyglutarate in IDH-mutated glioma patients by in vivo spectral-editing and 2D correlation magnetic resonance spectroscopy.** *Sci Transl Med* 2012;4:116ra4 CrossRef Medline
59. Chaumeil MM, Larson PE, Yoshihara HA, et al. **Non-invasive in vivo assessment of IDH1 mutational status in glioma.** *Nat Commun* 2013;4:2429 CrossRef Medline
60. An Z, Tiwari V, Baxter J, et al. **3D high-resolution imaging of 2-hydroxyglutarate in glioma patients using DRAG-EPSI at 3T in vivo.** *Magn Reson Med* 2019;81:795–802 CrossRef Medline
61. Provencher SW. **Automatic quantitation of localized in vivo 1H spectra with LCModel.** *NMR Biomed* 2001;14:260–64 CrossRef Medline
62. Huang LE. **Friend or foe-IDH1 mutations in glioma 10 years on.** *Carcinogenesis* 2019;40:1299–1307 CrossRef Medline
63. Wang HY, Tang K, Liang TY, et al. **The comparison of clinical and biological characteristics between IDH1 and IDH2 mutations in gliomas.** *J Exp Clin Cancer Res* 2016;35:86 CrossRef Medline
64. Molenaar RJ, Maciejewski JP, Wilmink JW, et al. **Wild-type and mutated IDH1/2 enzymes and therapy responses.** *Oncogene* 2018;37:1949–60 CrossRef Medline
65. Han S, Liu Y, Cai SJ, et al. **IDH mutation in glioma: molecular mechanisms and potential therapeutic targets.** *Br J Cancer* 2020;122:1580–89 CrossRef Medline
66. Louis DN, Perry A, Wesseling P, et al. **The 2021 WHO Classification of Tumors of the Central Nervous System: a summary.** *Neuro Oncol* 2021;23:1231–51 CrossRef Medline
67. Camelo-Piragua S, Jansen M, Ganguly A, et al. **Mutant IDH1-specific immunohistochemistry distinguishes diffuse astrocytoma from astrocytosis.** *Acta Neuropathol* 2010;119:509–11 CrossRef Medline
68. Takano S, Tian W, Matsuda M, et al. **Detection of IDH1 mutation in human gliomas: comparison of immunohistochemistry and sequencing.** *Brain Tumor Pathol* 2011;28:115–23 CrossRef Medline

69. Takano S, Kato Y, Yamamoto T, et al. **Immunohistochemical detection of IDH1 mutation, p53, and internexin as prognostic factors of glial tumors.** *J Neurooncol* 2012;108:361–73 CrossRef Medline
70. Hangel G, Cadrien C, Lazen P, et al. **High-resolution metabolic imaging of high-grade gliomas using 7T-CRT-FID-MRSI.** *Neuroimage Clin* 2020;28:102433 CrossRef Medline
71. Venkataramani V, Tanev DI, Strahle C, et al. **Glutamatergic synaptic input to glioma cells drives brain tumour progression.** *Nature* 2019;573:532–38 CrossRef Medline
72. Ye ZC, Sontheimer H. **Glioma cells release excitotoxic concentrations of glutamate.** *Cancer Res* 1999;59:4383–91 Medline
73. Hangel G, Jain S, Springer E, et al. **High-resolution metabolic mapping of gliomas via patch-based super-resolution magnetic resonance spectroscopic imaging at 7T.** *Neuroimage* 2019;191:587–95 CrossRef Medline
74. Nanga RP, DeBrosse C, Kumar D, et al. **Reproducibility of 2D GluCEST in healthy human volunteers at 7 T.** *Magn Reson Med* 2018;80:2033–39 CrossRef Medline
75. Libby CJ, Tran AN, Scott SE, et al. **The pro-tumorigenic effects of metabolic alterations in glioblastoma including brain tumor initiating cells.** *Biochim Biophys Acta Rev Cancer* 2018;1869:175–88 CrossRef Medline
76. Tardito S, Oudin A, Ahmed SU, et al. **Glutamine synthetase activity fuels nucleotide biosynthesis and supports growth of glutamine-restricted glioblastoma.** *Nat Cell Biol* 2015;17:1556–68 CrossRef Medline
77. Hingerl L, Strasser B, Moser P, et al. **Clinical high-resolution 3D-MR spectroscopic imaging of the human brain at 7 T.** *Invest Radiol* 2020;55:239–48 CrossRef Medline
78. Altman BJ, Stine ZE, Dang CV. **From Krebs to clinic: glutamine metabolism to cancer therapy.** *Nat Rev Cancer* 2016;16:619–34 CrossRef Medline
79. Koch K, Hartmann R, Tsiampali J, et al. **A comparative pharmacometabolomic study of glutaminase inhibitors in glioma stem-like cells confirms biological effectiveness but reveals differences in target-specificity.** *Cell Death Discov* 2020;6:20 CrossRef Medline
80. Wang JB, Erickson JW, Fuji R, et al. **Targeting mitochondrial glutaminase activity inhibits oncogenic transformation.** *Cancer Cell* 2010;18:207–19 CrossRef Medline
81. Ekici S, Risk BB, Neill SG, et al. **Characterization of dysregulated glutamine metabolism in human glioma tissue with ^{1}H NMR.** *Sci Rep* 2020;10:20435 CrossRef Medline
82. Obara-Michlewska M, Szeliga M. **Targeting glutamine addiction in gliomas.** *Cancers (Basel)* 2020;12:310 CrossRef Medline
83. Song M, Kim SH, Im CY, et al. **Recent development of small molecule glutaminase inhibitors.** *Curr Top Med Chem* 2018;18:432–43 CrossRef Medline
84. Wang Z, Liu F, Fan N, et al. **Targeting glutaminolysis: new perspectives to understand cancer development and novel strategies for potential target therapies.** *Front Oncol* 2020;10:589508 CrossRef Medline
85. Shen YA, Chen CL, Huang YH, et al. **Inhibition of glutaminolysis in combination with other therapies to improve cancer treatment.** *Curr Opin Chem Biol* 2021;62:64–81 CrossRef Medline
86. Choi C, Ganji SK, DeBerardinis RJ, et al. **Measurement of glycine in the human brain in vivo by 1H-MRS at 3 T: application in brain tumors.** *Magn Reson Med* 2011;66:609–18 CrossRef Medline
87. Kinoshita Y, Kajiwara H, Yokota A, et al. **Proton magnetic resonance spectroscopy of astrocytic tumors: an in vitro study.** *Neurol Med Chir (Tokyo)* 1993;33:350–59 CrossRef Medline
88. Righi V, Andronesi OC, Mintzopoulos D, et al. **High-resolution magic angle spinning magnetic resonance spectroscopy detects glycine as a biomarker in brain tumors.** *Int J Oncol* 2010;36:301–06 CrossRef Medline
89. Prisciandaro JJ, Schacht JP, Prescot AP, et al. **Evidence for a unique association between fronto-cortical glycine levels and recent heavy drinking in treatment naive individuals with alcohol use disorder.** *Neurosci Lett* 2019;706:207–10 CrossRef Medline
90. Stence NV, Fenton LZ, Levek C, et al. **Brain imaging in classic nonketotic hyperglycinemia: Quantitative analysis and relation to phenotype.** *J Inherit Metab Dis* 2019;42:438–50 CrossRef Medline
91. Tiwari V, Daoud EV, Hatanpaa KJ, et al. **Glycine by MRS is an imaging biomarker of glioma aggressiveness.** *Neuro Oncol* 2020;22:1018–29 CrossRef Medline
92. Seliger C, Schaertl J, Gerken M, et al. **Use of statins or NSAIDs and survival of patients with high-grade glioma.** *PLoS One* 2018;13:e0207858 CrossRef Medline
93. Avdievich NI, Pan JW, Baehring JM, et al. **Short echo spectroscopic imaging of the human brain at 7T using transceiver arrays.** *Magn Reson Med* 2009;62:17–25 CrossRef Medline
94. Strasser B, Chmelik M, Robinson SD, et al. **Coil combination of multichannel MRSI data at 7 T: MUSICAL.** *NMR Biomed* 2013;26:1796–805 CrossRef Medline
95. Feldman RE, Balchandani P. **A semiadiabatic spectral-spatial spectroscopic imaging (SASSI) sequence for improved high-field MR spectroscopic imaging.** *Magn Reson Med* 2016;76:1071–82 CrossRef Medline
96. Balchandani P, Pauly J, Spielman D. **Designing adiabatic radio frequency pulses using the Shinnar-Le Roux algorithm.** *Magn Reson Med* 2010;64:843–51 CrossRef Medline
97. Li N, Li S, Shen J. **High field *in vivo* ^{13}C magnetic resonance spectroscopy of brain by random radiofrequency heteronuclear decoupling and data undersampling.** *Front Phys*, 2017;5:26 CrossRef Medline
98. Wang Z, Lin JC, Mao W, et al. **SAR and temperature: simulations and comparison to regulatory limits for MRI.** *J Magn Reson Imaging* 2007;26:437–41 CrossRef Medline
99. Ogg RJ, Kingsley PB, Taylor JS. **WET, a T1- and B1-insensitive water-suppression method for in vivo localized 1H NMRS.** *J Magn Reson B* 1994;104:1–10 CrossRef Medline
100. Tkácõ I, Gruetter R. **Methodology of H NMR spectroscopy of the human brain at very high magnetic fields.** *Appl Magn Reson* 2005;29:139–57 CrossRef Medline
101. Stockmann J, Witzel T, Arango N, et al. (2017) *An integrated 32ch RF-shim array coil for improved B0 shimming of the brain at 7 Tesla.* A. A. Martinos Center for Biomedical Imaging, Charlestown, MA, United States. International Society for Magnetic Resonance in Medicine (ISMRM).
102. Verma G, Chawla S, Nagarajan R, et al. **Non-uniformly weighted sampling for faster localized two-dimensional correlated spectroscopy of the brain in vivo.** *J Magn Reson* 2017;277:104–12 CrossRef Medline
103. Fu Y, Ijare O, Thomas G, et al. **Implementation of wavelet encoding spectroscopic imaging technique on a 3 Tesla whole body MR scanner: in vitro results.** In: *Proceedings of the Annual International Conference of the IEEE Engineering in Medicine and Biology Society*, Minneapolis, MN, USA. September 3–6, 2009:2688–91
104. Geethanath S, Baek HM, Ganji SK, et al. **Compressive sensing could accelerate 1H MR metabolic imaging in the clinic.** *Radiology* 2012;262:985–94 CrossRef Medline
105. Cao P, Shin PJ, Park I, et al. **Accelerated high-bandwidth MR spectroscopic imaging using compressed sensing.** *Magn Reson Med* 2016;76:369–79 CrossRef Medline
106. Klauser A, Courvoisier S, Kasten J, et al. **Fast high-resolution brain metabolite mapping on a clinical 3T MRI by accelerated 1 H-FID-MRSI and low-rank constrained reconstruction.** *Magn Reson Med* 2019;81:2841–57 CrossRef Medline
107. Bogner W, Otazo R, Henning A. **Accelerated MR spectroscopic imaging-a review of current and emerging techniques.** *NMR Biomed* 2021;34:e4314 CrossRef Medline
108. Klauser A, Strasser B, Thapa B, et al. **Achieving high-resolution whole-brain slab 1H-MRSI with compressed-sensing and low-rank reconstruction at 7 Tesla.** *J Magn Reson* 2021;331:107048 CrossRef Medline

109. Verburg N, Koopman T, Yaqub MM, et al. **Improved detection of diffuse glioma infiltration with imaging combinations: a diagnostic accuracy study.** *Neuro Oncol* 2020;22:412–22 CrossRef Medline
110. Verburg N, Hoefnagels FWA, Barkhof F, et al. **Diagnostic accuracy of neuroimaging to delineate diffuse gliomas within the brain: a meta-analysis.** *AJNR Am J Neuroradiol* 2017;38:1884–91 CrossRef Medline
111. Croteau D, Scarpace L, Hearshen D, et al. **Correlation between magnetic resonance spectroscopy imaging and image-guided biopsies: semiquantitative and qualitative histopathological analyses of patients with untreated glioma.** *Neurosurgery* 2001;49:823–29 Medline
112. van der Kolk AG, Hendrikse J, Zwanenburg JJM, et al. **Clinical applications of 7 T MRI in the brain.** *Eur J Radiol* 2013;82:708–18 CrossRef Medline
113. Cordova JS, Shu HK, Liang Z, et al. **Whole-brain spectroscopic MRI biomarkers identify infiltrating margins in glioblastoma patients.** *Neuro Oncol* 2016;18:1180–89 CrossRef Medline
114. Hangel G, Strasser B, Povazõan M, et al. **Ultra-high resolution brain metabolite mapping at 7 T by short-TR Hadamard-encoded FID-MRSI.** *Neuroimage* 2018;168:199–210 CrossRef Medline
115. Moenninghoff C, Kraff O, Schlamann M, et al. **Assessing a dysplastic cerebellar gangliocytoma (Lhermitte-Duclos disease) with 7T MR imaging.** *Korean J Radiol* 2010;11:244–48 CrossRef Medline
116. Mönninghoff C, Maderwald S, Theysohn J, et al. **Imaging of brain metastases of bronchial carcinomas with 7 T MRI: initial results.** *Rofo* 2010;182:764–72 CrossRef Medline
117. Lupo JM, Banerjee S, Hammond KE, et al. **GRAPPA-based susceptibility-weighted imaging of normal volunteers and patients with brain tumor at 7 T.** *Magn Reson Imaging* 2009;27:480–88 CrossRef Medline
118. Tsien C, Galbán CJ, Chenevert TL, et al. **Parametric response map as an imaging biomarker to distinguish progression from pseudoprogression in high-grade glioma.** *J Clin Oncol* 2010;28:2293–99 CrossRef Medline
119. Leao DJ, Craig PG, Godoy LF, et al. **Response Assessment in Neuro-Oncology criteria for gliomas: practical approach using conventional and advanced techniques.** *AJNR Am J Neuroradiol* 2020;41:10–20 CrossRef Medline
120. Chukwueke UN, Wen PY. **Use of the Response Assessment in Neuro-Oncology (RANO) criteria in clinical trials and clinical practice.** *CNS Oncol* 2019;8:Cns28 CrossRef Medline
121. Brandsma D, Stalpers L, Taal W, et al. **Clinical features, mechanisms, and management of pseudoprogression in malignant gliomas.** *Lancet Oncol* 2008;9:453–61 CrossRef Medline
122. Hygino da Cruz LC, Rodriguez I, Domingues RC Jr, et al. **Pseudoprogression and pseudoresponse: imaging challenges in the assessment of posttreatment glioma.** *AJNR Am J Neuroradiol* 2011;32:1978–85 CrossRef Medline
123. Chen X, Wei X, Zhang Z, et al. **Differentiation of true-progression from pseudoprogression in glioblastoma treated with radiation therapy and concomitant temozolomide by GLCM texture analysis of conventional MRI.** *Clin Imaging* 2015;39:775–80 CrossRef Medline
124. Nasseri M, Gahramanov S, Netto JP, et al. **Evaluation of pseudoprogression in patients with glioblastoma multiforme using dynamic magnetic resonance imaging with ferumoxytol calls RANO criteria into question.** *Neuro Oncol* 2014;16:1146–54 CrossRef Medline
125. Zikou A, Sioka C, Alexiou GA, et al. **Radiation necrosis, pseudoprogression, pseudoresponse, and tumor recurrence: imaging challenges for the evaluation of treated gliomas.** *Contrast Media Mol Imaging* 2018;2018:6828396 CrossRef Medline
126. Ma B, Blakeley JO, Hong X, et al. **Applying amide proton transfer-weighted MRI to distinguish pseudoprogression from true progression in malignant gliomas.** *J Magn Reson Imaging* 2016;44:456–62 CrossRef Medline
127. Thust SC, van den Bent MJ, Smits M. **Pseudoprogression of brain tumors.** *J Magn Reson Imaging* 2018;48:571–89 CrossRef Medline
128. Brandes AA, Tosoni A, Spagnolli F, et al. **Disease progression or pseudoprogression after concomitant radiochemotherapy treatment: pitfalls in neurooncology.** *Neuro Oncol* 2008;10:361–67 CrossRef Medline
129. Gahramanov S, Muldoon LL, Varallyay CG, et al. **Pseudoprogression of glioblastoma after chemo- and radiation therapy: diagnosis by using dynamic susceptibility-weighted contrast-enhanced perfusion MR imaging with ferumoxytol versus gadoteridol and correlation with survival.** *Radiology* 2013;266:842–52 CrossRef Medline
130. Cha J, Kim ST, Kim H-J, et al. **Differentiation of tumor progression from pseudoprogression in patients with posttreatment glioblastoma using multiparametric histogram analysis.** *AJNR Am J Neuroradiol* 2014;35:1309–17 CrossRef Medline
131. Choi YJ, Kim HS, Jahng G-H, et al. **Pseudoprogression in patients with glioblastoma: added value of arterial spin labeling to dynamic susceptibility contrast perfusion MR imaging.** *Acta Radiol* 2013;54:448–54 CrossRef Medline
132. Shim H, Holder CA, Olson JJ. **Magnetic resonance spectroscopic imaging in the era of pseudoprogression and pseudoresponse in glioblastoma patient management.** *CNS Oncol* 2013;2:393–96 CrossRef Medline
133. Abbasi AW, Westerlaan HE, Holtman GA, et al. **Incidence of tumour progression and pseudoprogression in high-grade gliomas: a systematic review and meta-analysis.** *Clin Neuroradiol* 2018;28:401–11 CrossRef Medline
134. Andronesi OC, Esmaeili M, Borra RJ, et al. **Early changes in glioblastoma metabolism measured by MR spectroscopic imaging during combination of anti-angiogenic cediranib and chemoradiation therapy are associated with survival.** *NPJ Precis Oncol* 2017;1:120 CrossRef Medline
135. Li M, Ren X, Dong G, et al. **Distinguishing pseudoprogression from true early progression in isocitrate dehydrogenase wild-type glioblastoma by interrogating clinical, radiological, and molecular features.** *Front Oncol* 2021;11:627325 CrossRef Medline
136. Le Fevre C, Constans JM, Chambrelant I, et al. **Pseudoprogression versus true progression in glioblastoma patients: a multiapproach literature review, Part 2: radiological features and metric markers.** *Crit Rev Oncol Hematol* 2021;159:103230 CrossRef Medline
137. Kamada K, Houkin K, Abe H, et al. **Differentiation of cerebral radiation necrosis from tumor recurrence by proton magnetic resonance spectroscopy.** *Neurol Med Chir (Tokyo)* 1997;37:250–56 CrossRef Medline
138. Fink J, Born D, Chamberlain MC. **Pseudoprogression: relevance with respect to treatment of high-grade gliomas.** *Curr Treat Options Oncol* 2011;12:240–52 CrossRef Medline
139. Seeger A, Braun C, Skardelly M, et al. **Comparison of three different MR perfusion techniques and MRS for multiparametric assessment in distinguishing recurrent high-grade gliomas from stable disease.** *Acad Radiol* 2013;20:1557–65 CrossRef Medline
140. Elias AE, Carlos RC, Smith EA, et al. **MRS using normalized and non-normalized metabolite ratios for differentiating recurrent brain tumor from radiation injury.** *Acad Radiol* 2011;18:1101–08 CrossRef Medline
141. Smith EA, Carlos RC, Junck LR, et al. **Developing a clinical decision model: MRS to differentiate between recurrent tumor and radiation change in patients with new contrast-enhancing lesions.** *AJR Am J Roentgenol* 2009;192:W45–52 CrossRef Medline
142. Weybright P, Sundgren PC, Maly P, et al. **Differentiation between brain tumor recurrence and radiation injury using MRS.** *AJR Am J Roentgenol* 2005;185:1471–76 CrossRef Medline
143. Zeng QS, Li CF, Zhang K, et al. **Multivoxel 3D proton MRS in the distinction of recurrent glioma from radiation injury.** *J Neurooncol* 2007;84:63–69 CrossRef Medline
144. Knudsen-Baas KM, Moen G, Fluge Ø, et al. **Pseudoprogression in high-grade glioma.** *Acta Neurol Scand* 2013;127:31–37 CrossRef Medline
145. Verma G, Chawla S, Mohan S, et al. **Three-dimensional echo planar spectroscopic imaging for differentiation of true progression**

from pseudoprogression in patients with glioblastoma. *NMR Biomed* 2019;32:e4042 CrossRef Medline
146. Kong DS, Kim ST, Kim EH, et al. **Diagnostic dilemma of pseudoprogression in the treatment of newly diagnosed glioblastomas: the role of assessing relative cerebral blood flow volume and oxygen-6-methylguanine-DNA methyltransferase promoter methylation status.** *AJNR Am J Neuroradiol* 2011;32:382–87 CrossRef Medline
147. Pohmann R, Speck O, Scheffler K. **Signal-to-noise ratio and MR tissue parameters in human brain imaging at 3, 7, and 9.4 Tesla using current receive coil arrays.** *Magn Reson Med* 2016;75:801–09 CrossRef Medline
148. Wiggins GC, Potthast A, Triantafyllou C, et al. **Eight-channel phased array coil and detunable TEM volume coil for 7 T brain imaging.** *Magn Reson Med* 2005;54:235–40 CrossRef Medline
149. Oz G, Deelchand DK, Wijen JP, et al. **Advanced single voxel ^{1}H magnetic resonance spectroscopy techniques in humans: experts' consensus recommendations.** *NMR Biomed* 2020;e4236 CrossRef Medline
150. Tkac I, Oz G, Gruetter R. **Comparison of metabolite quantification in the human brain at 4 and 7 Tesla.** In: *Proceedings of the Scientific Meeting and Exhibition of the International Society for Magnetic Imaging in Medicine*, Miami Beach, Florida. May 7–13, 2005:2458
151. Su C, Liu C, Zhao L, et al. **Amide proton transfer imaging allows detection of glioma grades and tumor proliferation: comparison with Ki-67 expression and proton MR spectroscopy imaging.** *AJNR Am J Neuroradiol* 2017;38:1702–19 CrossRef Medline
152. Kim JH, Chang KH, Na DG, et al. **3T 1H-MRS in grading of cerebral gliomas: comparison of short and intermediate echo time sequences.** *AJNR Am J Neuroradiol* 2006;27:1412–18 Medline
153. Fudaba H, Shimomura T, Abe T, et al. **Comparison of multiple parameters obtained on 3T pulsed arterial spin-labeling, diffusion tensor imaging, and MRS and the Ki-67 labeling index in evaluating glioma grading.** *AJNR Am J Neuroradiol* 2014;35:2091–98 CrossRef Medline
154. Vamvakas A, Williams SC, Theodorou K, et al. **Imaging biomarker analysis of advanced multiparametric MRI for glioma grading.** *Phys Med* 2019;60:188–98 CrossRef Medline
155. Senft C, Hattingen E, Pilatus U, et al. **Diagnostic value of proton magnetic resonance spectroscopy in the noninvasive grading of solid gliomas: comparison of maximum and mean choline values.** *Neurosurgery* 2009;65:908–13; discussion 913 CrossRef Medline
156. Sakata A, Fushimi Y, Okada T, et al. **Diagnostic performance between contrast enhancement, proton MRS, and amide proton transfer imaging in patients with brain tumors.** *J Magn Reson Imaging* 2017;46:732–39 CrossRef Medline
157. Bradac O, Vrana J, Jiru F, et al. **Recognition of anaplastic foci within low-grade gliomas using MRS.** *Br J Neurosurg* 2014;28:631–36 CrossRef Medline
158. Chung C, Metser U, Menard C. **Advances in magnetic resonance imaging and positron emission tomography imaging for grading and molecular characterization of glioma.** *Semin Radiat Oncol* 2015;25:164–71 CrossRef Medline
159. Delikatny EJ, Chawla S, Leung D-J, et al. **MR-visible lipids and the tumor microenvironment.** *NMR Biomed* 2011;24:592–611 CrossRef Medline
160. Feng DX, McCauley JP, Morgan–Curtis FK, et al. **Evaluation of 39 medical implants at 7.0 T.** *Br J Radiol* 2015;88:20150633 CrossRef Medline
161. Kraff O, Wrede KH, Schoemberg T, et al. **MR safety assessment of potential RF heating from cranial fixation plates at 7 T.** *Med Phys* 2013;40:042302 CrossRef Medline
162. Chen B, Schoemberg T, Kraff O, et al. **Cranial fixation plates in cerebral magnetic resonance imaging: a 3 and 7 Tesla in vivo image quality study.** *MAGMA* 2016;29:389–98 CrossRef Medline
163. Kraff O, Quick HH. **7T: Physics, safety, and potential clinical applications.** *J Magn Reson Imaging* 2017;46:1573–89 CrossRef Medline
164. Okada T, Akasaka T, Thuy DH, et al. **Safety for human MR scanners at 7T.** *Magn Reson Med Sci* 2021 Aug 6 [Epub ahead of print] CrossRef Medline
165. Fagan AJ, Bitz AK, Björkman-Burtscher IM, et al; ISMRM Safety Committee. **7T MR safety.** *J Magn Reson Imaging* 2021;53:333–46 CrossRef Medline
166. Moser E, Stahlberg F, Ladd ME, et al. **7-T MR: from research to clinical applications?** *NMR Biomed* 2012;25:695–716 CrossRef Medline
167. Mikkelsen M, Rimbault DL, Barker PB, et al. **Big GABA II: water-referenced edited MRS at 25 research sites.** *Neuroimage* 2019;191:537–48 CrossRef Medline
168. Near J, Harris AD, Juchem C, et al. **Preprocessing, analysis and quantification in single-voxel magnetic resonance spectroscopy: experts' consensus recommendations.** *NMR Biomed* 2021;34:e4257 CrossRef
169. Branzoli F, Di Stefano AL, Capelle L, et al. **Highly specific determination of IDH status using edited in vivo magnetic resonance spectroscopy.** *Neuro Oncol* 2018;20:907–16 CrossRef Medline
170. Vareth M, Lupo J, Larson P, et al. **A comparison of coil combination strategies in 3D multi-channel MRSI reconstruction for patients with brain tumors.** *NMR Biomed* 2018;31:e3929 CrossRef Medline
171. Neal A, Moffat BA, Stein JM, et al. **Glutamate weighted imaging contrast in gliomas with 7 Tesla magnetic resonance imaging.** *Neuroimage Clin* 2019;22:101694 CrossRef Medline
172. Kudo H, Mio T, Kokunai T, et al. **Quantitative analysis of glutathione in human brain tumors.** *J Neurosurg* 1990;72:610–15 CrossRef Medline
173. Rocha CR, Garcia CC, Vieira DB, et al. **Glutathione depletion sensitizes cisplatin- and temozolomide-resistant glioma cells in vitro and in vivo.** *Cell Death Dis* 2014;5:e1505 CrossRef Medline
174. Prisciandaro JJ, Mikkelsen M, Saleh MG, et al. **An evaluation of the reproducibility of (1)H-MRS GABA and GSH levels acquired in healthy volunteers with J-difference editing sequences at varying echo times.** *Magn Reson Imaging* 2020;65:109–13 CrossRef Medline
175. Bottino F, Lucignani M, Napolitano A, et al. **In vivo brain GSH: MRS methods and clinical applications.** *Antioxidants (Basel)* 2021;10:1407 CrossRef Medline
176. Branco M, Linhares P, Carvalho B, et al. **Serum lactate levels are associated with glioma malignancy grade.** *Clin Neurol Neurosurg* 2019;186:105546 CrossRef Medline
177. Reuss AM, Gross D, Buchfelder M, et al. **The acidic brain-glycolytic switch in the microenvironment of malignant glioma.** *Int J Mol Sci* 2021;22:5518 CrossRef Medline
178. Daniele S, Giacomelli C, Zappelli E, et al. **Lactate dehydrogenase: A inhibition induces human glioblastoma multiforme stem cell differentiation and death.** *Sci Rep* 2015;5:15556 CrossRef Medline
179. de la Cruz-López KG, Castro-Muñoz LJ, Reyes-Hernández DO, et al. **Lactate in the regulation of tumor microenvironment and therapeutic approaches.** *Front Oncol* 2019;9:1143 CrossRef Medline
180. Bulik M, Jancalek R, Vanicek J, et al. **Potential of MRS for assessment of glioma grading.** *Clin Neurol Neurosurg* 2013;115:146–53 CrossRef Medline
181. Hérigault G, Zoula S, Rémy C, et al. **Multi-spin-echo J-resolved spectroscopic imaging without water suppression: application to a rat glioma at 7 T.** *MAGMA*2004;17:140–48 CrossRef Medline
182. Gonen OM, Moffat BA, Kwan P, et al. **Reproducibility of glutamate, glutathione, and GABA measurements in vivo by single-voxel STEAM magnetic resonance spectroscopy at 7-Tesla in healthy individuals.** *Front Neurosci* 2020;14:566643 CrossRef Medline

Call to Action: Women in Neuroradiology's Group (WINNERS)—Is There a Need?

A. Singhal and A. Aiken

It is well-known that radiology is one of the male-dominated specialties in medicine (33.5% women).[1] There has been extensive interest in studying gender disparities in all fields of medicine, including radiology recently.[2] Improving gender and cultural diversity helps to promote scientific advancement; increases diversity of perspectives, teamwork innovation, and creativity; produces more effective approaches to complex problems; and improves access to care for underserved groups.[3-7] The American Association of Medical Colleges recently launched a strong initiative imploring its member institutions and societies to be intentional in addressing gender inequities, emphasizing that gender equity is a key factor in achieving excellence in academic medicine.[8,9]

Gender Diversity in Medicine and the Motherhood Penalty

Female physicians are equally as likely as men to enter a career in academic medicine, but the overall proportion of women who are full professors is significantly lower, despite accounting for age, experience, specialty, and measures of research productivity.[10-12] Female faculty physicians are promoted more slowly than men, with more men than women on the tenure track.[11,13] Female physicians do not achieve the same level of career success, as measured by research funding, publications, promotions, and leadership positions.[12,14] Several studies have investigated the underlying factors and have shown less opportunity for academic advancement, lack of sponsorship, decreased availability of same-sex mentors, lack of research opportunities with greater difficulty in getting funding from the National Institutes of Health, the difficulty of raising a family while building a career, work-life integration, inequities and biases, and attrition of female faculty.[10,14-17] Lack of role models for combining career and family and work-life balance and the lack of a supportive environment were found to be important factors in a female physician's decision not only to leave an institution but also to leave the practice of medicine or work part-time.[18,19]

Physicians who are mothers are affected to a greater degree by societal norms, and a sociologic term called the "motherhood penalty" has been coined to describe discrimination to which mothers are subject in the workplace compared with men with or without children or women without children.[14,20,21] More than one-third of mothers particularly reported discrimination related to pregnancy, maternity leave, or breastfeeding, and discrimination is associated with higher burnout rates.[14] Motherhood in the workplace has been shown to be associated with decreased pay, perceptions of lower competence and of lower commitment to one's career, and being less likely to be hired and promoted.[21-23] Studies, however, contrarily have demonstrated increased productivity of mothers during a career compared with peers without children and that mothers bring unique skills to leadership roles.[19,21,24] Most female physicians felt the need for more support to thrive in their careers, especially for maternity leave and returning to work, including paid maternity leave, breastfeeding/pumping support, and schedule flexibility.[25] In a systematic review of challenges faced by physician mothers, a lack of dedicated women's networks, mentors, sponsors, coaches, role models, and professional development opportunities were found to be the most commonly cited organizational issues.[14] It has been further shown that female physicians were less likely than male physicians to receive career support through networking activities, with the effect increased more for those physicians with children than for those without.[14,26]

To clarify, mentorship is a longitudinal relationship in which a mentor advises, shares knowledge with, and gives feedback to a mentee for career development, whereas sponsorship is when a protégé is directly advocated and recommended by a sponsor for career-advancing opportunities.[27,28] Having an identifiable mentor increases a physician's chance of being promoted 2-fold.[29] Professionals with sponsors are 23% more likely than their peers to be promoted.[30,31] Female physician mentorship of female medical students or residents was found to be an important strategy for recruitment in a study in Japan.[32] Having facilitating colleague support groups is an effective, preventive intervention in mitigating burnout and distress among mothers at high risk for stress, leading to increased engagement at work and decreased parenting-associated stress.[14,33]

A study by Gordinier et al[34] emphasized that mentorship does not need to be only gender-specific because it reported the ability to successfully balance family and full-time practice as the most commonly cited quality in an ideal mentor. However, female physicians have reported lower satisfaction with existing mentorship programs than males.[16] Lack of women in leadership has been suggested as a factor; increasing the role of women in leadership positions could be a solution.[10,14] It is critical that physicians who are leaders with experience balancing career and family advocate for mothers who are junior physicians, not only as mentors but also to affect institutional changes including increased job flexibility and institutional support.

Gender Diversity in Radiology

Recent articles have highlighted gender disparities in radiology, including underrepresentation in leadership roles as well as higher promotion ranks in radiology.[2,10,35] Female radiologists, on average, had fewer total publications, fewer first or last author publications, and lower h-indexes and were less likely than men to have National Institutes of Health funding.[2,35] Women worked part-time more often and held fewer positions of power in hospitals and on editorial boards and in academic levels of associate and full professors.[2] Without accounting for any contributing factors in an analysis of US academic radiologists, female radiologists were less likely to hold the rank of full professor compared with men, but

Received June 20, 2022; accepted after revision July 6.
http://dx.doi.org/10.3174/ajnr.A7626

after multivariate adjustment, there was no significant difference found in 1 study. The authors concluded that female radiologists may lack sufficient opportunity to reach parity in research productivity.[35] Several barriers found by female radiologists are similar to those in other fields, such as a lack of mentorship, funding, and research opportunities; obstacles related to child rearing, work, and family alignment difficulties; and discrimination and sexual harassment.[2,10,36-38]

Gender Diversity in Neuroradiology

Specifically in neuroradiology, there are more men working relative to women, with highly significant gender disparity for leadership positions in neuroradiology (87.5% of leadership ranks within academic neuroradiology are held by men).[10] Gender disparity was not found when analyzing academic ranks, with women filling 25% of assistant, 23% of associate, and 21% of full professor positions. These proportions could simply be a reflection of the proportion of female radiology residents (27%), which otherwise points to general underrepresentation of women in radiology compared with the percentage of female medical students (47% in 2015).[10,39] The median h-index was higher for male (17.5) compared with female faculty members (9). Furthermore, the latest data regarding authorship in 155 international neurology-related journals showed the largest gender disparity in authorship in neuroradiology journals compared with neurology and neurology-related subspecialties.[6] The proportion of women authors in the studied neurological journals (which included neuroradiology journals) was not reflective of the gender proportions in the respective fields and fell short of them. There was also a tendency for same-gender senior and junior authors to publish together, increasing authorship gender inequities.[6] The greatest gender disparity was seen in the last authorship position, which likely reflects the proportion of senior leadership in the field. Gender proportion underrepresentation on editorial boards likely also contributes.[6,38]

Current Effort

American Association of Women in Radiology (AAWR) has a plethora of resources for women in radiology and their allies.[40,41] With increased momentum toward reducing gender disparities, several academic institutions in the United States have Women in Radiology programs,[42,43] and there is increased interest in outreach to the medical student levels.[39,44,45] Radiology societies such as the Society of Interventional Radiology have implemented Women In Radiology programs.[46] While just more than one-quarter of women are radiologists, which is already low, there is a further relative dearth of women in neuroradiology, with ASNR membership including <18% women in 2018. The ASNR leadership landscape has changed during the past decade with 5 of the 9 Presidents being women in the past decade compared with only 2 of the previous 46 Presidents until 2009.[47] While it is extremely important and inspirational to see women in top academic societal leadership positions, women in neuroradiology still often lack female colleagues within their institutions, and individual institutional level programs specific to neuroradiology are difficult to implement. Specialty-specific programs have a greater chance of networking opportunities for academic collaboration and mentorship. It is suggested that professional organizations adopt principles that strategically enhance diversity and inclusion.[9,48] Recognizing the contributions of women in leadership with awards, developing health policy documents, and reporting data on diversity and inclusion are some of the ways suggested in another specialty to enhance recruitment, retention, and career advancement of female physicians.[48] The Women in Neuroradiology award instituted by the ASNR in 2012 has also been a positive change in recognizing women with leadership potential and supporting their leadership development with positive outcomes.[47] Very recently, a new award called the American Society of Functional Neuroradiology-AAWR "Carolyn C. Meltzer" Joint Award has been instituted, aiming to increase the number of women engaged in the field of functional neuroradiology.

Gaps and Proposed Future Effort

While the current effort shows remarkable forward momentum, there are several other strategies, albeit more time- and labor-intensive as discussed above, which have been shown to be helpful in improving gender disparities such as mentorship and advocacy. It is critical to connect women with mentors who have successful work-life integration through positive formal and informal mentorship and sponsorship programs, such as support groups and female-focused networking events.[2,14,15,30,33,43,45,48,49] Mentorship and sponsorship of women and leadership programs directly impact advancement and career satisfaction and retention of female faculty.[14,47,50,51] Participation in a female-focused professional organization creates opportunities that facilitate scholarly work and leadership, which ultimately enhances retention and advancement of female physicians.[49] Additionally, the onus of increasing gender diversity by promoting, mentoring, and including women should not be on women only, especially when in male-dominated fields. Therefore, allyship from men and leaders is also necessary in improving gender equity in various fields.[8,52-54]

These data and discussions speak of a need to increase effort at a national and international societal level to help support advancement of women in neuroradiology and to attract more female medical students and residents into the field, thereby increasing diversity in the field. The authors, therefore, propose creation of an interest group/branch/subcommittee for women in neuroradiology with a suggested name of WINNERS (Women IN NEuroRadiology's group). We propose that this group welcome participation by women as well as allies.

The goal of the WINNERS group would be to bring interested female neuroradiologists and allies together for discussion, networking, mentoring, sponsorship opportunities, and academic collaboration to promote advancement and retention of women in neuroradiology and, thereby, increase diversity in the practice of radiology. WINNERS would be a great way to accomplish important goals to increase diversity of the neuroradiology workforce and include more female neuroradiologists in various roles, including leadership, and combat the motherhood penalty.[19,21] Areas of focus would include the following: 1) providing a forum for women to discuss and suggest processes and pathways that support workplace flexibility and work-life integration for neuroradiologists; 2) facilitating open and nonjudgmental discussions around the topic of work-life balance that can help reset the norm; 3) giving parents professional support and discussing pathways to

leadership; 4) finding innovative ways to research and better understand underlying barriers and ways to address them; and 5) discussing strategies for recruiting and retaining women in neuroradiology practice and neuroradiology academic departments and sharing aspects of work cultures of institutions they might consider joining. By way of example, the creation of such a group would encourage female radiologists and trainees to envision successful careers in neuroradiology. To achieve the goal of decreasing gender disparities in neuroradiology, current and future female neuroradiologists need to feel included and supported, and bringing them together would be the first step for this endeavor.

Disclosure forms provided by the authors are available with the full text and PDF of this article at www.ajnr.org.

REFERENCES

1. Cater SW, Yoon SC, Lowell DA, et al. **Bridging the gap: identifying global trends in gender disparity among the radiology physician workforce.** *Acad Radiol* 2018;25:1052–61 CrossRef Medline
2. Fichera G, Busch IM, Rimondini M, et al. **Is empowerment of female radiologists still needed? Findings of a systematic review.** *Int J Environ Res Public Health* 2021;18:1542 CrossRef Medline
3. Adjo J, Maybank A, Prakash V. **Building inclusive work environments.** *Pediatrics* 2021;148(Suppl 2):e2021051449E CrossRef Medline
4. Campbell LG, Mehtani S, Dozier ME, et al. **Gender-heterogeneous working groups produce higher quality science.** *PLoS One* 2013;8:e79147 CrossRef Medline
5. Kubik-Huch RA, Vilgrain V, Krestin GP, et al. **Women in radiology: gender diversity is not a metric, it is a tool for excellence.** *Eur Radiol* 2020;30:1644–52 CrossRef Medline
6. Nguyen AX, Yoffe L, Li A, et al. **Gender gap in neurology research authorship (1946-2020).** *Front Neurol* 2021;12:715428 CrossRef Medline
7. Valantine HA, Collins FS. **National Institutes of Health addresses the science of diversity.** *Proc Natl Acad Sci U S A* 2015;112:12240–42 CrossRef Medline
8. Acosta DA, Lautenberger DM, Castillo-Page L, et al. **Achieving gender equity is our responsibility: leadership matters.** *Acad Med* 2020;95:1468–71 CrossRef Medline
9. Association of American Medical Colleges. AAMC statement on gender equity. https://www.aamc.org/about-us/equity-diversity-inclusion/aamc-statement-gender-equity. Accessed March 5, 2022
10. Ahmadi M, Khurshid K, Sanelli PC, et al. **Influences for gender disparity in academic neuroradiology.** *AJNR Am J Neuroradiol* 2018;39:18–23 CrossRef Medline
11. Jena AB, Khullar D, Ho O, et al. **Sex differences in academic rank in US medical schools in 2014.** *JAMA* 2015;314:1149–58 CrossRef Medline
12. Jolly S, Griffith KA, DeCastro R, et al. **Gender differences in time spent on parenting and domestic responsibilities by high-achieving young physician-researchers.** *Ann Intern Med* 2014;160:344–53 CrossRef Medline
13. Tesch BJ, Wood HM, Helwig AL, et al. **Promotion of women physicians in academic medicine: glass ceiling or sticky floor?** *JAMA* 1995;273:1022–25 Medline
14. Chesak SS, Yngve KC, Taylor JM, et al. **Challenges and solutions for physician mothers: a critical review of the literature.** *Mayo Clin Proc* 2021;96:1578–91 CrossRef Medline
15. Howell LP, Beckett LA, Nettiksimmons J, et al. **Generational and gender perspectives on career flexibility: ensuring the faculty workforce of the future.** *Am J Med* 2012;125:719–28 CrossRef Medline
16. Kaplan SH, Sullivan LM, Dukes KA, et al. **Sex differences in academic advancement: results of a national study of pediatricians.** *N Engl J Med* 1996;335:1282–89 CrossRef Medline
17. Villablanca AC, Li Y, Beckett LA, et al. **Evaluating a medical school's climate for women's success: outcomes for faculty recruitment, retention, and promotion.** *J Womens Health (Larchmt)* 2017;26:530–39 CrossRef Medline
18. Webb AM, Hasty BN, Andolsek KM, et al. **A timely problem: parental leave during medical training.** *Acad Med* 2019;94:1631–34 CrossRef Medline
19. Polan RM, Mattei LH, Barber EL. **The motherhood penalty in obstetrics and gynecology training.** *Obstet Gynecol* 2022;139:9–13 CrossRef Medline
20. Jagsi R, Tarbell NJ, Weinstein DF. **Becoming a doctor, starting a family–leaves of absence from graduate medical education.** *N Engl J Med* 2007;357:1889–91 CrossRef Medline
21. Wang SS, Ackerman S. **The motherhood penalty: is it alive and well in 2020?** *J Am Coll Radiol* 2020;17:688–89 CrossRef Medline
22. Correll SJ. *Minimizing the Motherhood Penalty: What Works, What Doesn't and Why*. Gender and Work, Challenging Conventional Wisdom; 2013
23. Correll SJ, Benard S, Paik I. **Getting a job: is there a motherhood penalty?** *Am J Sociol* 2007;112:1297–1339 CrossRef
24. Krapf M, Ursprung HW, Zimmermann C. **Parenthood and productivity of highly skilled labor: evidence from the groves of academe.** *Journal of Economic Behavior & Organization* 2017;140:147–75 CrossRef
25. Juengst SB, Royston A, Huang I, et al. **Family leave and return-to-work experiences of physician mothers.** *JAMA Netw Open* 2019;2:e1913054 CrossRef Medline
26. Buddeberg-Fischer B, Stamm M, Buddeberg C, et al. **The impact of gender and parenthood on physicians' careers–professional and personal situation seven years after graduation.** *BMC Health Serv Res* 2010;10:40 CrossRef Medline
27. Ayyala MS, Skarupski K, Bodurtha JN, et al. **Mentorship is not enough: exploring sponsorship and its role in career advancement in academic medicine.** *Acad Med* 2019;94:94–100 CrossRef Medline
28. Deitte LA, McGinty GB, Canon CL, et al. **Shifting from mentorship to sponsorship-a game changer!** *J Am Coll Radiol* 2019;16:498–500 CrossRef Medline
29. Beasley BW, Simon SD, Wright SM. **A time to be promoted: the Prospective Study of Promotion in Academia (Prospective Study of Promotion in Academia).** *J Gen Intern Med* 2006;21:123–29 CrossRef Medline
30. Clark D. **How Women Can Develop — and Promote — Their Personal Brand.** *Harvard Business Review*. March 2, 2018. https://hbr.org/2018/03/how-women-can-develop-and-promote-their-personal-brand. Accessed March 5, 2022
31. Hewlett SA. *Forget a Mentor, Find a Sponsor: The New Way to Fast-Track Your Career*, Published September 10, 2013. Harvard Business Review Press; 2013
32. Yamazaki Y, Uka T, Marui E. **Professional fulfillment and parenting work-life balance in female physicians in basic sciences and medical research: a nationwide cross-sectional survey of all 80 medical schools in Japan.** *Hum Resour Health* 2017;15:65 CrossRef Medline
33. Luthar SS, Curlee A, Tye SJ, et al. **Fostering resilience among mothers under stress: "authentic connections groups" for medical professionals.** *Womens Health Issues* 2017;27:382–90 CrossRef Medline
34. Gordinier ME, Ramondetta LM, Parker LP, et al. **Survey of female gynecologic oncologists and fellows: balancing professional and personal life.** *Gynecol Oncol* 2000;79:309–14 CrossRef Medline
35. Kapoor N, Blumenthal DM, Smith SE, et al. **Gender differences in academic rank of radiologists in U.S. medical schools.** *Radiology* 2017;283:140–47 CrossRef Medline
36. Baker SR, Barry M, Chaudhry H, et al. **Women as radiologists: are there barriers to entry and advancement?** *J Am Coll Radiol* 2006;3:131–34 CrossRef Medline
37. Jutras M, Malekafzali L, Jung S, et al. **National Institutes of Health: gender differences in radiology funding.** *Acad Radiol* 2020;29:748–54 CrossRef Medline
38. Potterton VK, Ruan S, Sunshine JH, et al. **Why don't female medical students choose diagnostic radiology? A review of the current literature.** *J Am Coll Radiol* 2004;1:583–90 CrossRef Medline

39. Podsiadlo V, DeBenedectis CM. **Breaking the stereotype: interventions aimed at changing medical student misperceptions of radiology and increasing the female match rate.** *Acad Radiol* 2020;29(Suppl 5):527–33 CrossRef Medline
40. DeBenedectis CM, Schmitt C, Porter KK, et al. **American Association for Women in Radiology.** *Clin Imaging* 2021;80:353–58 CrossRef Medline
41. Spalluto LB, Arleo EK, Macura KJ, et al. **35 years of experience from the American Association for Women Radiologists: increasing the visibility of women in radiology.** *J Am Coll Radiol* 2017;14:426–30 CrossRef Medline
42. Kamel SI, Itani M, Leschied JR, et al. **Establishing a women-in-radiology group: a toolkit from the American Association for Women in Radiology.** *AJR Am J Roentgenol* 2021;217:1452–60 CrossRef Medline
43. Ladd LM, Bonaminio DN, Gonda AS, et al. **A mentorship and networking group for women in radiology.** *J Am Coll Radiol* 2017;14:987–90 CrossRef Medline
44. Forman HP, Larson DB, Kaye AD, et al. **Masters of radiology panel discussion: women in radiology: how can we encourage more women to join the field and become leaders?** *AJR Am J Roentgenol* 2012;198:145–49 CrossRef Medline
45. Gaetke-Udager K, Magid D, Smith M, et al. **Recruiting future radiologists: how can we do better?** *Acad Radiology* 2020;27:1311–15 CrossRef Medline
46. Society of Interventional Radiology. **Women in IR.** https://www.sirweb.org/member-central/volunteer/sections/women-in-ir-section/. Accessed March 5, 2022
47. Meltzer CC, Sanelli PC, Hepp MB, et al. **Women rising to the top: the tipping point for the ASNR.** *AJNR Am J Neuroradiol* 2019;40:2–4 CrossRef Medline
48. Sharma G, Sarma AA, Walsh MN, et al; American College of Cardiology Women in Cardiology Leadership Council and Diversity and Inclusion Task Force. **10 recommendations to enhance recruitment, retention, and career advancement of women cardiologists.** *J Am Coll Cardiol* 2019;74:1839–42 CrossRef Medline
49. Lin MP, Lall MD, Samuels-Kalow M, et al. **Impact of a women-focused professional organization on academic retention and advancement: perceptions from a qualitative study.** *Acad Emerg Med* 2019;26:303–16 CrossRef Medline
50. Weigel KS, Kubik-Huch RA, Gebhard C. **Women in radiology: why is the pipeline still leaking and how can we plug it?** *Acta Radiol* 2020;61:743–48 CrossRef Medline
51. Perry RE, Parikh JR. **Sponsorship: a proven strategy for promoting career advancement and diversity in radiology.** *J Am Coll Radiol* 2019;16:1102–07 CrossRef Medline
52. Bilal M, Balzora S, Pochapin MB, et al. **The need for allyship in achieving gender equity in gastroenterology.** *Am J Gastroenterol* 2021;116:2321–23 CrossRef Medline
53. Trudell AM, Frankel WC, Luc JG, et al. **Enhancing support for women in cardiothoracic surgery through allyship and targeted initiatives.** *Ann Thorac Surg* 2021;113:1676–83 CrossRef Medline
54. Wood DE. **How can men be good allies for women in surgery? #HeForShe.** *J Thorac Dis* 2021;13:492–501 CrossRef Medline

Neck Imaging Reporting and Data System: More Than Just a Template

P.A. Rhyner, A.A. Bhatt, K.L. Baugnon, and A.H. Aiken

ABSTRACT

SUMMARY: The Neck Imaging Reporting and Data System (NI-RADS) is a guide developed and introduced in 2017 by head and neck radiologists who worked in an academic radiology department. Based on the Breast Imaging Reporting and Data System, the initial goals of NI-RADS were to make posttreatment head and neck cancer imaging dictations more succinct and efficient, guide treating physicians in the next appropriate steps when recurrence was suspected, and encourage institutional and national research. NI-RADS is more than a dictation template, and it is best instituted after a head and neck imaging practice is established. We support the use of NI-RADS once a radiologist understands the nuances of head and neck cancer, including the biology, common subsites involved, essentials of tumor staging, common posttreatment benign imaging appearances, and subtleties of recurrent disease.

ABBREVIATIONS: CECT = contrast-enhanced CT; HN = head and neck; HNC = head and neck cancer; NI-RADS = Neck Imaging Reporting and Data System; TB = tumor board

The Neck Imaging Reporting and Data System (NI-RADS) is a guide developed and introduced in 2017 by head and neck radiologists who worked in an academic radiology department. Based on the widely successful Breast Imaging Reporting and Data System, the initial goals of NI-RADS were to make dictations of posttreatment head and neck cancer (HNC) imaging more succinct and efficient, guide treating physicians in the next appropriate steps when recurrence was suspected, and encourage research both within the institution and nationally.[1]

The clinical setting that allowed NI-RADS to develop and be successful is important. There were 4 neuroradiologists with extensive head and neck (HN) expertise, and all understood the HNC biology of the disease, clinical presentations, variations in imaging based on different pathology, treatment modalities including indications for each, and the nuances of recurrent disease and treatment complications. We were part of a large HNC practice with standardized imaging protocols, surveillance schedules and regimens, and weekly tumor boards (TBs). With time, we knew the accuracy of our interpretations, including results of our recommended biopsies for suspected recurrence at the primary site and pathologic adenopathy.

Formal TB presentations were succinct and direct because we knew exactly the clinical setting or issue, based on our knowledge of the disease. TB discussions and decisions were made with multidisciplinary input. When there was controversy regarding staging or treatment decisions, the conversations were spirited, and this scenario is when we learned the most, even as experienced HNC imagers. In our academic practice, neuroradiology fellows and radiology residents routinely reported that the TB experience added to their HNC knowledge base, but it also impacted their understanding of how critical it is to generate accurate imaging interpretations. As members of the HNC team, we were trusted by nonradiology team members. With this historical background, one can understand how our use of NI-RADS was readily accepted by the HNC team.[2]

As the volume increased, the need for efficiency in our reports was obvious. Surveillance imaging was a prime example. Does every incidental finding on each follow-up study in the patient with HNC need to be described again? Surveillance imaging goals are the following: 1) primary site treatment response, 2) status of lymph nodes in ipsilateral neck, 3) status of lymph nodes in the contralateral neck, 4) second primary disease, and 5) treatment complications, especially radiation-related soft-tissue or bone necrosis or carotid artery disease. Recommendations based on surveillance posttreatment imaging are limited and are the following:

1) Continue with established surveillance regimens if the study is negative for recurrence
2) Use shorter interval follow-up if recurrence is possible but not definite

Received April 15, 2022; accepted after revision July 5.

From the Department of Radiology (P.A.R., A.A.B.), Mayo Clinic, Jacksonville, Florida; and Department of Radiology and Imaging Sciences (K.L.B., A.H.A.), Emory University School of Medicine, Atlanta, Georgia.

Please address correspondence to Patricia A. Rhyner, MD, FACR, Department of Radiology, Mayo Clinic, 4500 San Pablo Rd, Jacksonville, FL 32224; e-mail: Rhyner.patricia3@gmail.com; @phudge54

http://dx.doi.org/10.3174/ajnr.A7627

NI-RADS history example

Tumor site	Right tonsil
Initial stage	T3 (tumor >4 cm), N2 (bilateral pathologic adenopathy)
Treatment	Definitive chemoradiation
Final treatment	12 Months ago
Initial posttreatment PET/CECT	No residual disease

3) Direct endoscopic assessment if a mucosal abnormality is present on imaging
4) Perform additional diagnostic imaging with another modality (usually MR imaging, as surveillance imaging was usually CECT)
5) Perform PET/CT or image-guided biopsy if a deep recurrence is suspected.

Except for endoscopy, the recommendations are based on imaging or biopsy with image guidance. Therefore, the responsibility for the posttreatment imaging recommendations is the purview of the radiologist.

NI-RADS is more than a simple template to improve dictating efficiency. When a radiologist uses such a specialized reporting system, especially when next-step treatment recommendations are part of the system, the user should be familiar with the disease process and all the variations. The bulk of the template is to assess the primary site and nodal drainage basins.[3] A brief bulleted history of the disease before the findings section of the report is helpful (Table). The date of presentation, initial tumor stage including primary and nodal disease, and the initial treatment technique and date can be listed. For radiation treatment, knowing the time since the final treatment is necessary because posttreatment imaging before 10–12 weeks after treatment is not recommended. Knowing the patient's status, whether the patient is asymptomatic, has a new palpable mass, has pain and what the specialist sees during the most recent outpatient visit is very important.

It is obvious, then, that adopting and using NI-RADS in daily practice is more than simply inputting a template into a speech-recognition program. Using NI-RADS is a final step, not an initial step, in radiology practice. Without an infrastructure of knowledge, experience, and trust between HN radiologists and a referral clinical practice, NI-RADS should not be used. It requires much more than finding soft-tissue "fullness" or unusual, vague contrast enhancement on imaging.

If a radiology practice does not have dedicated HN neuroradiologists, a subspecialized dictation template can be still be used, but it is best instituted after appropriate preparation and infrastructure development. The following recommendations can serve as a guide to developing an efficient HN service:

1) Standardize imaging protocols at all sites. CECT, MRI, and PET/CT techniques should be established for accurate comparisons among initial, posttreatment, and surveillance scans. This process includes scan acquisition parameters, scanner angulation, slice thickness, and even which series are sent to the PACS. Standardized intravenous contrast protocols are critical: dose, bolus technique, and timing of acquisition during or after the contrast bolus. In-service educational conferences for CT and MRI technologists help establish and maintain standardization and reinforce the team-based approach to the care of patients with HNC.
2) Establish imaging algorithms with referrers. Surgeons and oncologists must understand that the availability of both pretreatment and baseline posttreatment imaging results in the best patient care. This involves uploading imaging examinations from an outside institution and formal re-interpretation by an internal radiologist. It is important to have a pretreatment examination before biopsy because postbiopsy change can sometimes hinder accurate staging on imaging. Recognizing recurrent disease is facilitated by knowing what the tumor initially looked like and where it was located prior to treatment. In our experience, the concept of baseline posttreatment imaging was new to some providers. When we likened baseline imaging to the baseline posttreatment physical examination, referring clinicians better understood the need for a predictable time and modality for posttreatment imaging. In our practice, the modality was usually PET coupled with CECT at 12 weeks after the end of treatment. Universal surveillance imaging algorithms, with respect to timing and modality, have not been determined, but an individual HNC group can establish their own algorithm.
3) Establish a core group of radiologists to interpret HNC imaging. One goal of NI-RADS is consistency across imaging techniques, timing of surveillance, and interpretation. A small group of radiologists can more easily agree to standardized interpretations than a large group, with expected differences in interpretation styles, experience, and confidence levels. A smaller group, maybe 2–4 HN radiologists, can better agree on what constitutes worrisome or definite findings of recurrence. Even 1 outlier who routinely overcalls indeterminate findings can impact the practice. Routine meetings among the core group of radiologists helps standardize the imaging approach to a patient with HNC.
4) HN imagers must recognize the appearance of recurrent HN cancer. Recurrent HNC is rarely an easily appreciated "new necrotic peripherally enhancing mass." Recurrent tumor in the HN is often subtle: loss of fat planes, gradual changes in reconstructive flap morphology, perineural tumor, muscle denervation, or increasing size of small non-necrotic nodes that are in the expected draining nodal basin. Nodal size criteria are not a reliable predictor of nodal metastasis. Squamous cell carcinoma, the most common tumor, behaves in a different manner depending on the subsite. A true vocal cord tumor and a tonsil carcinoma have different imaging appearances, treatment, and recurrence patterns that are unique to each subsite. Therefore, it is critical that the radiologist know the HN subsites, normal and variant appearances, first- and second-order nodal drainage, common treatment modalities, and the specific imaging appearance of recurrent tumor. This knowledge requires a broad and detailed base because there is no universal and predictable recurrent-tumor appearance. Case sharing and discussion helped our group improve the knowledge base.
5) Attend TBs and routinely get clinical follow-up, including for operative and image-guided biopsies. Discussion at TBs helps the radiologist understand the nuances of HNC and what specific knowledge various treating clinicians need from imaging.

For example, radiation oncologists must know the proximity of the tumor to critical structures, such as the optic nerve or spinal cord. The presence of extranodal extension of tumor is important for medical oncologists to plan chemotherapeutic regimens. Routine follow-up after CT or MRI interpretations and next-step recommendations add to an individual HN radiologist's expertise.

In summary, our goals were to improve efficiency, standardize imaging and interpretations, clarify the HN radiologists' responsibilities, and improve patient care. Obviously, we enthusiastically support the use of NI-RADS. Introducing NI-RADS is best when all disciplines involved in caring for a patient with HNC trust that the HN radiologist is familiar with complex HN imaging, has a broad knowledge infrastructure for the disease, and understands the implications of further diagnostic recommendations. Implementing the NI-RADS template is the last step in developing a mature HNC imaging practice.

Disclosure forms provided by the authors are available with the full text and PDF of this article at www.ajnr.org.

REFERENCES

1. Aiken AH, Rath TJ, Anzai Y, et al. **ACR Neck Imaging Reporting and Data Systems (NI-RADS): a white paper of the ACR NI-RADS Committee.** *J Am Coll Radiol* 2018;15:1097–108 CrossRef Medline
2. Baugnon KL. **NI-RADS to predict residual or recurrent head and neck squamous cell carcinoma.** *Neuroimaging Clin N Am* 2022;32:1–18 CrossRef Medline
3. Strauss SB, Aiken AH, Lantos JE, et al. **Best practices: application of NI-RADS for posttreatment surveillance imaging of head and neck cancer.** *AJR Am J Roentgenol* 2021;216:1438–51 CrossRef Medline

Does Gadolinium Deposition Lead to Metabolite Alteration in the Dentate Nucleus? An MRS Study in Patients with MS

M. Mohammadzadeh, S. Kolahi, M.-M. Mehrabi Nejad, K. Firouznia, H. Naghibi, A. Mohammadzadeh, M. Shakiba, F. Mohebi, H. Komaki, H. Sharifian, H. Hashemi, M.H. Harirchian, A. Azimi, M.E. Adin, and D.M. Yousem

ABSTRACT

BACKGROUND AND PURPOSE: Repeat contrast-enhanced MR imaging exposes patients with relapsing-remitting MS to frequent administration of gadolinium-based contrast agents. We aimed to investigate the potential metabolite and neurochemical alterations of visible gadolinium deposition on unenhanced T1WI in the dentate nucleus using MRS.

MATERIALS AND METHODS: This prospective study was conducted in a referral university hospital from January 2020 to July 2021. The inclusion criteria for case and control groups were as follows: 1) case: patients with relapsing-remitting MS, visible gadolinium deposition in the dentate nucleus (ribbon sign), >5 contrast-enhanced MR images obtained; 2) control 1: patients with relapsing-remitting MS without visible gadolinium deposition in the dentate nucleus, >5 contrast-enhanced MR images obtained; 3) control 2: patients with relapsing-remitting MS without visible gadolinium deposition in the dentate nucleus, <5 contrast-enhanced-MR images obtained; and 4) control 3: adult healthy individuals, with no contrast-enhanced MR imaging. Dentate nucleus and pontine single-voxel 12 × 12 × 12 MRS were analyzed using short TEs.

RESULTS: Forty participants (10 per group; 27 [67.5%] female; mean age, 35.6 [SD, 9.6] years) were enrolled. We did not detect any significant alteration in the levels of NAA and choline between the studied groups. The mean concentrations of mIns were 2.7 (SD, 0.73) (case), 1.5 (SD, 0.8) (control 1), 2.4 (SD, 1.2) (control 2), and 1.7 (SD, 1.2) (control 3) ($P = .04$). The mean concentration of Cr and mIns ($P = .04$) and the relative metabolic concentration (dentate nucleus/pons) of lipid 1.3/Cr ($P = .04$) were significantly higher in the case-group than in healthy individuals (controls 1–3). Further analyses compared the case group with cumulative control 1 and 2 groups and showed a significant increase in lactate ($P = .02$), lactate/Cr ($P = .04$), and Cr (dentate nucleus/pons) ($P = .03$) in the case group.

CONCLUSIONS: Although elevated concentrations of Cr, lactate, mIns, and lipid in the dentate nucleus of the case group indicate a metabolic disturbance, NAA and choline levels were normal, implying no definite neuronal damage.

ABBREVIATIONS: CE = contrast-enhanced; DN = dentate nucleus; GBCA = gadolinium-based contrast agent; Gd = gadolinium; RRMS = relapsing-remitting MS; SI = signal intensity

MS is a chronic demyelinating, neurodegenerative disease of the CNS that affects >2 million people worldwide.[1] Contrast-enhanced (CE) MR imaging is extensively used and is vital for early diagnosis and follow-up of patients with MS because it can help fulfill the "dissemination in time" McDonald criteria. As a result, patients with MS are frequently exposed to the administration of gadolinium-based contrast agents (GBCAs) required for CE-MR imaging.[2] GBCAs have been considered very safe since the US Food and Drug Administration's approval in 1988. The first report of gadolinium deposition as a source of the high signal intensity (SI) in the dentate nucleus (DN) was published in 2014[3] and has led to extensive investigation of this phenomenon. Initially in patients with MS, radiologists linked the suspicious increase in SI on T1WI in the deep gray matter to MS itself,[4] but this etiology has since been discredited. The observed DN hyperintensity on unenhanced T1-weighted images was specifically attributed to the secondary-progressive disease MS subtype, but now there is no support for an independent association between MS and a hyperintense DN.

Received February 3, 2022; accepted after revision July 1.

From the Departments of Radiology (M.M., S.K., M.-M.M.N., K.F., H.N., M.S., H.S., H.H.) and Neurology (M.H.H., A.A.), Tehran University of Medical Sciences, Tehran, Iran; Department of Radiology (A.M.), Iran University of Medical Sciences, Tehran, Iran; Hass School of Business (F.M.), University of California, Berkeley, Berkeley, California; Khoury College of Computer Sciences (H.K.), Northeastern University, Boston, Massachusetts; Department of Radiology and Biomedical Imaging (M.E.A.), Yale School of Medicine, New Haven, Connecticut; and Department of Radiology (D.M.Y.), Johns Hopkins University School of Medicine, Baltimore, Maryland.

M. Mohammadzadeh and S. Kolahi had equal contribution as co-first authors.

Please address correspondence to David M. Yousem, MD, MBA, Johns Hopkins University School of Medicine, 600 N. Wolfe St, Phipps B100, Baltimore, MD 21287; e-mail: dyousem1@jhu.edu

Indicates article with online supplemental data.

http://dx.doi.org/10.3174/ajnr.A7623

The GBCAs are either linear or macrocyclic based on their type of polyamino-polycarboxylic ligand. Each of these groups is composed of nonionic and ionic classes of agents based on their electric charge. Despite the rigid cage wrapping around the Gd^{3+} in macrocyclic GBCAs, this cage is more flexible in the linear type. Because the agent's cage contributes to its stability, linear-type GBCAs are less stable than macrocyclic agents. As a general concept, the ionic macrocyclic and nonionic linear chelates are the most and least stable GBCAs, respectively.[5,6] The thermodynamic and kinetic stabilities of GBCAs are the main concerns in their safety because the stability of the gadolinium (Gd) agent determines the likelihood of its deposition.[5] Although several studies have found that hyperintensity in the DN on unenhanced T1-weighted images has the highest association with previous administration of linear GBCAs,[7,8] macrocyclic GBCAs can also lead to DN hyperintensity.[9]

Several studies have investigated the safety of GBCAs in pediatric[10,11] and adult patients.[12-14] The pooled evidence clearly supports the idea that GBCA administration is significantly, positively, and directly correlated with increased SI in the DN and globus pallidus on unenhanced T1WI assessments.[8,9] The aforementioned correlation was detected regardless of the patient's renal function.[6] Studies on patients with MS have also supported this evidence.[15,16] However, histologic findings on brain postmortem examinations in human and animal models have not detected any damage, despite the confirmed accumulation of gadolinium in affected structures.[17] Quantitative assessments of T1- and T2-weighted imaging also supported an association with previous GBCA administration and gadolinium accumulation, particularly in gray matter structures.[13]

To date, there is no study, to our knowledge, investigating the brain metabolite alterations following GBCA exposure in humans. A promising and relatively accessible technique is MRS because it has the unique ability to provide the chemical characteristics of MR imaging–visible lesions as well as normal-appearing brain tissue.[18] Therefore, we aimed to investigate the potential metabolite alterations in visually detectable Gd deposition in the DN following multiple prior GBCA exposure in patients with MS using a case-control design. Preclinical and clinical studies have reported in vitro neurotoxic effects of Gd exposure due to impairment of mitochondrial function and mitochondrial metabolic alterations subsequent to gadolinium deposition.[19,20] We hypothesize that Cr and lactate will show alterations due to disturbed mitochondrial metabolism. We also hoped this study would contribute to the understanding of the molecular and cellular ramifications of Gd deposition.

MATERIALS AND METHODS

Study Design and Participants

This prospective case-control study was reviewed and approved by Institutional Review Board of Imam Khomeini Hospital Complex and was conducted in a quaternary referral university hospital from January 2020 to July 2021. After all patients were informed about the study goals and assured that their medical data would remain confidential, consent was obtained. Patients were also assured that unwillingness to participate in the study or leaving the study would not affect their medical care.

The MS diagnosis was established according to an expert fellowship-trained neurologist based on the McDonald criteria.[2] The enrolled patients were selected from a specialized MS center. This center conducts all patients' follow-up imaging with the same protocol and GBCA type (gadoterate meglumine) that is used for the imaging in this study. No patient had prior GBCA exposure before the MS diagnosis. The inclusion criteria for case and control groups were as follows:

1) Case: adult patients with relapsing-remitting MS (RRMS) with visually detectable hyperintensity in the DN (ribbon sign; DN/pons SI ratio, >1) who underwent >5 CE-MRIs.
2) Control 1: adult patients with RRMS without visually detectable hyperintensity in the DN who underwent >5 CE-MRIs.
3) Control 2: adult patients with RRMS without visually detectable hyperintensity in the DN who underwent <5 CE-MRIs.
4) Control 3: healthy adult individuals with no history of CE-MRI.

Exclusion criteria were the following: 1) any MS plaques involving the infratentorial region, 2) any other previously diagnosed neurologic diseases, 3) impaired renal function (estimated glomerular filtration rate of <60 mL/min), 4) a history of cranial irradiation, or 5) any other disease requiring CE- MR imaging.

Image Acquisition and Interpretation

MR Imaging Protocol. All patients were in remission at the time of the examination, and no patient had MS plaques involving the infratentorial region. Patients were scanned on a 3T MR imaging machine (Discovery MR750; GE Healthcare) using a 32-channel phased array head coil. The protocol included axial, coronal, and sagittal T2 FSE: TR = 3000 ms, TE = 106 ms, matrix size = 352 × 256, FOV = 230 × 230, section thickness = 5 mm, flip angle = 142°; and an axial 3D T2*-weighted angiography gradient-echo sequence: TR = 75 ms, TE = 50 ms, section thickness = 2 mm, matrix size = 320 × 224, and FOV = 220 × 220. We used an axial T1 spin echo: TR = 600 ms, TE = 10 ms, section thickness = 5 mm, matrix size = 352 × 256, FOV = 230 × 230 to detect high intensity in the DN. A standard dose (0.1 mmol/kg) of a macrocyclic GBCA (gadoterate meglumine) was administered to all patients during each MR imaging acquisition.

Two fellowship-trained neuroradiologists (with 22 and 10 years of experience), blinded to clinical data, independently reviewed the images. Unenhanced T1WIs were used to draw a 4-mm^2 ROI in the middle of the pons and around the area with the highest intensity in the DN. The DN/pons SI ratio was calculated by dividing the mean SI within the DN by the mean SI within the central pons. Any disagreement was resolved by consensus.

MRS Evaluation

MRS imaging with the use of pointed-resolved spectroscopy was performed with the following configurations: long TE = 144 and short TE = 35 ms, FOV = 240 × 240, voxel size = 12 × 12 × 12 mm, TR1 = 500 ms, and number of samples per spectrum = 1024. A chemical shift selective suppression technique was used to suppress the water signal. Out-of-volume saturation bands were applied to suppress signal excited outside the FOV. No lipid suppression was applied. Manual shimming was performed.

Single-voxel 12 × 12 × 12 mm MRS was performed for the evaluation of the DN and pons area. Quantification-procedure MRS imaging data were obtained in TARQUIN (Version 4.3.10; https://sourceforge.net/projects/tarquin/) software. Quantification results for each metabolite were analyzed in the associated optimal TE with the metabolite peaks as follows: choline at 3.2 ppm; NAA at 2.02 ppm; Cr at 3 ppm; lactate at 1.3 ppm; lipid at 0.9- 1.3 ppm; Glx at 2.1–2.4 ppm; and mIns at 3.5 ppm (Online Supplemental Data).

MRS performed with short TE minimizes signal loss due to transverse relaxation, allowing higher quantification precision than long TE.[18] However, on short TE, broad macromolecule resonances are presented, which could be a confounding factor for quantification.[18] Because macromolecule lipid resonance and lactate resonances are closely located and might overlap each other, the macromolecule confounding problem mainly occurs at the spectra of lactate.[21] To confirm that the observed lactate change on short TE was clearly due to lactate, we compared the short TE and long TE spectra with TE = 144, in which the lactate peak was inverted. Then, the lactate quantification was performed on short TE spectra.

Statistical Analysis

We performed the analyses in SPSS for Windows, Version 18 (IBM). All P values $< .05$ were considered statistically significant. Descriptive data are presented in mean (SD) for continuous variables and frequency and percentage for categoric variables. To assess whether the recorded data have a normal distribution, we performed the Kolmogorov-Smirnov test. We conducted the comparisons by the following: 1) 1-way ANOVA with Tukey post hoc test and an independent 2-tailed sample t test for continuous variables with normal distribution and the relevant degree of freedom, 2) the Kruskal-Wallis test and the Mann-Whitney U test for the continuous variable with a significant lack of normality, and 3) a χ^2 test for nominal variables.

RESULTS

Participant Characteristics

Forty participants (10 in each group; 27 [67.5%] females; mean age , 35.6 [SD, 9.6] years; range, 20–57 years) were enrolled in this prospective study. The participants' demographic features are presented in Table 1. Considering that all patients were scanned with the same protocol and GBCA type, any reported differences are not due to different GBCA agents or scanning techniques. DN/pons SI ratios on T1WI were 1.04, 0.98, 0.94, and 0.94 in case and control 1–3 groups, respectively ($P < .001$), indicating appropriate selection of case and control groups.

DN Values

The absolute metabolite concentrations and calculated ratios in the DN in all 4 studied groups are presented in Table 2 and Figs 1 and 2. mIns was the only metabolite that was significantly different in all groups. The mean concentrations of mIns were 2.7 (SD, 0.73) (case), 1.5 (SD, 0.8) (control 1), 2.4 (SD, 1.2) (control 2), and 1.7 (SD, 1.2) (control 3) ($P = .04$). We observed intergroup differences in other metabolites as well, though they were not homogeneous in all 2 × 2 comparisons. The mean concentrations of Cr on short TE ($P = .04$) and mIns ($P = .04$) were significantly higher in the case group compared with healthy individuals (control 3). Further analyses compared the case group with an aggregated group of control 1 and 2 participants and showed significant elevation of lactate on short TE ($P = .02$) and lactate/Cr on short TE ($P = .04$) in the case group and elevation of Glx/Cr ($P = .04$) in the control groups.

DN-to-Pons Ratio Values

The relative metabolite concentrations and calculated ratios in DN/pons in all 4 studied groups are presented in Table 3. Among all variables, there were 2 statistically significant observations. First, the mean concentration of Cr on short TE ($P = .03$) was significantly higher in case participants than in a group of control 1 and 2 participants. Second, lipid 1.3/Cr ($P = .04$) was significantly higher in the case group than in control 3.

Table 1: Demographic features of participants

Variable	Case (n = 10)	Control 1 (n = 10)	Control 2 (n = 10)	Control 3 (n = 10)
Age (mean) (yr)	43.4 (SD, 8.6)	36.7 (SD, 10.2)	31.7 (SD, 10.0)	30.7 (SD, 2.9)
Sex (female)	8 (80%)	7 (70%)	9 (90%)	3 (30%)

Table 2: Absolute mean metabolite concentrations and calculated ratios in the DN in all 4 studied groups

Variable	Studied Groups				Comparisons (P Values)		
	Case	Control 1	Control 2	Control 3	Among 4 Groups	Case vs Control 3	Case vs. Controls 1 and 2
NAA	43.0 (SD, 7.3)	44.8 (SD, 11.7)	45.3 (SD, 10.5)	36.7 (SD, 10.8)	.24	.15	.59
Choline	32.8 (SD, 9.7)	25.7 (SD, 11.5)	28.8 (SD, 5.8)	23.5 (SD, 11.8)	.20	.07	.27
Cr on short TE	11.6 (SD, 1.3)	9.3 (SD, 4.3)	10.1 (SD, 1.8)	8.9 (SD, 3.3)	.21	.04[a]	.06
Lactate on short TE	4.6 (SD, 2.2)	2.3 (SD, 2.1)	2.1 (SD, 1.3)	3.2 (SD, 2.8)	.15	.33	.02[a]
mIns	2.7 (SD, 0.7)	1.5 (SD, 0.8)	2.4 (SD, 1.2)	1.7 (SD, 1.2)	.04[a]	.04[a]	.51
Glx	3.5 (SD, 1.7)	3.7 (SD, 1.7)	4.9 (SD, 1.8)	4.5 (SD, 2.7)	.36	.35	.10
Lipid 0.9	4.8 (SD, 2.0)	3.9 (SD, 2.4)	4.1 (SD, 1.8)	3.5 (SD, 2.2)	.65	.22	.44
Lipid 1.3	5.2 (SD, 2.7)	5.8 (SD, 4.1)	6.5 (SD, 3.6)	5.7 (SD, 3.0)	.92	.73	.42
NAA/Cr	1.7 (SD, 0.5)	2.1 (SD, 0.9)	1.6 (SD, 0.6)	2.8 (SD, 2.0)	.10	.11	.73
Lactate/Cr on short TE	0.4 (SD, 0.2)	0.3 (SD, 0.2)	0.2 (SD, 0.2)	0.3 (SD, 0.2)	.25	.50	.04[a]
mIns/Cr	0.2 (SD, 0.1)	0.2 (SD, 0.2)	0.2 (SD, 0.1)	0.2 (SD, 0.1)	.68	.16	.99
Glx/Cr	0.3 (SD, 0.1)	0.5 (SD, 0.3)	0.5 (SD, 0.2)	0.5 (SD, 0.3)	.35	.08	.04[a]
Lipid 0.9/Cr	0.4 (SD, 0.3)	0.4 (SD, 0.2)	0.4 (SD, 0.1)	0.4 (SD, 0.1)	.91	.50	.76
Lipid 1.3/Cr	0.4 (SD, 0.2)	0.9 (SD, 1.0)	0.6 (SD, 0.4)	0.8 (SD, 0.4)	.43	.05	.19

[a] Statistically significant.

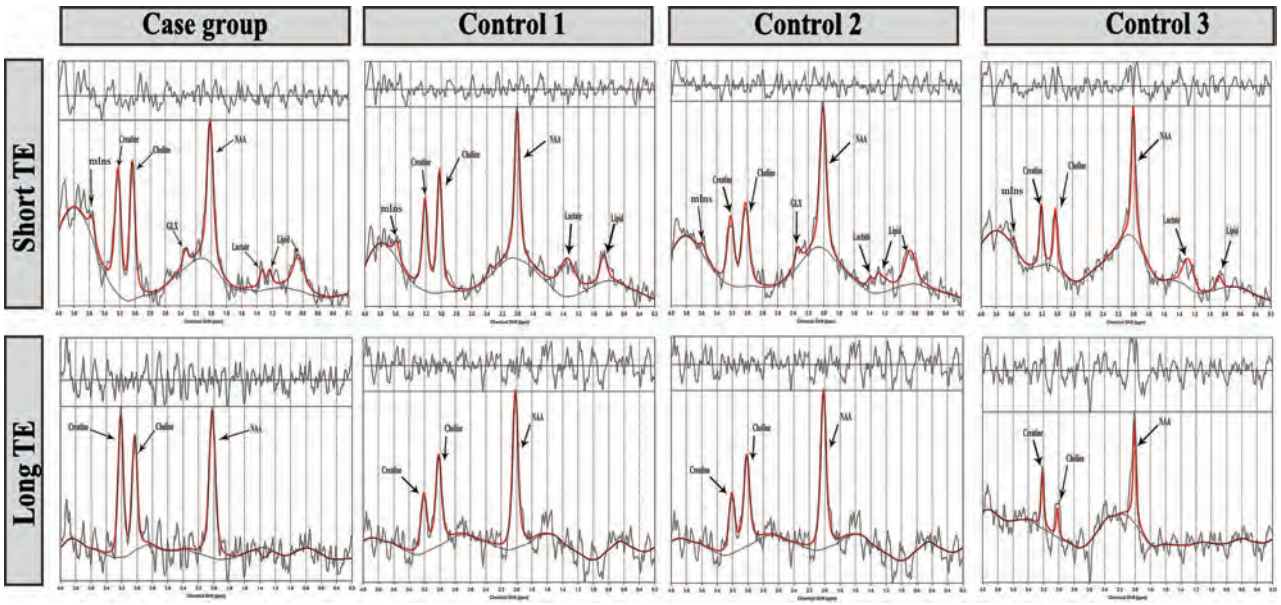

FIG 1. ^{1}H-MR spectra from the DN in 1 patient from both case and control groups. *Red lines* represent the TARQUIN fits. MRS at TE = 35 ms shows elevated mIns peaks at 3.5 ppm, creatine peaks at 3 ppm, lactate peaks at 1.3 ppm, and Glx peaks at 2.1–2.4 ppm.

DISCUSSION

Our findings support the hypothesis that Gd deposition could be related to metabolite alterations in the DN. Despite evidence of metabolite changes among the studied groups, these findings were minor and their clinical importance should be investigated in further studies. To elaborate, we did not detect any significant alteration in the levels of NAA and Cho among the studied groups, suggesting the absence of neuronal tissue damage in the DN with visually detectable Gd deposition. Nonetheless, the levels of mIns, Cr, lactate, and lipid showed a significant increase in the case group, which can be interpreted as a change in cellular metabolism as discussed below.

Two studies by McDonald et al[22,23] used inductively coupled plasma mass spectrometry and detected Gd deposition in the endothelial wall, neural tissue interstitium, and nuclei of neurons in the absence of any gross histologic changes. The concept of Gd crossing the blood-brain barrier and being deposited in neural nuclei raises concern about the potential cytotoxicity of Gd. To this end, preclinical in vitro studies provided insight about the time- and dose-dependent cytotoxic and neurotoxic mechanism of Gd through disturbance of mitochondrial function and oxidative stress.[19,24-26] The authors speculated that Gd, as a calcium antagonist due to their similar atomic radius, can interrupt the mitochondrial calcium metabolism leading to cellular death.[27]

Feng et al[19] observed that Gd exposure is associated with mitochondrial membrane depolarization, caspase-3 activation, cytochrome C release, lactate dehydrogenase increase, intracellular reactive oxygen species increase, adenosine triphosphate synthesis decrease, and subsequent DNA fragmentation. All the aforementioned cellular mechanisms indicate mitochondrial dysfunction and oxidative stress leading to neuronal cell apoptosis. The cellular studies of GBCA exposure in humans could help to predict its potential long-term clinical consequences. However, there is only 1 study using PET/CT in human subjects that has investigated the metabolic activity in Gd-deposition regions.[28] The authors found 16% and 27% lower [^{18}F] FDG uptake in the DN and globus pallidus, respectively, of individuals who received GBCAs.[28] Most interesting, a recent study used untargeted mass spectroscopy–based metabolomic analyses to investigate the plasma metabolite alterations after Gd administration.[20] Compared with healthy controls, patients with Gd-deposition disease showed differences in 45 biochemicals, mostly related to mitochondrial function, similar to our findings in the brain.[20]

We propose that the observed increased levels of Cr in case participants might indicate a disturbance in cellular energy homeostasis. Cr transmission through the blood-brain barrier is minimal, and most Cr is produced in the brain using the arginine:glycine amidinotransferase and guanidinoacetate methyltransferase enzymes.[29] Cr is the essential component of high-energy phosphate metabolism (pCr+ADP↔Cr+ATP) and plays a vital role in channeling energy into the cytosol to maintain cellular energy homeostasis.[30] Therefore, because MRS measures both Cr and creatine phosphate, compromised cellular energy production due to Gd accumulation could be caused by the responsive up-regulation of Cr as the substrate to compensate for an altered cellular energy system.

Lactate is the product of anaerobic glycolysis and increases in stroke, encephalopathies, lactic acidosis, neonatal hypoxia, and mitochondrial myopathies.[18] Neuronal metabolism appears to be mostly oxidative, and astrocytic metabolism is glycolytic according to the hypothesis of astrocyte-neuron lactate shuttle (Fig 3).[31-33] Astrocytes take up glucose through the glucose transporter 1 and metabolize it to lactate. Lactate, then, is conveyed to the outside of the astrocytes and is captured by neurons via monocarboxylate transporters. Neurons oxidize intracellular lactate to pyruvate and metabolize it through the oxidative phosphorylation pathway in the mitochondria.[31-33] Impaired mitochondrial function and the subsequent oxidative phosphorylation in neurons can result in accumulation of lactate. Therefore, the observed increased lactate

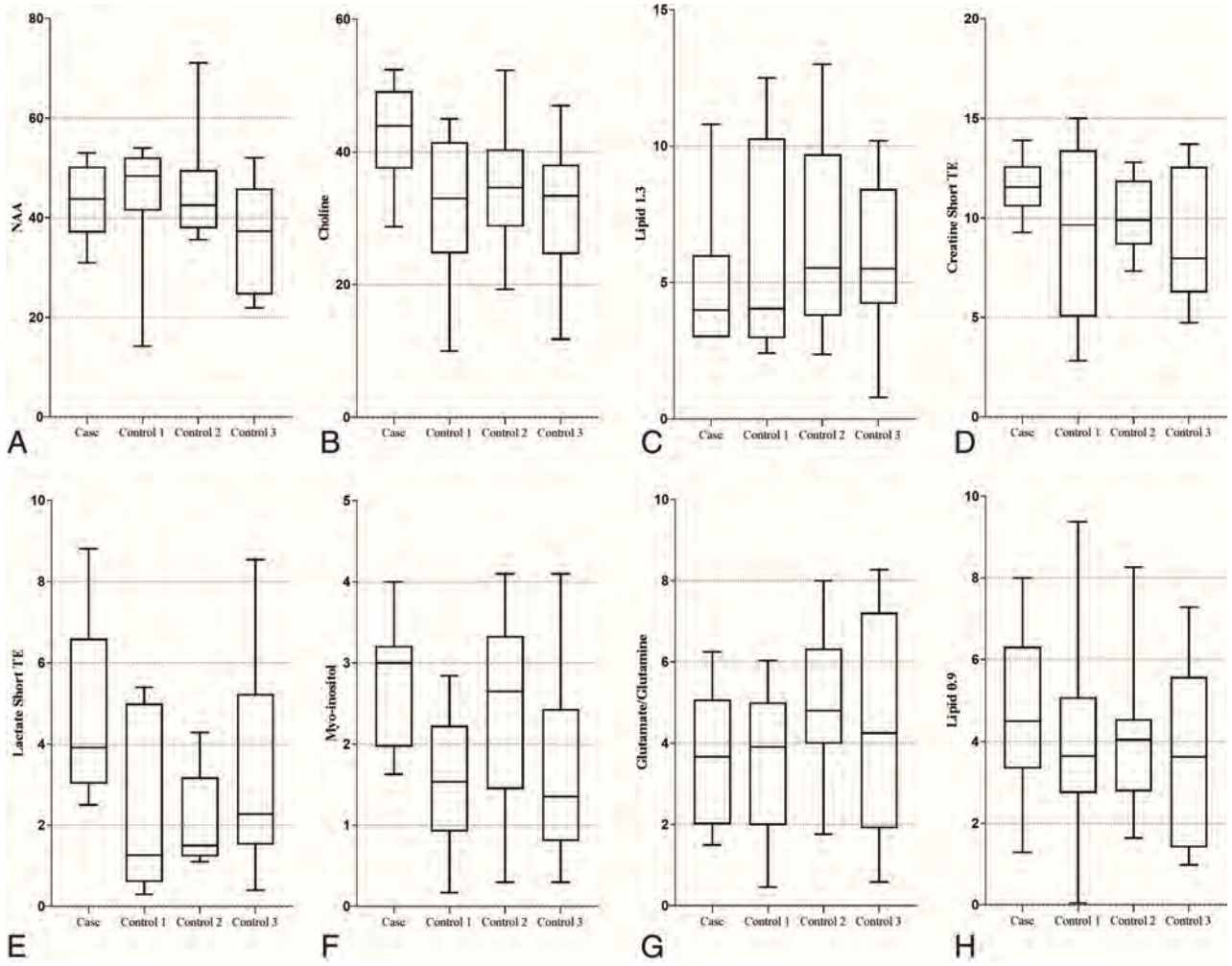

FIG 2. Boxplots of the metabolites. Differences between case and control groups.

Table 3: Relative mean metabolite concentrations and calculated ratios in DN/pons in all 4 studied groups

Variable	Studied Groups				Comparisons (*P* Values)		
	Case	Control 1	Control 2	Control 3	Among 4 Groups	Case vs. Control 3	Case vs Controls 1 and 2
NAA	0.7 (SD, 0.1)	1.1 (SD, 0.3)	0.8 (SD, 0.2)	0.9 (SD, 0.5)	.13	.38	.36
Choline	0.8 (SD, 0.3)	0.8 (SD, 0.4)	0.9 (SD, 0.3)	0.8 (SD, 0.4)	.98	.97	.70
Cr on short TE	1.4 (SD, 0.5)	1.1 (SD, 0.6)	1.0 (SD, 0.2)	1.8 (SD, 2.5)	.54	.61	.03[a]
Lactate on short TE	4.3 (SD, 7.4)	1.5 (SD, 2.0)	1.0 (SD, 1.6)	0.2 (SD, 0.4)	.32	.25	.26
mIns	0.9 (SD, 0.5)	0.5 (SD, 0.4)	1.3 (SD, 1.5)	1.1 (SD, 1.2)	.35	.69	.42
Glx	1.2 (SD, 0.8)	1.0 (SD, 0.6)	1.3 (SD, 1.0)	1.3 (SD, 0.6)	.84	.72	.81
Lipid 0.9	1.3 (SD, 0.8)	1.1 (SD, 0.7)	0.8 (SD, 0.5)	1.3 (SD, 1.0)	.43	.96	.13
Lipid 1.3	1.4 (SD, 1.0)	1.0 (SD, 1.3)	1.4 (SD, 1.0)	1.0 (SD, 0.5)	.74	.33	.93
NAA/Cr	0.7 (SD, 0.2)	0.8 (SD, 0.4)	0.6 (SD, 0.3)	0.9 (SD, 0.5)	.29	.44	.15
Lactate/Cr on short TE	0.2 (SD, 0.1)	0.2 (SD, 0.1)	0.1 (SD, 0.1)	0.2 (SD, 0.1)	.95	.56	.61
mIns/Cr	0.6 (SD, 0.3)	0.4 (SD, 0.2)	1.3 (SD, 1.5)	0.7 (SD, 0.5)	.11	.56	.20
Glx/Cr	1.1 (SD, 0.6)	0.9 (SD, 0.6)	1.5 (SD, 1.5)	1.2 (SD, 0.8)	.67	.58	.48
Lipid 0.9/Cr	1.0 (SD, 0.6)	1.0 (SD, 0.5)	0.8 (SD, 0.4)	1.0 (SD, 0.7)	.68	.83	.33
Lipid 1.3/Cr	1.5 (SD, 0.6)	1.3 (SD, 0.6)	1.8 (SD, 1.0)	0.8 (SD, 0.5)	.17	.04[a]	.45

[a] Statistically significant.

in the case group might indicate the existence of an impaired mitochondrial energy environment.

We also observed lower Glx levels in the case group. Glx is a mixture of similar amino acids that contribute to excitatory-inhibitory neurotransmission processes. Glutamate is released from the presynaptic neuron to stimulate glutamate receptors on the postsynaptic neuron. It enters the astrocytes through the synaptic gap via sodium (Na)-dependent excitatory amino acid activating transporters. Then,

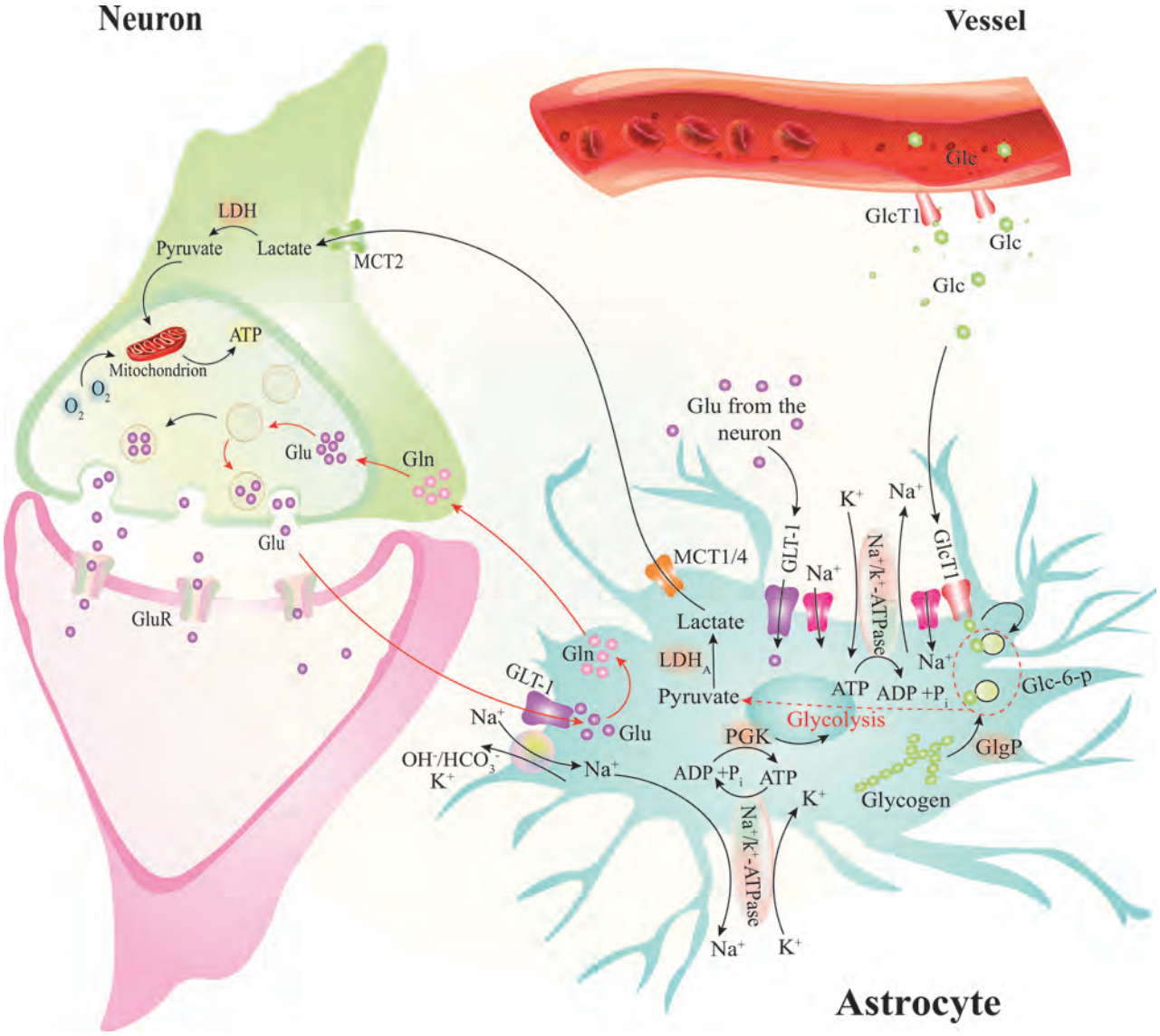

FIG 3. The astrocyte-neuron lactate shuttle and glutamate-glutamine cycles. After traveling through the endothelial cells, glucose (Glc) enters the astrocytes via Glc transporter 1 (GlcT1). It is metabolized to pyruvate and then lactate by lactate dehydrogenase (LDH5). The lactate is carried outside the astrocyte and inside the neuron via the monocarboxylate transporters (MCTs). The lactate inside the neuron is metabolized in the oxygen pathway. Glutamate (Glu) molecules released from presynaptic neurons are transported into the astrocytes through Na^+-dependent channels. In astrocytes, the Glu is transformed into Glutamine (Gln) or α-ketoglutarate to perform oxygen metabolism in the Krebs cycle. ATP indicates adenosine triphosphate; ADP, adenosine di-phosphate; P, phosphate; GluR, glutamate receptor; OH/HCO_3, hydroxide/bicarbonate; K+, potassium; GLT, glutamate transporter; PGK, phosphoglycerate kinase; ATPase, adenosine triphosphatase.

it is metabolized into glutamine (by the glutamine synthase enzyme or α-ketoglutarate by glutamate dehydrogenase) to process further oxygen metabolism in the tricarboxylic acid cycle (Krebs cycle) in the mitochondria. Glutamine, then, is transported to neurons to complete further glutamate production using phosphate-activated glutaminase (Fig 3).[31,33] Impairment of mitochondria functioning would lead to a compromised glutamate-glutamine cycle, which is dependent on the glutaminase enzyme in the mitochondria. In addition, impairment of the tricarboxylic acid cycle results in less use of α-ketoglutarate and, accordingly, impairment of the transformation of glutamate to α-ketoglutarate. Taken together, a glutamate/glutamine decrease can also be interpreted as a marker for metabolic impairment of neuronal cells.

Lipid levels were also significantly higher in the case group than in healthy controls. A recent study also detected elevated levels of 7-dehydrocholesterol, the cholesterol precursor, in patients with Gd deposition.[20] One of the degradation products of the leucine, 3-methylglutarate/2-methylglutarate, also showed increased levels after Gd deposition due to nicotinamide adenine dinucleotide phosphate/nicotinamide adenine dinucleotide phosphate–dependent enzyme impairment.[20] Sterol synthesis and leucine degradation are connected via the mevalonate shunt, leading to increased sterol production due to 3-methylglutarate/2-methylglutarate accumulation.[34,35] Hence, the authors believe that mitochondrial metabolism impairment due to Gd deposition leads to elevated levels of sterol biosynthesis through the mevalonate shunt.

Myo-inositol and its transporters may provide neuroprotection during or following brain ischemia[36] and are often increased in cerebral infarction. Impairment of mitochondrial function and oxidative phosphorylation can simulate a relatively hypoxic condition that leads to the accumulation of mIns. The H^+-mIns cotransporter is mainly expressed in the brain and is strongly stimulated by a decrease in pH.[37] Subsequently, brain exposure to a substantial lactate load—as discussed before—and a favorable H^+ gradient result in a significantly enhanced mIns uptake by the brain. Although mIns is known as a glial cell marker, studies have observed its elevated levels in neurodegenerative disorders without glial cell involvement, including Alzheimer disease, Huntington disease, and ataxia.[18] Taken together, the aforementioned mIns observations and the associated clinical conditions raise concerns regarding the long-term sequelae of Gd deposition.

Apart from the proposed notions, there is another potential mechanism behind the accumulation of these metabolites. There is a common understanding that mIns and Cr are the main osmolytes in the brain, which undergo alteration under chronic osmotic changes.[38] For instance, sodium-myo-inositol cotransporter-1 in the cortical astrocytes of rats was observed to up-regulate under a chronic hyperosmolar situation.[39] Therefore, chronic Gd deposition in the neural tissue interstitium could result in a hyperosmolar condition that induces the production of these osmolytes. Such hyperosmolarity has not been observed at clinical levels to date.

Our findings provide preliminary insight about a potential neurochemical alteration in patients with Gd deposition. Although we observed some degree of metabolite change in association with cellular metabolism and mitochondrial function, there were no significant changes in NAA and choline that would indicate the existence of any major neuronal damage. The authors posit that Gd deposition interrupts the mitochondrial function and results in some minor metabolite changes that are kept at the minimum level through the regulatory and compensatory cellular mechanisms. Nonetheless, the Gd deposition in the DN and evidence of malfunction of the mitochondrial energy pathway shown in animal and in vitro studies raise the specter of subclinical neurotoxicity effects of Gd deposition. Some animal studies have shown loss of motor coordination, including tremor, seizure, ataxia, and stereotyped movements and myoclonus.[40,41] In a recent study, patients with Gd-deposition disease reported symptoms similar to those with known mitochondrial-related diseases.[20] Although 2 other clinical studies reported lower verbal fluency in patients with MS with repetitive GBCA exposure,[42,43] there has not been a comprehensive study to indicate whether there are major adverse clinical effects attributed to multiple GBCA administrations in patients with MS.[6,27] We recommend that clinicians limit CE-MR imaging to the necessary indications and conform with the latest guidelines from such reputable bodies as the Consortium of Multiple Sclerosis Centers,[44] especially in those with chronic CNS diseases requiring repeat imaging.

Our study has several limitations. Our results indicate some statistically weak associations ($.05 < P < .10$), but we cannot ensure that they would remain the same if the sample size were larger. Second, although we enrolled patients with RRMS in similar stages of the disease, our case and control groups were not matched for age and sex. Several studies have hypothesized that MS therapeutic agents could alter the brain metabolites, but we did not include the treatment regimens in this study because we were interested in any potential harm of Gd, even if it was caused by an interaction with medications in patients with MS. In addition, our assessment did not include clinical evaluations of the patients and was limited to a specific macrocyclic GBCA. Moreover, this study requires more in-depth comparison of background information between the case and control groups in addition to age and sex, including, but not limited to, extensive medical history, smoking history, environmental exposures, and other neurologic conditions. We highly recommend conducting randomized controlled trials that incorporate information on the suggested background conditions that could help reveal the potential clinical significance of gadolinium deposition.

CONCLUSIONS

We found elevated concentrations of Cr, lactate, mIns, and lipid in the DN of patients with visible Gd deposition on their unenhanced T1WIs, indicating a metabolic disturbance in the affected patients. Our findings confirm previous studies implicating a potential adverse effect of Gd deposition on mitochondrial membrane and function. However, because we observed normal levels of NAA and choline in the DN, neuronal damage might be disavowed. Nevertheless, we require further clinical correlation and support for this notion. We recommend that clinicians remain cautious in their use of Gd, and that researchers should build on these preliminary findings by enrolling patients in a study with a larger sample size, with controlled and randomized design and full clinical assessment of the patients.

ACKNOWLEDGMENT

The authors thank the patients and hospital staff for their collaboration.

Disclosure forms provided by the authors are available with the full text and PDF of this article at www.ajnr.org.

REFERENCES

1. Mahad DH, Trapp BD, Lassmann H. **Pathological mechanisms in progressive multiple sclerosis.** *Lancet Neurol* 2015;14:183–93 CrossRef Medline
2. Polman CH, Reingold SC, Banwell B, et al. **Diagnostic criteria for multiple sclerosis: 2010 revisions to the McDonald criteria.** *Ann Neurol* 2011;69:292–302 CrossRef Medline
3. Kanda T, Ishii K, Kawaguchi H, et al. **High signal intensity in the dentate nucleus and globus pallidus on unenhanced T1-weighted MR images: relationship with increasing cumulative dose of a gadolinium-based contrast material.** *Radiology* 2014;270:834–41 CrossRef Medline
4. Roccatagliata L, Vuolo L, Bonzano L, et al. **Multiple sclerosis: hyperintense dentate nucleus on unenhanced T1-weighted MR images is associated with the secondary progressive subtype.** *Radiology* 2009;251:503–10 CrossRef Medline
5. Dekkers IA, Roos R, van der Molen AJ. **Gadolinium retention after administration of contrast agents based on linear chelators and the recommendations of the European Medicines Agency.** *Eur Radiol* 2018;28:1579–84 CrossRef Medline
6. Guo BJ, Yang ZL, Zhang LJ. **Gadolinium deposition in brain: current scientific evidence and future perspectives.** *Front Mol Neurosci* 2018;11:335 CrossRef Medline

7. Cao Y, Huang DQ, Shih G, et al. **Signal change in the dentate nucleus on T1-weighted MR images after multiple administrations of gadopentetate dimeglumine versus gadobutrol.** *AJR Am J Roentgenol* 2016;206:414–19 CrossRef Medline
8. Ozturk K, Nascene D. **Effect of at least 10 serial gadobutrol administrations on brain signal intensity ratios on T1-weighted MRI in children: a matched case-control study.** *AJR Am J Roentgenol* 2021;217:753–60 CrossRef Medline
9. Splendiani A, Corridore A, Torlone S, et al. **Visible T1-hyperintensity of the dentate nucleus after multiple administrations of macrocyclic gadolinium-based contrast agents: yes or no?** *Insights Imaging* 2019;10:1–10 CrossRef Medline
10. Hu HH, Pokorney A, Towbin RB, et al. **Increased signal intensities in the dentate nucleus and globus pallidus on unenhanced T1-weighted images: evidence in children undergoing multiple gadolinium MRI exams.** *Pediatr Radiol* 2016;46:1590–98 CrossRef Medline
11. Flood TF, Stence NV, Maloney JA, et al. **Pediatric brain: repeated exposure to linear gadolinium-based contrast material is associated with increased signal intensity at unenhanced T1-weighted MR imaging.** *Radiology* 2017;282:222–28 CrossRef Medline
12. Adin M, Kleinberg L, Vaidya D, et al. **Hyperintense dentate nuclei on T1-weighted MRI: relation to repeat gadolinium administration.** *AJNR Am J Neuroradiol* 2015;36:1859–65 CrossRef Medline
13. Kuno H, Jara H, Buch K, et al. **Global and regional brain assessment with quantitative MR imaging in patients with prior exposure to linear gadolinium-based contrast agents.** *Radiology* 2017;283:195–204 CrossRef Medline
14. Zhang Y, Cao Y, Shih GL, et al. **Extent of signal hyperintensity on unenhanced T1-weighted brain MR images after more than 35 administrations of linear gadolinium-based contrast agents.** *Radiology* 2017;282:516–25 CrossRef Medline
15. Stojanov DA, Aracki-Trenkic A, Vojinovic S, et al. **Increasing signal intensity within the dentate nucleus and globus pallidus on unenhanced T1W magnetic resonance images in patients with relapsing-remitting multiple sclerosis: correlation with cumulative dose of a macrocyclic gadolinium-based contrast agent, gadobutrol.** *Eur Radiol* 2016;26:807–15 CrossRef Medline
16. Tanaka M, Nakahara K, Kinoshita M. **Increased signal intensity in the dentate nucleus of patients with multiple sclerosis in comparison with neuromyelitis optica spectrum disorder after multiple doses of gadolinium contrast.** *Eur Neurol* 2016;75:195–98 CrossRef Medline
17. Kanda T, Oba H, Toyoda K, et al. **Brain gadolinium deposition after administration of gadolinium-based contrast agents.** *Jpn J Radiol* 2016;34:3–9 CrossRef Medline
18. Stagg C, Rothman D. *Magnetic Resonance Spectroscopy: Tools for Neuroscience Research and Emerging Clinical Applications*. Academic Press; 2014
19. Feng X, Xia Q, Yuan L, et al. **Impaired mitochondrial function and oxidative stress in rat cortical neurons: implications for gadolinium-induced neurotoxicity.** *Neurotoxicology* 2010;31:391–98 CrossRef Medline
20. Denmark D, Ruhoy I, Wittmann B, et al. **Altered plasma mitochondrial metabolites in persistently symptomatic individuals after a GBCA-assisted MRI.** *Toxics* 2022;10:56 CrossRef Medline
21. Lange T, Dydak U, Roberts T, et al. **Pitfalls in lactate measurements at 3T.** *AJNR Am J Neuroradiol* 2006;27:895–901 Medline
22. McDonald RJ, McDonald JS, Kallmes DF, et al. **Gadolinium deposition in human brain tissues after contrast-enhanced MR imaging in adult patients without intracranial abnormalities.** *Radiology* 2017;285:546–54 CrossRef Medline
23. McDonald RJ, McDonald JS, Kallmes DF, et al. **Intracranial gadolinium deposition after contrast-enhanced MR imaging.** *Radiology* 2015;275:772–82 CrossRef Medline
24. Ariyani W, Iwasaki T, Miyazaki W, et al. **Effects of gadolinium-based contrast agents on thyroid hormone receptor action and thyroid hormone-induced cerebellar Purkinje cell morphogenesis.** *Front Endocrinol (Lausanne)* 2016;7:115 CrossRef Medline
25. Bower DV, Richter JK, von Tengg-Kobligk H, et al. **Gadolinium-based MRI contrast agents induce mitochondrial toxicity and cell death in human neurons, and toxicity increases with reduced kinetic stability of the agent.** *Invest Radiol* 2019;54:453–63 Medline
26. Feng XD, Xia Q, Yuan L, et al. **Gadolinium triggers unfolded protein responses (UPRs) in primary cultured rat cortical astrocytes via promotion of an influx of extracellular Ca 2. +.** *Cell Biol Toxicol* 2011;27:1–12 CrossRef Medline
27. Mallio CA, Rovira À, Parizel PM, et al. **Exposure to gadolinium and neurotoxicity: current status of preclinical and clinical studies.** *Neuroradiology* 2020;62:925–34 CrossRef Medline
28. Bauer K, Lathrum A, Raslan O, et al. **Do gadolinium-based contrast agents affect 18F-FDG PET/CT uptake in the dentate nucleus and the globus pallidus? A pilot study.** *J Nucl Med Technol* 2017;45:30–33 CrossRef Medline
29. Kreider RB, Stout JR. **Creatine in health and disease.** *Nutrients* 2021;13:447 CrossRef Medline
30. Schlattner U, Tokarska-Schlattner M, Wallimann T. **Mitochondrial creatine kinase in human health and disease.** *Biochim Biophys Acta* 2006;1762:164–80 CrossRef Medline
31. Dienel GA. **Brain glucose metabolism: integration of energetics with function.** *Physiol Rev* 2019;99:949–1045 CrossRef Medline
32. Chen Y, Fry BC, Layton AT. **Modeling glucose metabolism and lactate production in the kidney.** *Math Biosci* 2017;289:116–29 CrossRef Medline
33. Falkowska A, Gutowska I, Goschorska M, et al. **Energy metabolism of the brain, including the cooperation between astrocytes and neurons, especially in the context of glycogen metabolism.** *Int J Mol Sci* 2015;16:25959–81 CrossRef Medline
34. Edmond J, Popjak G. **Transfer of carbon atoms from mevalonate to n-fatty acids.** *J Biol Chem* 1974;249:66–71 Medline
35. Kopito R, Murray DM, Story DL, et al. **The shunt pathway of mevalonate metabolism in the isolated perfused rat kidney.** *J Biol Chem* 1984;259:372–77 Medline
36. Villalba H, Shah K, Albekairi TH, et al. **Potential role of myo-inositol to improve ischemic stroke outcome in diabetic mouse.** *Brain Res* 2018;1699:166–76 CrossRef Medline
37. Uldry M, Ibberson M, Horisberger JD, et al. **Identification of a mammalian H+-myo-inositol symporter expressed predominantly in the brain.** *EMBO J* 2001;20:4467–77 CrossRef Medline
38. Knight LS, Piibe Q, Lambie I, et al. **Betaine in the brain: characterization of betaine uptake, its influence on other osmolytes and its potential role in neuroprotection from osmotic stress.** *Neurochem Res* 2017;42:3490–3503 CrossRef Medline
39. Videen JS, Michaelis T, Pinto P, et al. **Human cerebral osmolytes during chronic hyponatremia: a proton magnetic resonance spectroscopy study.** *J Clin Invest* 1995;95:788–93 CrossRef Medline
40. Ray D, Cavanagh J, Nolan C, et al. **Neurotoxic effects of gadopentetate dimeglumine: behavioral disturbance and morphology after intracerebroventricular injection in rats.** *AJNR Am J Neuroradiol* 1996;17:365–73 Medline
41. Roman-Goldstein S, Barnett P, McCormick C, et al. **Effects of gadopentetate dimeglumine administration after osmotic blood-brain barrier disruption: toxicity and MR imaging findings.** *AJNR Am J Neuroradiol* 1991;12:885–90 Medline
42. Forslin Y, Shams S, Hashim F, et al. **Retention of gadolinium-based contrast agents in multiple sclerosis: retrospective analysis of an 18-year longitudinal study.** *AJNR Am J Neuroradiol* 2017;38:1311–16 CrossRef Medline
43. Forslin Y, Martola J, Bergendal Å, et al. **Gadolinium retention in the brain: an MRI relaxometry study of linear and macrocyclic gadolinium-based contrast agents in multiple sclerosis.** *AJNR Am J Neuroradiol* 2019;40:1265–73 CrossRef Medline
44. Arevalo O, Riascos R, Rabiei P, et al. **Standardizing magnetic resonance imaging protocols, requisitions, and reports in multiple sclerosis: an update for radiologist based on 2017 Magnetic Resonance Imaging in Multiple Sclerosis and 2018 Consortium of Multiple Sclerosis Centers Consensus Guidelines.** *J Comput Assist Tomogr* 2019;43:1–12 CrossRef Medline

Cellular Density in Adult Glioma, Estimated with MR Imaging Data and a Machine Learning Algorithm, Has Prognostic Power Approaching World Health Organization Histologic Grading in a Cohort of 1181 Patients

E.D.H. Gates, D. Suki, A. Celaya, J.S. Weinberg, S.S. Prabhu, R. Sawaya, J.T. Huse, J.P. Long, D. Fuentes, and D. Schellingerhout

ABSTRACT

BACKGROUND AND PURPOSE: Recent advances in machine learning have enabled image-based prediction of local tissue pathology in gliomas, but the clinical usefulness of these predictions is unknown. We aimed to evaluate the prognostic ability of imaging-based estimates of cellular density for patients with gliomas, with comparison to the gold standard reference of World Health Organization grading.

MATERIALS AND METHODS: Data from 1181 (207 grade II, 246 grade III, 728 grade IV) previously untreated patients with gliomas from a single institution were analyzed. A pretrained random forest model estimated voxelwise tumor cellularity using MR imaging data. Maximum cellular density was correlated with the World Health Organization grade and actual survival, correcting for covariates of age and performance status.

RESULTS: A maximum estimated cellular density of >7681 nuclei/mm^2 was associated with a worse prognosis and a univariate hazard ratio of 4.21 ($P < .001$); the multivariate hazard ratio after adjusting for covariates of age and performance status was 2.91 ($P < .001$). The concordance index between maximum cellular density (adjusted for covariates) and survival was 0.734. The hazard ratio for a high World Health Organization grade (IV) was 7.57 univariate ($P < .001$) and 5.25 multivariate ($P < .001$). The concordance index for World Health Organization grading (adjusted for covariates) was 0.761. The maximum cellular density was an independent predictor of overall survival, and a Cox model using World Health Organization grade, maximum cellular density, age, and Karnofsky performance status had a higher concordance (C = 0.764; range 0.748–0.781) than the component predictors.

CONCLUSIONS: Image-based estimation of glioma cellularity is a promising biomarker for predicting survival, approaching the prognostic power of World Health Organization grading, with added values of early availability, low risk, and low cost.

ABBREVIATIONS: CD = cellular density; C-index = concordance index; KPS = Karnofsky performance status; max = maximum; ROC = receiver operating characteristic; WHO = World Health Organization

The most powerful prognostic factor currently known for patients with gliomas is the tumor grade as described by the World Health Organization (WHO).[1,2] The WHO grading system ranges from I to IV with a higher grade indicating increased malignancy and a worse prognosis. Historically, tissue histology has driven diagnosis and grading using characteristics like mitoses, microvascular proliferation, or necrosis.[3] Recent updates emphasize molecular characteristics in WHO grading.[1,2]

WHO grading depends on having tissue specimens. Obtaining these specimens is difficult, expensive, and includes a risk for the patient. In current practice, diagnostic tissue samples are often

Received February 10, 2022; accepted after revision July 1.

From the Departments of Imaging Physics (E.D.H.G., A.C., D.F.), Neurosurgery (D. Suki, J.S.W., S.S.P., R.S.), Translational Molecular Pathology (J.T.H.), Biostatistics (J.P.L.), Neuroradiology and Imaging Physics (D. Schellingerhout), and the University of Texas MD Anderson Cancer Center UTHealth Houston Graduate School of Biomedical Sciences (E.D.H.G.), Houston, Texas.

Data for this work have been obtained through a search of the integrated multidisciplinary Brain and Spine Center Database. The Brain and Spine Center Database was supported, in part, by an institutional MD Anderson database development grant. The High-Performance Research Computing facility at the University of Texas MD Anderson Cancer Center provided computational resources that have contributed to the research results reported in this work.

E.D.H. Gates was supported by a training fellowship from the Gulf Coast Consortia on the NLM Training Program in Biomedical Informatics & Data Science (T15LM007093). D. Fuentes, D. Schellingerhout, and A. Celaya were partially supported by R21CA249373. J.P. Long was partially supported by the National Cancer Institute and the National Center for Advancing Translational Sciences of the National Institutes of Health [P30CA016672 and CCTS UL1TR003167].

Please address correspondence to Dawid Schellingerhout, MD, Neuroradiology and Imaging Physics, UT MD Anderson Cancer Center, 1400 Pressler St, Unit 1482, Houston, TX 77030; e-mail: Dawid.Schellingerhout@mdanderson.org

Indicates open access to non-subscribers at www.ajnr.org

Indicates article with online supplemental data.

http://dx.doi.org/10.3174/ajnr.A7620

obtained during the first surgical procedure, meaning that, in effect, a definitive tumor grade is obtained after some treatment decisions have already been made. When tissue is collected before bulk resection, it takes the form of small biopsy samples.[4] All tissue-based approaches have some degree of risk with regard to sampling error and cannot capture the full range of heterogeneity present inside the tumor.

In contrast to tissue sampling, MR imaging is relatively inexpensive, safe, and easy to perform. Imaging does not have sampling error, and covers the whole brain, though not at the microscopic resolution of histology. Furthermore, imaging is available before the commencement of invasive therapies. Multiple imaging findings like contrast enhancement are strongly associated with a higher WHO grade[5] and have proved very useful in the clinical management of these patients. However, most imaging findings are qualitative in nature and cannot yet replace WHO grading.

There is great clinical need for a noninvasive imaging tool that can accurately grade and stage patients with gliomas. One way is to estimate pathologic characteristics used in formulating tumor grade. Cellular density (CD) is increased in all gliomas and correlates with increasing WHO grades.[2] CD is of additional clinical interest because the subtle infiltrative nature of diffuse gliomas, with increased CD blending into the healthy brain, makes these tumors difficult to treat. Several recent works have developed models capable of estimating heightened cellularity using MR imaging data.[6-9] However, the actual prognostic value of these model estimates has not been directly validated.

In this study, we investigated image-based estimates of CD as a low-cost and low-risk predictor of overall survival for patients with gliomas. We correlated CD and the gold standard of histology-based WHO grading to overall survival in a large retrospective cohort of patients with gliomas. We found that CD is a powerful and useful prognostic feature. While WHO grading is still superior, CD information is obtained at far lower cost and risk to the patient.

MATERIALS AND METHODS

Clinical Data

We collected clinical data under a Health Insurance Portability and Accountability Act–compliant retrospective chart review protocol approved by our institutional review board with a waiver of informed consent. Clinical databases were queried for all records of patients diagnosed with gliomas who ultimately underwent surgical resection at our institution. The returned records spanned 1993 to 2018. The resulting clinical data that were analyzed included age, preoperative performance status, surgery dates, imaging dates, follow-up dates, vital status, and diagnoses, including WHO grade. A majority of patients were treated before the introduction of integrated histomolecular diagnoses as introduced in the 2016 revision of the WHO grading system and further emphasized in the 2021 revision.[1,2] Therefore, the grades reported are based, for most cases, on morphologic characteristics consistent with the WHO 2007 grading scale. We staged patients on the basis of preoperative imaging data, similar to WHO staging, which is obtained at diagnosis and is not subsequently altered. Thus, the effects of operative, chemotherapy, and radiation therapy treatment were not considered in the current analysis. Overall survival was calculated from the surgery date to the last documented follow-up time, with appropriate right censoring. The patient cohort was further refined by inclusion criteria of 18 years of age or older, WHO grade II, III, or IV gliomas, and the availability of suitable preoperative MR imaging.

Imaging Data

For each patient, preoperative imaging was queried directly from the PACS system. A summary of the sequence parameters for each image type is given in the Online Supplemental Data, and a detailed description of the data processing is provided in the Online Supplemental Data.

Images were skull-stripped to remove nonbrain tissues and coregistered.[10,11] Then, tumors were segmented using a pretrained deep learning model, and CSF ROIs were generated using automated Gaussian mixture modeling.[12] Additional details of these methods are provided in the Online Supplemental Data. Each image was normalized by mapping modal intensities of healthy brain and CSF to 0 and 1. Note, this is a slightly different scheme than the one used by Gates et al[6] but achieves comparable modeling results.

Using the normalized images, we estimated the CD voxelwise throughout the brain of each patient by applying a pretrained random forest model, which has been previously reported.[6] This model was trained on imaging and pathology data from 52 image-guided biopsy samples and estimates CD with a root mean square error of 2099 nuclei/mm^2 (the total range in the training data was approximately 14,000 nuclei/mm^2) using 4 conventional imaging sequences (T1-weighted, T2-weighted, FLAIR, and T1 postcontrast). Examples of the CD maps are shown in Fig 2. As previously reported, these maps agree with literature values for white matter of around 3000 nuclei/mm^2 and clinical intuition showing more heterogeneous and highly cellular disease with increasing clinical WHO grade.[13] Using these maps, we measured the maximum (max) CD within the visible tumor ROI, defined by the extent of T2/T2-FLAIR hyperintensity, assuming that maximal cellularity is unlikely to occur outside the radiographically visible region. Specifically, we recorded the max CD in the visible lesion after excluding the values in the highest 0.01 cm^3 of the measurement ROI as outliers. This process provides a stabilized measure of the maximum that is less sensitive to outliers than the voxelwise maximum. A detailed description is provided in the Online Supplemental Data. For routine clinical use, this measurement could be manually approximated using the mean CD in a small circular ROI of about 10 voxels across (area, about 75 voxels) in the area of highest cellularity. CD maps and the MR imaging data were manually reviewed (by E.D.H.G., with 5 years of experience) using a custom data-review dashboard implemented in R Shiny.[14] Studies with unacceptable quality, like failed image registration or excessive artifacts, were excluded from further analysis.

Statistical Analysis

We used Cox proportional hazards modeling and concordance indices (C-indices) to correlate clinical and image features with survival.[15,16] We searched for an optimal stratifying threshold in terms of the hazard ratio to create two resulting groups. This procedure was performed within 10-fold cross-validation to prevent

overfitting and false discovery of survival differences.[17] Statistical differences between the pooled high- and low-risk groups were assessed using a log-rank test and the Kaplan-Meier method.

We performed both univariate and multivariate analysis with adjustments for age and performance status (Karnofsky performance status [KPS]), then again with adjustments for age, KPS, and high WHO grade. Patients who are older and have worse performance status are known to have a poorer prognosis irrespective of other prognostic factors.[18,19] We corrected the univariate significance level to account for the number of cellularity measurements tested, using the Benjamini-Hochberg method.[20] For simplicity, we report only the best-performing CD feature, max CD. Comparison of the overall correlation between max CD as a predictor (as opposed to a measurement at a single cutoff point) can be accomplished with the C-index, which measures the degree of agreement between a set of predictors and actual survival over the entire curve.[21] Comparisons of C-indices from proportional hazards models were performed using jackknife estimates of variance.[22] Last, we applied receiver operating characteristic (ROC) analysis with CD measurements and WHO grades to identify a pair of optimal thresholds to separate the WHO grade II, III, and IV tumors using max CD and compared the agreement.

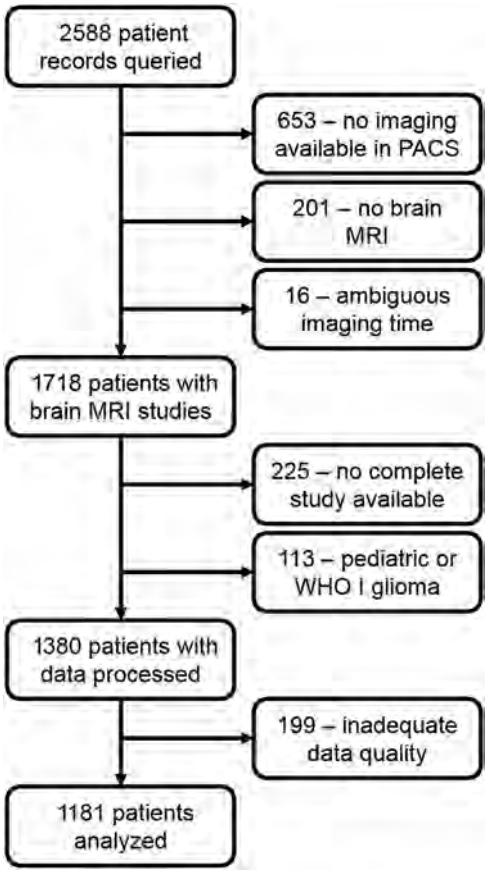

FIG 1. Flow chart for patient selection in the retrospective data. Ambiguous imaging time means the imaging and operation were on the same day. A complete study includes at least one of each of the following: T1-weighted precontrast, T1-weighted postcontrast, T2-weighted, and FLAIR images.

RESULTS

Clinical Data

A summary of the patient cohort selection process is shown in Fig 1. Among 2588 patients whose first resection was at our institution, 1718 had diagnostic imaging available. Of those, 329 had previous biopsies (as opposed to resections), and we elected to include these patients in the analysis. Exclusions were made for pediatric patients or those with WHO grade I ($n = 113$) and patients with insufficient MR imaging to apply predictive modeling ($n = 225$). After imaging data review, 199 further cases were excluded for unacceptable data quality. The most common failures were tumor segmentation (5.0% of data) and image registration (3.5% of data). The clinical characteristics of the remaining analyzable 1181 patients are summarized in Table 1.

Correlation between Survival and CD

We compared max CD (Fig 2) as a prognostic predictor with WHO grading, with age and KPS as covariates.[18,19] The univariate and multivariate hazard ratios are listed in Table 2. Max CD showed the largest survival difference among CD-based features. The optimal threshold of 7681 nuclei/mm^2 was very consistent in cross-validation (Online Supplemental Data). Low- and high-risk assignments between cross-validation and in-sample results differed for only 1 patient. The median survival for patients with highly cellular (max CD, >7681 nuclei/mm^2) tumors was 630 days compared with 5120 days for patients with low-cellularity tumors. The univariate hazard ratio between the 2 groups was 4.21, adjusted to 2.91 after correcting for covariates of age and KPS (all statistically significant), (Table 2 and Fig 3).

For comparison, the hazard ratio for histologically defined WHO grade IV disease was 7.57 on univariate analysis relative to WHO grade II and III, decreased to 5.25 for multivariate analysis when correcting for age and KPS. Max CD had C-indices of 0.662 alone, and 0.734 after adjusting for covariates, which compared well with WHO grading at 0.704, and 0.761 after adjusting for covariates (Online Supplemental Data). The concordance indices

Table 1: Clinical data summary of the 1181 cases analyzed[a]

WHO Grade	No.	Age (yr)	Sex (Male/Female)	Median KPS Score	Median Tumor Volume (mL)	Max CD (Nuclei/mm^2)	Median OS (Days)
II	207	40 (SD, 12)	121/86	90	37.16	8059 (SD, 1048)	NA[b]
III	246	43 (SD, 14)	135/111	90	47.25	8401 (SD, 1198)	5066
IV	728	59 (SD, 13)	446/282	90	72.64	10,218 (SD, 1167)	495

Note:—NA indicates not achieved; OS, overall survival.

[a] Tumor volume measurements were extracted from records collected before this study. Age and max CD are listed as means.

[b] Median survival was not reached for the WHO II group; the lowest fraction was 58% survival reached at 4147 days.

were significantly different from each other before ($P < .001$) and after ($P < .001$) adjusting for covariates.

In a combined model with age, KPS, WHO grade IV, and max CD analyzed together, the multivariate hazard ratio for CD was 1.36 ($P < .05$). The effect of WHO grade (hazard ratio = 4.60) was still larger, however, in the same model (Table 2). This combined model gave a risk score with a C-index of 0.764 with overall survival (95% CI, 0.748–0.781). This was significantly higher than the C-index for the model using just age, KPS, and a WHO grade of 0.761 ($P = .002$) (Online Supplemental Data). Again, this finding suggests some overlap but with nonredundant information present between WHO grading and max CD.

Correlation between CD and WHO Grade

The histogram of max CD values in Fig 3 shows a striking relationship between tumors with a high WHO grade (WHO IV) and larger maximum cellularity. The optimal threshold with respect to survival of 7681 nuclei/mm^2 effectively divides the high-grade (WHO grade IV) from the low-grade (WHO grade II and III) cases with a 93% sensitivity. Max CD showed no ability to differentiate WHO II from WHO III tumors due to the high overlap in the histograms. However, we were able to construct a trio of risk categories using CD that mimics the WHO II, III, and IV risk stratification, (Fig 4). We selected 2 cutoff points at 7443 and 8358 nuclei/mm^2 via ROC analysis to optimally mimic the WHO groups. These values are different from the previously mentioned 7681 nuclei/mm^2 cutoff, which was chosen to optimize overall survival differences between just two groups of patients. The number of patients and median survival for each group are tabulated in Table 3. These resulting three categories showed risk stratification visually similar to the WHO grades, though there were statistical differences in median overall survival (log-rank, $P = .004$).

One advantage of CD as a risk measure over WHO grading is that the estimated CD is a continuous measurement that can provide finer risk-stratification groups than the three-class categoric WHO grade (WHO I disease was not found in our adult population with gliomas, reducing the analysis to three categories). In proportional hazards modeling, the relation between a continuous measurement like CD and the hazard ratio is assumed to be log-linear. However, a nonlinear fit can be achieved using spline fitting. Figure 4 also shows the resulting nonlinear fit with the grade-matched cutoffs overlaid. The plateau at higher CD values (visually about >9000 nuclei/mm^2) suggests a saturation-type effect beyond which increased max CD does not further increase risk. At lower CD values, the curve is steeper (ie, greater sensitivity of risk to CD changes), suggesting that CD might allow more precise risk stratification for lower-grade gliomas. The nonlinear spline fit illustrates the relation between CD and risk at various CD levels but does not significantly improve concordance of the Cox model (C-index difference, 8×10^{-4}; $P = .65$).

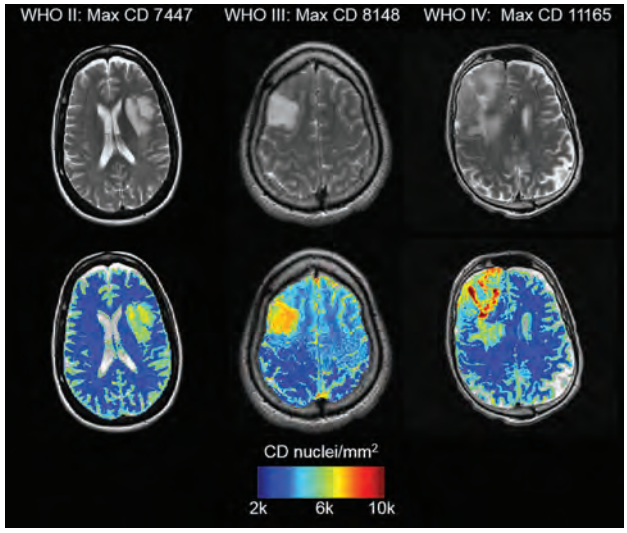

FIG 2. Maps of estimated CD for gliomas of known WHO grades. T2-weighted images are shown in the *upper row* for reference. Note the graphic nature of CD estimates and how CD maps can be used for image-guided therapy.

DISCUSSION

We estimated CD using MR imaging and a machine learning algorithm in a retrospective cohort of 1181 previously untreated

Table 2: Survival modeling for patients with all WHO grades (II, III, IV)[a]

	Univariate			Multivariate		
	HR	95% CI	*P*	HR	95% CI	*P*
Model A: C = 0.761						
Age older than 55 yr	3.69	(3.16–4.31)	<.001	2.05	(1.74–2 .42)	<.001
KPS <90	3.05	(2.61–3.57)	<.001	1.68	(1.43–1.98)	<.001
WHO grade IV	7.57	(6.18–9.27)	<.001	5.25	(4.23–6.53)	<.001
Model B: C = 0.734						
Age older than 55 yr	3.69	(3.16–4.31)	<.001	2.74	(2.33–3.22)	<.001
KPS <90	3.05	(2.61–3.57)	<.001	2.02	(1.72–2.38)	<.001
Max CD >7681	4.21	(3.05–4.42)	<.001	2.91	(2.28–3.71)	<.001
Model C: C = 0.764						
Age >older than 55 yr	3.69	(3.16–4.31)	<.001	2.02	(1.72–2.39)	<.001
KPS <90	3.05	(2.61–3.57)	<.001	1.67	(1.42–1.96)	<.001
WHO grade IV	7.57	(6.18–9.27)	<.001	4.60	(3.60–5.87)	<.001
Max CD >7681	4.21	(3.05–4.42)	<.001	1.36	(1.03–1.80)	.03

Note:—HR indicates hazard ratio; C, C-index.

[a] The univariate *P* values for max CD are corrected for multiple comparisons. The multivariate HRs are for models using only the factors listed in the specific panel. A) HRs for clinical factors and high WHO grade. B) HR for clinical factors and max CD (nuclei/square millimeter). C) HR for clinical factors, high WHO grade, and max CD. HRs for WHO grading are higher than those for max CD, but max CD retains a predictive value even when WHO grading is included in model C.

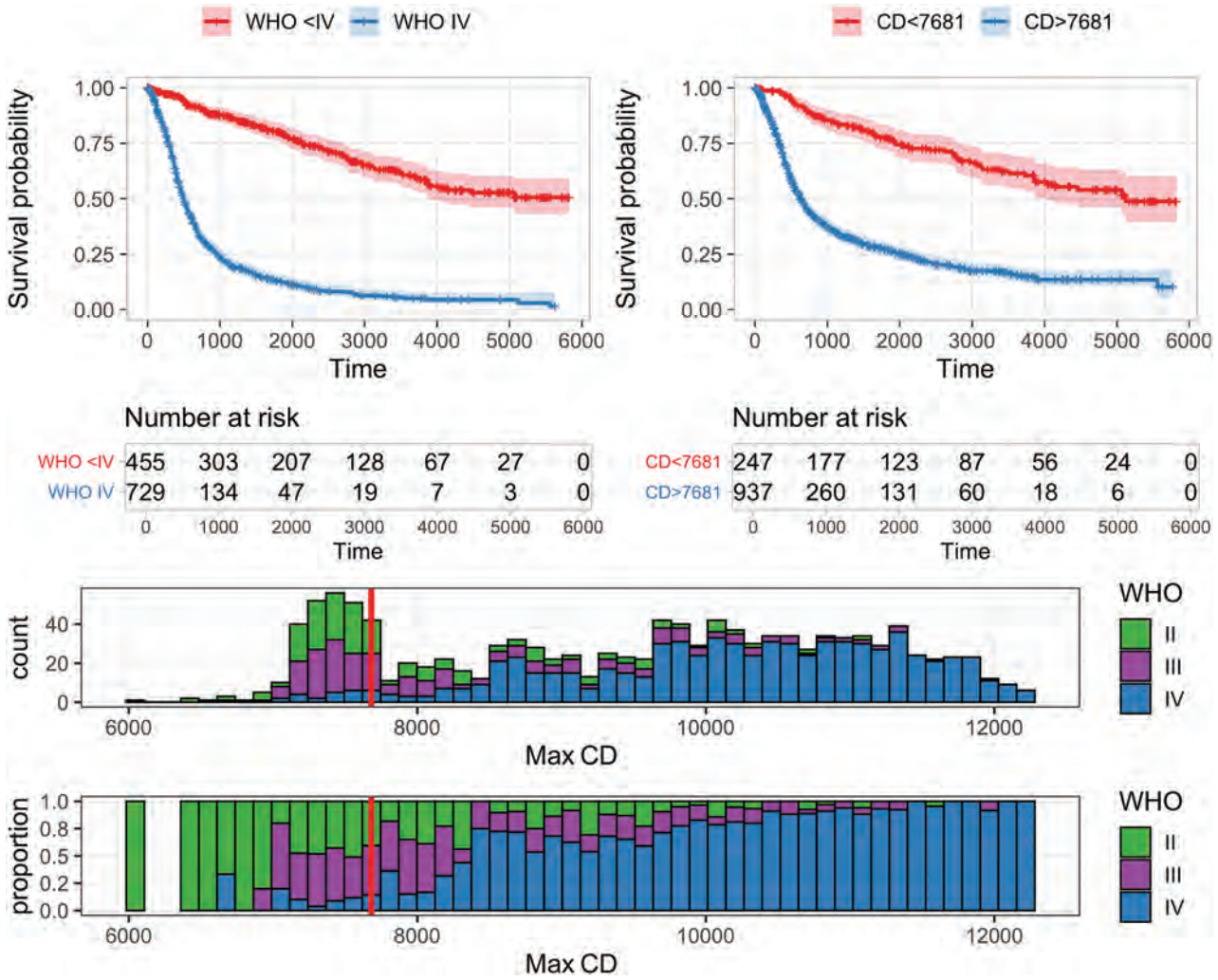

FIG 3. The best CD (in nuclei/square millimeters) measure for dichotomizing survival in adult gliomas is a max CD (stabilized with 0.01-cm^3 volume constraint) of 7681 nuclei/mm^2. *Upper left*: Patients with WHO grade IV gliomas have much worse overall survival (median, 497 days) than patients with WHO II or III gliomas (median unreached, 75% survival at 2131 days). *Upper right*: An optimal cutoff (maximizing hazard ratio) of 7681 nuclei/mm^2 divides the glioma population into groups with median survivals of 630 and 5120 days, respectively (log-rank, $P < .001$). *Lower row*: A histogram of all cases (bin size = 123 nuclei/mm^2) demonstrates stabilized max CD values ranging from 6089 to 12,260 with an interquartile range of 7632–10,717 and a mean of 9175. WHO grade II, III, and IV cases are color-coded, and the optimized cutoff value used in the *upper right panel* (7681 nuclei/mm^2) is shown with a *solid red line*. The *lower histogram* has all bins scaled to height 1 to show the relative proportion of each WHO grade in each bin.

patients with gliomas from our institution. We found that high max CD indicates worse prognosis independent of age, performance status, and even WHO tumor grade. The prognostic power of max CD is slightly less than that of the WHO grade but comes remarkably close, especially given the relatively low cost and risk of obtaining these CD estimates. The difference in concordance between a model based on WHO grade (and covariates) and the model based on CD (and covariates) was just 0.027 (95% CI, 0.016–0.037). CD estimates also have advantages over WHO grading, including timeliness, lower risk, and lower cost of the estimates. The graphic nature of the estimates also allows CD estimates to be used for image-guided therapies.

CD is known from the literature to correlate to survival.[23] Conventional and physiologic techniques like T2-FLAIR or DWI correlate with increased tissue cellularity.[24,25] Recently, several research studies have used machine learning trained on MR imaging and tissue data to quantitatively estimate CD in gliomas from imaging data alone. These models produce graphic mapping of CD that characterizes the full tumor heterogeneity and shows promising clinical applications such as identifying hypercellular regions outside contrast enhancement.[6-9] Our study differs from the current literature in that we directly evaluated the correlation between measures of cellularity and survival outcome. We focused specifically on simple, interpretable, first-order measures of cellularity rather than complex nonlinear feature combinations like texture analysis or deep filter features. Estimated cellularity maps already combine multiple sources of information from the MR images and tissue-training data, possibly rendering additional complexity unnecessary. Another key difference of our study is that we use a combined cohort of multiple WHO grades to correlate with survival, mimicking the actuality of practice before tissue diagnosis is known.

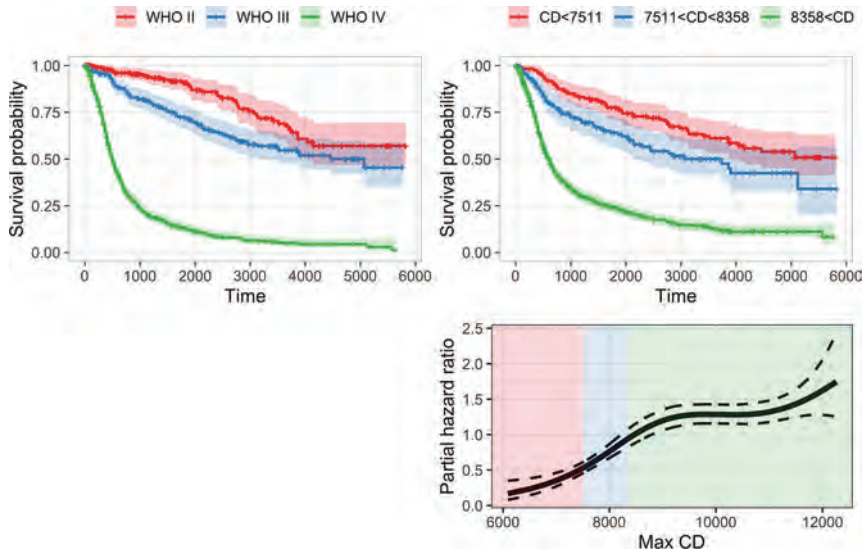

FIG 4. *Upper left*: Survival curves stratified by WHO grade. Median survival for WHO grades II, III, and IV: unreached, 3486 days, 497 days, respectively. *Upper right*: CD thresholds at 7443 and 8358 nuclei separate patients into 3 survival groups that are similar to the WHO II, III, and IV groups (median survival unreached, 3738 days, and 603 days, respectively). There is a significant difference in the *red and blue survival curves* (log-rank, $P = .004$). *Lower right*: P-spline fit (3 degrees of freedom) for nonlinear estimation of the hazard ratio with respect to CD for constant age and KPS. The reference point, hazard ratio 1, is arbitrary. The *shaded background* corresponds to the three groupings based on CD shown in the *upper right panel*. *Dashed lines* are 95% confidence intervals. Relative risk increases with increasing CD up to a max CD of about 9000 nuclei/mm^2, after which it plateaus. Max CD allows a continuous estimate of risk, unlike the categoric WHO grade.

Table 3: Patient numbers by max CD ranges (nuclei/square millimeter) and WHO grade[a]

Cellular Density Cutoff Ranges	WHO II Median OS: NA 95% CI, 4040 to NA	WHO III Median OS: 5066 95% CI, 3486 to NA	WHO IV Median OS: 495 95% CI, 463–538
CD, <7443 Median OS: NA 95% CI, 4444 to NA	65	69	13
7443 < CD < 8358 Median OS: 3738 95% CI, 2452 to NA	84	80	35
8358 < CD Median OS: 603 95% CI, 535–658	57	97	679

Note:—NA indicates not achieved; OS, overall survival.

[a] The cutoff values for CD were calibrated to separate WHO IV cases from WHO II and III cases and WHO II and III cases from each other using ROC analysis. The off-diagonal values in this matrix speak to the nonredundancy of information captured by CD and WHO grading, respectively.

One limitation of this work is gaps in the clinical data for the retrospective cohort. We account for overall survival of patients with different WHO-grade gliomas, ranging from about 12 months (WHO IV glioblastoma) to >5 years (WHO II).[26,27] However, we were not able to include therapeutic intervention or mutational profiles, which also affect outcomes.[18,27-29] Survival differences due to chemoradiation or total tumor resection range from a few months to more than a year,[27,30] and *IDH1* mutation is associated with a nearly 2-fold difference in median overall survival.[31] Most of the patients in our cohort were treated before 2015, when molecular information started being routinely collected.

Related to imaging, the retrospective nature of our study limited our control over specific imaging sequences. This issue caused some inaccuracy in the random forest that estimated cellularity because the forest was trained on data from a tightly controlled research protocol.[6] Intensity normalization accounts for much of the variability in image contrast and acquisition parameters, but the true accuracy on the retrospective data cannot be known without extensive histologic sample verification. Although the random forest estimates of CD using the conventional sequences have only a moderate correlation to actual measured CD ($R^2 = 0.52$),[6] survival models based on these estimates achieved a high concordance ($C = 0.73$) with overall survival. Two factors can explain this: First, the continuous CD estimates are binned with a threshold to designate high-risk and low-risk patients, generally an easier task than precise quantitative estimation. Second, clinical factors like age and KPS aid survival models. The fact that even rough estimates of cellularity are effective in estimating survival reinforces their potential value.

Additionally, DWI was not commonly available in the historic patient cohort. Given the well-established relationship between CD and DWI, we are eager to include this as part of future analyses. Finally, we examined the effect of preoperative cellularity on prognosis without explicitly accounting for treatment variables like gross total–versus-subtotal surgical resection or radiation treatment. While these are important, quantifying changes in CD after therapy is a very challenging image-processing task and is the subject of future investigation.

For future work, one of the most valuable directions is more accurately modeling cellularity in normal tissue like gray matter and white matter. Expanded training data in the random forest for these anatomic areas is a possible solution. Another potential solution is to apply methods from MR image synthesis to supplement the random forest to generate high-quality CD mappings (such as in Fig 2).[32] Graphical maps, either in their present form or future improved versions, will enable prospective clinical trials to validate the accuracy of cellular density estimates.

CONCLUSIONS

We evaluated the correlation between estimated glioma cellularity and survival in a large retrospective cohort of adults with infiltrative gliomas. We showed that imaging estimates of CD are a powerful and independent prognostic predictor of survival, only

slightly inferior to gold standard WHO grading. CD estimates are useful as a supplement to WHO grading due to the information being 1) timelier and available before any surgical procedures, 2) less risky to obtain than an open procedure, and 3) less costly than tissue sampling. CD estimates are useful beyond prognosis estimation in that graphic maps of CD can be used to guide biopsy and reduce the risk of undergrading and should be helpful in planning surgery and radiation treatment. In addition, CD as a continuous variable might allow more precise risk stratification, compared with the relatively coarse granularity of the categoric WHO grading scheme. Future clinical trials to prospectively test imaging-based CD estimates are justified.

Disclosure forms provided by the authors are available with the full text and PDF of this article at www.ajnr.org.

REFERENCES

1. Louis DN, Perry A, Wesseling P, et al. **The 2021 WHO Classification of Tumors of the Central Nervous System: a summary.** *Neuro Oncol* 2021;23:1231– 51 CrossRef Medline
2. Louis DN, Perry A, Reifenberger G, et al. **The 2016 World Health Organization Classification of Tumors of the Central Nervous System: a summary.** *Acta Neuropathol* 2016;131:803–20 CrossRef Medline
3. Huse JT. **Establishing a robust molecular taxonomy for diffuse gliomas of adulthood.** *Surg Pathol Clin* 2016;9:379–90 CrossRef Medline
4. Jackson RJ, Fuller GN, Abi-Said D, et al. **Limitations of stereotactic biopsy in the initial management of gliomas.** *Neuro Oncol* 2001;3:193–200 CrossRef Medline
5. Scott JN, Brasher PMA, Sevick RJ, et al. **How often are nonenhancing supratentorial gliomas malignant? A population study.** *Neurology* 2002;59:947–49 CrossRef Medline
6. Gates ED, Weinberg JS, Prabhu SS, et al. **Estimating local cellular density in glioma using MR imaging data.** *AJNR Am J Neuroradiol* 2021;42:102–08 CrossRef Medline
7. Chang PD, Malone HR, Bowden SG, et al. **A multiparametric model for mapping cellularity in glioblastoma using radiographically localized biopsies.** *AJNR Am J Neuroradiol* 2017;38:890–98 CrossRef Medline
8. Gaw N, Hawkins-Daarud A, Hu LS, et al. **Integration of machine learning and mechanistic models accurately predicts variation in cell density of glioblastoma using multiparametric MRI.** *Sci Rep* 2019;9:10063 CrossRef Medline
9. Bobholz SA, Lowman AK, Brehler M, et al. **Radio-pathomic maps of cell density identify glioma invasion beyond traditional MR imaging defined margins.** *AJNR Am J Neuroradiol* .2022;43:682–88 CrossRef Medline
10. Roy AG, Conjeti S, Navab N, et al. **Inherent Brain Segmentation Quality Control from Fully ConvNet Monte Carlo Sampling.** In: *Proceedings Part 1 of the Medical Image Computing and Computer Assisted Intervention, MICCAI 2018*, Granada, Spain. September 16–20, 2018
11. Avants BB, Tustison NJ, Song G, et al. **A reproducible evaluation of ANTs similarity metric performance in brain image registration.** *Neuroimage* 2011;54:2033–44 CrossRef Medline
12. Avants BB, Tustison NJ, Wu J, et al. **An open-source multivariate framework for n-tissue segmentation with evaluation on public data.** *Neuroinformatics* 2011;9:381–400 CrossRef Medline
13. Roetzer T, Leskovar K, Peter N, et al. **Evaluating cellularity and structural connectivity on whole brain slides using a custom-made digital pathology pipeline.** *J Neurosci Methods* 2019;311:215–21 CrossRef Medline
14. Gates ED, Celaya A, Suki D, et al. **Technical note: an efficient MR image data quality screening dashboard.** *J Appl Clin Med Phys* 2022;23: e13557 CrossRef
15. Cox DR. **Regression models and life-tables.** *J R Stat Soc Ser B Stat Methodol* 1972;34:187–220 CrossRef
16. Harrell FE Jr, Lee KL, Mark DB. **Multivariable prognostic models: issues in developing models, evaluating assumptions and adequacy, and measuring and reducing errors.** *Stat Med* 1996;15:361–87 CrossRef Medline
17. Simon RM, Subramanian J, Li MC, et al. **Using cross-validation to evaluate predictive accuracy of survival risk classifiers based on high-dimensional data.** *Brief Bioinform* 2011;12:203–14 CrossRef Medline
18. Lacroix M, Abi-Said D, Fourney DR, et al. **A multivariate analysis of 416 patients with glioblastoma multiforme: prognosis, extent of resection, and survival.** *J Neurosurg* 2001;95:190–98 CrossRef Medline
19. Li YM, Suki D, Hess K, et al. **The influence of maximum safe resection of glioblastoma on survival in 1229 patients: can we do better than gross-total resection?** *J Neurosurg* 2016;124:977–88 CrossRef Medline
20. Benjamini Y, Hochberg Y. **Controlling the false discovery rate: a practical and powerful approach to multiple testing.** *J R Stat Soc Ser B Stat Methodol* 1995;57:289–300 CrossRef
21. Therneau TM, Watson DA. **The Concordance Statistic and the Cox Model: Technical Report 85.** Department of Health Sciences Research, Mayo Clinic, Rochester, Minnesota; 2017. https://www.mayo.edu/research/departments-divisions/department-health-sciences-research/division-biomedical-statistics-informatics/publications/technical-reports.
22. Harrell FE Jr, Califf RM, Pryor DB, et al. **Evaluating the yield of medical tests.** *JAMA* 1982;247:2543–46 CrossRef Medline
23. Sahm F, Capper D, Jeibmann A, et al. **Addressing diffuse glioma as a systemic brain disease with single-cell analysis.** *Arch Neurol* 2012;69:523–26 CrossRef Medline
24. Ellingson BM, Malkin MG, Rand SD, et al. **Validation of functional diffusion maps (fDMs) as a biomarker for human glioma cellularity.** *J Magn Reson Imaging* 2010;31:538–48 CrossRef Medline
25. Latysheva A, Geier OM, Hope TR, et al. **Diagnostic utility of restriction spectrum imaging in the characterization of the peritumoral brain zone in glioblastoma: analysis of overall and progression-free survival.** *Eur J Radiol* 2020;132:109289 CrossRef Medline
26. Ohgaki H, Kleihues P. **Epidemiology and etiology of gliomas.** *Acta Neuropathol* 2005;109:93–108 CrossRef Medline
27. Stupp R, Mason WP, van den Bent MJ, et al. **Radiotherapy plus concomitant and adjuvant temozolomide for glioblastoma.** *N Engl J Med* 2005;352:987–96 CrossRef Medline
28. Hartmann C, Hentschel B, Simon M, et al; German Glioma Network. **Long-term survival in primary glioblastoma with versus without isocitrate dehydrogenase mutations.** *Clin Cancer Res* 2013;19:5146–57 CrossRef Medline
29. Reifenberger G, Wirsching HG, Knobbe-Thomsen CB, et al. **Advances in the molecular genetics of gliomas: implications for classification and therapy.** *Nat Rev Clin Oncol* 2017;14:434–52 CrossRef Medline
30. Van den Bent MJ, Hoang-Xuan K, Brandes AA, et al. **Long-term follow-up results of EORTC 26951: a randomized phase III study on adjuvant PCV chemotherapy in anaplastic oligodendroglial tumors (AOD).** *J Clin Oncol* 2012;30(18_Suppl):2–2 CrossRef
31. Yan H, Parsons DW, Jin G, et al. **IDH1 and IDH2 mutations in gliomas.** *N Engl J Med* 2009;360:765–73 CrossRef Medline
32. Wang T, Lei Y, Fu Y, et al. **A review on medical imaging synthesis using deep learning and its clinical applications.** *J Appl Clin Med Phys* 2021;22:11–36 CrossRef Medline

Arterial Spin-Labeling Parameters and Their Associations with Risk Factors, Cerebral Small-Vessel Disease, and Etiologic Subtypes of Cognitive Impairment and Dementia

B. Gyanwali, C.S. Tan, J. Petr, L.L.T. Escobosa, H. Vrooman, C. Chen, H.J. Mutsaerts, and S. Hilal

ABSTRACT

BACKGROUND AND PURPOSE: Cerebral small-vessel disease may alter cerebral blood flow (CBF) leading to brain changes and, hence, cognitive impairment and dementia. CBF and the spatial coefficient of variation can be measured quantitatively by arterial spin-labeling. We aimed to investigate the associations of demographics, vascular risk factors, location, and severity of cerebral small-vessel disease as well as the etiologic subtypes of cognitive impairment and dementia with CBF and the spatial coefficient of variation.

MATERIALS AND METHODS: Three hundred ninety patients with a diagnosis of no cognitive impairment, cognitive impairment no dementia, vascular cognitive impairment no dementia, Alzheimer disease, and vascular dementia were recruited from the memory clinic. Cerebral microbleeds and lacunes were categorized into strictly lobar, strictly deep, and mixed-location and enlarged perivascular spaces into the centrum semiovale and basal ganglia. Total and region-specific white matter hyperintensity volumes were segmented using FreeSurfer. CBF ($n = 333$) and the spatial coefficient of variation ($n = 390$) were analyzed with ExploreASL from 2D-EPI pseudocontinuous arterial spin-labeling images in white matter (WM) and gray matter (GM). To analyze the effect of demographic and vascular risk factors as well as the location and severity of cerebral small-vessel disease markers on arterial spin-labeling parameters, we constructed linear regression models, whereas logistic regression models were used to determine the association between arterial spin-labeling parameters and cognitive impairment no dementia, vascular cognitive impairment no dementia, Alzheimer disease, and vascular dementia.

RESULTS: Increasing age, male sex, hypertension, hyperlipidemia, history of heart disease, and smoking were associated with lower CBF and a higher spatial coefficient of variation. Higher numbers of lacunes and cerebral microbleeds were associated with lower CBF and a higher spatial coefficient of variation. Location-specific analysis showed mixed-location lacunes and cerebral microbleeds were associated with lower CBF. Higher total, anterior, and posterior white matter hyperintensity volumes were associated with a higher spatial coefficient of variation. No association was observed between enlarged perivascular spaces and arterial spin-labeling parameters. A higher spatial coefficient of variation was associated with the diagnosis of vascular cognitive impairment no dementia, Alzheimer's disease, and vascular dementia.

CONCLUSIONS: Reduced CBF and an increased spatial coefficient of variation were associated with cerebral small-vessel disease, and more specifically lacunes, whereas cerebral microbleeds and white matter hyperintensities were associated with WM-CBF and GM spatial coefficient of variation. The spatial coefficient of variation was associated with cognitive impairment and dementia, suggesting that hypoperfusion might be the key underlying mechanism for vascular brain damage.

ABBREVIATIONS: AD = Alzheimer's disease; ASL = arterial spin-labeling; ATT = arterial transit time; CIND = cognitive impairment no dementia; CMB = cerebral microbleed; NCI = no cognitive impairment; ePVS = enlarged perivascular spaces; PLD = post-labeling delay; sCoV = spatial coefficient of variation; SVD = cerebral small-vessel disease; VaD = vascular dementia; VCIND = vascular CIND; WMH = white matter hyperintensities

CBF ensures a constant delivery of oxygen and nutrients to brain tissue.[1] Recently, the assessment of CBF has become a common clinical investigation to evaluate vascular brain damage,[2] owing to the noninvasive and quantitative measurement by arterial spin-labeling (ASL).[1] Reduced CBF has been linked with normal aging[3] and systemic vascular risk factors such as

Received February 1, 2022; accepted after revision July 1.

From the Memory Aging and Cognition Centre (B.G., C.C., S.H.), National University Health System, Singapore; Saw Swee Hock School of Public Health (C.S.T., L.L.T.E., S.H.), National University of Singapore, and National University Health System, Singapore; Helmholtz-Zentrum Dresden-Rossendorf (J.P.), Institute of Radiopharmaceutical Cancer Research, Dresden, Germany; Department of Radiology and Nuclear Medicine (H.V.), Erasmus University Medical Center, Rotterdam, The Netherlands; Department of Pharmacology (C.C., S.H.), Yong Loo Lin School of Medicine, National University of Singapore, Singapore; Department of Radiology (H.J.M.), VU University Medical Center, Amsterdam, the Netherlands; and Department of Radiology (H.J.M.), Brain Center Rudolf Magnus, University Medical Center, Utrecht, the Netherlands.

This work was supported by the National Medical Research Council, Singapore (NMRC/CG/NUHS/2010, NMRC/CG/013/2013, NMRC/CIRG/1485/2018, NMRC/CAS-SI/007/2016), the National University of Singapore start-up grant (R-608-000-257-133), and the National University Health System Center Seed Funding Grant (R-608-000-275-511), Transition Award (A-0006310-00-00) and Ministry of Education, Academic Research Fund Tier 1 (A-0006106-00-00).

Please address correspondence to Saima Hilal, PhD, Saw Swee Hock School of Public Health, National University of Singapore, Tahir Foundation Building, 12 Science Dr 2, No. 10-03T, Singapore 117549; e-mail: saimahilal@nus.edu.sg; @bibek_BG; @HilalSaima; @AgingMACC

Indicates open access to non-subscribers at www.ajnr.org

Indicates article with online supplemental data.

http://dx.doi.org/10.3174/ajnr.A7630

hypertension, hyperlipidemia, and diabetes[4] and may manifest as cerebral small-vessel disease (SVD).[5]

SVD such as lacunes, white matter hyperintensities (WMH), cerebral microbleeds (CMBs), and enlarged perivascular spaces (ePVS) have been attributed to cerebral ischemia and hypoperfusion.[6,7] Previous studies used ASL to demonstrate the association between reduced CBF with the presence and severity of WMH,[8] an increased number of CMBs,[9,10] and lacunar infarcts.[11,12] However, the most important risk factors of hypoperfusion and how it contributes to SVD and cognitive impairment remain inconclusive. No studies have yet examined the association of ePVS with CBF parameters. Furthermore, the relationship between the location and severity of SVD with CBF in gray matter (GM) and white matter (WM) as measured by ASL has not yet been elucidated.

Reduced CBF due to vascular disease might be related to Alzheimer's disease (AD) as well as its preclinical stages, ie, mild cognitive impairment or cognitive impairment no dementia (CIND).[13,14] Previous ASL studies have focused on mild cognitive impairment and AD, showing marked CBF reduction in the cortical area,[14] with very limited studies on vascular CIND (VCIND) and vascular dementia (VaD).[14,15] This limitation is mainly attributed to vascular artifacts commonly encountered in the elderly, making it difficult to quantify CBF with the commonly used single post-labeling delay (PLD) ASL.[16] The spatial coefficient of variation (sCoV) of ASL images has been recently proposed to quantify the presence of vascular artifacts to overcome this issue.[16] While abnormality in the sCoV cannot be interpreted as abnormal CBF, a higher sCoV was shown to correlate with arterial transit time (ATT), age, and sex,[16] making it a potential proxy marker of vessel insufficiency. The sCoV can thus be used to quantify perfusion-related changes in combination with CBF and allow studying the ASL data in populations in which CBF alone is not conclusive. Previous research has mostly focused on the white American and European populations, with limited research on Southeast Asians, who have a higher prevalence of vascular risk factors, SVD, cognitive impairment, and dementia.[17]

We first aimed to determine the association between demographic and vascular risk factors as well as the location and severity of SVD with ASL perfusion parameters (GM-CBF, WM-CBF, GM-sCoV, and WM-sCoV). Second, we aimed to analyze the association of ASL parameters with etiologic subtypes of cognitive impairment and dementia: CIND, VCIND, AD, and VaD in a memory clinic population.

MATERIALS AND METHODS

Study Population

This study drew patients from a memory clinic of National University Hospital, Singapore, with the following diagnostic categories: no cognitive impairment (NCI), CIND, and dementia. The diagnosis of cognitive impairment was based on the clinical presentation as well as detailed neuropsychological assessments following the recommendation of the National Institute of Neurologic Disorders and Stroke and the Canadian Stroke Network (Online Supplemental Data).

From August 2010 to November 2017, a total of 579 participants were recruited who underwent clinical, physical, and neuropsychological assessments along with a 3T brain MR imaging at the National University of Singapore. Of 579 participants, 12 did not undergo MR imaging, and 52 had no ASL sequence, leaving 515 patients for ASL analysis.

Ethics approval was obtained from the National Healthcare Group Domain Specific Review Board. Written informed consent was obtained from all patients before their participation in this study.

Demographics and Vascular Risk Factors

A detailed questionnaire was administered to all participants to document age, sex, race, and education. Any history of hypertension, hyperlipidemia, and type 2 diabetes mellitus was noted and verified by medical records. A history of stroke was ascertained by a questionnaire and confirmed from medical records. A history of heart disease was defined as a previous diagnosis of myocardial infarction, congestive heart failure, atrial fibrillation, or intervention procedures such as angioplasty or stent placement. Smoking was categorized as "ever" versus "never."

Neuroimaging

MR imaging was performed at the National University of Singapore Clinical Imaging Research Center using a 3T Magnetom Trio, a Tim system (Siemens) with a 32-channel head coil. The standardized neuroimaging protocol in this study included 3D T1-weighted, T2-weighted, FLAIR, and SWI sequences.

MR imaging markers of SVD (CMBs, lacunes, ePVS) were defined on the basis of the Standards for Reporting Vascular Changes on Neuroimaging (STRIVE) criteria.[18] Quantitative MR imaging analyses for WMH volume were performed using FreeSurfer, Version 5.1.0 (http://surfer.nmr.mgh.harvard.edu) on T1-weighted images (Online Supplemental Data).

ASL Parameters. Pseudocontinuous ASL was acquired with a 2D gradient-echo echo-planar imaging readout with the following parameters: voxel size = $3 \times 3 \times 5\text{mm}^3$, 24 slices, labeling duration = 1656 ms, initial PLD = 1500 ms, section readout time = 49.94 ms leading to a PLD range of 1500–2649 ms across all slices or a mean PLD of 2074 ms, TR/TE = 4000/9 ms, and generalized autocalibrating partially parallel acquisitions factor = 3. Two ASL volumes of 23 control-label pairs were acquired with a 1-hour interval and were concatenated into 1 ASL time-series to decrease physiologic fluctuations. ASL image-processing was performed with ExploreASL software (https://github.com/ExploreASL/ExploreASL) (default settings without hematocrit correction) based on SPM (http://www.fil.ion.ucl.ac.uk/spm/software/spm12) and Matlab (MathWorks).[19] From the CBF map, we acquired 4 ASL parameters: GM-CBF, WM-CBF, GM-sCoV, and WM-sCoV. CBF reflects perfusion in milliliters of blood/100-g tissue/min and was calculated in total GM and WM regions of interest (ROIs). sCoV, which was shown to serve as a proxy for ATT, was defined as the SD of ASL signal/mean ASL signal within an ROI. We performed quality assessment of the ASL scans blinded to the clinical diagnosis. On the basis of visual assessment, 515 scans were classified into 1 of the 4 categories:

- Unusable scans that were incomplete, had labeling errors, or severe motion artifacts ($n = 125$)
- Angiography scans with dominant vascular artifacts and no or minimal tissue perfusion contrast ($n = 57$)

- Acceptable scans with minor (vascular) artifacts and reasonable tissue perfusion contrast ($n = 166$)
- Good artifact-free scans with tissue perfusion contrast ($n = 167$).

For the sCoV analysis, we used a total of 390 patients, including scans with angiography and acceptable and good scans. For the CBF analysis, the 57 patients who had an angiography-like ASL scan were excluded, resulting in 333 patients for the CBF analysis.

Statistical Analysis

In this study, CMBs, lacunes, WMH volume, and ePVS were treated as counts and categoric variables. For categoric data, we classified CMBs as 0, 1, 2–4, >4; lacunes as 0, 1, ≥2 and by their location (strictly lobar, strictly deep, and mixed-location); and ePVS as ≤10, 11–20, >20 and by location (centrum semiovale and basal ganglia). WMH volumes were logarithmically (log) transformed due to skewed distribution and were divided into tertiles (the first tertile was used as a reference) and by location (anterior and posterior).

For linear regression analysis, the log transformation of ASL parameter data (GM-CBF, WM-CBF, GM-sCoV, and WM-sCoV) was performed to ensure a normal distribution. Log-transformed ASL data were then standardized by dividing each variable by its SD. ASL data were used as continuous data (CBF: 1 SD unit decrease in 10 log; and sCoV: 1 SD unit increase in 10 log). Post-logarithmic transformation normality tests revealed normal distribution for most of the variables. To analyze the relationship between CBF (log GM-CBF) and sCoV (log GM-sCoV), we performed a Pearson correlation analysis. Finally, to analyze the effect of demographic and vascular risk factors on ASL parameters, we constructed linear regression models with the mean difference (β) and 95% CI. All models were first adjusted for age and sex and subsequently for hypertension, hyperlipidemia, diabetes, history of heart disease, history of stroke, and smoking. The same regression models were then conducted to analyze the association between location and severity of SVD markers with ASL parameters. In regression analyses, SVD markers were treated as determinants, and ASL parameters, as outcomes. We repeated these analyses for the 3 diagnostic groups: ie, NCI, CIND, and dementia.

Logistic regression models with ORs and 95% CIs were used to determine the association between ASL parameters and CIND, VCIND, AD, and VaD (NCI was used as the reference group). Models were adjusted for age, sex, education, and vascular risk factors. Results were considered significant at $P < .05$.

RESULTS

Baseline Characteristics

The characteristics of the study participants in CBF ($n = 333$) and sCoV ($n = 390$) analyses are shown in the Online Supplemental Data. There was a high prevalence of vascular risk factors and SVD in participants. In this study, we excluded 189 participants with ASL labeling errors or severe motion artifacts or no MR images. Excluded participants were significantly older, less educated, had a higher burden of vascular risk factors, and had dementia (Online Supplemental Data). Furthermore, those participants in whom CBF could not be measured ($n = 570$) were older (75 years versus 73 years), a significant number of participants were men (8.7% versus 42.0%), had a history of heart disease (31.6% versus 11.4%) and higher burden of cardiovascular risk factors, and more had dementia (47.4% versus 24.0%) compared with those in whom CMB could be measured ($n = 333$) (data not shown). We analyzed the correlation between GM-sCOV and GM-CBF in 333 subjects (with both CBF and sCoV data), and there was a negative correlation between log GM-CBF and log GM-sCOV ($r = -0.767$, $R^2 = 0.588$, $P < .001$) (data not shown).

WM-sCoV

The results for the association between WM-sCoV and demographics, vascular factors, SVD, and etiologic subtypes of cognitive impairment and dementia are shown in the Online Supplemental Data. However, WM-sCoV was associated with age, sex, vascular risk factors, and SVD in this study, and we did not further discuss these findings because the results were similar to the GM-sCoV results and did not add further insight into our findings. Furthermore, ASL measurements have a higher SNR and higher accuracy in GM compared with WM because CBF is higher and ATT is shorter in GM than in WM;[16,20] hence, our findings with respect to WM-sCoV may not be accurate.

Determinants of ASL Parameters

Among demographic and vascular risk factors, older age and male sex were associated with significant changes in all 3 ASL parameters (lower GM-CBF and WM-CBF, and higher GM-sCoV), whereas hyperlipidemia was associated with reduced GM-CBF; smoking, with a lower mean WM-CBF; and hypertension and a history of heart disease, with higher GM-sCoV. Moreover, there was borderline significance with smoking and higher GM-sCoV (Online Supplemental Data).

Location and Severity of SVD and ASL Parameters

An increased severity of lacunes was associated with changes in all 3 ASL parameters: lower GM-CBF, a comparable decrease in WM-CBF, and higher mean GM-sCoV. Similarly, the presence of ≥2 lacunes was associated with higher mean GM-sCoV. The increased severity of CMBs as well as the presence of >4 CMBs were associated with lower mean WM-CBF and higher mean GM-sCoV, but lower mean GM-CBF did not reach statistical significance. Similarly, total WMH volume and second and third tertiles of WMH volumes were associated with higher mean GM-sCoV. In addition, WMH volume in the third tertile was also associated with lower mean WM-CBF. However, the severity of ePVS was not associated with ASL parameters. Stratifying ePVS into ≤10 ePVS, 11–20 ePVS, and >20 ePVS also did not show any significant association (Online Supplemental Data).

An increased number of mixed-location lacunes were associated with lower GM- and WM-CBF and higher GM-sCoV. Similarly, an increased number of mixed-location CMBs were associated with lower WM-CBF and higher GM-sCoV, but not with GM-CBF. Higher volumes of anterior and posterior WMHs were associated with lower WM-CBF and higher GM-sCoV. WMH volumes in the anterior and posterior regions were not associated with lower GM-CBF. In contrast, ePVS in the centrum semiovale and basal ganglia were not associated with any of the 3 ASL parameters (Online Supplemental Data).

Stratified analysis among participants with NCI, CIND, and dementia also showed similar associations (Online Supplemental Data).

ASL Parameters with Etiologic Subtypes of Cognitive Impairment and Dementia

Lower GM-CBF was associated with AD, whereas lower WM-CBF was associated with CIND. There was borderline significance of lower WM-CBF with AD. Lower GM- and WM-CBF were not associated with the diagnosis of VCIND and VaD. By contrast, higher GM-sCoV was associated with VCIND, AD, and VaD, but not CIND (Online Supplemental Data).

DISCUSSION

In this study, we found that increasing age, male sex, hyperlipidemia, and smoking were associated with lower CBF, whereas increasing age, male sex, hypertension, and a history of heart disease were associated with higher GM-sCoV. With respect to SVD, increased severity of lacunes and mixed-location lacunes were associated with reduced CBF. Similarly, an increased severity of CMBs, specifically mixed-location CMBs, and total WMH volume including anterior and posterior regions were associated with lower WM-CBF and higher GM-sCoV. Higher GM-sCoV was associated with etiologic subtypes of cognitive impairment and dementia.

The association of increasing age with hypoperfusion is in line with findings in previous studies. Age was previously associated with endothelial dysfunction and vascular remodeling, leading to chronic hypoperfusion[21] and impaired cerebral autoregulation, causing several hemodynamic changes in the brain.[22] The tortuosity of cerebral microvascular vessels was found to be increased in the elderly compared with young adults[23] and was associated with reduced CBF.[24] Most of the tortuous arteries are found in the WM of the brain,[24] which may explain the lower WM-CBF in this study. Similarly, we found that men had more cerebral hypoperfusion compared to women, suggesting differences in brain structure, chemistry, and function.[24] Estrogen is found to be protective against ischemia.[26] Moreover, women tend to have smaller brain volume, higher cerebral metabolic rate, higher resting CBF, and lower vascular risk factors compared with men.[25]

Hypoperfusion due to hypertension can result from increased vessel stiffness due to atherosclerosis, disturbed hemodynamic flow patterns, and increased vascular resistance.[27] Hypertension can damage brain endothelial cells, which produce the vasodilator nitric oxide, contributing to cerebral hypoperfusion and hence higher GM-sCoV in our study.[28] Similarly, hyperlipidemia has been considered an important risk factor for decreased cerebral perfusion.[29] High levels of blood cholesterol and triglycerides lead to the accumulation of fatty deposits in the walls of arteries, resulting in narrowing of the lumen and reducing the supply of blood to the brain.[30] Smoking, on the other hand, increases the formation of plaque in blood vessels, which narrows the lumen of the blood vessels.[31] Furthermore, nicotine causes blood vessels to constrict and also stimulates the release of catecholamines and other free radicals, which injure arterial endothelium, promote atherogenesis, and eventually reduce CBF.[32] It has been shown that heart diseases such as myocardial infarction, congestive heart failure, and atrial fibrillation decrease cardiac output and reduce cerebral perfusion.[33] A previous study has shown that patients with heart disease are at increased risk of atrial thrombogenicity and cardioembolism, leading to ischemic brain disease.[34]

We found that SVD such as lacunes and CMBs was associated with lower WM-CBF and higher GM-sCoV, whereas total WMH volume was only associated with higher GM-sCoV. This finding could be because SVD markers are the consequence of cerebral amyloid angiopathy (CAA) and hypertensive arteriopathy. Lower CBF and higher sCoV due to SVD in this study may be due to amyloid deposition in the blood vessels and arteriosclerosis, which contributes to narrowing of the vessel lumen, leading to hypoperfusion.[6] Such reduced cerebral perfusion may lead to tissue damage, infarction, and additionally CMBs.[35]

We found that mixed-location lacunes and CMBs and WMH located in the anterior and posterior regions were associated with a lower CBF and higher sCoV. This finding can be because mixed lacunes and mixed CMBs represent mixed pathology, so patients with both CAA and hypertensive arteriopathy are more susceptible to cerebral ischemia and may exhibit mixed-location SVD on MR imaging.[6] By contrast, the location and severity of ePVS were not associated with ASL parameters. As ePVS are considered an early MR imaging marker of SVD,[36,37] we speculate that our study population might be already in the more advanced stage of the disease, which may explain the lack of association between the location and severity of ePVS with ASL parameters. Furthermore, it has been shown that perivascular spaces are present in abundance throughout the healthy brain[38] and may, thus, represent a nonpathologic process of aging with no contribution to hypoperfusion. As perivascular spaces are the fluid-filled spaces surrounding the penetrating vessels, responsible for regulating the immune response and drainage of interstitial fluids,[38] they are unlikely to affect cerebral perfusion.

We found that increased GM-sCoV was associated with the diagnoses of VCIND, AD, and VaD. These results indicate involvement of increased ATT and might reflect a reduction in the blood supply due to SVD, reduced neuronal activity, and cerebral atrophy.[39] It is further shown that hypoperfusion induces neurovascular dysfunction, triggering amyloid aggregation in the brain leading to cognitive impairment and dementia.[40] Accumulation of amyloid-β in the brain parenchyma and in the cerebral blood vessels starts decades before the onset of clinical symptoms of AD, implying that an early ischemic insult might initiate the disease process.[41] This possibility might explain the increased sCoV in our patients with VCIND and reduced CBF in patients with CIND, causing speculation that GM- and WM-CBF alone may not be reliable indicators of disease at the later stage. These results suggest that chronic vascular hypoperfusion could contribute to neuronal damage, cognitive impairment, and dementia; hence, the sCoV of ASL could be a marker of disease severity.

Moreover, higher sCoV was linked with increased ATT.[16] At the same time, WM-CBF is known to be difficult to measure, and ASL measurements are known to underestimate WM-CBF for a longer ATT, especially in deep WM.[20] However, we have observed that an increase in the sCoV was not necessarily connected with a decrease in WM-CBF or at least not a larger decrease than in GM-CBF.[19] It has been shown that measuring significant WM signal is possible, though this might be difficult with standard PLD and

acquisition duration in deep WM, and delayed ATT can manifest itself as lower CBF on ASL measurements, even though the perfusion might be intact.[42] A similar observation was made using healthy volunteers and very long breath-holds. A hypercapnic state leads to reduction of ATT, making the ATT/PLD combination much more favorable for measuring CBF than in normal settings that lead to a higher increase in WM-CBF than in GM-CBF, showing the important role of a short ATT in CBF measurement in WM with ASL.[43] Similarly, a decrease in WM-CBF was not always explained by an increase in the sCoV.[19] This finding leads us to an assumption that despite needing to be interpreted with care, real WM-CBF differences can be observed in our data. Similarly, certain redistributions between the macro- and microvascular compartments can be detected with the sCoV changes without being really reflected by changes in GM- or WM-CBF. Taken together, despite the WM-CBF measurement with ASL being difficult and absolute CBF values not being fully reliable, WM-CBF can still yield interesting information.

In our current study, there was negative correlation between CBF and sCOV in 333 subjects (with both CBF and sCoV data). This is partially correct because those 333 scans were labeled as good and acceptable. However, in this study, there are also another 57 scans labeled as angiography with scans with dominant vascular artifacts, and no-or-minimal tissue perfusion contrast when calculated CBF cannot be reliable. Analyzing the sCoV allows us to include more data in this study, especially when the study population is older adults with a higher burden of cerebrovascular disease. Thus, we believe that the sCoV is a good proxy parameter of global cerebrovascular health when CBF cannot be used interchangeably with sCoV.

The limitations of this study are, first, that ASL image quality can be affected by older age and dementia because these patients often find it difficult to stay still inside the scanner. To minimize this bias, we excluded those scans labeled as angiography and unusable. Furthermore, individuals who were more ill were excluded from the study, possibly affecting both the group analysis and individual clinical findings. Second, because this is a cross-sectional study, we cannot prove that SVD and a decrease in CBF or an increase in the sCoV across time caused hypoperfusion or vice versa. Future longitudinal studies are needed to understand the cause-effect relation between hypoperfusion and SVD. Third, in this study, not all participants underwent a brain PET scan to confirm the presence of amyloid or tau pathology; hence, the participants with AD could be considered as having probable AD. Finally, WM-CBF is difficult to measure with ASL, especially for longer ATTs.[20] However, we observed that an increase in the sCoV, associated with increased ATT,[16] was not necessarily connected with a decrease in WM-CBF.[19] We, therefore, assume that some true WM-CBF differences might be observed in our data.

CONCLUSIONS

In this study, we found that a higher sCoV of ASL images was associated with cognitive impairment and dementia, as well as with lacunes, WMH, and CMB, but not with ePVS. Our findings suggest that SVD may induce brain changes via vascular insufficiency, implying that chronic hypoperfusion may increase the risk for neuronal injury and neurodegeneration. Hence, sCoV of ASL images may be a useful indicator of vascular brain damage.

Disclosure forms provided by the authors are available with the full text and PDF of this article at www.ajnr.org.

REFERENCES

1. Petcharunpaisan S, Ramalho J, Castillo M. **Arterial spin-labeling in neuroimaging.** *World J Radiol* 2010;2:384–98 CrossRef Medline
2. Grade M, Hernandez Tamames JA, Pizzini FB, et al. **A neuroradiologist's guide to arterial spin-labeling MRI in clinical practice.** *Neuroradiology* 2015;57:1181–1202 CrossRef Medline
3. Wu C, Honarmand AR, Schnell S, et al. **Age-related changes of normal cerebral and cardiac blood flow in children and adults aged 7 months to 61 years.** *J Am Heart Assoc* 2016;5:e002657 CrossRef Medline
4. Bangen KJ, Nation DA, Clark LR, et al. **Interactive effects of vascular risk burden and advanced age on cerebral blood flow.** *Front Aging Neurosci* 2014;6:159 CrossRef Medline
5. Pantoni L, Poggesi A, Inzitari D. **Cognitive decline and dementia related to cerebrovascular diseases: some evidence and concepts.** *Cerebrovasc Dis* 2009;27 Suppl 1:191–96 CrossRef Medline
6. Gyanwali B, Shaik MA, Tan CS, et al. **Mixed-location cerebral microbleeds as a biomarker of neurodegeneration in a memory clinic population.** *Aging* 2019;11:10581–96 CrossRef Medline
7. Charidimou A, Boulouis G, Pasi M, et al. **MRI-visible perivascular spaces in cerebral amyloid angiopathy and hypertensive arteriopathy.** *Neurology* 2017;88:1157–64 CrossRef Medline
8. Bastos-Leite AJ, Kuijer JP, Rombouts SA, et al. **Cerebral blood flow by using pulsed arterial spin-labeling in elderly subjects with white matter hyperintensities.** *AJNR Am J Neuroradiol* 2008;29:1296–1301 CrossRef Medline
9. Hashimoto T, Yokota C, Koshino K, et al. **Cerebral blood flow and metabolism associated with cerebral microbleeds in small vessel disease.** *Ann Nucl Med* 2016;30:494–500 CrossRef Medline
10. Doi H, Inamizu S, Saito B-Y, et al. **Analysis of cerebral lobar microbleeds and a decreased cerebral blood flow in a memory clinic setting.** *Intern Med* 2015;54:1027–33 CrossRef Medline
11. Thamm T, Zweynert S, Piper SK, et al. **Diagnostic and prognostic benefit of arterial spin labeling in subacute stroke.** *Brain Behav* 2019;9:e01271 CrossRef Medline
12. Zaharchuk G. **Arterial spin-labeled perfusion imaging in acute ischemic stroke.** *Stroke* 2014;45:1202–07 CrossRef Medline
13. Riederer I, Bohn KP, Preibisch C, et al. **Alzheimer disease and mild cognitive impairment: integrated pulsed arterial spin-labeling MRI and 18F-FDG PET.** *Radiology* 2018;288:198–206 CrossRef Medline
14. Schuff N, Matsumoto S, Kmiecik J, et al. **Cerebral blood flow in ischemic vascular dementia and Alzheimer's disease, measured by arterial spin-labeling magnetic resonance imaging.** *Alzheimers Dement* 2009;5:454–62 CrossRef Medline
15. Sun Y, Cao W, Ding W, et al. **Cerebral blood flow alterations as assessed by 3D ASL in cognitive impairment in patients with subcortical vascular cognitive impairment: a marker for disease severity.** *Front Aging Neurosci* 2016;8:211 CrossRef Medline
16. Mutsaerts HJ, Petr J, Václavů L, et al. **The spatial coefficient of variation in arterial spin-labeling cerebral blood flow images.** *J Cereb Blood Flow Metab* 2017;37:3184–92 CrossRef Medline
17. Hilal S, Mok V, Youn YC, et al. **Prevalence, risk factors and consequences of cerebral small vessel diseases: data from three Asian countries.** *J Neurol Neurosurg Psychiatry* 2017;88:669–74 CrossRef Medline
18. Wardlaw JM, Smith EE, Biessels GJ, et al STandards for ReportIng Vascular changes on nEuroimaging (STRIVE v1). **Neuroimaging standards for research into small vessel disease and its contribution to ageing and neurodegeneration.** *Lancet Neurol* 2013;12:822–38 CrossRef Medline
19. Mutsaerts HJ, Petr J, Groot P, et al. **ExploreASL: an image processing pipeline for multi-center ASL perfusion MRI studies.** *Neuroimage* 2020;219:117031 CrossRef Medline

20. Skurdal MJ, Bjørnerud A, van Osch MJ, et al. **Voxel-wise perfusion assessment in cerebral white matter with PCASL at 3T: is it possible and how long does it take?** *PLoS One* 2015;10:e0135596 CrossRef Medline
21. El Assar M, Angulo J, Vallejo S, et al. **Mechanisms involved in the aging-induced vascular dysfunction.** *Front Physiol* 2012;3:132 CrossRef Medline
22. Wagner M, Jurcoane A, Volz S, et al. **Age-related changes of cerebral autoregulation: new insights with quantitative T2′-mapping and pulsed arterial spin-labeling MR imaging.** *AJNR Am J Neuroradiol* 2012;33:2081–88 CrossRef Medline
23. Thore CR, Anstrom JA, Moody DM, et al. **Morphometric analysis of arteriolar tortuosity in human cerebral white matter of preterm, young, and aged subjects.** *J Neuropathol Exp Neurol* 2007;66:337–45 CrossRef Medline
24. Xu X, Wang B, Ren C, et al. **Age-related impairment of vascular structure and functions.** *Aging Dis* 2017;8:590–610 CrossRef Medline
25. Cosgrove KP, Mazure CM, Staley JK. **Evolving knowledge of sex differences in brain structure, function, and chemistry.** *Biol Psychiatry* 2007;62:847–55 CrossRef Medline
26. Suzuki S, Brown CM, Wise PM. **Neuroprotective effects of estrogens following ischemic stroke.** *Front Neuroendocrinol* 2009;30:201–11 CrossRef Medline
27. de la Torre JC. **Cardiovascular risk factors promote brain hypoperfusion leading to cognitive decline and dementia.** *Cardiovasc Psychiatry Neurol* 2012;2012:367516 CrossRef Medline
28. Ramchandra R, Barrett CJ, Malpas SC. **Nitric oxide and sympathetic nerve activity in the control of blood pressure.** *Clin Exp Pharmacol Physiol* 2005;32:440–46 CrossRef Medline
29. Meyer JS, Rogers RL, Mortel KF, et al. **Hyperlipidemia is a risk factor for decreased cerebral perfusion and stroke.** *Arch Neurol* 1987;44:418–22 CrossRef Medline
30. Yaghi S, Elkind MS. **Lipids and cerebrovascular disease: research and practice.** *Stroke* 2015;46:3322–28 CrossRef Medline
31. Redgrave JN, Lovett JK, Rothwell PM. **Histological features of symptomatic carotid plaques in relation to age and smoking: the Oxford plaque study.** *Stroke* 2010;41:2288–94 CrossRef Medline
32. Powell JT. **Vascular damage from smoking: disease mechanisms at the arterial wall.** *Vasc Med* 1998;3:21–28 CrossRef Medline
33. Mishra RK, Li Y, Ricardo AC, et al. **Association of N-terminal pro-B-type natriuretic peptide with left ventricular structure and function in chronic kidney disease (from the Chronic Renal Insufficiency Cohort [CRIC]).** *Am J Cardiol* 2013;111:432–38 CrossRef Medline
34. Kim W, Kim EJ. **Heart failure as a risk factor for stroke.** *J Stroke* 2018;20:33–45 CrossRef Medline
35. Schreiber S, Bueche CZ, Garz C, et al. **The pathologic cascade of cerebrovascular lesions in SHRSP: is erythrocyte accumulation an early phase?** *J Cereb Blood Flow Metab* 2012;32:278–90 CrossRef Medline
36. Gyanwali B, Vrooman H, Venketasubramanian N, et al. **Cerebral small vessel disease and enlarged perivascular spaces-data from memory clinic and population-based settings.** *Front Neurol* 2019;10:669 CrossRef Medline
37. Francis F, Ballerini L, Wardlaw JM. **Perivascular spaces and their associations with risk factors, clinical disorders and neuroimaging features: a systematic review and meta-analysis.** *Int J Stroke* 2019;14:359–71 CrossRef Medline
38. Bouvy WH, Zwanenburg JJ, Reinink R, et al; Utrecht Vascular Cognitive Impairment (VCI) Study Group. **Perivascular spaces on 7 Tesla brain MRI are related to markers of small vessel disease but not to age or cardiovascular risk factors.** *J Cereb Blood Flow Metab* 2016;36:1708–17 CrossRef Medline
39. Kalaria RN. **Vascular basis for brain degeneration: faltering controls and risk factors for dementia.** *Nutr Rev* 2010;68 Suppl 2:S74–87 CrossRef Medline
40. ElAli A, Thériault P, Préfontaine P, et al. **Mild chronic cerebral hypoperfusion induces neurovascular dysfunction, triggering peripheral beta-amyloid brain entry and aggregation.** *Acta Neuropathol Commun* 2013;1:75–75 CrossRef Medline
41. Beason-Held LL, Goh JO, An Y, et al. **Changes in brain function occur years before the onset of cognitive impairment.** *J Neurosci* 2013;33:18008–14 CrossRef Medline
42. van Osch MJ, Teeuwisse WM, van Walderveen MA, et al. **Can arterial spin-labeling detect white matter perfusion signal?** *Magn Reson Med* 2009;62:165–73 CrossRef Medline
43. Keil VC, Eichhorn L, Mutsaerts H, et al. **Cerebrovascular reactivity during prolonged breath-hold in experienced freedivers.** *AJNR Am J Neuroradiol* 2018;39:1839–47 CrossRef Medline

Association between Early Ischemic Changes and Collaterals in Acute Stroke: A Retrospective Study

M. Laflamme, S. Carrondo-Cottin, M.-M. Valdès, D. Simonyan, M.-È. Audet, J.-L. Gariépy, M.-C. Camden, C. Gariépy, S. Verreault, and P. Lavoie

ABSTRACT

BACKGROUND AND PURPOSE: The quality of leptomeningeal collaterals may influence the speed of infarct progression in acute stroke. Our main objective was to evaluate the association of leptomeningeal collateral score and its interaction with time with ischemic changes on CT in patients with acute stroke.

MATERIALS AND METHODS: Adult patients with acute stroke symptoms and anterior circulation large-vessel occlusion on CTA from 2015 to 2019 were included. Routinely performed NCCT and multiphase CTA were reviewed to assess ASPECTS and the leptomeningeal collateral score. We built multivariate regression models to assess the association between leptomeningeal collateral score and its interaction with time and ASPECTS. Performance measures to predict poor ASPECTS at different time thresholds (identified with receiver operating characteristic curve analysis) were estimated in a subgroup of patients with poor leptomeningeal collateral scores.

RESULTS: Leptomeningeal collateral scores 0–1 were associated with lower ASPECTS, and the model with dichotomized and trichotomized leptomeningeal collateral score showed a significant multiplicative interaction between time and the leptomeningeal collateral score. The negative predictive value for poor ASPECTS was >0.9 for at least the first 3 hours from stroke onset to imaging, and the positive predictive value was <0.5 for every time threshold tested in the subgroup of patients with leptomeningeal collateral scores 0–3.

CONCLUSIONS: Poor (0–1) leptomeningeal collateral scores were associated with lower ASPECTS, and an increase in time has a multiplicative interaction with the leptomeningeal collateral score on ASPECTS.

ABBREVIATIONS: CollS = leptomeningeal collateral score; mCTA = multiphase CTA; NPV = negative predictive value; PPV = positive predictive value; ROC = receiver operating characteristic

Endovascular therapy decreases the risk of disability in patients with acute ischemic stroke due to anterior circulation large-vessel occlusion, particularly if the ischemic core is small enough compared with the rest of the hypoperfused brain.[1-6] Because the ischemic core tends to increase with time before revascularization is achieved, a delay between stroke onset and revascularization influences the efficiency of the treatment. However, some patients may still benefit from endovascular treatment as long as 24 hours after stroke onset.[3-6] This benefit includes patients living in remote areas who may be considered if the progression of the ischemic core is slow enough.[7] The ability to predict ischemic core progression in these patients has the potential to assist in their selection for transfer to stroke centers. However, predicting which patients will progress at which rate is still a challenge.[8]

Leptomeningeal collateral status may be a key element in this important decision-making process. The role of collaterals in acute stroke has been an important research topic and a subject of numerous publications during the past few years. Good collaterals are associated with a better functional outcome for patients with acute ischemic stroke,[9-12] especially in the context of endovascular therapy,[13-17] and more recently when considering endovascular therapy in patients with a low ASPECTS.[18,19]

Other authors have been focusing on radiologic parameters and the association among collaterals, the infarct core, and the infarct

Received February 10, 2021; accepted after revision July 13, 2022.

Form the Division of Neurosurgery, Department of Surgery (M.L., C.G., P.L.), Department of Radiology (M.-M.V., M.-È.A, J.-L.G.), Clinical and Evaluative Research Platform (D.S.), and Division of Neurology, Department of Medicine (M.-C.C., S.V.), Centre Hospitalier Universitaire de Québec -Université Laval, Quebec, Canada; and Department of Neurosciences, Centre Hospitalier Universitaire de Québec -Université Laval Research Center (S.C.C.), Quebec, Canada.

This study was funded by an educational grant from Stryker.

Please address correspondence to Pascale Lavoie, MD, CHU de Québec, Université Laval, Hôpital de l'Enfant-Jésus, 1401 18e rue, Québec City, Canada; e-mail: pascale.lavoie@mac.com

Indicates article with online supplemental data.

http://dx.doi.org/10.3174/ajnr.A7632

growth rate. Previous findings have shown that the ASPECTS and leptomeningeal collaterals may provide an indirect evaluation of the infarct core volume for a selection of patients with acute ischemic stroke and therefore assist in patient selection for endovascular therapy in an extended time window.[20-22] More recently, secondary analysis from the Randomized controlled trial to Optimize Patient's Selection for Endovascular Treatment in Acute Ischemic Stroke (SELECT) study showed that the early infarct growth rate strongly correlates with both collateral status and clinical outcomes after endovascular thrombectomy.[23] Regenhardt et al,[24] in 2022, also recently correlated symmetric collaterals with a low ischemic core growth rate. However, the relationship between leptomeningeal collaterals and the infarct core growth rate remains poorly understood with contradictory results in the literature[25-28] and lack of a thorough analysis of the effect of the interaction between time and leptomeningeal collaterals on ischemic core volume.

To evaluate the relation of leptomeningeal collaterals and time with infarct core volume in a pragmatic manner that reflects the real-life trajectories and resources of community centers, we conducted a single-center retrospective study, using the ASPECTS as a surrogate for the ischemic core volume. In this study, we aimed to analyze the effect of the leptomeningeal collateral score (CollS) and its interaction with time from stroke to imaging on the ASPECTS. We also sought to find a time threshold having the best performance values to predict ASPECTS, in patients with poor CollS.

MATERIALS AND METHODS

Design

We report this study in accordance with the REporting of studies Conducted by using Observational Routinely collected health Data (RECORD) statement.[29] The study received approval from our local institutional review board, and the need for patient consent was waived because data were exclusively collected on medical charts.

Setting

This study was conducted in a comprehensive stroke center located in Quebec city, Canada. All included patients underwent multiphase CTA (mCTA) for collaterals. Patients were identified through our radiology database (PACS) using a specific code related to acute stroke, from May 25, 2015 (on implementation of the mCTA protocol), to May 24, 2019. The entire protocol for patients with stroke includes an NCCT as well as mCTA. No data on perfusion studies were collected because CT perfusion was not available at our center at the above-mentioned dates.

Participants

We screened all consecutive patients admitted for acute ischemic stroke. The selected patients were all adults 18 years of age or older with acute stroke symptoms and large-vessel occlusion of the anterior cerebral circulation, including the ICA and proximal middle cerebral artery (M1 or proximal M2). Patients with either no occlusion, distal anterior circulation occlusion (distal M2 and A2), posterior circulation occlusion, or hemorrhagic stroke were excluded from the study.

Variables and Data Sources

The ASPECTS was evaluated independently by 1 vascular neurologist and 1 neurosurgeon with endovascular training. The assessment was made according to the guidelines published by the team who created this score, and both reviewers received appropriate training.[7,30] A third party (a vascular neurologist) was consulted in case of disagreement. This assessment was blinded to the quality of CollS and to all clinical data, including the time from stroke to imaging.

The assessment of collateral status on mCTA was performed separately and independently by 2 interventional neuroradiologists with a score ranging from 0 to 5 according to Menon et al.[31] A third party (a neurosurgeon specialized in neurointervention) reviewed all disagreements. If the third reviewer was not in agreement with one of the first 2 reviewers, the disagreement had to be resolved through discussion. This measurement was also blinded to clinical data. Because the CollS evaluation had to be independent of the ASPECTS, the investigators were required to mention all patients for whom a bad ASPECTS from large stroke could have been deduced on CTA images. The CollSs were trichotomized as poor (0–1), intermediate (2–3), and good (4–5) and dichotomized as poor (0–3) and good (4–5) for analyses.

Clinical data, including age, sex, NIHSS, time from stroke to imaging, smoking status, intravenous thrombolysis and thrombectomy status, and anticoagulant, antiplatelet, antihypertensive, lipid-lowering, and hypoglycemic drug use, were collected separately and independent from electronic medical records by 2 members of the team. For patients with no precise time from stroke onset, the time when the patient was last-seen-well was used. When the NIHSS was not available from the medical record, a retrospective scoring algorithm was used to estimate it.[32] Discrepancies were resolved through discussion.

The time from stroke to imaging was calculated afterward as the duration between the time of stroke onset (or last seen well) and the time of CT/CTA of the brain. All data collectors were blinded to the exact time from stroke to imaging.

Statistical Analyses

Sample size calculation was based on parameters issued from preliminary data collected from the first 23 patients. The mean (SD) of the time from stroke to imaging (2.3 hours and 1.74 hours, respectively) represented 60% of the bad ASPECTS in the poor CollS group. A sample size of $\geq$145 cases was sufficient to obtain 80% power in a multivariate logistic regression model with a conservative OR of 1.4 for the CollS factor. Furthermore, 10% of R-square was attributed to the time from stroke to imaging, and the significance level was set at .05. Considering the possible 20% of missing data, the final sample size was set at 175 cases.

Quantitative variables are described as mean (SD) and median, first (Q1) and third (Q3) quartiles, minimum, and maximum; qualitative variables are described as frequencies and percentages.

Interobserver agreement for ASPECTS and CollS data was measured with the Cohen κ for dichotomized and trichotomized data. The intraclass coefficient correlation was used to assess agreement with the original scales. The κ coefficient was defined as slight (0–0.20), fair (0.21–0.40), moderate (0.41–0.60), substantial (0.61–0.80), or excellent (0.81–1).[33] The intraclass correlation coefficient was categorized as follows: poor ($<$0.50), moderate (0.50–0.75), good (0.75–0.90), and excellent ($>$0.90).[34]

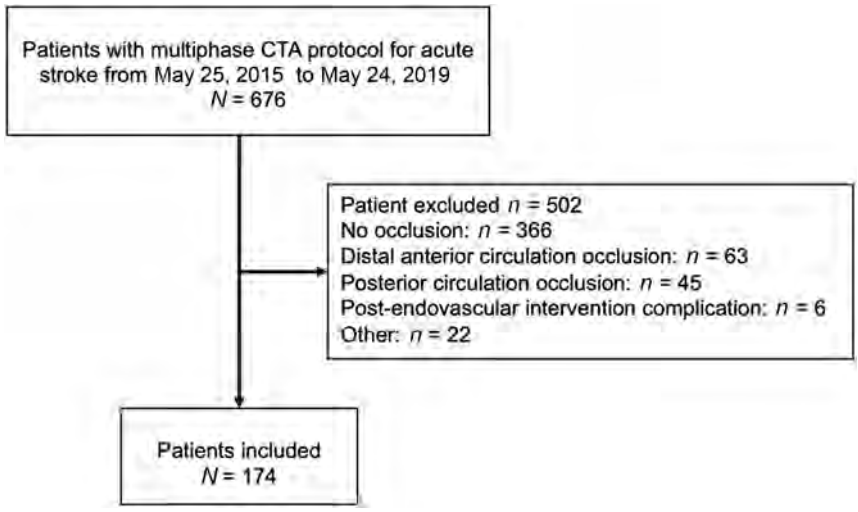

FIG 1. Flow chart of patient selection.

Receiver operating characteristic (ROC) curve analyses were used to find time thresholds from stroke to imaging having the best performance values to predict bad ASPECTS (0–5) in 2 subgroups of CollS (0–1 and 0–3). The performance measures of the different time thresholds for bad ASPECTS were estimated with asymptotic 95% CIs. For ROC curve analysis, the ASPECTS was dichotomized with scores ranging from 6 to 10 qualifying as good and scores and from 0 to 5 qualifying as bad. The threshold of ≥6 was chosen because it is an inclusion criterion for thrombectomy in the guidelines.[35,36]

The association of CollS and its interaction with time on ASPECTS was analyzed in multivariate linear regression models, entering CollS either as a continuous variable (model 1) or after dichotomization (model 2) or trichotomization (model 3). The time from stroke to imaging, age, NIHSS, intracranial occlusion location, the presence of tandem carotid occlusion, and an interaction term between time and the CollS were also entered in all models.

Statistical analyses were performed using SAS Statistical Software, Version.9.4 (SAS Institute) with a 2-sided significance level set at $P < .05$.

RESULTS

According to the radiologic database, 676 patients underwent mCTA at our institution between May 25, 2015, and May 24, 2019, and 174 patients were included in the analyses (Fig 1). Patients' demographic and clinical data are shown in the Table. Most the patients' CollSs were about equally distributed between 4 and 5 ($n = 81$; 46%) and 2 and 3 ($n = 82$; 47.1%). Very few patients had CollSs of 0–1 ($n = 11$; 6.3%). Poor CollSs were found in 10% (4/40) of ICA occlusions, 4.21% (4/95) of M1 occlusions, and 7.69% (3/39) of M2 occlusions.

The estimated simple κ for the CollS was 0.41 (95% CI, 0.27–0.54) after dichotomization and 0.42 (95% CI, 0.30–0.54) after trichotomization, while the intraclass correlation coefficient was 0.57 (95% CI, 0.46–0.66). The estimated simple κ for ASPECTS was 0.60 (95% CI, 0.42–0.78), and the intraclass correlation coefficient was 0.69 (95% CI, 0.61–0.76). The agreement when using a cutoff at 5 instead of 6 to dichotomize ASPECTS was only 0.26 (95% CI, 0.01–0.53).

Figure 2 shows the distribution of our cohort according to the CollS, ASPECTS, and time from stroke to imaging. Among patients with witnessed stroke onset and good collaterals (CollS = 4–5), good ASPECTS (6–10) were seen as late as 448 minutes (7.5 hours) after stroke onset, but bad ASPECTS (0–5) were also seen as soon as 158 minutes after stroke onset.

As shown in the Online Supplemental Data, in multivariate analysis, CollS 0–1 was independently associated with lower ASPECTS compared with CollS 4–5. The interaction term between poor CollS and time was also independently associated with ASPECTS in patients with CollS 2–3 and 0–3. For every 10-minute increase in time from stroke to imaging, there was a decrease in the ASPECTS of 0.07 (95% CI, 0.1–0.05; $P < .001$) in patients with CollS 2–3 and 0.06 (95% CI, 0.03–0.08; $P = .001$) in patients with CollS 0–3. In other words, a 1-point decay in the ASPECTS occurred for every 135 minutes (95% CI, 100–200) in the subgroup of patients with CollS 2–3 and for every 167 minutes (95% CI, 125–333) in the subgroup of patients with CollS 0–3.

According to ROC curve analyses (Fig 3), the time threshold for predicting poor ASPECTS (0–5) with the highest negative predictive value (NPV) was 100 minutes (NPV = 0.97; 95% CI, 0.87–0.99) in the instance of CollS 0–3. The NPV remains above 0.90 (95% CI, 0.82–0.97) for the time threshold of <190 minutes and 0.88 (95% CI, 0.78–0.94) for time thresholds of <236 minutes. The positive predictive values (PPVs) were <0.5 for all time thresholds in this subgroup. The subgroup of CollS 0–1 was too small to perform accurate ROC curve analyses and allow precise estimation of the predictive values.

DISCUSSION

In our study, a poor CollS (0–1) was independently associated with lower ASPECTS as was the multiplicative interaction of time with CollS. The NPV to predict poor ASPECTS was >0.9 for at least the first 3 hours from stroke onset to imaging, and the PPV was <0.5 for every time threshold in the subgroup of patients with CollS 0–3.

The association of ASPECTS and collaterals has been reported in many studies during the past decade, with varying results. While post hoc analysis of the Interventional Management of Stroke (IMS III) and Endovascular Therapy Following Imaging Evaluation for Ischemic Stroke (DEFUSE) 3 trials did not show a significant difference among patients according to their collateral status,[10,26] other studies have shown a protective effect of good collateralization.[37,38] Results from a retrospective cohort study suggested that collaterals can influence early ischemic changes; patients transferred from regional hospitals with poor collaterals were significantly more at risk of ASPECTS decay than those

Demographic and clinical characteristics of included patients (n = 174)

Demographics/Characteristics	
Age (mean) (yr)	73.35 (SD, 14.33)
Male (No.) (%)	74 (42.5)
NIHSS (mean)[a]	14.29 (SD, 6.46)
Time from stroke to imaging in minutes (mean)	166 (SD, 144.6)
Median; Q1–Q3; (min–max)	115.8; 66–231; 16.8–823.8
Stroke onset (No.) (%)	
Witnessed	136 (78.2)
Wake-up	38 (21.8)
Most proximal intracranial occlusion (No.) (%)	
ICA	40 (23.0)
M1	95 (54.6)
M2	39 (22.4)
Tandem carotid occlusion (No.) (%)	41 (23.6)
Smoking status (No.) (%)	
Never smoked	101 (58.7)
Active	29 (16.7)
Former	23 (13.2)
Unknown	21 (12.1)
Drugs (No.) (%)	
Anticoagulants	17 (9.8)
Antiplatelets	61 (35.1)
Antihypertensive	111 (63.8)
Diabetes	26 (14.9)
Cholesterol	72 (41.4)
Treatment received	
IVT only (No.) (%)	34 (19.5)
Endovascular therapy only (No.) (%)	34 (19.5)
IVT+endovascular therapy (No.) (%)	71 (40.8)
None (No.) (%)	35 (20.1)
ASPECTS (No.) (%)	
6–10	155 (89.1)
0–5[b]	19 (10.9)
Collateral status (No.) (%)	
4–5	81 (46.6)
2–3	82 (47.1)
0–1[c]	11 (6.3)

Note:—Q indicates quartile; min, minimum; max, maximum; IVT, intravenous thrombolysis.

[a] The retrospective scoring algorithm was used in 24 patients (13.8%) to assess NIHSS.

[b] ASPECTS was 5 in 12 patients.

[c] All had a score of 1.

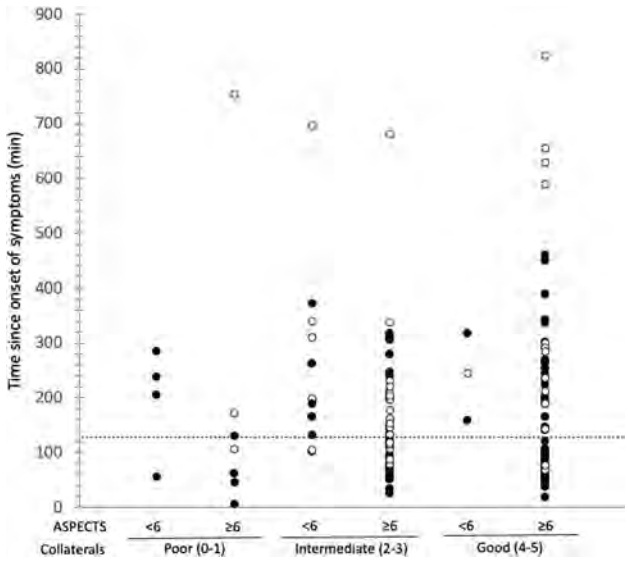

FIG 2. Time distribution since stroke onset in the stratified study population. Patients with witnessed time from stroke onset are represented as *solid circles*, and patients classified as last seen well or with wake-up stroke are represented by *open circles*.

with good/intermediate collaterals (OR = 5.14; 95% CI, 2.20–12.70).[39] Recent studies have shown that collateral status had the strongest association with infarct growth rate, while time from stroke onset did not reach statistical significance.[27,28,40] In our study, we found that poor collaterals (0–1) were significantly associated with lower ASPECTS. On the other hand, some patients in our cohort who had imaging as soon as 100 minutes from stroke onset had bad ASPECTS despite CollS 4–5, suggesting that good collaterals alone do not guarantee a slow infarct growth rate. A similar observation was made in a post hoc analysis of the Endovascular Treatment for Small Core and Anterior Circulation Proximal Occlusion with Emphasis on Minimizing CT to Recanalization Times (ESCAPE) trial, in which some fast-progressing patients had good collaterals.[41]

Finding a time threshold to select patients for treatment or to predict outcomes in acute ischemic stroke is still a challenge. The 6-hour threshold is used as the limit to discriminate between fast and slow progressors,[42] but most of our patients presented within this threshold. Therefore, we sought to identify a time threshold of patients with a poor CollS that would distinguish fast and very fast progressors. Given that the consequences of excluding a patient with stroke who was indeed eligible for endovascular therapy (good ASPECTS after a certain time threshold) are far worse than including a patient with stroke who is not eligible (bad ASPECTS within a certain time threshold), the ideal time threshold would offer the highest possible PPV. All time thresholds analyzed (within 4 hours) offer a low PPV in patients with CollS 0–3, meaning that, on the basis of our results, it was not possible to identify a time threshold after which patients with CollS 0–3 were more likely to have poor ASPECTS.

On the other hand, the NPV remains high for a long time despite CollS 0–3, meaning that the risk of including poor ASPECTS despite CollS 0–3 remains low within at least 3 hours. Indeed, the effect of time on the ASPECTS found in our study showed that it requires 135 minutes to decrease by only 1 the ASPECTS in patients with CollS 2–3, possibly suggesting that lower CollSs are responsible for ischemic core progression leading to poor ASPECTS on a time threshold after ≥6 hours and that it is not possible to distinguish very fast progressors on the basis of CollS 0–3 alone. Finally, poor CollS 0–1 may cause faster ischemic core progression, but a larger sample size with larger distribution of time from stroke to imaging is required to analyze the interaction with time in this subgroup.

In our study, 2 patients had ASPECTS of 5 after 130 minutes despite poor CollS 0–1. Using 5 instead of 6 as a cutoff to include patients for mechanical thrombectomy is an ongoing debate.[27,35,36,40-42] However, according to our results (κ = 0.2 for dichotomized ASPECTS at 5), it appears difficult to discriminate

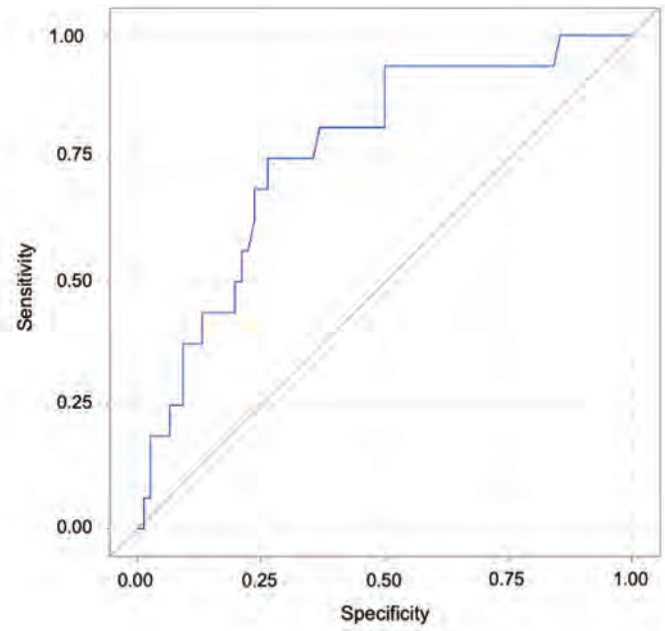

Time from stroke to imaging (minutes)	Sensitivity (95% CI)	Specificity (95% CI)	VPP (95% CI)	VPN (95% CI)	AUC** (95%CI)
≥ 100	0.94 (0.70 – 1.00)	0.50 (0.38 – 0.62)	0.28 (0.17 – 0.42)	0.97 (0.87 – 1.00)	0.76 (0.64 – 0.89)
≥ 189	0.69 (0.41 – 0.89)	0.76 (0.65 – 0.85)	0.38 (0.21 – 0.58)	0.92 (0.82 – 0.97)	0.73 (0.60 – 0.85)
≥ 205	0.50 (0.25 – 0.75)	0.80 (0.70 – 0.89)	0.35 (0.16 – 0.57)	0.88 (0.78 – 0.95)	0.76 (0.64 – 0.89)
≥ 237	0.44 (0.20 – 0.70)	0.87 (0.77 – 0.94)	0.41 (0.18 – 0.67)	0.88 (0.78 – 0.94)	0.65 (0.52 – 0.78)

** There was statistically significant difference of AUC at the significance level of .05.

FIG 3. ROC curves for determining best performances measures to predict bad ASPECTS at different time values. AUC indicates area under the curve.

between ASPECTS 0–4 and ASPECTS 5. Using a cutoff of 5 in our cohort could have wrongly included a bad (0–4) ASPECTS as a good ASPECTS. In a review article, authors mentioned the variable interobserver agreement, going from fair to good, for dichotomized ASPECTS at 7, but the agreement for lower ASPECTS dichotomization is less well-established in the literature.[43]

The interobserver agreement for CollS is only fair-to-moderate and is much lower than the one reported by the team that created the Calgary Collateral Score (κ coefficient = 0.81).[31] This difference may suggest a lack of external generalizability because we can expect that the team that created a radiologic score had a higher agreement than ours. Additionally, there are many examples of low agreement among readers assessing collaterals, even in the case of expert neuroradiologists.[30,44-46] These examples show that every physician involved in acute ischemic stroke care should, therefore, be very careful when excluding patients on behalf of a single radiologic interpretation. This suggestion places emphasis on the importance of specific training such as what already exists with the ASPECTS (http://aspectsinstroke.com/), even for experienced neuroradiologists and may be another argument in favor of computer-aided triage in acute stroke.[45]

The main limitation of our study is its retrospective and cross-sectional design. The ideal design to assess the association between ASPECTS and CollS and its interaction with time would have been a prospective longitudinal design and would have required multiple radiologic examinations on a single patient at different time points and the transfer of all outside patients to our center—even if not eligible for thrombectomy—to perform an mCTA. Such a design would have been ethically questionable. Furthermore, because the images were obtained at only 1 time point, we implicitly assumed that the CollS does not change with time. Proving this point would have required multiple examinations during a short time, which are not routinely performed in our center and could add unnecessary delays to proper patient treatment.

Our design could also have been vulnerable to selection bias because we included transferred patients who were previously judged as potential candidates for thrombectomy, while those who were not eligible stayed at their referring center and were, therefore, excluded from our sample. Although this design should not have biased our results, it precluded us from studying the effect of collateral status with a longer delay. Also, our study has a low number of patients with CollS 0–1 (n = 11, 6%). This number is at the lowest limit of what is described in the literature, in which, depending on the scale, between 5% and 36% of the patients were identified with poor collaterals.[47,48] Less than 11% of our patients presented with bad ASPECTS (≤5). Although this is a relatively small proportion of our cohort, it is still within the range found in the literature in which some cohorts had as low as 5% of bad ASPECTS.[49] The radiologic reviewers were completely blinded to the time from stroke onset and other clinical and radiologic data. However, the ASPECTS was deduced by mCTA readers in 5 patients overall, but no significant change was found when carrying out sensitivity analysis excluding these data. The inclusion of unwitnessed stroke onset in our study may have biased the performance measures of a higher time threshold toward higher NPV and biased the time required to lose 1 point on ASPECTS toward higher estimates. Finally, our study shows good external validity because it was pragmatic and reflects real life with simple radiologic data that stroke clinicians must consider every time they decide on acute ischemic stroke management. It also reinforces the hypothesis of a relationship between faster ischemic changes and poor collateral status, which is frequently assumed and deliberately sought in only a few studies in literature.[25,28,50]

CONCLUSIONS

Poor (0–1) CollSs were associated with lower ASPECTS, and an increase in time has a multiplicative interaction with CollS on

ASPECTS. Patients presenting within 4 hours may still have a good ASPECTS despite CollS 0–3, given the high NPV of this time threshold in this subgroup. Transferred patients with poor and intermediate collaterals should be rescanned at arrival in case of more rapid ASPECTS decay with time, to support endovascular therapy decisions. Finally, good collaterals alone are not a guarantee of a slow infarct growth rate, and moderate interobserver agreement for CollS mandates special attention—particularly when excluding patients on the basis of this criterion alone.

Disclosures: Marie-Ève Audet—*RELATED: Grant*: Stryker, *Comments*: Educational grant.* Jean-Luc Gariépy—*RELATED: Grant*: Stryker, *Comments*: Educational grant.* Pascale Lavoie—*RELATED: Grant*: Stryker, *Comments*: Educational grant.* Marie-Christine Camden—*UNRELATED: Payment for Lectures Including Service on Speakers Bureaus:* Bristol-Myers-Squibb.* Steve Verreault—*UNRELATED: Grants/Grants Pending:* Bristol Myers Squibb, Portola; Public Health Research Institute; *Payment for Lectures Including Service on Speakers Bureaus:* Servier, Bristol Myers Squibb, Pfizer.* Money paid to the institution.

REFERENCES

1. Berkhemer OA, Fransen PS, Beumer D, et al. MR CLEAN Investigators. **A randomized trial of intraarterial treatment for acute ischemic stroke.** *N Engl J Med* 2015;372:11–20 CrossRef Medline
2. Campbell BC, Mitchell PJ, Kleinig TJ, et al. **Endovascular therapy for ischemic stroke with perfusion-imaging selection.** *N Engl J Med* 2015;372:1009–18 CrossRef Medline
3. Jovin TG, Chamorro A, Cobo E, et al. REVASCAT Trial Investigators. **Thrombectomy within 8 hours after symptom onset in ischemic stroke.** *N Engl J Med* 2015;372:2296–306 CrossRef Medline
4. Goyal M, Demchuk AM, Menon BK, et al. **Randomized assessment of rapid endovascular treatment of ischemic stroke.** *N Engl J Med* 2015;372:1019–30 CrossRef Medline
5. Saver JL, Goyal M, Bonafe A, et al. **Stent-retriever thrombectomy after intravenous t-PA vs. t-PA alone in stroke.** *N Engl J Med* 2015;372:2285–95 CrossRef Medline
6. Bracard S, Ducrocq X, Mas JL, et al; THRACE Investigators. **Mechanical thrombectomy after intravenous alteplase versus alteplase alone after stroke (THRACE): a randomised controlled trial.** *Lancet Neurol* 2016;15:1138–47 CrossRef Medline
7. Pexman JH, Barber PA, Hill MD, et al. **Use of the Alberta Stroke Program Early CT Score (ASPECTS) for assessing CT scans in patients with acute stroke.** *AJNR Am J Neuroradiol* 2001;22:1534–42 Medline
8. Powers WJ, Derdeyn CP, Biller J, et al. American Heart Association Stroke Council. **2015 American Heart Association/American Stroke Association Focused Update of the 2013 Guidelines for the Early Management of Patients with Acute Ischemic Stroke Regarding Endovascular Treatment: A Guideline for Healthcare Professionals from the American Heart Association/American Stroke Association.** *Stroke* 2015;46:3020–35 CrossRef Medline
9. Fanou EM, Knight J, Aviv RI, et al. **Effect of collaterals on clinical presentation, baseline imaging, complications, and outcome in acute stroke.** *AJNR Am J Neuroradiol* 2015;36:2285–91 CrossRef Medline
10. Liebeskind DS, Tomsick TA, Foster LD, et al. **Collaterals at angiography and outcomes in the Interventional Management of Stroke (IMS) III trial.** *Stroke* 2014;45:759–64 CrossRef Medline
11. Yeo LL, Paliwal P, Teoh HL, et al. **Assessment of intracranial collaterals on CT angiography in anterior circulation acute ischemic stroke.** *AJNR Am J Neuroradiol* 2015;36:289–94 CrossRef Medline
12. Yeo LL, Paliwal P, Low AF, et al. **How temporal evolution of intracranial collaterals in acute stroke affects clinical outcomes.** *Neurology* 2016;86:434–41 CrossRef Medline
13. Wufuer A, Wubuli A, Mijiti P, et al. **Impact of collateral circulation status on favorable outcomes in thrombolysis treatment: a systematic review and meta-analysis.** *Exp Ther Med* 2018;15:707–18 CrossRef Medline
14. Ravindran AV, Killingsworth MC, Bhaskar S. **Cerebral collaterals in acute ischaemia: implications for acute ischaemic stroke patients receiving reperfusion therapy.** *Eur J Neurosci* 2021;53:1238–61 CrossRef Medline
15. Bang OY, Saver JL, Kim SJ, et al. **Collateral flow predicts response to endovascular therapy for acute ischemic stroke.** *Stroke* 2011;42:693–99 CrossRef Medline
16. Berkhemer OA, Jansen IG, Beumer D, et al; MR CLEAN Investigators. **Collateral status on baseline computed tomographic angiography and intra-arterial treatment effect in patients with proximal anterior circulation stroke.** *Stroke* 2016;47:768–76 CrossRef Medline
17. Boers AM, Jansen IG, Berkhemer OA, et al; MR CLEAN Trial Investigators. **Collateral status and tissue outcome after intra-arterial therapy for patients with acute ischemic stroke.** *J Cereb Blood Flow Metab* 2017;37:3589–98 CrossRef Medline
18. Broocks G, Kniep H, Schramm P, et al. **Patients with low Alberta Stroke Program Early CT Score (ASPECTS) but good collaterals benefit from endovascular recanalization.** *J Neurointerv Surg* 2020;12:747–52 CrossRef Medline
19. Tan BY, Wan-Yee K, Paliwal P, et al. **Good intracranial collaterals trump poor ASPECTS (Alberta Stroke Program Early CT Score) for intravenous thrombolysis in anterior circulation acute ischemic stroke.** *Stroke* 2016;47:2292–98 CrossRef Medline
20. Consoli A, Andersson T, Holmberg A, et al; CAPRI Collaborative Group. **CT perfusion and angiographic assessment of pial collateral reperfusion in acute ischemic stroke: the CAPRI study.** *J Neurointerv Surg* 2016;8:1211–16 CrossRef Medline
21. Dehkharghani S, Bammer R, Straka M, et al. **Performance of CT ASPECTS and collateral score in risk stratification: can target perfusion profiles be predicted without perfusion imaging?** *AJNR Am J Neuroradiol* 2016;37:1399–404 CrossRef Medline
22. Mehrkhani F, Berkhemer OA, Majoie C, et al. **Combined evaluation of noncontrast CT ASPECTS and CT angiography collaterals improves detection of large infarcts in proximal artery occlusive stroke.** *J Neuroimaging* 2018;28:524–59 CrossRef Medline
23. Sarraj A, Hassan AE, Grotta J, et al; for the SELECT Investigators. **Early infarct growth rate correlation with endovascular thrombectomy clinical outcomes: analysis from the SELECT Study.** *Stroke* 2021;52:57–69 CrossRef Medline
24. Regenhardt RW, Gonzalez RG, He J, et al. **Symmetric CTA collaterals identify patients with slow-progressing stroke likely to benefit from late thrombectomy.** *Radiology* 2022;302:400–07 CrossRef Medline
25. Kimmel ER, Al Kasab S, Harvey JB, et al. **Absence of collaterals is associated with larger infarct volume and worse outcome in patients with large vessel occlusion and mild symptoms.** *Journal of Stroke and Cerebrovascular Diseases* 2019;28:1987–92 CrossRef Medline
26. de Havenon A, Mlynash M, Kim-Tenser MA, et al; DEFUSE 3 Investigators. **Results from DEFUSE 3: good collaterals are associated with reduced ischemic core growth but not neurologic outcome.** *Stroke* 2019;50:632–38 CrossRef Medline
27. Jiang B, Ball RL, Michel P, et al. **Factors influencing infarct growth including collateral status assessed using computed tomography in acute stroke patients with large artery occlusion.** *Int J Stroke* 2019;14:603–12 CrossRef Medline
28. Vagal A, Aviv R, Sucharew H, et al. **Collateral clock is more important than time clock for tissue fate.** *Stroke* 2018;49:2102–27 CrossRef Medline
29. Benchimol EI, Smeeth L, Guttmann A, et al; RECORD Working Committee. **The REporting of studies Conducted using Observational Routinely-collected health Data (RECORD) statement.** *PLoS Med* 2015;12:e1001885 CrossRef Medline
30. Barber PA, Demchuk AM, Zhang J, et al. **Validity and reliability of a quantitative computed tomography score in predicting outcome of hyperacute stroke before thrombolytic therapy: ASPECTS Study Group—Alberta Stroke Programme Early CT Score.** *Lancet* 2000;355:1670–74 CrossRef Medline

31. Menon BK, d'Esterre CD, Qazi EM, et al. **Multiphase CT angiography: a new tool for the imaging triage of patients with acute ischemic stroke.** *Radiology* 2015;275:510–20 CrossRef Medline
32. Williams LS, Yilmaz EY, Lopez-Yunez AM. **Retrospective assessment of initial stroke severity with the NIH Stroke Scale.** *Stroke* 2000;31:858–62 CrossRef Medline
33. Landis JR, Koch GG. **The measurement of observer agreement for categorical data.** *Biometrics* 1977;33:159–74 CrossRef Medline
34. Portney LG, Watkins MP. *Foundations of Clinical Research: Applications to Practice*. Prentice Hall; 4th Edition, 2020
35. Boulanger JM, Lindsay MP, Gubitz G, et al. **Canadian Stroke Best Practice Recommendations for Acute Stroke Management: Prehospital, Emergency Department, and Acute Inpatient Stroke Care, 6th Edition, Update 2018.** *Int J Stroke* 2018;13:949–84 CrossRef Medline
36. Powers WJ, Rabinstein AA, Ackerson T, et al. **Guidelines for the Early Management of Patients with Acute Ischemic Stroke: 2019 Update to the 2018 Guidelines for the Early Management of Acute Ischemic Stroke: A Guideline for Healthcare Professionals From the American Heart Association/American Stroke Association.** *Stroke* 2019;50:e344–418 CrossRef Medline
37. Nannoni S, Sirimarco G, Cereda CW, et al. **Determining factors of better leptomeningeal collaterals: a study of 857 consecutive acute ischemic stroke patients.** *J Neurol* 2019;266:582–88 CrossRef Medline
38. Renu A, Laredo C, Montejo C, et al. **Greater infarct growth limiting effect of mechanical thrombectomy in stroke patients with poor collaterals.** *J Neurointerv Surg* 2019;11:989–93 CrossRef
39. Boulouis G, Lauer A, Siddiqui AK, et al. **Clinical imaging factors associated with infarct progression in patients with ischemic stroke during transfer for mechanical thrombectomy.** *JAMA Neurol* 2017;74:1361–67 CrossRef Medline
40. Puhr-Westerheide D, Tiedt S, Rotkopf LT, et al. **Clinical and imaging parameters associated with hyperacute infarction growth in large vessel occlusion stroke.** *Stroke* 2019;50:2799–804 CrossRef Medline
41. Ospel JM, Hill MD, Kappelhof M, et al. **Which acute ischemic stroke patients are fast progressors? Results from the ESCAPE Trial Control Arm.** *Stroke* 2021;52:1847–50 CrossRef Medline
42. Rocha M, Desai SM, Jadhav AP, et al. **Prevalence and temporal distribution of fast and slow progressors of infarct growth in large vessel occlusion stroke.** *Stroke* 2019;50:2238–40 CrossRef Medline
43. Prakkamakul S, Yoo AJ. **ASPECTS CT in acute ischemia: review of current data.** *Top Magn Reson Imaging* 2017;26:103–12 CrossRef Medline
44. Ben Hassen W, Malley C, Boulouis G, et al. **Inter- and intraobserver reliability for angiographic leptomeningeal collateral flow assessment by the American Society of Interventional and Therapeutic Neuroradiology/Society of Interventional Radiology (ASITN/SIR) scale.** *J Neurointerv Surg* 2019;11:338–41 CrossRef Medline
45. Grunwald IQ, Kulikovski J, Reith W, et al. **Collateral automation for triage in stroke: evaluating automated scoring of collaterals in acute stroke on computed tomography scans.** *Cerebrovasc Dis* 2019;47:217–22 CrossRef Medline
46. Barber PA, Hill MD, Eliasziw M, et al. **Imaging of the brain in acute ischaemic stroke: comparison of computed tomography and magnetic resonance diffusion-weighted imaging.** *J Neurol Neurosurg Psychiatry* 2005;76:1528–33 CrossRef Medline
47. Menon BK, Qazi E, Nambiar V, et al. **Differential effect of baseline computed tomographic angiography collaterals on clinical outcome in patients enrolled in the Interventional Management of Stroke III Trial.** *Stroke* 2015;46:1239–44 CrossRef Medline
48. Zhu J, Ma M, Guo Y, et al. **Pre-stroke warfarin enhancement of collateralization in acute ischemic stroke: a retrospective study.** *BMC Neurol* 2018;18:194 CrossRef Medline
49. Wirtz MM, Hendrix P, Goren O, et al. **Predictor of 90-day functional outcome after mechanical thrombectomy for large vessel occlusion stroke: NIHSS score of 10 or less at 24 hours.** *J Neurosurg* 2019 Dec 20 [Epub ahead of print] CrossRef Medline
50. Verma RK, Gralla J, Klinger-Gratz PP, et al. **Infarction distribution pattern in acute stroke may predict the extent of leptomeningeal collaterals.** *PLoS One* 2015;10:e0137292 CrossRef Medline

In Vitro Analysis of the Efficacy of Endovascular Thrombectomy Techniques according to the Vascular Tortuosity Using 3D Printed Models

J.H. Kim B.M. Kim, and D.J. Kim

ABSTRACT

BACKGROUND AND PURPOSE: Achieving complete recanalization with the front-line endovascular thrombectomy device improves the outcome of acute stroke. The aim of this study was to evaluate whether various thrombectomy techniques including contact aspiration, stent retriever thrombectomy, and combination therapy differ in first-pass effect and distal emboli in acute large-vessel occlusion simulated using 3D printed nontortuous and tortuous cerebrovascular anatomy models.

MATERIALS AND METHODS: 3D printed flow models were manufactured using angiographic data of nontortuous and acutely angulated tortuous vascular anatomy from real patients. Three thrombectomy techniques, contact aspiration, stent retriever, and combined methods, were tested under proximal protection with the balloon-guiding catheter. The first-pass effect and distal emboli rates were analyzed in addition to the thrombectomy-failure mechanisms of the respective techniques.

RESULTS: A total of 30 thrombectomy experiments were performed. The overall incidence of first-pass effect in the nontortuous and tortuous anatomy was 80.0% versus 46.7%. The overall incidence of distal emboli in the nontortuous and tortuous anatomy was 26.7% versus 46.7%. The contact aspiration technique showed better first-pass effect (80.0%) and distal emboli rates (20%) in the tortuous model compared with other techniques. The combined technique did not show remarkable superiority of the first-pass effect and distal emboli in either the nontortuous or tortuous anatomy. Shearing off of the thrombus was the main mechanism of thrombectomy failure in the combined group.

CONCLUSIONS: The tortuous vascular anatomy may worsen the first-pass effect and distal emboli rates. The combined techniques failed to show improvement in outcome due to the shearing-off phenomenon of the thrombus during retrieval.

ABBREVIATIONS: ACA = anterior cerebral artery; BGC = balloon-guided catheter; CA = contact aspiration; DE = distal emboli; EVT = endovascular thrombectomy; FPE = first-pass effect; SR = stent retriever

Endovascular thrombectomy (EVT) has become the treatment of choice for acute ischemic stroke due to large-vessel occlusion through several randomized controlled studies.[1] The use of a stent retriever (SR) has an effective recanalization rate and acceptable safety.[1] With the introduction of new large-bore aspiration catheters, direct contact aspiration (CA) has comparable results compared with SR thrombectomy.[2] Additional use of a balloon-guided catheter (BGC) for proximal flow control is recommended for the prevention of distal emboli (DE) and improvement of the first-pass effect (FPE) rate during thrombectomy and improved outcome.[3-5] Recently, techniques using a combination of these devices have garnered interest in terms of the potential improvement in the successful recanalization rates and clinical outcome.[6,7]

With the development of these techniques and devices, recent emphasis has moved on from successful recanalization to effectively achieving fast and complete recanalization. Clinical indices such as the FPE, which achieves complete recanalization with the first thrombectomy attempt, have been shown to improve the clinical outcome of EVT and lower the mortality rate.[8] Thrombus fragmentation and DE migration occur in 12%–22% of cases, which may affect the prognosis of the patients after treatment.[9] Optimization of the efficacy of EVT by improving these indices (FPE, DE) may be achieved by tailoring to the occlusion characteristics of the individual patient.

Tortuous vessel anatomy is one of the most common challenges that neurointerventionists encounter in clinical practice

Received May 12, 2022; accepted after revision July 17.

From the Department of Radiology (J.H.K.), Yongin Severance Hospital, Yonsei University College of Medicine, Yongin-si, Gyeonggi-do, Korea; and Department of Radiology (B.M.K., D.J.K.), Research Institute of Radiological Science, Severance Hospital, Yonsei University College of Medicine, Seoul, Korea.

This study was supported by a research grant of the Department of Radiology, Severance Hospital, Research Institute of Radiological Science (4-2017-0877).

Please address correspondence to Dong Joon Kim, MD, PhD, Department of Radiology, Research Institute of Radiological Science, Severance Hospital, Yonsei University College of Medicine, 50-1 Yonsei-ro, Seodaemun-gu, Seoul 120-752, Korea; e-mail: djkimmd@yuhs.ac
http://dx.doi.org/10.3174/ajnr.A7633

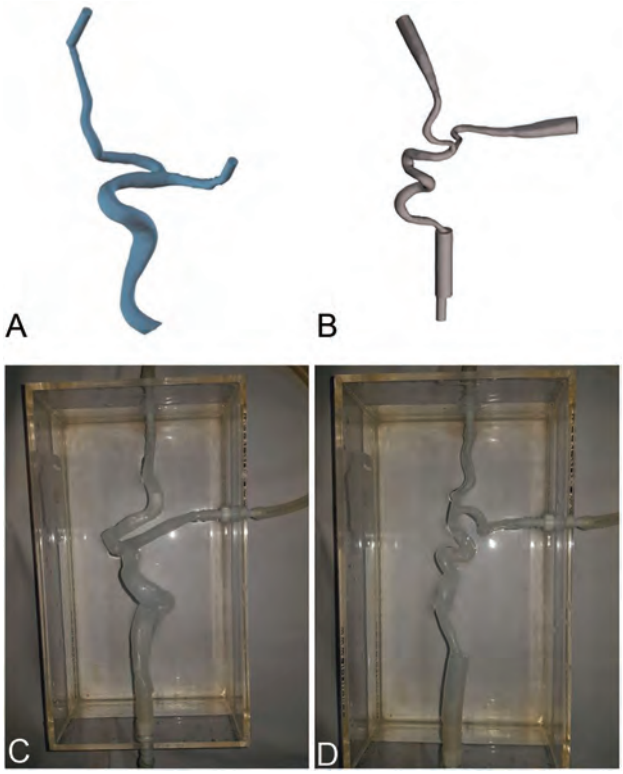

FIG 1. CAD-processed 3D images of the nontortuous (*A*) and tortuous (*B*) cerebrovascular angiographic data. Silicone vascular models of the nontortuous (*C*) and tortuous (*D*) anatomy manufactured from the 3D printing models.

and may be one of the major causes of recanalization failure.[10] However, the exact mechanism of how the tortuous anatomy affects the efficacy of EVT is not well-known. Fortunately, with the recent development of 3D printing and modeling techniques, it has become possible to replicate this difficult anatomy with a flow model matching the real patient that can be tested in vitro.

Therefore, the aim of this study was to compare the efficacy of various thrombectomy techniques including CA, SR thrombectomy, and combination therapy in terms of FPE and DE and to elucidate the mechanisms of thrombectomy failure in acute large-vessel occlusion simulated using 3D printed nontortuous and tortuous cerebrovascular anatomy flow models obtained from real patient data.

MATERIALS AND METHODS

Model Anatomy

3D DSA data were obtained from 2 patients who had been treated by EVT for acute ischemic stroke at our stroke center. Data were obtained from a patient with nontortuous cerebrovascular anatomy who achieved FPE and a patient with very tortuous anatomy who achieved recanalization only after multiple retrieval attempts. The collection and use of the patient's angiographic data were approved by the institutional review board. Blood vessel data were extracted from the distal cervical segment of the ICA, through the carotid bifurcation, to include the M1 segment of the MCA and the A2 segment of the anterior cerebral artery (ACA). The tortuosity of the vessel was visually verified and also numerically confirmed (arc-to-chord ratio) by comparing the distance between the 2 points on a straight line between the distal M1 and the distal cervical ICA in each model and the total length of blood vessels between the 2 points (arc-to-chord ratio: 1.77 for the tortuous model and 1.49 for the nontortuous model).[11]

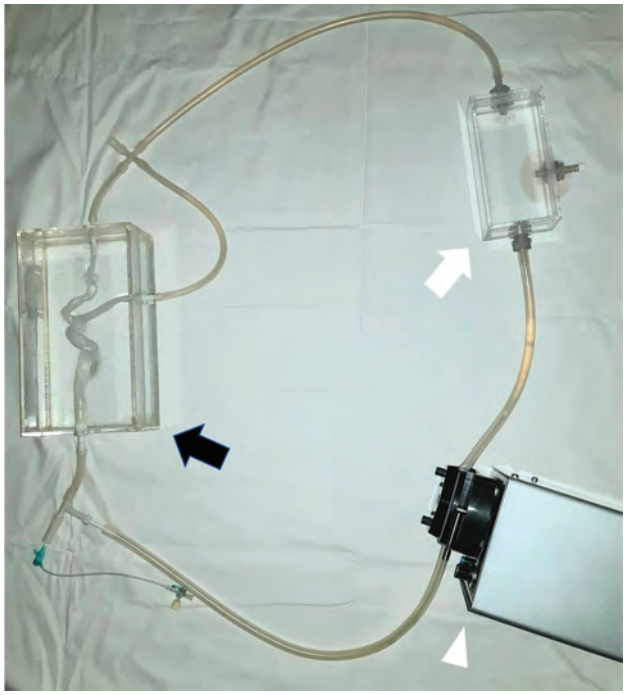

FIG 2. A vascular model was placed in the acrylic tank and connected to the closed circuit. The *black arrow* indicates the flow model in a water-filled tank. The *white arrow* indicates a separate tank for collecting distal embolus. The *white arrowhead* indicates the peristaltic pump.

Flow Model

The angiographic DICOM data were extracted in Virtual Reality Modeling Language (Matlab; MathWorks) format using the 3D Workstation (IntelliSpace Portal; Philips Healthcare). These were converted into a stereolithography file using CAD software (MeshLab; Cignoni et al). Using these files, we produced semitranslucent vascular models with photopolymerization resin (standard Clear Resin, Version 4; Formlabs) with a 3D printer (Form2; Formlabs). After printing, we applied multiple silicone coatings to the surface of the models, and removed the inner mold to produce a flexible, hollow, and transparent vascular model (Fig 1). The manufactured model was placed in a water-filled tank made of acryl and connected to a water-circulation system at the proximal ICA, MCA, and ACA. The system was connected to a transparent silicone tube and was connected to a peristaltic pump (EMP-100; EMS technologies), which maintains a pulse rate of 80 beats per minute to simulate blood circulation. A separate water tank was connected to collect the distally migrated embolus. The entire model was filled with a mixture of normal saline fluid and glycerin (60/40 volume saline/glycerin) to mimic the characteristics of blood. A route through which a guiding catheter and thrombectomy devices can be inserted was separately connected to the proximal ICA of the circulation system (Fig 2). Experimental procedures were recorded with video and photographs using a high-resolution digital camera.

Table 1: Incidence of FPE and DE in nontortuous and tortuous models according to the EVT technique

	FPE		DE	
	Nontortuous	Tortuous	Nontortuous	Tortuous
Total	12/15 (80.0%)	7/15 (46.7%)	4/15 (26.7%)	7/15 (46.7%)
CA	5/5 (100.0%)	4/5 (80.0%)	0/5 (0%)	1/5 (20.0%)
SR	4/5 (80.0%)	2/5 (40.0%)	1/5 (20.0%)	3/5 (60.0%)
Combined	3/5 (60.0%)	1/5 (20.0%)	3/5 (60.0%)	3/5 (60.0%)

Table 2: Incidence of failure of complete recanalization in nontortuous and tortuous models according to the EVT technique

	Failure of Complete Recanalization	
	Nontortuous	Tortuous
Total	5/15 (33.3%)	9/15 (60.0%)
CA	0/5 (0%)	1/5 (20.0%)
SR	2/5 (40.0%)	4/5 (80.0%)
Combined	3/5 (60.0%)	4/5 (80.0%)

Thrombus Analog

The method of producing a fresh thrombus analog is well-documented and has been used in many prior studies.[12,13] Per 4 mL of fresh swine blood, 32 mg of fibrinogen from bovine plasma (Sigma-Aldrich) and 1 U of thrombin from bovine plasma were mixed, put in a plastic cage, and incubated at room temperature for 60 minutes. The prepared clot was cut into 10-mm lengths and inserted into the flow system using an 8F guiding catheter.

Endovascular Thrombectomy Techniques

After connecting the 8F sheath to the flow model through a silicone tube, an 8F BGC (Flowgate2; Stryker) was inserted and placed in the distal cervical ICA portion of the model. The thrombus was placed in the MCA M1 portion through the guiding catheter. EVT in the SR group was performed using a Solitaire FR 4/20 (Medtronic) or Trevo 4/20 (Stryker) stent after passing the thrombus with a 0.021-inch microcatheter and a 0.014-inch microwire. The active push deployment technique was performed when deploying the SR. In the CA group, manual aspiration thrombectomy was performed using an AXS Catalyst 6 aspiration catheter (Stryker) and a 20-mL syringe after direct catheter tip contact with the thrombus. In the combined group, a microwire and a microcatheter were navigated across the occlusion site followed by coaxial advancement of the aspiration catheter (Catalyst 6) close to the occlusion site. After the deployment of the SR through the occlusion site, the aspiration catheter was advanced just proximal to the portion of the SR-engaged thrombus. Then, with simultaneous suction via the aspiration catheter, the entire system was cautiously retrieved as a unit. In all groups, proximal flow arrest was achieved using the BGC.

FPE was defined as complete flow restoration without any remaining thrombus in the MCA, ACA, or ICA segments after a single thrombectomy attempt. DE was defined as identification of a visible, migrated embolus that reached the reservoir tank through the MCA, ACA, or ICA segment regardless of the size of the embolus. FPE and DE were evaluated at the end of the procedure after BGC deflation mimicking the real-world procedure. Successful first-pass recanalization with a DE small enough to migrate distally and enter the reservoir tank system was considered as both FPE and DE. If the thrombus was fragmented but large enough to remain in the MCA or ICA segment without distal migration, it was considered as an FPE failure and not classified as DE. Moreover, we defined failure of complete recanalization by combining all cases of failure to achieve FPE and cases of DE. Analyses of the video recordings were performed to identify the mechanisms of thrombectomy failure.

RESULTS

A total of 30 thrombectomy experiments were performed for the CA ($n = 10$), SR ($n = 10$), and combined groups ($n = 10$), respectively. Of these, half in each group ($n = 5$) were tested in the nontortuous anatomy model, and the remaining half ($n = 5$) were tested in the tortuous anatomy model.

EVT Results according to the Vascular Tortuosity

In terms of the tortuosity of the vessel, the FPE rate of the nontortuous anatomy model was higher than that of the tortuous anatomy model (80.0%, 12/15, versus 46.7%, 7/15). The incidence of DE was lower in the nontortuous anatomy model (26.7%, 4/15, versus 46.7%, 7/15) (Table 1). The failure of the complete recanalization rate in the nontortuous anatomy model was lower than that in the tortuous anatomy model (33.3%, 5/15, versus 60.0%, 9/15) (Table 2).

Comparison of Various Thrombectomy Techniques

CA showed the best FPE and DE rates in both the nontortuous and the tortuous models compared with the SR or combined techniques. In the nontortuous model, FPE/DE rates were 100%/0% versus 80%/20% versus 60%/60% for the CA, SR, and combined techniques, respectively. In the tortuous model, the FPE/DE rates worsened for all devices compared with the nontortuous model; however, CA maintained a relatively favorable outcome compared with the SR or combined techniques (80%/20% versus 40%/60% versus 20%/60%) (Table 1). The combined technique failed to show superior results compared with the other techniques in all aspects, with notably poor FPE outcome in the tortuous anatomy model (80% versus 40% versus 20%).

Mechanism of Thrombectomy Failure

The analysis of the video recordings revealed the mechanisms of thrombectomy failure for the respective techniques. In the CA technique, FPE and no DE were observed when the thrombus was completely ingested at the site of occlusion. However, when the clot was not completely ingested, deflection and straightening of the tip of the aspiration catheter occurred when passing through the curved angle of the vessel, resulting in an increase in the angle between the axis of the aspiration catheter tip and the axis of the captured thrombus, causing fragmentation and detachment of the thrombus (Fig 3*A*, -*D*). In the SR technique, the stent was elongated, resulting in partial collapse of its lumen when passing through the curved segments such as the carotid siphon. These

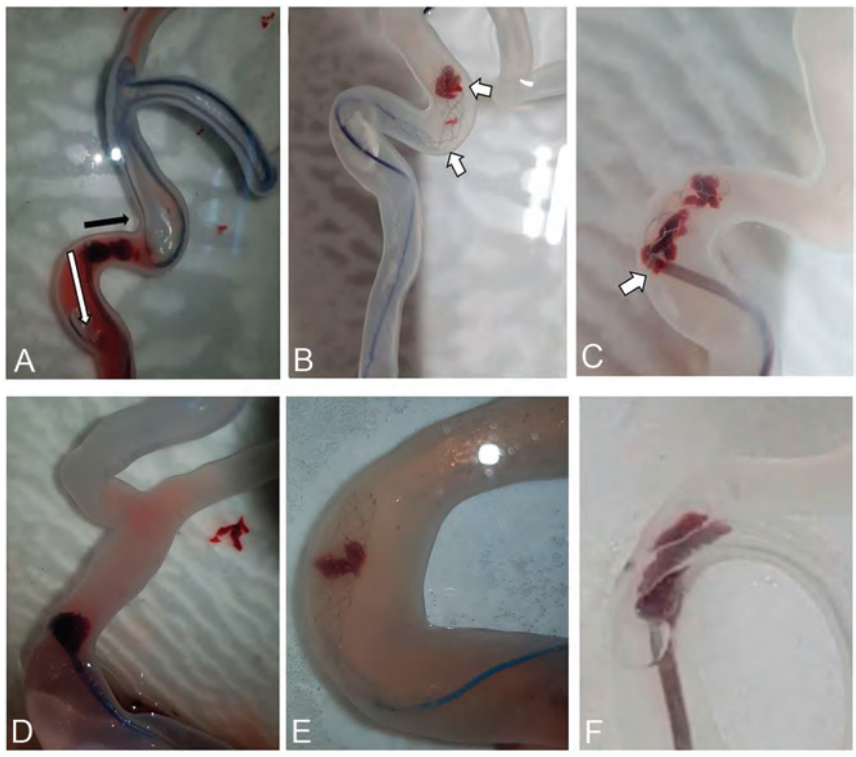

FIG 3. Mechanisms of thrombectomy failure in the tortuous anatomy model. *A–C*, Tortuous anatomy model. *D–F*, Nontortuous anatomy model. *A*, In the CA experiment, the thrombus is clogged at the tip of the aspiration catheter. The thrombus brushes against the tortuous vessel wall during retrieval and fragments when the aspiration catheter tip deflects perpendicular to the axis of the lumen at the angulated curve (*white arrow*, catheter tip alignment; *black arrow*, axis of the lumen and thrombus alignment). *B*, In the SR experiment, elongation and segmental collapse of the stent are noted (*white arrows*) when retrieving across the curved segment of the vessel, causing fragmentation of the thrombus. *C*, In the combined experiment, shearing of the thrombus occurred (*white arrow*) while crossing the curved segment when the SR was inadvertently pulled into the aspiration catheter during retrieval of the SR-CA unit due to aggravation of the length mismatch. *D*, In the CA experiment, the clogged thrombus and aspiration catheter show a more obtuse angle and are less deflected in the nontortuous anatomy model. *E*, The SR shows no elongation or segmental collapse at the curved segment of the vessel in the SR experiment, and there is no fragmentation or missing thrombus. *F*, In the combined experiment, the SR is not pulled into the aspiration catheter, and no shearing-off phenomenon is seen.

collapsed segments caused rolling, detachment, and fragmentation of the captured thrombus (Fig 3*B*, -*E*). In the case of the combined technique, shearing of the thrombus occurred when the thrombus-engaged SR was pulled into the aspiration catheter tip and during retrieval of the devices. This shearing phenomenon was more pronounced in the tortuous vessels (Fig 3*C*, -*F*).

DISCUSSION

The current in vitro study shows that the tortuosity of the cerebral vessels may impact the outcome of EVT techniques. The efficacy of EVT was inferior in the tortuous anatomy compared with the nontortuous anatomy irrespective of the techniques used. We found that both CA and SR techniques with proximal flow arrest showed acceptable FPE and DE results in the nontortuous anatomy. On the other hand, in the tortuous anatomy model showing severe angulations, the application of the CA technique was more effective in achieving better FPE and DE results than other techniques. The combined technique failed to show its effectiveness in terms of the FPE and DE in both the nontortuous and tortuous anatomy models.

In our experiment, CA showed the best FPE achievement with no DE in the nontortuous anatomy. It also showed relatively favorable FPE and DE results (FPE, 80%; DE, 20%) in the tortuous model. Many studies have reported that the CA technique shows angiographic and clinical outcomes comparable with those of conventional SR.[2,14] However, in a real-world patient, whether to pursue CA in the face of a tortuous anatomy or switch early to another technique may be a dilemma. Our in vitro study suggests that CA may be preferred in terms of improving the FPE and preventing DE in the tortuous anatomy scenario. Our analysis showed that complete ingestion of the thrombus was the main reason for the better results of CA in the tortuous anatomy. When the thrombus was completely ingested into the catheter lumen, DE did not occur. Arslanian et al[15] also reported the positive effects of CA on FPE and DE when the clot was completely ingested into the catheter lumen. On the other hand, Madjidyar et al[16] showed, with a flow model study, that the likelihood of DE increased when the thrombus was clogged without being completely ingested into the catheter tip.

Our results also showed that the thrombus fragmentation could occur when the catheter tip was clogged with a long segment of the thrombus outside the catheter tip. The catheter-clogged thrombus remaining outside the catheter failed to remain intact due to the friction with the vessel wall, especially when deflection and straightening of the catheter tip occurred while passing through the angled curvature. According to Alverne et al,[17] the retraction force of the thrombectomy devices can be physically reduced as it disperses through the different vectors in the tortuous vessels. Bernava et al[18] showed that the angle of interaction between the aspiration catheter tip and the thrombus also influences the thrombectomy efficacy at MCA branches in an in vitro study. In this regard, larger inner-diameter aspiration catheters capable of complete ingestion of the clot may be the best solution for patients with severely tortuous vascular anatomy.[19] However, despite the in vitro advantages of CA clot retrieval in the tortuous anatomy shown in this experiment, the tortuous anatomy may preclude fast and safe navigation of the aspiration catheter to the occlusion site in real-world patients. Development of more flexible and soft-tipped aspiration catheters with larger inner diameters is warranted.

The FPE and DE rates were 80.0% and 20.0%, respectively, in the nontortuous anatomy model when the SR technique was used with a BGC. In the tortuous anatomy model, the FPE rate decreased (40.0%) and DE was observed with a higher incidence (60.0%). The mechanisms of thrombectomy failure with the SR has been reported in several studies.[20,21] Insufficient thrombus integration into the stent strut and thrombus rolling between the vessel wall and the strut are known to be common mechanisms and were observed in our analysis as well.[20] Elongation and collapse of the device was observed in several cases of our tortuous anatomy model. The integrated thrombus was dislodged from the stent lumen at these collapsed segments. It has been reported that the elongation and collapse of the SR mesh may occur in curved and angulated segments.[21,22] Also, the longer retrieval length of the SR due to the tortuous anatomy is thought to be associated with failure of thrombus retrieval. The physical elongation and collapse of the stent together with the increased length of the retrieval from the M1 to the cervical ICA in the severely angulated vessel may be the cause of the poor performance of SR in these cases. Considering these mechanisms of thrombectomy failure shown in this study, SR may be a suboptimal technique, especially in patients with a tortuous vascular anatomy. A longer length of the SR may be an alternative option. Recent introduction of many new SRs with modified structures such as segmented/hybrid design, dual-layer, and closed-end structures of the device may show improvement in the outcome.[23-26]

Although a synergistic effect of the combined method may have been expected, our results show that there was no obvious advantage in achieving FPE and reducing DE compared with other techniques (Table 1). Rather, the FPE rate was quite low, especially in the tortuous anatomy (20%). Several SR-aspiration catheter combination thrombectomy techniques have been studied.[7,27] Prior reports have reported that these combination techniques may be effective in improving the recanalization rate and reducing the distal embolization compared with single-device techniques.[28] However, Yoo et al[29] reported that when the SR was retrieved inside the aspiration catheter, there could be a risk of shearing off the thrombus between the aspiration catheter tip and thrombus-engaged SR. McTaggart et al[30] emphasized the importance of appropriate tension adjustments to prevent shearing of the clot from the length mismatch of the SR and the aspiration catheter during retrieval. This shearing-off phenomenon may be difficult to visualize during the real-world patient treatment. However, the analysis of our study revealed that as the SR is retrieved into the tip of aspiration catheter, shearing off or squeezing out of the noningested thrombus occurs followed by fragmentation. This phenomenon was more pronounced in cases of tortuous curves where control of the length and tension mismatch between the stent and the aspiration catheter may be more difficult during retrieval.

Also, the stent struts may actually pin the clot to the vessel wall and interfere in the ingestion process of the thrombus by the CA catheter. Recently, Koge et al[31] reported that the combined method showed more superior FPE results than in the SR and CA groups in the nontortuous ICA curve group, but the superiority was lost in the tortuous curve group. This finding seems to partly contradict our experimental results, which showed no superiority of the combined method in both the nontortuous and the tortuous models. Our analysis suggests that the shearing-off phenomenon is associated with not only vascular tortuosity but also multiple other factors. Our experiment included only M1 occlusions, but Okuda et al[32] showed that the efficacy of the combined method may be influenced by the location of the occlusion, ie, it is more effective in ICA and M2 occlusions. Another concern of the combined method in the tortuous anatomy may be the safety of the procedure. Although the tensile force for retrieval of the devices was not analyzed in our study, more force was often necessary to retrieve the aspiration catheter and stent retriever together, probably due to the higher friction related to the combined use of the devices.

This study has some limitations inherently related to the in vitro nature of the experiment. Although the main arterial flow and its arrest with the BGC were simulated, the effects of the collateral flow on the thrombus could not be completed replicated. Other limitations include the endothelium and the coagulation factors and their effects on the friction and tension of the actual vessel wall. Also, only 1 type of red blood cell–rich thrombus analog and single models of the nontortuous and tortuous vascular anatomy were used. Another limitation is that although video recordings were used, the thrombectomy failure mechanisms could not be identified in some of the experiments; thus, quantitative analysis was not performed. The angle of the video recording was not optimal to visualize and identify the exact mechanism in some of the cases.

On the other hand, the major strength of this study is the anatomic simulation of the real human vasculature. Various model studies have attempted to simulate the real human cerebrovascular anatomy. Animal experiments may simulate relatively angulated vascular anatomy, but the anatomy and blood vessel size are different from those of actual human arteries. Fabrications of silicone or glass tubes may allow angulated and tortuous curvature models. However, this procedure also has limitations in simulating the actual curvature of human blood vessels. Flow-model production using 3D printing has the advantage of being able to accurately depict the cerebrovascular structure of a real patient. Furthermore, with a transparent material, the mechanisms of the device-thrombus-anatomic interaction can be directly observed. More diverse experiments such as the impact of the different histologic clot components and the efficacy of various devices/techniques in various models should be the subject of future studies.

CONCLUSIONS

We observed that the tortuous vascular anatomy may worsen the FPE and DE rates. Deflection and straightening of the aspiration catheter, elongation of the SR, and the shearing-off phenomenon during combined techniques were the main mechanisms of thrombectomy failure. CA was effective despite the tortuous anatomy when complete ingestion of the thrombus was achieved.

Disclosure forms provided by the authors are available with the full text and PDF of this article at www.ajnr.org.

REFERENCES

1. Goyal M, Menon BK, van Zwam WH, et al. **Endovascular thrombectomy after large-vessel ischaemic stroke: a meta-analysis of individual patient data from five randomised trials.** *Lancet* 2016;387:1723–31 CrossRef Medline

2. Lapergue B, Blanc R, Gory B, et al; ASTER Trial Investigators. **Effect of Endovascular Contact Aspiration vs Stent Retriever on Revascularization in Patients with Acute Ischemic Stroke and Large Vessel Occlusion: The ASTER Randomized Clinical Trial.** *JAMA* 2017;318:443–52 CrossRef Medline
3. Chueh JY, Kuhn AL, Puri AS, et al. **Reduction in distal emboli with proximal flow control during mechanical thrombectomy: a quantitative in vitro study.** *Stroke* 2013;44:1396–401 CrossRef Medline
4. Nguyen TN, Malisch T, Castonguay AC, et al. **Balloon guide catheter improves revascularization and clinical outcomes with the Solitaire device: analysis of the North American Solitaire Acute Stroke Registry.** *Stroke* 2014;45:141–45 CrossRef Medline
5. Teleb MS. **Endovascular acute ischemic stroke treatment with FlowGate Balloon Guide Catheter: a single-center observational study of FlowGate Balloon Guide Catheter Use.** *Interv Neurol* 2018;7:327–33 CrossRef Medline
6. Maegerlein C, Berndt MT, Mönch S, et al. **Further development of combined techniques using stent retrievers, aspiration catheters and BGC.** *Clin Neuroradiol* 2020;30:59–65 CrossRef Medline
7. Pampana E, Fabiano S, De Rubeis G, et al. **Switch strategy from direct aspiration first pass technique to Solumbra improves technical outcome in endovascularly treated stroke.** *Int J Environ Res Public Health* 2021;18:2670 CrossRef Medline
8. Zaidat OO, Castonguay AC, Linfante I, et al. **First pass effect: a new measure for stroke thrombectomy devices.** *Stroke* 2018;49:660–66 CrossRef Medline
9. Gascou G, Lobotesis K, Machi P, et al. **Stent retrievers in acute ischemic stroke: complications and failures during the perioperative period.** *AJNR Am J Neuroradiol* 2014;35:734–40 CrossRef Medline
10. Yamamoto S, Yamagami H, Todo K, et al. **Correlation of middle cerebral artery tortuosity with successful recanalization using the Merci retrieval system with or without adjunctive treatments.** *Neurol Med Chir (Tokyo)* 2014;54:113–19 CrossRef Medline
11. Kim BJ, Kim SM, Kang DW, et al. **Vascular tortuosity may be related to intracranial artery atherosclerosis.** *Int J Stroke* 2015;10:1081–86 CrossRef Medline
12. Chueh JY, Wakhloo AK, Hendricks GH, et al. **Mechanical characterization of thromboemboli in acute ischemic stroke and laboratory embolus analogs.** *AJNR Am J Neuroradiol* 2011;32:1237–44 CrossRef Medline
13. Mokin M, Setlur Nagesh SV, Ionita CN, et al. **Comparison of modern stroke thrombectomy approaches using an in vitro cerebrovascular occlusion model.** *AJNR Am J Neuroradiol* 2015;36:547–51 CrossRef Medline
14. Phan K, Maingard J, Kok HK, et al. **Contact aspiration versus stent-retriever thrombectomy for distal middle cerebral artery occlusions in acute ischemic stroke: meta-analysis.** *Neurointervention* 2018;13:100–09 CrossRef Medline
15. Arslanian RA, Marosfoi M, Caroff J, et al. **Complete clot ingestion with cyclical ADAPT increases first-pass recanalization and reduces distal embolization.** *J Neurointerv Surg* 2019;11:931–36 CrossRef Medline
16. Madjidyar J, Nerkada L, Larsen N, et al. **Choosing an effective and safe direct aspiration setup for tortuous anatomy in acute ischemic stroke: in vitro study in a physiological flow model.** *Rofo* 2021;193:544–50 CrossRef Medline
17. Alverne F, Lima FO, Rocha FA, et al. **Unfavorable vascular anatomy during endovascular treatment of stroke: challenges and bailout strategies.** *J Stroke* 2020;22:185–202 CrossRef Medline
18. Bernava G, Rosi A, Boto J, et al. **Experimental evaluation of direct thromboaspiration efficacy according to the angle of interaction between the aspiration catheter and the clot.** *J Neurointerv Surg* 2021;13:1152–56 CrossRef Medline
19. Pampana E, Fabiano S, De Rubeis G, et al. **Tailored vessel-catheter diameter ratio in a direct aspiration first-pass technique: is it a matter of caliber?** *AJNR Am J Neuroradiol* 2021;42:546–50 CrossRef Medline
20. Madjidyar J, Hermes J, Freitag-Wolf S, et al. **Stent-thrombus interaction and the influence of aspiration on mechanical thrombectomy: evaluation of different stent retrievers in a circulation model.** *Neuroradiology* 2015;57:791–97 CrossRef Medline
21. Schwaiger BJ, Gersing AS, Zimmer C, et al. **The curved MCA: influence of vessel anatomy on recanalization results of mechanical thrombectomy after acute ischemic stroke.** *AJNR Am J Neuroradiol* 2015;36:971–76 CrossRef Medline
22. Machi P, Jourdan F, Ambard D, et al. **Experimental evaluation of stent retrievers' mechanical properties and effectiveness.** *J Neurointerv Surg* 2017;9:257–63 CrossRef Medline
23. Zaidat OO, Bozorgchami H, Ribo M, et al. **Primary results of the multicenter ARISE II Study (Analysis of Revascularization in Ischemic Stroke With EmboTrap).** *Stroke* 2018;49:1107–15 CrossRef Medline
24. Gruber P, Zeller S, Garcia-Esperon C, et al. **Embolus Retriever with Interlinked Cages versus other stent retrievers in acute ischemic stroke: an observational comparative study.** *J Neurointerv Surg* 2018;10:e31–31 CrossRef Medline
25. Kaneko N, Komuro Y, Yokota H, et al. **Stent retrievers with segmented design improve the efficacy of thrombectomy in tortuous vessels.** *J Neurointerv Surg* 2019;11:119–22 CrossRef Medline
26. Vogt ML, Kollikowski AM, Weidner F, et al. **Safety and effectiveness of the new generation APERIO hybrid stent-retriever device in large vessel occlusion stroke.** *Clin Neuroradiol* 2022;32:141–51 CrossRef Medline
27. Dumont TM, Mokin M, Sorkin GC, et al. **Aspiration thrombectomy in concert with stent thrombectomy.** *J Neurointerv Surg* 2014;6:e26 CrossRef Medline
28. Wong J, Telischak N, Heit J, et al. **E-083 Acute Stroke Intervention for Large Vessel Occlusion with Combined Stent Retriever and Suction Thrombectomy (Solumbra Technique): a retrospective analysis of 85 patients.** *J NeuroInterv Surg* 2016;8(Suppl 1):A86 CrossRef
29. Yoo AJ, Andersson T. **Thrombectomy in acute ischemic stroke: challenges to procedural success.** *J Stroke* 2017;19:121–30 CrossRef Medline
30. McTaggart RA, Ospel JM, Psychogios MN, et al. **Optimization of endovascular therapy in the neuroangiography suite to achieve fast and complete (Expanded Treatment in Cerebral Ischemia 2c-3) reperfusion.** *Stroke* 2020;51:1961–68 CrossRef Medline
31. Koge J, Tanaka K, Yoshimoto T, et al. **Internal carotid artery tortuosity: impact on mechanical thrombectomy.** *Stroke* 2022;53:2458–67 CrossRef Medline
32. Okuda T, Arimura K, Tokunaga S, et al. **Efficacy of combined use of a stent retriever and aspiration catheter in mechanical thrombectomy for acute ischemic stroke.** *J Neurointerv Surg* 2022;53:892–97 CrossRef Medline

Surgical or Endovascular Treatment of MCA Aneurysms: An Agreement Study

W. Boisseau, T.E. Darsaut, R. Fahed, J.M. Findlay, R. Bourcier, G. Charbonnier, S. Smajda, J. Ognard, D. Roy, F. Gariel, A.P. Carlson, E. Shotar, G. Ciccio, G. Marnat, P.B. Sporns, T. Gaberel, V. Jecko, A. Weill, A. Biondi, G. Boulouis, A.L. Bras, S. Aldea, T. Passeri, S. Boissonneau, N. Bougaci, J.C. Gentric, J.D.B. Diestro, A.T. Omar, H.M. Al-Jehani, G. El Hage, D. Volders, Z. Kaderali, I. Tsogkas, E. Magro, Q. Holay, J. Zehr, D. Iancu, and J. Raymond

ABSTRACT

BACKGROUND AND PURPOSE: MCA aneurysms are still commonly clipped surgically despite the recent development of a number of endovascular tools and techniques. We measured clinical uncertainty by studying the reliability of decisions made for patients with middle cerebral artery (MCA) aneurysms.

MATERIALS AND METHODS: A portfolio of 60 MCA aneurysms was presented to surgical and endovascular specialists who were asked whether they considered surgery or endovascular treatment to be an option, whether they would consider recruitment of the patient in a randomized trial, and whether they would provide their final management recommendation. Agreement was studied using κ statistics. Intrarater reliability was assessed with the same, permuted portfolio of cases of MCA aneurysm sent to the same specialists 1 month later.

RESULTS: Surgical management was the preferred option for neurosurgeons (n = 844/1320; [64%] responses/22 raters), while endovascular treatment was more commonly chosen by interventional neuroradiologists (1149/1500 [76.6%] responses/25 raters). Interrater agreement was only "slight" for all cases and all judges (κ = 0.094; 95% CI, 0.068–0.130). Agreement was no better within specialties or with more experience. On delayed requestioning, 11 of 35 raters (31%) disagreed with themselves on at least 20% of cases. Surgical management and endovascular treatment were always judged to be a treatment option, for all patients. Trial participation was offered to patients 65% of the time.

CONCLUSIONS: Individual clinicians did not agree regarding the best management of patients with MCA aneurysms. A randomized trial comparing endovascular with surgical management of patients with MCA aneurysms is in order.

ABBREVIATIONS: ISFD = intrasaccular flow disruptors; RCT = randomized controlled trial

Whether the best management of MCA aneurysms is surgical or endovascular remains uncertain. MCA aneurysms commonly present endovascular challenges such as a wide neck that incorporates arterial branch origins, yet they are usually readily treatable with surgical clipping.[1-3] Despite recent trends favoring endovascular repair, many patients with MCA aneurysm are still treated surgically.

Received March 30, 2022; accepted after revision June 28.

From the Department of Radiology (W.B., D.R., A.W., D.I., J.R.), Division of Neuroradiology, and Department of Neurosurgery (G.E.H.), Centre Hospitalier de l'Université de Montréal, Montreal, Québec, Canada; Department of Surgery (T.E.D., J.M.F.), Division of Neurosurgery, University of Alberta Hospital, Mackenzie Health Sciences Centre, Edmonton, Alberta, Canada; Department of Medicine (R.F.), Division of Neurology, The Ottawa Hospital, Ottawa Hospital Research Institute and University of Ottawa, Ottawa, Ontario, Canada; Department of Neuroradiology (R.B.), University Hospital of Nantes, Nantes, France; Departments of Interventional Neuroradiology (G. Charbonnier, A.B.) and Neurosurgery (N.B.), Besançon University Hospital, Besançon, France; Departments of Interventional Neuroradiology (S.S.) and Neurosurgery (S.A.), Fondation Ophtalmologique Adolphe de Rothschild, Paris, France; Department of Interventional Neuroradiology (J.O., J.C.G.), Hôpital de la Cavale Blanche, Brest, Bretagne, France; Departments of Neuroradiology (F.G., G.M.) and Neurosurgery (V.J.), University Hospital of Bordeaux, Bordeaux, France; Department of Neurosurgery (A.P.C.), University of New Mexico Hospital, Albuquerque, New Mexico; Department of Neuroradiology (E.S.), Groupe Hospitalier de Pitié Salpêtrière, Paris, France; Department of Interventional Neuroradiology (G. Ciccio), Centre Hospitalier de Bastia, Bastia, Corse, France; Department of Neuroradiology (P.B.S., I.T.), Clinic of Radiology and Nuclear Medicine, University Hospital Basel, Basel, Switzerland; Department of Diagnostic and Interventional Neuroradiology (P.B.S.), University Medical Center Hamburg-Eppendorf, Hamburg, Germany; Department of Neurosurgery (T.G.), University Hospital of Caen, Caen, France; Department of Neuroradiology (G.B.), University Hospital of Tours, Tours, Indre et Loire, France; Department of Radiology (A.L.B.), Groupement Hospitaliser Bretagne Atlantique–Hôpital Chubert, Vannes, Bretagne, France; Department of Neurosurgery (T.P.), Lariboisière Hospital, Assistance Publique Hôpitaux de Paris, University of Paris, Paris, France; Department of Neurosurgery (S.B.), La Timone Hospital, and L'Institut National de la Santé et de la Recherche Médicale (S.B.), Institut de Neurosciences des Systèmes, Aix Marseille University, Marseille, France; Division of Diagnostic and Therapeutic Neuroradiology (J.D.B.D.), Department of Medical Imaging, St. Michael's Hospital, University of Toronto, Toronto, Ontario, Canada; Division of Neurosurgery (A.T.O.), Department of Surgery, St. Michael's Hospital, University of Toronto, Toronto, Ontario, Canada; Department of Neurosurgery, Radiology and Critical Care Medicine (H.M.A.-J.), King Fahad Hospital of the University, Imam Abdulrahman bin Faisal University, Alkhobar, Saudi Arabia; Department of Radiology (D.V.), Dalhousie University, Halifax, Nova Scotia, Canada; Division of Neurosurgery (Z.K.), GB1-Health Sciences Centre, Winnipeg, Manitoba, Canada; Department of Neurosurgery (E.M.), Centre Hospitalier Universitaire Cavale Blanche, UBO L'Institut National de la Santé et de la Recherche Médicale, LaTIM UMR 1101, Brest, France; Department of Radiology (Q.H.), Hôpital d'Instruction des Armées Saint-Anne, Toulon, France; and Department of Mathematics and Statistics (J.Z.), Pavillon André-Aisenstadt, Montreal, Québec, Canada.

Please address correspondence to Jean Raymond, MD, Centre Hospitalier de l'Université de Montréal (CHUM), Department of Radiology, Room D03.5462b, Montreal, PQ, CANADA H2X 0C1; e-mail: jean.raymond@umontreal.ca

Indicates article with online supplemental data.

http://dx.doi.org/10.3174/ajnr.A7648

Aneurysm rupture status impacts the decision regarding surgery versus endovascular management. Although randomized evidence in favor of coiling ruptured aneurysms exists, it may not apply to MCA aneurysms. The International Subarachnoid Aneurysm Trial (ISAT) included 301 patients with MCA aneurysms, with similar results: Forty-six of 162 (28%) had poor outcomes for coiling, and 39/139 (28%), for clipping.[4,5] In the prerandomized Barrow Ruptured Aneurysm Trial (BRAT) trial,[6] most patients with MCA aneurysm allocated to coiling were crossed over to clipping, while the early Finnish trial excluded most patients with MCA aneuryms.[7]

Whether unruptured aneurysms in any location should be preventively treated at all remains controversial.[8] Yet, when the goal of treatment is lifetime protection from bleeding, the reputed better long-term occlusion provided by clipping may be an advantage. A recent exploratory analysis of the MCA subgroups of 2 ongoing randomized trials showed similar clinical outcomes but better treatment efficacy with surgical management than with coiling.[9] Multiple comparative case series have suggested that clipping may be better,[1-3,9] but trial subgroup analyses and observational studies should be interpreted with caution.[10]

To address the endovascular difficulties of wide-neck bifurcation aneurysms, innovative endovascular devices continue to be introduced, including stent-assisted coiling,[11] off-label use of flow diverters,[12] and intrasaccular flow disruptors (ISFD).[13] Yet, there is currently no convincing evidence that new devices improve endovascular results.[14-16] A randomized trial comparing endovascular and surgical management of MCA aneurysms is needed to address the uncertainty and establish the best way to care for these patients.[17]

Showing the presence of clinical uncertainty and, therefore, community equipoise between treatment options is a useful preparatory step to the design and conduct of a randomized trial. Clinical uncertainty can be measured by studying the variability of clinical decisions made by various clinicians on the same cases using agreement study methodology.[18,19]

In the present work, we sought to investigate the uncertainty and agreement between aneurysm experts for the endovascular or surgical management of patients with MCA aneurysms.

MATERIALS AND METHODS

This study was prepared in accordance with the Guidelines for Reporting Reliability and Agreement Studies.[20]

Patients

An electronic portfolio of 60 anonymized patients with MCA aneurysms (30 ruptured and 30 unruptured) was prepared (Online Supplemental Data). Each patient in the portfolio had a catheter angiographic "working projection" of the aneurysm to delineate the neck and parent and branching vessels and a short case vignette (age, sex and World Federation of Neurosurgical Societies score if ruptured). Three authors (W.B., T.E.D., and J.R.) selected the cases to include a wide spectrum of patients typically considered for surgical or endovascular treatment. MCA aneurysms were selected from 5 pragmatic clinical trials (ISAT-2,[21] Canadian UnRuptured Endovascular versus Surgery [CURES],[22] Stenting in Aneurysm Treatments [STAT],[23] Flow Diversion in Aneurysms Trial [FIAT].[24] and Randomized Trial on Intra-Saccular Endobridge devices [RISE][25]. To minimize κ paradoxes,[26] case selection included approximately one-third of cases for whom endovascular treatment was expected to be a frequent (for example, small saccular aneurysms with narrow necks), one-third of cases for whom surgical clipping was expected to be frequent (wide-neck aneurysms incorporating MCA branch origins), and one-third "gray zone" cases, for whom surgical clipping or endovascular treatment choices might be more balanced.

Raters

All raters were clinicians who actively manage aneurysms. Anonymity was ensured, but some demographic information was collected. Raters were asked to specify their training background (interventional neuroradiology, neurosurgery, or dual-trained), the number of years treating aneurysms (<5 years, 6–10 years, 11–20 years, or >20 years), the number of patients they have treated with flow diverters and ISFDs (none, 1–19 patients, >20 patients), and the estimated proportion of patients with MCA aneurysms treated by surgery and endovascular treatment at their center.

Ratings

For each case, raters were asked (question 1) whether surgical management was an option (yes/no), (question 2) whether there was another option they would offer (choose from: no, surgical clipping only or yes, endovascular treatment), (question 3) whether they would be willing to recruit the patient in an randomized controlled trial (RCT) that would give a 50% chance of surgical management and a 50% of endovascular treatment (yes/no), and (question 4) their final best treatment choice (choose from surgical management or endovascular treatment).

If the responder chose endovascular treatment, he or she was asked (question 5) to specify the method, and to choose from: 1) coils ± balloon remodeling, 2) coils ± stent, 3) flow diverter, or 4) intrasaccular flow disruptor, the WEB (ie, Woven EndoBridge; Sequent Medical). Finally, (question 6) responders were asked to gauge their confidence regarding their final treatment choice (in 10% increments, ranging from 0% to 100%). The entire survey is available in the Online Supplemental Data. To evaluate intrarater agreement, raters were asked to re-assess the same cases in a permuted order at least 1 month later. The present study did not address the fundamental problem regarding whether unruptured aneurysms should be treated at all. Raters were required to choose surgery or endovascular treatment for each and all patients, whether the aneurysms were ruptured or unruptured.

Statistical Analyses

Descriptive statistics are presented using percentage for categoric variables and mean (SD) for continuous variables. The proportions of answers for each question among different groups of aneurysms or patients (all cases/ruptured/unruptured aneurysms) or different groups of raters (background: years of experience, practice location, flow diverters, or ISFD experience) were compared using a 1-way ANOVA. When applicable, pair-wise comparisons were performed using a Bonferroni adjustment. Correlations between treatment choice and continuous variables (aneurysm and neck size) were analyzed using the Pearson correlation coefficient. Confidence in

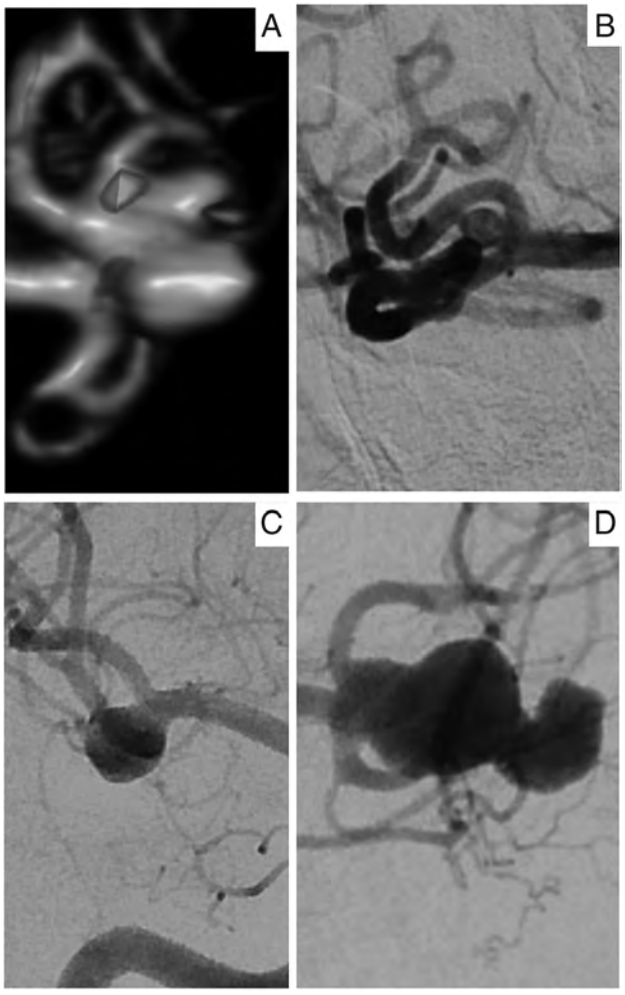

FIG 1. Cases of high (*A* and *B*) and low (*C* and *D*) agreement: Seventy-seven percent of respondents selected surgical management for case *A* and 87% selected endovascular management for case *B*, while 51% and 49% selected surgical management for *C* and *D*.

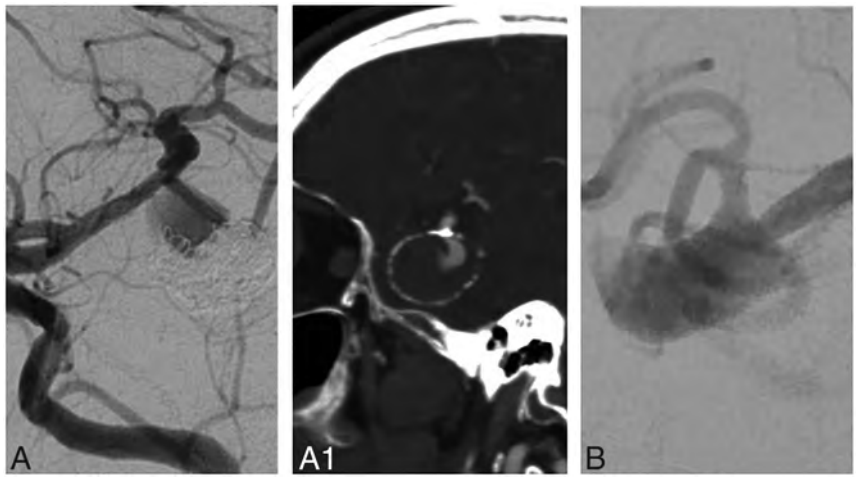

FIG 2. Cases in which surgical management (*A* and *A1*) or endovascular treatment (EVT) *(B*) were rarely considered to be an option. *A* and *A1* show a recurrent, previously coiled, calcified, partially thrombosed-but-unruptured left MCA aneurysm. Only 64% of the respondents considered surgical management an option. *B*, A large, wide-neck, ruptured, right MCA aneurysm. Only 39% of the respondents considered EVT to be an option for this case.

decision-making (scale of 0–100) was analyzed using ANOVA. χ^2 tests were used to compare willingness to recruit patients in a RCT. Agreement between and within raters was measured using κ statistics and 95% bootstrap confidence intervals (the preferred method to estimate κ confidence intervals) and interpreted according to Landis and Koch.[27] κ values ranged from −1 (perfect disagreement) to +1 (perfect agreement), with 0 indicating no agreement among the raters other than what would be expected by chance alone. Analyses were performed using STATA (Version 16.1; StataCorp) and SPSS software (Version 26; IBM) with significance set at 5%.

RESULTS

Patient and aneurysm characteristics included in the portfolio are detailed in the Online Supplemental Data, with typical cases depicted in Fig 1, and more difficult cases, in Fig 2.

There were 47 respondents to the survey: 25 interventional neuroradiologists, 15 open vascular neurosurgeons, and 7 dual-trained (open and endovascular) neurosurgeons. Raters were from North America ($n = 19$), Europe ($n = 27$), or the Middle East ($n = 1$). Raters had <5 years ($n = 18$), 6–10 years ($n = 16$), 11–20 years ($n = 6$), or >20 years' experience ($n = 7$). The numbers of surgical and endovascular choices for each of the 60 MCA aneurysm cases are illustrated in Fig 3.

Surgical management was always judged to be a treatment option, for all patients (mean, 41 [SD, 6] positive responses from 47 responders). Interrater agreement regarding whether surgical management was an option was poor ($\kappa = 0.092$; 95% CI, 0.047–0.146), even for subgroups according to experience, specialty, or location of practice (Online Supplemental Data).

Endovascular treatment was judged to always be an option (mean, 41 [SD, 5] positive responses to question 2). Interrater agreement regarding whether endovascular treatment was an alternative option was poor ($\kappa = 0.056$; 95%, CI, 0.039–0.077) for all subgroups of raters (Online Supplemental Data).

Overall, endovascular treatment was most frequently selected as final best management: 1625/2820 responses (58%; 95% CI, 56%–60%), with surgical management garnering 1195 votes (42%; 95% CI, 41%–44%) (Online Supplemental Data). The proportion of final treatment choices for all raters, according to background and expertise, for unruptured, ruptured, and all MCA aneurysms is illustrated in Fig 4.

Final treatment choices did not vary according to years of experience ($P = .32$) or practice location ($P = .49$) but differed between specialties and according to local use. Interventional neuroradiologists preferred endovascular treatment in 77% of cases, while open and dual-trained neurosurgeons selected endovascular treatment only 30% and 46% of the time, respectively; $P = .000$). There was a significant correlation between the self-

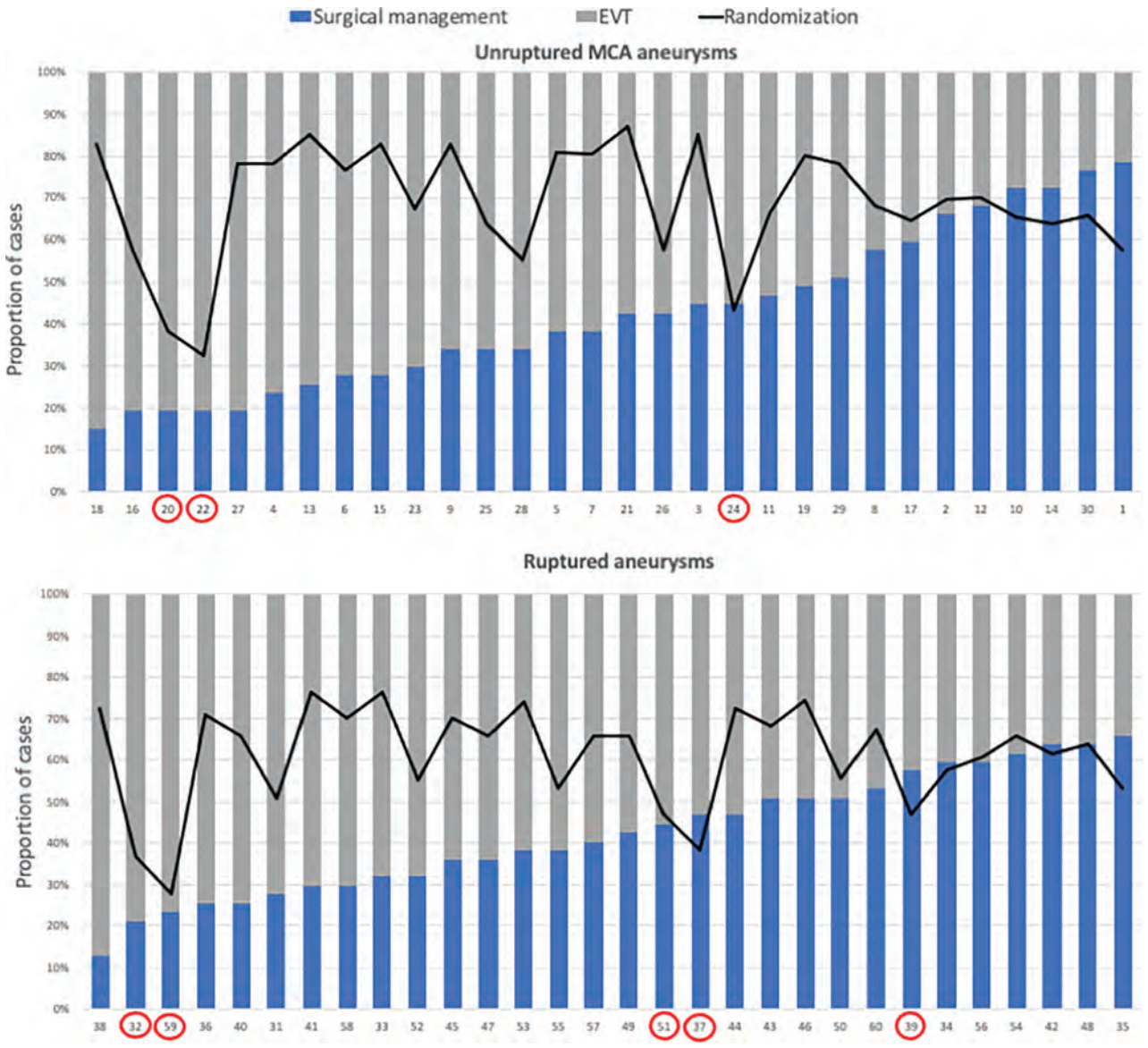

FIG 3. Proportions of votes for surgical and for endovascular treatment (EVT) for unruptured (*upper graph*) and ruptured (*lower graph*) MCA aneurysms and the proportion of clinicians willing to include the patient in an RCT (*line*). *Red circles* indicate cases with <50% of raters willing (3/30 for unruptured and 5/30 ruptured MCA aneurysms).

declared frequency of using surgical management at each center and the proportions of final decisions for surgery ($r = 0.587$; $P = .000$).

Interrater agreement regarding the final management decision was "slight" ($\kappa = 0.110$; 95% CI, 0.090–0.135) and did not improve when answers were dichotomized (surgical management versus any endovascular option) or when respondents were grouped according to experience, specialty, or location of practice (Table or Fig 5).

The proportion of final decisions for surgery, intrarater agreement between the 2 rating sessions, and the proportion of patients recruited in an RCT for each rater and ordered by numbers and classified by training are illustrated in Fig 6.

Intrarater κ values regarding the best final management (surgical management versus endovascular treatment) were affected by paradoxes (ie, high agreement and yet low κ values) in many cases. Intrarater κ values reached a substantial level for 8/35 (23%) raters. On delayed requestioning, 11 of 35 raters (31%) disagreed with themselves on at least 20% of cases (Online Supplemental Data).

Regarding the specific endovascular management options, coiling ± balloon remodelling was the most frequently selected endovascular option (Online Supplemental Data) for ruptured ($n = 506/960$, 52.7%) but not for unruptured ($n = 256/960$, 26.7%) aneurysms. Endovascular strategies requiring antiplatelet agents (stents and flow diverter, $n = 441/1605$, 27.5%) were less frequently chosen for both ruptured and unruptured MCA aneurysms than other endovascular strategies (coiling, balloon-assisted coiling, and ISFD, $n = 1164/1605$, 72.5%).

The size of the aneurysm and the width of the neck correlated ($P = .000$) with fewer endovascular choices (–0.142 for aneurysm

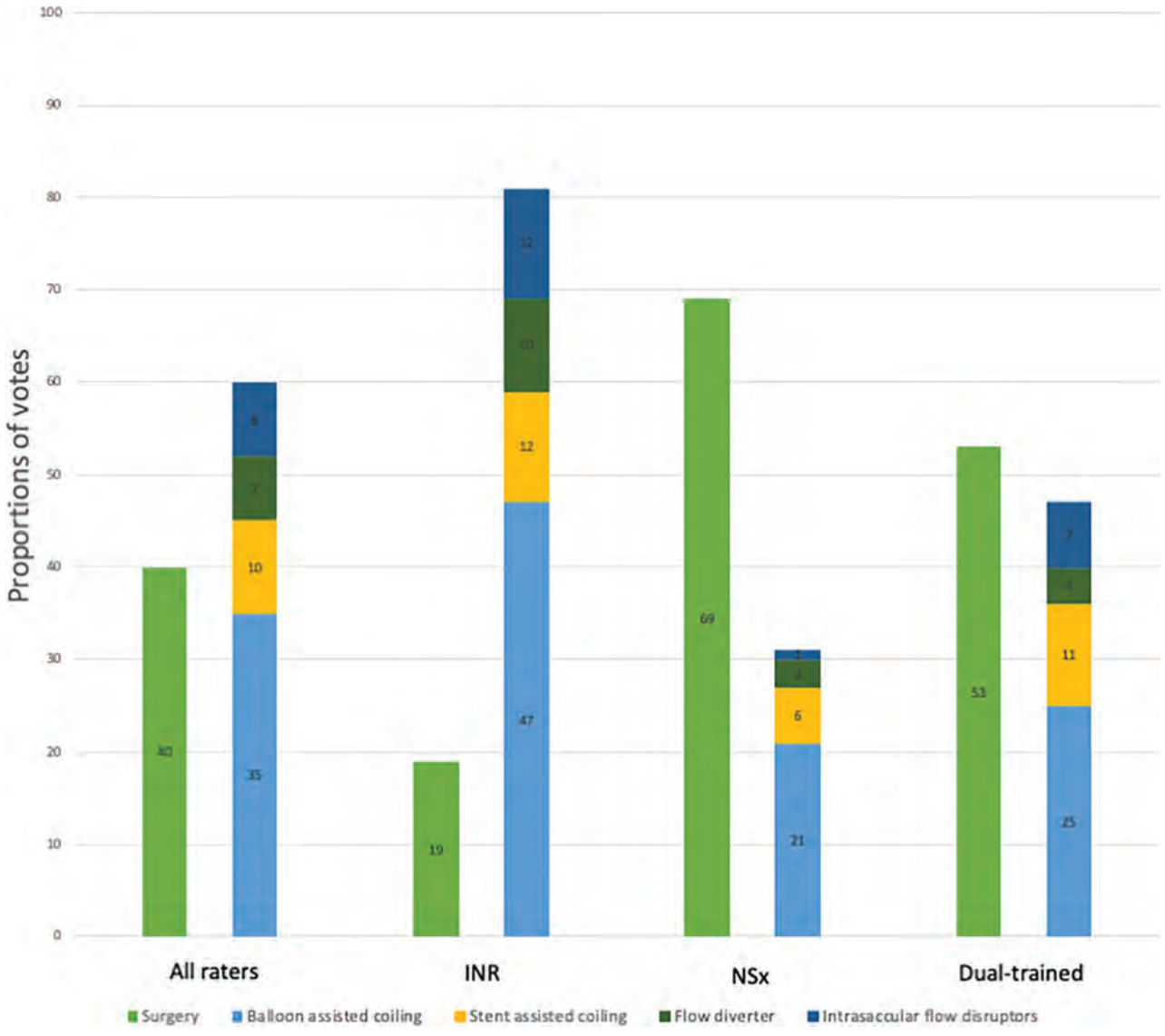

FIG 4. Proportions of final treatment choices for all raters, according to background and expertise, for all MCA aneurysms. Note the strong correlation between training background and choice of treatment. INR indicates interventional neuroradiologists; NSx, neurosurgeons.

size, −0.496 for neck size), more choices for flow diversion (+0.596, +0.550), and less confidence in the treatment decision (−0.629, −0.434). Clinicians were generally confident in their final decision (mean confidence, 75%; minimum-maximum, 53–98).

Recruitment of patients in an RCT comparing surgical and endovascular management is graphically displayed in Fig 3 (per patient) and Fig 6 (per rater). Trial participation was offered 64.9% of the time (1815/2795 yes responses to question 3). In 52/60 (87%) patients, a majority (≥51%) of responders were willing to include the patient in a randomized trial, which did not change substantially on the basis of rupture status: 27/30 (90%) for unruptured and 25/30 (83%) for ruptured aneurysms. Trial participation was offered by North American clinicians in 78% of cases and by European clinicians in 66% of cases ($P = .011$), regardless of specialty or training background ($P = .91$) or years of experience ($P = .969$). Interrater agreement regarding recruitment in an RCT was slight ($\kappa = 0.059$; 95% CI, 0.033–0.090) (Online Supplemental Data).

DISCUSSION

The current study shows that the best management of patients with MCA aneurysms, ruptured or unruptured, is uncertain. While surgical clipping was always a treatment option, endovascular treatment of some type was always judged to be an alternative. There was extreme variability in the final treatment decisions. Agreement regarding surgical or endovascular management was well below the "substantial" level, even between experts of the same specialty, with the same experience, and working on the same continent. There was also substantial variability at the level of individual clinicians. Inconsistency and lack of agreement occurred despite raters being individually and in general confident in their treatment decisions. Many raters (up to 30%) did not recommend the same approach (endovascular or surgical) when asked twice about the same patient in ≥20% of cases.

The most influential factors affecting clinical decisions were the training background of the clinician making the decision and

Interrater agreement (κ) regarding best final management choice

	All Cases	Landis and Koch Interpretation
All raters ($n = 47$)		
Dichotomized[a]	0.094 (0.068–0.130)	Poor
All categories	0.110 (0.090–0.135)	Poor
Specialty		
Open neurosurgeons ($n = 15$)		
Dichotomized[a]	0.109 (0.063–0.172)	Poor
All categories	0.072 (0.040–0.119)	Poor
INR ($n = 25$)		
Dichotomized[a]	0.177 (0.135–0.233)	Poor
All categories	0.185 (0.155–0.224)	Poor
Dual-trained neurosurgeons ($n = 7$)		
Dichotomized[a]	0.132 (0.065–0.203)	Poor
All categories	0.120 (0.079–0.176)	Poor
Location of practice		
North America ($n = 19$)		
Dichotomized[a]	0.060 (0.031–0.101)	Poor
All categories	0.076 (0.055–0.101)	Poor
Europe ($n = 27$)		
Dichotomized[a]	0.118 (0.084–0.167)	Poor
All categories	0.130 (0.103–0.166)	Poor

Note:—INR indicates interventional neuroradiologists.

[a] All categories (surgical management, coiling ± balloon remodelling, coiling ± stent, flow diverter, and intrasaccular flow disruptor) were dichotomized as surgical management versus all others.

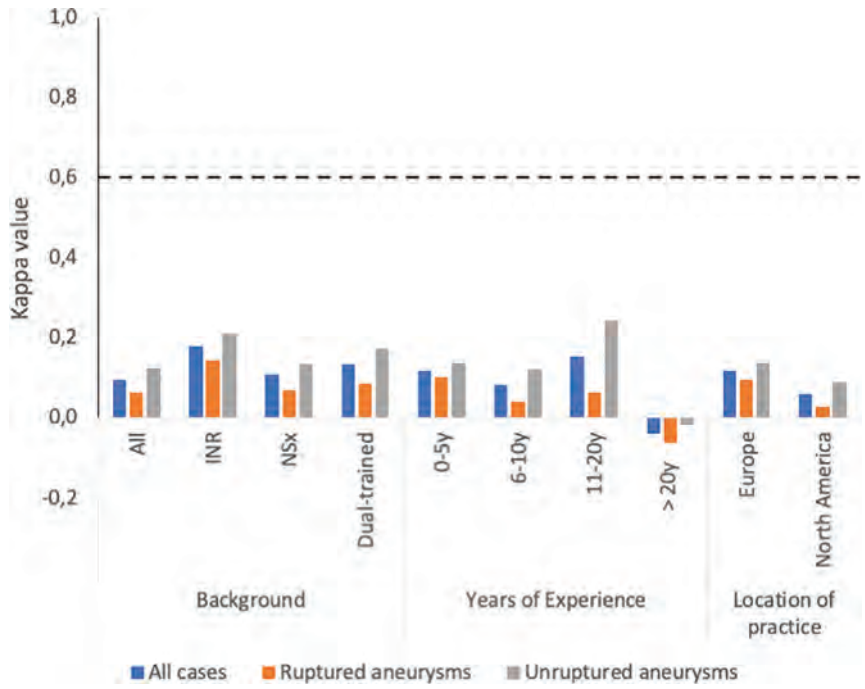

FIG 5. Interrater agreement for final treatment choices (surgical management versus any endovascular treatment) for all raters, according to background, experience, and practice location, for unruptured, ruptured, and all MCA aneurysms. All κ values are well below the *dashed substantial line* (0.600). INR indicates interventional neuroradiologists; NSx, neurosurgeons; y, year.

the frequency of use of an operation or endovascular treatment at the rater's institution. Perhaps, unsurprisingly, neurosurgeons and dual-trained neurosurgeons had a propensity for selecting clipping, while interventional neuroradiologists generally opted for endovascular treatment.

Aneurysm and neck sizes were also influential in determining surgical or endovascular management choices. The larger the neck, the less likely clinicians would be to consider endovascular treatment using coiling or balloon-assisted coiling. Wide-neck aneurysms were also associated with lower confidence in decision-making, with more frequent RCT participation.

Raters with an endovascular background more frequently selected strategies that did not require antiplatelet agents, especially for patients with ruptured aneurysms. The added risk of antiplatelet therapies in the ruptured context and the potential risk of thromboembolic complications with stents and flow diverters probably explain this result.[11,12] Our study also highlights new devices, such as intrasaccular flow disruptors (the WEB for example), being increasingly considered for MCA aneurysms.

While it seems natural that clinicians would tend to propose the intervention they practice, the clinical community, clinicians and patients alike, should be aware that diverse options are commonly being proposed for many patients with MCA aneurysms. Many clinicians believe that the real question is not whether MCA aneurysms should be clipped or treated endovascularly, but rather which MCA aneurysms should be clipped and which should be treated endovascularly. This latter question is impossible to translate into a workable trial hypothesis, and the underlying belief is directly responsible for widely divergent opinions and practices. Recognizing the uncertainty revealed by this study may be an important step in encouraging members of our community to proceed with the clinical research necessary to address the uncertainty regarding best management. If the first step of a science of practice is to recognize uncertainty, the second step is to change practice to take into account that uncertainty.[19] Our study may show the necessity of changing the way we practice, from unrepeatable, unverifiable decisions, to a more prudent and systematic approach that takes uncertainty into account. When no one really knows what to do, integrating research methods into clinical care may be in the best medical interest of individual patients. The questionnaire was designed with a randomized trial in view, one which hypothesizes that surgical clipping may still be better than

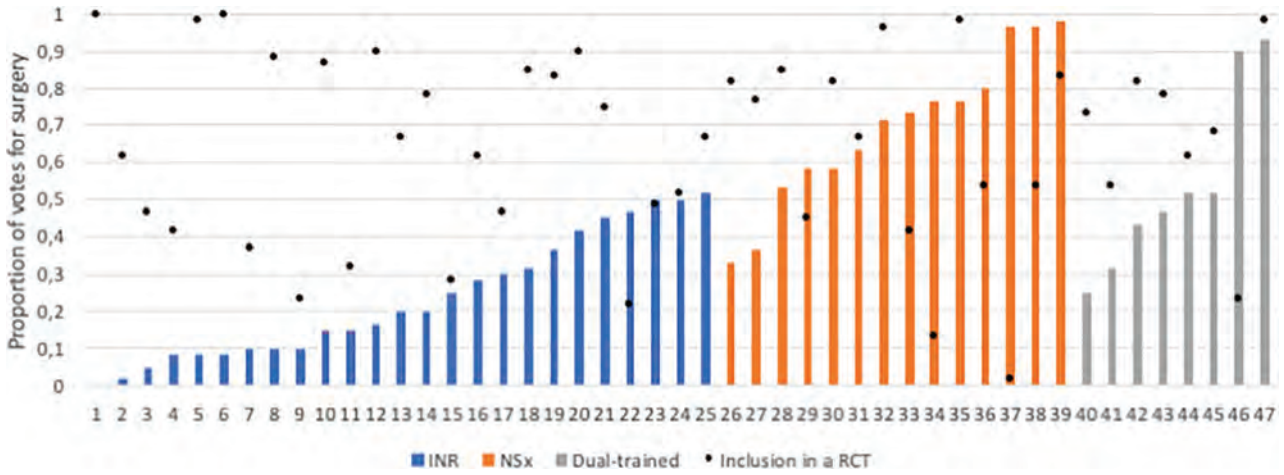

FIG 6. Proportions of votes for surgical management and inclusion in an RCTs (*black dots*) for each rater and rater's background. INR indicates interventional neuroradiologists; NSx, neurosurgeons.

endovascular options.[17] Disparities in management decisions provide evidence of collective uncertainty and community equipoise regarding the best management of patients with both ruptured and unruptured MCA aneurysms. A reassuring finding of our survey is that 33/47 clinicians (or 70%) would propose RCT participation to at least 50% of patients with MCA aneurysms. These results support the feasibility of an RCT that compares surgical and endovascular management.[17]

Surgical clipping, the time-honored-but-more invasive treatment, may still be best for patients with MCA aneurysms, yet clipping is "an uphill battle fought with fewer and fewer troops" against less invasive, increasingly popular endovascular options.[28] Endovascular treatment of MCA aneurysms is not always straightforward, but innovations to address the clinical challenge are proliferating. We believe that in the presence of uncertainty, patients are best managed in the context of a care trial,[18,29] in which they have a 50% chance of receiving a promising treatment of yet-unknown benefit, but an equal 50% chance of receiving the time-honored treatment.[30] To be eligible for participation in such a trial, patients must be treatable with either surgical or endovascular treatment. As our survey showed, this was the case for nearly all patients.

There are several limitations to this study. The patient series used cases selected from 5 ongoing pragmatic trials, including 2 RCTs that compared surgical and endovascular treatments. The artificial construction of a portfolio of balanced cases is necessary to minimize κ paradoxes,[26] but the series may not be representative of naturally occurring MCA aneurysms. A different case selection might have produced different results. Raters were not a random sample representative of a population of clinicians, and the intrarater agreement study was restricted to self-selected clinicians willing to answer the questionnaire twice. The background of raters was not perfectly balanced. A preponderance of responders from an interventional neuroradiology background might explain the frequency of endovascular choices. However, such an imbalance has no impact on the interrater agreement within the same specialty, which remained poor for any specialty or background. Finally, completing an electronic survey and caring for real patients are very different activities. The degree to which responders imagined that they were dealing with serious clinical decisions can only be surmised.

CONCLUSIONS

Clinicians do not agree regarding the best management of patients with unruptured or ruptured MCA aneurysms. There is sufficient uncertainty to conduct a randomized trial comparing endovascular with surgical management of patients with MCA aneurysms.

Disclosure forms provided by the authors are available with the full text and PDF of this article at www.ajnr.org.

REFERENCES

1. Alreshidi M, Cote DJ, Dasenbrock HH, et al. **Coiling versus microsurgical clipping in the treatment of unruptured middle cerebral artery aneurysms: a meta-analysis.** *Neurosurgery* 2018;83:879–89 CrossRef Medline
2. Berro DH, L'Allinec V, Pasco-Papon A, et al. **Clip-first policy versus coil-first policy for the exclusion of middle cerebral artery aneurysms.** *J Neurosurgery* 2020;133:1124–1131 CrossRef Medline
3. Rodriguez-Hernandez A, Sughrue ME, Akhavan S, et al. **Current management of middle cerebral artery aneurysms: surgical results with a "clip first" policy.** *Neurosurgery* 2013;72:415–27 CrossRef Medline
4. Molyneux A, Kerr R, Stratton I, et al International Subarachnoid Aneurysm Trial (ISAT) Collaborative Group. **International Subarachnoid Aneurysm Trial (ISAT) of neurosurgical clipping versus endovascular coiling in 2143 patients with ruptured intracranial aneurysms: a randomised trial.** *Lancet* 2002;360:1267–74 CrossRef Medline
5. Molyneux AJ, Kerr RS, Yu LM, et al; International Subarachnoid Aneurysm Trial (ISAT) Collaborative Group. **International Subarachnoid Aneurysm Trial (ISAT) of neurosurgical clipping versus endovascular coiling in 2143 patients with ruptured intracranial aneurysms: a randomised comparison of effects on survival, dependency, seizures, rebleeding, subgroups, and aneurysm occlusion.** *Lancet* 2005;366:809–17 CrossRef Medline
6. McDougall CG, Spetzler RF, Zabramski JM, et al. **The Barrow Ruptured Aneurysm Trial.** *J Neurosurg* 2012;116:135–44 CrossRef Medline

7. Koivisto T, Vanninen R, Hurskainen H, et al. **Outcomes of early endovascular versus surgical treatment of ruptured cerebral aneurysms.** *Stroke* 2000;31:2369–77 CrossRef Medline
8. Raymond J, Molyneux AJ, Fox AJ, et al; TEAM Collaborative Group. **The TEAM trial: safety and efficacy of endovascular treatment of unruptured intracranial aneurysms in the prevention of aneurysmal hemorrhage—a randomized comparison with indefinite deferral of treatment in 2002 patients followed for 10 years.** *Trials* 2008;9:43 CrossRef Medline
9. Darsaut TE, Keough MB, Sagga A, et al. **Surgical or endovascular management of middle cerebral artery aneurysms: a randomized comparison.** *World Neurosurg* 2021;149:e521–34 CrossRef Medline
10. Rothwell PM. **Subgroup analysis in randomised controlled trials: importance, indications, and interpretation.** *Lancet* 2005;365:176–86 CrossRef
11. Piotin M, Blanc R, Spelle L, et al. **Stent-assisted coiling of intracranial aneurysms.** *Stroke* 2010;41:110–15 CrossRef Medline
12. Cagnazzo F, Mantilla D, Lefevre PH, et al. **Treatment of middle cerebral artery aneurysms with flow-diverter stents: a systematic review and meta-analysis.** *AJNR Am J Neuroradiol* 2017;38:2289–94 CrossRef Medline
13. Pierot L, Klisch J, Cognard C, et al. **Endovascular WEB flow disruption in middle cerebral artery aneurysms: preliminary feasibility, clinical, and anatomical results in a multicenter study.** *Neurosurgery* 2013;73:27–34; discussion 34–25 CrossRef Medline
14. Raymond J, Gentric JC, Darsaut TE, et al. **Flow diversion in the treatment of aneurysms: a randomized care trial and registry.** *J Neurosurg* 2017;127:454–62 CrossRef Medline
15. Chapot R, Mosimann PJ, Darsaut TE, et al. **Retreatments must be included in the evaluation of device performance.** *J Neurointerv Surg* 2021;13:e5 CrossRef Medline
16. Raymond J, Darsaut TE. **Stenting for intracranial aneurysms: how to paint oneself into the proverbial corner.** *AJNR Am J Neuroradiol* 2011;32:1711–13 CrossRef Medline
17. Darsaut TE, Keough MB, Boisseau W, et al. **Middle Cerebral Artery Aneurysm Trial (MCAAT): a randomized care trial comparing surgical and endovascular management of MCA aneurysm patients.** *World Neurosurg* 2022;160:e49–54 CrossRef Medline
18. Fahed R, Darsaut TE, Farzin B, et al. **Measuring clinical uncertainty as a preliminary step to randomized controlled trials.** *J Clin Epidemiol* 2019;112:96–98 CrossRef Medline
19. Fahed R, Darsaut TE, Farzin B, et al. **Measuring clinical uncertainty and equipoise by applying the agreement study methodology to patient management decisions.** *BMC Med Res Methodol* 2020;20:214 CrossRef Medline
20. Kottner J, Audigé L, Brorson S, et al. **Guidelines for Reporting Reliability and Agreement Studies (GRRAS) were proposed.** *J Clin Epidemiol* 2011;64:96–106 CrossRef Medline
21. Darsaut TE, Jack AS, Kerr RS, et al. **International Subarachnoid Aneurysm Trial –ISAT, Part II: study protocol for a randomized controlled trial.** *Trials* 2013;14:156 CrossRef Medline
22. Darsaut TE, Findlay JM, Raymond J; CURES Collaborative Group. **The design of the Canadian UnRuptured Endovascular versus Surgery (CURES) trial.** *Can J Neurol Sci* 2011;38:236–41 CrossRef Medline
23. Darsaut TE, Raymond J; STAT Collaborative Group. **The design of the STenting in Aneurysm Treatments (STAT) trial.** *J Neurointerv Surg* 2012;4:178–81 CrossRef Medline
24. Raymond J, Darsaut TE, Guilbert F, et al. **Flow diversion in aneurysms trial: the design of the FIAT study.** *Interv Neuroradiol* 2011;17:147–53 CrossRef Medline
25. Raymond J, Januel AC, Iancu D, et al. **The RISE trial: A Randomized Trial on Intra-Saccular Endobridge devices.** *Interv Neuroradiol* 2020;26:61–67 CrossRef Medline
26. Feinstein AR, Cicchetti DV. **High agreement but low kappa, I: the problems of two paradoxes.** *J Clin Epidemiol* 1990;43:543–49 CrossRef Medline
27. Landis JR, Koch GG. **The measurement of observer agreement for categorical data.** *Biometrics* 1977;33:159–74 CrossRef Medline
28. Macdonald RL. **Editorial: Clip or coil? Six years of follow-up in BRAT.** *J Neurosurg* 2015;123:605–07 CrossRef Medline
29. Raymond J, Darsaut TE, Altman DG. **Pragmatic trials can be designed as optimal medical care: principles and methods of care trials.** *J Clin Epidemiol* 2014;67:1150–56 CrossRef Medline
30. Raymond J, Fahed R, Darsaut TE. **Randomize the first patient.** *J Neuroradiol* 2017;44:291–94 CrossRef Medline

Testing an Adapted Auditory Verbal Learning Test Paradigm for fMRI to Lateralize Verbal Memory in Patients with Epilepsy

E. Conde-Blanco, J.C. Pariente, M. Carreño, T. Boget, S. Pascual-Díaz, M. Centeno, I. Manzanares, A. Donaire, L. Pintor, J. Rumià, P. Roldán, X. Setoain, and N. Bargalló

ABSTRACT

BACKGROUND AND PURPOSE: fMRI is a noninvasive tool for predicting postsurgical deficits in candidates with pharmacoresistant temporal lobe epilepsy. We aimed to test an adapted paradigm of the Rey Auditory Verbal Learning Test to evaluate differences in memory laterality indexes between patients and healthy controls and its association with neuropsychological scores.

MATERIALS AND METHODS: We performed a prospective study of 50 patients with temporal lobe epilepsy and 22 healthy controls. Participants underwent a block design language and memory fMRI. Laterality indexes and the hippocampal anterior-posterior index were calculated. Language and memory lateralization was organized into typical and atypical on the basis of laterality indexes. A neuropsychological assessment was performed with a median time from fMRI of 8 months and was compared with fMRI performance.

RESULTS: We studied 40 patients with left temporal lobe epilepsy and 10 with right temporal lobe epilepsy. Typical language occurred in 65.3% of patients and 90.9% of healthy controls ($P = .04$). The memory fMRI laterality index was obtained in all healthy controls and 92% of patients. The verbal memory laterality index was bilateral (24.3%) more frequently than the language laterality index (7.69%) in patients with left temporal lobe epilepsy. Atypical verbal memory was greater in patients with left temporal lobe epilepsy (56.8%) than in healthy controls (36.4%), and the proportion of bilateral laterality indexes (53.3%) was larger than right laterality indexes (46.7%). Atypical verbal memory might be associated with higher cognitive scores in patients. No relevant differences were seen in the hippocampal anterior-posterior index according to memory impairment.

CONCLUSIONS: The adapted Rey Auditory Verbal Learning Test paradigm fMRI might support verbal memory lateralization. Temporal lobe epilepsy laterality influences hippocampal memory laterality indexes. Left temporal lobe epilepsy has shown a higher proportion of atypical verbal memory compared with language, potentially to memory functional reorganization.

ABBREVIATIONS: AVLT = Rey Auditory Verbal Learning Test; APi = hippocampal anterior-posterior index; ATLR = anterior temporal lobe resection; HC = healthy controls; IQR = interquartile range; LI = laterality index; LMI = immediate Logical Memory; LMII = delayed Logical Memory; SISCOM = substraction of ictal and interictal SPECT coregistered to MR Imaging; VMI = immediate Visual Reproduction; VMII = delayed Visual Reproduction; TLE = temporal lobe epilepsy

Refractory mesial temporal lobe epilepsy (TLE) usually concurs with progressive cognitive impairment.[1-3] Material-specific memory dysfunction has been associated with left and right temporal lobe lesions. Verbal memory processes were hindered by left-sided lesions, whereas visuospatial memory deficits were related to right TLE.[4] Focal epilepsies arising in eloquent areas or in the vicinity of the dominant hemisphere have been associated with cerebral plasticity, such as reorganization of adjacent or even distant and contralateral cortical areas to maintain function.[5] Factors such as the age of seizure onset, seizure frequency, the presence of hippocampal sclerosis, the duration of the disease, and antiseizure medication may play a relevant role in cognitive function.[6,7] Lack of

Received March 6, 2022; accepted after revision July 1.

From the Departments of Neurology (E.C.-B., M. Carreño, M. Centeno, I.M., A.D.), Radiology (N.B.), Neuropsychology (T.B.), Psychiatry (L.P.), Neurosurgery (J.R., P.R.), and Nuclear Medicine (X.S.), Epilepsy Program, Hospital Clínic de Barcelona, Barcelona, Spain; Institut d'Investigacions Biomèdiques August Pi i Sunyer (E.C.-B., M. Carreño, M. Centeno, A.D., T.B., L.P., J.R., P.R., X.S., N.B.), Barcelona, Spain; Magnetic Resonance Imaging Core Facility (J.C.P., S.P.-D.), Institut d'Investigacions Biomèdiques August Pi i Sunyer, Barcelona, Spain; Biomedical Research Networking Center in Bioengineering, Biomaterials and Nanomedicine (A.D., X.S.), Barcelona, Spain; and EpiCARE: European Reference Network for Epilepsy (E.C.-B., M. Carreño, M. Centeno, A.D.), Dublin, Ireland.

This study was supported by project PI19/00348, financed by the Instituto de Salud Carlos III and the European Regional Development Fund. This research did not receive any specific grant from commercial or not-for-profit sectors. E.C.-B. was supported by the fellowship grant RH041910.

Please address correspondence to Nuria Bargalló, Carrer de Villarroel 170, Barcelona 08029, Spain; e-mail: bargalló@clinic.cat; @ECondeBlanco

Indicates open access to non-subscribers at www.ajnr.org

Indicates article with online supplemental data.

http://dx.doi.org/10.3174/ajnr.A7622

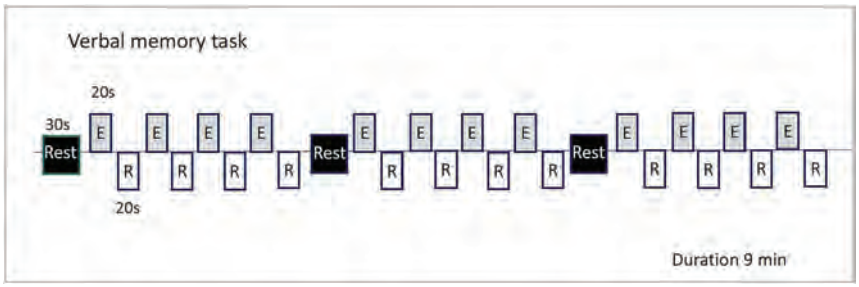

FIG 1. Verbal memory paradigm. E indicates encoding; R, retrieval; Min, minutes.

cognitive dysfunction in TLE may also occur, even when patients had similar clinical features to those who do have cognitive deficits.

The left hippocampus has often been associated with verbal memory encoding.[8] Its relationship to the seizure-onset zone has been regarded as a determinant factor in changes in verbal memory function.[9] From a network perspective, hippocampal sclerosis has been associated with a dysfunction of long-range network connections.[10] Neuropsychological testing has been the main diagnostic tool to evaluate memory function before anterior temporal lobe resection (ATLR); however, it is operator-dependent and does not provide information about the underlying functional anatomy.[11] fMRI has become a helpful tool to investigate cognitive processes and to predict memory deficits before ATLR.[12]

To date, memory fMRI studies have methodologic differences, particularly regarding the memory task itself, with complex paradigms difficult to apply on an everyday clinical basis for patients with epilepsy.[13] Cognition evaluation in patients with epilepsy is increasingly a multidisciplinary team effort.[14] However, neuropsychological tests cannot lateralize memory function before surgical intervention and do not provide information on functional anatomy. fMRI could be a useful noninvasive tool to identify the lateralization and localization of memory functions before surgical intervention in individual patients with TLE.[15-19] Prior studies have found that preoperative posterior fMRI activation in the ipsilateral hippocampus during memory encoding was associated with better memory outcome after ATLR.[20]

In this study, we examined the use of a simple and robust paradigm based on a well-established neuropsychological test on fMRI for verbal memory laterality outcome. We hypothesize that by using this list-learning paradigm we could obtain results in lateralization similar to those in the neuropsychological assessment, incorporating the functional anterior-posterior distribution of the hippocampal formation activity. Our main aim was to test this adapted paradigm for evaluating differences in memory hippocampal anterior-posterior indexes (APIs) and laterality indexes (LIs) between healthy controls (HC) and patients with right and left TLE and to search for associations and comparisons in performance with neuropsychological test scores.

MATERIALS AND METHODS

Design and Patients

This was a prospective study of consecutive patients with TLE who were evaluated for presurgical assessment at our multidisciplinary Patient Management Conference. Patients underwent language and memory fMRI based on clinical needs, particularly when there was reasonable doubt about language distribution. Participants were scanned between December 2018 and March 2020.

We included 50 patients with an age range between 18 and 65 years who underwent a presurgical evaluation for potential epilepsy surgery with a neuropsychological assessment. Participants were excluded from the study if diagnosed with neuropsychiatric disorders, were unable to tolerate the fMRI, or when artifacts invalidated the analysis. We also studied 23 HC with no history of neurologic or psychiatric disease using the same paradigm. One subject was excluded because of MR imaging artifacts.

The study was approved by the Ethics Committee of the Hospital Clinic of Barcelona. Informed consent was obtained from all participants in the study. Patients underwent a video-electroencephalography, structural MR imaging, and, additionally in some cases, FDG-PET scan and SISCOM, which established seizure onset location and lateralization. Neuropsychological assessment was obtained for all patients but only for 13 of the 22 HC due to the test being canceled during the pandemic restrictions.

MR Imaging

All scans were performed on a 3T Magnetom Tim Trio (Siemens) scanner or Prisma Fit scanner (Siemens), at the Magnetic Resonance Image Core Facility at August Pi i Sunyer Biomedical Research Institute located in the Diagnostic Imaging Center at Hospital Clinic of Barcelona using a 32- or 64-channel head coil. Each subject underwent a 3D structural high-resolution T1-weighted MPRAGE sequence with a 7.48-minute acquisition, which consisted of a set of 240 adjacent sagittal images with an isometric voxel size of 1 × 1 × 1 mm. A spoiled gradient-echo sequence (TR, 2.30 s; TE, 2.98 s; number of excitations, 1; flip angle, 9°; FOV, 256 × 256) was used to coregister with the fMRI activation maps.

fMRI images were acquired in the axial plane with an echo-planar sequence. For language lateralization, we used 3 different paradigms; and for verbal memory lateralization, a single paradigm: 1) language tasks: TR, 3.00 s; TE, 0.03 s; flip angle, 90°; pixel matrix, 3 × 3 mm; section thickness, 3 mm; 2) memory tasks: TR, 2.00 s; TE, 0.21 s; flip angle, 90°; pixel matrix, 3.8 × 3.8 mm; section thickness, 3 mm.

Paradigms. Before a scanning session, an explanation of the memory and language tasks was given to patients. Outside the scanner, for quality assurance, participants were asked about how well they comprehended and performed the commands of the undergone tasks. Paradigms were all block design and are displayed in Fig 1 and the Online Supplemental Data.

Verbal Memory Paradigm. We used an adapted version of the Rey Auditory Verbal Learning Test (AVLT)[21] that evaluates both

encoding and retrieval verbal memory with the aim of achieving a sensitive LI of hippocampal involvement. The control task consisted of the patient hearing a list of incomprehensible words (passive listening), followed by an understandable list of 15 words that the patient must memorize, and silent periods in which the patient must recall as many words from the list as possible. Stimuli were presented in 3 blocks, alternating 30 seconds of the control task (incomprehensible words), followed by 4 cycles consisting of 20 seconds of the encoding task (memorizing the list of words) and 20 seconds of retrieval (recalling the list of words) (Fig 1).

We used 3 different block design paradigms to lateralize language activation: a phonemic verbal fluency task, a semantic verbal fluency task, and an auditory comprehension task (Online Supplemental Data).

All images were processed and analyzed using Statistical Parametric Mapping (SPM12; http://www.fil.ion.ucl.ac.uk/spm/software/spm12) and the MAGIC fMRI toolbox,[23] an in-house application developed with MATLAB 2017b (MathWorks) (Online Supplemental Data).

LI for Language and Verbal Memory

Language or verbal memory lateralization was considered typical when the LI was left-lateralized and atypical when it was bilateral or right-lateralized. To determine language lateralization in the case of different results among the 3 language paradigms, we took lateralization from the 2 concordant paradigms.

Activation was classified as "left-sided" if the LI was >0.2, "right-sided" if it was <0.2, and bilateral when the LI ranged between 0.2 and -0.2 (Online Supplemental Data).

Anterior-Posterior Index of the Hippocampus

The APi frames the difference between voxel count in the anterior and posterior parts of the hippocampus. The anterior and posterior segmentation was defined by identifying the section on the Montreal Neurological Institute space where the last part of the uncal apex is appreciated.[21] Anterior activation was classified if the APi was >0.2; and posterior activation, if the APi was <0.2. Whole-hippocampal activation was established when the APi fell between 0.2 and -0.2.

Neuropsychological Assessment

Participants underwent a comprehensive neuropsychological assessment with a median time lapse from MR imaging of 8 months. Verbal memory was assessed with the AVLT using total learning and delayed recall to evaluate the patient's ability to encode, consolidate, and retrieve verbal information.[21] T scores for each test and for each subject were calculated on the basis of the normative control group's means and SDs. Participants with scores of $\leq$1.5 SD were classified as neurologically impaired.

Wechsler Adult Intelligence Scale-3rd Edition[22] and subsets from the Wechsler Memory Scale III such as the immediate Logical Memory (LMI), delayed Logical Memory (LMII), immediate (VMI) and delayed (VMII) Visual Reproduction, and executive functions[22] were used for the evaluation (Online Supplemental Data). Naming functions by the Boston Naming Test (BNT)[23] were also carried out.

Statistics

The statistical analysis was performed using STATA/IC 14.2 (StataCorp).

A descriptive analysis of the variables collected was performed. Qualitative variables were expressed as a percentage, and the quantitative variables, using standard deviation (SD) or median (interquartile range [IQR]) if they had a normal distribution.

Demographic data and volumetric findings are reported as number (percentage) or median and IQR. To check the impact of the TLE side in the LI, we evaluated it using the Kruskal-Wallis 1-way ANOVA test (χ^2 [2]) followed by post hoc analysis with Bonferroni correction (t), and we also used a multivariate ANOVA for influential variables. An analysis of the neuropsychological test scores and the verbal memory LI was performed using the χ^2 test or Fisher exact test. Quantitative variables were compared using the Student t test, the Mann Whitney U test, or the Kruskal-Wallis 1-way ANOVA test (χ^2 [2]) when appropriate.

A first-level analysis was performed by fitting a general linear model on a voxelwise basis to model the brain activation of each condition. Condition-specific effects were modeled by creating a boxcar function convolved with a canonical hemodynamic response function. Additionally, motion parameters were entered as regressors of no interest. A criterion for statistically significant activation was set at a threshold of $P < .001$, and a family-wise error cluster threshold of $P < .05$ was applied to correct for multiple comparisons (Online Supplemental Data).

RESULTS

Clinical and Neuropsychological Profiles

The Table shows clinical variables and the characteristics of the sample. Twenty-three patients had unilateral hippocampal sclerosis, of which 18 (78.3%) were on the left.

Intelligence quotients of patients ranged from above average to below average, with no significant differences between groups ($P = .92$). Of 50 patients, 19 (38%) showed low-average intelligent quotient; 18 (36%), an average intelligence quotient; 12 (24%), above-average intelligence quotient; and 1 (2%), below-average intelligence quotient. HC showed predominantly average scores in 6 (46.1%) participants with 5 (38.5%) having above-average and 2 (15.4%) low-average scores.

Logical memory, visual reproduction, verbal memory learning and recall, attention, and mental flexibility were significantly lower in patients with TLE compared with HC ($P < .05$) (Online Supplemental Data). Severely impaired verbal learning was more frequent in patients compared with HC (Pearson χ^2 [2] $= 10.7$; Fisher exact test, $P = .003$). Verbal memory encoding ($t = 3.58$, $P = .002$) and retrieval ($t = 2.73$, $P = .025$) were significantly worse in left TLE compared with HC but not significantly different from right TLE.

In verbal learning encoding, 29 (58%) patients scored -1 SD or below, and 21 (42%) patients between -1 SD and $+1$ SD. HC showed significantly higher verbal learning scores (median, 47; IQR 6.1) than patients with left TLE (median, 36.2; IQR, 17.3) ($t = 3.58$, $P = .002$), while patients with right TLE (median, 39.9; IQR, 12.0) showed no significant differences compared with HC ($t = 1.79$; $P = .218$). Delayed recall was also significantly lower in left TLE (median, 40.47; IQR, 17.32) than in HC (median, 52.86;

Participant characteristics

	All Patients ($n = 50$)	LTLE ($n = 40$)	RTLE ($n = 10$)	HC ($n = 22$)	*P* Value
Sex					
Female	32 (64%)	25 (62.5%)	7 (70%)	14 (63.6%)	>.05
Male	18 (36%)	15 (37.5%)	3 (30%)	8 (36.4%)	
Seizures					
FAS	7 (14%)	6 (15%)	1 (10%)	NA	
FIAS	45 (90%)	36 (90%)	9 (90%)	NA	
FBTCS	7 (14%)	5 (12.5%)	2 (20%)	NA	
FIAS frequency per mo (mean)	5.5 (SD, 6.1)	6 (SD, 6.5)	4 (SD, 3.4)	NA	
FBTCS frequency per mo (mean)	0.8 (SD, 2.0)	0.35 (SD, 0.95)	0.3 (SD, 1.0)	NA	
Age and duration (mean) (yr)					
Age at scan	37 (SD, 13)	37 (SD, 13)	35 (SD, 13)	34 (SD, 11)	>.05
Age at seizure onset	14 (SD, 10)	14 (SD, 10)	15 (SD, 6)	NA	
Epilepsy duration at scan	23 (SD, 15)	23 (SD, 16)	20 (SD, 12)	NA	
Pathology[a]					
HS	23 (46%)	18 (45%)	5 (50%)	NA	
Cavernoma	3 (6%)	2 (5%)	1 (10%)	NA	
DNT	1 (2%)	0 (0%)	1 (10%)	NA	
Focal cortical dysplasia	7 (14%)	7 (17.5%)	0 (0%)	NA	
Gliosis	2 (4%)	1 (2.5%)	1 (10%)	NA	
Other	6 (12%)	6 (15%)	0 (0%)	NA	
No abnormality	11 (22%)	8 (20%)	3 (30%)	NA	

Note:—FAS indicates focal aware seizures; FIAS, focal with impaired awareness seizures; FBTCS, focal to bilateral tonic-clonic seizures; DNT, dysembryoplastic neuroepithelial tumor; HS, hippocampal sclerosis; LTLE, left TLE; NA, not applicable; RTLE, right TLE. Significant ($P < .05$) difference compared with controls.
[a] Location of the lesions are detailed in supplementary material table S.

IQR, 14.64) ($t = 2.73$, $P = .025$), while no significant differences were found between HC and patients with right TLE ($t = 1.75$, $P = .235$).

fMRI Language Lateralization Profiles

Forty-nine patients showed activation during the language fMRI tasks. One patient did not show activation in any of the 3 paradigms.

The LI was achieved in >94% of patients and HC for the 3 verbal tasks (phonemic verbal fluency, 98% HC/95% patients). Atypical language occurred more frequently in patients (32 of 49 [65.3%]) than in HC (2/22 [9.1%]) ($P = .04$) (Fig 2*A*).

In both phonemic verbal fluency and semantic verbal fluency tasks, the LI was significantly different depending on handedness only for left TLE. Patients with left TLE who were left-handed had a significantly higher proportion of atypical language ($\chi^2 = 6.62$; Fisher exact test, $P = .002$), but no differences were seen in right TLE or HC regardless of handedness. For the auditory comprehension task this effect was not seen.

Compared with atypical activation, patients with left TLE with typical language showed significantly lower scores in LMI, LMII, VMI, VMII, verbal learning, and Boston Naming Test subtests of the neuropsychological assessment (Online Supplemental Data).

fMRI Verbal Memory Lateralization Profiles

For the verbal memory task, LI was seen in all (100%) HC and 46 of 50 (92.0%) patients. Three patients with left TLE and 1 patient with right TLE did not show hippocampal activation. Of the 4 patients who did not show activation, 3 were left-handed. According to language distribution, we found no hippocampal activation in 2 patients with typical and 2 patients with atypical language. The proportion of patients with each hippocampal activation distribution and handedness is described in the Online Supplemental Data.

Typical verbal memory was seen in a higher proportion of HC (14/22, 63.6%), compared with patients (21/46, 45.6%). Atypical verbal memory in left TLE (16/37, 56.8%) was greater compared with right TLE (4/9, 44.4%). In patients with atypical verbal memory, the right LI was more frequent than bilateral LI. However, the proportion of bilateral LI was twice as high in patients with left TLE than in those with right TLE (Fig 2*B* and Fig 3*A*).

fMRI Verbal Memory Lateralization Profile in Typical and Atypical Language. Of 21 HC with typical language, 13/20 (65.0%) demonstrated typical memory lateralization. The verbal memory LI was obtained in 30/32 (93.7%) patients with typical language. Typical verbal memory was seen in 12/30 (40%) of them (Fig 3*B*). In patients with left TLE, atypical memory was more frequent (15/25; 60.0%). In patients with left TLE with atypical memory, the proportion of bilateral LIs (8/15, 53.3%) was higher than right LIs (7/15, 46.7%).

Only 2 HC showed atypical language. One of them had typical verbal memory, and the other showed atypical verbal memory (right LI). The verbal memory LI was obtained in 15/17 (88.2%) patients with atypical language. Typical verbal memory was seen in 8/15 (53.3%) of them. In patients with left TLE, 11/15 (73.3%), atypical memory was more frequent (6/11, 54.5%). In left TLE with atypical memory, the proportion of right LI (5/11, 45.5%) was higher than bilateral LI (1/11, 9%).

APi Distribution. The APi was obtained in 19/22 (86.0%) HC and in 46/50 (92.0%) patients. Accounting for both hippocampi, the APi was seen in 20/22 (90.9%) HC and 43/46 (93.5%) patients. Both hippocampi showed activation in 35/40 (87.5%) patients with left TLE and in 8/10 (80%) with right TLE.

The distribution of the APi in both hippocampi according to HC or patients with left TLE and right TLE is shown in Fig 2*B*.

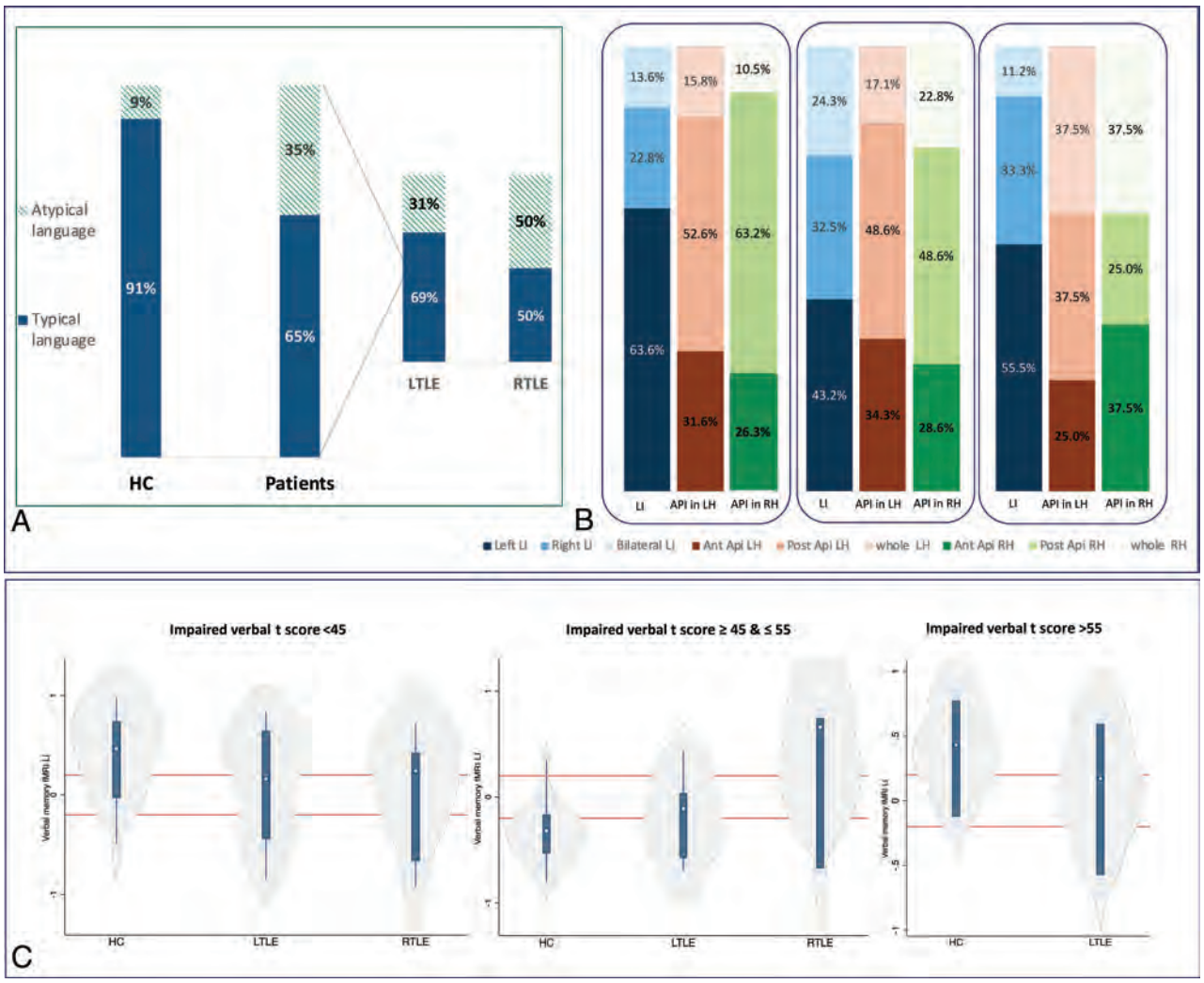

FIG 2. *A*, LI . *B*, APi. *C*, Verbal memory LI according to verbal learning impairment of patients and HC.

In the left hippocampus, the posterior APi was the most frequent pattern both in HC and those with left TLE, while posterior and whole activation was most frequently seen in those with right TLE with an equal proportion. In the right hippocampus, anterior activation was most frequently observed in those with right TLE compared with HC and those with left TLE (Fig 2*B*).

We evaluated potential associations of the anterior-posterior distribution and handedness, age at seizure onset, duration of epilepsy, and learning or delayed verbal recall, but no significant association was found ($P > .05$). We found a significant association between age and the APi, the older the patient the more anterior activation ($\beta = 0.014$, $P = .03$). The APi was significantly different in the left and right hippocampi of patients with severely impaired verbal learning, but not different in patients with moderate and slight impairment.

Association of Language and Verbal Memory fMRI with Neuropsychological Performance

Patients with atypical language scored −0.5 SD or below their age-matched peers in 12 (70.6%) cases, between −0.5 and +0.5 SDs in 4 (23.5%) cases, and +0.5 SD or above in 1 (5.9%) case.

The Online Supplemental Data show neuropsychological tests scores related to typical and atypical verbal memory according to HC and patients with left and right TLE. Immediate and delayed logical memory, visual reproduction, and naming scores (BNT) were significantly lower in patients with left TLE with typical verbal memory compared with HC. LMII and VMI were also significantly lower in patients with right TLE with typical verbal memory compared with HC. Patients with left TLE with atypical verbal memory showed a tendency toward higher scores in every subtest of the Wechsler Memory Scale, but significance was not achieved.

HC and patients with left TLE with a bilateral verbal memory LI showed a nonsignificant tendency toward higher scores in verbal memory encoding and retrieval compared with those participants who had more unilateral lateralization.

Patients with left TLE showed a nonsignificant tendency toward bilateral memory independent of verbal memory impairment (Fig 2*C*). No significant differences were seen in APis in memory impairment (Online Supplemental Data).

The proportion of patients with right-handedness was significantly lower in those with atypical language ($\chi = 11.40$; Fisher exact test, $P = .001$), but it was not significantly different in

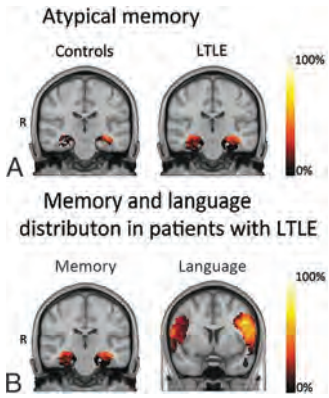

FIG 3. *A*, Atypical verbal memory was greater in patients with left TLE (56.8%) than in HC (36.4%). *B*, The verbal memory LI was bilateral (24.3%) more frequently than the language LI (7.7%) in patients with left TLE. The scale on the right indicates the percentage of the overlapping activation of the group (first-level analysis, $P = .01$), in which 100% represents a zone activated in the whole group. For visual purposes, the zones with activation in <5% of the group were considered noise and excluded. Warmer colors indicate higher overlapping, and darker colors, lesser overlapping. R indicates right.

patients with atypical memory ($\chi = 0.61$; Fisher exact test, $P = .568$).

DISCUSSION

ATLR is the most established treatment for drug-refractory TLE.[24] A surgical approach in refractory TLE has been associated with a 5-year increase in life expectancy.[25] Prediction of cognitive decline after ATLR is essential to counsel patients regarding potential memory loss. To our knowledge, there is not a highly sensitive verbal learning paradigm standardized to use during memory fMRI. This prospective study focused on testing a verbal memory paradigm based on an established memory test to evaluate differences in memory LI and its association with neuropsychological impairment and language. The AVLT-adapted paradigm was able to elicit hippocampal activation in 100% of HC and 92% of patients. Our results suggest a distinctive redistribution of verbal memory and language systems in left TLE.

Verbal Memory Paradigm in Epilepsy

American and European task forces from the American College of Radiology and European Society of Neuroradiology have worked diligently to standardize the use of language fMRI in clinical practice.[26] However, the nature of memory is complex, and activation depends on the task, paradigm design, data acquisition, and analysis. Tasks have varied across memory fMRI studies, leading to unsuccessful result replication. Thus, a prominent center such as UCL-Queen Square has used a task that involves making a judgment on whether each presented stimuli is pleasant, with an event-related analysis. We found that an AVLT-adapted paradigm based on word encoding or a recall task and analyzed with a blocked analysis elicited hippocampal activation. Event-related analysis was associated with a more reliable activation of anterior hippocampal activity.[27] However, this approach is less powerful at detecting activation, more vulnerable to hemodynamic response function, time-consuming, and more demanding for patients and staff in a clinical setting.

Language and Verbal Memory Lateralization and Clinical Repercussions

Dominant TLE has been associated with extensive effects on the language systems. Patients have been associated with higher atypical language representation.[28,29] In our study, atypical language occurred significantly more often in patients than in HC, similar to results in previous work (34.7% versus 9%).[5] In left TLE, language was more lateralized than verbal memory, which was more bilateral. Patients with atypical language and slight verbal memory impairment showed a more frequent right verbal memory LI compared with a more bilateral LI in moderately and severely impaired patients. Memory and language systems seem to differ in their functional redistribution when affected by the epileptogenic network in TLE.[30] Our findings agreed with the hypothesis that temporal pathology might first affect close areas, leading to more dysfunction during tasks specifically relying on them.[31] Also, patients with TLE were associated with reduced flexibility and increased intra- and interregional communication involved in the cognitive task.[32] These findings might suggest functional regulation to other regions capable of better meeting the current cognitive goal. Prior reports described a tendency of a left-to-right shift of language activation in left-hemisphere pathology.[33,34] Atypical dominance in adults with left-hemispheric lesions was associated with both poorer[35] and better cognitive abilities.[29,36] We found that patients with left TLE and better memory scores showed a more atypical activation in comparison with those with right TLE and HC. Also, verbal learning and delayed recall were significantly lower in left TLE compared with right TLE and HC. Hand dominance did not significantly influence the memory LI compared to the language LI with the semantic and phonemic fluency tasks.

APi

A posterior hippocampal remnant might support postoperative memory in patients with TLE[37] We found that half of the patients with left TLE showed predominant posterior hippocampal activation in both the left and right hippocampi. Prior work described distinct connections of hippocampal functionally. The anterior hippocampus is connected to the entorhinal cortex, temporal pole, and orbitofrontal cortex and is associated with verbal memory. The posterior hippocampus is linked to memory retrieval and polysynaptic-pathway propagation.[38-41] The posterior remnant of the ipsilateral hippocampus, rather than the functional reserve of the contralateral hippocampus, was designated as the relevant structure for maintaining verbal memory function after ATLR.[23,35,41] In addition, it was postulated that patients with left TLE with retained verbal memory function had an adaptive functional reorganization mediated by the right temporal lobe to keep higher memory scores.[6,27,37,41] In our sample, patients with left TLE showed a higher proportion of whole activation in the right hippocampus compared with HC, which could be related to complex functional network plasticity with increased intrahemispheric connectivity that extends to the contralateral hippocampus. Additionally, patients with right TLE also showed a high proportion of whole

activation and a higher proportion of posterior activation in the left compared with the right hippocampus. We found a tendency toward higher verbal learning scores in patients with a more posterior activation, which favors this hypothesis.

Neurophysiologic connectivity studies during a cognitive task found significant reductions of high-frequency oscillations rates in epileptic hippocampi.[42] We hypothesize that a complete verbal memory transfer to the contralateral hippocampus might be associated with less severe memory impairment. This hypothesis could explain why some patients with TLE have memory impairment, while others do not. Complete transfer might increase the chance of preserving memory function after epilepsy surgery.

Limitations

Memory fMRI in the temporal lobe is prone to geometric distortions and blood oxygen level–dependent signal drop-out related to susceptibility of the echo-planar imaging sequence and to the field strength of the magnet, fMRI pulse sequence, and the level of cooperation and education of the participants.[43] We used a block design approach to maximize signal changes. One limitation is the small number of patients with right TLE and that half of them were left-handed because scanning was based on clinical uncertainty of language distribution, which might bias results. Also, the acquisition time is relatively long for patients with cognitive decline and might cause fatigue that could influence performance. Additionally, all neuropsychological test scores were collected for patients but were available for a proportion of healthy controls. Other factors such as the amount of interictal activity on the day of testing or antiseizure medication might also have had an impact. This is a single-center study, moderate in size, and it only addresses patients with TLE. Larger databases of patients with epilepsy with temporal and extratemporal epilepsy with various pathologies would provide with a deeper knowledge.

CONCLUSIONS

The AVLT-adapted paradigm was able to elicit hippocampal activation. The laterality of a dysfunctional hippocampus in TLE induces specific processes of functional reorganization that affect verbal memory and language systems differently. Left TLE shows a higher proportion of bilateral LI in verbal memory compared with language, potentially secondary to reorganization in memory function, which happens more frequently than language function. That may lead to a discrepancy between language and memory laterality, which could potentially be relevant for predicting memory function after surgery. Right and especially bilateral memory activation patterns are much more frequent in patients with left TLE compared with HC and are generally associated with better memory function. Future studies will clarify whether this paradigm could be used to predict memory function after surgery.

ACKNOWLEDGMENTS

The authors would also like to thank the patients and their caregivers for their contribution.

Disclosure forms provided by the authors are available with the full text and PDF of this article at www.ajnr.org.

REFERENCES

1. Golby AJ, Poldrack RA, Brewer JB, et al. **Material-specific lateralization in the medial temporal lobe and prefrontal cortex during memory encoding.** *Brain* 2001;124:1841–54 CrossRef Medline
2. Helmstaedter C. **Neuropsychological aspects of epilepsy surgery.** *Epilepsy Behav* 2004;5:(Suppl 1)45–55 CrossRef Medline
3. Elger CE, Helmstaedter C, Kurthen M. **Chronic epilepsy and cognition.** *Lancet Neurol* 2004;3:663–72 CrossRef Medline
4. Milner B. **Disorders of learning and memory after temporal lobe lesions in man.** *Clin Neurosurg* 1972;19:421–46 CrossRef Medline
5. Janszky J, Jokeit H, Heinemann D, et al. **Epileptic activity influences the speech organization in medial temporal lobe epilepsy.** *Brain* 2003;126:2043–51 CrossRef Medline
6. Richardson MP, Strange BA, Duncan JS, et al. **Preserved verbal memory function in left medial temporal pathology involves reorganisation of function to right medial temporal lobe.** *Neuroimage* 2003;20(Suppl 1):S112–19 CrossRef Medline
7. Saling MM. **Verbal memory in mesial temporal lobe epilepsy: beyond material specificity.** *Brain* 2009;132:570–82 CrossRef Medline
8. Baxendale S, Thompson PJ, Sander JW. **Neuropsychological outcomes in epilepsy surgery patients with unilateral hippocampal sclerosis and good preoperative memory function.** *Epilepsia* 2013;54: e131–34 CrossRef Medline
9. Chelune GJ. **Hippocampal adequacy versus functional reserve: Predicting memory functions following temporal lobectomy.** *Arch Clin Neuropsychol* 1995;10:413–32 CrossRef Medline
10. Vaughan DN, Rayner G, Tailby C, et al. **MRI-negative temporal lobe epilepsy.** *Neurology* 2016;87:1934–42 CrossRef Medline
11. Vogt VL, Äikiä M, del Barrio A, et al; E-PILEPSY consortium. **Current standards of neuropsychological assessment in epilepsy surgery centers across Europe.** *Epilepsia* 2017;58:343–55 CrossRef Medline
12. Helmstaedter C, Elger CE. **Cognitive consequences of two-thirds anterior temporal lobectomy on verbal memory in 144 patients: a three-month follow-up study.** *Epilepsia* 1996;37:171–80 CrossRef Medline
13. Buck S, Sidhu MK. **A guide to designing a memory fMRI paradigm for pre-surgical evaluation in temporal lobe epilepsy.** *Front Neurol* 2019;10:1354 CrossRef Medline
14. Wilson SJ, Baxendale S, Barr W, et al. **Indications and expectations for neuropsychological assessment in routine epilepsy care: report of the ILAE Neuropsychology Task Force, Diagnostic Methods Commission, 2013-2017.** *Epilepsia* 2015;56:674–81 CrossRef Medline
15. Thornton R, Powell R, Lemieux L. fMRI in epilepsy. In: Filippi M, ed. *fMRI Techniques and Protocols. Neuromethods*, Humana Press; 2009:41:681–745 CrossRef
16. Limotai C, Mirsattari SM. **Role of functional MRI in presurgical evaluation of memory function in temporal lobe epilepsy.** *Epilepsy Res Treat* 2012;2012:687219 CrossRef Medline
17. Rabin ML, Narayan VM, Kimberg DY, et al. **Functional MRI predicts post-surgical memory following temporal lobectomy.** *Brain* 2004;127:2286–98 CrossRef Medline
18. Jokeit H, Okujava M, Woermann FG. **Memory fMRI lateralizes temporal lobe epilepsy.** *Neurology* 2001;57:1786–93 CrossRef Medline
19. Sidhu MK, Stretton J, Winston GP, et al. **Memory fMRI predicts verbal memory decline after anterior temporal lobe resection.** *Neurology* 2015;84:1512–19 CrossRef Medline
20. Bonelli SB, Powell RH, Yogarajah M, et al. **Imaging memory in temporal lobe epilepsy: predicting the effects of temporal lobe resection.** *Brain* 2010;133:1186– 99 CrossRef Medline
21. Rey A. *L'examen clinique en psychologie*. Paris: Presses universitaires de France; 1964
22. David ST, Nancy DC, Barton W, et al. **The Wechsler Memory Scale, Third Edition.** In: David S, ed. *Clinical Interpretation of the WAIS-III and WMS-III*. Academic Press, San Diego 2003;93–139
23. LaBarge E, Edwards D, Knesevich JW. **Performance of normal elderly Boston Naming Test.** *Brain Lang* 1986;27:380–84 CrossRef Medline

24. Wiebe S, Blume WT, Girvin JP, et al. **A randomized, controlled trial of surgery for temporal-lobe epilepsy.** *N Engl J Med* 2001;345:311–18 CrossRef Medline
25. Choi H, Sell RL, Lenert L, et al. **Epilepsy surgery for pharmacoresistant temporal lobe epilepsy: a decision analysis.** *JAMA* 2008;300:2497–2505 CrossRef Medline
26. Bargalló N, Cano-López I, Rosazza C, et al. **Clinical practice of language fMRI in epilepsy centers: a European survey and conclusions by the ESNR Epilepsy Working Group.** *Neuroradiology* 2020;62:549–62 CrossRef Medline
27. Powell HW, Richardson MP, Symms MR, et al. **Reorganization of verbal and nonverbal memory in temporal lobe epilepsy due to unilateral hippocampal sclerosis.** *Epilepsia* 2007;48:1512–25 CrossRef Medline
28. Janszky J, Mertens M, Janszky I, et al. **Left-sided interictal epileptic activity induces shift of language lateralization in temporal lobe epilepsy: an fMRI study.** *Epilepsia* 2006;47:921–27 CrossRef Medline
29. Berl MM, Balsamo LM, Xu B, et al. **Seizure focus affects regional language networks assessed by fMRI.** *Neurology* 2005;65:1604–11 CrossRef Medline
30. Roger E, Pichat C, Torlay L, et al. **Hubs disruption in mesial temporal lobe epilepsy: a resting-state fMRI study on a language-and-memory network.** *Hum Brain Mapp* 2020;41:779–96 CrossRef Medline
31. He X, Bassett DS, Chaitanya G, et al. **Disrupted dynamic network reconfiguration of the language system in temporal lobe epilepsy.** *Brain* 2018;141:1375– 89 CrossRef Medline
32. Caciagli L, Paquola C, He X, et al. **Disorganization of language and working memory systems in frontal versus temporal lobe epilepsy.** *Brain* 2022;awac150 CrossRef Medline
33. Helmstaedter C, Fritz NE, González Pérez PA, et al. **Shift-back of right into left hemisphere language dominance after control of epileptic seizures: evidence for epilepsy driven functional cerebral organization.** *Epilepsy Res* 2006;70:257–62 CrossRef Medline
34. Helmstaedter C, Kurthen M, Gleissner U, et al. **Natural atypical language dominance and language shifts from the right to the left hemisphere in right hemisphere pathology.** *Naturwissenschaften* 1997;84:250–52 CrossRef Medline
35. Sone D, Ahmad M, Thompson PJ, et al. **Optimal surgical extent for memory and seizure outcome in temporal lobe epilepsy.** *Ann Neurol* 2022;91:131–44 CrossRef Medline
36. Cano-López I, Calvo A, Boget T, et al. **Typical asymmetry in the hemispheric activation during an fMRI verbal comprehension paradigm is related to better performance in verbal and non-verbal tasks in patients with epilepsy.** *Neuroimage Clin* 2018;20:742–52 CrossRef Medline
37. Bonelli SB, Thompson PJ, Yogarajah M, et al. **Memory reorganization following anterior temporal lobe resection: a longitudinal functional MRI study.** *Brain* 2013;136:1889–1900 CrossRef Medline
38. Li H, Ji C, Zhu L, et al. **Reorganization of anterior and posterior hippocampal networks associated with memory performance in mesial temporal lobe epilepsy.** *Clin Neurophysiol* 2017;128:830–38 CrossRef Medline
39. Fanselow MS, Dong HW. **Are the dorsal and ventral hippocampus functionally distinct structures?** *Neuron* 2010;65:7–19 CrossRef Medline
40. Langnes E, Sneve MH, Sederevicius D, et al. **Anterior and posterior hippocampus macro- and microstructure across the lifespan in relation to memory: a longitudinal study.** *Hippocampus* 2020;30:678–92 CrossRef Medline
41. Postma TS, Cury C, Baxendale S, et al. **Hippocampal shape is associated with memory deficits in temporal lobe epilepsy.** *Ann Neurol* 2020;88:170–82 CrossRef Medline
42. Pail M, Cimbálník J, Roman R, et al. **High frequency oscillations in epileptic and non-epileptic human hippocampus during a cognitive task.** *Sci Rep* 2020;10:1–12 CrossRef Medline
43. Lipschutz B, Friston KJ, Ashburner J, et al. **Assessing study-specific regional variations in fMRI signal.** *NeuroImage* 2001;13:392–38 CrossRef Medline

Adaptive Language Mapping Paradigms for Presurgical Language Mapping

E. Diachek, V.L. Morgan, and S.M. Wilson

ABSTRACT

BACKGROUND AND PURPOSE: Functional MR imaging is widely used for preoperative language assessment in candidates for resective neurosurgery. Language mapping paradigms that are adaptive to participant performance have the potential to engage the language network more robustly and consistently, resulting in more accurate functional maps. The aim of the current study was to compare two adaptive paradigms with the recommended language mapping paradigms that constitute the current standard of care.

MATERIALS AND METHODS: Seventy-three patients undergoing fMRI for language lateralization and/or localization completed an adaptive semantic matching paradigm, an adaptive phonological judgment paradigm, and two standard paradigms: sentence completion and word generation. The paradigms were compared in terms of the degree to which they yielded lateralized language maps and the extent of activation in frontal, temporal, and parietal language regions.

RESULTS: The adaptive semantic paradigm resulted in the most strongly lateralized activation maps, the greatest extent of frontal and temporal activations, and the greatest proportion of overall satisfactory language maps. The adaptive phonological paradigm identified anterior inferior parietal phonological encoding regions in most patients, unlike any of the other paradigms.

CONCLUSIONS: The adaptive language mapping paradigms investigated have several psychometric advantages compared with currently recommended paradigms. Adoption of these paradigms could increase the likelihood of obtaining satisfactory language maps in each individual patient.

ABBREVIATION: LI = lateralization index

fMRI is widely used for presurgical language mapping in patients who are candidates for resective surgery for epilepsy, brain tumors, and vascular malformations.[1-3] One goal of presurgical language mapping is to determine language lateralization, and fMRI compares favorably with the invasive Wada test for this purpose.[4-7] A second goal is to identify indispensable language regions to aid in tailoring surgical margins; fMRI is also widely used for this purpose,[3] though its validity has not been established.[8] Many different paradigms are used for language mapping (eg, sentence completion, word generation, and so forth), and numerous studies have compared the validity and reliability of various sets of paradigms.[1,9-13] In 2017, a task force of American Society of Functional Neuroradiology members reviewed this literature and recommended sentence completion and word generation as the first two tasks that should be performed in adult patients.[2] However, this recommendation was based primarily on practical considerations, including widespread existing use, rather than a detailed assessment of the psychometric properties of different paradigms that have been proposed.

Recently, we have described a pair of semantic and phonological language mapping paradigms that are adaptive to patient performance; that is, the difficulty of the tasks is dynamically modulated on the basis of the patient's responses.[13-15] The motivation for developing these adaptive paradigms was to perform language mapping in individuals with aphasia, whose language deficits may preclude performance of many tasks used in clinical practice. We found that the adaptive tasks could be performed successfully by most individuals with aphasia and had superior psychometric properties compared with several other tasks in individuals with aphasia and

Received February 1, 2022; accepted after revision July 12.

From the Departments of Psychology and Human Development (E.D., S.M.W.) and Biomedical Engineering (V.L.M.), Vanderbilt University, Nashville, Tennessee; and Departments of Radiology and Radiological Sciences (V.L.M., S.M.W.), Neurological Surgery (V.L.M.), and Hearing and Speech Sciences (S.M.W.), Vanderbilt University Medical Center, Nashville, Tennessee.

This work was supported by the National Institute on Deafness and Other Communication Disorders, R01 DC013270; and the National Institute of Neurological Disorders and Stroke, R01 NS110130, R01 NS108445.

Please address correspondence to Stephen M. Wilson, MD, Department of Hearing and Speech Sciences, Vanderbilt University Medical Center, 1215 21st Ave S, MCE 8310, Nashville, TN 37232; e-mail: stephen.m.wilson@vanderbilt.edu

Indicates open access to non-subscribers at www.ajnr.org

Indicates article with online supplemental data.

http://dx.doi.org/10.3174/ajnr.A7629

Table 1: Characteristics of the 73 participants

Age (mean) (range) (yr)	38.6 (SD, 12.6) (20–70)
Sex	32 Male; 41 female
Handedness[a]	57 Right-handed; 6 left-handed; 10 mixed (of whom 6 write with right and 4 write with left); mean laterality quotient: 68.8 (SD, 59.4)
Education (mean) (range) (yr)	13.7 (SD, 2.5) (range, 8–19)
Race	58 White; 10 black; 1 Asian; 4 did not state
Native speaker	71 Native; 2 fluent but non-native
Etiology	Epilepsy 55
	Tumor 16
	Arteriovenous malformation 1
	Cavernous malformation 1
Duration of etiology (mean) (range)	3170 (SD, 3722) days (range, 6 days to 39 yr)
Language deficit	42 (58%) Yes; 31 (42%) no

[a] Handedness was assessed with the 4-item modification of the Edinburgh Handedness Inventory by Veale.[29]

neurologically healthy controls.[13-15] The adaptive nature of the tasks entails that they remain challenging yet feasible at all times, thus tightly constraining participants' cognitive states, resulting in robust recruitment of the language network and good test-retest reproducibility.

The aim of the present study was to investigate the utility of these adaptive semantic and phonological language mapping paradigms for presurgical language mapping. Most candidates for resective surgery have no language deficits or mild language deficits, but occasionally, patients present with moderate or even severe aphasia. The ability of the adaptive paradigms to reliably identify language areas in patients with and without language deficits suggests that they have strong potential to be appropriate for this population. We administered both paradigms, along with the currently recommended sentence completion and word generation paradigms, to map language regions in patients with epilepsy, brain tumors, or vascular malformations who were referred for presurgical language mapping. We operationalized success as the ability of each paradigm to yield lateralized language maps that included activation of known frontal, temporal, and anterior parietal language regions.

MATERIALS AND METHODS

Patients

All patients referred for presurgical language mapping at Vanderbilt University Medical Center between September 2019 and December 2021 were considered for inclusion. During this time period (and continuing), it was our practice to perform all 4 language mapping paradigms whenever possible for clinical purposes.

A total of 73 patients provided written informed consent to participate in the study. Demographic information is provided in Table 1. Patients were diagnosed with epilepsy ($n = 55$), tumor ($n = 16$), AVM ($n = 1$), or a cavernous malformation ($n = 1$). Forty-two of 73 patients (58%) reported some degree of language impairment. Language deficits were mild in most cases. The sample was consecutive for the first half of the study period and constituted approximately every second patient during the second half of the study period, with inclusion determined by scheduling and not by any patient factor. No patients declined consent. A minority of patients were not asked to consent because language mapping was expected to be based on <4 paradigms due to time constraints; this was most often the case when extensive motor mapping was required as well.

The study was approved by the institutional review board at Vanderbilt University Medical Center.

Language Mapping Paradigms

Each of the 4 paradigms involved a simple 2-condition block design with 6 blocks per condition and 20 seconds per block, for a total scan time of exactly 4 minutes.

The adaptive semantic paradigm has been described in detail previously,[13] but in brief, there were 2 conditions: a semantic matching task and a perceptual matching task. In the semantic matching condition, participants saw 2 words in the middle of the screen, one above the other, and were instructed to press a button if the words were semantically related (eg, boy-girl) and to do nothing if the words were unrelated (eg, walnut-bicycle). In the perceptual matching condition, participants saw 2 strings of symbols in the middle of the screen, one above the other, and were instructed to press a button if the 2 strings were identical (eg, [ΔΘδЂЊ-ΔΘδЂЊ]) and to do nothing if they were different (eg, [ΔΘδЂЊ-ЊΔЊѓΔ]). Each condition had 7 levels of difficulty, and participants progressed to the next level every time they made 2 consecutive correct responses and stepped back 2 levels every time they made an error. Difficulty was modulated in the semantic condition by manipulating word frequency, concreteness, length, age of acquisition, degree of semantic relatedness, and presentation rate and, in the perceptual condition, by manipulating the degree of similarity of mismatching items and presentation rate.

The adaptive phonological paradigm has also been described previously.[15] The language condition was a rhyme judgment task in which participants saw 2 pseudowords in the middle of the screen, one above the other, and were instructed to press a button if the pseudowords rhymed (eg, mulky-tulkie) and to do nothing if they did not (eg, shofy-sheffy). Difficulty was modulated by manipulating pseudoword length, orthographic transparency, stress pattern, and presentation rate. The perceptual control condition was the same as for the semantic paradigm.

Both adaptive paradigms were implemented in Matlab (MathWorks) using Psychtoolbox[16,17] and are freely available online at https://langneurosci.org/alm.

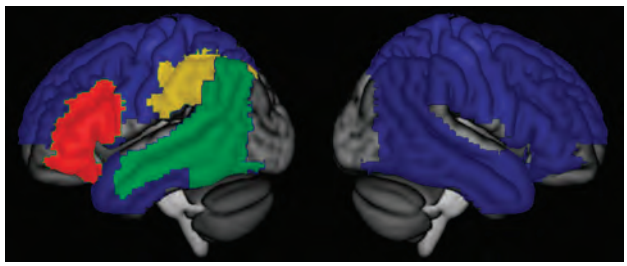

FIG 1. ROIs. LIs were calculated on the basis of activation throughout the wide region shown in blue (or any of the other colors), while sensitivity was determined on the basis of activations in frontal (red), temporal (green), and anterior parietal (yellow) language regions.

The sentence completion paradigm was implemented as recommended by the American Society of Functional Neuroradiology,[2] and the stimuli were downloaded from their Web site (https://www.asfnr.org/paradigms). In the language condition, participants saw 4 sentences per block (5 seconds each) with a blank space instead of the final word and were instructed to silently think of one or more words that could fit into the blank. In the control condition, participants saw scrambled letters matching the sentences in the number of characters and placement of spaces and were instructed to do nothing.

The word generation paradigm was also presented as recommended,[2] with the stimuli provided. In the language condition, participants saw a letter in the middle of the screen (2 per block, 10 seconds each) and were instructed to think of as many words as possible that start with that letter. In the control condition, participants saw symbols in the middle of the screen and were instructed to do nothing.

Before scanning, patients were trained on all 4 paradigms by 1 of the 3 authors. Training items were not repeated in the scanning session. For the adaptive paradigms, each trial type was demonstrated and discussed; then patients practiced a few blocks with actual task timing and adaptive features.[13,15] The sentence completion and word generation paradigms were practiced out loud to ensure task compliance; then the patient was instructed to perform the tasks silently in the scanner. In the scanner, the order of the 4 paradigms was counterbalanced across participants, to ensure that results were not confounded by presentation order. We cycled through 4 presentation orders so that each of the 4 paradigms was equally likely to be performed first, second, third, or fourth.

Neuroimaging

MR imaging data were acquired on a Philips Achieva 3T scanner (n = 57) or a Philips Ingenia Elition 3T scanner (n = 16) (Philips Healthcare) with 32-channel head coils at Vanderbilt University Medical Center. All paradigms were controlled by a laptop computer (Thinkpad T490s; Lenovo) running Matlab (Mathworks) Version R2019a and Psychtoolbox Version 3.0.16.[16,17] Visual stimuli were presented using a projector and a screen in front of the bore (n = 57) or on a monitor positioned behind the bore (n = 16), either of which patients viewed through a mirror mounted on the head coil. In the adaptive paradigms, patients responded on an MR imaging–compatible button box connected to the laptop.

For each of the 4 language mapping paradigms, sequences of T2*-weighted blood oxygen level–dependent echo-planar images were collected with the following parameters: 120 volumes + 5 initial volumes discarded; 35 or 36 axial slices in interleaved order; slice thickness = 3.5 mm with a 0.5-mm gap; FOV = 240 × 240 mm; matrix = 64 × 64; TR = 2000 ms; TE = 35 ms; flip angle = 78°; sensitivity-encoding factor = 2; voxel size = 3.75 × 3.75 × 4 mm.

For anatomic reference, T1-weighted (voxel size = 1 × 1 × 1 mm) and FLAIR images that were coplanar with the functional images (voxel size = 0.5 × 0.5 × 4 mm) were also acquired.

The imaging data were processed using standard methods as described previously.[13,15] The functional data were first preprocessed with AFNI: Slice timing and head motion were corrected, then the data were detrended and smoothed with a 6-mm full width at half maximum Gaussian kernel. Next, independent-component analysis was performed using the FSL tool MELODIC. Noise components were manually identified and removed using fsl_regfilt. All paradigms were modeled with boxcar functions convolved with a hemodynamic response function and fit to the data with the FMRISTAT program fmrilm. The 6 head-motion parameters were included as covariates, as were time-series from white matter and CSF regions to account for nonspecific global fluctuations and 3 cubic spline temporal trends. The T1-weighted anatomic images were warped to Montreal Neurological Institute space using unified segmentation in SPM12. Functional images were coregistered with structural images via coplanar FLAIR images using SPM and warped to Montreal Neurological Institute space. Individual activation maps were thresholded with a 5% relative threshold[18] and a minimum cluster extent of 2 cm^3, as described previously.[13,15]

To compare the paradigms in terms of their ability to reveal hemispheric dominance, we calculated lateralization indices (LIs) in an extensive bilateral ROI (Fig 1) comprising the inferior, middle, and superior frontal gyri, supplementary motor area, precentral and postcentral gyri, all of the lateral parietal lobe, and all of the temporal lobe (lateral and medial) except for the dorsal (auditory) part of the superior temporal gyrus. This same a priori ROI has been used previously.[13]

Frontal, temporal, and anterior parietal language ROIs were defined to assess the sensitivity for detection of activation in these 3 language regions (Fig 1). These ROIs were defined in the dominant hemisphere, according to our clinical judgment of language lateralization based on all 4 paradigms, or in the left hemisphere in patients with bilateral language. Regions were deemed activated when there was ≥4 cm^3 activation within the region. The frontal ROI was defined as the inferior frontal gyrus, as defined previously[13,15] on the basis of the Automated Anatomical Labelling atlas.[19] The temporal ROI was defined previously[13,15] as the ventral part of the superior temporal gyrus, the middle temporal gyrus, and the angular gyrus; in this study, this ROI was expanded to also include the lateral and posterior parts of the inferior temporal and fusiform gyri ($|x| \geq 38$, $y \leq -38$). The anterior parietal ROI was defined as the supramarginal gyrus and the inferior parietal lobule, as previously defined;[15] a language region within this territory has been shown to be critical for phonological encoding.[15,20-23]

Language maps were defined as satisfactory when they met 3 conditions: 1) $|LI| \geq 0.25$, in the correct direction or for patients

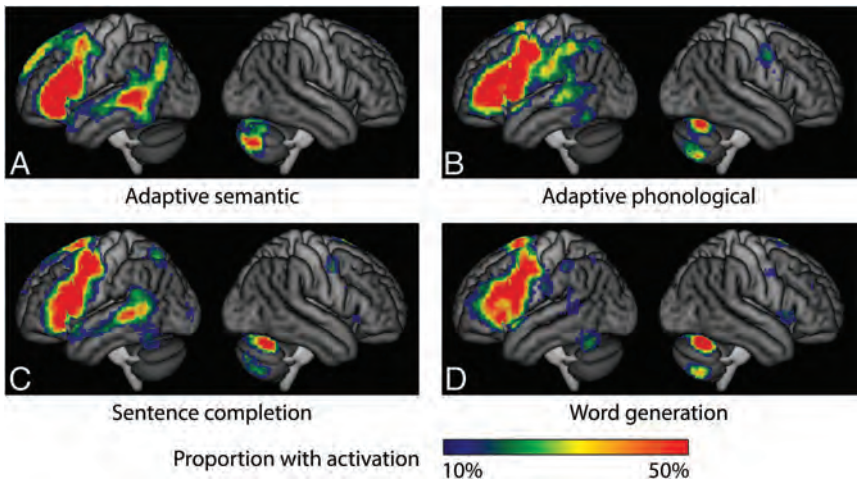

FIG 2. Activation maps for each paradigm. The color map indicates the number of individual patients with activation, with a whole-brain ROI, relative threshold of 5%, and minimum cluster extent of 2 cm^3. Activation maps for patients with right-hemisphere dominance were flipped for these maps. *A*, Adaptive semantic. *B*, Adaptive phonological. *C*, Sentence completion. *D*, Word generation.

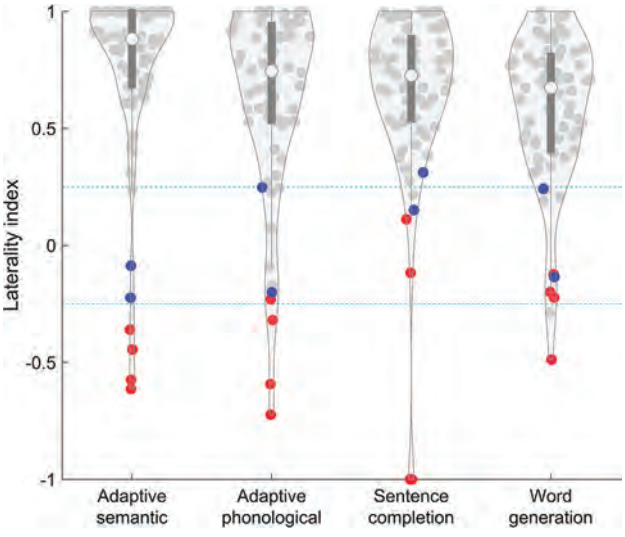

FIG 3. Lateralization indices by paradigm. Violin plots show the distribution of patients. *Red dots* indicate patients with right-hemisphere language, and *blue dots* indicate patients with bilateral language lateralization. *Teal dotted lines* show cutoffs for lateralization categories.

with bilateral language, $-0.25 < LI < 0.25$; these cutoffs are based on those proposed by Janecek et al;[5] 2) frontal activation of $\geq 4\ cm^3$ in the dominant hemisphere (left hemisphere for patients with bilateral language); and 3) temporal activation of $\geq 4\ cm^3$ in the dominant hemisphere (left hemisphere for patients with bilateral language).

Test-retest reproducibility was assessed in a preliminary manner by splitting each run in half, analyzing the 2 halves separately, and calculating the Dice coefficient of similarity[24] between the 2 resultant activation maps. Head motion was compared between paradigms by calculating the mean framewise displacement for each run.

LIs, activation extents, Dice coefficients, and head-motion measures were compared among paradigms using repeated measures ANOVAs and post hoc paired *t* tests. The proportions of satisfactory language maps were compared with a χ^2 test, followed by post hoc Fisher exact tests.

RESULTS

The mean accuracy on the adaptive semantic task was 84.1% (SD, 5.0%) (range, 58.3%–95.0%), indicating that all patients performed the task above chance. Accuracy on the adaptive phonological task was 77.8% (SD, 9.5%) (range, 33.3%–91.1%), indicating that most but not all patients performed the task above chance. The mean difficulty level of items presented was 4.1 (SD, 2.8) (on a 7-point scale) (range, 1.7–6.1) for the semantic task and 2.8 (SD, 1.1) (range, 1.2–6.2) for the phonological task; these means are about 1 point lower than previously observed in neurologically healthy individuals.[15] Because the sentence completion and word generation paradigms were performed covertly, it was not possible to evaluate performance, but all patients were able to perform both paradigms during prescan training.

On the basis of our clinical judgments, taking into account all 4 paradigms, language was localized to the left hemisphere in 67 patients, localized to the right hemisphere in 4 patients, and bilaterally distributed in 2 patients. The brain regions activated by each of the 4 paradigms are shown in Fig 2, in which activations for the 4 patients with right-lateralized language have been mirror-reversed around the midline. All 4 paradigms yielded extensive activation in the inferior frontal lobe. In the posterior temporal lobe, the most robust language activation was observed for the adaptive semantic paradigm, followed by the sentence completion paradigm. In contrast, the adaptive phonological paradigm activated temporal language areas in many but not all patients, while the word generation paradigm yielded temporal activation in even fewer patients. The anterior parietal region was activated by the adaptive phonological paradigm in most patients, but rarely by the other 3 paradigms. Finally, all 4 paradigms activated the contralateral cerebellum.

All 4 paradigms revealed satisfactory lateralization determinations (ie, $|LI| \geq 0.25$, in the correct direction) in most patients (adaptive semantic: 72 of 73; adaptive phonological: 67 of 73; sentence completion: 71 of 73; word generation: 69 of 73) (Fig 3). However, the 4 paradigms did differ in the degree to which language activations were lateralized ($F(3,216) = 12.029$, $P < .001$). Note that for the 4 patients with right-lateralized language, LIs were negated in the statistical analysis (but not in the figure). Post hoc tests indicated that the adaptive semantic paradigm (mean $|LI| = 0.80 \pm 0.25$) yielded higher LIs than the other 3 paradigms (all, $t(72) \geq 3.05$; all $P \leq .003$). The adaptive phonological paradigm (mean $|LI| = 0.68$ [SD, 0.31]) did not differ from the 2 standard paradigms (all $P \geq .060$), while the sentence completion paradigm (mean $|LI| = 0.71$ [SD, 0.25]) yielded higher absolute LIs than the word generation paradigm (mean $|LI| = 0.60$ [SD, 0.27], $P = .003$).

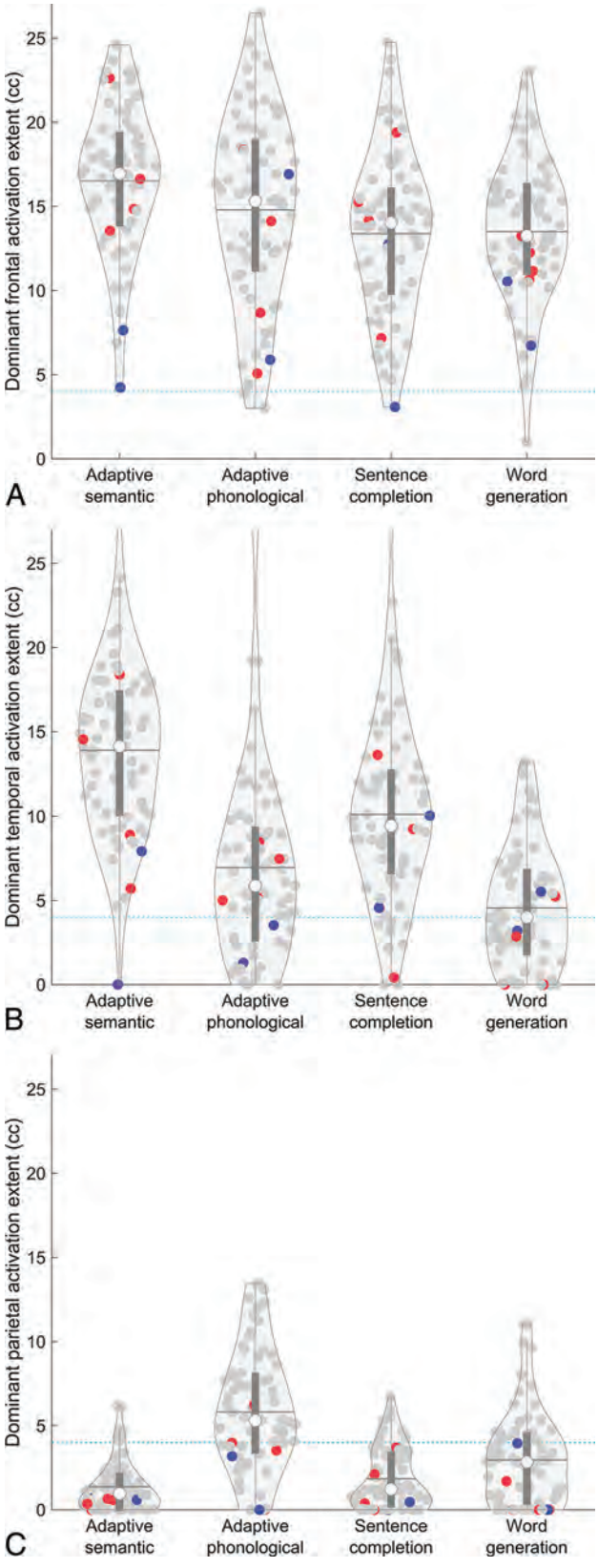

FIG 4. Sensitivity for identifying language regions in the dominant hemisphere. Violin plots show the extent of activation in each region for each paradigm. *Red dots* indicate patients with right-hemisphere language, and *blue dots* indicate patients with bilateral language lateralization. *Horizontal lines* show means. *Teal dotted lines* show cutoffs for assessment of sensitivity. *A*, Inferior frontal language region. *B*, Posterior temporal language region. *C*, Anterior parietal language region.

Table 2: Proportions of patients with satisfactory language maps

Paradigm	Proportion	Percentage
Adaptive semantic	71 of 73	97%
Adaptive phonological	49 of 73	67%
Sentence completion	63 of 73	86%
Word generation	37 of 73	51%

All 4 paradigms activated the frontal language region of the dominant hemisphere in most patients (adaptive semantic: 73 of 73; adaptive phonological: 70 of 73; sentence completion: 72 of 73; word generation: 72 of 73) (Fig 4*A*). However, the 4 paradigms differed in the extent of dominant-hemisphere frontal activation ($F(3,216) = 12.43$, $P < .001$). Post hoc tests indicated that the adaptive semantic paradigm produced the greatest extent of activation (all $P \leq .005$), followed by the adaptive phonological paradigm (all $P \leq .031$), then the 2 standard paradigms, which did not differ from each other ($P = .83$).

The 4 paradigms differed markedly in their capacity to activate the dominant-hemisphere temporal language region (adaptive semantic: 72 of 73; adaptive phonological: 52 of 73; sentence completion: 64 of 73; word generation: 37 of 73) (Fig 4*B*). The differences in the extent of activation in this region were statistically significant ($F(3,216) = 90.06$, $P < .001$). Post hoc tests indicated that the adaptive semantic paradigm produced the greatest extent of activation (all $P < .001$), followed by the sentence completion paradigm (all $P < .001$), then the adaptive phonological paradigm ($P < .001$), and finally, the word generation paradigm.

The 4 paradigms also differed markedly in their capacity to activate the dominant-hemisphere anterior parietal language region involved in phonological encoding (adaptive semantic: 7 of 73; adaptive phonological: 48 of 73; sentence completion: 9 of 73; word generation: 22 of 73) (Fig 4*C*). The differences in the extent of activation in this region were statistically significant ($F(3,216) = 70.12$, $P < .001$). Post hoc tests indicated that the adaptive phonological paradigm produced the greatest extent of activation (all $P < .001$), followed by the word generation paradigm (all $P < .001$), then the sentence completion paradigm ($P = .031$), and last, the adaptive semantic paradigm.

Finally, the paradigms were compared in terms of the number of patients for whom overall satisfactory language maps were obtained, ie, correctly lateralized with dominant-hemisphere frontal and temporal activations each exceeding 4 cm^3. These proportions differed significantly across the 4 paradigms ($\chi^2[3] = 50.14$, $P < .001$) (Table 2). The adaptive semantic paradigm met these 3 criteria in the most patients (71 of 73, 97%), followed by the sentence completion paradigm (63 of 73, 86%), the adaptive phonological paradigm (49 of 73, 67%), and the word generation paradigm (37 of 73, 51%). All pair-wise differences were significant (Fisher exact test, all $P \leq .031$), except for the difference between the phonological and word generation paradigms ($P = .064$).

Neither test-retest reliability ($F(3,216) = 1.99$, $P = .12$) nor head motion ($F(3, 216) = 0.97$, $P = .41$) differed across the 4 paradigms. The relative performance of the 4 paradigms was

maintained across different choices of analysis parameters, including ROIs, absolute or relative voxelwise thresholds, and cluster-extent thresholds (Online Supplemental Data).

DISCUSSION

Our data indicate that the adaptive semantic paradigm has the strongest psychometric properties of the 4 paradigms investigated, and for most purposes, it is most likely to result in satisfactory maps of individual patient language networks. For determination of language lateralization and for identification of the frontal language region of the dominant hemisphere, all 4 paradigms performed well in most patients, and the advantages of the adaptive semantic paradigm, though statistically significant, were modest. However, for identification of the temporal language region of the dominant hemisphere, the adaptive semantic paradigm performed markedly better than the other 3 paradigms, and consequently, it was the paradigm most likely to produce language maps that were satisfactory overall.

In our clinical practice, we continue to use all 4 paradigms whenever possible. A panel of tasks provides multiple fallback possibilities, and several studies have demonstrated the advantages of panels of tasks relative to single tasks.[11,25,26] However, there are often situations in which time is limited and paradigms must be prioritized over one another. For example, patients who are at risk of experiencing a seizure in the scanner or patients who are claustrophobic may not be able to complete a full panel of tasks. On the basis of our data, we recommend that the adaptive semantic paradigm be administered first, so if a patient cannot complete a full panel of tasks for any reason, the likelihood of obtaining a satisfactory language map is maximized.

The only exception is in patients with tumors or epileptogenic foci in the parietal lobe, for whom there is an interest in localizing language regions with respect to the intended resection site. The adaptive phonological paradigm excelled at activating the anterior parietal language region, which is involved in phonological encoding.[20-23] This region was activated by this paradigm in about two-thirds of the patients, greatly exceeding the other 3 paradigms, which usually do not reveal this language region. Parietal resections are relatively uncommon relative to temporal and frontal resections, but they are certainly sometimes indicated. In these patients, the adaptive phonological paradigm should be prioritized. Because sensitivity for this region was only 66%, we recommend that the paradigm be repeated more than once because it is likely that additional data would increase sensitivity.[15] Other paradigms such as syllable counting, which also activates this region, could also be considered.[15,20]

There are several design factors that may account for the good performance of the adaptive paradigms. First, the adaptive nature of the tasks ensures that participants are always performing tasks that are challenging, yet within their abilities. This feature means that the language network is strongly driven during the language condition, while other brain regions are robustly recruited during the control condition, thus maximizing differences between the conditions. Second, the control conditions are tightly matched to the language conditions for task demands, thus avoiding spurious activations due to visual processing, decision-making, and so forth. Third, the combination of active decision-making and comprehension is well-suited to activating both frontal and temporal language areas in the case of the semantic task,[27] while reading and phonological encoding of pseudowords place a heavy load on the phonological system in the case of the phonological task.[15] Another advantage of the adaptive tasks is that they allow observation of responses and assessment of accuracy, which can be helpful in the interpretation of atypical activation maps.

There are two practical considerations in using the adaptive paradigms. First, an MR imaging–compatible button box is required to collect the responses that are used to select subsequent stimuli. Second, the adaptive language mapping software depends on Matlab and Psychtoolbox, the former being expensive and the latter requiring modest technical expertise to install correctly. A stand-alone version of the adaptive language mapping software is a priority for future work.

The present study has one noteworthy limitation, which is that successful language mapping was defined relative to expected patterns (lateralization and identification of known language regions), rather than with reference to clinical outcomes after surgery.[28] Studies of outcomes in relation to alternative methods of localizing eloquent regions are generally difficult to perform because it would not be ethical to resect brain regions that one method (but perhaps not another) indicated were critical for language function. Therefore, the present evidence may be the strongest that is feasible to obtain in practice.

CONCLUSIONS

We found that the adaptive semantic paradigm is most likely to yield satisfactory language maps compared with the other paradigms investigated, and we, therefore, recommend this paradigm in most circumstances. When parietal localization is of particular concern, we recommend the adaptive phonological paradigm. If there is sufficient time, then we recommend that a panel of all 4 paradigms be used.

ACKNOWLEDGMENTS

We thank all patients who took part in this research, and 2 anonymous reviewers for their constructive suggestions.

Disclosure forms provided by the authors are available with the full text and PDF of this article at www.ajnr.org.

REFERENCES

1. Binder JR, Swanson SJ, Hammeke TA, et al. **A comparison of five fMRI protocols for mapping speech comprehension systems.** *Epilepsia* 2008;49:1980–97 CrossRef Medline
2. Black DF, Vachha B, Mian A, et al. **American Society of Functional Neuroradiology-recommended fMRI paradigm algorithms for presurgical language assessment.** *AJNR Am J Neuroradiol* 2017;38:E65–73 CrossRef Medline
3. Benjamin CF, Li AX, Blumenfeld H, et al. **Presurgical language fMRI: clinical practices and patient outcomes in epilepsy surgical planning.** *Hum Brain Mapp* 2018;39:2777–85 CrossRef Medline
4. Sabsevitz DS, Swanson SJ, Hammeke TA, et al. **Use of preoperative functional neuroimaging to predict language deficits from epilepsy surgery.** *Neurology* 2003;60:1788–92 CrossRef Medline
5. Janecek JK, Swanson SJ, Sabsevitz DS, et al. **Language lateralization by fMRI and Wada testing in 229 patients with epilepsy: rates and predictors of discordance.** *Epilepsia* 2013;54:314–22 CrossRef Medline

6. Janecek JK, Swanson SJ, Sabsevitz DS, et al. **Naming outcome prediction in patients with discordant Wada and fMRI language lateralization.** *Epilepsy Behav* 2013;27:399–403 CrossRef Medline
7. Szaflarski JP, Gloss D, Binder JR, et al. **Practice guideline summary: use of fMRI in the presurgical evaluation of patients with epilepsy—report of the Guideline Development, Dissemination, and Implementation Subcommittee of the American Academy of Neurology.** *Neurology* 2017;88:395–402 CrossRef Medline
8. Giussani C, Roux FE, Ojemann J, et al. **Is preoperative functional magnetic resonance imaging reliable for language areas mapping in brain tumor surgery? Review of language functional magnetic resonance imaging and direct cortical stimulation correlation studies.** *Neurosurgery* 2010;66:113–20 CrossRef Medline
9. Rutten GJ, Ramsey NF, van Rijen PC, et al. **Development of a functional magnetic resonance imaging protocol for intraoperative localization of critical temporoparietal language areas.** *Ann Neurol* 2002;51:350–60 CrossRef Medline
10. Pillai JJ, Zaca D. **Relative utility for hemispheric lateralization of different clinical fMRI activation tasks within a comprehensive language paradigm battery in brain tumor patients as assessed by both threshold-dependent and threshold-independent analysis methods.** *Neuroimage* 2011;54(Suppl 1):S136–45 CrossRef Medline
11. Zaca D, Jarso S, Pillai JJ. **Role of semantic paradigms for optimization of language mapping in clinical fMRI studies.** *AJNR Am J Neuroradiol* 2013;34:1966–71 CrossRef Medline
12. Wilson SM, Bautista A, Yen M, et al. **Validity and reliability of four language mapping paradigms.** *Neuroimage Clin* 2017;16:399–408 CrossRef Medline
13. Wilson SM, Yen M, Eriksson DK. **An adaptive semantic matching paradigm for reliable and valid language mapping in individuals with aphasia.** *Hum Brain Mapp* 2018;39:3285–3307 CrossRef Medline
14. Wilson SM, Eriksson DK, Yen M, et al. **Language mapping in aphasia.** *J Speech Lang Hear Res* 2019;62:3937–46 CrossRef Medline
15. Yen M, DeMarco AT, Wilson SM. **Adaptive paradigms for mapping phonological regions in individual participants.** *Neuroimage* 2019;189:368–79 CrossRef Medline
16. Brainard DH. **The psychophysics toolbox.** *Spat Vis* 1997;10:433–36 CrossRef Medline
17. Pelli DG. **The VideoToolbox software for visual psychophysics: transforming numbers into movies.** *Spat Vis* 1997;10:437–42 CrossRef Medline
18. Gross WL, Binder JR. **Alternative thresholding methods for fMRI data optimized for surgical planning.** *Neuroimage* 2014;84:554–61 CrossRef Medline
19. Tzourio-Mazoyer N, Landeau B, Papathanassiou D, et al. **Automated anatomical labeling of activations in SPM using a macroscopic anatomical parcellation of the MNI MRI single-subject brain.** *Neuroimage* 2002;15:273–89 CrossRef Medline
20. Price CJ, Moore CJ, Humphreys GW, et al. **Segregating semantic from phonological processes during reading.** *J Cogn Neurosci* 1997;9:727–33 CrossRef Medline
21. McDermott KB, Petersen SE, Watson JM, et al. **A procedure for identifying regions preferentially activated by attention to semantic and phonological relations using functional magnetic resonance imaging.** *Neuropsychologia* 2003;41:293–303 CrossRef Medline
22. Pillay SB, Stengel BC, Humphries C, et al. **Cerebral localization of impaired phonological retrieval during rhyme judgment.** *Ann Neurol* 2014;76:738–46 CrossRef Medline
23. Mirman D, Chen Q, Zhang Y, et al. **Neural organization of spoken language revealed by lesion-symptom mapping.** *Nat Commun* 2015;6:6762 CrossRef Medline
24. Rombouts SA, Barkhof F, Hoogenraad FG, et al. **Test-retest analysis with functional MR of the activated area in the human visual cortex.** *AJNR Am J Neuroradiol* 1997;18:1317–22 Medline
25. Rutten GJ, Ramsey NF, van Rijen PC, et al. **Reproducibility of fMRI-determined language lateralization in individual subjects.** *Brain Lang* 2002;80:421–37 CrossRef Medline
26. Gaillard WD, Balsamo L, Xu B, et al. **fMRI language task panel improves determination of language dominance.** *Neurology* 2004;63:1403–08 CrossRef Medline
27. Mbwana J, Berl MM, Ritzl EK, et al. **Limitations to plasticity of language network reorganization in localization related epilepsy.** *Brain* 2009;132:347–56 CrossRef Medline
28. Binder JR, Sabsevitz DS, Swanson SJ, et al. **Use of preoperative functional MRI to predict verbal memory decline after temporal lobe epilepsy surgery.** *Epilepsia* 2008;49:1377–94 CrossRef Medline
29. Veale JF. **Edinburgh Handedness Inventory-Short Form: a revised version based on confirmatory factor analysis.** *Laterality* 2014;19:164–77 CrossRef Medline

Sagittal Angle of the Trigeminal Nerve at the Porus Trigeminus: A Novel Measurement to Distinguish Different Causes of Classic Trigeminal Neuralgia

B.F. Branstetter, N. Reddy, K. Patel, and R. Sekula

ABSTRACT

BACKGROUND AND PURPOSE: Classic trigeminal neuralgia is a clinical syndrome of facial pain, most often attributable to vascular compression of the proximal cisternal segment of the trigeminal nerve and treatable with microvascular decompression of the nerve. Some patients, however, meet all clinical criteria for classic trigeminal neuralgia yet do not respond to microvascular decompression. Because the reasons for surgical failure are not well understood, the aim of this study was to determine if a subset of patients with classic trigeminal neuralgia could be distinguished by measuring the angle of the trigeminal nerve in the sagittal plane as the nerve traverses the porus trigeminus.

MATERIALS AND METHODS: We retrospectively identified patients with either classic trigeminal neuralgia ($n = 300$) or hemifacial spasm ($n = 300$) who had undergone MR imaging, including 3-plane steady-state free precession imaging. Patients with hemifacial spasm served as controls. On sagittal steady-state free precession images, we measured the angle of each trigeminal nerve as it crosses through the porus trigeminus into the Meckel cave (SATNaPT). In patients with classic trigeminal neuralgia, we separated the nerves into symptomatic and asymptomatic sides. We compared these 3 groups using the Student *t* test.

RESULTS: Control patients had a mean SATNaPT of 170° (SD, 11°) with a normal distribution. The contralateral asymptomatic nerve in patients with classic trigeminal neuralgia had the same distribution of angles. The symptomatic nerves in patients with classic trigeminal neuralgia had a bimodal distribution; 83% of patients fell into the same distribution as the asymptomatic nerves, but the other 15% had an average angle of 143° (SD, 7°). This difference was statistically significant ($P < .0001$).

CONCLUSIONS: Patients with the clinical syndrome of classic trigeminal neuralgia fell into 2 categories based on the radiologic measurement of the SATNaPT. Most patients had an anatomically normal nerve that was affected by vascular compression, but 17% of these patients had aberrant anatomy that may cause or contribute to their clinical presentation. Further study is needed to determine whether this subset of patients should receive a different surgery to better address their underlying anatomic abnormality. The SATNaPT measurement should be included in every MR imaging interpretation performed on patients with classic trigeminal neuralgia.

ABBREVIATIONS: cTN = classic trigeminal neuralgia; HFS = hemifacial spasm; MVD = microvascular decompression; SATNaPT = sagittal angle of the trigeminal nerve at the porus trigeminus; SSFP = steady-state free precession

Trigeminal neuralgia is a syndrome of pain in the distribution of the trigeminal nerve. Although trigeminal neuralgia can be caused by diseases such as multiple sclerosis or tumors, the most common form is classic trigeminal neuralgia (cTN). The International Headache Society has established objective criteria for the diagnosis of cTN, including paroxysms that last from a fraction of a second to 2 minutes; severe intensity of pain; electric, stabbing, or sharp pain; and episodes precipitated by innocuous stimuli to the face.[1]

In 80%–90% of patients, cTN is associated with arterial compression of the trigeminal nerve.[2,3] A tortuous artery, most frequently the superior cerebellar artery, abuts (and often distorts or displaces) the trigeminal nerve near its root entry point.[4] Although not well-understood, pulsations from the artery presumably irritate the adjacent nerve, causing the characteristic pain syndrome.

Voltage-gated sodium channel blockers such as carbamazepine and oxcarbazepine are considered first-line therapy for cTN.[1] Unfortunately, most patients progress despite medical therapy and

Received November 25, 2021; accepted after revision July 19, 2022.

From the Departments of Radiology (B.F.B.), Otolaryngology (B.F.B.), and Neurosurgery (R.S.), University of Pittsburgh School Medicine, Pittsburgh, Pennsylvania; and University of Pittsburgh (N.R., K.P.), Pittsburgh, Pennsylvania.

Please address correspondence to Barton Branstetter, MD, FACR, FSIIM, 200 Lothrop St, Pittsburgh, PA 15213; e-mail: BFB1@pitt.edu

http://dx.doi.org/10.3174/ajnr.A7634

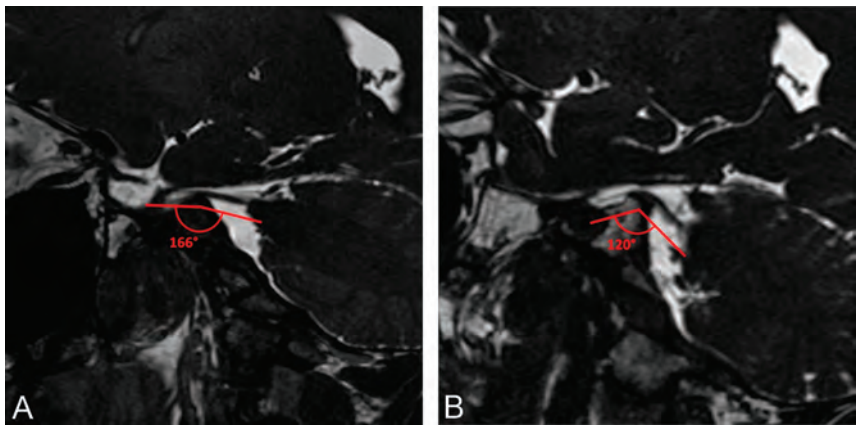

FIG 1. Sample measurements of the SATNaPT. Sagittal SSFP MR images show a normal angle of 166° (*A*) and a decreased angle of 120° (*B*). The angle measurements are shown below the nerves to avoid obscuring the anatomy.

eventually require surgery. The surgical procedure of choice is microvascular decompression (MVD), in which the compressive artery is isolated from the trigeminal nerve and an interpositional pledget is placed between the artery and nerve to prevent further injury. MVD has a high success rate when performed on patients who meet all the criteria for cTN.[2,5,6]

MR imaging of the cranial nerves using high-resolution T2-weighted sequences is the technique of choice for imaging patients with cTN before surgery.[4] The offending artery is identified, and the degree of compression in quantified. This process is useful not only for surgical planning, but it also conveys prognostic information.[2,7]

Some patients meet all the criteria for cTN yet still do not respond to surgical therapy. Although the degree of neurovascular compression and response to medication help predict which patients will respond to MVD,[7,8] there may be other anatomic differences between responders and nonresponders that could predict surgical success or suggest alternative treatments. In particular, some patients have bony distortions of their skull base that result in superior displacement of the porus trigeminus (the opening between the prepontine cistern and the Meckel cave). This aberrant anatomy displaces the trigeminal nerve upward, forming an acute angle between the cisternal and cavernous portions of the nerve when viewed in the sagittal plane. We refer to this angle as the sagittal angle of the trigeminal nerve at the porus trigeminus (SATNaPT).

The purpose to this study was to establish normal measurements for the SATNaPT in asymptomatic individuals and to determine whether the SATNaPT differs between asymptomatic individuals and patients with cTN.

MATERIALS AND METHODS

The institutional review board of University of Pittsburgh approved this study as performed on retrospective data and thus waived informed consent.

Patient Selection

From the surgical registry at the University of Pittsburgh, we identified 300 consecutive patients with cTN who had undergone MR imaging before surgery. We then identified 300 consecutive patients with hemifacial spasm (HFS) who had undergone MR imaging. All patients in the registry were screened for facial nerve and trigeminal nerve symptoms; patients with both were excluded from this study. Because the patients with HFS had no symptoms attributable to their trigeminal nerves, they served as controls for measurement of the trigeminal nerves. We recorded age, sex, and symptom laterality for all patients. All patients were imaged between 2013 and 2018 at a single academic hospital. Patients were excluded (and not counted toward the total of 300 patients) if they had been previously treated with MVD or if motion artifacts prevented measurement.

Imaging Protocol

Our MR imaging protocol for patients with presumed vascular compression of the cranial nerves consists of sagittal T1 and axial FLAIR images through the entire brain. Balanced steady-state free precession (SSFP) images with dual excitation, which are often referred to by vendor acronyms such as FIESTA or CISS, are performed in the axial, coronal, and sagittal planes through the cranial nerves. We do not rely on reformatted images because we have found them to be less reliable than multiplanar imaging, allowing us to use a single protocol for evaluating compression of the trigeminal, facial, and glossopharyngeal nerves. The SSFP sequences use optimized TR and TE (usually about 5.5 and 2 ms), a flip angle of 65°, FOV of 18 cm, matrix of 384 × 256, 1.0-mm section thickness, 0.5-mm section interval, and NEX of 2.

Measurements

The images were evaluated by a single dedicated head and neck radiologist with 20 years of experience in practice. On a single sagittal SSFP image, the angle between the trunk of the trigeminal nerve (in the prepontine cistern) and the uppermost branch of the trigeminal nerve (within the Meckel cave) was measured (Fig 1). This constitutes the SATNaPT. Each trigeminal nerve angle was measured separately on each patient using the angle measurement tool in the PACS. The observer was blinded to the patients' symptoms and the scans were presented in random order.

Statistical Analysis

We analyzed 3 groups of nerves: asymptomatic nerves in control patients, asymptomatic (contralateral) nerves in patients with cTN, and symptomatic nerves in patients with cTN. Normal distribution of data was confirmed, and normal (bell-shaped) curves were fitted to the histogram of angles in each population. For populations with a bimodal distribution, the least-squares method was used to optimize a sum of 2 normal curves. In anticipation of similar normal distributions between left and right ears as well as between control patients and uninvolved ears in patients with trigeminal neuralgia, equivalence testing was used to demonstrate

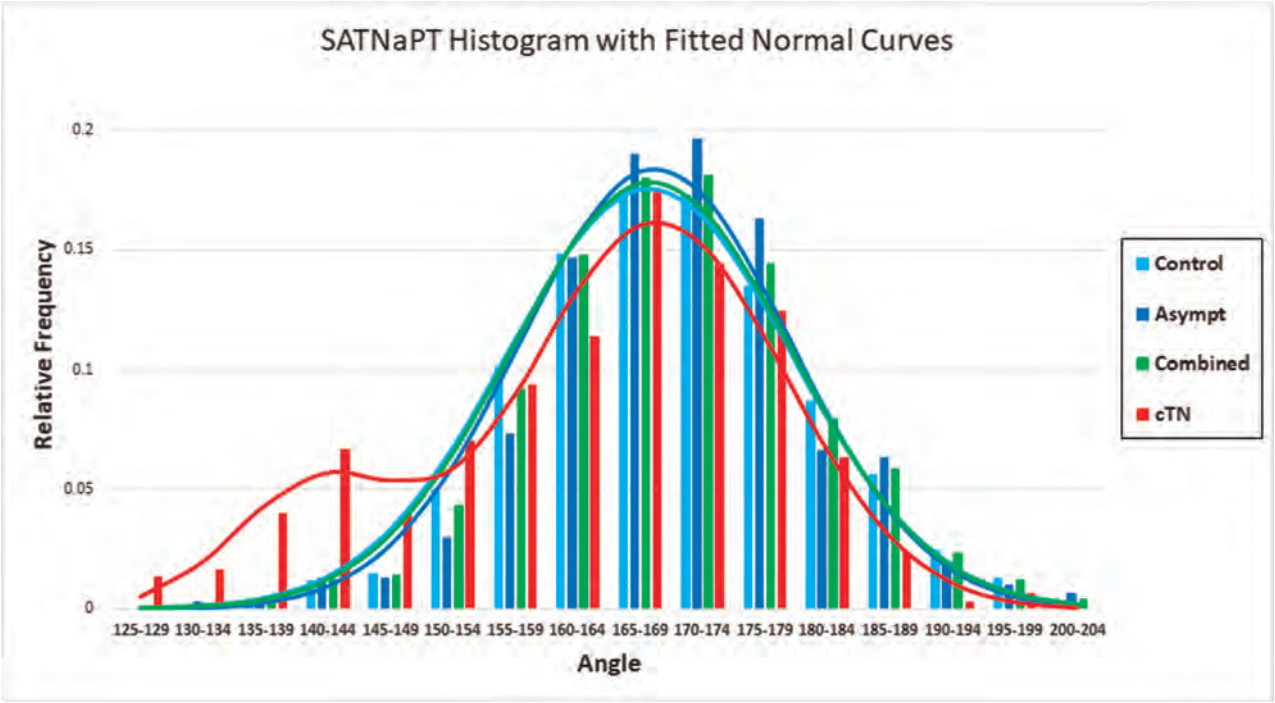

FIG 2. Histogram of SATNaPT in different patient populations. The horizontal axis angle is measured in 5° intervals. The vertical axis is the percentage of patients. A best-fit normal curve is also shown for each histogram. Note that all curves are similar except the cTN curve, which has a bimodal distribution in which 17% of the nerves form a separate population with decreased SATNaPT. Asympt indicates the contralateral asymptomatic nerve in patients with cTN; Control, patient scanned for other reasons; Combined, all asymptomatic nerves (control plus Asympt).

similarities among these groups.[9] The Student *t* test was used to demonstrate pair-wise differences between those with affected trigeminal nerves and the other groups.

RESULTS

We accrued 306 patients with HFS as controls; 6 were excluded because of excessive motion artifacts on their scans. Of the remaining 300 controls, 88 (29%) were men and 212 (71%) were women, with an average age of 56 years (range, 20–88 years). We accrued 331 patients with cTN; 13 were excluded for motion artifacts and 18 were excluded because they had prior MVD surgery. Of the remaining 300 patients, 116 (39%) were men and 184 (61%) were women, with an average age of 63 years (range, 23–87 years). Although some patients had bilateral symptoms, 1 side was always dominant and that side was considered symptomatic for our analyses.

In the healthy population, the SATNaPT has an average value of 170°. It follows a normal distribution with an SD of 11° (Fig 2). Equivalence testing showed no differences based on sex, age (dichotomized to the median), or side (left/right), using $\Delta = 10°$. The asymptomatic (contralateral) nerves of patients with cTN also have an average SATNaPT of 170° (SD, 11°). There was no statistical difference between the SATNaPT for controls and the asymptomatic nerves of patients with cTN ($P = .48$).

The symptomatic nerves in patients with cTN followed a bimodal distribution (Fig 2); 83% of patients had the larger peak, which had an average SATNaPT of 170° (SD, 10°) (similar to that in controls). The remaining 17% of patients had an average SATNaPT of 143° (SD, 7°). The symptomatic nerves differed significantly from the nerves in control patients and also the contralateral asymptomatic nerves in patients with cTN ($P < .0001$).

DISCUSSION

We have identified 2 distinct groups of patients who present with cTN. These 2 groups are distinguishable by the anatomy of the trigeminal nerve as it passes through the porus trigeminus. Most patients have normal trigeminal nerve anatomy, and their symptoms are attributable to vascular compression in the traditional model popularized by Jannetta.[10]

However, about one-fifth of patients have aberrant anatomy with a decreased SATNaPT. It is unclear how this underlying anatomy, which is rare in the asymptomatic population, contributes to the symptoms of cTN. One possibility is that the trigeminal nerve becomes stretched as it extends over an elevated porus trigeminus; this stretching may inherently injure the nerve or may make it more susceptible to vascular compression. It is unclear whether patients with a decreased SATNaPT are less likely to respond to MVD; this is an area for further research that may provide insight into the role that the SATNaPT plays in the pathogenesis of cTN.

This study is limited by its single-institution design, in which all measurements were made by a single experienced radiologist. We did not attempt to assess interobserver variability. Another potential criticism of this work is that severe displacement of the cisternal segment of the trigeminal nerve by a compressing artery could result in a decreased SATNaPT, in which case the effect on the SATNaPT would be a consequence of vascular compression rather than a cause of disease. Subjective evaluation of the

patients in our series does not support this theory because the degree of nerve displacement was mild or absent in most patients with a decreased SATNaPT.

It is difficult to define a precise threshold for an "abnormal" SATNaPT because there is overlap between the patients with a normal SATNaPT and those with a decreased SATNaPT. Outcome analysis is needed to define an optimal cutoff point for prediction of surgical success. However, a value below 150° should prompt concern.

It is possible that patients with a decreased SATNaPT would benefit from additional or different surgery at the time of MVD. Further study is needed on the rates of coexistence between radiologic vascular compression and decreased SATNaPT and on outcomes for these groups of patients.

CONCLUSIONS

Patients with the clinical syndrome of cTN fall into 2 categories based on the radiologic measurement of the SATNaPT. Most patients have an anatomically normal nerve that is affected by vascular compression, but 17% of these patients have aberrant anatomy that may cause or contribute to their clinical presentation. Further study is needed to determine whether this subset of patients should undergo different surgery to better address their underlying anatomic abnormality. Radiologists should be aware of this potentially important anatomic variant and should know how to measure the SATNaPT.

Disclosure forms provided by the authors are available with the full text and PDF of this article at www.ajnr.org.

REFERENCES

1. Headache Classification Committee of the International Headache Society (IHS). **The International Classification of Headache Disorders, 3rd ed** . *Cephalalgia* 2018 Jan;38:629–808 CrossRef Medline
2. Hughes MA, Jani RH, Fakhran S, et al. **Significance of degree of neurovascular compression in surgery for trigeminal neuralgia.** *J Neurosurg* 2019 Jun 14. [Epub ahead of print] CrossRef Medline
3. Maarbjerg S, Wolfram F, Gozalov A, et al. **Significance of neurovascular contact in classical trigeminal neuralgia.** *Brain* 2015;138:311–19 CrossRef Medline
4. Hughes MA, Frederickson AM, Branstetter BF, et al. **MRI of the trigeminal nerve in patients with trigeminal neuralgia secondary to vascular compression.** *AJR Am J Roentgenol* 2016;206:595–600 CrossRef Medline
5. Barker FG 2nd, Jannetta PJ, Bissonette DJ, et al. **The long-term outcome of microvascular decompression for trigeminal neuralgia.** *N Engl J Med* 1996;334:1077–83 CrossRef Medline
6. Linskey ME, Ratanatharathorn V, Penagaricano J. **A prospective cohort study of microvascular decompression and gamma knife surgery in patients with trigeminal neuralgia.** *J Neurosurg* 2008;109:160–72 CrossRef Medline
7. Panczykowski DM, Jani RH, Hughes MA, et al. **Development and evaluation of a preoperative trigeminal neuralgia scoring system to predict long-term outcome following microvascular decompression.** *Neurosurgery* 2020;87:71–79 CrossRef Medline
8. Sekula RF. **Letter: the spectrum of trigeminal neuralgia without neurovascular compression.** *Neurosurgery* 2020;86:E472 CrossRef Medline
9. Ahn S, Park SH, Lee KH. **How to demonstrate similarity by using noninferiority and equivalence statistical testing in radiology research.** *Radiology* 2013;267:328–38 CrossRef Medline
10. Jannetta PJ. **Arterial compression of the trigeminal nerve at the pons in patients with trigeminal neuralgia.** *J Neurosurg* 1967;26:159–62 CrossRef Medline

Correlation between Histopathology and Signal Loss on Spin-Echo T2-Weighted MR Images of the Inner Ear: Distinguishing Artifacts from Anatomy

B.K. Ward, A. Mair, N. Nagururu, M. Bauer, and B. Büki

ABSTRACT

BACKGROUND AND PURPOSE: MR imaging of the inner ear on heavily T2-weighted sequences frequently has areas of signal loss in the vestibule. The aim of the present study was to correlate the anatomic structures of the vestibule with areas of low signal intensity.

MATERIALS AND METHODS: We reviewed T2-weighted spin-echo MR imaging studies of the internal auditory canal from 27 cases and cataloged signal intensity variations in the vestibulum of inner ears. Using a histologic preparation of a fully mounted human ear, we prepared 3D reconstructions showing the regions of sensory epithelia (semicircular canal cristae, utricular, and saccular maculae). Regions of low signal intensity were reconstructed in 3D, categorized by appearance, and compared with the 3D histologic preparation.

RESULTS: The region corresponding to the lateral semicircular canal crista showed signal loss in most studies (94%). In the utricle, a focus of signal loss occurred in the anterior-cranial portion of the utricle and corresponded to the location of the utricular macula and associated nerve on histopathologic specimens (63% of studies). Additional areas of low signal were observed in the vestibule, corresponding to the fluid-filled endolymphatic space and not to a solid anatomic structure.

CONCLUSIONS: Small foci of signal loss within the inner ear vestibule on T2-weighted spin-echo images correlate with anatomic structures, including the lateral semicircular canal crista and the utricular macula. More posterior intensity variations in the endolymphatic space are likely artifacts, potentially representing fluid flow within the endolymph caused by magneto-hydrodynamic Lorentz forces.

MR imaging of the temporal bone and lateral skull base has become common practice in the work-up of many clinical conditions, including sensorineural hearing loss, cholesteatoma, and infections of the lateral skull base. Increasingly, attention is being directed to the inner ear, for example in decisions about cochlear implant candidacy and in patients with Ménière disease.[1-3] The inner ear has been difficult to image with MR imaging techniques due to its small size and environment, which includes a mixture of tissues of different proton densities, leading to susceptibility artifacts.[4] T2*-weighted sequences using either gradient-echo (eg, CISS) or FIESTA are used at many centers but are prone to banding artifacts.[5] Other centers have used 3D fast spin-echo sequences (T2-weighted sampling perfection with application-optimized contrasts by using flip angle evolution [SPACE; Siemens]), which are less prone to magnetic susceptibility artifacts.[6]

In T2-weighted images generated using SPACE sequences, the labyrinthine fluids have a high signal intensity in sharp contrast with the low signal intensity of the surrounding bone of the otic capsule. The vestibule, however, is not entirely homogeneous, often showing patchy or filamentous areas of lower signal intensity. In the internal auditory canal, areas of low signal intensity on SPACE sequences are considered anatomic structures such as nerves and blood vessels. The increasing attention paid to inner ear structures on T2-weighted sequences prompted us to assess these areas of reduced signal intensity in the context of labyrinthine anatomy.

Received March 4, 2022; accepted after revision July 5.

From the Department of Otolaryngology-Head and Neck Surgery (B.K.W., N.N.), The Johns Hopkins University School of Medicine, Baltimore, Maryland; and Departments of Otolaryngology (A.M., B.B.) and Radiology (M.B.), Karl Landsteiner University Hospital Krems, Krems an der Donau, Austria.

B.K. Ward is supported by a clinician-scientist award K23DC018302 from the National Institutes of Health and by the Robert and Kate Niehaus Foundation. B. Büki is supported by the grants RTO005 and SF06 from the Karl Landsteiner Private University of Health Sciences, Krems an der Donau, Austria.

Please address correspondence to Béla Büki, MD, Department of Otolaryngology, Karl Landsteiner University Hospital Krems, Mitterweg 10, 3500 Krems an der Donau, Austria; e-mail: bela.bueki@krems.lknoe.at

Indicates open access to non-subscribers at www.ajnr.org

http://dx.doi.org/10.3174/ajnr.A7625

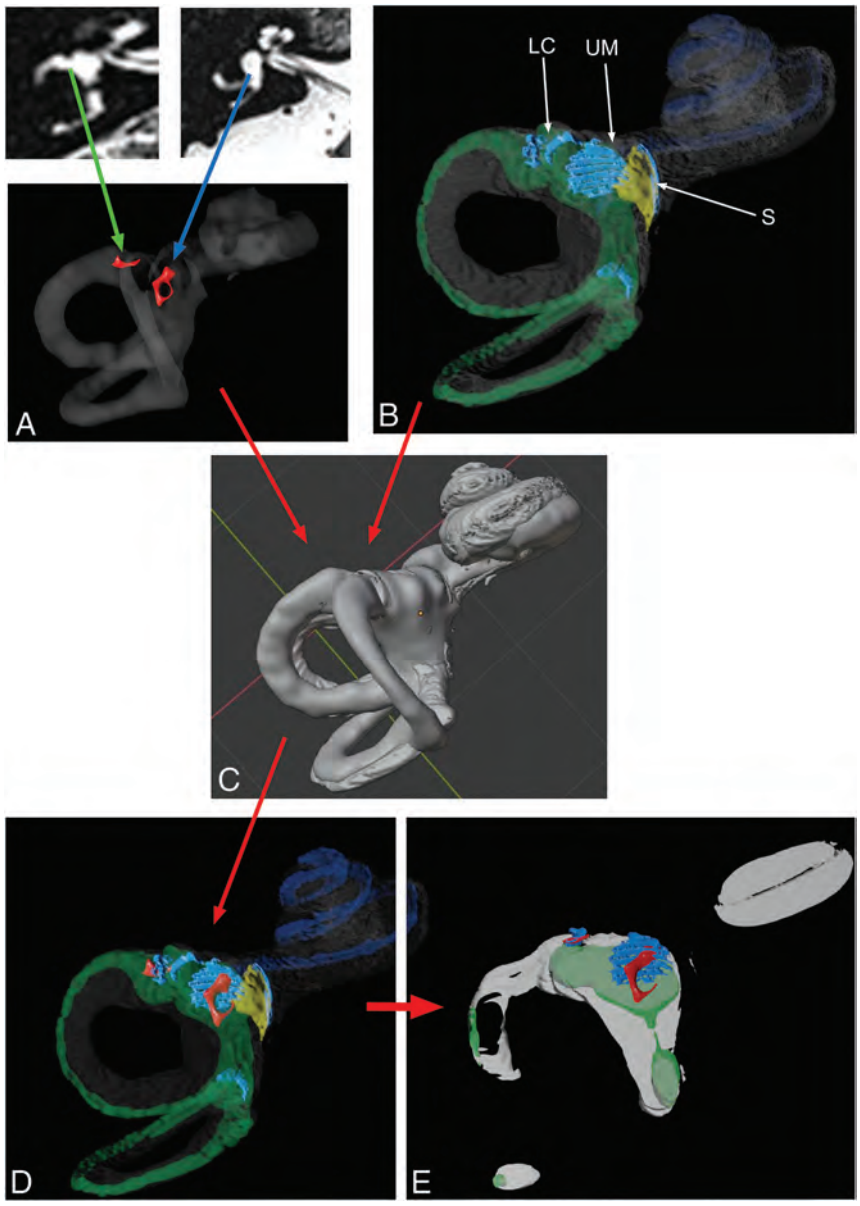

FIG 1. Demonstration of a morphologic fitting procedure, which was applied to search for correlations between MR images and anatomy observed in histologic sections. *A*, Inner ear fluid-filled spaces (right ear) as seen in the SPACE images were reconstructed in 3D (the 3D reconstruction has been mirrored to fit the anatomy of the left ear). Red: Note 2 landmarks in the MR images: an indentation in the region of the lateral canal crista (*green arrow*) and a diamond-shaped area of low signal (*blue arrow*). *B*, 3D reconstruction of the histologic sections (left ear) showing the lateral canal crista (LC), utricular macula (UM), and saccular macula (S). *C*, The two 3D reconstructions (MR imaging and histology) are fitted together according to their outer (perilymphatic) fluid boundary. *D*, Results of the fitting (green: histologic endolymphatic space of the utricle and semicircular canals). *E*, The composite fitted MR imaging and histologic 3D compartments are re-sectioned in the plane of the MR imaging sections to create a virtual MR image based on histology in which the regions with low signal intensity are embedded. In this image, the indentation in the region of the lateral canal crista on MR imaging (red) is colocalized with the same structure from histology (blue) and the diamond-shaped area shown in red projected more cranially to the utricular macula (blue).

Our aim in this retrospective study was to classify these foci of low signal intensity within the vestibulum according to their topography and to determine whether they correspond to anatomic structures.

MATERIALS AND METHODS

Research Design and Patients/Subjects

In this retrospective study, we reviewed T2-weighted SPACE sequence MR images from patients who were examined at the Department of Otolaryngology, Karl Landsteiner University Hospital Krems, Krems an der Donau, Austria, between January 1, 2019, and June 30, 2020. The study had been authorized by the Bioethics Committee of Lower Austria (GS4-EK-4/676–2020). All patients were older than 18 years of age, and in all cases, the radiologic evaluation showed normal high signal intensity representing the fluid-filled spaces of the inner ear, including the cochlea, vestibule, and semicircular canals.

MR Imaging Data Acquisition and Processing

The SPACE technique consists of a 3D-fast (turbo) spin-echo acquisition using very long echo-train lengths (typically 100–250 echoes), ultrashort echo spacing (typically 3–4 ms), nonselective refocusing pulses, and reduced flip angles. The examinations used a Magnetom Verio 3T MR imaging system (Siemens) with the following sequence parameters: TR, 1000 ms; TE, 135 ms; section thickness, 0.5 mm; bandwidth, 289 Hz/pixel; flip angle, 120°; echo spacing, 6.84 ms.

The MR imaging SPACE sequences were evaluated independently by 2 investigators for foci of low signal intensity in the vestibule without any processing using the DICOM viewer MagicView DANUBE (Siemens). Images were exported as JPEGs, and a scalar volume was created using Slicer (Version 4.10.2; http://www.slicer.org). The areas of low signal intensity in the vestibule were manually defined and registered in Slicer. The MR images were then three-dimensionally reconstructed (as illustrated in Fig 1*A*).

Processing of the Histology Sections

One normal ear (left side) from the temporal bone collection of the Otopathology Laboratory at the Massachusetts Eye and Ear Infirmary was examined (National Institute on Deafness and Other Communication Disorders National Temporal Bone Registry; institutional review board ethical commission permission number: 92–04-017X). The

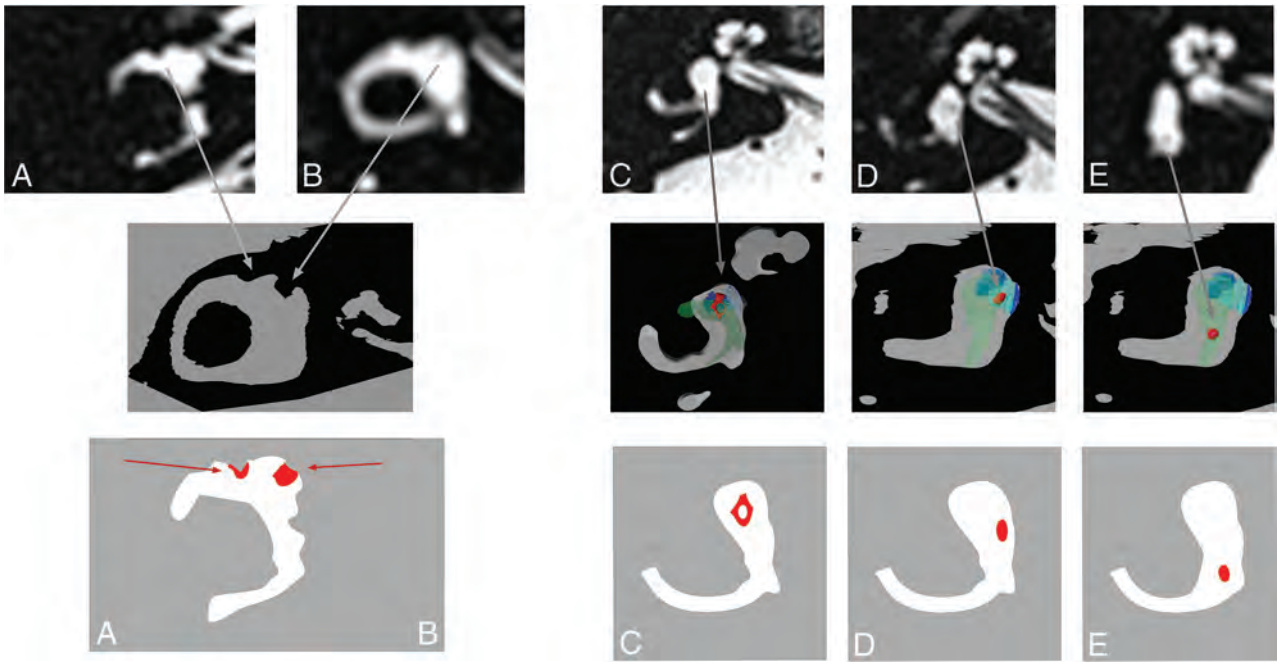

FIG 2. Landmarks identified in the MR images (*upper row*) and in the histologic images (*middle row*; red: foci of low intensity from the MR imaging projected into the histologic section after the 3D fitting procedure). Red: MR imaging hypointensities reconstructed in 3D. Dark blue: utricular macula. Transparent green: endolymphatic space. Light blue, saccule (for an explanation also see *D*). *Lower row*: Schematic drawing depicting the 5 areas of interest. *A*, Lateral canal crista. *B*, Utricular root region. *C*, Utricular "diamond." *D*, Focus of low intensity in the saccular region. *E*, Focus of low intensity in the posterior vestibulum. Red: ROIs, statistically evaluated.

donor was a 71-year-old man, and the specimen was acquired 14 hours postmortem. The ear was horizontally sectioned (ie, in the axial plane) with a section thickness of 20 μm with every section stained with H&E and mounted. The histologic slides were scanned using an Aperio AT2 scanner and viewed using Aperio ImageScope (Leica Biosystems). The ROIs were captured using a resolution of 3264 × 1836 and stored in JPEG format. Anatomic details such as the lateral canal crista, utricular macula, and saccular macula were manually defined and registered in Slicer. The 440 images were manually aligned using Fiji ImageJ (National Institutes of Health, Bethesda) and three-dimensionally reconstructed using Slicer [7] (as illustrated in Fig 1*B*). By means of Blender 2.82 (https://www.blender.org/download/releases/2-82/), a composite 3D model of the temporal bone histology including membranous spaces was built and virtually re-sectioned in the plane of the MR image sections. This process was necessary because the histologic sections are much thinner than the MR image slices, and the radiologic plane differed from the plane of the histologic sections.

Preliminary Fitting of the MR Images to the Histology

After the 3D reconstruction of the histologic sections was completed, the 3D MR imaging and 3D histology were scaled and fit. Using Blender, the location of the areas of low signal intensity on MR imaging were compared with the anatomic details from the reconstructed histology of the inner ear (Fig 1). After patterns of low signal intensity were identified, to focus on normal anatomy, we excluded patients with a diagnosis of a peripheral vestibular disorder from the final analysis.

Statistical Methods

The frequency of observation of areas of low signal intensity was compared between the left and right inner ears using a Fisher exact test. Statistical analyses were performed using Graph Pad Prism, Version 5.03 for Windows (GraphPad Software). A P value $< .05$ was considered statistically significant.

RESULTS

Originally 43 cases were identified that met the inclusion criteria. After a preliminary examination of the MR images for regions of low signal intensity, 5 patterns of low signal intensity in the vestibule were identified (Fig 2): 1) a focus near the anterior takeoff of the lateral semicircular canal; 2) the anterior-cranial part of the vestibule we called the utricular root; 3) a rhomboid or diamond-shaped filamentous area of decreased signal within the middle portion of the vestibule; 4) a focus near the saccule (saccular region); and 5) a focus in the posterior vestibule. The MR imaging SPACE sequences were evaluated independently by 2 investigators and the interrater agreement for identifying the regions of low signal intensity for the 2 examiners was 97.9% (Cohen $\kappa = 0.907$).

After the classification of these ROIs, 5 cases with the clinical diagnosis of vestibular neuritis, 3 cases with Ménière disease, and 8 cases with benign paroxysmal positional vertigo were excluded from the analysis because we intended to focus on normal peripheral vestibular anatomy. Ultimately, scans from 27 patients (13 women, 14 men) were processed (average age, 63 years; range, 35–89 years). Clinical diagnoses were hypertensive crisis ($n = 3$), idiopathic sudden hearing loss ($n = 12$), tinnitus ($n = 2$), central downbeat nystagmus ($n = 1$), minor cerebral hemorrhage

Frequency of foci of low signal intensity among vestibular ROIs

	ROIs (No.)				
	Lateral Semicircular Canal Crista	Utricular Root Region	Utricular "Diamond"	Saccular Region	Posterior Vestibular Region
Right side	25/27 (93%)	17/27 (63%)	23/27 (85%)	0/27 (0%)	25/27 (93%)
Left side	26/27 (96%)	17/27 (63%)	13/27[a] (48%)	0/27 (0%)	20/27 (74%)

[a] Significant difference between left and right sides (Fisher exact test, 2-tailed *P* value = .0084).

($n = 1$), subependymal tumor ($n = 1$), migraine ($n = 1$), transient ischemic attack ($n = 2$), trigeminal neuralgia ($n = 1$), syncope ($n = 2$), and vestibular schwannoma ($n = 1$).

The Table shows the frequency of the areas of low signal intensity for the left and right inner ears. The indentation caused by low signal intensity near the anterior takeoff of the lateral semicircular canal corresponded, on histology, to the lateral semicircular canal crista and was found in 93% of the right ears and in 96% of the left ears (Fig 2*A*). A signal loss adjacent to the anterior-superior part of the bony vestibule corresponded to the attachment or "root" of the utricular macula and could be seen in 63% of both left and right inner ears (Fig 2*B*). The remaining 3 areas of low signal intensity within the vestibule did not correspond to solid anatomic structures on the histologic specimen. The rhomboid or diamond-shaped area of reduced signal in the middle of the vestibule was observed with variable frequency for the inner ears on both sides, being significantly more commonly seen in the right inner ear than in the left (85% versus 48%, significant by the Fisher exact test; the 2-tailed *P* value = .0084) (Fig 2*C*). The low signal around the anatomic location of the saccule was not found in the final group of examined ears. The regions of low signal intensity were decided before excluding cases of peripheral vestibular disorders (Materials and Methods). There was 1 right ear in which a focus of low signal intensity was seen in this saccular region, and this case was excluded because of the diagnosis of ipsilateral benign paroxysmal positional vertigo (Fig 2*D*). In the more posterior-caudal region of the vestibule a small, round focus of low signal intensity was seen in 93% of right ears and 74% of the left inner ears (not significantly different by the Fisher exact test; the 2-tailed *P* value = .1415) (Fig 2*E*). The diamond-shaped area of low signal in the middle of the vestibule and the small round gray area in the posterior-caudal vestibule projected into the fluid-filled endolymphatic spaces on histology (Fig 2C, -*D*).

DISCUSSION

In this study, by comparing conventional spin-echo T2-weighted images with a detailed 3D histologic reconstruction of inner ear anatomy, we found 2 inner ear anatomic structures that can be identified frequently by reduced signal intensity and 2 areas of low signal that do not correspond to a solid anatomic structure. An indentation is found consistently on both right and left inner ears at the anterior attachment of the lateral semicircular canal to the vestibule, corresponding to the anatomic position of the lateral semicircular canal crista. More medially and somewhat caudal from the crista, foci of low signal intensity were observed in more than half of the cases on both sides approximately at the anatomic position of the root of the utricular macula. The bulk of the utricular root spreads over 400 μm along the z-axis (ie, 20 histologic slices), and the section thickness of the MR images was 500 μm, which means that this tiny tissue mass protruding into the fluid-filled vestibule may have been missed due to partial volume averaging, with the high signal intensity of the surrounding fluid perhaps accounting for its being found only in 63% of the ears. The frequency by which the root of the utricular macula could be seen was exactly the same on the left and right sides, supporting the hypothesis that the signal loss corresponds to an anatomic structure.

The additional 2 areas of low signal intensity within the vestibule did not correlate with solid anatomic structures but rather corresponded to regions of the endolymph-filled space of the vestibule on histology. The inner ear houses a thin membranous labyrinth that contains potassium-enriched fluid called endolymph and is surrounded by sodium-enriched perilymph. The sensory epithelia of the inner ear are located within the endolymph-filled space of the membranous labyrinth. The composition of these fluids is like water, indicating that endolymph and perilymph ought to have similar proton density and therefore a similar signal intensity on T2-weighted spin-echo images. The loss of signal within this space is likely an artifact.

An advantage of T2-weighted spin-echo sequences like SPACE over T2*-weighted gradient-echo sequences is fewer magnetic susceptibility artifacts.[8] T2-weighted TSE sequences like SPACE, however, are especially susceptible to movement artifacts.[9] The imaging characteristics of CSF cause it to manifest as intense signal on T2-weighted images.[10] The loss of signal, caused, for instance, when protons in fluid move during image acquisition, is called a flow void. Although considered an artifact, flow void has been used to examine the movement of the CSF in cases with normal-pressure hydrocephalus.[11-14] Areas of low signal intensity within the CSF can be caused by CSF flow-related phenomena and are divided into 2 categories: time-of-flight (TOF) effects and phase-related effects from turbulent flow, with turbulent flow creating greater loss of signal.[10]

Previously, the inner ear was modelled as a closed system with relatively little fluid flow. Increasingly, however, attention is being paid to flow phenomena in the inner ear.[15] In 2011, Roberts et al[16] discovered that healthy humans have a beating of the eyes called nystagmus in MR imaging machines of at least 3T. They reported nystagmus in all ($n = 10$) of their healthy human volunteers with the effect being greater at 7T than at 3T magnetic fields. The authors proposed that the effect is caused by a magneto-hydrodynamic Lorentz force occurring in the inner ear vestibule, induced by the interaction of normal ionic currents entering utricle hair cells and the strong static magnetic field of the MR imaging machine.[16,17] The Lorentz force has been attributed primarily to the ionic currents within endolymph associated with the utricle, though the effect would not be on the utricle macula and hair cells themselves but through the movement of the endolymph into the nearby openings of the lateral and superior semicircular canals, pushing on the cupulae and producing a nystagmus.[17] The nystagmus effect

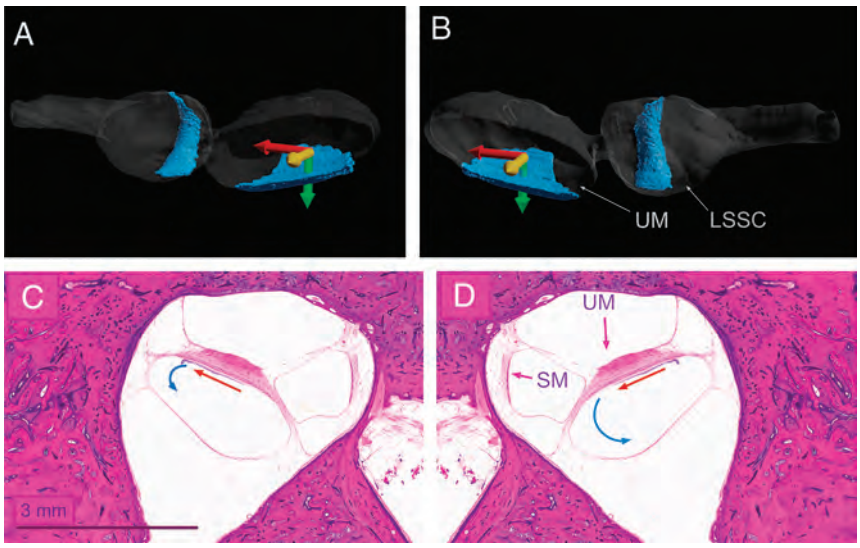

FIG 3. Cartoon presentation of the hypothetical mechanism of asymmetric turbulent fluid movements in the left and right ears caused by Lorentz forces. The Lorentz force (*red arrow*) is evoked, the direction determined by the right-hand rule, by the combination of the magnetic field (*yellow arrow*) and the utricle current (*green arrow*) as described in Roberts et al.[16] The anterior part of the utricle and lateral semicircular canal viewed from posterior on the left (*A*) and right (*B*) side. 3D reconstruction of the endolymphatic space from the histologic specimen. UM indicates utricular macula; LSSC, lateral semicircular canal crista in the ampulla. *C* and *D*, Original axial histologic section of the left inner ear across the utricular macula. Image *C* was mirrored horizontally to create the impression of the right inner ear. UM indicates utricular macula; SM, saccular macula; *red arrows*, magneto-hydrodynamic Lorentz force; *blue arrows*, hypothetical turbulent endolymph movements.

persists the entire time the person lies within the static magnetic field, physiology that could only occur if there was a continuous fluid flow constantly displacing the semicircular canal cupulae. On the 3D reconstruction in this study, additional foci of low signal were located within the endolymph space, both cranial to the utricular root and in the posterior vestibule, the first of which corresponds directly to the location of endolymphatic fluid vortices that could cause the nystagmus observed in MR imaging machines.

We hypothesized that the 2 foci of low signal within the vestibule that do not correlate with anatomic structures are caused by local endolymph movement. Low signal from TOF effects occurs in spin-echo imaging like SPACE sequences when protons do not experience both the initial radiofrequency pulse and the subsequent radiofrequency refocusing pulse. Turbulent flow results in a broader spectrum of proton velocities and a wide range of flow directions that are not seen in laminar flow. The varied flow velocities and directions result in more rapid dephasing and signal loss, termed "intravoxel dephasing."[10,18] TOF effects are also more pronounced (lower signal) with faster proton velocity, thinner slices, longer TEs, and an imaging plane perpendicular to flow.[10] In our case, the section thickness was 0.5 mm; the TE was long at 135 ms; and the imaging plane was perpendicular to the hypothetic flow direction (Fig 3). The frequency of these putative flow void artifacts was different between the ears on the left and right sides, potentially related to the mirrored anatomy across the ears, yet with the identical direction of flow based on the mechanism of the Lorentz force. These factors all may have augmented the flow artifacts even with a relatively slow-but-turbulent flow in the vestibule.

A limitation of the study is that only 1 normal cadaveric temporal bone was fully processed and reconstructed to compare with the MR images of the study population. Observations from the cadaver may not correlate perfectly with findings in the imaged patients. The spatial resolution of a 3D reconstructed, fully processed cadaveric specimen exceeds that of standard histologic preparations, and due to the time-intensive process of digitizing and manually aligning the specimen, few fully processed specimens have been reported in the literature.[19,20] Nevertheless, on the basis of the appearance of normal labyrinthine fluid spaces from other lower-resolution specimens, we are confident that the specimen used in this study represents a typical distribution of the different scalar volumes in a normal specimen.

In this study, we excluded cases in which pathology may have affected the peripheral vestibular system. The aim was to describe the findings in the normal inner ear; however, the included participants all had a clinical indication for the imaging study that may have affected the frequency of the observed findings. Nevertheless, the findings may have implications for patients who could demonstrate different patterns of low signal intensity, as in the single case in which low signal was seen near the saccule in an individual with ipsilateral benign paroxysmal positional vertigo but in none of the cases without a peripheral vestibular disorder. In cases with utricular endolymphatic hydrops, flow void artifacts may appear differently compared with normal ears. Changes in inner ear signal intensity, for instance in cases with dysfunction of the utricular macula (vestibular neuritis) or intralabyrinthine schwannoma, could benefit from more precise localization of affected inner ear structures. More precise localization of signal abnormalities can aid clinicians treating patients with inner ear abnormalities.

CONCLUSIONS

In this study, we identified foci of low signal intensity in the vestibule in T2-weighted spin-echo MR images. While some areas of low signal corresponded on histology to structures like the lateral semicircular canal crista and the utricular macula, others corresponded to the fluid-filled endolymphatic space of the utricle. We hypothesize that these latter areas are artifacts caused by fluid movements in the endolymphatic space and could result from magneto-hydrodynamic Lorentz forces.

ACKNOWLEDGMENTS

The authors thank Joseph B. Nadol Jr and MengYu Zhu from the National Institute on Deafness and Other Communication

Disorders National Temporal Bone, Hearing and Balance Pathology Registry Resource (U24DC013983-01) for access to the histologic preparations and for their support in 2020. We also thank Margit Kirschbaum for her technical help and are grateful for the dedicated work of 3 anonymous reviewers.

Disclosure forms provided by the authors are available with the full text and PDF of this article at www.ajnr.org.

REFERENCES

1. Lopez-Escamez JA, Attye A. **Systematic review of magnetic resonance imaging for diagnosis of Meniere disease.** *J Vestib Res* 2019;29:121–29 CrossRef Medline
2. Pyykko I, Zou J, Poe D, et al. **Magnetic resonance imaging of the inner ear in Meniere's disease**. *Otolaryngol Clin North Am* 2010;43:1059–80 CrossRef Medline
3. Gerb J, Ahmadi SA, Kierig E, et al. **VOLT: a novel open-source pipeline for automatic segmentation of endolymphatic space in inner ear MRI.** *J Neurol* 2020;267:185–96 Medline
4. Oehler MC, Schmalbrock P, Chakeres D, et al. **Magnetic susceptibility artifacts on high-resolution MR of the temporal bone.** *AJNR Am J Neuroradiol* 1995;16:1135–43 Medline
5. Lane JI, Ward H, Witte RJ, et al. **3-T imaging of the cochlear nerve and labyrinth in cochlear-implant candidates: 3D fast recovery fast spin-echo versus 3D constructive interference in the steady state techniques.** *AJNR Am J Neuroradiol* 2004;25:618–22 Medline
6. Naganawa S, Koshikawa T, Fukatsu H, et al. **MR cisternography of the cerebellopontine angle: comparison of three-dimensional fast asymmetrical spin-echo and three-dimensional constructive interference in the steady-state sequences.** *AJNR Am J Neuroradiol* 2001;22:1179–85 Medline
7. Fedorov A, Beichel R, Kalpathy-Cramer J, et al. **3D Slicer as an image computing platform for the Quantitative Imaging Network.** *Magn Reson Imaging* 2012;30:1323–41 CrossRef Medline
8. Mugler JP, 3rd, Bao S, Mulkern RV, et al. **Optimized single-slab three-dimensional spin-echo MR imaging of the brain.** *Radiology* 2000;216:891–99 CrossRef Medline
9. Ucar M, Guryildirim M, Tokgoz N, et al. **Evaluation of aqueductal patency in patients with hydrocephalus: three-dimensional high-sampling-efficiency technique (SPACE) versus two-dimensional turbo spin echo at 3 Tesla.** *Korean J Radiol* 2014;15:827–35 CrossRef Medline
10. Lisanti C, Carlin C, Banks KP, et al. **Normal MRI appearance and motion-related phenomena of CSF.** *AJR Am J Roentgenol* 2007;188:716–25 CrossRef Medline
11. Kartal MG, Algin O. **Evaluation of hydrocephalus and other cerebrospinal fluid disorders with MRI: an update.** *Insights Imaging* 2014;5:531–41 CrossRef Medline
12. Bradley WG Jr, Scalzo D, Queralt J, et al. **Normal-pressure hydrocephalus: evaluation with cerebrospinal fluid flow measurements at MR imaging.** *Radiology* 1996;198:523–29 CrossRef Medline
13. Sherman JL, Citrin CM. **Magnetic resonance demonstration of normal CSF flow.** *AJNR Am J Neuroradiol* 1986;7:3–6 Medline
14. Algin O, Turkbey B, Ozmen E, et al. **Evaluation of spontaneous third ventriculostomy by three-dimensional sampling perfection with application-optimized contrasts using different flip-angle evolutions (3D-SPACE) sequence by 3T MR imaging: preliminary results with variant flip-angle mode.** *J Neuroradiol* 2013;40:11–18 CrossRef Medline
15. Obrist D. **Flow phenomena in the inner ear.** *Annu Rev Fluid Mech* 2019;51:487–510 CrossRef
16. Roberts DC, Marcelli V, Gillen JS, et al. **MRI magnetic field stimulates rotational sensors of the brain.** *Curr Biol* 2011;21:1635–40 CrossRef Medline
17. Ward BK, Roberts DC, Otero-Millan J, et al. **A decade of magnetic vestibular stimulation: from serendipity to physics to the clinic.** *J Neurophysiol* 2019;121:2013–19 CrossRef Medline
18. Bradley WG Jr. **Carmen lecture: flow phenomena in MR imaging.** *AJR Am J Roentgenol* 1988;150:983–94 CrossRef Medline
19. Buki B, Mair A, Pogson JM, et al. **Three-dimensional high-resolution temporal bone histopathology identifies areas of vascular vulnerability in the inner ear.** *Audiol Neurootol* 2022;27:249–59 CrossRef Medline
20. Buki B, Ward BK. **Length of the narrow bony channels may not be the sole cause of differential involvement of the nerves in vestibular neuritis.** *Otol Neurotol* 2021;42:e918–24 CrossRef Medline

Exploratory Study of the Brain Response in Facial Synkinesis after Bell Palsy with Systematic Review and Meta-analysis of the Literature

N.A. Krane, M. Loyo, J. Pollock, M. Hill, C.Z. Johnson, and A.A. Stevens

ABSTRACT

BACKGROUND: Facial synkinesis, characterized by unintentional facial movements paired with intentional movements, is a debilitating sequela of Bell palsy.

PURPOSE: Our aim was to determine whether persistent peripheral nerve changes arising from Bell palsy result in persistent altered brain function in motor pathways in synkinesis.

DATA SOURCES: A literature search using terms related to facial paralysis, Bell palsy, synkinesis, and fMRI through May 2021 was conducted in MEDLINE and EMBASE. Additionally, an fMRI study examined lip and eyeblink movements in 2 groups: individuals who fully recovered following Bell palsy and individuals who developed synkinesis.

STUDY SELECTION: Task-based data of the whole brain that required lip movements in healthy controls were extracted from 7 publications. Three studies contributed similar whole-brain analyses in acute Bell palsy.

DATA ANALYSIS: The meta-analysis of fMRI in healthy control and Bell palsy groups determined common clusters of activation within each group using activation likelihood estimates. A separate fMRI study used multivariate general linear modeling to identify changes associated with synkinesis in smiling and blinking tasks.

DATA SYNTHESIS: A region of the precentral gyrus contralateral to the paretic side of the face was hypoactive in synkinesis during lip movements compared with controls. This region was centered in a cluster of activation identified in the meta-analysis of the healthy controls but absent from individuals with Bell palsy.

LIMITATIONS: The meta-analysis relied on a small set of studies. The small sample of subjects with synkinesis limited the power of the fMRI analysis.

CONCLUSIONS: Premotor pathways show persistent functional changes in synkinesis first identifiable in acute Bell palsy.

ABBREVIATIONS: ALE = activation likelihood estimate; BLINK = eye blinking; BP = Bell palsy; HC = healthy controls; PoC = postcentral gyrus; PrC = precentral gyrus; SMILE = smiling; REST = rest blocks

Facial synkinesis is characterized by unintentional facial movements occurring simultaneously with intentional movements and develops weeks or months after facial nerve injury, most commonly following Bell palsy (BP). Periocular, midface, perioral, chin, and neck muscles can all be affected by synkinesis. Most commonly, facial synkinesis manifests as inadvertent lip movement during blinking or unintentional eye closure with smiling (Online Supplemental Data). The smile is frequently affected; patients often have uncoordinated activation of oral elevators and depressors, resulting in a lack of oral commissure elevation. The resulting asymmetric appearance of the face and uncoordinated facial movements impair facial expressions and conveyance of emotions, thereby negatively impacting a patient's social life, work life, and self-image, which may lead to social isolation.[1]

Although the initial lesion in BP localizes outside the CNS, there is evidence that injury extends to the facial nucleus in the pontine

Received January 24, 2022; accepted after revision June 28.

From the Division of Facial Plastic and Reconstructive Surgery (N.A.K., M.L., C.Z.J.), Department of Otolaryngology–Head and Neck Surgery; Division of Neuroradiology (J.P.), Department of Diagnostic Radiology; and Advanced Imaging Research Center (A.A.S.), Oregon Health & Science University, Portland, Oregon; and Department of Otolaryngology–Head and Neck Surgery (M.H.), University of Colorado Anschutz Medical Campus, Aurora, Colorado.

This work was supported by the OHSU Shared Resources Core Pilot Program, and by NIH S10OD021701 and NIH S10OD018224 for imaging and computing resources in OHSU's Advanced Imaging Research Center.

Please address correspondence to Alexander A. Stevens, PhD, Advanced Imaging Research Center, Oregon Health & Science University, 3181 SW Sam Jackson Park Rd, Portland, OR 97239; e-mail: stevenal@ohsu.edu; @axlander1

Indicates article with online supplemental data.

http://dx.doi.org/10.3174/ajnr.A7619

brainstem, resulting in disorganized motor neuron axonal projections and loss of somatotopic organization.[2,3] In animal models, injury of the facial nerve results in loss of somatotopic organization of the facial nucleus.[2] The degree of somatotopic reorganization depends on the degree of injury and may contribute to abnormal recovery from BP and the development of synkinesis.[4,5] Furthermore, synkinesis is thought to occur secondary to both aberrant peripheral nerve regeneration and neuronal reorganization in the facial nucleus following recovery from the original facial nerve injury.[6] CNS alterations may, therefore, reflect compensatory mechanisms compounding the peripheral nerve abnormality that patients with synkinesis experience, but this idea has not yet been explored.

Although there are data indicating that CNS changes occur in patients with BP in the acute phase of illness,[7-9] which may persist in some brain regions following recovery,[9] there are scarce data on the changes in the brain due to synkinesis.[10] In this study, we used fMRI during motor tasks that elicit facial synkinesis to characterize the brain changes associated with synkinesis. We first performed a meta-analysis of fMRI studies of facial movements in healthy controls (HC) and individuals scanned during acute BP to identify brain regions where there was convergent validation of brain activity specifically related to lip movements. Then, using fMRI to study facial movements in participants with synkinesis and those who had fully recovered following BP (control), we tested whether activation differences between the synkinesis and control groups converged on the regions identified in the meta-analysis. We hypothesized that synkinesis reflects persistent alterations in brain somatomotor pathways reported to be affected by BP; therefore, areas consistent with BP-related changes may also be affected in synkinesis.

MATERIALS AND METHODS

Systematic Review

A literature search using the Medical Subject Headings search terms, "facial paralysis," "bells palsy," "facial nerve disease," "facial nerve paralysis," "synkinesis," "facial nerve," "MR imaging," "brain mapping," "fmri," "hemifacial," was conducted from 1990 to May 5, 2020, to identify articles published in MEDLINE and EMBASE. Articles with only abstracts available, nonhuman studies, and non-English articles were excluded. Three independent investigators (N.A.K, M.L, and A.A.S.) reviewed the articles and collected data on standardized forms following the Preferred Reporting Items for Systematic Reviews and Meta-Analyses guidelines. Inclusion criteria required studies that performed whole-brain analyses, used tasks requiring lip movement (smiling or lip pursing), and were contrasted to a resting condition; included participants with a history of BP and/or healthy individuals; and included BP participants imaged during the acute phase of illness. Studies were excluded if they were performed using a priori ROI-based analyses, rather than whole-brain analysis. While ROI-based studies are typically well-justified as a way to control statistical power and test specific hypotheses,[9,11] they cannot be used in the meta-analysis because they introduce spatial biases associated with the selected brain regions.

Whole-Brain Meta-analysis

The meta-analysis of fMRI studies of facial movements in HC and BP groups was performed using the GingerALE software (Versions 3.0.2; http://www.brainmap.org).[12-14] This approach estimates the above-chance probability of spatial clustering of activation loci from separate experiments compared with a random distribution across the spatial extent of the brain.[13] The activation likelihood estimate (ALE) determines the spatial consistency across studies analyzed. The activation peaks of each study are modeled as spatial Gaussian distributions weighted by the sample size of the study. The distributions across studies estimate the modeled activation at each voxel.[14] The resulting ALE is compared with a probability of a null distribution generated by a permutation test (1000 permutations).[14] ALE maps are thresholded using a cluster-level family-wise error and a cluster-size threshold to reduce the probability of false-positive clusters.

Data in the included studies from the meta-analysis were converted into the Montreal Neurological Institute Colin27 template (http://neuro.debian.net/pkgs/mni-colin27-nifti.html) coordinate space. Data from BP groups were aligned so that the paretic side was on the left side of the body. For the studies that reported alignment of the paretic side of the face on the right, the left/right x-coordinates were flipped (positive-negative) for consistency.

Exploratory fMRI Study Methods

The study was approved by the Oregon Health & Science University institutional review board. Participants were identified for recruitment by searching the electronic medical record for International Classification of Diseases codes consistent with the diagnosis of BP.

Participants

Individuals were screened for eligibility on the basis of the following criteria: >1 year from the onset of BP and 18 years of age or older. Participants were excluded if pregnant, lacked decision-making capacity, were unable to safely undergo MR imaging, and/or had a history of viral skin lesions, epilepsy, dementia, brain tumors, multiple sclerosis, or stroke. Two groups of participants were enrolled: individuals with synkinesis following BP and a control group who fully recovered following BP.

All participants provided informed consent and underwent clinical assessment of their facial function, including photography/videography to capture the face at rest and during smiling and eye blinking. Photographs and videos were evaluated to assess facial function using the electronic clinician-graded facial function scale (eFACE; https://eface.ai/).[15] eFACE provides reliable and reproducible measurements of facial function and disfigurement in those with facial paralysis.[15] Additionally, participants completed the Synkinesis Assessment Questionnaire, a validated patient-graded instrument designed to assess facial synkinesis.[16] Hand dominance was assessed by the Edinburgh Handedness Inventory.[17]

Image Acquisition

Scanning took place at OHSU's Advanced Imaging Research Center using a 3T Magnetom Prisma whole-body scanner (Siemens), fitted with a 32-channel head coil. A T1-weighted MPRAGE anatomic scan was acquired with the following parameters: TR/TE = 2.4 sec/2.22 ms, TI = 1.0 sec, flip angle = 8°, matrix = 320 × 300, FOV = 320 × 300, section orientation = sagittal, voxel size = 1.0 × 1.0 × 0.8 mm. fMRI data consisted of 4–6 EPI blood oxygen level–

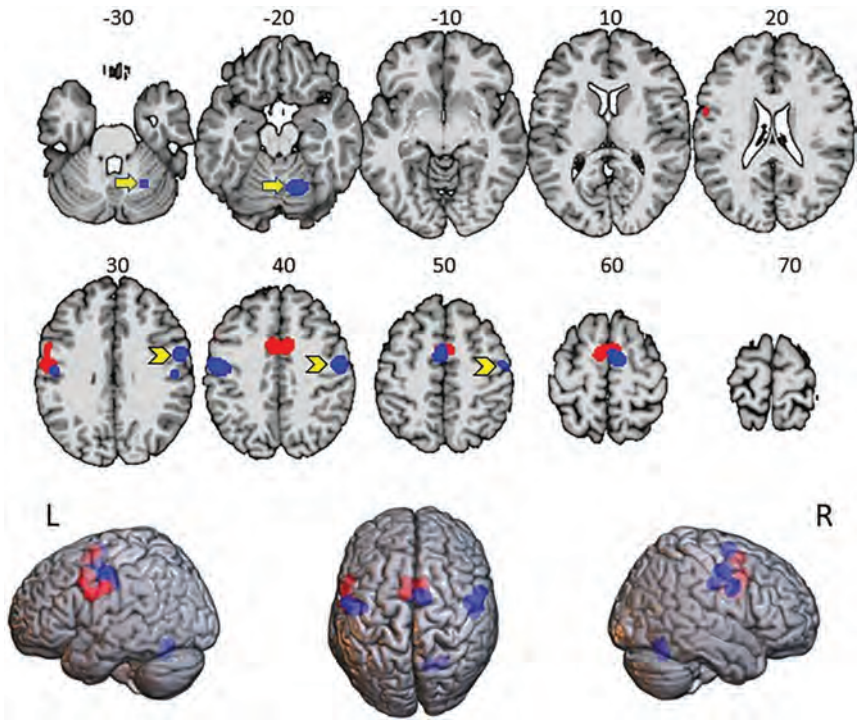

FIG 1. ALE of the foci for HC studies (blue) from the 5 separate studies ($n = 103$) and BP studies (red) from 3 separate studies ($n = 78$). *Yellow arrows* indicate the location of significant ALE in the cerebellum of the HC group. *Yellow chevrons* indicate significant ALE in the left precentral gyrus, exclusively in the HC analysis. The *lower row* shows the same results on glass brains. Numbers indicate Montreal Neurological Institute z-coordinates. Left (L) is on left. R indicates right.

dependent scans. Scans were acquired with the following parameters: TR/TE = 2000/30 ms, flip angle = 90°, slices = 35, in-plane resolution = 2 × 2 mm, section thickness = 2 mm, volumes = 140, acquisition time = 4 minutes 46 seconds.

Participants practiced and then performed a series of motor tasks during fMRI acquisition. Each scan contained alternating blocks of bilateral eye blinking (BLINK) and smiling (SMILE) separated by rest blocks (REST). These specific movements were chosen given the high likelihood of involvement of the smile and/or blepharospasm in facial synkinesis. Each block was 16 seconds long and repeated 5 times during each scan. A recorded message presented through MR imaging–compatible in-ear speakers (http://www.sensimetrics.com, model S-15) spoke "ready" 2 seconds before the onset of each block and then repeated the gesture to be executed (SMILE or BLINK) at 0.5 Hz during the task blocks to maintain a similar cadence between all participants. A "rest" command was presented at the beginning of the REST block.

The fMRI data were preprocessed and analyzed using the Analysis of Functional Neuro Images (AFNI) software suite (https://afni.nimh.nih.gov/). Slices from each volume were temporally aligned to account for differences in section time acquisition, motion corrected by realigning each volume to the minimum outlier volume from each fMRI time-series, and then aligned to the high-resolution anatomic volume. All runs were concatenated and voxel intensities were normalized and spatially smoothed with a 5.0-mm Gaussian filter. The 6 motion estimates and their derivatives were entered as nuisance regressors into the model. Volume-to-volume displacements of >0.3 mm in each time-series were censored in the regression model. The "ready" and "REST" signals were included as nuisance variables. The regressors for SMILE and BLINK were separately modelled with a canonical hemodynamic response function convolved with the task blocks. The data were aligned to the Montreal Neurological Institute 152_2009c template using linear and nonlinear warps to permit group-level data analysis. Synkinesis data were aligned with the synkinetic side on the left of the body.

Statistical analyses of the fMRI data were first performed at the subject-level and then entered into a group-level analysis using a linear mixed-effects analysis with 1 between-groups (control, synkinesis) factor and 1 (SMILE, BLINK) within-groups factor.[18] A spatial threshold filter of 100 contiguous voxels was applied, and the family-wise error significance threshold was set to $P < .005$.

RESULTS

Systematic Review and Whole-Brain Meta-analysis

Following the Preferred Reporting Items for Systematic Reviews and Meta-Analyses guidelines, 14 articles were identified for full review (Online Supplemental Data). For the final meta-analysis, task-based data involving smiling were extracted from 7 publications, of which 5 studies included HC groups (Buendia et al;[19] Calistri et al;[20] Hesselmann et al;[21] Song et al;[11] Wang et al[22]) with a total combined sample size of 103 participants and 33 separate foci reported. Three studies contributed whole-brain analysis of acute BP participants (Calistri et al;[20] Klingner et al;[23] Klingner et al[24]) with a total combined sample of 78 BP participants and 60 foci reported across paretic and nonparetic sides (Online Supplemental Data).

The meta-analyses for the HC and BP studies were performed separately. In the HC group analysis, we identified 4 major clusters associated with lip movements (Fig 1 and Online Supplemental Data): 1) the left hemisphere comprising foci in the precentral gyrus (PrC) and postcentral gyrus (PoC); 2) along the medial wall of the prefrontal cortex; and 3) the left hemisphere, analogous to the first cluster, including the PrC and PoC; and 4) the right cerebellum.

The BP meta-analysis showed substantial overlap with the HC group in the left hemisphere (Fig 1 and Online Supplemental Data) ipsilateral to the paretic side, including the PrC and extending anteriorly into the middle frontal gyrus. The second cluster was detected along the medial wall of the prefrontal cortex, similar to the findings in the HC studies. A third cluster lay anterior and inferior to the second cluster in the anterior cingulate gyrus.

A random-effects conjunction analysis of ALE maps[14] from the HC and BP groups indicated consistency between the groups along the medial wall of the frontal lobe (Online Supplemental Data). A

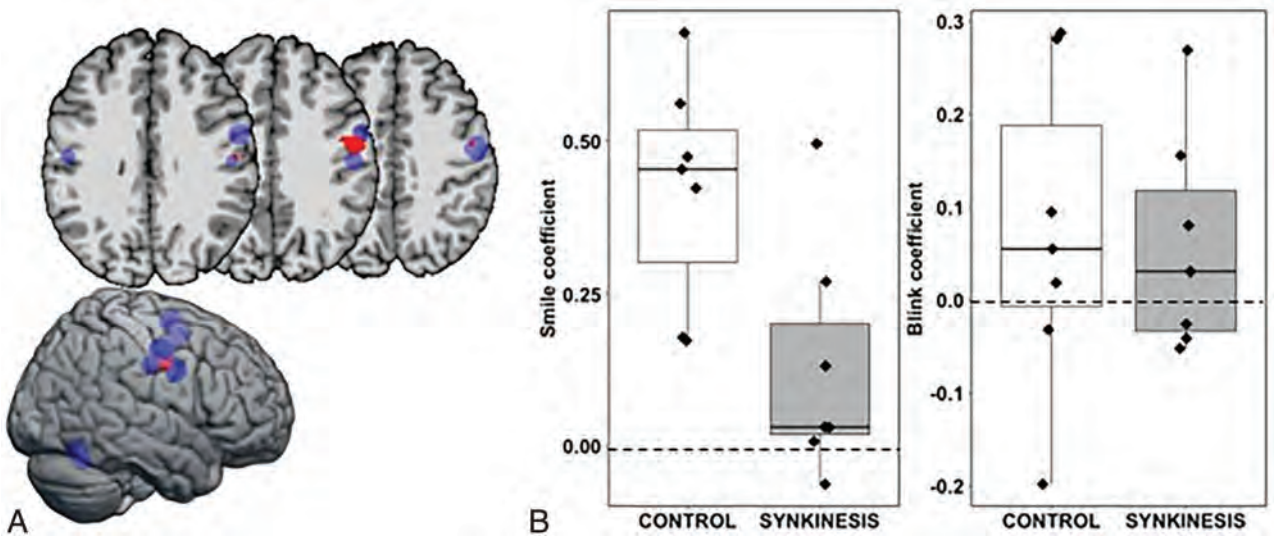

FIG 2. *A*, Significant group (control, synkinesis) by condition (SMILE, BLINK) interaction ($P < .005$) (red). The ROI falls in the precentral gyrus and central sulcus in the right hemisphere contralateral to the synkinetic side of the face (Montreal Neurological Institute coordinates: x = 55, y = 7, z = 35). HC clusters from the meta-analysis are shown for reference (blue). *B*, Boxplots of the regression coefficients for the SMILE condition and BLINK condition by group.

second volume of conjunction appeared in the left hemisphere at the junction of the PrC and PoC (Online Supplemental Data). A contrast analysis performed to identify differences between the groups detected no significant differences between clusters. Nevertheless, we noted in the BP group analysis no detection of a cluster in the right PrC and PoC areas, as was observed in the HC analysis.

Results of the fMRI Study

A total of 14 subjects, all right-handed, were included in the study; 7 subjects (1 woman) in the control group (61 [SD, 12] years of age) and 7 subjects (6 women) in the synkinesis group (60 [SD, 15] years of age). The control mean Synkinesis Assessment Questionnaire was 23.2 (SD, 4.77), compared with 73.3 (SD, 20.16) ($P < .01$) in synkinesis, consistent with facial synkinesis. The mean eFACE synkinesis score was 99.0 (SD, 1.91) in the control group and 70.6 (SD, 16.1) in the synkinesis group ($P < .01$), while the mean eFACE dynamic score was 97.9 (SD, 1.78) in the control group and 77.0 (16.1) in the synkinesis group ($P = .02$), confirming synkinesis and asymmetry with movement in the synkinesis group.

Using fMRI, the SMILE task produced greater signal change than BLINK bilaterally in the somatomotor areas, with activation foci centered on the central sulcus and the BLINK task producing greater signal change in the medial occipital cortex in areas corresponding to primary and secondary visual areas (Online Supplemental Data). The control group demonstrated greater activation across both SMILE and BLINK tasks in the medial supplementary motor cortex (Online Supplemental Data).

A single cluster associated with a group by task interaction was detected in the right PrC extending into the central sulcus, contralateral to the synkinetic side of the face (Fig 2). The interaction effect was examined by extracting β coefficients from the right PrC cluster for each subject, revealing that the synkinesis group had significantly lower signal in the SMILE condition compared with controls (Wilcoxon sum rank test: W = 42, $P = .026$) but did not differ under the BLINK condition (W = 28, $P = .710$) (Fig 2). No clusters associated with the BLINK task differed between the 2 groups.

DISCUSSION

Facial paralysis and synkinesis following BP alter the functional brain response in similar somatomotor cortical areas. A meta-analysis to identify common areas of activation by lip movements in healthy individuals and individuals with acute BP revealed that the PrC area active in HC studies was absent contralateral to the paretic side of the face in BP. In the fMRI study of synkinesis, the same PrC location contralateral to the synkinetic side of the face had significantly decreased signal, but only during the SMILE task (Online Supplemental Data and Figs 1 and 2). This finding in synkinesis suggests that that PrC changes are linked with aberrant nerve fiber regeneration and facial nucleus changes thought to be responsible for disorganized facial movements.[6] Together with the meta-analysis of BP, the data suggest that synkinesis may reflect chronic changes in the PrC associated with the early effects of acute BP shown in prior studies, while hypoactivity in the Supplementary Motor Area (SMA) may reflect generalized chronic changes.

Previous fMRI studies of acute BP using both whole-brain and ROI analyses characterized changes in the brain during mouth movements as decreased signal in the somatomotor areas contralateral to the paretic side of the face.[7,23] Smit et al[9] demonstrated that as recovery progressed following BP, activation increased in the somatomotor region contralateral to the affected side of the face. However, in synkinesis, the hypoactivity in the PrC appeared to persist (Fig 2 and Online Supplemental Data). Changes in the CNS arising from peripheral nerve damage have been documented in several sensory pathways; for example, phantom limb sensations in upper limb amputation alter contralateral somatomotor areas[25] and tinnitus affects the organization

of auditory cortical fields.[26] In these cases, there is evidence of remodeling within somatotopic sensory areas[27] and in auditory cortical and subcortical pathways,[28] respectively. A study of the effects of movement restriction for 2 weeks using casting of a healthy arm led to decreased connectivity between the ipsilateral and contralateral somatomotor areas, which returned to normal following removal of the cast.[29] Similarly, there is evidence to support CNS involvement and cortical changes in BP, a disorder secondary to pure peripheral motor deafferentation without an effect on sensory afferents[7-9,11,23] and the restoration of signal following recovery from BP.[9] The results of the meta-analysis and synkinesis study indicate that the contralateral PrC in BP and synkinesis may be a common node; how the changes seen in the PrC during acute BP are linked to the aberrant innervation of facial musculature in synkinesis remains unclear. The PrC sits at the apex of the motor system, and its hypoactivity may reflect functional changes at multiple levels of the motor pathway.[9,22,24]

The study has several limitations. While there appears to be continuity between changes observed in the PrC from the BP meta-analysis and the fMRI study evaluating synkinesis, how this hypoactivity relates to peripheral changes and synkinesis is unknown. Additionally, the meta-analysis relied on a small set of studies that qualified for the analysis. Therefore, the relatively weak power of the analysis likely underestimated the brain locations affected by acute BP. The failure to detect significant activation clusters that differed between the BP and HC groups was also likely a reflection of the small sample sizes of the studies. The fMRI study also relied on a small sample and had limited statistical power. Consequently, changes in other cortical and subcortical areas may not have been detected. Additionally, the task design of simple lip movements and blinking provided a test of changes in hemodynamic function linked to these facial gestures and was consistent with prior studies of BP, providing a first step in examining the effects of synkinesis.

CONCLUSIONS

Premotor pathways show persistent functional changes in synkinesis, some of which are first identifiable in acute BP. The changes observed in the brains of participants with synkinesis likely reflect a confluence of neurophysiologic and behavioral adaptations to synkinesis. Understanding the CNS response to peripheral nerve injury and its sequelae can lead to improved clinical practices that enhance adaptation.

Disclosure forms provided by the authors are available with the full text and PDF of this article at www.ajnr.org.

REFERENCES

1. Husseman J, Mehta RP. **Management of synkinesis.** *Facial Plast Surg* 2008;24:242–49 CrossRef Medline
2. Angelov DN, Neiss WF, Streppel M, et al. **Nimodipine accelerates axonal sprouting after surgical repair of rat facial nerve.** *J Neurosci* 1996;16:1041–48 CrossRef Medline
3. Choi D, Raisman G. **Somatotopic organization of the facial nucleus is disrupted after lesioning and regeneration of the facial nerve: the histological representation of synkinesis.** *Neurosurgery* 2002;50:355–62; discussion 362–63 CrossRef Medline
4. Yagi N, Nakatani H. **Crocodile tears and thread test of lacrimation.** *Ann Otol Rhinol Laryngol Suppl* 1986;122:13–16 CrossRef Medline
5. Baker RS, Stava MW, Nelson KR, et al. **Aberrant reinnervation of facial musculature in a subhuman primate: a correlative analysis of eyelid kinematics, muscle synkinesis, and motoneuron localization.** *Neurology* 1994;44:2165–73 CrossRef Medline
6. Moran CJ, Neely JG. **Patterns of facial nerve synkinesis.** *Laryngoscope* 1996;106:1491–96 CrossRef Medline
7. Klingner CM, Volk GF, Maertin A, et al. **Cortical reorganization in Bell's palsy.** *Restor Neurol Neurosci* 2011;29:203–14 CrossRef Medline
8. Rijntjes M, Tegenthoff M, Liepert J, et al. **Cortical reorganization in patients with facial palsy.** *Ann Neurol* 1997;41:621–30 CrossRef Medline
9. Smit A, van der Geest J, Metselaar M, et al. **Long-term changes in cerebellar activation during functional recovery from transient peripheral motor paralysis.** *Exp Neurol* 2010;226:33–39 CrossRef Medline
10. Wang Y, Wang WW, Hua XY, et al. **Patterns of cortical reorganization in facial synkinesis: a task functional magnetic resonance imaging study.** *Neural Regen Res* 2018;13:1637–42 CrossRef Medline
11. Song W, Cao Z, Lang C, et al. **Disrupted functional connectivity of striatal sub-regions in Bell's palsy patients.** *Neuroimage Clin* 2017;14:122–29 CrossRef Medline
12. Turkeltaub PE, Eickhoff SB, Laird AR, et al. **Minimizing within-experiment and within-group effects in activation likelihood estimation meta-analyses.** *Hum Brain Mapp* 2012;33:1–13 CrossRef Medline
13. Eickhoff SB, Bzdok D, Laird AR, et al. **Activation likelihood estimation meta-analysis revisited.** *Neuroimage* 2012;59:2349–61 CrossRef Medline
14. Eickhoff SB, Laird AR, Grefkes C, et al. **Coordinate-based activation likelihood estimation meta-analysis of neuroimaging data: a random-effects approach based on empirical estimates of spatial uncertainty.** *Hum Brain Mapp* 2009;30:2907–26 CrossRef Medline
15. Banks CA, Bhama PK, Park J, et al. **Clinician-graded Electronic Facial Paralysis Assessment: the eFACE.** *Plast Reconstr Surg* 2015;136:223e–30e CrossRef Medline
16. Mehta RP, WernickRobinson M, Hadlock TA. **Validation of the Synkinesis Assessment Questionnaire.** *Laryngoscope* 2007;117:923–26 CrossRef Medline
17. Oldfield RC. **The assessment and analysis of handedness: the Edinburgh Inventory.** *Neuropsychologia* 1971;9:97–113 CrossRef Medline
18. Chen G, Saad ZS, Britton JC, et al. **Linear mixed-effects modeling approach to FMRI group analysis.** *Neuroimage* 2013;73:176–90 CrossRef Medline
19. Buendia J, Loayza FR, Luis EO, et al. **Functional and anatomical basis for brain plasticity in facial palsy rehabilitation using the masseteric nerve.** *J Plast Reconstr Aesthet Surg* 2016;69:417–26 CrossRef Medline
20. Calistri V, Mancini P, Raz E, et al. **fMRI in Bell's palsy: cortical activation is associated with clinical status in the acute and recovery phases.** *J Neuroimaging* 2021;31:90–97 CrossRef Medline
21. Hesselmann V, Sorger B, Lasek K, et al. **Discriminating the cortical representation sites of tongue and up movement by functional MRI.** *Brain Topogr* 2004;16:159–67 CrossRef Medline
22. Wang Y, Yang L, Wang WW, et al. **Decreased distance between representation sites of distinct facial movements in facial synkinesis: a task fMRI study.** *Neuroscience* 2019;397:12–17 CrossRef Medline
23. Klingner CM, Volk GF, Brodoehl S, et al. **The effects of deefferentation without deafferentation on functional connectivity in patients with facial palsy.** *Neuroimage Clin* 2014;6:26–31 CrossRef Medline
24. Klingner CM, Brodoehl S, Witte OW, et al. **The impact of motor impairment on the processing of sensory information.** *Behav Brain Res* 2019;359:701–08 CrossRef Medline
25. Nikolajsen L, Jensen TS. **Phantom limb pain.** *Br J Anaesth* 2001;87:107–16 CrossRef Medline

26. Kleinjung T, Steffens T, Strutz J, et al. **Curing tinnitus with a cochlear implant in a patient with unilateral sudden deafness: a case report.** *Cases J* 2009;2:7462 CrossRef Medline
27. Lotze M, Flor H, Grodd W, et al. **Phantom movements and pain: an fMRI study in upper limb amputees.** *Brain* 2001;124:2268–77 CrossRef Medline
28. Engineer ND, Moller AR, Kilgard MP. **Directing neural plasticity to understand and treat tinnitus.** *Hear Res* 2013;295:58–66 CrossRef Medline
29. Newbold DJ, Laumann TO, Hoyt CR, et al. **Plasticity and spontaneous activity pulses in disused human brain circuits.** *Neuron* 2020;107:580–86 CrossRef Medline

Imaging Characteristics of CNS Neuroblastoma-*FOXR2*: A Retrospective and Multi-Institutional Description of 25 Cases

A.Tietze, K. Mankad, M.H. Lequin, L. Ivarsson, D. Mirsky, A. Jaju, M. Kool, K.V. Hoff, B. Bison, and U. Löbel

ABSTRACT

BACKGROUND AND PURPOSE: The 5th edition of the World Health Organization Classification of CNS tumors defines the CNS neuroblastoma *FOXR2* in the group of embryonal tumors. Published clinical outcomes tend to suggest a favorable outcome after resection, craniospinal irradiation, and chemotherapy. This multicenter study aimed to describe imaging features of CNS neuroblastoma-*FOXR2*, which have been poorly characterized thus far.

MATERIALS AND METHODS: On the basis of a previously published cohort of tumors molecularly classified as CNS neuroblastoma-*FOXR2*, patients with available imaging data were identified. The imaging features on preoperative MR imaging and CT data were recorded by 8 experienced pediatric neuroradiologists in consensus review meetings.

RESULTS: Twenty-five patients were evaluated (13 girls; median age, 4.5 years). The tumors were often large (mean, 115 [SD, 83] mL), showed no (24%) or limited (60%) perilesional edema, demonstrated heterogeneous enhancement, were often calcified and/or hemorrhagic (52%), were always T2WI-hyperintense to GM, and commonly had cystic and/or necrotic components (96%). The mean ADC values were low (687.8 [SD 136.3] $\times$ 10^{-6} mm^2/s). The tumors were always supratentorial. Metastases were infrequent (20%) and, when present, were of nodular appearance and leptomeningeal.

CONCLUSIONS: In our cohort, CNS neuroblastoma *FOXR2* tumors showed imaging features suggesting high-grade malignancy and, at the same time, showed characteristics of less aggressive behavior. There are important differential diagnoses, but the results of this study may assist in considering this diagnosis preoperatively.

ABBREVIATIONS: ATRT = atypical teratoid/rhabdoid tumors; CNS NB-*FOXR2* = CNS neuroblastoma *FOXR2*-activated; CNS-PNET = primitive neuroectodermal tumors of the CNS; ETMR = embryonal tumor with multilayered rosettes; ITD = internal tandem duplication; WHO = World Health Organization

In the recent 5th edition of the World Health Organization (WHO) Classification of CNS Tumors, published in 2021,[1] the CNS neuroblastoma *FOXR2*-activated (CNS NB-*FOXR2*) has been included as a new entity in the group of embryonal tumors that are highly malignant CNS tumors mainly occurring in children, adolescents, or young adults.[2] In the 2016 update of the WHO Classification, the embryonal tumors had emerged from the primitive neuroectodermal tumors of the CNS (CNS-PNET), which were replaced after an increasing number of molecular markers and genetic alterations had substantially advanced diagnostic specificity. In their important re-analysis of previously diagnosed CNS-PNET using DNA methylation profiles, Sturm et al[3] were able to show that this group of tumors is highly heterogeneous, consisting of many known entities, eg, medulloblastoma, embryonal tumor with multilayered rosettes (ETMR), or atypical teratoid/rhabdoid tumors (ATRT) among others. In

Received March 28, 2022; accepted after revision July 27.

From the Institute of Neuroradiology (A.T.) and Department of Pediatric Oncology and Hematology (K.V.H.), Charité–Universitätsmedizin Berlin, corporate member of Freie Universität Berlin and Humboldt-Universität zu Berlin, Berlin, Germany; Department of Radiology (K.M., U.L.), Great Ormond Street Hospital, London, UK; Department of Radiology (M.H.L.), University Medical Center Utrecht, Utrecht, the Netherlands; Department of Pediatric Radiology (L.I.), Queen Silvias Children´s Hospital, Sahlgrenska University Hospital, Gothenburg, Sweden; Department of Pediatric Radiology and Imaging (D.M.), Children's Hospital Colorado, Denver, Colorado; Department of Medical Imaging (A.J.), Ann and Robert H. Lurie Children's Hospital of Chicago, Chicago, Illinois; Hopp Children's Cancer Center (M.K.), Heidelberg, Germany; Division of Pediatric Neurooncology (M.K.), German Cancer Research Center and German Cancer Consortium, Heidelberg, Germany; Princess Máxima Center for Pediatric Oncology (M.K.), Utrecht, the Netherlands; and Department of Neuroradiology (B.B.), University Hospital Augsburg, Ausburg, Germany.

A. Tietze and K. Mankad shared first authorship.

B. Bison and U. Löbel shared last authorship.

This work was supported by the German Research Foundation (DFG, SFB295RETUNE).

Please address correspondence to Anna Tietze, MD, Institute of Neuroradiology, Charité–Universitätsmedizin Berlin, corporate member of Freie Universität Berlin and Humboldt-Universität zu Berlin, Augustenburger Platz 1, D. 13353 Berlin, Germany; e-mail: anna.tietze@charite.de

http://dx.doi.org/10.3174/ajnr.A7644

addition, DNA methylation analyses revealed several new tumor types in this group, one of which is the CNS NB-*FOXR2*.

Available clinical data so far suggest that favorable rates of overall survival can be achieved for patients with CNS NB-*FOXR2* when treated with surgical resection, craniospinal irradiation, and chemotherapy.[4,5] Imaging characteristics suggesting the diagnosis are currently based on the description of single patients,[6,7] and to the best of our knowledge, larger series are not yet available. The reason is undoubtedly the increasingly detailed tumor classification, which results in a low incidence of confirmed cases in single centers and makes international collaboration essential to pool imaging data.

The aim of this article was to describe the imaging characteristics of CNS NB-*FOXR2* based on an international patient cohort and, at the same, establish a practical approach to collect and evaluate larger series across multiple centers.

MATERIALS AND METHODS

The cohort is based on a previously published cohort of pathology samples with the original diagnosis of CNS-PNET, which was subsequently molecularly reclassified as CNS NB-*FOXR2*.[4] This study was evaluated and approved by the ethics board of the coordinating institutions. Molecular diagnosis was confirmed by DNA methylation classification (Version 11b4 or higher; www.molecularneuropathology.org) in each included case.[8] Informed consent was obtained by the patients or legal representatives at the time of the initial study or registry inclusion, or for some centers, the requirement for informed consent was waived. Imaging data for 2 of the cases have been published previously.[6]

The image evaluation team consisted of at least 1 local neuroradiologist. Consensus decisions were made in joint online meetings on a weekly basis for 12 weeks regarding the following characteristics on pseudonymized images: 1) location, 2) cortical and/or WM involvement, 3) assumed tumor origin, 4) calvarial involvement, 5) approximation of volume (calculated [transverse × craniocaudal × anterior-posterior diameter]/2), 6) strength of enhancement compared with the choroid plexus (none, mild, intermediate, strong), 7) extent of enhancement (in categories: 0%, 0%–25%, 25%–50%, 50%–75%, 75%–100%, or 100% of the solid tumor component), 8) T2WI intensity compared with unaffected cortex, 9) susceptibility indicating calcification and/or hemorrhage on gradient-echo imaging (T2* or SWI, potentially further specified by CT, T1WI, T2WI), 10) average $ADC_{minimum}$, ADC_{mean}, $ADC_{maximum}$ values (±SD), in an ROI, 0.14–0.65 cm^2 in size, in visually determined areas with the lowest values, 11) multifocality, 12) multilobulated appearance, 13) the presence/extent of perifocal edema (in categories: none, < 25% of the perimeter, 25%–75%, 100%), 14) the presence of nonsolid components (thin-walled cysts and/or necrotic regions defined as having irregular and thick borders), 15) extent of nonsolid components (in categories: 0%, 0%–25%, 25%–50%, 50%–75%, 75%–100%, or 100% of solid-to-entire tumor), 16) the presence and extent of hydrocephalus (in categories: none, mild with ventricular dilation, moderate with ventricular dilation and periventricular edema, and severe with additional sulcal effacement),[9] and 17) laminar and/or nodular intracranial and/or spinal metastases. Results of arterial spin-labeling perfusion-weighted imaging or MRS were reported when available. Descriptive statistics were used to describe the data including median/interquartile range for non-normally distributed data and mean (SD) for normally distributed nominal data. All other variables were reported as percentages.

RESULTS

Patients

MR imaging data were available for 25 treatment-naïve patients (13 girls) with CNS NB-*FOXR2* diagnosed between 2003 and 2021. The median age was 4.5 years (interquartile range, 3.1–9 years; range, 1.4–16 years).

Imaging

MR imaging data consisted of T1WI, T2WI, FLAIR, and contrast-enhanced T1WI for all patients, gradient-echo imaging (T2* or SWI) for 14 patients, and DWI for 21 patients. Arterial spin-labeling PWI and single-voxel MRS (short TE) were available for 1 patient. All MR images were acquired before total/partial/subtotal tumor resection or treatment initiation. In a single patient, MR imaging was performed after the insertion of an external ventricular drain; all other patients were treatment-naïve. Four patients had a baseline CT scan.

Imaging Features

Results are summarized in the Online Supplemental Data, and representative imaging features in selected patients are shown in Fig 1. Further examples are available in the Online Supplemental Data, and all results are given as Online Supplemental Data. The brain regions most frequently affected were the frontal lobe (72%), followed by the parietal (44%) and temporal (36%) lobes, as well as the basal ganglia (32%). Typically, >1 region was involved. In most cases (80%), 1 or 2 anatomic compartments were involved, mostly the frontal lobe with or without the basal ganglia/thalami. In most cases, the tumor directly abutted the ventricular system without normal tissue seen between the tumor and the ventricular wall. Often, the ventricular wall was infiltrated (64%; Fig 1*A*). In 60% of cases, the right hemisphere was affected. The WM was always infiltrated. In 80% of cases, there was also infiltration of the cortex, while in 20%, the cortex was merely compressed. Generally, we found it difficult to determine the origins of the tumors owing to their large sizes, but assuming that the epicenter of the tumor usually reflects the origin, 52% appeared to originate in the WM, and 32%, in the cortex. In only 8% of cases, did the tumors seem to originate from the deep GM and/or the WM of the internal capsule. None of the cases occurred in the brainstem or the infratentorial compartment.

Calvarial remodeling was found in 48%, associated with calvarial signal changes in 33%. The average tumor size was 115 (SD, 83) mL and was often larger in the 48% of cases with associated skull remodeling and scalloping (148 [SD, 68] mL) compared with cases without remodeling (85 [SD, 87] mL; Fig 1*G*).

In most cases, solid tumor components showed intermediate-but-inhomogeneous enhancement as well as peripheral enhancement of necrotic elements (Fig 1*E*, *-F*) or cyst walls. Dural infiltration was noted in 2 cases.

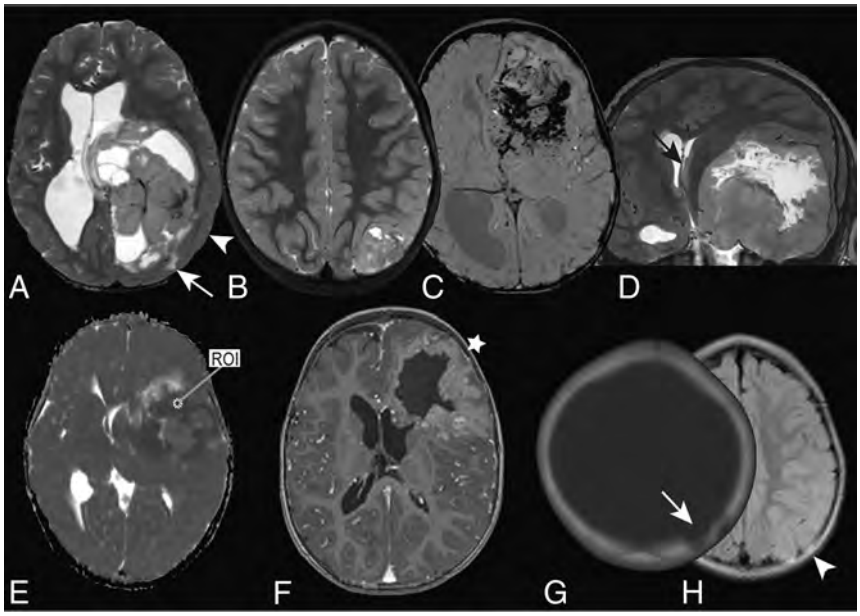

FIG 1. Typical imaging characteristics of CNS NB-*FOXR2* in different patients (*A*, A 2.5-year-old girl; *B*, *G*, *H*, A 3-year-old girl; *C*, A 4.2-year-old girl; *D*, A 16-year-old boy; *E*, A 4-year-old boy; *F*, A 2.7-year-old boy). Most tumors were characterized by T2WI signal heterogeneity but always contained hyperintense regions compared with cortical GM (*A* and *B*). In most, no or-limited perilesional edema (*arrow* in *A*) was found. When gradient-echo images (T2*, SWI) were available, signal loss was detected in about half of the cases (*C*). An example of nodular, leptomeningeal metastases at the foramen of Monro is shown in *D* (*black arrow*). In general, ADC values were relatively low. An example is given in *E*: ADC_{mean} in a ROI placed within the solid tumor component is 660 × 10^{-6} mm^2/s ($ADC_{minimum}$, 550 × 10^{-6} mm^2/s, $ADC_{maximum}$, 760 × 10^{-6} mm^2/s). Contrast enhancement on T1WI was mostly mild to-intermediate compared with the choroid plexus and seen in larger parts of the solid component (*F*). Nonsolid tumor components with thick, irregular borders were often noted representing necrotic regions (*F*). The main tumor load was often located in the WM with compression (*arrowhead* in *A*) or infiltration (*star* in *F*) of the overlying cortex, or it appeared to originate from the cortex (*B*). Skull remodeling was detected in about half of the cases (*arrow* on CT in *G*), often associated with bony signal changes (*arrowhead*, *H*).

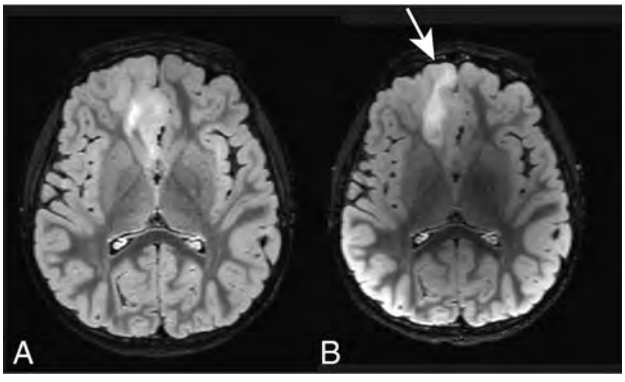

FIG 2. Axial FLAIR of a 4.5-year-old boy presenting with seizures. Initially, a focal cortical dysplasia of the right frontal lobe was proposed (*A*). The follow-up MR imaging 8 months later shows disease progression (*arrow* in *B*). After resection, the diagnosis of a CNS NB-*FOXR2* was made, whereas the diagnosis of a focal cortical dysplasia was dismissed.

In all cases, the solid component was at least in some parts T2WI hyperintense compared with normal cortex but was increasingly heterogeneous in larger tumors (T2WI hyper-, iso-, and hypointense; Fig 1*A*, -*B*).

Signal loss was noted in 43% of cases with available SWI or T2* data (Fig 1*C*). It was not possible to confidently determine the cause of increased susceptibility (hemorrhage versus calcification) even if phase images were available. However, in 3 patients, calcifications were unequivocally identified by CT, and in 1 patient, associated fluid levels confirmed the presence of hemorrhage on MR imaging. Altogether in 48% of cases, calcifications or hemorrhages or both were diagnosed on the basis of a combination of T1WI, T2WI, T2*, SWI, and the B_0 series of DWI data.

ADC values varied considerably between and within tumors (Fig 1*D*), but generally low values were probed in the solid portion, with an average ADC_{mean} of 687.8 (SD, 136.3) × 10^{-6} mm^2/s.

Most tumors showed a multilobulated appearance (64%; Fig 1*A*–*F*), and 20% were multifocal. Perifocal edema was not particularly pronounced and, at most, of intermediate degree. Almost all tumors had nonsolid parts (Fig 1*A*, -*B* and *E*, -*F*) except the second smallest, which had a volume of only 10.5 mL. Unequivocal necrosis with thick, irregular, enhancing walls was diagnosed in 16% of cases (Fig 1*A*, -*E*); cysts, in 25%; and both, in another 25%.

Intracranial metastases were detected in 5 patients (20%), characterized by nodular leptomeningeal disease. One of these patients (a 4.5-year-old boy) also showed intraspinal dissemination.

High lipid and lactate peaks were noted in the enhancing part of the tumor with available MRS (single-voxel, short TE). Enhancing and nonenhancing tumor components showed a decrease in the NAA/Cr ratio (0.8 and 0.96, respectively) and an increase in Cho/NAA (3.12 and 1.74, respectively) and Cho/Cr (2.5 and 1.66, respectively) ratios. CBF was elevated on arterial spin-labeling data in the same patients.

The tumor of 1 patient, a 5-year-old boy presenting with seizures, was initially suspected to represent focal cortical dysplasia based on MR imaging findings (Fig 2*A*). He was treated for epilepsy under regular MR imaging surveillance. After 8 months, interval growth was noted (Fig 2*B*), prompting total resection. A CNS NB-*FOXR2* tumor was diagnosed, whereas the diagnosis of a focal cortical dysplasia was dismissed.

DISCUSSION

CNS NB-*FOXR2* has recently been added as a tumor type in the 2021 WHO Classification of CNS tumors. Therefore, only a few case series describing its imaging features exist.[6,7,10-13] In our international cohort of 25 patients, we found that these were

supratentorial, often large, multilobulated tumors with little-or-no perifocal edema. Tumors nearly always showed a mix of solid and cystic/necrotic components. Involvement of the cortex was present in most cases, and the WM was involved in all patients. Lesions showed intermediate and inhomogeneous contrast enhancement and high vascularity with the presence of hemorrhage and/or calcifications. The epicenter of the tumor appeared to be in the periventricular and subcortical WM or the cortex. In almost half of the cases, the adjacent skull was remodeled with thinning of the inner table, and in some cases, pathologic signal changes in the affected bone were present. The T2WI intensity in the solid parts was heterogeneous, but always hyperintense to GM. The ADC values were relatively low but fluctuated considerably within the solid components. Multifocality and dissemination were seen, but rarely.

CNS NB-*FOXR2* tumors in our cohort showed several imaging features suggesting a high-grade malignancy, such as low ADC values, large volumes, and necrosis. However, they also showed characteristics of less aggressive tumors, including relative T2WI hyperintensity, little perifocal edema, and remodeling of the skull. Imaging characteristics described in our study are not specific, and ependymoma and other embryonal tumors such as ETMR, CNS tumor with *BCOR* internal tandem duplication (CNS *BCOR*-ITD), and ATRT need to be considered in the differential diagnosis. Of these tumors, CNS NB-*FOXR2* is the only type that, to the best of our knowledge, has exclusively presented in a supratentorial location, whereas the other tumor types can develop infratentorially with varying frequencies.[4,10,11,13-19] In addition, patient age may help with differentiation because the median age at diagnosis for patients with CNS NB-*FOXR2* is 5 years (range, 1–20 years), while patients rarely present within the first 2 years of life.[4] In contrast, patients with ATRT are typically younger than 2 years of age, with 33% younger than 1 year of age at diagnosis.[20] ETMR usually presents in the first 4 years of life,[4,21,22] and the median age for presentation with CNS *BCOR*-ITD is 4 years (range, 0.6–22 years). The presentation age for supratentorial ependymomas is highly dependent on the molecular subtype. Supratentorial ependymoma, *YAP1* fusion–positive, occurs at a median age of 1.4 years,[23] while *ZFTA* fusion–positive ependymoma presents at a median age of 8 years (largely overlapping with tumors previously diagnosed as ependymoma, *RELA*-fused).[23,24]

The discrepancy between restricted diffusion, usually attributed to high cellularity, and high signal on T2WI that is typically seen in low-proliferative processes has previously been described in ATRT.[14] High cellularity is, however, only one of several causes for restricted diffusion. The microenvironment, neuropil density, cell size, or nuclear volume fraction may contribute to low ADC values, possibly without necessarily decreasing the T2WI signal.[25] With the current data, we are not able to specify these contributions in more detail. Skull remodeling was found in nearly half of our patients. While this is a relatively common feature in low-grade CNS tumors, we found additional calvarial signal changes in some of these cases, which has also been described at initial diagnosis in ATRT[19] but appears to be rare in other pediatric high-grade tumors.

Only 1 previously published case can be compared with our series[7] because the 2 patients described previously by Holsten et al[6] are included in our cohort. However, because the focus of the case report by Furuta et al[7] was not primarily on imaging characteristics, the comparison remains limited. Furuta et al also found a relatively large, partially enhancing, centrally necrotic tumor with scattered calcification but, in their case, with extensive perilesional edema.

As stated previously, some of the cases we included represent a subcohort of a previously published pathology series of retrospectively re-classified CNS NB-*FOXR2* tumors.[4] In this study of 307 tumors with an initial diagnosis of CNS-PNET, 36 (12%) were classified as CNS NB-*FOXR2* by DNA methylation profiling in this series. In a pooled cohort of 63 patients with CNS NB-*FOXR2*, which included additionally identified cases, the 5-year progression-free survival and overall survival was 63% and 85%.[4] The frequency of relapses was lowest among patients treated with surgical resection and craniospinal irradiation combined with chemotherapy. This finding is in agreement with another published series that includes overlapping patients.[5]

We did not use the Visually AcceSAble Rembrandt Images (VASARI) criteria[26] for our assessments because the criteria were not judged fit for our purpose, too detailed in some respects, and not pediatric-specific.

Due to the retrospective nature of our study, the imaging data were sometimes incomplete (eg, missing DWI and T2*/SWI series). While CT images were especially helpful in verifying calcifications or bony changes, they were only available for 4 patients. In addition, advanced MR imaging may have been useful to characterize the tumors in more detail, eg, by shedding some light on neo-angiogenesis with PWI or on metabolic and microstructural changes by MRS or advanced diffusion-weighted techniques, but the multi-institutional approach and the long inclusion period of >18 years due to the rarity of these tumors precluded the availability of these imaging techniques in this study.

The integrated diagnosis of molecular and morphologic features in CNS tumor diagnostics has radically changed the classification system. The knowledge of an increasing number of molecular profiles and the revision of previous classification groups has entailed and will entail a far more detailed taxonomy. Multicenter collaboration becomes pivotal as cases become rarer, and tumor entities will have to be phenotyped through consensus reading. Our experience with weekly joint online meetings was excellent to achieve this objective.

CONCLUSIONS

We described typical imaging characteristics of CNS NB-*FOXR2* tumors in a multicenter series of 25 patients, the largest to date. Our findings contribute further to the description of new tumor types included in the 5th edition of the WHO Classification of CNS tumors. Important work lies ahead of radiologists to describe and possibly differentiate these emerging entities. Because an increasing subdivision will inevitably be accompanied by fewer cases per center, further multi-institutional reviews will be needed in the future.

ACKNOWLEDGMENTS

We thank Magnus Sabel and Elizabeth Schepke (Queen Silvias Children's Hospital, Sahlgrenska University Hospital, Gothenburg, Sweden), Stefan Rutkowski (Department of Paediatric Haematology

and Oncology, University Medical Centre Hamburg-Eppendorf, Hamburg, Germany), Barbara von Zezschwitz (Department of Pediatric Oncology and Hematology, Charité–Universitätsmedizin Berlin, Germany), Darren Hargrave (Pediatric Oncology Unit, UCL Great Ormond Street Institute of Child Health, London, UK), Tom Jacques (Developmental Biology and Cancer Research & Teaching Department, UCL Great Ormond Street Institute of Child Health, London, UK), and Pieter Wesseling (Department of Pathology, Amsterdam University Medical Centers/VU Medisch Centrum, Amsterdam, the Netherlands) for contributing clinical and molecular data. All research at Great Ormond Street Hospital NHS Foundation Trust and UCL Great Ormond Street Institute of Child Health is made possible by the NIHR Great Ormond Street Hospital Biomedical Research Centre. The views expressed are those of the author(s) and not necessarily those of the NHS, the NIHR or the Department of Health.

Disclosure forms provided by the authors are available with the full text and PDF of this article at www.ajnr.org.

REFERENCES

1. Louis DN, Perry A, Wesseling P, et al. **The 2021 WHO Classification of Tumors of the Central Nervous System: a summary.** *Neuro Oncol* 2021;23:1231–51 CrossRef Medline
2. Louis DN, Ohgaki H, Wiestler OD, et al. **The 2007 WHO classification of tumours of the central nervous system.** *Acta Neuropathol* 2007;114:97–109 CrossRef Medline
3. Sturm D, Orr BA, Toprak UH, et al. **New brain tumor entities emerge from molecular classification of CNS-PNETs.** *Cell* 2016; 164:1060–72 CrossRef Medline
4. von Hoff K, Haberler C, Schmitt-Hoffner F, et al. **Therapeutic implications of improved molecular diagnostics for rare CNS embryonal tumor entities: results of an international, retrospective study.** *Neuro Oncol* 2021;23:1597–611 CrossRef Medline
5. Korshunov A, Okonechnikov K, Schmitt-Hoffner F, et al. **Molecular analysis of pediatric CNS-PNET revealed nosologic heterogeneity and potent diagnostic markers for CNS neuroblastoma with FOXR2-activation.** *Acta Neuropathol Commun* 2021;9:20 CrossRef Medline
6. Holsten T, Lubieniecki F, Spohn M, et al. **Detailed clinical and histopathological description of 8 cases of molecularly defined CNS neuroblastomas.** *J Neuropathol Exp Neurol* 2021;80:52–59 CrossRef Medline
7. Furuta T, Moritsubo M, Muta H, et al. **Central nervous system neuroblastic tumor with FOXR2 activation presenting both neuronal and glial differentiation: a case report.** *Brain Tumor Pathol* 2020; 37:100–104 CrossRef Medline
8. Capper D, Jones DTW, Sill M, et al. **DNA methylation-based classification of central nervous system tumours.** *Nature* 2018;555:469–74 CrossRef Medline
9. Stock A, Mynarek M, Pietsch T, et al. **Characteristics of wingless pathway subgroup medulloblastomas: results from the German Imaging HIT/SIOP-Trial Cohort.** *AJNR Am J Neuroradiol* 2019; 40:1811–17 CrossRef Medline
10. Ferris SP, Velazquez Vega J, Aboian M, et al. **High-grade neuroepithelial tumor with BCOR exon 15 internal tandem duplication: a comprehensive clinical, radiographic, pathologic, and genomic analysis.** *Brain Pathol* 2020;30:46–62 CrossRef Medline
11. De Lima L, Sürme MB, Gessi M, et al. **Central nervous system high-grade neuroepithelial tumor with BCOR alteration (CNS HGNET-BCOR): case-based reviews.** *Childs Nerv Syst* 2020;36:1589–99 CrossRef Medline
12. Hu W, Wang J, Yuan L, et al. **Case report: a unique case of pediatric central nervous system embryonal tumor harboring the CIC–LEUTX fusion, germline NBN variant and somatic TSC2 mutation: expanding the spectrum of CIC-rearranged neoplasia.** *Front Oncol* 2020;10:598970 CrossRef Medline
13. Cardoen L, Tauziède-Espariat A, Dangouloff-Ros V, et al. **Imaging features with histopathologic correlation of CNS high-grade neuroepithelial tumors with a BCOR internal tandem duplication.** *AJNR Am J Neuroradiol* 2022;43:151–56 CrossRef Medline
14. Jin B, Feng XY. **MRI features of atypical teratoid/rhabdoid tumors in children.** *Pediatr Radiology* 2013;43:1001–08 CrossRef Medline
15. Meyers SP, Khademian ZP, Biegel JA, et al. **Primary intracranial atypical teratoid/rhabdoid tumors of infancy and childhood: MRI features and patient outcomes.** *AJNR Am J Neuroradiol* 2006; 27:962–71 Medline
16. Yamasaki K, Kiyotani C, Terashima K, et al. **Clinical characteristics, treatment, and survival outcome in pediatric patients with atypical teratoid/rhabdoid tumors: a retrospective study by the Japan Children's Cancer Group.** *J Neurosurg Pediatr* 2019;15:1–10 CrossRef Medline
17. Mangalore S, Aryan S, Prasad C, et al. **Imaging characteristics of supratentorial ependymomas: study on a large single institutional cohort with histopathological correlation.** *Asian J Neurosurg* 2015;10:276–81 CrossRef Medline
18. Wang Q, Cheng J, Li J, et al. **The survival and prognostic factors of supratentorial cortical ependymomas: a retrospective cohort study and literature-based analysis.** *Front Oncol* 2020;10:1585 CrossRef Medline
19. Warmuth-Metz M, Bison B, Gerber NU, et al. **Bone involvement in atypical teratoid/rhabdoid tumors of the CNS.** *AJNR Am J Neuroradiol* 2013;34:2039–42 CrossRef Medline
20. WHO Classification of Tumours Editorial Board. *Central Nervous System Tumours: Who Classification of Tumours. 5th ed*. International Agency for Research on Cancer; December 2021
21. Frühwald MC, Hasselblatt M, Nemes K, et al. **Age and DNA methylation subgroup as potential independent risk factors for treatment stratification in children with atypical teratoid/rhabdoid tumors.** *Neuro Oncol* 2020;22:1006–17 CrossRef Medline
22. Khan S, Solano-Paez P, Suwal T, et al. **Clinical phenotypes and prognostic features of embryonal tumours with multi-layered rosettes: a Rare Brain Tumor Registry study.** *Lancet Child Adolesc Health* 2021;5:800–13 CrossRef Medline
23. Pajtler KW, Witt H, Sill M, et al. **Molecular classification of ependymal tumors across all CNS compartments, histopathological grades, and age groups.** *Cancer Cell* 2015;27:728–43 CrossRef Medline
24. Andreiuolo F, Varlet P, Tauziède-Espariat A, et al. **Childhood supratentorial ependymomas with YAP1-MAMLD1 fusion: an entity with characteristic clinical, radiological, cytogenetic and histopathological features.** *Brain Pathol* 2019;29:205–16 CrossRef Medline
25. Maier SE, Sun Y, Mulkern RV. **Diffusion imaging of brain tumors.** *NMR Biomed* 2010;23:849–64 CrossRef Medline
26. **VASARI Research Project.** March 30, 2020. https://wiki.cancerimagingarchive.net/display/Public/VASARI+Research+Project. Accessed May 29, 2022

Fine, Vascular Network Formation in Patients with Vein of Galen Aneurysmal Malformation

T. Shigematsu, M.J. Bazil, J.T. Fifi, and A. Berenstein

ABSTRACT

BACKGROUND AND PURPOSE: A vein of Galen aneurysmal malformation is known to present with recruitment of dural feeders and, in our cohort, a fine, vascular network formation. The vessels we have observed differ from dural vascular recruitment in that they produce a hairlike, collateral network of vessels. We reviewed treatment courses of vein of Galen aneurysmal malformation treatments in a series of 36 cases that displayed a fine, vascular network formation.

MATERIALS AND METHODS: We retrospectively analyzed 36 cases of vein of Galen aneurysmal malformation, including tectal/thalamic AVMs, treated at our center from January 2004 to September 2021, and reviewed fine, vascular network formations in the subarachnoid space and subependymal zone alongside the vein of Galen aneurysmal malformation.

RESULTS: Patients at first endovascular treatment ranged from neonates to 157 months (median age, 4.3 months). Patients with preinterventional fine, vascular network formations were significantly older at the initial angiogram than patients with postinterventional fine, vascular network formations ($P < .05$). On average, for 20 control choroidal/mural vein of Galen aneurysmal malformations whose treatment course had been completed and in which no plexiform network was visualized, a mean of 2.63 (SD, 1.64) treatments were required to achieve a radiographic cure. For the 36 choroidal/mural vein of Galen aneurysmal malformations whose treatment course had been completed and in which a fine, vascular network formation was visualized, a mean of 5.94 (SD, 2.73) treatments were required to achieve a radiographic cure ($P < .01$).

CONCLUSIONS: Development of a fine, vascular network formation is an acquired and reversible phenomenon that differs from typical dural vessel recruitment, given the hairlike nature of the network and its rapid onset postinterventionally. It typically resolves after completion of treatment, and this resolution correlates with closure of the vein. We recommend that neurointerventionalists avoid delays in treatment wherever possible to reduce the likelihood of a fine, vascular network formation.

ABBREVIATIONS: FVN = fine, vascular network; FVNF = fine, vascular network formation; SAS = subarachnoid space; SEZ = subependymal zone; TAE = transarterial embolization; TVE = transvenous embolization; VGAM = vein of Galen aneurysmal malformation; VOG = vein of Galen

Vein of Galen aneurysmal malformation (VGAM) occurs in early embryonic development and accounts for a minor fraction of all vascular malformations, but a far greater portion of neonatal and pediatric vascular malformations.[1-3] A VGAM develops between 6 and 11 weeks of gestation. While most VGAMs are diagnosed antenatally or as neonates, some patients survive to adulthood relatively asymptomatic and present with hemorrhage or other manifestations.[4-8] VGAMs entail a dilated vein of Galen (VOG), but the true fistula occurs between the persistent prosencephalic vein of Markowski (the mature VOG precursor) and the arterial limbic system (pericallosal arcade and anterior-posterior choroidal arteries).

A VGAM is characterized as either choroidal and mural.[9-11] Choroidal VGAMs are more common in the neonatal period and are more complex, with a larger number of high-flow fistulas; in our experience, they are more likely to produce medically untreatable, high-cardiac-output failure. Additionally, Lasjaunias et al[11] reported that a choroidal-type VGAM "is encountered in most neonates with low clinical scores." It is supplied by numerous feeder vessels from the limbic system (pericallosal arcade, choroidal arteries, and occasionally thalamoperforating/transmesencephalic arteries).[12] These vessels mostly converge at the anterior portion of the median prosencephalic vein. Mural VGAMs contain fistulas at the inferolateral margin in the wall of the median prosencephalic

Received March 30, 2022; accepted after revision July 27.

From the Departments of Neurosurgery (T.S., M.J.B., J.T.F., A.B.) and Neurology (J.T.F.), Icahn School of Medicine at Mount Sinai, New York, New York.

Please address correspondence to Maximilian J. Bazil, BS, Icahn School of Medicine at Mount Sinai, 1 Gustave Levy Place, Annenberg 20-225, New York, NY 10029; e-mail: maximilian.bazil@mountsinai.org; @SciMaximilian

Indicates article with online supplemental data.

http://dx.doi.org/10.3174/ajnr.A7649

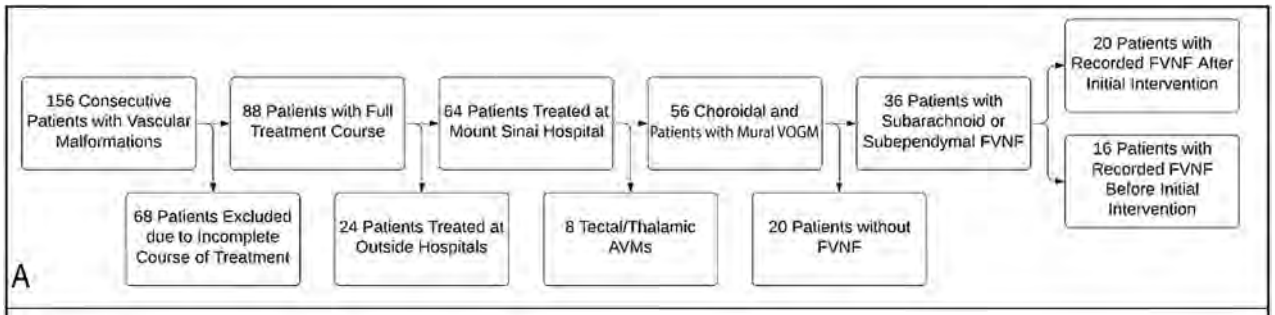

Location of FVNF	Right	Left	Bilateral
Thalamus	4,10,22, 30,32	2,6,13, 26,27	8,11,17,20,23,24,29,33, 34,36
Cisternal Space	19,30	6,9,25	2,3,4,5,7,8,10,11,12,13, 14,15,16,18,20,21,22,23, 24,26,27,28,29,31,32, 33,34,35,36

B

FIG 1. Patient inclusion flow chart and FVNF geography. Patients were considered if they presented to our practice with an AVM between January 2004 and August 2021. Exclusion criteria included incomplete courses of treatment, treatment at centers outside our practice, tectal/thalamic AVM, or no observable FVNF. *A*, An FVNF was generalized as being present in either the thalamus, the cisternal space surrounding the VOG, or both with a description of laterality (*B*). VOGM indicates vein of galen malformation.

vein.[5] Mural VGAMs manifest later in infancy as macrocephaly, hydrocephalus, or delayed cognitive development (especially if associated with venous occlusions/thrombosis). A smaller number of feeders and greater outflow obstruction has often led to a more drastic dilation of the median prosencephalic vein in our experience. Cardiac failure is milder than in the choroidal subtype, and cardiomegaly may be asymptomatic.[9,11]

Endovascular embolization is a criterion standard treatment for VGAM.[2,13-16] Embolization is generally staged during several sessions. Embolization aims to safely reduce the risk of cardiac failure, venous hypertension, and hydrocephalus by closing AVFs at the arteriovenous junction, contributing to the lesion. If untreated or if arterial feeders are closed without closing the venous shunt, dramatic remodeling can occur, such as the formation of a "fine," vascular network that reaches the arteriovenous shunts, which further supply the lesion. This finding has been noted as recruitment of dural feeders and a general, collateral network in other publications:[17-21] We describe a dynamic progression of feeders in the subependymal zone (SEZ) and the subarachnoid space (SAS) as a reversible, physiologic phenomenon dependent on flow demand, low venous pressure, and/or tissue ischemia.

A previous study from our practice assessed dural recruitment and contribution to VGAM fistulas.[22] We built on these findings with a further analysis of a larger cohort to assess a fine, vascular network formation (FVNF) in the SAS/SEZ. The vessels we have observed accompanying initial imaging or arising with time in cases of a VGAM differ from dural recruitment in that they produce a hairlike, collateral network of vessels. We reviewed treatment courses of patients with VGAMs in a series of 36 cases that had FVNF shunting into the lesion. Some of these cases presented with an FVNF in pretreatment imaging. In these cases, the FVNF may cause confusion by resembling a "true" thalamic AVM (Online Supplemental Data). In some cases, initial imaging in the neonate period shows high-flow AVFs; then at 3-month follow-up, it shows an FVNF. We also observed this phenomenon after coil embolization of feeders that failed to close the AVF and on follow-up after the primary stage of embolization with liquid embolic agents (*n*-BCA), with incomplete closure of these AVFs. We have seen regression of the FVNF after proper closure of the arteriovenous shunt without embolization of the FVNF itself. This represents a delayed anatomic change related to the hemodynamic demands of the high flow. We discuss the significance of these observations, their influence on the treatment paradigm our practice uses for incidences of VGAMs with visible FVNFs, the various presentations that our practice has encountered, the locations of FVNF feeders, and correlations with resolution of the VGAM and FVNF therein.

MATERIALS AND METHODS

This study was approved by the appropriate institutional review board. All imaging was reviewed by neuroendovascular surgery attending physicians (T.S., J.T.F., A.B.). We retrospectively analyzed 156 consecutive cases of all VGAMs, including tectal/thalamic AVMs, treated at our center from January 2004 to September 2021 (Fig 1*A*). We selected patients whose treatment course was completed and ended in complete or near-complete occlusion (>95%) for a total of 88 patients. We included only patients whose treatment course and imaging series were complete, to demonstrate the difference between closure of the malformation and amelioration of the FVNF. Of these, we extracted 64 cases whose complete treatment course was performed at our practice rather than at multiple institutions. We defined tectal or thalamic AVMs as those without obvious large feeders or fistulas (which often resemble but are distinctly not a VGAM) to ensure

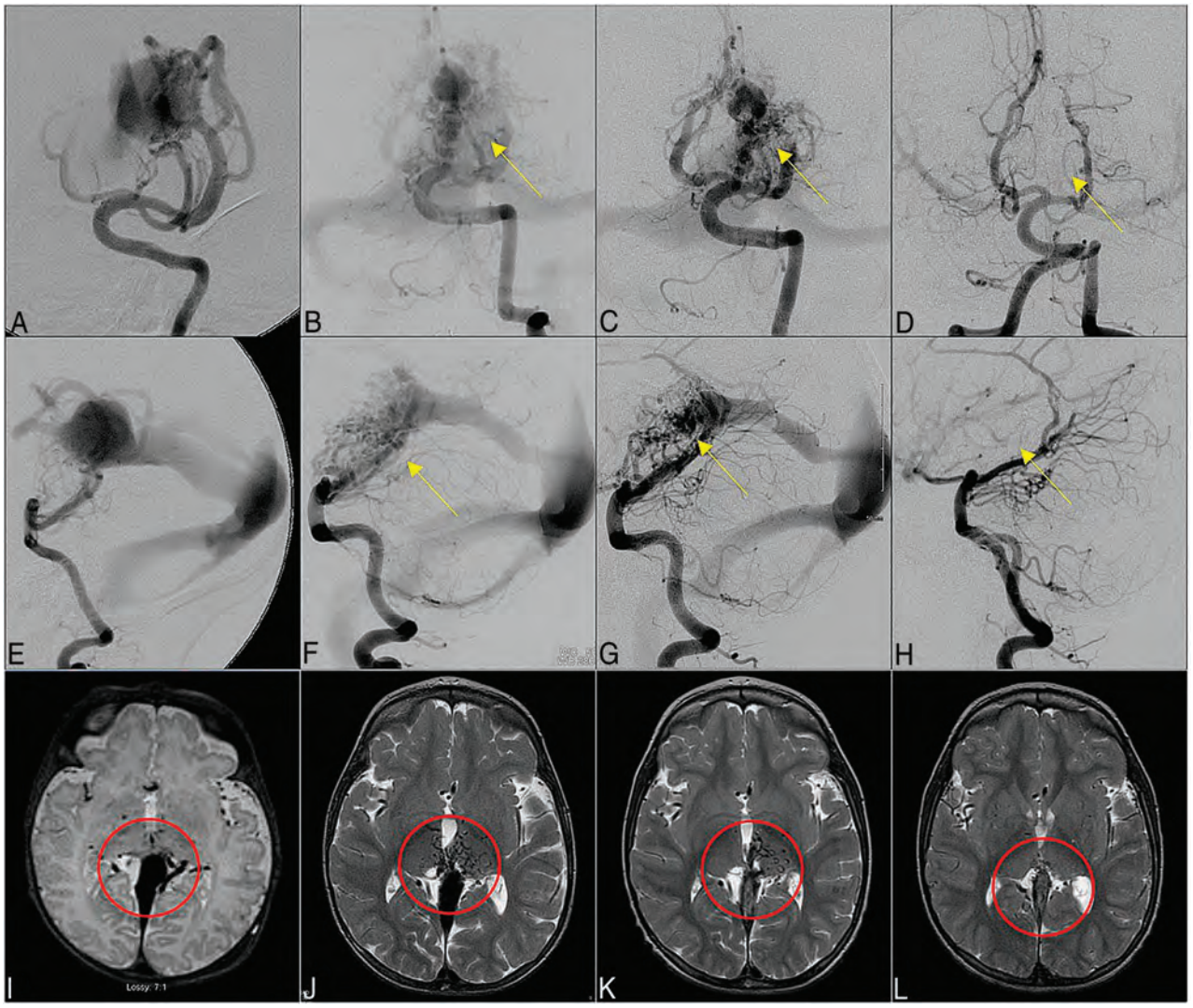

FIG 2. Angiogram. Anterior-posterior (*A–D*) and lateral (*E–H*) views of the angiogram and T2-weighted MR imaging (*I–L*) of case 4. We show a progressive diminution of the FVNF at the thalamus and quadrigeminal cistern (*B–D*, *F* and *G*, *J–L*) observed after initial treatment (*A*, *E*, *I*). This reduction was achieved through staged embolization of feeder vessels to the VGAM from 4.2 to 10 to 20 to 40 months. The *yellow arrows* indicate location of FVNF on AP and Lateral view of cerebral angiography sections. The *red circle* indicates the location of FVNF on axial MRI plane.

that no VGAMs were excluded. We excluded tectal/thalamic AVMs for a total of 56 choroidal or mural-type VGAMs. We gathered information from clinical case records and MR imaging/angiography on presentation and during follow-up. We recorded patient demographics, presentation, and the patient's timeline to cure. MR imaging was used to identify anatomic locations of the FVNF. A FVNF was defined as the hairlike, hypervascular, collateral network around the VGAM on angiography and T2 MR imaging. The findings were analyzed to aid discussion of the FVNF in the SAS/SEZ alongside the VGAM.

RESULTS

Among the 56 cases selected for detailed review, we identified 36 patients with SAS/SEZ FVNFs (Fig 1). We present 36 cases of VGAMs that we evaluated on the basis of the FVNF, a classification, treatment strategy, anatomic location, patient demographics, and procedure quantity required to achieve complete obliteration of the malformation.

Overall FVNF Cohort

Ages at the time of the first endovascular treatment ranged from neonate to 157 months (mean age, 12.1 months; median age, 4.3 months). In 16 patients (44.4%), the vascular network was identified on the initial angiogram and drained into the VOG (Figs 2*A* and 3*A*). In 20 patients (55.6%), the FVNF was observed after the initial angiogram (Fig 4*A*, Online Supplemental Data). The cohort of patients with FVNFs before intervention was significantly older at the initial angiogram compared with the patients who developed these networks after ≥1 session of endovascular embolization (mean, 12 [SD, 40.1] months versus 4.0 [SD, 5.4] months; $P < .05$). We compared the 20 VGAMs for which no FVNF had been visualized (Fig 1) with our FVNF cohort on the basis of the treatment number. On average, for the 20 choroidal/mural VGAMs whose treatment course had been completed and in which no plexiform network was visualized, a mean of 2.63 (SD, 1.64) treatments were required to achieve a radiographic cure. For the 36 choroidal/mural VGAMs whose treatment course had been completed and in which

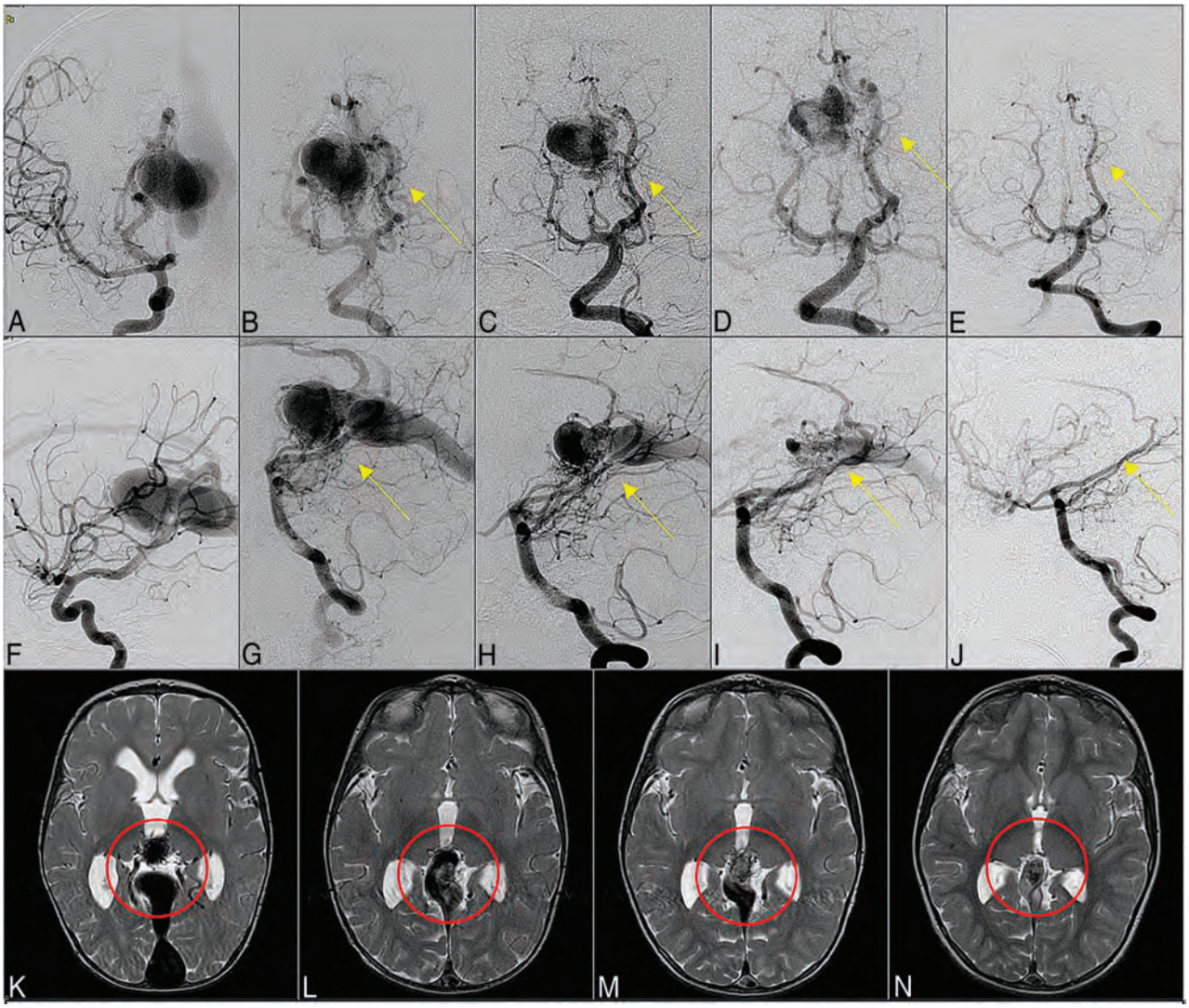

FIG 3. Angiogram. Anterior-posterior (*A–E*) and lateral (*F–J*) views of the angiogram and T2-weighted MR imaging (*K–N*) of case 23. We show a progressive diminution of the FVNF bilaterally at the thalamus with a bias for the right side (*B–E*, *G–J*, *K–M*) observed after initial treatment (*A* and *F*). This reduction was achieved through staged embolization of feeder vessels to the VGAM staged from 0.5 to 3 to 20 to 72 months.

an FVNF was visualized, a mean of 5.94 (SD, 2.73) treatments were required to achieve a radiographic cure ($P < .01$).

Patients were categorized into left, right, or bilateral subarachnoid/thalamic fine, vascular networks (FVNs) (Fig 1*B*). The FVNF was localized to either the left, right, or bilateral thalamus in 2 cases, the cisternal space surrounding the VOG in 16 cases, and both for 18 cases. We also noted 3 patterns of FVN expansion/regression during the treatment course of our cohort: 1) progressive decrease in the FVNF after initial presentation (20/36; 55.56%), 2) an original increase in the FVNF after initial presentation followed by progressive decrease (7/36; 19.44%), and 3) cycling of increases and decreases in the FVNF after initial presentation followed by eventual cure (9/36; 25%).

Demonstrative Cases

Subject 4, who was first imaged via cerebral angiography at 4.2 months and was found to have a mural VGAM, underwent staged embolization therapy (Fig 2). No FVNF was initially observed around the dilated VOG (Fig 2*A*, *-E*, *-I*). Six months following this initial imaging and subsequent embolization, we discovered an obvious, novel FVN in the right thalamus and quadrigeminal cistern (Fig 2*B*, *-F*, *-J*). We were able to successfully regress this FVN through staged, transarterial embolization, and we observed continuing regression at the 19-month follow-up (Fig 2*C*, *-G*, *-K*). After complete obliteration of the fistulas dilating the VOG (cured), we no longer found visible FVNs as evidenced by images obtained at a 40-month follow-up (Fig 2*D*, *-H*, *-L*).

Subject 23, initially imaged at 16.4 months and found to have a choroidal VGAM, presented with an observable FVNF on the initial imaging series (Fig 3*A*, *-F*, *-K*). On the angiography/MR imaging at 3 months (Fig 3*B*, *-C*, *-G*, *-H*, *-L*) and 15 months (Fig 3*D*, *-I*, *-M*) after the first procedure, during the staged embolization that followed, the FVN receded little by little. After the complete obliteration of the VGAM had been achieved, no FVN was seen at the final follow-up at 6 years of age (Fig 3*E*, *-J*, *-N*).

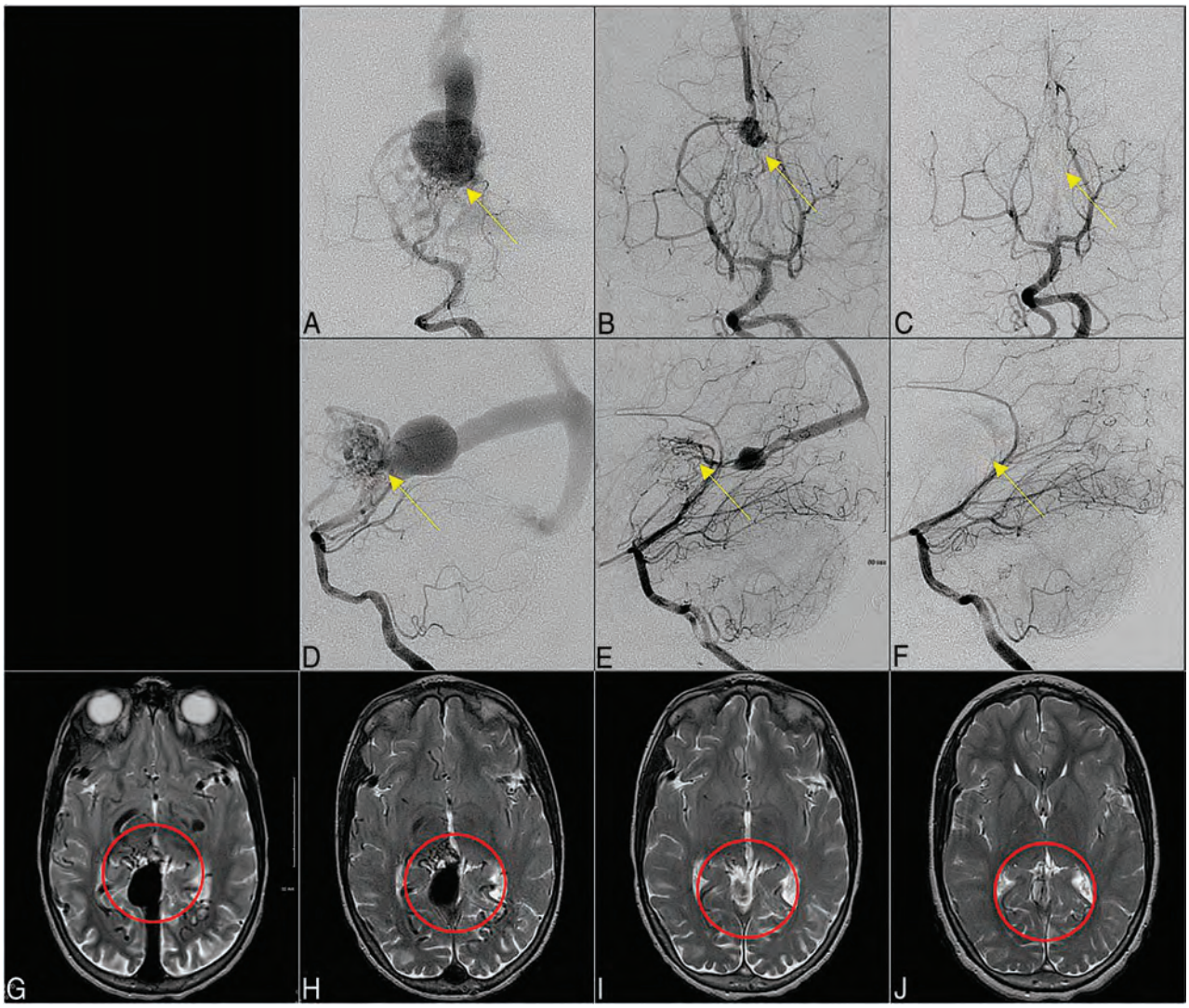

FIG 4. Angiogram. Anterior-posterior (*A–C*) and lateral (*D–F*) views of the angiogram and T2-weighted MR imaging (*G–J*) of case 22. We show an up-regulation (*H*) and waning (*B* and *C*, *E* and *F*, *I* and *J*) of a plexiform network centered around the right hypothalamus and quadrigeminal cistern. The FVNF observed at 4 months post-initial consultation was rectified with staged embolization and obliterated by the 6-year follow-up (*C*, *F*, *J*).

Subject 22 presented to our practice with a choroidal VGAM and a nascent FVNF on initial screening (Fig 4*G*). This patient presented to our practice at 5 years of age with an FVNF localized to the posterior right hypothalamus and quadrigeminal cistern. The diagnostic angiogram and MR imaging that preceded the initial embolization revealed an FVNF. The first session of embolization treatment was planned for only 4 months following the original consultation, yet the imaging performed on arrival to the angiosuite revealed an up-regulation of the FVNF (Fig 4*A*, *-D*, *-H*). Fortunately, it seemed that the observed FVNF regressed after 2 stages of transarterial embolization at 10 months (Fig 4*B*, *-E*,- *I*) and was completely absent after total occlusion of the VGAM fistulas (Fig 4*C*, 4*F*, 4*J*) at 6 years post-initial imaging.

Subject 30 presented to our practice as a neonate, imaged via CT 1 day postnatal, with a choroidal VGAM without observable FVNF (Online Supplemental Data). At 5 months of age, after a single embolization, we identified an FVNF in the right thalamus and SAS (Online Supplemental Data). After 4 embolization treatments, we found an initial regression of the plexiform network (Online Supplemental Data), which had abated entirely by the tenth treatment, at which point closure of the vein had been achieved (Online Supplemental Data).

DISCUSSION

Summary of Findings

Most of our cohort had FVNFs identified on a follow-up angiogram following a stage or multiple stages of embolization therapy. Those who presented with an FVNF at the initial angiography were significantly older at presentation than those whose FVNF was identified during a follow-up angiography. Even after removal of a large outlier (case 31) from the initial FVNF presentation group, we still observed a significantly higher mean age at presentation compared with the postinterventional group. We reasoned that this finding may be due to the "secondary" nature of the FVNF. Case 31 experienced a delay in treatment until just older than 13 years of age because the VGAM diagnosis occurred in a

work-up to determine the cause of headaches. This was the first of our findings that suggested that one should not delay treatment, particularly considering the greater treatment burden identified in the cohort with FVNF at initial presentation. The importance of this observation can be seen in cases 4 and 30 (Fig 2 and Online Supplemental Data) in which the MR imaging/MRA in the neonatal period clearly showed an AVF angioarchitecture, whereas the MR imaging and angiography at 6 and 5 months of age, respectively, clearly showed the acquired FVNF in the thalamic region. We found that those with an FVNF required more treatment to achieve cure than those without an FVNF. Unsurprisingly, a significant association was observed between the choroidal VGAM subtype and presentation of the FVNF relative to a mural VGAM (4/14 mural versus 32/42 choroidal; $P < .01$). The anatomic locations of the observed FVNFs were mainly centered around the thalamus, surrounding the SAS and/or the quadrigeminal cistern; they were usually attached or very close to the dilated the venous sac of the VOG.

VGAM Treatments

A FVNF poses a number of challenges to diagnosis and treatment of VGAMs, specifically, due to the difficulty of differentiating a tectal/thalamic or traditional VGAM surrounded by an FVN (Online Supplemental Data). On identification of an FVNF, our strategy is still to embolize the fistulous connections where feeders communicate with the vein. Focus is placed on penetrating the embolic material through to the vein to ensure closure of the fistula; occasionally, multiple fistulas may be targeted through 1 injection rather than each individual abnormal feeder vessel. The ideal strategy in our practice is cannulation of the primary feeder of the malformation, as close to the fistula as possible, and injection of highly concentrated *n*-BCA glue (70%–90%). After multiple rounds of staged embolization, remaining feeders become considerably less dilated and are difficult to distinguish from the observed FVNF. In this pattern, we use low-concentrate *n*-BCA (40%–50%) from an identifiable, proximal feeder and occlude the venous component of the fistula. SEZ/SAS FVNFs cause no symptoms in our patients; subsequently, we describe a clinical focus on embolization of major feeders rather than FVNFs. Most important, the expansion of the FVNF after beginning staged transarterial embolization (TAE) leaves only transvenous embolization (TVE) or TAE through the fine vasculature as endovascular treatment options. These are both technically difficult options and, in areas such as the thalamus, carry a higher risk of stroke. While our practice has begun to favor a TVE approach using the Chapot pressure cooker technique after multiple rounds of TAE, a large FVNF can lead us to decide against this otherwise effective approach due to the possible increased risk of hemorrhage.[23] Indeed, a member of our TVE cohort with extensive FVNFs at the time of treatment experienced a hemorrhage in the SAS surrounding the malformation adjacent to the FVNF (Online Supplemental Data).

FVNF and Shunt Formation

Members of our research group published a case series on dural arteriovenous shunt formation secondary to VGAM.[22] They noted that the FVNF occurred in 26/87 patients in 3 distinct patterns: 1) feeders arising predominantly from pial vessels, 2) feeders arising from both pial and dural vessels, and 3) feeders arising predominantly from the dural vessels. In the 2 latter cases, they posited that "angiogenic stimuli from the partially thrombosed Galenic venous pouch located in the SAS and in near direct contact with the dura baring the thin arachnoid results in an angiogenic response from the dura." We suspect that proangiogenic stimuli from the local vascular environment may play a role in recruiting vessels to the malformation, which should be investigated further. We are pursuing this hypothesis further by organizing a large-scale, multiomics analysis of the VGAM at our practice. Contrary to our observations, in other forms of AVM, it is often observed that increased vascularization occurs as a result of incomplete or staged embolization.[1] As a result, we believe that the physiology of VGAM may be unique among AVMs and should be examined further in the form of a multiomics analysis.

Patterns of FVNF

We chiefly observed 2 patterns of FVNF with VGAM: 1) an FVNF that was present at the initial diagnostic angiogram and MR imaging, diminishing with time as the shunts are closed, and 2) an FVNF that developed during the staged embolization treatment course of the patient. We believe the latter to be due likely to incomplete shunt occlusion or shunt increase. It may also be related to increases in flow and/or tissue ischemia secondary to arterial insufficiency or venous hypertension, resulting in tissue hypoperfusion. If properly treated, this FVNF will diminish with time and regress with closure of the malformation.

CONCLUSIONS

Development of an SEZ/SAS FVNF is common during the multisession treatment of the VGAM. We believe this is an acquired and reversible phenomenon that differs from typical dural vessel recruitment, given the hairlike nature of the network and its rapid onset in cases in which it is not observed at initial imaging postinterventionally. This finding is limited by the resolution of currently available imaging modalities and will require a future pathologic study to validate. These networks regress and progress as we treat the VGAM, targeting the venous side of the fistula. It typically resolves after completion of treatment, and this resolution correlates with closure of the vein. We recommend that neurointerventionalists avoid delays in treatment wherever possible to lower the likelihood of an FVNF. In cases in which an FVNF appears spontaneously, we recommend treating the VGAM with staged TAE without embolizing individual FVNF feeders, which tend to resolve after closure of the vein.

Ethics Approval

This study was approved by the Mount Sinai Hospital institutional review board with a consent waiver under IRB STUDY 21–00749.

Disclosure forms provided by the authors are available with the full text and PDF of this article at www.ajnr.org.

REFERENCES

1. Buell TJ, Ding D, Starke RM, et al. **Embolization-induced angiogenesis in cerebral arteriovenous malformations.** *J Clin Neurosci* 2014;21:1866–71 CrossRef Medline

2. Khullar D, Andeejani AM, Bulsara KR. **Evolution of treatment options for vein of Galen malformations: a review.** *J Neurosurg Pediatr* 2010;6:444–51 CrossRef Medline
3. Nuñez FB, Dohna-Schwake C. **Epidemiology, diagnostics, and management of vein of Galen malformation.** *Pediatr Neurol* 2021;119:50–55 CrossRef Medline
4. Pareek K, Shrivastava T, Sinha VD. **Choroidal type of vein of Galen aneurysmal malformation in adult patient with unusual presentation of orthostatic headache.** *Asian J Neurosurg* 2018;13:418–20 CrossRef Medline
5. Ribeiro, Valentina T, et al. **Choroidal type aneurysmal malformation of the vein of Galen associated with Dandy-Walker malformation in an adult** (in Portuguese). *Acta Med Port* 2003;16.3:217–20 Medline
6. Xu DS, Usman AA, Hurley MC, et al. **Adult presentation of a familial-associated vein of Galen aneurysmal malformation: case report.** *Neurosurgery* 2010;67:E1845–51; discussion 1851 CrossRef Medline
7. Muquit S, Shah M, Bassi S. **Vein of Galen malformation presenting in adulthood.** *Br J Neurosurg* 2008;22:692–94 CrossRef Medline
8. Marques RM, Lobão CA, Sassaki VS, et al. **Vein of Galen aneurysm in an adult: case report.** *Arq Neuropsiquiatr* 2006;64:862–64 CrossRef Medline
9. Berenstein A, Niimi Y. Vein of Galen aneurysmal malformation. In: Winn HR, ed. *Youmans Neurological Surgery*. Vol 2. 6th ed. Elsevier/Saunders; 2011;2150–65
10. Lasjaunias PL. *Vascular Diseases in Neonates, Infants and Children: Interventional Neuroradiology Management*. Springer; 1997
11. Lasjaunias PL, Chng SM, Sachet M, et al. **The management of vein of Galen aneurysmal malformations.** *Neurosurgery* 2006;59(5 Suppl 3):S184–94; discussion S3–13 CrossRef Medline
12. Lasjaunias P, ter Brugge KG, Berenstein A. *Surgical Neuroangiography: Clinical and Interventional Aspects in Children*. Vol 3. Springer; 2007
13. Bhatia K, Mendes Pereira V, Krings T, et al. **Factors contributing to major neurological complications from vein of Galen malformation embolization.** *JAMA Neurol* 2020;77:992–99 CrossRef Medline
14. Sivasankar R, Limaye V, Wappalapati S, et al. **Endovascular management of vein of Galen aneurysmal malformations: a retrospective analysis over a 15-year period.** *J Vasc Interv Neurol* 2019;10:23–29 Medline
15. Berenstein A, Fifi JT, Niimi Y, et al. **Vein of Galen malformations in neonates: new management paradigms for improving outcomes.** *Neurosurgery* 2012;70:1207–14 CrossRef Medline
16. Berenstein A, Paramasivam S, Sorscher M, et al. **Vein of Galen aneurysmal malformation: advances in management and endovascular treatment.** *Neurosurgery* 2019;84:469–78 CrossRef Medline
17. Agarwal H, Sebastian LJ, Gaikwad SB, et al. **Vein of Galen aneurysmal malformation: clinical and angiographic spectrum with management perspective—an institutional experience.** *J Neurointerv Surg* 2017;9:159–64 CrossRef Medline
18. Brinjikji W, Krings T, Murad MH, et al. **Endovascular treatment of vein of Galen malformations: a systematic review and meta-analysis.** *AJNR Am J Neuroradiol* 2017;38:2308–14 CrossRef Medline
19. Adair TH, Montani JP. Angiogenesis. *Colloquium Series on Integrated Systems Physiology: from Molecule to Function* 2010;2:1–84 CrossRef
20. Sato S, Kodama N, Sasaki T, et al. **Perinidal dilated capillary networks in cerebral arteriovenous malformations.** *Neurosurgery* 2004;54:163–70 CrossRef Medline
21. Takemae T, Kobayashi S, Sugita K. **Perinidal hypervascular network on immediate postoperative angiogram after removal of large arteriovenous malformations located distant from the arterial circle of Willis.** *Neurosurgery* 1993;33:400–06 Medline
22. Paramasivam S, Niimi Y, Meila D, et al. **Dural arteriovenous shunt development in patients with vein of Galen malformation.** *Interv Neuroradiol* 2014;20:781–89 CrossRef Medline
23. Shigematsu T, Bazil MJ, Matsoukas S, et al. **Transvenous embolization of vein of Galen aneurysmal malformations using the "Chapot pressure cooker" technique.** *Interv Neuroradiol* 2021 Dec 23. [Epub ahead of print] CrossRef Medline

Refining the Neuroimaging Definition of the Dandy-Walker Phenotype

M.T. Whitehead, M.J. Barkovich, J. Sidpra, C.A. Alves, D.M. Mirsky, Ö. Öztekin, D. Bhattacharya, L.T. Lucato, S. Sudhakar, A. Taranath, S. Andronikou, S.P. Prabhu, K.A. Aldinger, P. Haldipur, K.J. Millen, A.J. Barkovich, E. Boltshauser, W.B. Dobyns, and K. Mankad

ABSTRACT

BACKGROUND AND PURPOSE: The traditionally described Dandy-Walker malformation comprises a range of cerebellar and posterior fossa abnormalities with variable clinical severity. We aimed to establish updated imaging criteria for Dandy-Walker malformation on the basis of cerebellar development.

MATERIALS AND METHODS: In this multicenter study, retrospective MR imaging examinations from fetuses and children previously diagnosed with Dandy-Walker malformation or vermian hypoplasia were re-evaluated, using the choroid plexus/tela choroidea location and the fastigial recess shape to differentiate Dandy-Walker malformation from vermian hypoplasia. Multiple additional measures of the posterior fossa and cerebellum were also obtained and compared between Dandy-Walker malformation and other diagnoses.

RESULTS: Four hundred forty-six examinations were analyzed (174 fetal and 272 postnatal). The most common diagnoses were Dandy-Walker malformation (78%), vermian hypoplasia (14%), vermian hypoplasia with Blake pouch cyst (9%), and Blake pouch cyst (4%). Most measures were significant differentiators of Dandy-Walker malformation from non-Dandy-Walker malformation both pre- and postnatally ($P < .01$); the tegmentovermian and fastigial recess angles were the most significant quantitative measures. Posterior fossa perimeter and vascular injury evidence were not significant differentiators pre- or postnatally ($P > .3$). The superior posterior fossa angle, torcular location, and vermian height differentiated groups postnatally ($P < .01$), but not prenatally ($P > .07$).

CONCLUSIONS: As confirmed by objective measures, the modern Dandy-Walker malformation phenotype is best defined by inferior predominant vermian hypoplasia, an enlarged tegmentovermian angle, inferolateral displacement of the tela choroidea/choroid plexus, an obtuse fastigial recess, and an unpaired caudal lobule. Posterior fossa size and torcular location should be eliminated from the diagnostic criteria. This refined phenotype may help guide future study of the numerous etiologies and varied clinical outcomes.

ABBREVIATIONS: BPC = Blake's pouch cyst; DWM = Dandy-Walker malformation; RL = rhombic lip; TTC = taenia–tela choroidea complex; TVA = tegmentovermian angle; VH = vermian hypoplasia

The traditionally described Dandy-Walker malformation (DWM) comprises a range of structural abnormalities involving the cerebellum and posterior cranial fossa.[1] While classic imaging features are firmly established, the inclusion and exclusion criteria used

Received April 20, 2022; accepted after revision June 28.

From the Department of Radiology (M.T.W.) and Prenatal Pediatrics Institute (M.T.W.), Children's National Hospital, Washington DC; The George Washington University School of Medicine and Health Sciences (M.T.W.), Washington DC; Division of Neuroradiology (M.T.W., C.A.A., S.A.), Children's Hospital of Philadelphia, Philadelphia, Pennsylvania; Department of Radiology, Perelman School of Medicine (M.T.W., S.A), University of Pennsylvania, Philadelphia, Pennsylvania; Department of Radiology and Biomedical Imaging (M.J.B., A.J.B.) University of California, San Francisco, San Francisco, California; Neuroradiology Section (M.J.B., A.J.B.), University of California, San Francisco-Benioff Children's Hospital, San Francisco, California; Developmental Biology and Cancer Section (J.S., K.M.), University College London Great Ormond Street Institute of Child Health, London, UK; Department of Neuroradiology (J.S., S.S., K.M.), Great Ormond Street Hospital for Children National Health Service Foundation Trust, London, UK; Department of Radiology (D.M.M.), Children's Hospital Colorado, University of Colorado School of Medicine, Aurora, Colorado; Department of Neuroradiology (Ö.Ö.), Bakırçay University, Çi li Education and Research Hospital, İzmir, Turkey; Department of Neuroradiology (D.B.), Royal Victoria Hospital, Belfast, UK; Division of Diagnostic Neuroradiology (L.T.L.), Hospital das Clínicas da Faculdade de Medicina da Universidade de São Paulo, São Paulo, Brazil; Department of Medical Imaging (A.T.), Women's and Children's Hospital, North Adelaide, South Australia, Australia; Faculty of Medicine (A.T.), University of Adelaide, Adelaide, South Australia, Australia; Department of Neuroradiology (S.P.P.), Boston Children's Hospital, Harvard Medical School, Boston, Massachusetts; Center for Integrative Brain Research (K.A.A., P.H., K.J.M.), Seattle Children's Research Institute, Seattle, Washington; University of Washington School of Medicine (K.J.M.), Seattle, Washington; Department of Pediatric Neurology (E.B.), University Children's Hospital, Zürich, Switzerland; and Department of Genetics and Metabolism (W.B.D.), Department of Pediatrics, University of Minnesota, Minneapolis, Minnesota.

First authorship is shared between M.T. Whitehead and M.J. Barkovish, order as listed.

Please address correspondence to Matthew Whitehead, MD, Division of Neuroradiology, Children's Hospital of Philadelphia, 3401 Civic Center Blvd, Philadelphia, PA 19104; e-mail: WhiteheadM@CHOP.edu

Indicates article with online supplemental data.

http://dx.doi.org/10.3174/ajnr.A7659

to define less typical imaging patterns are inexact, both in theory and in practice. Indeed, though "Dandy-Walker variant," a term that was introduced as a means of describing milder phenotypes, has been strongly discouraged due to misuse, it still appears regularly in the literature and in the clinical practice of institutions around the world.[2-4] Although one could advocate abandoning the eponym altogether, we instead designate DWM as a structural phenotype as a way to succinctly define its complex-but-specific anatomic composition. DWM is indeterminant in etiology when isolated and may be acquired or genetic.[5,6] Thus, its causes, risk factors, prognoses, and outcomes will remain enigmatic, and counseling challenges will linger until its neuroimaging phenotype is better defined and issues pertaining to classification/categorization and ascertainment bias are resolved.

Recently recognized features that can help distinguish DWM from its mimics, including the tail sign,[7] choroid plexus/tela choroidea location,[6,8,9] and fastigial recess shape,[10,11] have not yet been incorporated into the diagnostic criteria. On the other hand, as we demonstrate here, posterior fossa enlargement and torcular location should probably be discarded because these are variable in and are not specific for DWM.

Using the choroid plexus/tela choroidea location and fastigial recess shape, together with conventional qualitative and quantitative cerebellar and posterior fossa measures, we retrospectively evaluated a large series of fetal and postnatal brain MRIs from children determined to have DWM at initial imaging to achieve the following: 1) refining the phenotypic imaging criteria for DWM; 2) estimating the diagnostic accuracy of historical MR imaging examinations; and, 3) using our refined criteria of DWM (tail sign, choroid plexus/tela choroidea location, and fastigial recess angle) to compare DWM and non-DWM groups with regard to conventional qualitative and quantitative cerebellar and posterior fossa measures.

MATERIALS AND METHODS

This 11-center international study was conducted after site-specific institutional review board approval. Written informed consent was waived due to the retrospective nature of the study. Institution-specific radiology information systems were searched for all fetal and postnatal pediatric (19 years of age or younger) brain MR imaging examinations with radiology reports containing the terms "Dandy-Walker" and/or "vermian hypoplasia." An additional 21 postnatal MRIs from patients with DWM included in a previous study were also included.[5] Examinations were manually reviewed to confirm the diagnoses. After excluding incomplete examinations, examinations with severe motion artifacts, and those without posterior fossa anomalies or malformations, each case was evaluated for the following (to the extent allowed by the technique): indication, magnet and imaging parameters, vermian size/morphology, fastigial recess angle, posterior fossa size/morphology, choroid plexus and taenia–tela choroidea complex (TTC) location, torcular location, evidence of prior injury (hemorrhage and/or encephalomalacia), brainstem abnormalities, and supratentorial findings. Specific vermian measures included the following: anterior-posterior diameter (millimeter), height (millimeter), lobe number, vermian ratio, tail sign, fastigial recess angle, and tegmentovermian angle (TVA).[5,7,11-17] On the basis of recent histopathologic studies of normal human vermian embryologic development, the vermian ratio was considered abnormal when the collective size of the posterior and central lobes was less than approximately twice the size of the anterior lobe using a line drawn from the fastigial point to the primary fissure (Online Supplemental Data).[10,11]

Specific posterior fossa assessments included the following: torcular location, posterior fossa perimeter (millimeter), superior posterior fossa angle, falx cerebelli abnormalities (absent, truncated, or multiplied), and cisterna magna depth (millimeter).[12,13,18] Given the technical and motion-related challenges inherent in fetal MR imaging, measurements were obtained on the images that best approximated conventional imaging planes. If certain measurements could not be obtained accurately in a particular case, those data were excluded. Age, sex, history of prematurity, twinning history, shunt history, and known genetic abnormalities were obtained from the medical record where available.

All cases were independently reviewed by senior neuroradiologists at each participating institution. To ensure standardization across centers, a board-certified pediatric neuroradiologist (K.M.) with 14 years of posttraining experience independently reviewed all anonymized images to verify the diagnosis, qualitative and quantitative measures, and the reporting of additional brainstem malformations. Discrepancies in qualitative and quantitative measures and the reporting of additional brainstem malformations were resolved via independent review by a third author (J.S.).

Working definitions for this study were based on literature review and group consensus (Online Supplemental Data). DWM was defined by vermian hypoplasia with an inferior severity gradient, vermian under-rotation with an increased TVA, an enlarged fourth ventricle with an obtuse fastigial recess, an unpaired caudal lobule (tail sign when visible), and inferior and/or lateral displacement of the TTC and/or the choroid plexus when visible (Figure) (Online Supplemental Data).[6,10,11] "Vermian hypoplasia" was defined as global reduction in vermian volume without vermian ratio reduction, lobe deficit, fissural enlargement, fastigial recess angle blunting, or inferolateral TTC/choroid plexus displacement. "Inferior vermian hypoplasia" was defined as inferior-predominant vermian hypoplasia, a decreased vermian ratio with/without lobe reduction, an acute fastigial recess angle, and lack of inferolateral TTC/choroid plexus displacement (Online Supplemental Data). Blake pouch cyst (BPC) was defined by a normally sized vermis, enlarged TVA, and TTC/choroid plexus location at the inferomedial cerebellar margin (when visible). We compared the original and updated diagnoses on the basis of this classification scheme.

Imaging Technique

Sixty-eight patients (15%) were scanned at 3T (60 postnatal; 8 fetal), and the other 339 patients (173 postnatal; 166 fetal) were scanned at 1.5T. Due to the number of participating centers and the several decades of imaging included in the patient cohort, there was significant heterogeneity in terms of scanner manufacturer, sequences acquired, and imaging parameters. Minimum postnatal MR imaging sequences for inclusion were sagittal T1WI and axial T2WI, all with ≤5-mm section thicknesses. Additional sequences including T2 FLAIR, SWI, DWI/DTI, and

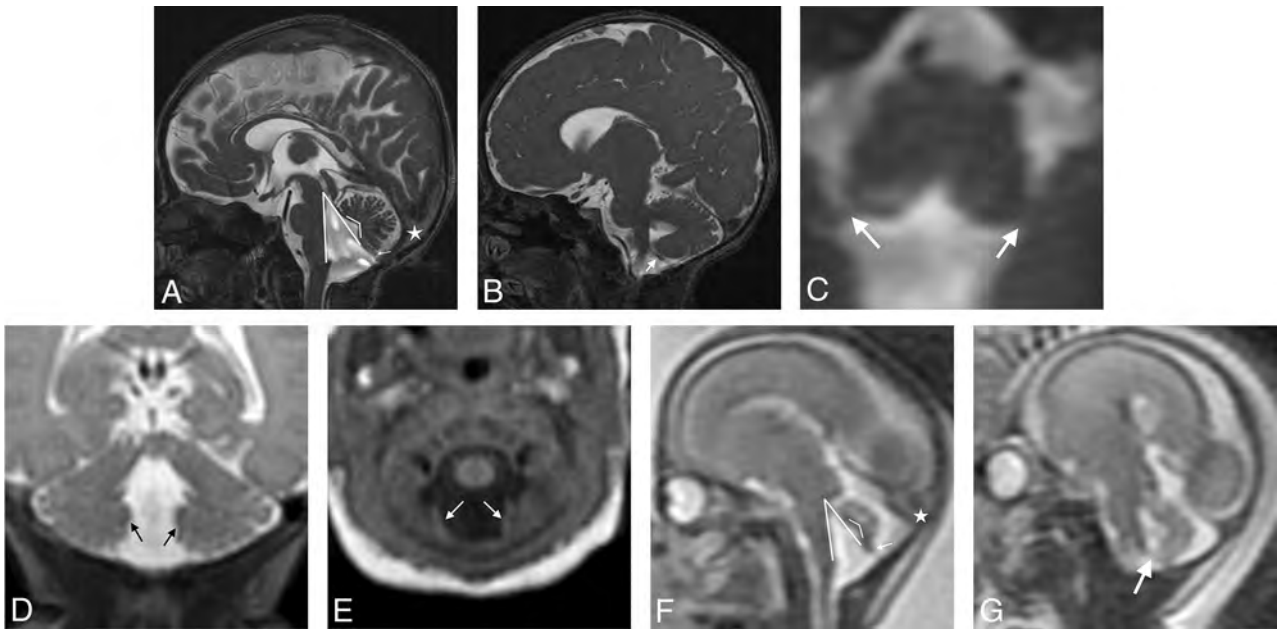

FIGURE. Dandy-Walker phenotype: MR imaging criteria. Balanced steady-state sequence (0.8-mm section thickness, 0.4-mm section spacing) in the sagittal (*A*), parasagittal (*B*), and axial (*C*) planes and coronal T2WI (1-mm section thickness, 0-mm section spacing, *D*) and axial TIWI (1-mm section thickness, 0-mm section spacing, *E*) from a neonate show inferior predominant VH, an enlarged tegmentovermian angle at 35° (*thick-lined angle*, *A*), an obtuse fastigial angle at 119° (*thin-lined angle*, *A*), an unpaired caudal lobe (ie, tail-sign; *thin arrow*, *A*), and inferolateral displacement of the taenia–tela choroidea complex and choroid plexus distant from the vermis (*thick arrows*, *B–E*). Similar findings are seen in the same patient on fetal MR imaging at 22 weeks' gestational age in sagittal (*F*) and parasagittal single-shot T2WI (3-mm section thickness, 0-mm section spacing, *G*). Note a normal torcular position (*stars*); the torcular position is variable in all forms of posterior fossa abnormalities/anomalies and should not be considered in isolation as an interpretive criterion in the differential diagnosis.

gradient recalled-echo were reviewed in most cases (when available). Multiplanar single-shot FSE/TSE sequences with section thickness ranging from 2 to 5 mm were acquired in all fetal MR imaging examinations.

Statistical Analysis

The Mann-Whitney *U* test was performed to evaluate differences in continuous variables between the DWM and non-DWM groups. The χ^2 test was used for categoric variables. Receiver operating characteristic curves and concordance statistics comparing the DWM and non-DWM groups were generated for the continuous variables in both the prenatal and postnatal groups. An optimized linear model for discriminating DWM from non-DWM groups was created by the stepwise Akaike information criterion optimization in both the prenatal and postnatal cohorts. Receiver operating characteristic curves and concordance statistics were generated for both the empirically generated and stepwise Akaike information criterion–optimized linear models. Missing data were encountered at random, and corresponding patients were discarded from subsequent, associated statistical analyses. Statistical analyses were performed using R Version 4.1.1 (http://www.r-project.org/) and approved by a consulting statistician.

RESULTS

Four hundred seventy-six brain MR imaging examinations were evaluated. Thirty examinations were excluded due to insufficient image quality and/or deficient data, leaving 446 examinations (fetal: $n = 174$, 39.0%; median gestational age/interquartile range/range = 21.9 weeks/6.2 weeks/17–39 weeks, male/female = 1:1.0; postnatal: $n = 272$ [61.0%]; median age/interquartile range = 190 days/1472 days, male/female = 1:1.2) from 407 patients. Thirty-nine patients were imaged both prenatally and postnatally. Of these, 9 (23.1%) diagnoses were revised postnatally though no single diagnosis was significantly affected. Most patients had either DWM (78%, $n = 329$) (Online Supplemental Data) or vermian hypoplasia (VH; 13.9%, $n = 62$) (Online Supplemental Data) as would be expected on the basis of the method of case acquisition. However, a minority of cases were re-classified as either BPS ($n = 16$, 3.6%) or concurrent VH and BPC ($n = 39$, 8.7%) (Online Supplemental Data).

Seventy-five percent ($n = 129$) of fetal MR imaging cases and 73% ($n = 200$) of postnatal examinations had DWM. The remaining were diagnosed with VH (fetal: $n = 12$, 6.9%; postnatal: $n = 50$, 18.3%), BPC (fetal: $n = 8$, 4.6%; postnatal: $n = 8$, 2.9%), and VH with BPC (fetal: $n = 24$, 13.9%; postnatal: $n = 15$, 5.5%). The original diagnosis was updated/re-classified in 96 (21.5%) cases (fetal: $n = 42$, 24%; postnatal: $n = 54$, 19%) on the basis of our revised DWM criteria. There were no discrepancies identified in the updated diagnosis using our consensus criteria, and all diagnoses were equally misdiagnosed. Ventricular shunts were present in 43/273 (15.7%) postnatal examinations: Forty of 43 (93%) had DWM, 2 had VH, and 1 had VH with BPC. One hundred ten (23.1%) patients were found to have a genetic anomaly or abnormality; however, genetic information was available in only a minority of cases.

Most of the analyzed variables were found to be significant differentiators of DWM from non-DWM both prenatally and

postnatally (Online Supplemental Data). Posterior fossa perimeter and evidence of prior vascular injury were not significant differentiators of DWM and non-DWM phenotypes prenatally or postnatally (Online Supplemental Data). Superior posterior fossa angle, torcular location, and VH differentiated groups postnatally but not prenatally.

In the postnatal cohort, using TVA alone to differentiate patients with DWM from those without DWM resulted in a concordance (C) statistic of 0.901 (Online Supplemental Data). A linear model using TVA and patient age resulted in C-statistics of 0.901 (prenatally) and 0.925 (postnatally) for differentiating DWM and non-DWM (Online Supplemental Data). Optimized linear models generated with the stepwise Akaike information criterion resulted in C-statistics of 0.927 (prenatally) and 0.944 (postnatally) for differentiating DWM and non-DWM (Online Supplemental Data). The Akaike information criterion–optimized prenatal linear model included age, TVA, fastigial angle, and VH. The Akaike information criterion–optimized postnatal linear model included age, TVA, and fastigial angle.

Brainstem dysmorphism was found in 66.9% ($n = 220$) of children with DWM in comparison with 60.7% ($n = 71$) of children in the non-DWM group. Of the 220 children with DWM and brainstem abnormalities, most had pontine hypoplasia (86.0%; $n = 189$), while a minority had either a thickened pons and/or medulla (6.4%; $n = 14$) or a dysplastic, elongated brainstem (3.6%; $n = 8$). Pontine hypoplasia was also the most common phenotype present in children without DWM with brainstem abnormalities (84.5%; $n = 60$).

DISCUSSION

The literature is rife with confusing terminology regarding abnormalities of the posterior fossa. Imprecise definitions and inconsistent use of DWM and related terms (variant, continuum, spectrum), VH, inferior vermian hypoplasia, and partial caudal vermian agenesis have contributed to poor correlations between neuroimaging phenotypes and clinical outcome. Clarification would improve counseling for pregnancy planning, prognosis, and genetic work-up. In our cohort, we found evidence of this ongoing confusion and descriptive heterogeneity. If we used vermian structure, choroid plexus/tela choroidea location, and fastigial recess angles as primary diagnostic criteria, 96 of 407 (23.6%) posterior fossa malformations were originally misdiagnosed with a predominant bias of intraventricular hemorrhage and BPC ($n = 29$) and intraventricular hemorrhage ($n = 17$) instead of DWM.

Current diagnostic imaging criteria for DWM include VH with enlargement of the fourth ventricle and posterior fossa.[1] However, there is wide variability in the degree of vermian underdevelopment and posterior fossa enlargement, sometimes without correlation between the 2. Our results support this variability in that posterior fossa enlargement was not a significant differentiator between the DWM and non-DWM groups. Often, there are imaging features that approach but do not meet the full diagnostic criteria. While Dandy-Walker variant is an antiquated, poorly defined label, its intended use once served an important purpose: to indicate less pronounced phenotypes that appeared similar to a DWM proper. The problem with the term Dandy-Walker variant was not an intrinsic one; rather, it was that its misuse in the literature left it without a clear definition and even rendered it, at times, misleading. Abandonment was necessary, leaving a descriptive void.

We are reluctant to overly emphasize the imaging appearance of these malformations for fear of overstating the importance of the imaging phenotype for prognosis and management. Ultimately, clinical outcome is the most important factor for prognosis, so there is a need for long-term longitudinal clinical follow-up to determine to what extent an imaging subclassification scheme matters, if at all. In addition, myriad causative mechanisms (postmigrational insult, infection, germline genetic abnormality, somatic mutation) must be better elucidated and understood in the context of the mechanism of normal cerebellar development. Evidence of prior vascular injury was found in a minority of our cohort but did not differentiate the DWM from the non-DWM group. Nevertheless, MR imaging sensitivity for hemorrhage detection wanes with time, and prior injury may be indiscernible on fetal MR imaging, particularly with insufficient resolution or when motion artifacts are present.

To fully appreciate the developmental pathogenesis of any brain malformation, one must identify the approximate timing of the insult following which development goes awry. DWM is characterized by upward, under-rotation of a hypoplastic vermis vis-à-vis the brainstem. Extensive analysis points to the posterior vermis being disproportionately hypoplastic.[10,11] Our updated imaging criteria stem from an improved understanding of the mechanism of injury (disrupted growth of the posterior vermis) during a specific developmental epoch generally thought to result in the Dandy-Walker phenotype—that is, inferior vermian–predominant hypoplasia with an unpaired caudal lobule, an obtuse fastigial recess, a large TVA, and inferolateral displacement of the taenia–tela choroidea complex and choroid plexus, the latter due to failed resolution of the anterior membranous area.

Fourth ventricular size, posterior fossa size, and torcular location are poor imaging criteria for DWM because they are largely related to the degree of fourth ventricular outflow impedance and are not direct sequelae of the injury or malformation. Rather, imaging determination should hinge on the appearance of the vermis, choroid plexus, and tela choroidea in accordance with the time that the abnormality developed. Our receiver operating characteristic analysis quantitatively demonstrates the robust distinction between DWM and non-DWM cases with C-statistics of >0.9 when evaluating structures such as the fastigial recess or measuring the TVA. As objective measures of the more subjective DWM imaging features, these strongly predictive quantitative data may facilitate neuroimaging classification by those with less clinical expertise than our expert panel or by, yet developed, artificial intelligence tools. Although more complex linear models were more predictive (Online Supplemental Data), the strong predictive value of TVA alone suggests that such complexity may be unnecessary in most cases; however, it would be necessary to compare patients with posterior fossa abnormalities to a cohort of healthy control subjects to better determine the importance of predictive imaging variables for diagnosis.

Histopathologically, DWM is thought to be underpinned by disruption in the structure of the rhombic lip (RL), a stem cell zone located in the posterior cerebellum that gives rise to ~80% of

all neurons in the human brain, including all glutamatergic neurons in the cerebellum.[10,11] During embryonic development, the human RL is trigonal but later expands into a tail-like structure trailing from the posterior cerebellum, with ventricular and subventricular compartments separated by a vascular bed. During this time, the fastigial recess remains flat. With an increase in size of the posterior cerebellum brought about by the outward growth of the nodulus beginning at 14 postconceptional weeks, the tail-like RL becomes integrated into the posterior-most lobule, causing the fastigial recess to sharpen (>14 postconceptional weeks).[10,11] In comparisons of DWM and VH, it is evident that in DWM, the fastigial angle remains flat or obtuse, while in VH, the angle becomes acute. This finding provides us with some clues to the potential timing of the insult and leads to the hypothesis that in DWM, RL disruption occurs before RL internalization, while in VH, aberrations in RL development and other processes occur following internalization. The delay in RL disruption leading to restricted hypoplasia of the posterior-most lobule suggests that the early RL likely contributes to the growth of the entire cerebellum, but post-internalization helps in the growth and maintenance of the posterior lobe only. Hence, the extent of hypoplasia would depend on the timing of the RL insult, with further work required to define this developmental stage.

The concomitant presence of brainstem dysmorphism in children with abnormalities of cerebellar development is unsurprising, given that the cerebellum is a dorsal derivative of the anterior hindbrain, rhombomere 1.[19,20] Developmentally, the neurons of the pontine nuclei arise from the both the cerebellar RL in rhombomere 1 and the RL of other more posterior hindbrain rhombomeres. These neurons migrate tangentially to their final position in rhombomeres 3 and 4.[19,20] Because both DWM and VH exhibit similar and statistically indifferentiable rates of pontine hypoplasia, this feature suggests that the pontine hypoplasia seen in these conditions is most likely due to a combination of deficient pontine nuclear neurogenesis/histogenesis and WM fiber reduction commensurate with the degree of cerebellar hypoplasia.

The growth and development of the posterior vermis are the most protracted of all regions, making it especially vulnerable to disruptive events.[10,11,21] The inferior vermis is the most common and most severely involved region in DWM and isolated vermian hypogenesis, ie, partial agenesis.[11] Nonetheless, inferior VH should be diagnosed only if it can be documented that the inferior vermis is small. Otherwise, the more general term "vermian hypoplasia" should be used.[21] "Hypoplasia" should be reserved for a small but otherwise structurally normal-for-age vermis.[22] The other less discussed and appreciated fact is that in some circumstances, one or more of these diagnoses may be present, further hampering interpretation (eg, VH and Blake pouch anomalies). Larger Blake pouch anomalies cause vermian measurement inaccuracies,[6] thereby making vermian height in isolation an inadequate determinant for the Dandy-Walker phenotype, as seen in our prenatal cohort. Furthermore, the TVA is variable in both DWM and BPC. Although marked TVA enlargement strongly supports the diagnosis of DWM, the opposite is not true: Mild TVA elevation may be present in either DWM or BPC.

The retrospective nature of this cohort study and imaging review is a limitation and is subject to case-selection bias. Because the bulk of the cohort was accrued from imaging reports containing the terms "Dandy-Walker" and "vermian hypoplasia," it lacks an unknown number of cases that were missed, misinterpreted, or mislabeled by the original interpreting radiologist. It also lacks a control group. This study, although the largest reported, is only the first step toward a more complete understanding of the Dandy-Walker phenotype and its (likely numerous) etiologies and diverse clinical presentations. Future work must involve more clinical outcome data, longitudinal clinical and imaging data, histopathologic and genomic analysis, healthy controls, and prenatal clinical history if we hope to bridge the divide between imaging appearance and clinical outcome. Ultimately, we aim to better understand the causes and contributing factors that result in the Dandy-Walker phenotype, and with that mechanistic understanding, we hope that we will one day be able to predict outcomes, heritability, and the likelihood of similar abnormalities in future pregnancies.

CONCLUSIONS

Objective measures have confirmed statistically the modern phenotypic features of DWM and allow differentiation from VH and BPC, causing misclassification in nearly one-quarter of prior reports. The modern DWM phenotype is best defined by inferior, predominant VH (mandatory), inferolateral displacement of the tela choroidea/choroid plexus (mandatory when visible), an unpaired caudal lobule (mandatory when visible), an enlarged tegmentovermian angle, and an obtuse fastigial recess, the latter 2 being the most significant qualitative measures. Posterior fossa size and torcular location should be eliminated from the diagnostic criteria. We highlight the fact that the structural phenotype, while providing some information about developmental timing, bears no relevance to the etiology, whether genetic or acquired, except in rare cases where there is evidence of prior hemorrhage, inflammation, or other injury. This refined imaging phenotype may help guide future study of the numerous etiologies and varied clinical outcomes.

ACKNOWLEDGMENTS

Biostatistician W. John Boscardin, PhD, reviewed the data and assisted with the statistical analysis.

Disclosure forms provided by the authors are available with the full text and PDF of this article at www.ajnr.org.

REFERENCES

1. Barkovich AJ, Raybaud CA. **Congenital malformations of the brain and skull.** In: Barkovich AJ, Raybaud CA, eds. *Pediatric Neuroimaging.* 6th ed. Wolters Kluwer; 2019:531
2. Wüest A, Surbek D, Wiest R, et al. **Enlarged posterior fossa on prenatal imaging: differential diagnosis, associated anomalies and postnatal outcome.** *Acta Obstet Gynecol Scand* 2017;96:837–43 CrossRef Medline
3. Lerman-Sagie T, Prayer D, Stöcklein S, et al. **Fetal cerebellar disorders.** *Handb Clin Neurol* 2018;155:3–23 CrossRef Medline

4. Nagaraj UD, Kline-Faith BM, Horn PS, et al. **Evaluation of posterior fossa biometric measurements on fetal MRI in the evaluation of Dandy-Walker continuum.** *AJNR Am J Neuroradiol* 2021;42:1716–21 CrossRef Medline
5. Aldinger KA, Timms AE, Thomson Z, et al. **Redefining the etiologic landscape of cerebellar malformations.** *Am J Hum Genet* 2019;105:606–15 CrossRef Medline
6. Whitehead MT, Vezina G, Schlatterer SD, et al. **Taenia-tela choroidea complex and choroid plexus location help distinguish Dandy-Walker malformation and Blake pouch cysts.** *Pediatr Radiol* 2021;51:1457–70 CrossRef Medline
7. Bernardo S, Vinci V, Saldari M, et al. **Dandy-Walker malformation: is the "tail sign" the key sign?** *Prenat Diagn* 2015;35:1358–64 CrossRef Medline
8. Paladini D, Donarini G, Parodi S, et al. **Hindbrain morphometry and choroid plexus position in differential diagnosis of posterior fossa cystic malformations.** *Ultrasound Obstet Gynecol* 2019;54:207–14 CrossRef Medline
9. Nelson MD, Maher K, Gilles FH. **A different approach to cysts of the posterior fossa.** *Pediatr Radiol* 2004;34:720–32 CrossRef Medline
10. Haldipur P, Aldinger KA, Bernardo S, et al. **Spaciotemporal expansion of the primary progenitor zones in the developing human cerebellum.** *Science* 2019;366:454–60 CrossRef Medline
11. Haldipur P, Bernardo S, Aldinger K, et al. **Evidence of disrupted rhombic lip development in the pathology of Dandy-Walker malformation.** *Acta Neuropathol* 2021;142:761–76 CrossRef Medline
12. Twickler DM, Reichel T, McIntire DD, et al. **Fetal central nervous system ventricle and cisterna magna measurements by magnetic resonance imaging.** *Am J Obstet Gynecol* 2002;187:927–31 CrossRef Medline
13. Chapman T, Menashe SJ, Zare M, et al. **Establishment of normative values for the fetal posterior fossa by magnetic resonance imaging.** *Prenat Diagn* 2018;38:1035–41 CrossRef Medline
14. Jandeaux C, Kuchcinski G, Ternynck C, et al. **Biometry of the cerebellar vermis and brain stem in children: MR imaging reference data from measurements in 718 children.** *AJNR Am J Neuroradiol* 2019;40:1835–41 CrossRef Medline
15. Dovjak GO, Brugger PC, Gruber GM, et al. **Prenatal assessment of cerebellar vermian lobulation: fetal MRI with 3-Tesla postmortem validation.** *Ultrasound Obstet Gynecol* 2018;52:623–30 CrossRef Medline
16. Kline-Faith B, Bulas D, Bahado-Singh R. *Fundamental and Advanced Fetal Imaging: Ultrasound and MRI*. Wolters Kluwers; 2015
17. Pertl B, Eder S, Stern C, et al. **The fetal posterior fossa on prenatal ultrasound imaging: normal longitudinal development and posterior fossa anomalies.** *Ultraschall Med* 2019;40:692–721 CrossRef Medline
18. Whitehead MT, Vezina G. **The fetal falx cerebelli.** *Pediatr Radiol* 2020;50:984–89 CrossRef Medline
19. Watson C, Bartholomaeus C, Puelles L. **Time for radical changes in brain stem nomenclature-applying the lessons from developmental gene patterns.** *Front Neuroanat* 2019;13:10 CrossRef Medline
20. Leto K, Arancillo M, Becker EB, et al. **Consensus paper: cerebellar development.** *Cerebellum* 2016;15:789–828 CrossRef Medline
21. Robinson AJ, Blaser S, Toi A, et al. **The fetal cerebellar vermis: assessment for abnormal development by ultrasonography and magnetic resonance imaging.** *Ultrasound Q* 2007;23:211–23 CrossRef Medline
22. Malinger G, Lev D, Lerman-Sagie T. **The fetal cerebellum: pitfalls in diagnosis and management.** *Prenat Diagn* 2009;29:372–80 CrossRef Medline

Intracranial Hemorrhage in Term and Late-Preterm Neonates: An Institutional Perspective

A.G. Sandoval Karamian, Q.-Z. Yang, L.T. Tam, V.L. Rao, E. Tong, and K.W. Yeom

ABSTRACT

BACKGROUND AND PURPOSE: Distribution of intracranial hemorrhage in term and late-preterm neonates is relatively unexplored. This descriptive study examines the MR imaging–detectable spectrum of intracranial hemorrhage in this population and potential risk factors.

MATERIALS AND METHODS: Prevalence and distribution of intracranial hemorrhage in consecutive term/late-preterm neonates who underwent brain MR imaging between January 2011 to August 2018 were assessed. MRIs were analyzed to determine intracranial hemorrhage distribution (intraventricular, subarachnoid, subdural, intraparenchymal, and subpial/leptomeningeal), and chart review was performed for potential clinical risk factors.

RESULTS: Of 725 term/late-preterm neonates who underwent brain MR imaging, intracranial hemorrhage occurred in 63 (9%). Fifty-two (83%) had multicompartment intracranial hemorrhage. Intraventricular and subdural were the most common hemorrhage locations, found in 41 (65%) and 39 (62%) neonates, respectively. Intraparenchymal hemorrhage occurred in 33 (52%); subpial, in 19 (30%); subarachnoid, in 12 (19%); and epidural, in 2 (3%) neonates. Twenty infants (32%) were delivered via cesarean delivery, and 5 (8%), via instrumented delivery. Cortical vein thromboses were present in 34 (54%); periventricular or medullary vein thromboses, in 37 (59%); and cerebral venous sinus thrombosis, in 5 (8%). Thirty-seven (59%) had elevated markers of coagulopathy (international normalized ratio $>$ 1.2, fibrinogen level $<$ 234), 9 (14%) had a clinically meaningful elevation in the international normalized ratio ($>$1.4), and 3 (5%) had a clinically meaningful decrease in the fibrinogen level ($<$150). Three (5%) neonates had thrombocytopenia (platelet count $< 100 \times 10^3/\mu L$).

CONCLUSIONS: While relatively infrequent, there was a wide distribution of intracranial hemorrhage in term and late-preterm infants; intraventricular and subdural hemorrhages were the most common types. We report a high prevalence of venous congestion or thromboses accompanying neonatal intracranial hemorrhage.

ABBREVIATIONS: GA = gestational age; ICH = intracranial hemorrhage; INR = international normalized ratio; IPH = intraparenchymal hemorrhage; IVH = intraventricular hemorrhage; SWAN = susceptibility-weighted angiography

Intracranial hemorrhages (ICHs) in term (gestational age [GA] $\geq$ 37 weeks) and late-preterm (GA = 34–36 weeks) neonates can range in clinical manifestations from asymptomatic to potentially devastating.

In preterm neonates, intraventricular hemorrhage (IVH) is the most common ICH type due to immature vessels of the germinal matrix.[1-3] In older neonates, however, ICH is less common and differs in location, etiology, and outcome.[4] A case-control study of infants born in the Northern California Kaiser Permanente Medical Group identified 20 cases of neonatal ICH with a population prevalence of 6.2 in 100,000 live births, but without investigations into a specific intracranial compartment.[5] The clinical presentation of the term neonate with ICH might include encephalopathy, strokes, seizures, apnea, and respiratory distress.[5-7]

There are conflicting data regarding the association of ICH with traumatic or instrumented delivery via assistance with vacuum or forceps.[5,8-11] One Swedish study of vacuum-assisted vaginal delivery of term neonates described 9-fold increased odds of ICH, with protracted extractions compared with extractions adhering to safety

Received February 20, 2022; accepted after revision July 27.

From the Division of Child Neurology (A.G.S.K.), University of Utah, Salt Lake City, Utah; Division of Child Neurology (Q.-Z.Y.), University of North Carolina, Chapel Hill, North Carolina; Stanford University School of Medicine (L.T.T., V.L.R.), Palo Alto, California; and Department of Radiology (E.T., K.W.Y.), Lucile Packard Children's Hospital, Stanford University, Palo Alto, California.

A. G. Sandoval Karamian is supported by a grant from the American Epilepsy Society; V.L. Rao is supported by the Stanford MedScholars Fellowship.

Please address correspondence to Kristen W. Yeom, MD, 725 Welch Rd, Lucile Packard Children's Hospital G516, Palo Alto, CA 94304; e-mail: kyeom@stanford.edu

Indicates article with online supplemental data.

http://dx.doi.org/10.3174/ajnr.A7642

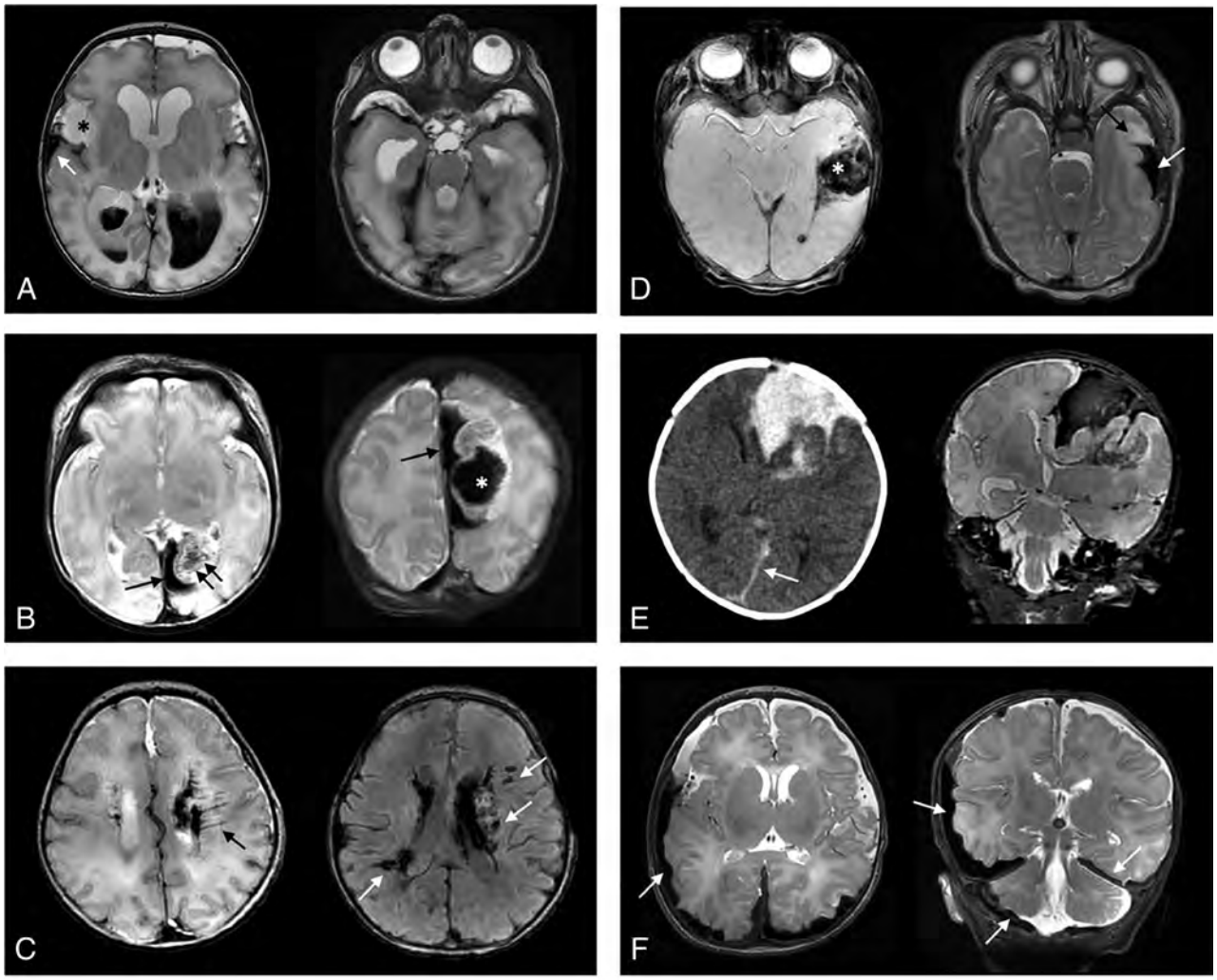

FIG 1. Examples of various anatomic distributions of intracranial hemorrhages in term or late-preterm neonates. *A*, IVH and associated ventriculomegaly are present. Tentorial subdural hemorrhage is also present, as well as hemorrhage overlying the bilateral temporal poles. Right temporal lobe swelling (*asterisk*) is present and associated with subpial hemorrhage (*arrow*). *B*, Left occipital subpial hemorrhage (*single arrow*) is present, as well as left parieto-occipital lobe parenchymal hemorrhage (*asterisk*). Linear low signal intensities (*double arrows*) suggest either venous congestion or thromboses. *C*, Intra- and periventricular hemorrhages are present. Linear intensities (*black arrow*) and nodular intensities (*white arrows* on T2* imaging) suggest a perimedullary vein congestion and/or thromboses. *D*, Subpial hemorrhage is seen (*white arrow*) with subjacent temporal lobe deformity and edema (*black arrow*). On T2* imaging, parenchymal hemorrhage is also seen (*asterisk*), as well as punctate intraventricular blood products. *E*, Combined left frontal subpial and parenchymal hemorrhages are shown on CT and MR imaging. Small falcine subdural hemorrhage is also shown (*arrow*). *F*, Bilateral cerebral convexity, posterior fossa, and tentorial subdural hemorrhages (*arrows*) are present in a neonate with hemophilia.

recommendations.[12] In another study, instrument-assisted birth was not associated with higher odds of intracranial hemorrhage or hemorrhagic stroke.[5]

There are also conflicting data on the association of coagulopathy with neonatal ICH.[6,7] For example, 1 small case series of 17 neonates with subpial hemorrhage, a rare neonatal ICH pattern with hemorrhage interposed between the brain surface and pia mater, observed a relatively high incidence of acute thrombocytopenia and coagulation abnormalities.[6] However, in another small series of 7 neonates with subpial or subarachnoid hemorrhage, none had coagulopathy.[7]

Limited data exist on the prevalence and location of intracranial hemorrhage in term and late-preterm neonates, and less is known about potential risk factors for these hemorrhages. This study describes the spectrum of ICH in late-preterm and term neonates from a large cohort at a single institution.

MATERIALS AND METHODS

Study Design

This was a retrospective descriptive study of neonates who underwent brain MR imaging at Lucile Packard Children's Hospital at Stanford from January 2011 to August 2018. The study and waiver of consent were approved by the Stanford University Institutional Review Board. Clinical and radiographic data were de-identified.

Participants

The following served as the inclusion criteria: term (GA $\geq$ 37 weeks) or late-preterm (GA $\geq$ 34 weeks) neonates with brain

Table 1: Sample characteristics

Variable	Result
GA (median) (IQR) (wk)	38.3 (37.0–39.8)
Birth weight (mean) (SD) (kg)	3.1 (0.7)
Maternal age (median) (IQR) (yr)	31 (28.0–34.0)
Cesarean delivery (No.) (%)	20 (32)
Scheduled (No.) (%)	9 (45)
Urgent (No.) (%)	11 (55)
Instrumented delivery (No.) (%)	5 (8)
Apgar at 1 minute (median) (IQR)	7 (2–8)
Apgar at 5 minutes (median) (IQR)	9 (7–9)
HIE as indication for MR imaging (No.) (%)	11 (17)
Seizure as indication for MR imaging, (No.) (%)	15 (24)
Sepsis/meningitis (No.) (%)	5 (8)

Note:—HIE indicates hypoxic-ischemic encephalopathy.

MR imaging that included both anatomic scans and iron-sensitive T2* imaging (gradient-echo or susceptibility-weighted angiography [SWAN]) obtained before 45 weeks postmenstrual age. Patients with nondiagnostic brain MR imaging (eg, motion degradation or other artifacts) and lack of T2* MR imaging were excluded. Subjects were identified from a database of patients in the Lucile Packard Children's Hospital at Stanford Neonatal Intensive Care Unit who underwent brain MR imaging.

Hemorrhage Locations

The ICH location was based on the following criteria: 1) intraventricular hemorrhage, hemorrhage in the cerebral ventricles; 2) subdural hemorrhage, hemorrhage in the subdural space between the dura mater and arachnoid mater; 3) subarachnoid hemorrhage, hemorrhage in the subarachnoid space between the pia mater and arachnoid mater; 4) subpial hemorrhage, hemorrhage overlying the cortex or between the cortical surface and the pia mater; and 5) intraparenchymal hemorrhage (IPH), hemorrhage in the brain parenchyma. Small blood products in the posterior fossa and tentorium typically present after birth were not considered pathologic ICH.

Clinical Information

Chart review was conducted for the following: birth weight, GA, maternal age, method of delivery, instrumented delivery, Apgar scores, indication for imaging, underlying congenital heart disease, history of extracorporeal membrane oxygenation, history of seizures, and coagulation laboratory values. Normal value ranges for the laboratory where the coagulation studies were performed were 234–395 mg/dL for fibrinogen levels and 0.9–1.2 for the international normalized ratio (INR).

Imaging Technique and Analysis

All patients underwent brain MR imaging at either 1.5T (Signa; GE Healthcare) or 3T (Discovery MR750; GE Healthcare). The routine infant brain MR imaging protocol included either a T2* axial gradient-echo (TR = 500–600 ms, TE = 20–30 ms, section thickness = 5 mm, and skip = 1.5 mm) or SWAN (TR = 50–70 ms, TE = 45–25 ms, section thickness = 4 mm, 0 skip). Other imaging sequences included T1 FLAIR, T1 spoiled gradient-recalled, T2 FSE, DWI, and arterial spin-labeling.

Two board-certified neuroradiologists (E.T. and K.W.Y.), blinded to clinical information, independently reviewed the brain MRIs and cataloged hemorrhage distribution. Additionally, the reviewers recorded the presence of lesions suspicious for venous thromboses, eg, thick, linear, and expansile T2* lesions that followed the anatomic distribution of medullary/periventricular or cortical veins or filling defects/flow gaps associated with dural venous sinus thromboses. Any disagreement between the reviewers was resolved by a consensus review among the 2 neuroradiologists and 2 child neurologists (A.G.S.K., Q.-Z.Y.). Examples of ICH categorization are shown in Fig 1.

Statistical Analysis

Descriptive statistics included mean (SD) for normally distributed variables and median and interquartile ranges (IQRs) for non-normally distributed variables.

RESULTS

Hemorrhage

Of 1542 neonates who underwent brain MR imaging between January 2011 and August 2018, seven hundred twenty-five neonates (median day of life = 5.0 days, IQR = 3.0–8.5) met the inclusion criteria: 576 term (GA ≥ 37 weeks) and 149 late-preterm neonates (GA = 34–36.9 weeks). Of 725 neonates, 63 (9%) were found to have ICH: 47 of the 576 (8.2%) term neonates and 16 of the 149 (10.7%) late-preterm neonates. Table 1 summarizes demographics and clinical features. Fifty-two neonates (83%) had >1 type of hemorrhage. IVH and subdural hemorrhage were the most common hemorrhage locations, occurring in 41 (65%) and 39 (62%), respectively. IPH occurred in 33 (52%); subpial hemorrhage, in 19 (30%); SAH, in 12 (19%); and epidural hemorrhage, in 2 (3%) (Figs 2 and 3). T2* lesions suspicious for venous thromboses were identified in more than half of the subjects (Table 2).

Clinical Features

Thirty-seven (59%) subjects had elevated markers of coagulopathy (INR > 1.2, fibrinogen level <234 mg/dL). Nine (14%) had a clinically meaningful elevation in the INR of >1.4, and 3 (5%) had a clinically meaningful decrease in fibrinogen levels of <150 mg/dL (Table 2). Three (5%) neonates had platelet counts of $<100 \times 10^3/\mu L$. Four neonates were found to have possible genetic etiologies of coagulopathy. One was heterozygous for a factor V Leiden mutation, 1 was heterozygous for prothrombin 20210A mutation, 1 was homozygous for the *MTHFR* mutation, and 1 was found to have factor VIII hemophilia.

Delivery was instrumented in 5 subjects: 4 with vacuum-assisted delivery and 1 with forceps-assisted delivery. Eight (13%) had congenital heart disease, and 2 (3%) had undergone extracorporeal membrane oxygenation before MR imaging.

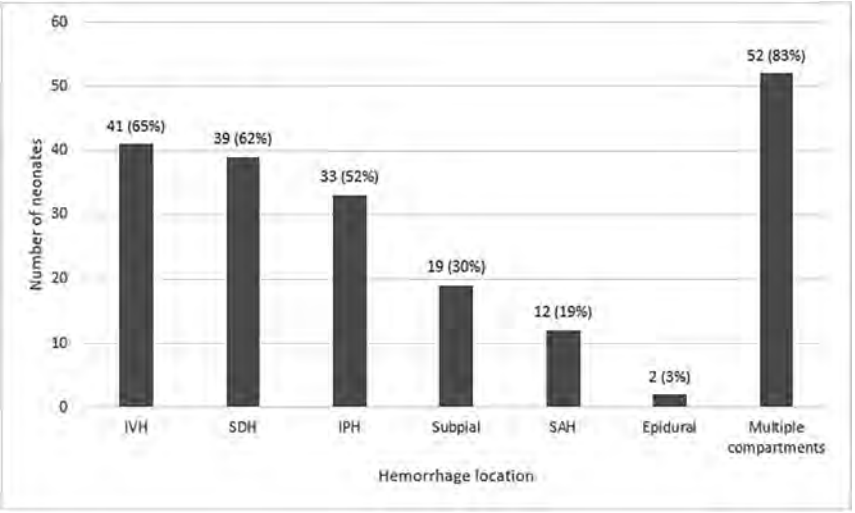

FIG 2. Distribution of hemorrhages by CNS location. SDH indicates subdural hemorrhage.

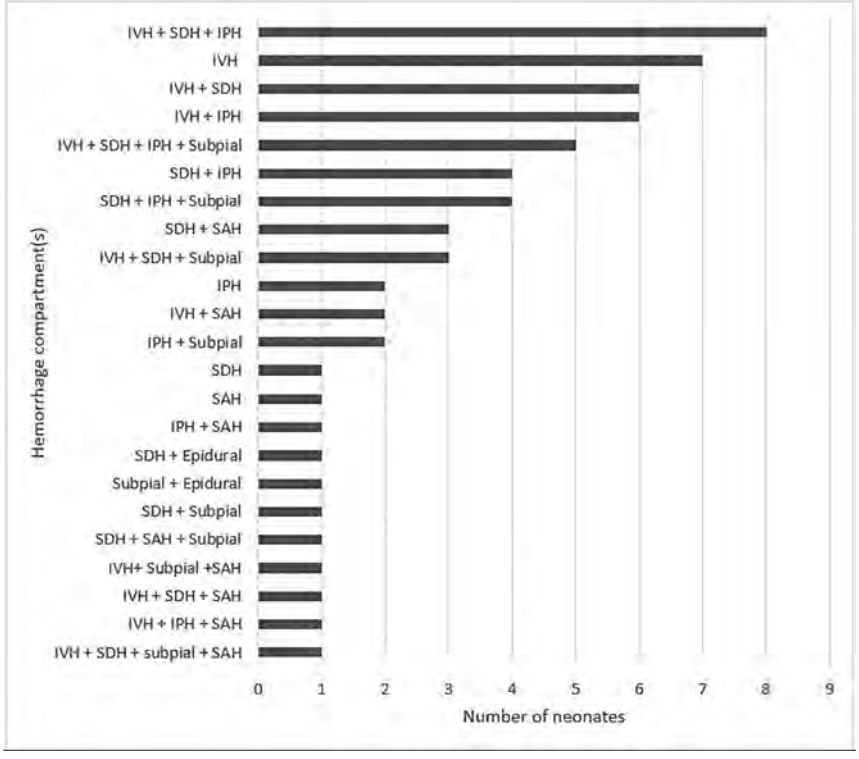

FIG 3. Distribution of hemorrhages by CNS location, subdivided by a combination of compartments when multiple compartments were involved. SDH indicates subdural hemorrhage.

The indications for MR imaging were clinical suspicion of hypoxic-ischemic encephalopathy in 11 (17%), seizures in 15 (24%), and abnormal findings on head sonography in 20 (32%). Five subjects (8%) had sepsis or meningitis. Most patients (n = 56, 89%) were discharged home, 5 (8%) were transferred to an outside facility, and 2 (3%) died. Both of the 2 patients who died had chromosomal abnormalities and congenital heart disease.

DISCUSSION

We observed a wide range in ICH distribution in term and late-preterm neonates, with most presenting with multicompartment hemorrhages and intraventricular hemorrhage and subdural hemorrhage representing the most common hemorrhage locations. To date, this is the first study to systematically categorize ICH in term and late-preterm neonates at a large quaternary care pediatric center.

Clinical presentation and indications for MR imaging in our cohort are concordant with prior neonatal studies that examined ICH,[5,6] including clinical suspicion of hypoxic-ischemic encephalopathy, seizures, and abnormal findings on head sonography. Intraventricular hemorrhage has been widely studied in premature neonates and remains the most common ICH type affecting preterm infants.[1-3] Our sample, although a single-center experience, suggests that IVH is also a common ICH presentation in term and late-preterm neonates, occurring in 65% (n = 41) of those with ICH. However, given the multicompartment ICH distribution in most of our neonates with ICH (83%), we postulate pathophysiology or hemodynamic dysregulation that is distinct from the germinal matrix fragility typically implicated in preterm neonates (Figs 2 and 3). Similarly, a recent small cohort study of 17 neonates with subpial hemorrhages also found concomitant hemorrhages in other brain locations, eg, IPH or IVH.[6]

Although the relationship between ICH and traumatic or instrumented delivery via vacuum assistance or forceps remains debated, most studies report low rates of ICH with instrumented delivery.[5,8-11] Similarly, we report a low rate of instrumented delivery, occurring in only 5 of the 63 subjects (8%). Prior studies have identified an association between fetal distress via emergent cesarean delivery: bradycardia, decelerations, and low Apgar scores with neonatal ICH. However, the rates of delivery by cesarean birth in our sample were similar to those in the general population at 32%, with 9 (45%) scheduled and 11 (55%) for urgent indications; and the median Apgar score at 5 minutes was 9 (IQR = 7–9).[13]

One potential contributor to neonatal ICH is coagulopathy, despite conflicting data in the literature.[6,7] While most (59%) of our neonates with ICH had elevated coagulopathy markers based

Table 2: Venous thromboses and thrombocytopenia/coagulopathy in neonates with ICH

Variable	Result
Cortical vein thromboses present (No.) (%)	34 (54)
Periventricular or medullary vein thromboses present (No.) (%)	37 (59)
CVST present (No.) (%)	5 (8)
MRA performed (No.) (%)	26 (41)
MRA, abnormal finding (No.) (%)	2 (3)
MRV performed (No.) (%)	27 (43)
MRV, abnormal findings (No.) (%)	5 (8)
Platelet count (median) (IQR) ($\times 10^3/\mu$L)	186 (147–271)
Platelet count <100 $\times 10^3/\mu$L (No.) (%)	3 (5)
INR (median) (IQR)	1.2 (1.1–1.4)
INR >1.2 (No.) (%)	22 (35)
INR >1.4 (No.) (%)	9 (14)
PTT (median) (IQR) (sec)	37.4 (32.1–41.9)
PTT >35.7 sec (No.) (%)	26 (41)
Fibrinogen level (median) (IQR) (mg/dL)	266 (216–392.5)
Fibrinogen level <234 mg/dL (No.) (%)	15 (24)
Fibrinogen level <150 mg/dL (No.) (%)	3 (5)

Note:—CVST indicates cerebral venous sinus thrombosis; PTT, partial thromboplastin time.

Table 3: Thromboses and coagulopathy by bleed location

	Thrombosis (No.) (%)[a]				Increased Bleeding Risk (No.) (%)[a]	
Hemorrhage Location	Cortical Vein Alone	Periventricular Vein Alone	Both Cortical and Periventricular Veins	CVST	Coagulopathy[b]	Thrombocytopenia[c]
IVH ($n = 41$)	4 (10)	9 (22)	17 (41)	5 (12)	9 (22)	2 (5)
SDH ($n = 39$)	7 (18)	9 (23)	17 (44)	2 (5)	12 (31)	1 (3)
Subpial ($n = 19$)	4 (21)	7 (37)	4 (21)	2 (11)	3 (16)	0 (0)
SAH ($n = 12$)	4 (33)	1 (8)	3 (25)	0 (0)	3 (25)	1 (8)
IPH ($n = 33$)	5 (15)	9 (27)	16 (48)	3 (9)	8 (24)	3 (9)
Epidural ($n = 2$)	0 (0)	0 (0)	1 (50)	0 (0)	0 (0)	0 (0)
Multiple compartments ($n = 52$)[d]	8 (15)	9 (17)	23 (44)	3 (6)	12 (23)	3 (6)

Note:—SDH indicates subdural hemorrhage.
[a] Percentages are row-based.
[b] INR >1.4 and/or fibrinogen level < 150 mg/dL.
[c] Platelet count < 100 $\times 10^3$/uL.
[d] Most of the sample (83%) had hemorrhages in multiple compartments.

on the laboratory cutoff values, only 14% had a clinically relevant elevation in the INR of >1.4, and only 5% had either a clinically relevant decrease in platelet count of <100 $\times 10^3/\mu$L or in fibrinogen levels of <150 mg/dL. A small minority had genetic etiologies of coagulopathy, including 1 patient with hemophilia. Nevertheless, coagulopathy and thrombocytopenia represent important modifiable potential contributors, whereby early identification and correction of coagulopathy, along with maintenance of homeostasis and hemodynamic stability, are key in the management of critically ill neonates.

Most interestingly, T2* lesions suspicious for periventricular/medullary vein and cortical vein thromboses were common in our sample, occurring in 59% and 54%, respectively, with 37% having both (Table 3). Despite some reports of neonatal IPH associated with cortical vein thrombosis,[14] studies on neonatal venous thromboses are sparse. A study of subpial hemorrhages in 17 neonates also found a high incidence of enlarged perimedullary veins (65%–76%) and suggested that medullary venous congestion or thromboses may account for these hemorrhages.[6] While the mechanisms for periventricular/medullary or cortical vein thromboses remain unknown, it is possible that they represent sequelae of ICH and associated venous hypertension and congestion or primary/exacerbating contributors to hemorrhage and hemodynamic dysregulation in inflammatory or procoagulant states.

The 2 patients who died in this study each had chromosomal abnormalities and congenital heart disease; thus, ICH was not considered a major or primary contributor to mortality. Long-term neurodevelopmental outcomes are beyond the scope of this study but remain important points of future investigation.

This study has several limitations, primarily the sample size and selection bias inherent in a single quaternary pediatric center. Although this study represents the largest cohort of term or late-preterm neonatal ICHs to date, the sample in each ICH category remains small, which limits group comparisons for potential contributing risk factors or for outcome analysis. The relatively higher prevalence of ICH in our sample compared with prior studies[5] may relate to selection bias in our cohort at a quaternary, referral center or a high rate of brain MR imaging use that facilitated ICH detection unique to our academic practice.

CONCLUSIONS

While ICH in preterm infants is well-studied, it is less explored in term or late-preterm neonates. To date, this is the first and the

largest study to systematically categorize ICH in this population. We observed a wide range in ICH distribution in term and late-preterm neonates, with most neonates presenting with multicompartment hemorrhages, which might reflect global hemodynamic dysregulation. Periventricular and cortical vein thromboses were common; instrumented delivery was less frequent; and despite abnormal coagulopathy laboratory markers in >50% of the patients with ICH, clinically meaningful coagulopathy was less frequent. Further investigation is needed to determine the association of ICH subtypes in term and late-preterm neonates with later neurodevelopmental outcomes.

Disclosure forms provided by the authors are available with the full text and PDF of this article at www.ajnr.org.

REFERENCES

1. Schindler T, Koller-Smith L, Lui K, et al; New South Wales and Australian Capital Territory Neonatal Intensive Care Units' Data Collection. **Causes of death in very preterm infants cared for in neonatal intensive care units: a population-based retrospective cohort study.** *BMC Pediatr* 2017;17:59 CrossRef Medline
2. Khwaja O, Volpe JJ. **Pathogenesis of cerebral white matter injury of prematurity.** *Arch Dis Child Fetal Neonatal Ed* 2008;93:F153–61 CrossRef Medline
3. Osborn DA, Evans N, Kluckow M. **Hemodynamic and antecedent risk factors of early and late periventricular/intraventricular hemorrhage in premature infants.** *Pediatrics* 2003;112:33–39 CrossRef Medline
4. Gupta SN, Kechli AM, Kanamalla US. **Intracranial hemorrhage in term newborns: management and outcomes.** *Pediatr Neurol* 2009;40:1–12 CrossRef Medline
5. Armstrong-Wells J, Johnston SC, Wu YW, et al. **Prevalence and predictors of perinatal hemorrhagic stroke: results from the Kaiser pediatric stroke study.** *Pediatrics* 2009;123:823–28 CrossRef Medline
6. Cain DW, Dingman AL, Stence NV, et al. **Subpial hemorrhage of the neonate.** *Stroke* 2020;51:315–18 CrossRef Medline
7. Huang AH, Robertson RL. **Spontaneous superficial parenchymal and leptomeningeal hemorrhage in term neonates.** *AJNR Am J Neuroradiol* 2004;25:469–75 Medline
8. Castillo M, Fordham LA. **MR of neurologically symptomatic newborns after vacuum extraction delivery.** *AJNR Am J Neuroradiol* 1995;16:816–18 Medline
9. Towner D, Castro MA, Eby-Wilkens E, et al. **Effect of mode of delivery in nulliparous women on neonatal intracranial injury.** *N Engl J Med* 1999;341:1709–14 CrossRef Medline
10. Whitby EH, Griffiths PD, Rutter S, et al. **Frequency and natural history of subdural haemorrhages in babies and relation to obstetric factors.** *Lancet* 2004;363:846–51 CrossRef Medline
11. Looney CB, Smith JK, Merck LH, et al. **Intracranial hemorrhage in asymptomatic neonates: prevalence on MR images and relationship to obstetric and neonatal risk factors.** *Radiology* 2007;242:535–41 CrossRef Medline
12. Åberg K, Norman M, Pettersson K, et al. **Protracted vacuum extraction and neonatal intracranial hemorrhage among infants born at term: a nationwide case-control study.** *Acta Obstet Gynecol Scand* 2019;98:523–32 CrossRef Medline
13. Cole L, Dewey D, Letourneau N, et al. **Clinical characteristics, risk factors, and outcomes associated with neonatal hemorrhagic stroke: a population-based case-control study.** *JAMA Pediatr* 2017;171:230–38 CrossRef Medline
14. Gunny RS, Lin D. **Imaging of perinatal stroke.** *Magn Reson Imaging Clin N Am* 2012;20:1–33 CrossRef Medline

The Needed Studies Trying to Untangle the Complex Nature of Neonatal Intracranial Bleeds Occurring around Birth

The challenge of understanding mechanisms beyond insults and the resulting brain lesions in term or near-term neonates facing delivery time is far from being fully untangled. We believe considering together near-term and term neonates is justified because major achievements in brain maturation have been obtained for fetuses after 34 weeks of gestation.[1] Karamian et al[2] produced this very useful and large single-center retrospective study on intracranial hemorrhages that we know are highly heterogeneous with a complex and often unclear nature. Data on the multicompartment character of intracranial hemorrhages emerges as one of the principal findings of the study, reinforcing a generic hemodynamic identity of these intracranial bleeds but minimizing the contribution of instrumented delivery and of coagulopathy favoring bleeding.

Intraventricular hemorrhages (IVHs) also remain well-represented in this population of neonates close to or at term gestation. IVH in very premature neonates is undoubtedly due to the vascular vulnerability at the caudothalamic notch of the remaining germinal matrix, so prone to bleed into the ventricles in the first 3–4 days of life, making obvious the origin of the IVH.[3] At term gestation, many cerebral developmental features are changing; the germinal matrix undergoes anatomic involution, though IVH also remains rather frequent in less premature neonates as this study confirms. Knowledge of the origin of IVH in such neonates near or at term is only based on pioneer and very old postmortem studies[4] showing the likely origin from the choroid plexus.

The present work further highlights the role of brain venous thrombosis phenomena, because we know IVH may disclose cerebral sinovenous thrombosis (CSVT) in term neonates[5] and also in near-term preterm neonates.[6] In these mildly premature neonates, a late appearance of IVH (in very preterm neonates IVH occurs in the first 3–4 days) reveals the phenomenon of progression of CSVT into the deep, venous system of the brain with frontal medullary vein involvement, an anatomic area that is the last one to mature.[1] In these neonates, thrombophilic abnormalities are more significantly represented.[7] Conversely, it is not so uncommon to also find medullary vein involvement in the brain of term neonates in the first days of life, mimicking local venous thrombotic phenomena without evident CSVT and potentially representing a different form of neonatal encephalopathy that we have already described.[8] These abnormalities despite possibly resulting in "linear" periventricular leukomalacia–like lesions, again atypically more frequent in the frontal part of the brain, represent a different entity from the better known white matter diseases of premature neonates first described by Banker and Larroche in 1962[9] and clinically identified exactly one hundred years before by William J. Little.[10]

We believe one of the major merits of the present study is to stress the important role of periventricular, medullary, and cortical vein involvement, a phenomenon described as thrombosis by the authors and perhaps a potential sign of a venous congestion in the pathogenesis of an intracranial bleed occurring around the time of labor and delivery. This sequence of events may reproduce what already observed decades ago for understanding the pathogenesis of IVH from the germinal matrix of premature neonates, originally thought to be an arterial kind of bleeding more than a venous one, the "venous hypothesis" we all trust currently.

REFERENCES

1. Childs AM, Ramenghi LA, Cornette L, et al. **Cerebral maturation in premature infants: quantitative assessment using MR imaging.** *AJNR Am J Neuroradiol* 2001;22:1577–82 Medline
2. Karamian AG, Yang QZ, Tam LT, et al. **Intracranial hemorrhage in term and late-preterm neonates: an institutional perspective.** *AJNR Am J Neuroradiol* 2022;43:1494–99 CrossRef
3. Tortora D, Severino M, Malova M, et al. **Differences in subependymal vein anatomy may predispose preterm infants to GMH-IVH.** *Arch Dis Child Fetal Neonatal Ed* 2018;103:F59–65 CrossRef Medline
4. Donat JF, Okazaki H, Kleinberg F, et al. **Intraventricular hemorrhages in full-term and premature infants.** *Mayo Clin Proc* 1978;53:437–41 Medline
5. Wu YW, Hamrick SE, Miller SP, et al. **Intraventricular hemorrhage in term neonates caused by sinovenous thrombosis.** *Ann Neurol* 2003;54:123–26 CrossRef Medline
6. Ramenghi LA, Govaert P, Fumagalli M, et al. **Neonatal cerebral sinovenous thrombosis.** *Semin Fetal Neonatal Med* 2009;14:278–83 CrossRef Medline

7. Ramenghi LA, Gill BJ, Tanner SF, et al. **Cerebral venous thrombosis, intraventricular haemorrhage and white matter lesions in a preterm newborn with factor V (Leiden) mutation.** *Neuropediatrics* 2002;33:97–99 CrossRef Medline
8. Arrigoni F, Parazzini C, Righini A, et al. **Deep medullary vein involvement in neonates with brain damage: an MR imaging study.** *AJNR Am J Neuroradiol* 2011;32:2030–36 CrossRef Medline
9. Banker BQ, Larroche JC. **Periventricular leukomalacia of infancy. A form of neonatal anoxic encephalopathy.** *Arch Neurol* 1962;7:386–410 CrossRef Medline
10. Little WJ. **On the influence of abnormal parturition, difficult labours, premature birth, and asphyxia neonatorum, on the mental and physical condition of the child, especially in relation to deformities.** *Trans Obstet Soc Lond* 1861–1862;293–344

L.A. Ramenghi
Istituto Pediatrico "G.Gaslini"
DINOGMI Department, University of Genoa
Italy

http://dx.doi.org/10.3174/ajnr.A7651

Involvement of the Thalamus, Hippocampus, and Brainstem in Hypsarrhythmia of West Syndrome: Simultaneous Recordings of Electroencephalography and fMRI Study

Y. Maki, J. Natsume, Y. Ito, Y. Okai, E. Bagarinao, H. Yamamoto, S. Ogaya, T. Takeuchi, T. Fukasawa, F. Sawamura, T. Mitsumatsu, S. Maesawa, R. Saito, Y. Takahashi, and H. Kidokoro

ABSTRACT

BACKGROUND AND PURPOSE: West syndrome is a developmental and epileptic encephalopathy characterized by epileptic spasms, neurodevelopmental regression, and a specific EEG pattern called hypsarrhythmia. Our aim was to investigate the brain activities related to hypsarrhythmia at onset and focal epileptiform discharges in the remote period in children with West syndrome using simultaneous electroencephalography and fMRI recordings.

MATERIALS AND METHODS: Fourteen children with West syndrome underwent simultaneous electroencephalography and fMRI at the onset of West syndrome. Statistically significant blood oxygen level–dependent responses related to hypsarrhythmia were analyzed using an event-related design of 4 hemodynamic response functions with peaks at 3, 5, 7, and 9 seconds after the onset of each event. Six of 14 children had focal epileptiform discharges after treatment and underwent simultaneous electroencephalography and fMRI from 12 to 25 months of age.

RESULTS: At onset, positive blood oxygen level–dependent responses were seen in the brainstem (14/14 patients), thalami (13/14), basal ganglia (13/14), and hippocampi (13/14), in addition to multiple cerebral cortices. Group analysis using hemodynamic response functions with peaks at 3, 5, and 7 seconds showed positive blood oxygen level–dependent responses in the brainstem, thalamus, and hippocampus, while positive blood oxygen level–dependent responses in multiple cerebral cortices were seen using hemodynamic response functions with peaks at 5 and 7 seconds. In the remote period, 3 of 6 children had focal epileptiform discharge–related positive blood oxygen level–dependent responses in the thalamus, hippocampus, and brainstem.

CONCLUSIONS: Positive blood oxygen level–dependent responses with hypsarrhythmia appeared in the brainstem, thalamus, and hippocampus on earlier hemodynamic response functions than the cerebral cortices, suggesting the propagation of epileptogenic activities from the deep brain structures to the neocortices. Activation of the hippocampus, thalamus, and brainstem was still seen in half of the patients with focal epileptiform discharges after adrenocorticotropic hormone therapy.

ABBREVIATIONS: ACTH = adrenocorticotropic hormone; BOLD = blood oxygen level–dependent; ED = epileptiform discharge; EEG-fMRI = simultaneous recordings of electroencephalography and fMRI; HRF = hemodynamic response function; MNI = Montreal Neurological Institute; WS = West syndrome

West syndrome (WS) is a developmental and epileptic encephalopathy of infancy characterized by epileptic spasms, neurodevelopmental regression, and a specific electroencephalography (EEG) pattern called hypsarrhythmia.[1] Hypsarrhythmia consists of high-voltage slow waves and multifocal spikes without interhemispheric and intrahemispheric synchrony.[2,3] In the concept of developmental and epileptic encephalopathy, the abundant epileptiform activity interferes with psychomotor development, resulting in cognitive slowing and regression.[4] In that sense, it is important to know which brain structures and networks are involved in the form of hypsarrhythmia to understand the mechanism of WS leading to cognitive slowing and regression.

Previous neuroimaging studies have implied the involvement of widespread cortical and subcortical structures in the

Received February 28, 2022; accepted after revision July 27.

From the Departments of Pediatrics (Y.M., J.N., Y.I., Y.O., H.Y., F.S., T.M., Y.T., H.K.), Developmental Disability Medicine (J.N.), and Neurosurgery (S.M., R.S.), Nagoya University Graduate School of Medicine, Nagoya, Japan; Brain and Mind Research Center (J.N., Y.I., Y.O., E.B., H.Y., S.M., H.K.), Nagoya University, Nagoya, Japan; Department of Pediatrics (Y.I.), Aichi Prefectural Mikawa Aoitori Medical and Rehabilitation Center, Okazaki, Japan; Department of Pediatric Neurology (Y.O.), Toyota Municipal Child Development Center, Toyota, Japan; Department of Pediatric Neurology (S.O.), Aichi Developmental Disability Center Central Hospital, Kasugai, Japan; Department of Pediatrics (T.T.), Japanese Red Cross Nagoya First Hospital, Nagoya, Japan; and Department of Pediatrics (T.F.), Anjo Kosei Hospital, Anjo, Japan.

This work was supported by JSPS Kakenhi grant No. JP16K09987.

Please address correspondence to Jun Natsume, MD, PhD, Department of Pediatrics, Nagoya University Graduate School of Medicine, 65 Tsurumai-cho, Showa-ku, Nagoya, 466-8550, Japan; e-mail: junnatsu@med.nagoya-u.ac.jp

Indicates open access to non-subscribers at www.ajnr.org

Indicates article with online supplemental data.

http://dx.doi.org/10.3174/ajnr.A7646

pathophysiology of WS. FDG-PET shows hypermetabolism of the lenticular nuclei and brainstem.[5,6] DTI has shown restricted diffusion in the brainstem at the onset of WS.[7] However, because of the low temporal resolution of PET and DTI, it is difficult to assess the relationship of hypermetabolism and restricted diffusion with hypsarrhythmia directly.

Simultaneous recording of EEG and fMRI (EEG-fMRI) is a technique for evaluating hemodynamic changes by blood oxygenation level–dependent (BOLD) signals related to EEG activities. A previous EEG-fMRI study of hypsarrhythmia in children with WS showed a positive correlation between the Δ power of the occipital slow wave and a positive BOLD response in the brainstem and putamen.[8] EEG-fMRI is a promising tool to identify the brain structures involved in hypsarrhythmia and to clarify the role of these structures in developmental and epileptic encephalopathies.

In the present study, EEG-fMRI was performed in patients with WS to evaluate the brain structures related to hypsarrhythmia. An event-related design of 4 hemodynamic response functions (HRFs) that peak at 3, 5, 7, and 9 seconds after the onset of clusters of the epileptiform discharge was used to assess the temporospatial propagation of the epileptiform activities. Additionally, EEG-fMRI was re-evaluated in the remote period after adrenocorticotropic hormone (ACTH) therapy in patients who had remaining epileptiform discharges (EDs), and the results were compared with seizure outcomes.

MATERIALS AND METHODS

Ethics Approval

The present study was approved by the research ethics committee of Nagoya University Graduate School of Medicine. Written, informed consent was obtained from the children's caregivers before participation.

Patients and Clinical Data

Children with new-onset WS who were referred to Nagoya University Hospital between January 2016 and December 2021 were recruited. The diagnosis of WS was made from epileptic spasms in clusters confirmed by video-EEG recording and interictal EEG findings of hypsarrhythmia. The search for the etiology included laboratory tests and MR imaging, and the etiology of WS was regarded as unknown in children without abnormal findings on these examinations. Children were treated according to the following protocol: First, oral antiepileptic drugs were administered for at least 1 week, or ACTH was started. When spasms were not controlled by the oral antiepileptic drug, ACTH therapy was initiated immediately. Intramuscular injection of ACTH was administered for 2–4 weeks, followed by alternate-day administration for 1 week. The effectiveness was evaluated on the basis of the frequency of spasms and interictal EEG findings.

EEG-fMRI Acquisition

Patients underwent EEG-fMRI before the initiation of ACTH therapy. In patients who had remaining focal EDs after ACTH therapy, another EEG-fMRI scan was performed.

MR images were obtained using a Magnetom Verio (Siemens) 3T scanner with a 32-channel head coil using the same protocol as in previous studies.[9] fMRIs were recorded in a single, continuous session for 15 minutes using a T2-weighted gradient-echo echo-planar imaging sequence with the following imaging parameters: TR, 2.5 seconds; TE, 30 ms; FOV, 192 mm; matrix dimension, 64 × 64; 39 transverse slices with a 0.5-mm interslice interval and 3-mm thickness; flip angle, 80°; and a total of 360 volumes. EEGs and electrocardiograms were recorded simultaneously during fMRI scans using an MR imaging–compatible system (GES 400 MR, Electrical Geodesics, EGI; https://www.egi.com/). A 32-channel EEG cap was worn by the child throughout the scan and was connected to a combined digitizer-amplifier system. Data from the amplifier sampled at 1 kHz were continuously retrieved. Children were sedated in a drug-induced sleep condition with triclofos sodium, 80 mg/kg of body weight.

Image Preprocessing

Anatomic T1-weighted images and fMRIs were preprocessed using SPM12 software (http://www.fil.ion.ucl.ac.uk/spm/software/spm12) running on Matlab (MathWorks). For fMRI, the first 5 images were discarded to remove signal inhomogeneity. The remaining 355 images were corrected for temporal differences in section acquisitions, resampled relative to the middle image (20th of the 39 transverse slices), and corrected for head motion. The fMRI images were normalized to the Montreal Neurological Institute (MNI) space and smoothed with an 8-mm full width at half maximum Gaussian kernel.

EEG Preprocessing

Raw EEG data were preprocessed using EGI's Net Station software (https://www.egi.com/clinical-division/net-station). Gradient artifacts were removed using the template subtraction method, and ballistocardiogram artifacts were also removed using principal component analysis.[10,11] The cleaned EEG was band-pass filtered within the frequency range from 0.1 to 100 Hz. Two epileptologists (Y.M. and Y.I.) independently marked the onset and end of intermittent hypsarrhythmia bursts during sleep for EEGs at WS onset and the onset of EDs for EEGs in the remote period. Each hypsarrhythmia burst was regarded as an event with duration, similar to that in a previous approach used in ictal EEG-fMRI analysis in childhood absence epilepsy or Lennox-Gastaut syndrome.[12,13] The events for which 2 epileptologists obtained consensus were used for the subsequent analysis.

Individual-Level fMRI Analysis

fMRI data were analyzed using SPM12 software. Identified hypsarrhythmia bursts or ED onsets were used to generate a series of bursts or spikes, which were then convolved with HRFs and used in the statistical analyses of preprocessed fMRI data using an FSL General Linear Model approach (http://fsl.fmrib.ox.ac.uk/fsl/fslwiki/GLM). Four different HRFs that peaked at 3, 5, 7, and 9 seconds (P3, P5, P7, and P9) after the onset of each event were used for the analyses, as described previously.[13] One-tailed t tests were applied to test hypsarrhythmia bursts or ED-related BOLD signal changes. A significant BOLD response was defined as at least 5 contiguous voxels above a t value of 3.1, which is equivalent to a P value $< .01$.[14] All significant clusters obtained from 4 HRFs using this significance level were also regarded as significant for total individual-level analysis, and the results were superimposed on T1-weighted images of

each child. To combine the images of multiple HRFs, we followed the method that Gotman Lab described (https://www.mcgill.ca/gotman-lab/research/combined-eeg-fmri-recordings/creating-combined-hrf-tmap). A new image file was created using the *t*-maps for the individual models as the template. Each voxel was independently examined, and the value of the *t*-map with the highest absolute value was written into that voxel. Anatomic segmentation was according to Automated Anatomical Labeling (https://www.gin.cnrs.fr/en/tools/aal/).[15]

Group-Level fMRI Analysis

Group-level analysis was performed for individual results at the onset of WS. Analysis was first performed for each HRF (P3, P5, P7, and P9) using the SPM12 software. Age at scanning was used as a covariate. The significance level was set at $P < .01$ for multiple comparisons using family-wise error cluster-level correction with a cluster-forming threshold of $P = .001$. All significant clusters obtained from 4 HRFs using this significance level were also regarded as significant for the total group-level analysis, similar to findings in a previous EEG-fMRI study that used a time-shift model of a single HRF.[16] The results were superimposed on the common T1-weighted image in MNI space.

RESULTS

Patient Demographics

Fourteen children with new-onset WS were included in the study (Online Supplemental Data). The median age at the onset of WS was 5 months (range, 3–10 months). Two children (patients 5 and 6) had tuberous sclerosis complex and focal motor seizures before the onset of spasms. In the remaining 12 children, the etiology of WS was unknown at the onset. Patient 7 had delayed myelination and WM volume loss on MR imaging, but gene panel exome sequencing of developmental and epileptic encephalopathies did not show causative abnormalities.

In 5 patients, clonazepam, valproate, levetiracetam, topiramate, or vigabatrin was administered before ACTH therapy. In other patients, ACTH therapy was the first medication. After ACTH therapy, patients 5, 7, and 12 had epileptic spasms and patients 5 and 7 received another course of ACTH therapy. In the other 11 patients, spasms and hypsarrhythmia were resolved by a single course of ACTH therapy. Four patients (patients 1, 2, 3, and 5) experienced focal seizures during the follow-up period. Patients 1 and 3 had focal seizures 12 and 42 months after completing ACTH therapy, respectively. Patients 2 and 5 had onset of focal seizures within a month after completing ACTH therapy. Patient 2 underwent right temporal lobe resection at 23 months of age, and pathology showed focal cortical dysplasia type IIa.

Of the 8 patients who did not have focal EDs after ACTH therapy, 3 (patients 7, 12, and 14) had generalized EDs, relapse of seizures, and mild-to-severe developmental delays. In the other 5 patients who did not have focal or generalized EDs, 4 had normal psychomotor development and 1 (patient 10) had a mild delay of language development.

On EEG during the follow-up period, 6 of 14 patients (patients 1–6) had focal EDs after ACTH therapy. Patient 7 had frequent diffuse sharp-slow waves on interictal EEG. Patient 12 had multifocal EDs on interictal EEG.

BOLD Responses Related to Hypsarrhythmia at Onset of WS

The median interval between the onset of WS and the first EEG-fMRI scan was 10.5 days (range 3–112 days). In the patient who underwent EEG-fMRI 112 days after the onset of WS, the family did not recognize the spasms as epileptic seizures and the diagnosis of WS was delayed to 84 days after onset. This patient had a series of epileptic spasms and typical hypsarrhythmia at diagnosis and was included in the present study.

The median number of bursts of EDs in a 15-minute scan of each patient was 55 (range, 11–129). BOLD responses related to ED bursts of each patient are in seen in Fig 1*A*. In cerebral neocortices, all children showed multiple positive BOLD responses in the bilateral frontal, temporal, parietal, and occipital lobes, and the cingulate gyri. Positive BOLD responses in the bilateral insulae were also observed in all except 1 patient. Negative BOLD responses were observed in the frontal (12/14 patients), temporal (10/14), parietal (12/14), and occipital lobes (12/14) of the cerebral cortices, though the areas were smaller than those of positive BOLD responses. Regarding subcortical structures and the hippocampus, positive BOLD responses were observed in the brainstem (14/14 patients), thalami (13/14), and hippocampi (13/14). Positive BOLD responses in the brainstem were observed in the pons in 13 patients. Positive BOLD responses in the thalami were observed bilaterally in 12 patients and unilaterally in 1. Positive BOLD responses in the hippocampi were observed bilaterally in 11 patients and unilaterally in 1. Positive BOLD responses in the basal ganglia were observed in 8 patients. Negative BOLD responses were observed in the brainstem in 2 patients, the thalami in 3, and the hippocampi in 2. Negative BOLD responses in the basal ganglia were observed in 12 of 14 patients. The BOLD responses with maximum *t* values were positive BOLD responses in all children and were observed in the cerebral neocortex in 8 patients, in the pons in 3, the hippocampus in 1, the pulvinar in 1, and the posterior cingulate gyrus in 1.

The result of group-level analysis is shown in Fig 2. No clusters with significant negative BOLD responses were identified. Group analysis using a P3 HRF showed significant positive BOLD responses in the dorsal pons, midbrain, bilateral hippocampus, bilateral thalami, and bilateral opercula, whereas positive BOLD responses in the cerebral neocortex were scarce. P5 and P7 HRFs showed significant positive BOLD responses in the cerebral neocortex, pons, midbrain, bilateral thalami, and left hippocampus. The P9 HRF yielded scattered positive BOLD responses in the cerebral neocortex and positive BOLD responses in the bilateral thalami and hippocampi.

BOLD Responses Related to Focal EDs after ACTH Therapy

The median age at the second EEG-fMRI scan was 16 months (range, 12–25 months) in 6 patients (patients 1–6) with focal EDs after ACTH therapy. The median number of focal EDs during a 15-minute scan was 27 (range, 13–76). Four of the 6 patients with focal EDs after ACTH therapy had focal seizures.

BOLD responses related to focal EDs are described in the Online Supplemental Data and Fig 1*B*. Patients 1–3 showed positive BOLD responses in the brainstem, thalami, and hippocampi, in addition to the cerebral cortex; maximum *t* values

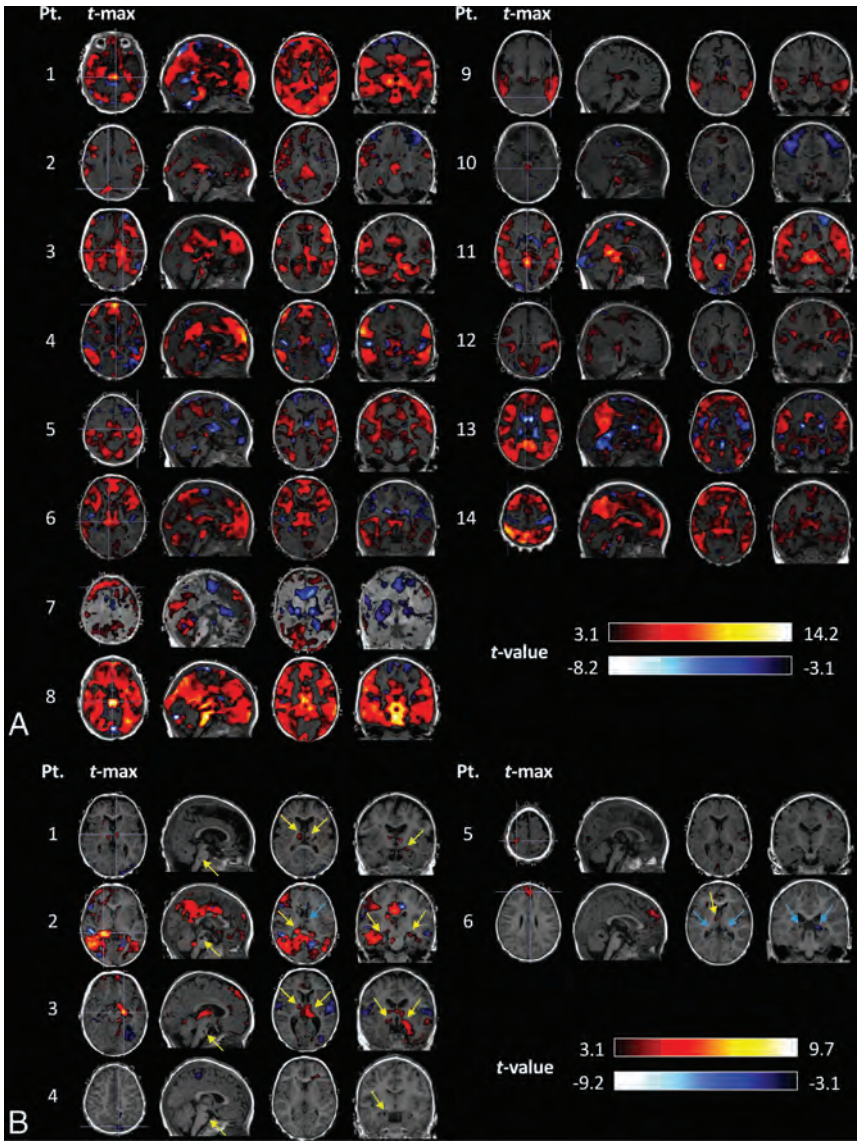

FIG 1. EEG-fMRI findings of all patients with WS. *A*, Combined *t*-maps of 4 HRFs on EEG-fMRI of all patients at the onset of WS. The first (leftmost) axial image of each patient shows the axial slice with the maximum *t* value. All children showed significant BOLD response in the brainstem, hippocampus, thalamus, and basal ganglia, as well as multiple cerebral neocortices. *B*, EEG-fMRI findings of 6 children who had focal epileptiform discharges in the remote period after ACTH therapy. Significant BOLD responses in the brainstem, thalamus, and hippocampus are shown by *arrows* on sagittal, axial, and coronal sections of each patient. Positive BOLD responses are indicated by *yellow arrows*, and negative BOLD responses are indicated by *blue arrows*. The MNI coordinates of maximum *t* values are described in the Online Supplemental Data. In both *A* and *B*, all significant BOLD responses from 4 HRFs are shown. Pt. indicates patient; *t*-max, time-to-maximum.

were observed in the hippocampus or thalamus. Patient 4 showed positive BOLD responses in the brainstem and right hippocampus. Of patients with tuberous sclerosis complex, patient 5 showed positive BOLD responses only in the cerebral cortices, and patient 6 showed significant BOLD responses in the thalamus and hippocampus, as well as in the cerebral cortices. The areas with positive BOLD responses in the cerebral cortices decreased in all except 1 patient (patient 2). The areas with positive BOLD responses in the brainstem, thalami, hippocampi, and basal ganglia decreased in all patients.

DISCUSSION

In the present study, individual and group analyses of EEG-fMRI with hypsarrhythmia showed activation of the brainstem, hippocampus, and thalamus, as well as the cerebral neocortices. In the group-level analysis, positive BOLD responses in the hippocampus, thalamus, and brainstem were obtained from the earlier timing of multiple HRFs than in the cerebral neocortex. On EEG-fMRI of focal EDs during the follow-up period after ACTH therapy, the hippocampus, thalamus, and brainstem were still activated with focal EDs in 3 of 6 children.

Previous neuroimaging studies stressed the importance of the brainstem in the pathophysiology of WS. An FDG-PET study by Chugani et al[5] showed glucose hypermetabolism in the lenticular nuclei and brainstem in patients with WS, and they hypothesized that epileptic activity propagates from the brainstem to the basal ganglia and cerebral cortex. In a case report of ictal SPECT, increased perfusion in the brainstem was observed in a patient with a defective left hemisphere and symmetric epileptic spasms.[17] Our DTI study showed increased fractional anisotropy and reduced mean diffusivity in the dorsal brainstem at the onset of WS.[7] The finding of reduced diffusion may suggest cytotoxic edema of the dorsal brainstem. The dorsal raphe area of the brainstem has a large number of serotonergic cell bodies, and it has been hypothesized that raphe-cortical interactions induce hypsarrythmia.[6] The individual and group-level results of the present study support the involvement of the brainstem in the epileptic brain activities of WS. Furthermore, the results of the group analysis in the present study showing positive BOLD responses in the brainstem obtained from a P3 HRF and positive BOLD responses in the cerebral cortex from P5 or P7 HRFs support the hypothesis about the propagation pattern of epileptic activity in children with WS.[6] Multiple HRF analyses provide interesting information about the formation of epileptic networks in WS, though the multiple HRF analyses were originally developed to cover the variable hemodynamics with EDs, and the difference in the HRF does not necessarily mean different timing of epileptiform activities.

The present study found group-level significant positive BOLD responses in the thalamus and hippocampus from P3, P5, and P7

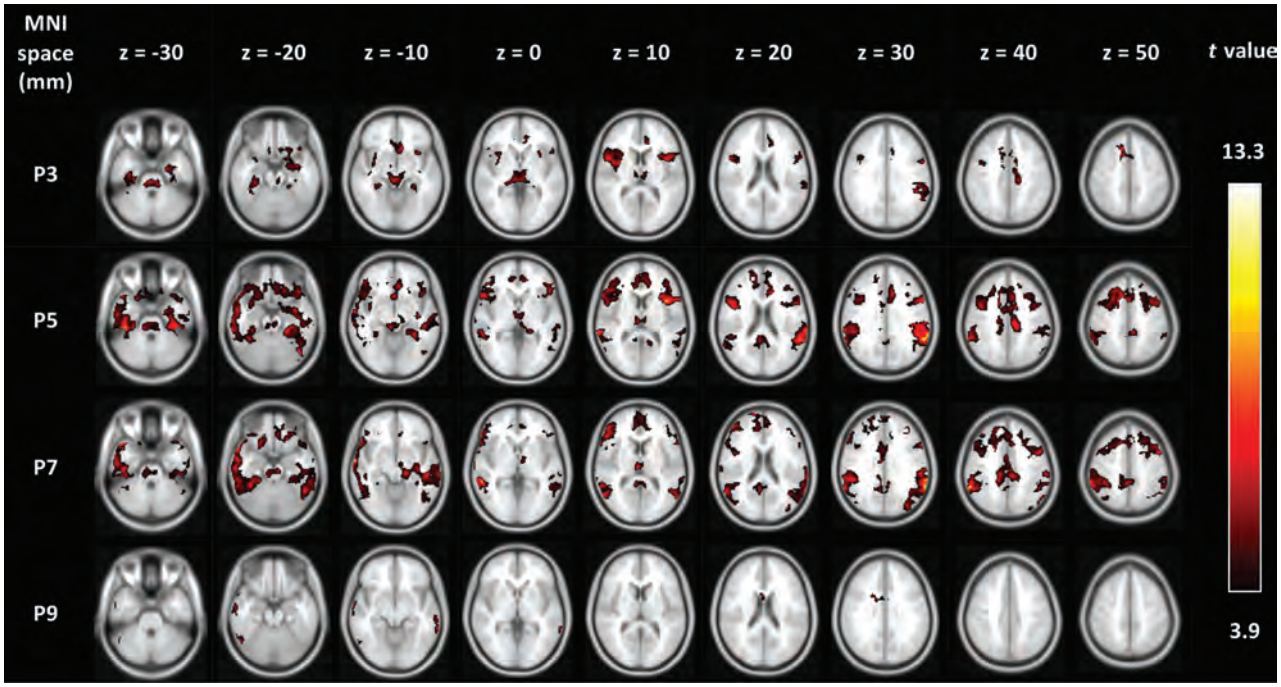

FIG 2. The results of group-level analysis at the onset of WS. With the P3 HRF, significant positive BOLD responses were observed in the brainstem, bilateral hippocampi, and bilateral thalami. Positive BOLD responses in the cerebral cortices were observed mainly with P5 and P7 HRFs, and these HRFs also yielded positive BOLD responses in the pons, midbrain, bilateral thalami, and left hippocampus. No group-level significant negative BOLD responses were observed.

HRFs. The role of the thalamus and hippocampus in WS and hypsarrhythmia is intriguing. It has been hypothesized that the thalamus and hippocampus form a limbic network with the role of distribution and synchronization of hyperexcitability determined from the results of animal model studies of temporal lobe epilepsy.[18] The role of the thalamus and hippocampus in epilepsy has also been discussed in other types of focal and generalized epilepsy.[19,20] On the other hand, the roles of the hippocampus and thalamus in WS are not fully understood. A previous study of interictal SPECT showed decreased perfusion of the thalamus and hippocampus in children with WS.[21] The present EEG-fMRI study suggests that epileptogenic activities during hypsarrhythmia are associated with abnormal activities in the hippocampus and thalamus and lead to dysfunction of the limbic system. This hypothesis supports the idea that early cessation of the hypsarrhythmia is important for cognitive outcomes in WS.

The present results also showed that the hippocampus, thalamus, and brainstem were still activated with focal EDs in 3 of 6 children during the follow-up period. All 3 patients with activation in the hippocampus, thalamus, and brainstem with focal EDs had focal epilepsies and developmental delay. Previous EEG-fMRI studies indicated the involvement of subcortical GM, especially the thalamus, in patients with pharmacoresistant focal or multifocal epilepsies.[22-24] The present findings indicate that part of the subcortical epileptic activities at the onset of WS remains in some children with focal epilepsies, even after the disappearance of hypsarrhythmia.

A previous EEG-fMRI study of 8 children with WS by Siniatchkin et al[8] showed a positive correlation between occipital Δ power of the hypsarrhythmia and BOLD responses in the brainstem, thalamus, and putamen. There are differences in analysis methods between the study by Siniatchkin et al and the present one. The method of the former study was capable of assessing spike components and slow waves of hypsarrhythmia separately. The present method included all spikes and slow waves of each hypsarrhythmia burst in each event and has a weak point in that it does not involve analyzing spike and slow-wave components separately. Another difference is that Siniatchkin et al used the canonical HRF, which has high amplitude with its peak at approximately 5 seconds after an event, and the present study used 4 HRFs with different temporal peaks and lower amplitude. The present method could reduce the *t* values of BOLD responses due to lower amplitude and could raise the sensitivity of significant BOLD responses by covering the temporal gap of the hemodynamic response among brain regions. Although it is uncertain how the methodologic difference affected the results, the present study confirmed the results of Siniatchkin et al, showing activation in the brainstem, thalamus, and basal ganglia, and it additionally found activation in the hippocampus with hypsarrhythmia.

There were some limitations in the present study. First, the number of patients was small. Second, the follow-up period was relatively short, and seizure and long-term developmental outcomes were not examined. Third, because EEG-fMRI is analyzed by marking the EDs on EEG, it cannot be performed in patients without EDs in the follow-up period. Therefore, it was not possible to evaluate the change of activity in the thalami, hippocampi, and brainstem in patients without EDs after ACTH therapy. Despite these limitations, the present results provide important insight into the pathophysiology of WS.

CONCLUSIONS

The present EEG-fMRI study showed the presence of subcortical epileptic networks involving the brainstem, hippocampus, and thalamus at the onset of WS. Activation of the hippocampus, thalamus, and brainstem was still seen in half of the patients with focal EDs after ACTH therapy.

ACKNOWLEDGMENTS

The authors thank Mr Akira Ishizuka of the Brain and Mind Research Center, Nagoya University, for providing technical support for EEG-fMRI scanning.

Disclosure forms provided by the authors are available with the full text and PDF of this article at www.ajnr.org.

REFERENCES

1. Pavone P, Striano P, Falsaperla R, et al. **Infantile spasms syndrome, West syndrome and related phenotypes: what we know in 2013.** *Brain Dev* 2014;36:739–51 CrossRef Medline
2. Gibbs FA, Gibbs EL. *Atlas of Electroencephalography*. Vol. 2. Chap 6. Addison-Wesley; 1952:24–30
3. Hrachovy RA, Frost JD. **Infantile epileptic encephalopathy with hypsarrhythmia (infantile spasms/West syndrome).** *J Clin Neurophysiol* 2003;20:408–25 CrossRef Medline
4. Scheffer IE, Berkovic S, Capovilla G, et al. **ILAE classification of the epilepsies: Position Paper of the ILAE Commission for Classification and Terminology.** *Epilepsia* 2017;58:512–21 CrossRef Medline
5. Chugani HT, Shewmon DA, Sankar R, et al. **Infantile spasms, II. lenticular nuclei and brain stem activation on positron emission tomography.** *Ann Neurol* 1992;31:212–19 CrossRef Medline
6. Juhasz C, Chugani HT, Muzik O, et al. **Neuroradiological assessment of brain structure and function and its implication in the pathogenesis of West syndrome.** *Brain Dev* 2001;23:488–95 CrossRef Medline
7. Ogawa C, Kidokoro H, Fukasawa T, et al. **Cytotoxic edema at onset in West syndrome of unknown etiology: a longitudinal diffusion tensor imaging study.** *Epilepsia* 2018;59:440–48 CrossRef Medline
8. Siniatchkin M, van Baalen A, Jacobs J, et al. **Different neuronal networks are associated with spikes and slow activity in hypsarrhythmia.** *Epilepsia* 2007;48:2312–21 CrossRef Medline
9. Ito Y, Maki Y, Okai Y, et al. **Involvement of brain structures in childhood epilepsy with centrotemporal spikes.** *Pediatr Int* 2021;64:e15001 CrossRef Medline
10. Allen PJ, Josephs O, Turner R. **A method for removing imaging artifact from continuous EEG recorded during functional MRI.** *Neuroimage* 2000;12:230–99 CrossRef Medline
11. Niazy RK, Beckmann CF, Iannetti GD, et al. **Removal of FMRI environment artifacts from EEG data using optimal basis sets.** *Neuroimage* 2005;28:720–37 CrossRef Medline
12. Warren AE, Harvey AS, Vogrin SJ, et al. **The epileptic network of Lennox-Gastaut syndrome: cortically driven and reproducible across age.** *Neurology* 2019;93:e215–26 CrossRef
13. Moeller F, Siebner HR, Wolff S, et al. **Simultaneous EEG-fMRI in drug-naive children with newly diagnosed absence epilepsy.** *Epilepsia* 2008;49:1510–19 CrossRef Medline
14. Bagshaw AP, Aghakhani Y, Benar CG, et al. **EEG-fMRI of focal epileptic spikes: analysis with multiple haemodynamic functions and comparison with gadolinium-enhanced MR angiograms.** *Hum Brain Mapp* 2004;22:179–92 CrossRef Medline
15. Tzourio-Mazoyer N, Landeau B, Papathanassiou D, et al. **Automated anatomical labeling of activations in SPM using a macroscopic anatomical parcellation of the MNI MRI single-subject brain.** *Neuroimage* 2002;15:273–89 CrossRef Medline
16. Usami K, Matsumoto R, Sawamoto N, et al. **Epileptic network of hypothalamic hamartoma: an EEG-fMRI study.** *Epilepsy Res* 2016;125:1–9 CrossRef Medline
17. Haginoya K, Kon K, Tanaka S, et al. **The origin of hypsarrhythmia and tonic spasms in West syndrome: evidence from a case of porencephaly and hydrocephalus with focal hypsarrhythmia.** *Brain Dev* 1999;21:129–31 CrossRef Medline
18. Bertram EH, Zhang DX, Mangan P, et al. **Functional anatomy of limbic epilepsy: a proposal for central synchronization of a diffusely hyperexcitable network.** *Epilepsy Res* 1998;32:194–205 CrossRef Medline
19. Dell KL, Cook MJ, Maturana MI. **Deep brain stimulation for epilepsy: biomarkers for optimization.** *Curr Treat Options Neurol* 2019;21:47 CrossRef Medline
20. Ilyas A, Pizarro D, Romeo AK, et al. **The centromedian nucleus: anatomy, physiology, and clinical implications.** *J Clin Neurosci* 2019;63:1–7 CrossRef Medline
21. Hamano S, Higurashi N, Koichihara R, et al. **Interictal cerebral blood flow abnormality in cryptogenic West syndrome.** *Epilepsia* 2010;51:1259–65 CrossRef Medline
22. Fahoum F, Lopes R, Pittau F, et al. **Widespread epileptic networks in focal epilepsies: EEG-fMRI study.** *Epilepsia* 2012;53:1618–27 CrossRef Medline
23. An D, Dubeau F, Gotman J. **BOLD responses related to focal spikes and widespread bilateral synchronous discharges generated in the frontal lobe.** *Epilepsia* 2015;56:366–74 CrossRef Medline
24. Siniatchkin M, Moehring J, Kroeher B, et al. **Multifocal epilepsy in children is associated with increased long-distance functional connectivity: an explorative EEG-fMRI study.** *Eur J Paediatr Neurol* 2018;22:1054–65 CrossRef Medline

Arterial Spin-Labeling Perfusion Metrics in Pediatric Posterior Fossa Tumor Surgery

S.M. Toescu, P.W. Hales, J. Cooper, E.W. Dyson, K. Mankad, J.D. Clayden, K. Aquilina, and C.A. Clark

ABSTRACT

BACKGROUND AND PURPOSE: Pediatric posterior fossa tumors often present with hydrocephalus; postoperatively, up to 25% of patients develop cerebellar mutism syndrome. Arterial spin-labeling is a noninvasive means of quantifying CBF and bolus arrival time. The aim of this study was to investigate how changes in perfusion metrics in children with posterior fossa tumors are modulated by cerebellar mutism syndrome and hydrocephalus requiring pre-resection CSF diversion.

MATERIALS AND METHODS: Forty-four patients were prospectively scanned at 3 time points (preoperatively, postoperatively, and at 3-month follow-up) with single- and multi-inflow time arterial spin-labeling sequences. Regional analyses of CBF and bolus arrival time were conducted using coregistered anatomic parcellations. ANOVA and multivariable, linear mixed-effects modeling analysis approaches were used. The study was registered at clinicaltrials.gov (NCT03471026).

RESULTS: CBF increased after tumor resection and at follow-up scanning ($P = .045$). Bolus arrival time decreased after tumor resection and at follow-up scanning ($P = .018$). Bolus arrival time was prolonged ($P = .058$) following the midline approach, compared with cerebellar hemispheric surgical approaches to posterior fossa tumors. Multivariable linear mixed-effects modeling showed that regional perfusion changes were more pronounced in the 6 children who presented with symptomatic obstructive hydrocephalus requiring pre-resection CSF diversion, with hydrocephalus lowering the baseline mean CBF by 20.5 (standard error, 6.27) mL/100g/min. Children diagnosed with cerebellar mutism syndrome (8/44, 18.2%) had significantly higher CBF at follow-up imaging than those who were not ($P = .040$), but no differences in pre- or postoperative perfusion parameters were seen.

CONCLUSIONS: Multi-inflow time arterial spin-labeling shows promise as a noninvasive tool to evaluate cerebral perfusion in the setting of pediatric obstructive hydrocephalus and demonstrates increased CBF following resolution of cerebellar mutism syndrome.

ABBREVIATIONS: AIC = Akaike information criterion; ASL = arterial spin-labeling; BAT = bolus arrival time; BuxCBF = Buxton-modeled CBF from multi-TI ASL data; CMS = cerebellar mutism syndrome; EVD = external ventricular drain; HCP = hydrocephalus; ICP = intracranial pressure; mod = model; (mod_hcp) = addition of HCP with an interaction term for the time point; (mod_hcpcms) = full model including terms for CMS and HCP; PLD = post-labeling delay; TI = inflow time

CBF is a physiologic parameter with a well-established relationship to intracranial pressure (ICP) and systemic arterial blood pressure.[1-3] Changes in CBF follow open craniotomy in adult patients,[4] but less is known about the effect of neurosurgery on CBF in children.[5] Brain tumors commonly occur in the posterior fossa in children, who often present with symptoms of raised ICP due to obstruction of CSF flow.[6] Obstructive hydrocephalus (HCP) can be severe enough to warrant emergency CSF diversion as a life-saving procedure before tumor resection. There are few reports of alterations in perfusion metrics in children with HCP.[5,7,8] Following tumor resection, up to one-quarter of patients develop cerebellar mutism syndrome (CMS),[9] characterized by a delayed onset of mutism and emotional lability,[10] which tend to resolve during weeks to months. Damage to the superior cerebellar peduncles is thought to disturb reciprocal cerebrocerebellar pathways, giving rise to the striking symptomatology of the condition. Frontal perfusion deficits in patients with CMS have previously been shown using SPECT imaging,[11,12] DSC MR imaging,[13] and, more recently, arterial spin-labeling (ASL).[14,15]

ASL quantifies brain perfusion in physiologically relevant units by subtracting an image with radiofrequency-labeled blood

Received January 3, 2022; accepted after revision July 27.

From the Departments of Neurosurgery (S.M.T., E.W.D., K.A.) and Neuroradiology (J.C., K.M., C.A.C.), Great Ormond Street Hospital, London, UK; and Developmental Imaging and Biophysics Section (S.M.T., P.W.H., J.D.C.), University College London Great Ormond Street Institute of Child Health, London, UK.

This work was supported by Children With Cancer UK, CwC-UK-15-203, and the Great Ormond Street Hospital Charity, 174385.

Please address correspondence to Sebastian M. Toescu, MD, Developmental Imaging and Biophysics Section, UCL-GOS Institute of Child Health, 30 Guilford St, London, UK, WC1N 1EH; e-mail: Sebastian.toescu@ucl.ac.uk; @sebmigueltoescu

http://dx.doi.org/10.3174/ajnr.A7637

from a control image at a suitable post-labeling delay (PLD, also known as single inflow time [TI] or single-TI data). By acquiring data at multiple TIs (multi-TI), it is possible to extract further parameters such as the bolus arrival time (BAT) of labeled blood. BAT varies regionally, making single-PLD acquisitions susceptible to underestimation of CBF due to incomplete delivery of the bolus of labeled blood at the chosen TI. The advantage of multi-TI ASL is that this issue is accounted for by imaging at serially increasing TIs.

The aim of this study was to characterize perfusion metrics of CBF and BAT of labeled blood using single- and multi-TI ASL in children with posterior fossa tumors. We also aimed to investigate how changes in perfusion metrics were modulated by perioperative surgical and clinical features of CMS and HCP requiring pre-resection CSF diversion. We hypothesized that children with CMS would have reduced CBF postoperatively and that HCP would cause a reduction in preoperative CBF and prolong preoperative BAT.

MATERIALS AND METHODS

Patients

Children referred to our institution with posterior fossa tumors underwent MR imaging before tumor resection, within 72 hours of tumor resection, and at 3-month follow-up. Scans were performed with the patient under general anesthesia in younger children to avoid movement artifacts; otherwise, all scanning was performed in unsedated patients. Sedation requirements were assessed by experienced pediatric neuroradiographers before scanning and were primarily determined by patient age. Only 1 patient required general anesthesia at a follow-up scan appointment, having previously tolerated unsedated scanning.

Children presenting with symptomatic HCP (signs of raised ICP, such as headache, vomiting, or deteriorating conscious levels) were treated with urgent CSF diversion in the form of an external ventricular drain (EVD) before tumor resection. Those who did not undergo pre-resection EVD were temporized with glucocorticoid administration until tumor resection. Operative notes were contemporaneously reviewed, and the intradural surgical approach to the tumor was categorized into midline, hemispheric, and miscellaneous groups. Postoperative CMS status was determined by prospective clinical evaluation by attending neurosurgical and multidisciplinary staff. The diagnosis was primarily based on the presence of mutism or reduced speech output in the early postoperative phase. Patients were followed up at 2 months postoperatively to assess ongoing symptoms of CMS. Ethics approval was granted by the National Health Service Health Research Authority (18/LO/0501), and the study was registered at clinicaltrials.gov (NCT03471026).

MR Imaging Acquisition

Imaging was performed on a 3T MR imaging scanner (Magnetom Prisma; Siemens) using a 20-channel receive head coil. The scanning protocol comprised structural imaging (including T1 MPRAGE), multishell diffusion imaging, and ASL. Imaging at the preoperative time point was acquired before CSF diversion.

Single-PLD ASL was performed using a prototype pseudocontinuous labeling sequence with background suppression and a 3D gradient-echo and spin-echo readout. Imaging parameters were set according to international consensus recommendations,[16] with a labeling duration of 1800 ms, a 1500-ms PLD, and 10 repetitions. The FOV was 220 mm with a 64 × 62 matrix reconstructed to 1.7 × 1.7 mm^2 in-plane spatial resolution (interpolation factor = 2). Additional sequence parameters were the following: 24 partitions; turbo factor = 12; EPI factor = 31; segments = 2 (with parallel imaging, generalized autocalibrating partially parallel acquisition = 2); section thickness = 4.0 mm; TR = 4620 ms; TE = 21.8 ms. A proton density–weighted (M0) image was also acquired, with a readout identical to that of the ASL acquisition but with the labeling radiofrequency pulses removed for CBF quantification.

Multi-TI pulsed ASL data comprised acquisitions at 10 TIs ranging from 350 to 2600 ms in 250-ms steps, with a single acquisition per TI. The TR was 3300 ms; all other readout parameters were the same as above.

Image Processing

Cortical parcellation and subcortical segmentation were performed on volumetric T1-weighted images using FreesSurfer (http://surfer.nmr.mgh.harvard.edu),[17] and these were registered into the patient's diffusion space using Niftyreg (http://sourceforge.net/projects/niftyreg/).[18] Repetitions of raw ASL images were checked for motion artifacts before averaging. Preprocessing of all ASL data was performed in Matlab (R2017b, MathWorks). Single-PLD data were preprocessed using the method of Alsop et al[16] to calculate voxelwise CBF (milliliter/100 g/min). The kinetic model described by Buxton et al[19] was used on noise-masked multi-TI ASL data to calculate voxelwise maps of BAT (seconds) and CBF (milliliter/100g/min; referred to in the Results section as Buxton-modeled CBF from multi-T1 ASL data [BuxCBF] to avoid confusion with CBF from single-PLD data). Details of the model-fitting procedure are described elsewhere.[20] Each patient's ASL parameter maps were registered into the patient's diffusion space using FLIRT[21] (https://fsl.fmrib.ox.ac.uk/fsl/fslwiki/FLIRT). Diffusion space was chosen as a symmetric registration space because its resolution was midway between that of ASL and structural images. Time point– and subject-specific median perfusion parameters were then extracted for regions corresponding to frontal, parietal, occipital, temporal, and motor (precentral, paracentral, and caudal middle frontal gyri) cortices, thalamus, and cerebellum.

Statistical Analysis

Statistical analysis was performed in R (Version 3.6.1).[22] Continuous data were tested for differences in means using a 2-tailed Student *t* test after assessing assumptions of normality using the Shapiro-Wilk test. Non-normally distributed data were tested using the Wilcoxon rank-sum test. A prespecified α of .05 was chosen. A 1-way repeated-measures ANOVA was performed to examine the effect of the scanning time point on perfusion metrics. Subsequent group comparisons using pair-wise *t* tests were corrected for multiple comparisons using the false discovery rate.

A multivariable linear mixed-effects modeling analysis was performed in which subject identification was taken as a random effect, and fixed effects included scanning time point, brain region, age, sedation status, HCP, and CMS. The Akaike information criterion (AIC) and marginal/conditional R^2 values[23] were

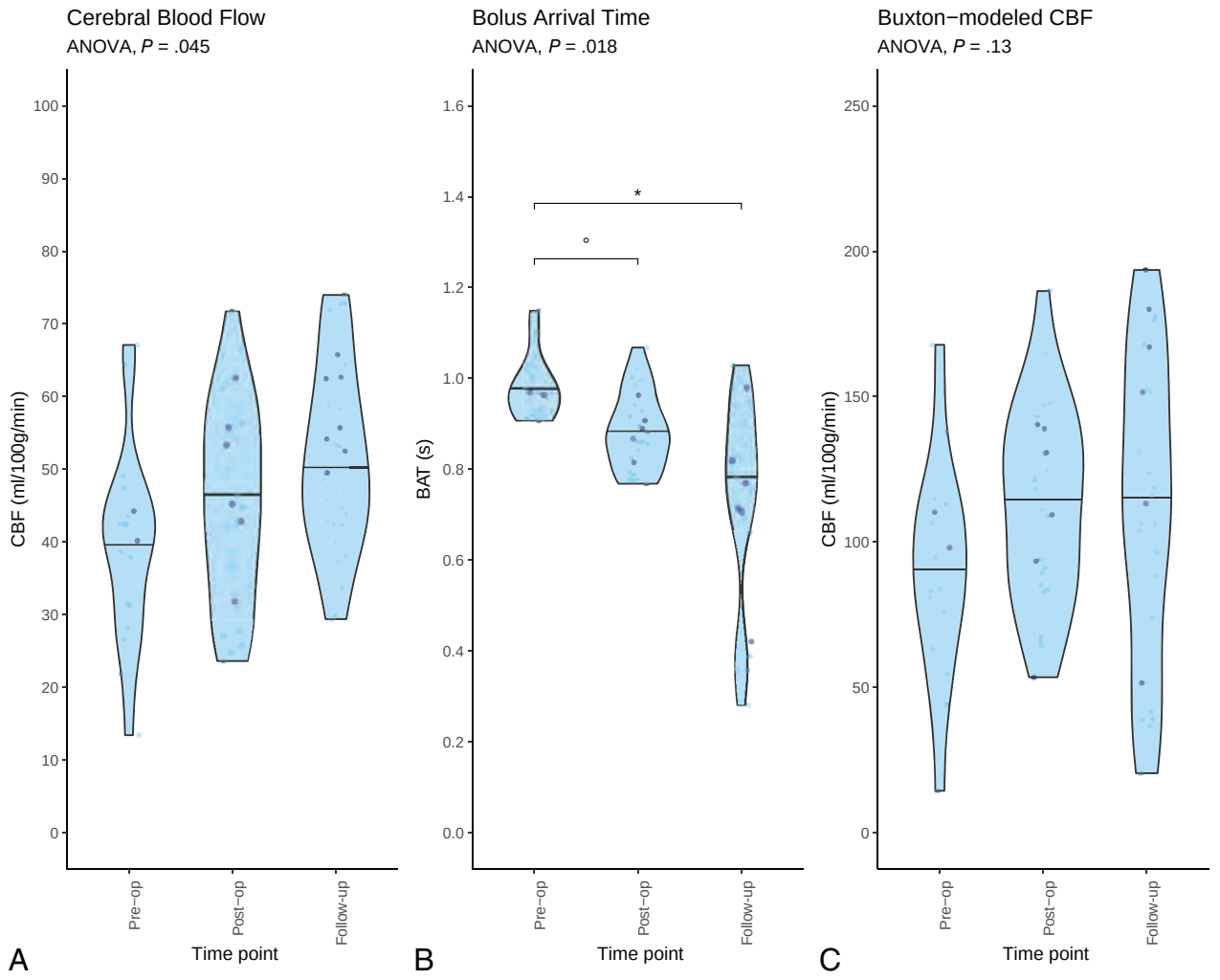

FIG 1. Violin plots showing changes in perfusion metrics across time points for all patients' brain regions. The *horizontal line* within the plot indicates the median. *Darker data points* indicate patients with CMS. *A*, CBF derived from single-PLD ASL. *B*, BAT derived from multi-TI ASL. *C*, CBF derived from multi-TI ASL. *Horizontal significance bars* show false discovery rate–adjusted *P* values from *t* test pair-wise comparisons (*degree sign* indicates $P < .1$; *asterisk*, $P < .05$). Pre-op indicates preoperative; Post-op, postoperative.

used to assess model performance. Model performance was taken to be improved with a lower AIC and/or an increase in R^2. The likelihood ratio ANOVA tests were used to assess the effects of additive model terms.

RESULTS

Forty-four patients were prospectively recruited to the study, with a mean age of 6.69 (SD, 3.68) years; range, 1.04–14.6 years; 23 were female. The most common tumor histology encountered at the operation was pilocytic astrocytoma ($n = 22$), followed by medulloblastoma ($n = 14$), ependymoma ($n = 2$), diffuse midline glioma ($n = 2$), and atypical teratoid/rhabdoid tumor, ganglioglioma, hemangioblastoma, and high-grade glioma (1 each). Six patients (13.6%) underwent preoperative CSF diversion due to symptomatic obstructive HCP. Most patients (23/44, 52.3%) underwent midline intradural surgical approaches to the tumor. Eleven patients (25.0%) underwent lateral transcerebellar hemispheric approaches, and the remaining 10 patients (22.7%) had heterogeneous surgical approaches to their tumor, including biopsy only and cerebellopontine angle or direct access to large tumors presenting to the parenchymal surface. Eight patients (18.2%) were diagnosed with CMS in the postoperative period. The cardinal symptom of mutism was improved in 5 of these patients at follow-up. Eleven patients in the cohort (25.0%, all having medulloblastomas) underwent adjuvant photon radiation therapy.

Change in Gross Perfusion Metrics

Mean CBF in the cerebral cortex increased across the 3 time points (preoperative: 39.6 [SD, 13.3] mL/100g/min; postoperative: 45.5 [SD, 13.3] mL/100g/min; follow-up: 51.5 [SD, 12.6] mL/100g/min; Fig 1*A*). Repeated-measures ANOVA revealed statistically significant differences among the 3 time points ($P = .045$), though post hoc tests did not survive multiple comparison correction. Mean regional BAT decreased with time (preoperative: 0.982 [SD, 0.069] seconds; postoperative: 0.884 [SD, 0.083] seconds; and follow-up: 0.747 [SD, 0.217] seconds; Fig 1*B*). Repeated-measures ANOVA revealed statistically significant differences

among the 3 time points ($P = .018$), and post hoc tests confirmed a significant difference between the preoperative and follow-up time points ($P = .034$). Single-PLD CBF results were echoed by similar trends in mean BuxCBF, though these did not reach statistical significance (preoperative: 90.2 [SD, 36.9] mL/100g/min; postoperative: 113 [SD, 33.3] mL/100g/min; follow-up: 112 [SD, 51.7] mL/100g/min; $P = .129$; Fig 1*C*). Examples of single-PLD and multi-TI ASL data from a single representative patient are shown in Fig 2.

Table 1 shows differences in perfusion metrics of the cerebral cortex at the postoperative time point, depending on the surgical approach used. There was no significant difference in postoperative CBF between midline and lateral surgical approaches ($P = .212$ and .209, respectively) and no difference in mean age between the 2 groups ($P = .527$). The cortical BAT appeared to be prolonged in children who had undergone a midline approach to the tumor, though this did not reach statistical significance ($P = .058$).

Perfusion and HCP

There was no significant difference in age between those with and without symptomatic obstructive HCP requiring pre-resection CSF diversion ($P = .277$). In patients with HCP, preoperative mean cortical CBF was lower than in those who had not required CSF diversion (mean, 22.2 [SD, 8.95] versus 43.1 [SD, 11.2] mL/100g/min, $P = .032$). These effects were observed for all brain regions studied (Fig 3*A*), and differences in all regions reached a level of statistical significance apart from the frontal and motor cortices. Postoperatively, mean cortical CBF returned to normal levels, with no statistically significant difference in mean cortical CBF between those who underwent CSF diversion and those who did not (48.3 [SD, 10.7] versus 45.0 [SD, 13.8] mL/100g/min, $P = .562$). At follow-up imaging, mean cortical CBF was 57.5 (SD, 16.5) mL/100g/min in the HCP group compared with 50.3 (SD, 11.8) mL/100g/min in those without HCP ($P = .396$). These results were echoed by the findings from cortical BuxCBF, though they did not reach statistical significance at any time point (all, $P = .183$). Furthermore, a regional analysis did not reveal any statistically significant differences in BuxCBF among groups, other than in the thalamus at the preoperative time point ($P = .014$).

There was a statistically significant prolongation of mean BAT to the cerebral cortex preoperatively in children with symptomatic HCP (1.09 [SD, 0.07] versus 0.954 [SD, 0.037] seconds, $P = .048$). Figure 3*B* shows that this was more striking in some supratentorial cortical regions, especially the frontal, motor, and occipital. Postoperatively and at follow-up, there were no significant differences in mean cortical BAT depending on pre-resection HCP treatment ($P = .153$ and .558, respectively).

Perfusion and CMS

There was a significant difference in age between children diagnosed with CMS postoperatively and those without (mean, 4.00 [SD,1.90] versus 7.20 [SD, 3.72] years, $P = .002$). Preoperative (42.2 [SD, 2.88] versus 39.3 [SD, 14.1] mL/100g/min, $P = .488$) and postoperative (48.6 [SD, 10.9] versus 44.8 [SD, 13.9] mL/100g/min, $P = .484$) mean cortical CBF was similar between children with CMS and those without. There was a significantly higher mean CBF at the follow-up time point in the CMS group (57.5 [SD, 6.08] versus 49.7 [SD, 13.6] mL/100g/min, $P = .040$). There were no significant differences in BAT or BuxCBF at any time point, and no significant differences in any perfusion metrics on a regional analysis.

Linear Mixed-Effects Modeling

Multivariable linear mixed-effects models were used to explore the effect of HCP and CMS on CBF in the cohort. Models were fit on a 3-region sample of CBF values: the mean across the whole cortex, thalamus, and cerebellum. This

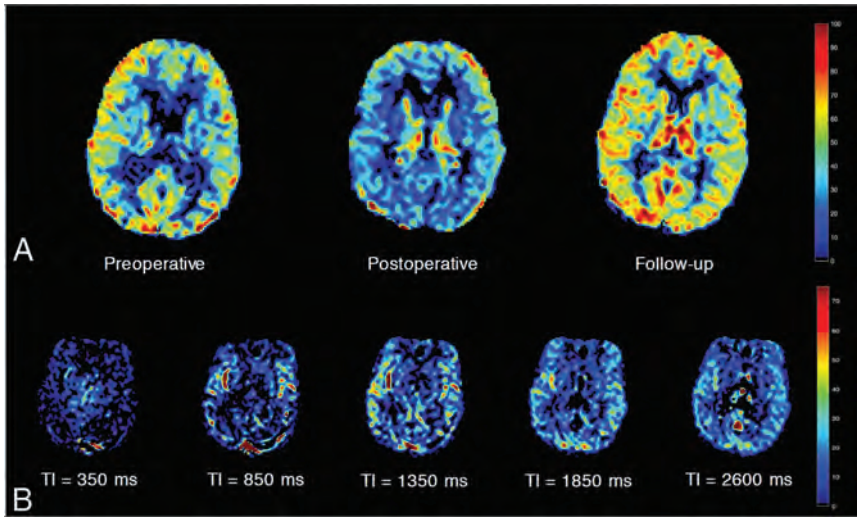

FIG 2. Sample ASL maps of a patient with a posterior fossa pilocytic astrocytoma on a midthalamic axial section. *A*, Single-PLD CBF maps at preoperative, postoperative, and follow-up time points. *Color bar* indicates milliliters/100g/min. *B*, Raw multi-TI ASL data show a difference in magnetization (d*M*) between control and label scans at selected sequentially increasing TIs at a follow-up scan. *Color bar* indicates arbitrary units of *dM*.

Table 1: Mean postoperative cortical perfusion metrics by surgical approach[a]

	Midline	Hemispheric	95% CI Difference	*P*
Age (yr)	6.22 (SD, 3.45)	7.05 (SD, 3.5)	–3.49–1.84	.527
CBF (mL/100g/min)	44.7 (SD, 11.5)	53.4 (SD, 15.5)	–23.3–5.97	.212
BAT (sec)	0.891 (SD, 0.076)	0.828 (SD, 0.056)	–0.002–0.128	.0576
BuxCBF (mL/100g/min)	109 (SD, 27.8)	135 (SD, 42.3)	–70.3–18.6	.209

[a] Values are means and 95% CIs; *P* values are from unpaired *t* tests.

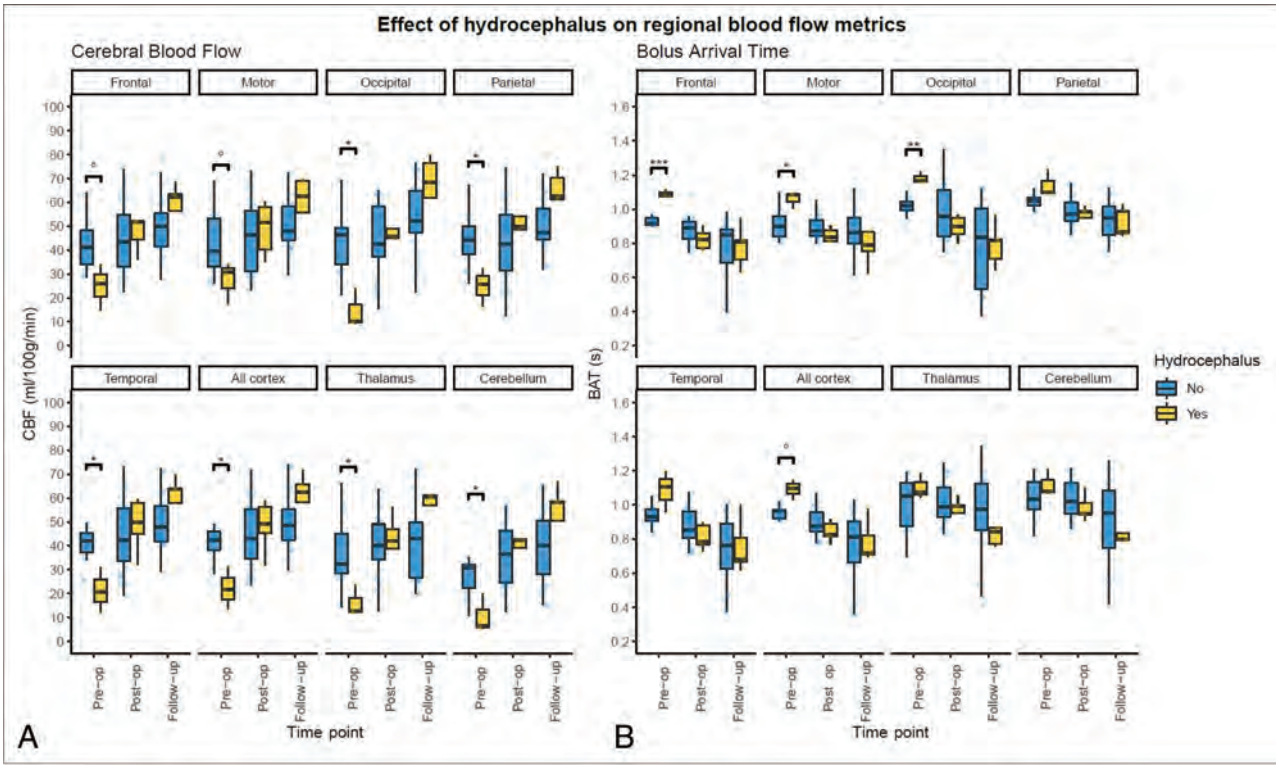

FIG 3. *Boxplots* depicting perfusion metrics stratified by brain regions in patients with and without symptomatic HCP. *A*, CBF derived from single-PLD ASL. *B*, BAT derived from multi-TI ASL. False discovery rate–adjusted *P* values: Degree sign indicates $P < .1$; *asterisk*, $P < .05$; *double asterisks*, $P < .01$; *triple asterisks*, $P < .001$. Pre-op indicates preoperative; Post-op, postoperative.

process began with the fitting of a baseline model (mod_baseline), which did not include the effects of interest, to estimate the effects of time point, age, and brain region on CBF. Model terms and their fixed-effect coefficients are shown in Table 2, along with comparisons of model characteristics.

The addition of HCP with an interaction term for time point (mod_hcp) reduced the AIC and increased R^2 values. Likelihood ratio testing of (mod_hcp2) and (mod_baseline) indicated a significant effect of HCP and its interaction with the time point on the model ($P < .001$). The full model (mod_hcpcms) included terms for CMS and HCP and their interactions with the time point. Likelihood ratio testing between the 2 best-performing models, (mod_hcp) and (mod_hcpcms), showed a statistically significant difference between the 2 in favor of the full model ($P = .03$), which also had the lowest AIC and higher R^2 values.

DISCUSSION

In this prospective study of children with posterior fossa tumors, mean cortical CBF increased after tumor resection and at follow-up imaging. For the first time, we show reductions in the BAT of labeled blood to the cerebral cortex after tumor resection. Children presenting with symptomatic obstructive HCP requiring pre-resection CSF diversion had significantly reduced preoperative CBF and prolonged BAT. A regional analysis according to standardized brain parcellations revealed that CBF was significantly lower preoperatively in many cortical regions in patients with HCP and that BAT was significantly prolonged in the frontal, motor, and occipital cortices of patients with HCP. There was a significantly higher CBF at follow-up in children who developed CMS. A multivariable linear mixed-effects modeling approach confirmed that both HCP and CMS had a powerful effect on CBF by time point. In fact, these 2 factors emerged as more significant features of determining postoperative CBF in the final model than the time point alone.

Our results indicate weak evidence of prolonged BAT after midline approaches to posterior fossa tumors, which entail more extensive dissection of neural parenchyma, greater exposure of CSF spaces, and increased handling and manipulation of large infratentorial arteries, such as the PICA. It is possible that vasospasm could have led to prolonged BAT following midline approaches. This scenario has been described following posterior fossa tumor resection in children[24,25] and even described as a cause of CMS in an adolescent.[26]

Perfusion Metrics and Hydrocephalus

Seventy-to-ninety percent of children with posterior fossa tumors present with HCP.[27] However, the relation between ventricular size, compliance, and pressure is complex, and ventricular size can be equivocal with regard to underlying CSF mechanics.[28] In this series, the need for pre-resection CSF diversion was judged clinically by experienced pediatric neurosurgeons on the basis of features of raised ICP. It is to be expected that resection of a posterior fossa tumor alone will increase CBF due to the removal of an obstructing mass;[5] however, we demonstrate that in patients with symptomatic HCP before tumor resection, the mean cortical CBF was lower and BAT was higher, with statistically significant differences in these parameters among groups.

Table 2: Multivariable linear mixed-effects modeling of CBF based on clinical, demographic, and study factors[a]

	Mod_Baseline	Mod_HCP	Mod_HCPCMS
(Intercept)	43.3 (3.86)[b]	48.4 (4.06)[b]	50.1 (4.70)[b]
Postop time point	6.21 (2.00)[c]	3.01 (2.08)	1.55 (2.20)
Follow-up time point	14.8 (2.07)[b]	10.5 (2.15)[b]	7.74 (2.31)[b]
Age	−0.686 (0.45)	−1.17 (0.53)[d]	−1.34 (0.59)[d]
Thalamus	−5.55 (1.60)[b]	−5.59 (1.51)[b]	−5.60 (1.45)[b]
Cerebellum	−10.0 (1.59)[b]	−10.0 (1.50)[b]	−10.0 (1.44)[b]
Unsedated (vs GA)	–	3.57 (3.79)	5.73 (3.93)
Hydrocephalus	–	−19.4 (6.04)[c]	−20.5 (6.27)[c]
Postop time point + HCP	–	21.5 (5.17)[b]	24.0 (5.13)[b]
Follow-up time point + HCP	–	26.0 (5.22)[b]	27.2 (5.18)[b]
CMS	–	–	−10.9 (6.46)[e]
Postop time point + CMS	–	–	8.74 (5.26)[e]
Follow-up time point + CMS	–	–	15.6 (5.28)[c]
AIC	1841.5	1824.7	1821.8
Marginal R^2	0.224	0.290	0.295
Conditional R^2	0.607	0.650	0.692

Note:—– indicates not included in model; GA, general anesthesia; Post-op, postoperative.

[a] Values are coefficients (standard error).

[b] $P < .001$.

[c] $P < .01$.

[d] $P < .05$.

[e] $P < .1$.

The first study to evaluate the role of ASL in HCP compared 19 patients with HCP secondary to posterior fossa tumors with 16 healthy controls.[7] The former group was found to have significantly lower CBF at baseline. CBF was significantly increased in this group after "alleviation of HCP," ie, tumor resection (with additional CSF diversion in 6 patients). The present study replicates these findings, and by adding a temporal dimension in the form of multi-TI ASL, it is the first demonstration that reduction of CBF in symptomatic obstructive HCP occurs in conjunction with a prolonged arterial transit time. A regional analysis of perfusion metrics showed that CBF was lower in the HCP group for all brain regions other than the frontal and motor cortices. This finding is likely due to the raised ICP related to HCP causing reduced cerebral perfusion pressure. However, because the ICP was not directly measured in this study, we cannot provide any mechanistic evidence for this finding.

Changes in the BuxCBF in the HCP group were corresponding in direction, though only the comparison of the preoperative thalamic BuxCBF reached a level of statistical significance. BuxCBF values are inevitably higher than single-PLD CBF values because they capture blood flow in large arteries at earlier TIs. The concordance between these 2 metrics provides reassurance that the single-PLD CBF changes were not due to incomplete delivery of the labeled bolus at the PLD of 1.5 seconds.

The results of the linear multivariable mixed-effects modeling confirmed the effects of HCP on CBF seen by statistical hypothesis testing of the data. This confirmation indicated that HCP had a significant effect on CBF dependent on the time point, once age, sedation status, brain region, scanning time point, and CMS by time point were controlled for, reducing the mean CBF by 20.5 (SD, 6.27) mL/100g/min preoperatively ($P < .01$). Following tumor resection, children who had been treated with CSF diversion had significant increases in mean CBF at postoperative imaging (24.0 [SD, 5.13] mL/100g/min, $P < .001$) and at follow-up imaging (27.2 [SD, 5.18] mL/100g/min, $P < .001$).

One potential clinical implication of these results, when taken along with those of Yeom et al,[7] is that in the presence of equivocal symptomatology of raised ICP, perfusion metrics from ASL may help in decisions regarding perioperative CSF diversion. To further investigate this possibility, dedicated studies using real-time ICP measurements, ventricular volumetry, and detailed clinical correlates are needed.

Perfusion Metrics and CMS

CMS is a common postoperative complication after posterior fossa tumor resection, occurring in around one-quarter of cases.[6] The putative mechanism posits damage to the superior cerebellar peduncle at the operation as a key element causing a disturbance in cerebellocerebral circuitry. This, in turn, is thought to lead to diaschisis causing a loss of function in widespread supratentorial cortical areas, and the corollary hypoperfusion can be quantified with perfusion imaging. Thus, SPECT[11,12] and DSC-MRI[13] studies have shown frontal hypoperfusion in patients with CMS. Similarly, ASL-derived CBF was found to be reduced in the frontal lobes in a patient with CMS, recovering to normal levels after resolution of the syndrome.[15] This result was later confirmed in a small cohort study of children with posterior fossa tumors (11 patients with CMS compared with 10 without).[14] A modest reduction in CBF in the right frontal lobe was observed postoperatively, with significant increases in CBF in both frontal lobes after clinical improvement. A systematic review of 5 studies concluded that cerebral perfusion is reduced in children with CMS postoperatively, though none of the included studies incorporated preoperative comparison imaging.[29]

In this study, we were unable to replicate the findings of a statistically significant difference in postoperative CBF with respect to CMS status. However, we provide confirmatory evidence of increased CBF in children with CMS at the follow-up time point—after improvement of CMS symptoms in most—on single-PLD CBF ($P = .0403$). The multi-TI ASL results did not demonstrate any differences in BAT or BuxCBF among groups.

The presence of an unbalanced age distribution among groups may help explain the results from statistical hypothesis testing of the data. Age is known to be broadly negatively correlated with CBF in children[20] (confirmed by its significance in the final mixed-effects model with a model coefficient of −1.34), so the CMS group having a much younger mean age may have increased the CBF at all time points for this group. Other reasons for the lack of distinction in postoperative CBF include a small sample size in the CMS group, which will have hindered comparative statistical testing. Furthermore, the repeated-measures data are unbalanced due to the substantial logistic challenges in obtaining preoperative scans in many patients.

The linear mixed-effects models described above are able to circumvent this drawback to give meaningful insight into the effects of the age parameter in the cohort. The full model, which included both HCP and CMS with their time point interactions as terms, confirmed a significant increase in CBF in the CMS group at follow-up, and coefficients for the other time points almost reached the threshold for statistical significance. The results presented here indicate that future studies investigating perfusion in CMS must take clinical features such as HCP and tumor location (and therefore surgical approach) into account.

Limitations

The lack of a clear, objective determination of CMS status is a perennial issue in studies reporting neuroimaging correlates of the syndrome, and this criticism applies to this study as much as all others in the field. To mitigate this issue, the definition of CMS applied in this study was pragmatic, based on the key criterion of mutism or reduced speech output, applied contemporaneously by an experienced neurosurgical multidisciplinary team. Because the key clinical correlate in this study was a speech deficit in CMS, it is not known from the data presented here whether CBF alterations exist postoperatively in the setting of CMS symptoms other than a speech deficit. The development of a validated scoring system for CMS is essential to objectively classify CMS phenotypes and their imaging correlates.

The regional ASL analysis did not take into account laterality because the assumption was made that symmetric vasculature leads to symmetric blood delivery. This assumption is perfectly valid in healthy brains, yet it may not be entirely true in a postoperative cohort with data acquisition shortly after surgery. For instance, unilateral manipulation of major infratentorial arteries, such as the PICA, a necessary step during midline tumor approach in dissection of the posterior fossa, may have conceivably caused a degree of arterial spasm leading to a variation in CBF by laterality.

The parcellation of the brain into regions of cortical lobes in this analysis was a pragmatic one because we are ultimately interested in behavioral effects of CBF changes in this cohort. However, we recognize that the cerebral lobes are functional-not-vascular units, and interrogating perfusion on a truly vascular basis would require territorial ASL,[30] which is technically challenging, even more so in unwell perioperative pediatric patients. The multi-TI ASL acquisition was a research sequence that is not widely available, limiting the generalizability of the results.

With regard to the insights shown on CBF in symptomatic HCP in the setting of pediatric posterior fossa tumors, these findings may not be entirely generalizable to more chronic or complex HCP syndromes seen in the wider neurosurgical population, such as low-pressure hydrocephalic states,[31] or those with an altered CSF constitution, such as following subarachnoid or intraventricular hemorrhage or CNS infection. In the adult literature, there is cautionary evidence that in normal-pressure HCP, CBF measured using ASL is reduced in deep-seated brain regions[32] but that changes in CBF do not correlate with clinical improvement following shunting.[33]

Radiation therapy has been shown to affect ASL CBF in children with posterior fossa tumors,[34] and this variable, in dichotomized form due to the lack of variation in the total dose, was included in the modeling analysis. It is possible that some of the increase in CBF and BuxCBF seen at the follow-up time point will have been accounted for by this effect, though radiation therapy was a nonsignificant feature of the model and diminished model performance; therefore, it was discarded.

CONCLUSIONS

In children with posterior fossa tumors, CBF increases after tumor resection and at follow-up scanning, and it is demonstrated for the first time that this increase occurs in conjunction with a decrease in the arrival time of labeled blood to several brain regions. Given the differences in BAT in this cohort, quantification of CBF using a single-PLD method alone has serious drawbacks; here we describe a thorough approach to CBF estimation using combined multi-TI ASL. Multivariable linear mixed-effects modeling confirms that perfusion changes are more pronounced in children presenting with symptomatic obstructive HCP requiring CSF diversion. Children with CMS had significantly higher CBF at follow-up imaging, but no differences were seen in perioperative CBF compared with those without CMS. ASL shows promise as a noninvasive tool to evaluate cerebral perfusion in the setting of pediatric obstructive HCP.

Disclosure forms provided by the authors are available with the full text and PDF of this article at www.ajnr.org.

REFERENCES

1. Johnston IH, Rowan JO, Harper AM, et al. **Raised intracranial pressure and cerebral blood flow, I: cisterna magna infusion in primates.** *J Neurol Neurosurg Psychiatry* 1972;35:285–96 CrossRef Medline
2. Johnston IH, Rowan JO. **Raised intracranial pressure and cerebral blood flow, 4: intracranial pressure gradients and regional cerebral blood flow.** *J Neurol Neurosurg Psychiatry* 1974;37:585–92 CrossRef Medline
3. Grubb RL, Raichle ME, Phelps ME, et al. **Effects of increased intracranial pressure on cerebral blood volume, blood flow, and oxygen utilization in monkeys.** *J Neurosurg* 1975;43:385–98 CrossRef Medline
4. Jabre A, Symon L, Richards PG, et al. **Mean hemispheral cerebral blood flow changes after craniotomy: significance and prognostic value.** *Acta Neurochir (Wien)* 1985;78:13–20 CrossRef Medline
5. Kerscher S, Schoning M, Schuhmann M. **Raised ICP decreases cerebral blood flow volume in pediatric patients.** In: *Proceedings of the Annual Meeting of the International Society for Paediatric Neurosurgery*, Birmingham, UK. October 20–24, 2019
6. Toescu S, Samarth G, Layard Horsfall H, et al. **Fourth ventricle tumours in children: complications and influence of surgical approach.** *J Neurosurg Pediatr* 2020;27:52–61 CrossRef Medline

7. Yeom KW, Lober RM, Alexander A, et al. **Hydrocephalus decreases arterial spin-labeled cerebral perfusion.** *AJNR Am J Neuroradiol* 2014;35:1433–39 CrossRef Medline
8. Keil VC, Hartkamp NS, Connolly DJ, et al. **Added value of arterial spin labeling magnetic resonance imaging in pediatric neuroradiology: pitfalls and applications.** *Pediatr Radiol* 2019;49:245–53 CrossRef Medline
9. Robertson PL, Muraszko KM, Holmes EJ, et al; Children's Oncology Group. **Incidence and severity of postoperative cerebellar mutism syndrome in children with medulloblastoma: a prospective study by the Children's Oncology Group.** *J Neurosurg* 2006;105:444–51 CrossRef Medline
10. Gudrunardottir T, Sehested A, Juhler M, et al. **Cerebellar mutism: definitions, classification and grading of symptoms.** *Childs Nerv Syst* 2011;27:1361–63 CrossRef Medline
11. Germanò A, Baldari S, Caruso G, et al. **Reversible cerebral perfusion alterations in children with transient mutism after posterior fossa surgery.** *Childs Nerv Syst* 1998;14:114–19 CrossRef Medline
12. De Smet HJ, Baillieux H, Wackenier P, et al. **Long-term cognitive deficits following posterior fossa tumor resection: a neuropsychological and functional neuroimaging follow-up study.** *Neuropsychology* 2009;23:694–704 CrossRef Medline
13. Miller NG, Reddick WE, Kocak M, et al. **Cerebellocerebral diaschisis is the likely mechanism of postsurgical posterior fossa syndrome in pediatric patients with midline cerebellar tumors.** *AJNR Am J Neuroradiol* 2010;31:288–94 CrossRef
14. Yecies D, Shpanskaya K, Jabarkheel R, et al. **Arterial spin-labeling perfusion changes of the frontal lobes in children with posterior fossa syndrome.** *J Neurosurg Pediatr* 2019 Aug 2. [Epub ahead of pirnt] CrossRef Medline
15. Watanabe Y, Yamasaki F, Nakamura K, et al. **Evaluation of cerebellar mutism by arterial spin-labeling perfusion magnetic resonance imaging in a patient with atypical teratoid/rhabdoid tumor (AT/RT): a case report.** *Childs Nerv Syst* 2012;28:1257–60 CrossRef Medline
16. Alsop DC, Detre JA, Golay X, et al. **Recommended implementation of arterial spin-labeled perfusion MRI for clinical applications: a consensus of the ISMRM perfusion study group and the European consortium for ASL in dementia.** *Magn Reson Med* 2015;73:102–16 CrossRef Medline
17. Dale AM, Fischl B, Sereno MI. **Cortical surface-based analysis.** *Neuroimage* 1999;9:179–94 CrossRef Medline
18. Modat M, Cash DM, Daga P, et al. **Global image registration using a symmetric block-matching approach.** *J Med Imaging (Bellingham)* 2014;1:024003 CrossRef Medline
19. Buxton RB, Frank LR, Wong EC, et al. **A general kinetic model for quantitative perfusion imaging with arterial spin-labeling.** *Magn Reson Med* 1998;40:383–96 CrossRef Medline
20. Hales PW, Kawadler JM, Aylett SE, et al. **Arterial spin-labeling characterization of cerebral perfusion during normal maturation from late childhood into adulthood: normal "reference range" values and their use in clinical studies.** *J Cereb Blood Flow Metab* 2014;34:776–84 CrossRef Medline
21. Jenkinson M, Bannister P, Brady M, et al. **Improved optimization for the robust and accurate linear registration and motion correction of brain images.** *Neuroimage* 2002;17:825–41 CrossRef Medline
22. R Core Team. **A language and environment for statistical computing.** R Foundation for Statistical Computing; 2017. https://www.r-project.org/. Accessed March 3, 2020
23. Barton K. **MuMIn: Multi-Model Inference.** 2020. https://cran.microsoft.com/snapshot/2020-11-30/web/packages/MuMIn/index.html. Accessed March 3, 2020
24. Rao VK, Haridas A, Nguyen TT, et al. **Symptomatic cerebral vasospasm following resection of a medulloblastoma in a child.** *Neurocrit Care* 2013;18:84–88 CrossRef Medline
25. Gocmen S, Acka G, Karaman K, et al. **Cerebral vasospasm after posterior fossa tumor surgery: a case report and literature review.** *Pediatr Neurosurg* 2020;55:393–96 CrossRef Medline
26. Deghedy M, Pizer B, Kumar R, et al. **Basilar artery vasospasm as a cause of post-operative cerebellar mutism syndrome.** *Case Rep Pediatr* 2022;2022:9148100–05 CrossRef Medline
27. Lin CT, Riva-Cambrin JK. **Management of posterior fossa tumors and hydrocephalus in children: a review.** *Childs Nerv Syst* 2015;31:1781–89 CrossRef Medline
28. Borgesen SE, Gjerris F. **Relationships between intracranial pressure, ventricular size, and resistance to CSF outflow.** *J Neurosurg* 1987;67:535–39 CrossRef Medline
29. Ahmadian N, van Baarsen M, Robe, PA, et al. **Association between cerebral perfusion and paediatric postoperative cerebellar mutism syndrome after posterior fossa surgery: a systematic review.** *Childs Nerv Syst* 2021;37:2742–51 CrossRef Medline
30. Hartkamp NS, Petersen ET, De Vis JB, et al. **Mapping of cerebral perfusion territories using territorial arterial spin-labeling: techniques and clinical application.** *NMR Biomed* 2013;26:901–12 CrossRef Medline
31. Pang D, Altschuler E. **Low-pressure hydrocephalic state and viscoelastic alterations in the brain.** *Neurosurgery* 1994;35:643–56 CrossRef Medline
32. Virhammar XJ, Laurell XK, Ahlgren XA, et al. **Arterial spin-labeling perfusion MR imaging demonstrates regional CBF decrease in idiopathic normal pressure hydrocephalus.** *AJNR Am J Neuroradiol* 2017;38:2081–88 CrossRef Medline
33. Virhammar J, Ahlgren A, Cesarini KG, et al. **Cerebral perfusion does not increase after shunt surgery for normal pressure hydrocephalus.** *J Neuroimaging* 2020;30:303–07 CrossRef Medline
34. Li MD, Forkert ND, Kundu P, et al. **Brain perfusion and diffusion abnormalities in children treated for posterior fossa brain tumors.** *J Pediatr* 2017;185:173–80.e3 CrossRef Medline

Arterial Spin-Labeling Perfusion Imaging in the Early Stage of Sturge-Weber Syndrome

G. Pouliquen, L. Fillon, V. Dangouloff-Ros, M. Kuchenbuch, C. Bar, N. Chemaly, R. Levy, C.-J. Roux, A. Saitovitch, J. Boisgontier, R. Nabbout, and N. Boddaert

ABSTRACT

BACKGROUND AND PURPOSE: Sturge-Weber syndrome is a rare congenital neuro-oculo-cutaneous disorder. Although the principal mechanism of Sturge-Weber syndrome is characterized by a leptomeningeal vascular malformation, few data regarding perfusion abnormalities of the brain parenchyma are available. Therefore, the aim of this study was to assess the diagnostic performance of arterial spin-labeling perfusion imaging in the early stage of Sturge-Weber syndrome before 1 year of age until 3.5 years of age. We hypothesized that a leptomeningeal vascular malformation has very early hypoperfusion compared with controls with healthy brains.

MATERIALS AND METHODS: We compared the CBF using arterial spin-labeling perfusion imaging performed at 3T MR imaging in the brain parenchymal regions juxtaposing the leptomeningeal vascular malformation in patients with Sturge-Weber syndrome ($n = 16$; 3.5 years of age or younger) with the corresponding areas in age-matched controls with healthy brains ($n = 58$). The analysis was performed following two complementary methods: a whole-brain voxel-based analysis and a visual ROI analysis focused on brain territory of the leptomeningeal vascular malformation.

RESULTS: Whole-brain voxel-based comparison revealed a significant unilateral decrease in CBF localized in the affected cortices of patients with Sturge-Weber syndrome ($P < .001$). CBF values within the ROIs in patients with Sturge-Weber syndrome were lower than those in controls (in the whole cohort: median, 25 mL/100g/min, versus 44 mL/100g/min; $P < .001$). This finding was also observed in the group younger than 1 year of age, emphasizing the high sensitivity of arterial spin-labeling in this age window in which the diagnosis is difficult.

CONCLUSIONS: Arterial spin-labeling perfusion imaging in the early stage of Sturge-Weber syndrome can help to diagnose the disease by depicting a cortical hypoperfusion juxtaposing the leptomeningeal vascular malformation.

ABBREVIATIONS: ASL = arterial spin-labeling; AUC = area under the curve; FWE = family-wise error; IQR = interquartile range; LVM = leptomeningeal vascular malformation; MNI = Montreal Neurological Institute; PWB = port-wine birthmark; SWS = Sturge-Weber syndrome

Sturge-Weber syndrome (SWS) is a congenital disorder characterized by a triad, variably including an ipsilateral port-wine birthmark (PWB) typically involving the forehead, a leptomeningeal vascular malformation (LVM), and ocular abnormalities.[1-3]

A sporadic, somatic activating mutation in the *GNAQ* gene leads to cell proliferation and inhibition of apoptosis leading to an SWS spectrum.[2,4] Depending on the time in development when the mutation occurs, it may simply provoke PWB or SWS.[2] The main progressive symptoms include seizures, neurodevelopmental delay, and visual defects.[5]

Because the isolated PWB is not referred to as SWS, the brain involvement confirms the diagnosis[5] and may be detected in infants with a high-risk PWB, even before the onset of neurologic symptoms.[6] 3T MR imaging is the primary technique recommended[7] for the diagnosis by the visualization of the LVM on post-contrast-weighted images.[3,5] Other MR imaging signs provide indirect evidence of LVM: ipsilateral choroid plexus enlargement, cerebral atrophy, and signal inversion of the affected WM on T2WI.[3]

Few studies regarding brain perfusion abnormalities are available.[8-18] The latest studies were performed using T2* dynamic

Received February 20, 2022; accepted after revision July 27.

From the Department of Pediatric Radiology (G.P., V.D.-R., R.L., C.-J.R., N.B.) and Centre de Reference Epilepsies Rares (M.K., C.B., N.C., R.N.), Department of Pediatric Neurology, Necker Children's Hospital, Assistance Publique-Hôpitaux de Paris, Université de Paris, Paris, France; and Imagine Institute for Genetic Diseases (G.P., L.F., V.D.-R., R.L., C.-J.R., A.S., J.B., R.N., N.B.), L'Institut National de la Santé et de la Recherche Médicale U1163, Paris, France.

R. Nabbout and N. Boddaert contributed equally to this work

Please address correspondence to Geoffroy Pouliquen, MD, Department of Pediatric Radiology, Necker Children's Hospital, Assistance Publique-Hôpitaux de Paris, University of Paris, 149 Rue de Sèvres, 75015 Paris, France; e-mail: geoffroy.pouliquen@gmail.com

http://dx.doi.org/10.3174/ajnr.A7643

susceptibility contrast material–enhanced imaging, which does not reflect the routine practice in children in expert centers currently. Its application has been limited due to reduced patient comfort and technical difficulties required by high-flow injection of contrast media in small veins.[19]

Arterial spin-labeling (ASL) is a perfusion imaging technique that does not require injection, making it suitable for pediatric patients.[20] Our aim was to assess the diagnostic performance of ASL in the early stage of SWS before 1 year of age until 3.5 years of age by comparing cortical perfusion juxtaposing the LVM with the corresponding areas in controls with healthy brains. We hypothesized that LVM shows an early hypoperfusion compared with controls with healthy brains and investigated this hypothesis following 2 methods: a whole-brain voxel-based analysis and an ROI analysis focused on the brain territory of LVM.

MATERIALS AND METHODS

Subjects

We retrospectively reviewed patients with a confirmed diagnosis of SWS followed at our institution from May 2015 to March 2021. They were recruited from the pediatric neurology department using the full-text search engine database DR WAREHOUSE (https://www.trademarkelite.com/trademark/trademark-detail/87158029/DR-WAREHOUSE).[21] Inclusion criteria were a confirmed diagnosis of SWS in children between 0 and 3.5 years of age obtained on 3T MR imaging during the interictal period with a routine protocol including ASL. Patients were excluded from the study if MR imaging revealed an atypical SWS syndrome (eg, including diagnostic uncertainty or association with other diseases such as scaphocephaly, subdural hematoma, or subarachnoid cyst) or was compromised by artifacts. Age-matched controls were included with the following criterion: examination for various reasons during the time of the study with scans with strictly normal findings (nonexhaustively morphologic evaluation of upper-limit head circumference, feeding difficulties, abnormal eye movements, benign nystagmus, isolated strabismus).

Analyses were performed for the whole cohort and in age groups before or after 1 year of age to focus on young patients when the SWS diagnosis was peculiarly difficult. According to local regulations, institutional review board approval was not required because this was a retrospective study using anonymized data. Consent was waived for this retrospective analysis.

Data Acquisition

Images were acquired in the Department of Pediatric Radiology on a 3T MR imaging scanner (Discovery MR750; GE Healthcare). The standard routine protocol included a 3D T1WI with and without postgadolinium acquisitions, T2WI, FLAIR, SWI, and ASL perfusion imaging.

ASL images were obtained with a 3D pseudocontinuous ASL sequence using an FSE acquisition with spiral filling of the *k*-space and the following parameters: TR = 4453 ms; TE = 10.96 ms; 8 spiral arms in each 3D partition with 512 points per arm; labeling duration = 1500 ms; postlabeling delay = 1025 ms; flip angle = 155°; resolution in plane = 1.875 × 1.875 mm; section thickness = 4 mm; FOV = 240 × 240 mm; acquisition time = 4 minutes 17 seconds.

The standard routine protocol included sedation using intrarectal pentobarbital (5 mg/kg of the child's weight, <20 kg) to avoid motion artifacts in children younger than 5 years of age. In this study, all children (patients and controls) were sedated.

Data Processing

For the data preprocessing and statistical analysis, we used the rest CBF quantification produced automatically by the processing console (GE Healthcare) using a proton-density image for signal normalization during CBF quantification.[22]

Whole-Brain Voxel-Based Analysis

Images were analyzed using Statistical Parametric Mapping 12 (SPM12; http://www.fil.ion.ucl.ac.uk/spm) and Matlab R2018b (MathWorks). Native T1WIs were segmented into GM, WM, and CSF maps using the Computational Anatomy Toolbox 12 (http://www.neuro.uni-jena.de/cat/) in SPM12. Deformation fields between native space and the Montreal Neurological Institute (MNI) space were obtained in this step. The MNI template used for tissue segmentation has been adapted according to the age of the given subject: a pediatric template created with Template-O-Matic toolbox[23] using the National Institutes of Health Pediatric MRI Data Repository (https://www.nitrc.org/projects/pediatric_mri/) for children older than 1 year of age, and the Infant Brain Probability Templates[24] for children younger than 1 year of age.

For each child, the coregistration between the native CBF image and the native GM image was estimated. Then, the combination of the deformation fields and the estimated coregistration was applied to the CBF image to spatially normalize this image in the MNI space with an in-plane resolution of 1.5 × 1.5 mm and a section thickness of 1.5 mm. The resulting image was checked for proper registration and smoothed with a Gaussian kernel of 6-mm full width at half-maximum.

Leptomeningeal Vascular Malformation Analysis

Images were analyzed using a medical image viewer (Vue PACS, Version 12.1.6.0117; Carestream Health). A 2D ROI was manually placed on CBF images in the LVM location for each patient with SWS found on T1-weighted contrast-enhanced images. Similarly, ROIs were placed in the corresponding areas in controls. They were round, with a mean area of 50 mm^2 (range, 40–60 mm^2). Figure 1 displays an illustration of an MR imaging from a patient with SWS.

Statistical Analysis

Whole-Brain Voxel-Based Analysis. For each subgroup, comparisons between children with SWS and controls were performed to investigate voxelwise cortical perfusion differences using a 2-sample *t* test design in the framework of the FSL General Linear Model (http://fsl.fmrib.ox.ac.uk/fsl/fslwiki/GLM). All results were thresholded with a *P* value of .001. Because we had an a priori hypothesis concerning the location of the LVM, we showed the results without the family-wise error (FWE) correction. When significant, results with the FWE correction were also indicated.

LVM-Focused Analysis. CBF values in the angioma ROI for patients and in the corresponding areas for controls were reported as median and interquartile range (IQR). Comparisons

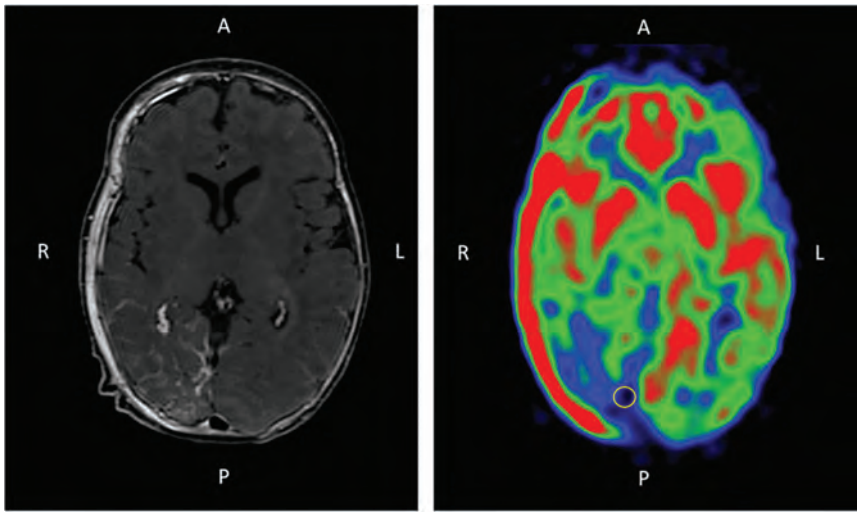

FIG 1. Illustration of a 3-month-of-age patient with SWS with a right occipito-temporo-parietal LVM. Axial slices of the brain on T1-weighted imaging after contrast injection (*left*) and ASL perfusion imaging (*right*) show, respectively, the contrast enhancement and the hypoperfusion associated with the LVM. A ROI (*yellow circle*) was placed in the cortical area juxtaposing the LVM on ASL. Note that an osseous angioma is also present and responsible for the hyperperfused area of the right part of the skull. A indicates anterior; P, posterior; R, right; L, left.

between children with SWS and controls were performed to investigate perfusion differences using Wilcoxon tests. $P \leq .05$ was considered statistically significant.

To explore the diagnostic accuracy of these ROIs to diagnose SWS, we performed receiver operating characteristic curves per age and in the whole cohort; the area under the curve (AUC) was computed, as well as sensitivities and specificities. A bootstrap method was used to calculate the 95% CI of the AUC, sensitivities, and specificities.

RESULTS

Patients

Sixteen patients with 26 scans were identified for this study. Seventeen scans were obtained in children younger than younger than 1 year of age, and 9 scans, in children between 1 and 3.5 years of age. The demographic details of the patients are listed in Table 1. Fifty-eight controls with healthy brains were identified with 25 younger than 1 year of age and 33 from 1 to 3.5 years of age.

Subjects were divided into 4 subgroups based on age and lateralization of the disease. There were 2 subgroups of children younger than 1 year of age with the following: 1) left LVM with 7 examinations, and 2) right LVM with 10 examinations both compared with the 25 controls younger than 1 year of age. There were 2 subgroups of children between 1 and 3.5 years of age with the following: 1) left LVM with 2 examinations, and 2) right LVM with 9 examinations, both compared with the 33 controls with the same age interval. Two patients with bilateral LVMs were included and allocated twice, depending on their age, to the subgroups left and right, independently.

Whole-Brain Voxel-Based Comparisons

For each subgroup, whole-brain voxel-based comparison between CBF in patients with SWS and controls with healthy brains revealed a significant unilateral decrease in CBF localized on the affected cortex of patients with SWS ($P < .001$). Figure 2 shows the

Table 1: Demographics and morphologic imaging data of patients with SWS

Patient	Sex	Examination Age[a] (months)	Leptomeningeal Vascular Malformation		Epilepsy	Atrophy	Calcifications
			Side	Extension (Lobe)			
1	Female	3	Left	FTP	None	None	None
2	Female	0/11	Bilateral	LO/RO	None	None	None
3	Female	0/9	Left	OT	None	None	None
4	Male	1	Left	HS	None	None	Present
5	Male	11	Left	OP	None	None	None
6	Female	1	Right	O	None	None	None
7	Female	2/25	Right	O	Present	None	None
8	Male	3/18	Right	OTP	Present	Present	Present
9	Female	4/6/17	Right	HS	Present	Present	Present
10	Female	4/11	Right	O	None	None	None
11	Male	9	Right	OTP	None	None	None
12	Female	27	Left	O	Present	None	Present
13	Female	42	Bilateral	LFP/ROTP	Present	None	None
14	Male	16	Right	OTP	Present	Present	Present
15	Male	18	Right	O	Present	None	Present
16	Male	30	Right	O	None	None	None

Note:—F indicates frontal; O, occipital; HS, hemisphere; OP, occipito-parietal; OTP, occipito-temporo-parietal; LFP, left fronto-parietal; ROTP, Right occipito-temporo-parietal; FTP, fronto-temporo-parietal; LO, left occipital; RO, right occipital; OT, occipito-temporal.

[a] Two or 3 numbers are reported in this column when several examinations were performed for the same patient.

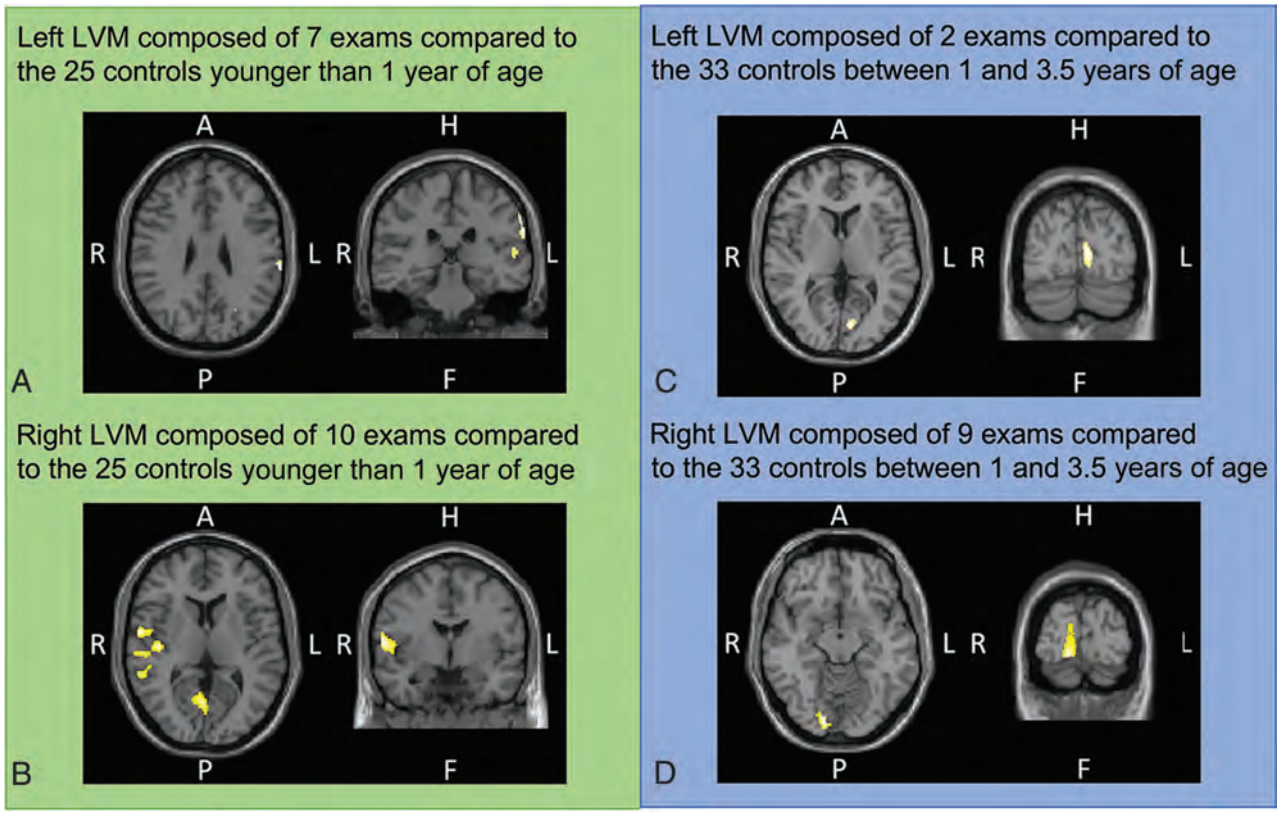

FIG 2. Whole-brain voxel-by-voxel SPM analyses in children with SWS and controls with healthy brains younger than 1 year of age (*A* and *B*) and from 1 to 3.5 years of age (*C* and *D*). Templates are shown with the radiologic convention in the axial and coronal plains. Significant hypoperfusion is labeled by *yellow areas*. A indicates anterior; P, posterior; H, head; F, foot; L, left; R, right.

Table 2: CBF in LVM of patients with SWS and corresponding area in controls

CBF (mL/100g/min)	Patients (Median) (IQR)	Controls (Median) (IQR)	Wilcoxon *P*
A, Left, younger than 1 year of age	17 (13–33)	41 (33–47)	.02
B, Right, younger than 1 year of age	23 (20–29)	38 (32–45)	.01
C, Left, between 1 and 3.5 years of age	25 (24–26)	52 (41–62)	.02
D, Right, between 1 and 3.5 years of age	28 (13–33)	48 (39–64)	.003
Whole cohort	25 (14–30)	44 (34–55)	<.0001

significant hypoperfusion areas, depending on the analyzed subgroup. Children with SWS who were younger than 1 year of age with a left LVM (Fig 2*A*) had a significant CBF decrease in the left parietotemporal cortex (main cluster: $t = 4.44$; $z_{(score)} = 3.85$; $P_{(uncorrected)} < .001$; MNI coordinates: x = −64, y = −28, $z = 28$). Children with SWS who were younger than 1 year of age with a right LVM (Fig 2*B*) had a significant CBF decrease in the right occipital, temporal cortex (main cluster: $t = 5.07$; $z_{(score)} = 4.31$; $P_{(uncorrected)} < .001$; $P_{(FWE\text{-}corrected\ cluster\text{-}level)} < .001$; MNI coordinates: x = 60, y = −3, z = 8).

Children with SWS between 1 and 3.5 years of age with a left LVM (Fig 2*C*) had a significant CBF decrease in the left parieto-occipital cortex ($t = 4.49$; $z_{(score)} = 3.66$; $P_{(uncorrected)} < .001$; MNI coordinates: x = −8, y = −80, z = 6). Children with SWS between 1 and 3.5 years of age with a right LVM (Fig 2*D*) had a significant CBF decrease in the occipital cortex (main cluster: $t = 5.12$; $z_{(score)} = 4.43$; $P_{(uncorrected)} < .001$; $P_{(FWE\text{-}corrected\ cluster\text{-}level)} = .016$; MNI coordinates: x = 16, y = −90, z = −12).

ROI-Based Analysis

CBF values in the ROIs in patients with SWS were lower than those in controls (in the whole cohort: median, 25 mL/100g/min [IQR = 14–30 mL/100g/min] versus 44 mL/100g/min [IQR = 34–55 mL/100g/min], respectively, $P < .0001$). This significant difference was found for all subgroups regardless of the patient's age and side of the LVM (Table 2 and Fig 3).

Diagnostic Accuracy

As shown in Fig 4, the receiver operating characteristic curve for the whole cohort had an AUC of 0.84 (95% CI, 0.75–0.93). The optimal threshold for the global analysis including all patients and controls was a CBF at 30 mL/100g/min with a specificity of 77% (95% CI, 75–93) and sensitivity of 88% (95% CI, 75–93).

In the subgroup of patients younger than 1 year of age, the AUC was 0.78 (95% CI, 0.63–0.93). A threshold of 36 mL/100g/min yielded a specificity of 89% (95% CI, 67–100) and a sensitivity of 82% (95% CI, 73–91) in this subgroup.

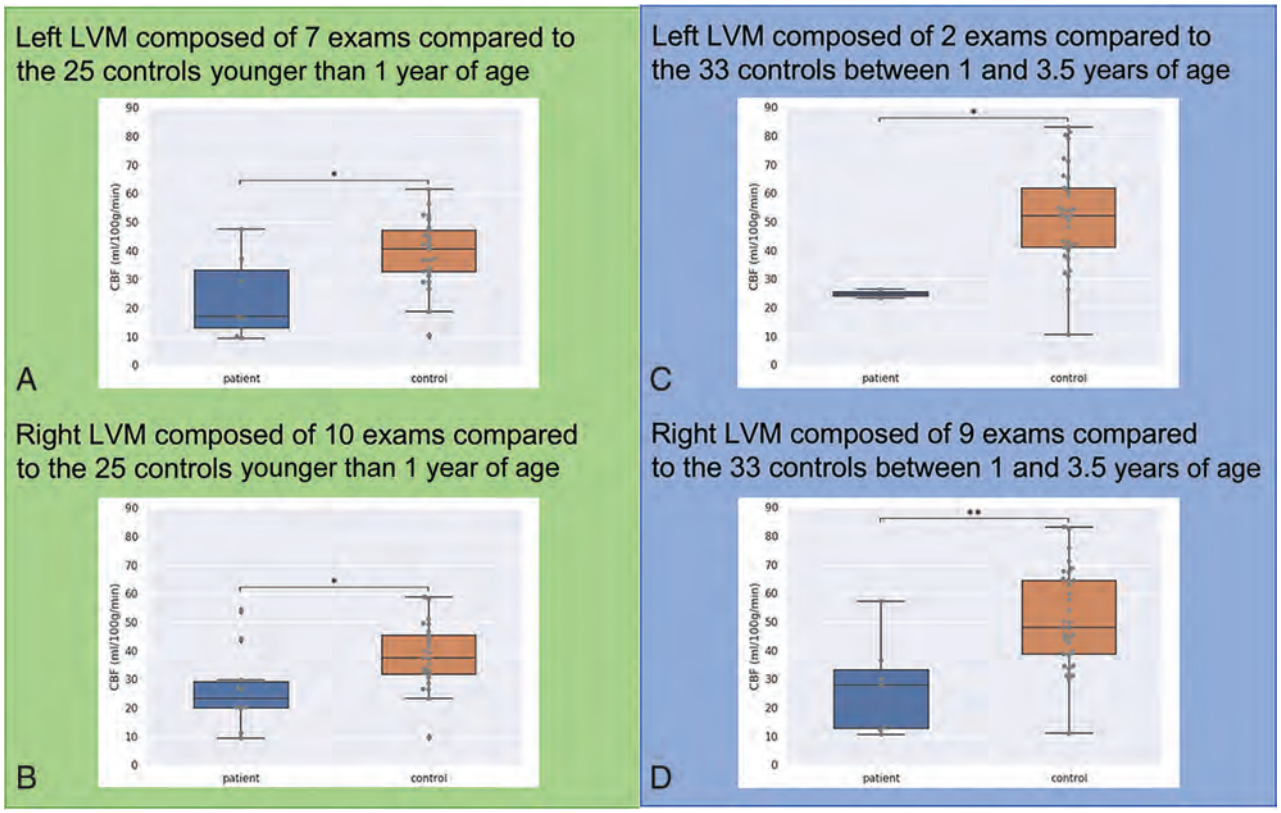

FIG 3. Comparison of CBF values between LVMs in children with SWS and corresponding areas in controls for subgroups matched for age and side. Horizontal bars on the top of the graphs show significant differences. *Asterisk* indicates $P < .05$; *double asterisks*, $P < .01$.

DISCUSSION

In this series of 16 young patients with SWS (3.5 years of age or younger), ASL perfusion imaging had a cortical hypoperfusion juxtaposing the LVM compared with pair-wise controls. This finding was observed in the group younger than 1 year of age, emphasizing the high sensitivity of ASL in this age window in which the diagnosis is difficult. These results were not driven by atrophy or calcification of the diseased cortex. Each subgroup showed a significant hypoperfusion including the subgroup in which no patient had cortical atrophy. In the same way, it was unlikely driven by calcifications because in the age group younger than 1 year, only 3 patients of 11 had calcifications.

Such findings are in line with histologic studies. The cortical blood flow reduction could have been speculated as secondary to the venous stasis and hypertension due to malformation of the cortical vessels as well as venous thrombosis leading to impaired cortical perfusion and ischemia.[17] In our study, the brain hypoperfusion corresponding to the LVM was unchanging during development up to 3.5 years of age and did not show the normal cortical maturation increasing with age.[20]

Data in the literature reported the role of brain perfusion to unravel the difficulty of detection of LVM,[8,10-16] which can be slight or discrete at an early stage. Our results were consistent because these studies have demonstrated decreased perfusion in the parenchyma regions juxtaposing the leptomeningeal enhancement. Whitehead et al[25] reported hypoperfusion in 2 patients with SWS without leptomeningeal abnormalities. All patients in our cohort with obvious hypoperfusion also had leptomeningeal enhancement.

Presymptomatic use and optimal timing of MR imaging in the investigation of PWB have been controversial issues.[1] A recent expert consensus concluded that for neonates and infants with a high-risk PWB and no history of seizures or neurologic symptoms, routine screening for brain involvement was not recommended; MR imaging should be reserved for symptomatic infants or children.[6] This guidance was mainly based on 2 observations: First, negative findings on neuroimaging in a normally developing asymptomatic infant with a facial PWB do not exclude brain involvement and may provide false reassurance. Such false-negative findings have been reported in 3%–23% of the cases in retrospective studies.[6] Second, even if an LVM is confirmed, neurologically asymptomatic children are unlikely to undergo immediate therapeutic intervention.[6] Nevertheless, other reasons drive pediatric neurologists to perform early MR imaging, including parental expectations, anxieties, or discomfort with diagnostic uncertainty.[1] It also may be performed to confirm the pathology when an atypical presentation is encountered or to exclude a differential diagnosis that includes variable and overlapping phenotypes such as *PIK3CA*-related disorders with no decreased CBF. This consensus was built on a literature review from 2008 to 2018, so it could not take into consideration 2 recent studies.

Bar et al[3] reported that leptomeningeal enhancement invisible before 1 year of age may appear afterward and proposed an MR imaging protocol to diagnose SWS during the presymptomatic stage in this difficult age window, obtaining a sensitivity of 100% and a

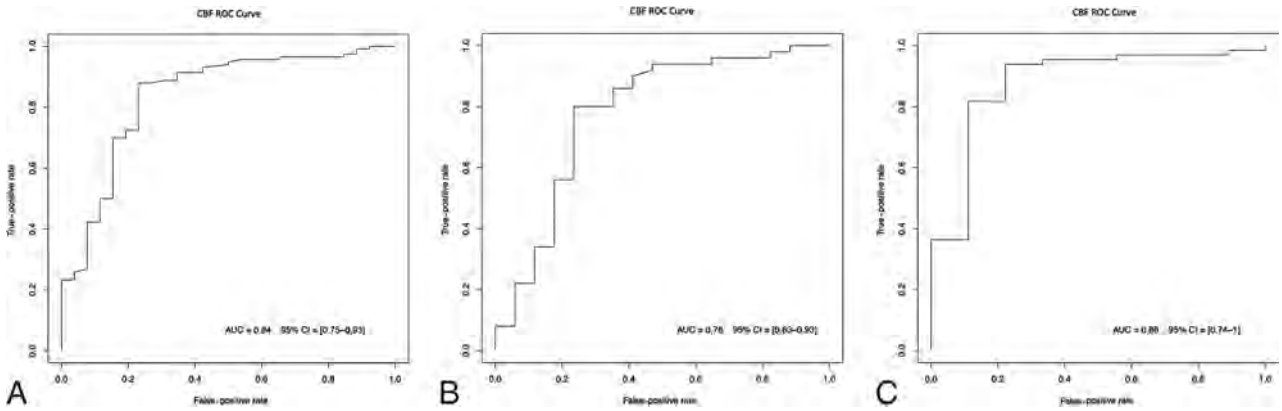

FIG 4. Receiver operating characteristic (ROC) curves for the whole cohort (*A*), patients younger than 1 year of age (*B*), and patients older than 1 year of age (*C*).

specificity of 94%. Day et al[26] assessed the presymptomatic treatment before seizure onset in SWS compared with postsymptomatic treatment on pair-wise subjects. By reducing seizure scores in presymptomatically treated subjects, they hypothesized that prophylaxis may delay seizure onset. These studies put in perspective the possible key role of imaging to early and presymptomatically detect LVM, while waiting for more evidence of the benefit of early and presymptomatic treatment. Hypoperfusion detected on ASL in our study (decreased around 20 mL/100g/min in comparison with age-matched controls) may either help to increase vigilance in children younger than 1 year of age suspected of having SWS if there is a doubtful LVM enhancement, or may increase confidence to diagnose the LVM. This ASL sign could be added to indirect MR imaging anatomic signs already described by Bar et al[3] to detect the LVM in this difficult age window before the age of 1 year. Larger prospective cohorts with serial MR imaging in the same patients are warranted to assess the time course of perfusion abnormalities and other MR imaging signs.

Limits in our study should be mentioned. The study had a small sample size effect, which prevented sound analysis of small subgroups. Moreover, considering the small sample size of our diseased group, several scans from some patients were considered independently, introducing a representation bias. The advantage of a voxelwise analysis was to display a global tendency among the studied individuals. However, because it takes into consideration the average perfusion of all subjects while they had a different brain expression, the analysis mixed LVM and healthy brain areas, resulting in an averaging effect. Therefore, the abnormality-focused analysis using an ROI was complementary because the measured CBF in each patient was not averaged by others who had a different location of the disease. Finally, patients who did not have a concomitant electroencephalogram and had subtle nonmotor seizures during the ASL acquisition, though not the most frequent type in this population, could have been unnoticed.

CONCLUSIONS

ASL perfusion imaging may help to diagnose SWS during the early stage by showing a cortical hypoperfusion and could be very useful before the age of 1 year. This ASL sign could be added to other MR imaging signs already described to detect the LVMs in this difficult age window. Even if the place of screening and prophylactic treatment to prevent the seizure onset still needs to be clarified, ASL perfusion imaging gives valuable information about LVMs without the injection of contrast media. Included in an adapted MR imaging protocol, it could promote the MR imaging screening for SWS.

Disclosure forms provided by the authors are available with the full text and PDF of this article at www.ajnr.org.

REFERENCES

1. Zallmann M, Leventer RJ, Mackay MT, et al. **Screening for Sturge-Weber syndrome: a state-of-the-art review.** *Pediatr Dermatol* 2018; 35:30–42 CrossRef Medline
2. Silverstein M, Salvin J. **Ocular manifestations of Sturge-Weber syndrome.** *Curr Opin Ophthalmol* 2019;30:301–05 CrossRef Medline
3. Bar C, Pedespan JM, Boccara O, et al. **Early magnetic resonance imaging to detect presymptomatic leptomeningeal angioma in children with suspected Sturge-Weber syndrome.** *Dev Med Child Neurol* 2020;62:227–33 CrossRef Medline
4. Shirley MD, Tang H, Gallione CJ, et al. **Sturge-Weber syndrome and port-wine stains caused by somatic mutation in *GNAQ*.** *N Engl J Med* 2013;368:1971–79 CrossRef Medline
5. Comi AM. **Sturge-Weber syndrome.** *Handb Clin Neurol* 2015; 132:157–68 CrossRef Medline
6. Sabeti S, Ball KL, Bhattacharya SK, et al. **Consensus Statement for the Management and Treatment of Sturge-Weber Syndrome: Neurology, Neuroimaging, and Ophthalmology Recommendations.** *Pediatr Neurol* 2021;121:59–66 CrossRef Medline
7. De la Torre AJ, Luat AF, Juhász C, et al. **A multidisciplinary consensus for clinical care and research needs for Sturge-Weber syndrome.** *Pediatr Neurol* 2018;84:11–20 CrossRef Medline
8. Riela AR, Stump DA, Roach ES, et al. **Regional cerebral blood flow characteristics of the Sturge-Weber syndrome.** *Pediatr Neurol* 1985; 1:85–90 CrossRef Medline
9. Pinton F, Chiron C, Enjolras O, et al. **Early single-photon emission computed tomography in Sturge-Weber syndrome.** *J Neurol Neurosurg Psychiatry* 1997;63:616–21 CrossRef Medline
10. Griffiths PD, Boodram MB, Blaser S, et al. **99mTechnetium HMPAO imaging in children with the Sturge-Weber syndrome: a study of nine cases with CT and MRI correlation.** *Neuroradiology* 1997;39:219–24 CrossRef Medline
11. Maria BL, Neufeld JA, Rosainz LC, et al. **High prevalence of bihemispheric structural and functional defects in Sturge-Weber syndrome.** *J Child Neurol* 1998;13:595–605 CrossRef Medline
12. Maria BL, Neufeld JA, Rosainz LC, et al. **Central nervous system structure and function in Sturge-Weber syndrome: evidence of**

neurologic and radiologic progression. *J Child Neurol* 1998;13:606–18 CrossRef Medline

13. Evans AL, Widjaja E, Connolly DJA, et al. **Cerebral perfusion abnormalities in children with Sturge-Weber syndrome shown by dynamic contrast bolus magnetic resonance perfusion imaging.** *Pediatrics* 2006;117:2119–25 CrossRef Medline
14. Lin DD, Barker PB, Hatfield LA, et al. **Dynamic MR perfusion and proton MR spectroscopic imaging in Sturge-Weber syndrome: correlation with neurological symptoms.** *J Magn Reson Imaging* 2006;24:274–81 CrossRef Medline
15. Yu TW, Liu HM, Lee WT. **The correlation between motor impairment and cerebral blood flow in Sturge-Weber syndrome.** *Eur J Paediatr Neurol* 2007;11:96–103 CrossRef Medline
16. Wu J, Tarabishy B, Hu J, et al. **Cortical calcification in Sturge-Weber syndrome on MRI-SWI: relation to brain perfusion status and seizure severity.** *J Magn Reson Imaging* 2011;34:791–98 CrossRef Medline
17. Miao Y, Juhász C, Wu J, et al. **Clinical correlates of white matter blood flow perfusion changes in Sturge-Weber syndrome: a dynamic MR perfusion-weighted imaging study.** *AJNR Am J Neuroradiol* 2011;32:1280–85 CrossRef Medline
18. Alkonyi B, Miao Y, Wu J, et al. **A perfusion-metabolic mismatch in Sturge-Weber syndrome: a multimodality imaging study.** *Brain Dev* 2012;34:553–56 CrossRef Medline
19. Hales PW, Kawadler JM, Aylett SE, et al. **Arterial spin-labeling characterization of cerebral perfusion during normal maturation from late childhood into adulthood: normal "reference range" values and their use in clinical studies.** *J Cereb Blood Flow Metab* 2014;34:776–84 CrossRef Medline
20. Lemaître H, Augé P, Saitovitch A, et al. **Rest functional brain maturation during the first year of life.** *Cereb Cortex* 2021;31:1776–85 CrossRef Medline
21. Garcelon N, Neuraz A, Salomon R, et al. **A clinician friendly data warehouse oriented toward narrative reports: Dr. Warehouse.** *J Biomed Inform* 2018;80:52–63 CrossRef Medline
22. Zaharchuk G, Bammer R, Straka M, et al. **Arterial spin-label imaging in patients with normal bolus perfusion-weighted MR imaging findings: pilot identification of the borderzone sign.** *Radiology* 2009;252:797–807 CrossRef Medline
23. Wilke M, Holland SK, Altaye M, et al. **Template-O-Matic: a toolbox for creating customized pediatric templates.** *Neuroimage* 2008;41:903–13 CrossRef Medline
24. Altaye M, Holland SK, Wilke M, et al. **Infant brain probability templates for MRI segmentation and normalization.** *Neuroimage* 2008;43:721–30 CrossRef Medline
25. Whitehead MT, Vezina G. **Osseous intramedullary signal alteration and enhancement in Sturge-Weber syndrome: an early diagnostic clue.** *Neuroradiology* 2015;57:395–400 CrossRef Medline
26. Day AM, Hammill AM, Juhász C, et al; National Institutes of Health Sponsor: Rare Diseases Clinical Research Network (RDCRN) Brain and Vascular Malformation Consortium (BVMC) SWS Investigator Group. **Hypothesis: presymptomatic treatment of Sturge-Weber syndrome with aspirin and antiepileptic drugs may delay seizure onset.** *Pediatr Neurol* 2019;90:8–12 CrossRef Medline

MR Imaging and Clinical Characteristics of Diffuse Glioneuronal Tumor with Oligodendroglioma-like Features and Nuclear Clusters

M. Benesch, T. Perwein, G. Apfaltrer, T. Langer, A. Neumann, I.B. Brecht, M.U. Schuhmann, H. Cario, M.C. Frühwald, K. Vollert, M. van Buiren, M.Y. Deng, A. Seitz, C. Haberler, M. Mynarek, C. Kramm, F. Sahm, P.A. Robe, J.W. Dankbaar, K.V. Hoff, M. Warmuth-Metz, and B. Bison

ABSTRACT

BACKGROUND AND PURPOSE: Diffuse glioneuronal tumor with oligodendroglioma-like features and nuclear clusters (DGONC) is a new, molecularly defined glioneuronal CNS tumor type. The objective of the present study was to describe MR imaging and clinical characteristics of patients with DGONC.

MATERIALS AND METHODS: Preoperative MR images of 9 patients with DGONC (median age at diagnosis, 9.9 years; range, 4.2–21.8 years) were reviewed.

RESULTS: All tumors were located superficially in the frontal/temporal lobes and sharply delineated, displaying little mass effect. Near the circle of Willis, the tumors encompassed the arteries. All except one demonstrated characteristics of low-to-intermediate aggressiveness with high-to-intermediate T2WI and ADC signals and bone remodeling. Most tumors ($n = 7$) showed a homogeneous ground-glass aspect on T2-weighted and FLAIR images. On the basis of the original histopathologic diagnosis, 6 patients received postsurgical chemo-/radiotherapy, 2 were irradiated after surgery, and 1 patient underwent tumor resection only. At a median follow-up of 61 months (range, 10–154 months), 6 patients were alive in a first complete remission and 2 with stable disease 10 and 21 months after diagnosis. The only patient with progressive disease was lost to follow-up. Five-year overall and event-free survival was 100% and 86±13%, respectively.

CONCLUSIONS: This case series presents radiomorphologic characteristics highly predictive of DGONC that contrast with the typical aspects of the original histopathologic diagnoses. This presentation underlines the definition of DGONC as a separate entity, from a clinical perspective. Complete resection may be favorable for long-term disease control in patients with DGONC. The efficacy of nonsurgical treatment modalities should be evaluated in larger series.

ABBREVIATIONS: DNET = dysembryoplastic neuroepithelial tumor; HIT = Brain Tumor Network; DGONC = diffuse glioneuronal tumor with oligodendroglioma-like features and nuclear clusters; PNET = primitive neuroectodermal tumor

For decades, the pathologic diagnosis and classification of tumors of the CNS have been almost exclusively based on histomorphologic features.[1] Recently, molecular profiling has revolutionized our understanding of CNS tumors, leading to the definition of new entities and improved risk stratification.[2-5] Further effort has been made to correlate newly defined molecular subgroups with clinical features and neuroradiologic findings.[6-13]

Received January 25, 2022; accepted after revision June 28.

From the Division of Pediatric Hematology and Oncology (M.B., T.P.), Department of Pediatrics and Adolescent Medicine, and Division of Pediatric Radiology (G.A.), Department of Radiology, Medical University Graz, Graz, Austria; Departments of Pediatrics (T.L.) and Neuroradiology (A.N.), University Medical Center Schleswig-Holstein, Campus Lübeck, Lübeck, Germany; Pediatric Hematology and Oncology (I.B.B.), Children's Hospital, and Division of Pediatric Neurosurgery (M.U.S.), Department of Neurosurgery, Eberhard-Karls University Tübingen, Tübingen, Germany; Department of Pediatrics and Adolescent Medicine (H.C.), Ulm University Medical Center, Ulm, Germany; Swabian Children's Cancer Center (M.C.F.), Pediatric and Adolescent Medicine and Departments of Diagnostic and Interventional Radiology and Neuroradiology (K.V., B.B.), University Medical Center Augsburg, Augsburg, Germany; Department of Pediatric Hematology and Oncology (M.v.B.), Center for Pediatrics, Medical Center-University of Freiburg, Freiburg, Germany; Hopp Children's Cancer Center Heidelberg (M.Y.D., F.S.), German Cancer Research Center and Department of Neuroradiology (A.S.), Department of Neuropathology (F.S.), Institute of Pathology, and Clinical Cooperation Unit Neuropathology (F.S.), German Cancer Consortium, German Cancer Research Center, Heidelberg University Hospital, Heidelberg, Germany; Division of Neuropathology and Neurochemistry (C.H.), Department of Neurology, Medical University of Vienna, Vienna, Austria; Department of Pediatric Hematology and Oncology (M.M.) and Mildred Scheel Cancer Career Center (M.M.), University Medical Center Hamburg-Eppendorf, Hamburg, Germany; Division of Pediatric Hematology and Oncology (C.K.), University Medical Center Göttingen, Göttingen, Germany; Department of Neurology and Neurosurgery (P.A.R.) and Department of Radiology (J.W.D.), University Medical Center Utrecht, Utrecht, the Netherlands; Department of Pediatric Oncology and Hematology (K.V.H.), Charité–Universitätsmedizin Berlin, corporate member of Freie Universität Berlin, Humboldt-Universität zu Berlin, and Berlin Institute of Health, Berlin, Germany; and Institute of Diagnostic and Interventional Neuroradiology (M.W.-M.), University Hospital Würzburg, Würzburg, Germany.

Since the late 1980s, the Brain Tumor Network (HIT) of the Society of Pediatric Oncology and Hematology (GPOH, Gesellschaft für Pädiatrische Onkologie und Hämatologie) in Germany, Austria and Switzerland has run a series of disease-specific treatment optimization and observational studies for children with CNS tumors.

These studies have allowed exploring novel therapeutic options and provide standardized treatment recommendations as well as a system of high-quality reference diagnostics and expert counseling for diagnostics and therapy. Along with neuropathologic reference diagnostics, the central neuroradiologic review at the Neuroradiological Reference Center of the HIT group (Department of Diagnostic and Interventional Neuroradiology, University Hospital, Augsburg, Germany) has become a mandatory practice for all recruited patients. The MR imaging series of the HIT studies have been archived on the Medical Data and Picture Exchange server by the Medical Informatics Group at the University Hospital, Frankfurt, Germany, which enables their rapid access for re-review to address scientific questions. Thus, the objective of performing the present case series was to describe MR imaging and corresponding clinical characteristics of diffuse glioneuronal tumors with oligodendroglioma-like features and nuclear clusters (DGONC), a molecularly defined glioneuronal CNS tumor class that has been described recently and has been included as a provisional tumor type in the 2021 World Health Organization Classification of CNS Tumors.[5,14,15]

MATERIALS AND METHODS

The (retrospective) neuropathologic diagnosis of DGONC was initially made according to the DNA methylation profile and other criteria (nuclear clusters of small-to-medium-sized cells with oligodendroglioma-like morphology, *OLIG2* and synaptophysin expression, and the absence of widespread glial fibrillary acidic protein expression, monosomy 14) as previously described.[5,14] MR images of 9 patients were then retrospectively re-evaluated by an experienced neuroradiologist (B.B.). MR imaging series from 8 patients had been sent for central neuroradiologic review at the time of diagnosis, allowing their inclusion in the respective treatment optimization study or registry. In the ninth patient, the MR imaging was provided by colleagues from the Princess Máxima Center for Pediatric Oncology, Utrecht, Netherlands. In all cases, MR images were obtained at the initial diagnosis.

MR imaging data were generated at local centers with MR imaging scanners from different manufacturers at 1.5T or 3T field strength. In all patients, basic MR imaging data sets of the brain included T2WI, FLAIR, or proton density sequences; T1WI without and with contrast enhancement; as well as DWI with ADC. In 6 patients, additional MRIs of the spine, including T1WI with contrast enhancement of the entire dural sac, were available.

The evaluation was performed according to standardized MR imaging criteria adapted from the routine image evaluation at the Neuroradiological Reference Center, including localization, size (calculated as an approximation of the ellipsoid formula and using the maximum diameters in the 3 standard planes [axial × coronal × sagittal × 0.5 cm^3]), contour, peritumoral edema, mass effect, and contrast enhancement estimated as part of the tumor volume. The intensity of the contrast enhancement was compared with the choroid plexus and quantified in 3 subjective steps of intensity. Clinical characteristics and treatment-related and outcome parameters were retrieved from the respective study centers and retrospectively analyzed without direct personal identification. All patients had received treatment according to their respective original diagnosis before the diagnosis of DGONC was established. Survival curves were calculated with the Kaplan-Meier method using the SPSS Statistics 26 software package (IBM). Informed consent was obtained from the patients or their legal representatives at the time of study inclusion. The present study was approved by the institutional review board of the Ludwig-Maximilians University of Munich, Germany (Publication No. 21–0493). Data were updated as of October 31, 2020.

RESULTS

Imaging Characteristics

Representative MR imaging slices at diagnosis are shown in the Figure (patients 1—9 [P1–P9]). Major MR imaging characteristics are summarized in the Online Supplemental Data. All tumors were localized in the supratentorial region in the frontal or temporal lobes; in 2 cases, the tumor crossed the midline and extended into both frontal lobes (patients 1 and 5). In another patient (patient 2), both the frontal and temporal lobes of the right hemisphere were involved. Eight tumors were located at the basal part of the brain with 4 oriented directly toward the frontobase, with a temporomesial manifestation in 3 cases. Only 1 tumor was located along the convexity (patient 8). Tumors formed a broad basis of the surface of the lobe, involving the cortex and medullary WM in all cases. Displacement of the basal ganglia was common, without definite signs of infiltration of the deep GM. The median initial tumor volume was 35.83 mL (range, 2.28–80.14 mL). Tumors in the temporomesial region and along the convexity were smaller (2.28, 4.86, 10.05, and 5.82 mL) than the remaining tumors.

All tumors were clearly demarcated and sharply contoured, masking the underlying tissue, and had a relatively low mass effect in comparison with their size. This observation was more pronounced in larger tumors (eg, Figure, P1AB, P2AB, P5AB). Edema was absent in 6 and was small (up to 0.7 cm, measured perpendicular to the tumor) in 2 patients (Figure, P4AB, P8AB). A marked edema of 2 cm was found in only 1 patient (Figure, P3A, short gray/white arrows). Of note, imaging characteristics in this patient differed from those of the other patients in several respects. Contrast enhancement was detectable in only 3 patients (patients 3, 8, and 9), all with an intermediate intensity (Figure, P3C, P8C, P9C, Online Supplemental Data); in 2 of these patients, almost the

Martin Benesch and Thomas Perwein share first authorship.

The Neuroradiologic Reference Center of the Brain Tumor Network Consortium, University Würzburg (grant Nos. 2001.05, 2003.09, 2005.07, 2008.07, 2011.02, 2013.21, 2014.15, 2017.07, 2018.02 to M. Warmuth-Metz, B. Bison) were supported by the German Children's Cancer Foundation (Deutsche Kinderkrebsstiftung). M. Benesch and T. Perwein receive support from the Styrian Childhood Cancer Foundation (Steirische Kinderkrebshilfe).

Please address correspondence to Thomas Perwein, MD, Division of Pediatric Hematology and Oncology, Department of Pediatrics and Adolescent Medicine, Medical University of Graz, Auenbruggerplatz 34/2, 8036 Graz, Austria; e-mail: thomas.perwein@medunigraz.at

Indicates article with online supplemental data.

http://dx.doi.org/10.3174/ajnr.A7647

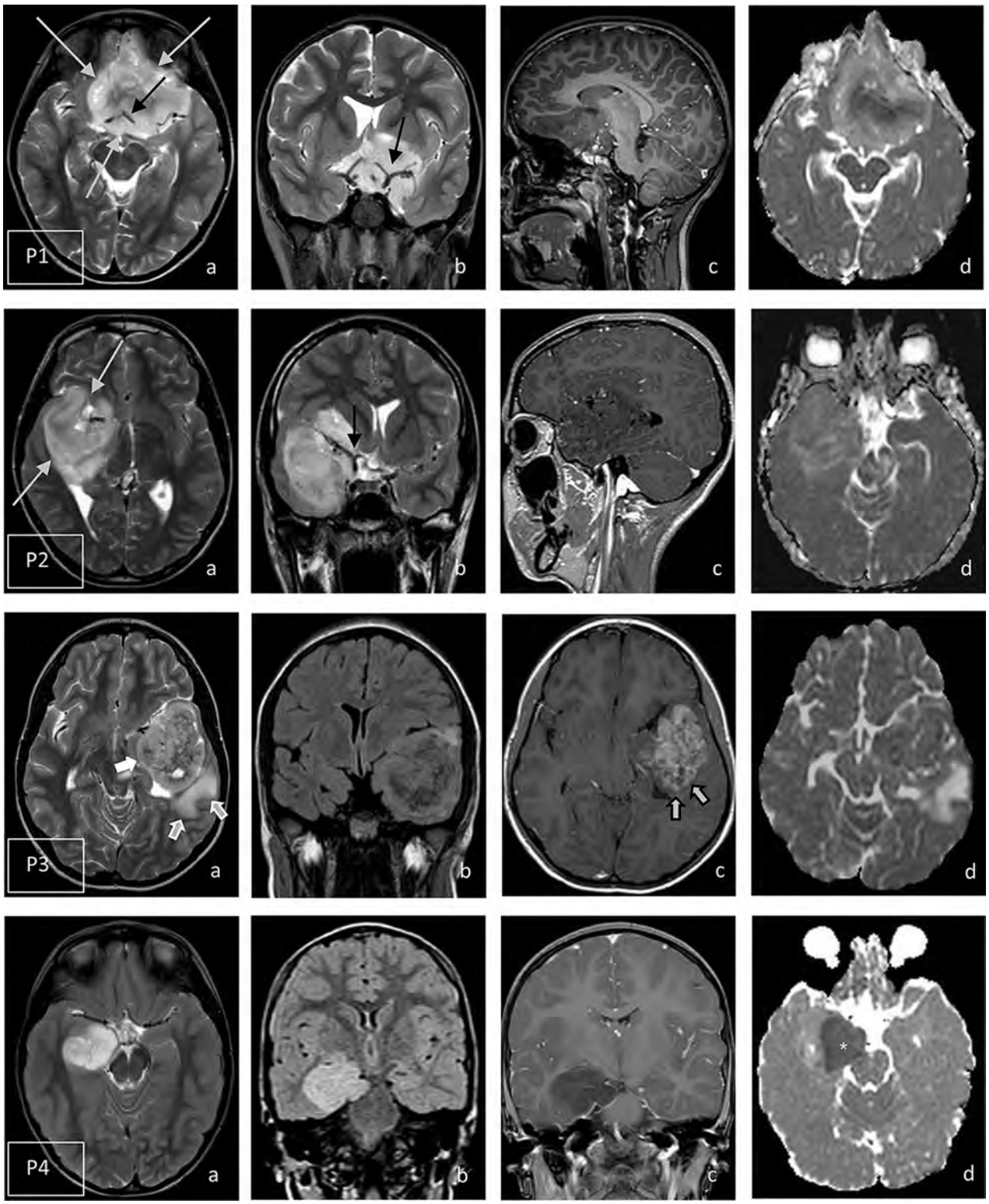

FIGURE. Representative MR imaging slices of all 9 patients (P1–P9). Columns: *A*, Axial T2WI in all MRIs; *B*, Coronal T2WI (P1, P2, P5) and coronal FLAIR (P3, P4, P6, P7, P8, P9); *C*, Contrast-enhanced T1WI, sagittal (P1, P2, P5), axial (P3, P6, P8, P9), or coronal (P4, P7); *D*, axial DWI/ADC in all MRIs. Long gray arrows, centrally decreased T2 signal suggestive of diffuse calcification (P1A, P2A); black arrows, tumor encompassing the circle of Willis and adjacent arteries without compression (P1AB, P2B, P5B, P9B); short gray/white arrows, marked edema (P3A); short white arrows, band-like pattern with intermediate signal on T2WI (P3A, P8A); short gray/black arrows, inhomogeneous band-like CE of the solid tumor part (P3C, P8C); white asterisk, restricted diffusion (P4D); white arrow, patchy pattern of CE affecting <25% of the tumor volume (P9C).

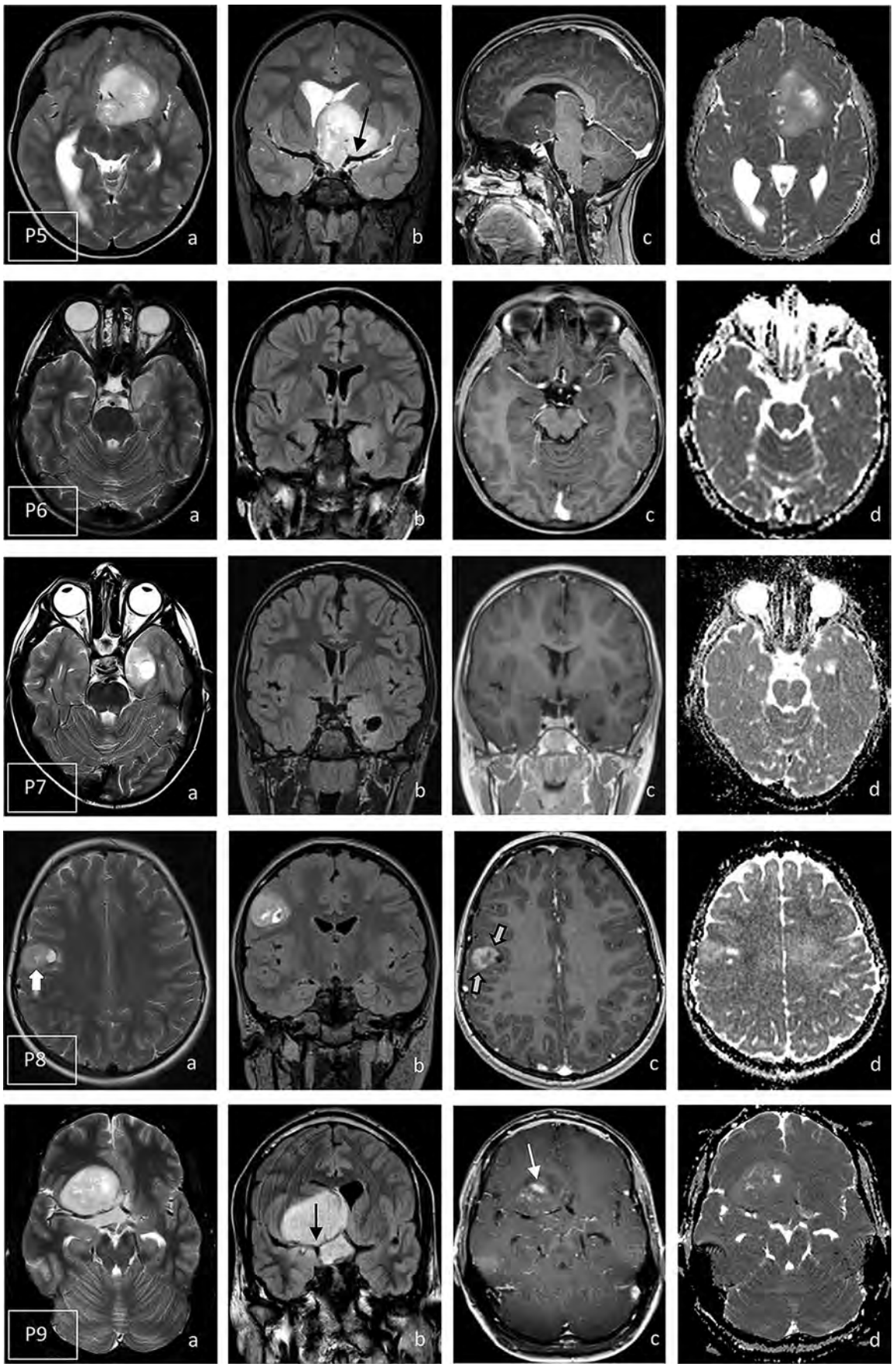

FIGURE. Continued

complete solid part showed an inhomogeneous bandlike enhancement (Figure, P3C and P8C, short gray/black arrows); and in 1 case, the contrast enhancement displayed a patchy pattern that affected <25% of the tumor volume (Figure, P9C, white arrow). The tumor structure was predominantly homogeneous in 7 cases, with a high signal on T2WI in 5 cases (Figure, P1AB, P4AB, P5AB, P7A, P9A) and an intermediate-to-high T2WI signal in 2 cases (Figure, P2AB, P8AB). As a characteristic pattern, we called this homogeneous and sharply contoured aspect "ground-glass-like." In the 2 largest of these structures, the T2 signal was centrally decreased, which was suggestive of diffuse calcification (Figure, P1A, P2A, long gray arrows).

In 2 patients, a bandlike pattern with an intermediate signal on T2WI corresponding to the contrast enhancement was noted (patients 3 and 8; Figure, P3A, P8A, short white arrows). In all except 1 patient, diffusion signals were inhomogeneous, equaling the adjacent brain. Only the patient who had experienced progressive disease before the initiation of treatment had restricted diffusion (patient 4; Figure, P4D, white asterisk). Bone remodeling was present in all cases in which the bone was immediately adjacent to the tumor. Small, not clearly definable defects (either small necroses or cysts or prominent Virchow-Robin spaces) were detected in 8 cases. No relevant necroses or cysts exceeding 10% of tumor volume were found. In the 4 patients with larger frontal or frontotemporal tumors (35.83, 44.46, 64.45, and 80.14 mL), the circle of Willis and adjacent arteries were surrounded by the tumor without any signs of compression visible on the basic MR imaging (Figure, P1B, P2B, P5B, P9B, black arrows). Although blood-sensitive sequences were not available, large areas of hemorrhage and blood-degradation products were not detectable. None of the patients had a leptomeningeal dissemination. Follow-up scans 3.5 months after the initial imaging were available in 1 patient (Online Supplemental Data) and showed a 3-fold tumor volume increase accompanied by a reduction in the T2WI and FLAIR signals. The patient did not receive any treatment between the first and second MR imaging.

Clinical Characteristics

Clinical and treatment characteristics are shown in the Online Supplemental Data. The median age at diagnosis was 9.9 years (range, 4.2–21.8 years) with a female predominance of 2:1. The primary diagnosis was anaplastic glioma in 4 (oligodendroglioma, $n = 3$; oligoastrocytoma, $n = 1$), as well as CNS primitive neuroectodermal tumor (CNS PNET) and CNS neuroblastoma in 2 patients each, respectively. One patient was initially diagnosed with dysembryoplastic neuroepithelial tumor (DNET).

Information about the clinical presentation was available for 6 of 9 patients. Compatible with the tumor site, the most common presenting symptoms were seizures (mainly complex-partial; $n = 5$), while double vision and nausea were reported in 1 patient each.

Treatment Response, Status of Remission, and Survival

Initial complete resection was achieved in 4 patients (Online Supplemental Data). The remaining 5 patients underwent a partial or subtotal resection. In one of these, a complete surgical remission was achieved by a second surgery. Postoperative nonsurgical treatment was guided by the primary histopathologic diagnosis. Only 1 patient (patient 6 with mesial temporal DNET) was treated by surgery (complete resection) alone. All patients with the primary diagnosis of anaplastic glioma ($n = 4$) underwent local irradiation; in 3 of these, temozolomide was administered with concomitant radiation therapy, followed by temozolomide maintenance therapy for 12–18 months. In 1 patient (patient 4), a watch-and-wait strategy was pursued after initial imaging. Three months later, a second MR imaging showed massive progression, leading to surgery and adjuvant therapy. Patients with CNS PNET ($n = 2$) received craniospinal irradiation with tumor boost followed by 8 cycles of maintenance chemotherapy in one of them. One patient with CNS neuroblastoma was also treated with craniospinal irradiation, tumor boost, and maintenance therapy. In the second patient with the initial diagnosis of CNS neuroblastoma, an individualized chemotherapy was administered followed by local irradiation.

With a median follow-up of 61 months (range, 10–154 months), 6 patients were alive in the first continuous complete remission. Two patients were alive with stable residual lesions 10 and 21 months after the initial diagnosis, respectively. The only progression occurred in 1 patient (patient 2) who developed a single metastatic lesion in the right posterior horn of the lateral ventricle following the initial partial resection and local irradiation. After complete re-resection, she received various chemotherapies and was lost to follow-up with progressive disease. The overall and event-free survival rates at 5 years were 100% and 86±13%, respectively.

DISCUSSION

In recent years, there has been an effort to describe imaging features in histopathologically and molecularly defined CNS tumor entities. Ideally, a pathognomonic spectrum of imaging characteristics would allow the number of potential differential diagnoses to be narrowed down on the basis of the neuroradiologic appearance of a tumor. However, previous reports have shown that in general, imaging characteristics, even within a particular tumor subtype, are quite heterogeneous and overlap with various CNS tumor entities.[9-13] Although special criteria exist in childhood brain tumors, the rarity of most brain tumor subtypes hampers the ability to identify unique imaging features and to conduct a reliable statistical analysis. In addition, the availability of standardized, centrally reviewed MR images is limited and is possible only in the context of clinical trials.

The aim of the present analysis was to describe neuroradiologic features with corresponding clinical characteristics in patients with DGONC, a recently and molecularly defined CNS tumor entity.[5,14] Despite their distinct DNA methylation profile, DGONCs display a spectrum of histologic differentiation that varies from well-differentiated tumors with a low mitotic index to undifferentiated cases with brisk mitotic activity. This variability reflects that of the original diagnosis, which ranged from DNET to anaplastic oligodendroglioma and CNS-PNET/neuroblastoma. Still, 7 of the 9 patients in our series had highly similar radiologic characteristics that were distinct from the features expected on the basis of the original diagnoses. In 2 of these 7 patients with cellular, undifferentiated tumors (original diagnosis of CNS neuroblastoma in patient 1 and CNS PNET in patient 9), this

characteristic aspect was particularly remarkable because such tumors would generally have neuroradiologic signs of high cellularity with a low T2WI signal, at least a partly restricted diffusion, an inhomogeneous bandlike or nodular contrast enhancement, extensive necroses, and hemorrhage.

In our cohort, all tumors were located in the frontal and/or temporal lobes in a superficial position, involving the cortical and subcortical white matter. This observation is in accordance with all cases of DGONC reported to date being supratentorial.[5,14,15] Tumor margins were sharp with little mass effect and hyperintense on T2- and FLAIR-weighted sequences, as also described by Pickles et al.[15] Most tumors showed a characteristic homogeneous ground-glass-like aspect on the T2WI and FLAIR images. They displayed characteristics of low-grade tumors without restricted diffusion, the adjacent arteries were surrounded by the tumor without signs of compression, and all tumors near the bone demonstrated bone remodeling, suggesting a clinical behavior similar to that of low-grade glioneuronal tumors, as originally proposed by Deng et al.[14]

Contrast enhancement was seen in only 3 patients, all with an intermediate intensity. One of these patients had the characteristic appearance with a discrete, diffuse contrast enhancement. In 2 of the 9 patients (patients 3 and 8) with the original diagnosis of a World Health Organization grade IV CNS neuroblastoma and CNS PNET, respectively, the radiomorphologic appearance differed from this characteristic aspect, showing a bandlike structure both on the T2WI and contrast-enhanced images. Although the experience in CNS neuroblastoma is still limited, a large size, nodular aspect, severe edema, and contrast enhancement are radiomorphologic features that have been described in these tumors.[16] Former PNET, according to the World Health Organization 2007 classification, would demonstrate aggressive behavior with restricted diffusion, necroses, and hemorrhage. This appearance contrasts with both the regular bandlike aspect of the tumors in these 2 patients, without restricted diffusion or signs of aggressiveness, and the imaging features regarded as characteristic of DGONC in the present study, though PNETs like the DGONCs we describe here appear clearly delineated and mostly without any perifocal edema and little-or-no contrast enhancement.

In 2 patients with relatively small, temporomesial tumors, T2WI signals were elevated but lower compared with the larger tumors. Whether the intensity of the T2WI signal correlates with the tumor size (ie, getting brighter while growing) remains to be explored.

One noteworthy point is that restricted diffusion, usually a sign of high cellularity, was observed in only 1 case (patient 4) in our series and contrasted with the high T2WI signal, typically indicating low cellularity, in this case. This patient developed a 3-fold tumor growth when a watch-and-wait strategy was applied. Further experience is needed to explore whether restricted diffusion in this case is a sign of higher aggressiveness compared with the 8 other cases. Here, the T2WI and FLAIR signals became darker in the follow-up MR imaging examination, though no treatment was administered. Regarding the MR imaging aspect, this finding can be explained by a higher cellularity, which has to be proved in additional patients with DGONC. The histomorphologic diagnosis of DNET is associated with radiomorphologic signs of extremely low cellularity with a very bright signal on T2WI and ADC, as well as a multicystic structure, which also contrasts with the images in our case series. Larger tumors showed a more pronounced inhomogeneity with a centrally lower T2WI signal. On the basis of the diffuse distribution, this phenomenon is highly suggestive of diffuse calcifications.

Most patients in our series had the histopathologic diagnosis of anaplastic oligodendroglioma. Here, we would expect a high level of congruence with DGONC because these are typically well-delineated, cortically-based tumors. However, signs of clumped calcifications, as described by Pickles et al,[15] or hemorrhage were not detectable in our cases. Whether the orientation toward the skull base is another distinct feature suggestive of DGONC needs to be evaluated in future research.

CONCLUSIONS

Most DGONCs (7 of 9) in our series had uniform, characteristic MR imaging features despite a spectrum of histologic differentiation that ranged from well-differentiated to undifferentiated tumors, emphasizing the definition of DGONC as a separate entity from a clinical perspective. These radiomorphologic characteristics clearly differ from the typical MR imaging aspect of the original histomorphologic diagnoses, become increasingly obvious in larger tumors, and are highly predictive of a DGONC. Typical features include the superficial, supratentorial localization with an orientation toward the skull base, as well as involvement of the cortex and white matter, causing only the displacement of the deep gray matter with little-to-no perifocal edema. DGONCs are sharply delineated from the adjacent tissue with little mass effect for their size and display a relatively homogeneous structure that masks the underlying tissue with a bright-to-intermediate T2WI signal, which we call the ground glass-like aspect. In a suprasellar localization, they engulf the arteries of the circle of Willis without any sign of compression or infiltration. Adjacent to bone, they induce bone remodeling.

These aspects resemble low-grade tumors and suggest an intermediate aggressiveness, which is also reflected by the better survival rates compared with those reported for highly malignant CNS tumors. The clinical course ranged from continuous complete remission after total resection to metastatic tumor recurrence with subsequent treatment-refractory progressive disease. Still, no patient died in our series, and disease control was attained in almost 90% of patients following resection with and without adjuvant radio-/chemotherapy. Complete resection may be favorable for long-term disease control in patients with DGONC. Of note, restricted diffusion was found in only 1 patient, though all other criteria of the characteristic DGONC aspect were present. Additional cases have to be analyzed to gain more insight into the relationship between the MR imaging morphology and histologic and molecular diagnoses, as well as into clinical features in patients with DGONC, with the aim of explaining apparent discrepancies in this respect.

Disclosure forms provided by the authors are available with the full text and PDF of this article at www.ajnr.org.

REFERENCES

1. Scheithauer BW. **Development of the WHO classification of tumors of the central nervous system: a historical perspective.** *Brain Pathol* 2009;19:551–64 CrossRef Medline

2. Capper D, Jones DT, Sill M, et al. **DNA methylation-based classification of central nervous system tumours.** *Nature* 2018;555:469–74 CrossRef Medline
3. Sturm D, Orr BA, Toprak UH, et al. **New brain tumor entities emerge from molecular classification of CNS-PNETs.** *Cell* 2016;164:1060–72 CrossRef Medline
4. Louis DN, Perry A, Reifenberger G, et al. **The 2016 World Health Organization classification of tumors of the central nervous system: a summary.** *Acta Neuropathol* 2016;131:803–20 CrossRef Medline
5. Louis DN, Perry A, Wesseling P, et al. **The 2021 WHO Classification of Tumors of the Central Nervous System: a summary.** *Neuro Oncol* 2021;23:1231–51 CrossRef
6. Pajtler KW, Mack SC, Ramaswamy V, et al. **The current consensus on the clinical management of intracranial ependymoma and its distinct molecular variants.** *Acta Neuropathol* 2017;133:5–12 CrossRef Medline
7. Guerreiro Stucklin AS, Ramaswamy V, Daniels C, et al. **Review of molecular classification and treatment implications of pediatric brain tumors.** *Curr Opin Pediatr* 2018;30:3–9 CrossRef Medline
8. Jünger ST, Mynarek M, Wohlers I, et al. **Improved risk-stratification for posterior fossa ependymoma of childhood considering clinical, histological and genetic feature: a retrospective analysis of the HIT ependymoma trial cohort.** *Acta Neuropathol Commun* 2019;7:181 CrossRef Medline
9. Nowak J, Jünger ST, Huflage H, et al. **MRI phenotype of RELA-fused pediatric supratentorial ependymoma.** *Clin Neuroradiol* 2019;29:595–604 CrossRef Medline
10. Jaju A, Hwang EI, Kool M, et al. **MRI features of histologically diagnosed supratentorial primitive neuroectodermal tumors and pineoblastomas in correlation with molecular diagnoses and outcomes: a report from the Children's Oncology Group ACNS0332 trial.** *AJNR Am J Neuroradiol* 2019;40:1796–1803 Medline
11. Nowak J, Seidel C, Berg F, et al. **MRI characteristics of ependymoblastoma: results from 22 centrally reviewed cases.** *AJNR Am J Neuroradiol* 2014;35:1996–2001 CrossRef Medline
12. Stock A, Mynarek M, Pietsch T, et al. **Imaging characteristics of wingless pathway subgroup medulloblastomas: results from the German HIT/SIOP-trial cohort.** *AJNR Am J Neuroradiol* 2019;40:1811–17 CrossRef Medline
13. Nowak J, Nemes K, Hohm A, et al. **Magnetic resonance imaging surrogates of molecular subgroups in atypical teratoid/rhabdoid tumor.** *Neuro Oncol* 2018;20:1672–79 CrossRef Medline
14. Deng MY, Sill M, Sturm D, et al. **Diffuse glioneuronal tumour with oligodendroglioma-like features and nuclear clusters (DGONC): a molecularly defined glioneuronal CNS tumour class displaying recurrent monosomy 14.** *Neuropathol Appl Neurobiol* 2020;46:422–30 CrossRef Medline
15. Pickles JC, Mankad K, Aizpurua M, et al. **A case series of diffuse glioneuronal tumours with oligodendroglioma-like features and nuclear clusters (DGONC).** *Neuropathol Appl Neurobiol* 2020;47:464–67 CrossRef Medline
16. Holsten T, Lubieniecki F, Spohn M, et al. **Detailed clinical and histopathological description of 8 cases of molecularly defined CNS neuroblastomas.** *J Neuropathol Exp Neurol* 2021;80:52–59 CrossRef Medline

Evaluation of 2 Novel Ratio-Based Metrics for Lumbar Spinal Stenosis

U.U. Bharadwaj, A.R. Ben-Natan, J. Huang, V. Pedoia, D. Chou, S. Majumdar, T.M. Link, and C.T. Chin

ABSTRACT

BACKGROUND AND PURPOSE: Quantitative metrics of the dural sac such as the cross-sectional area are commonly used to evaluate central canal stenosis. The aim of this study was to analyze 2 new metrics to measure spinal stenosis on the basis of the ratio between the dural sac and disc cross-sectional areas (DDRCA) and the dural sac and disc anterior-posterior diameters (DDRDIA) and compare them with established quantitative metrics of the dural sac.

MATERIALS AND METHODS: T2-weighted axial MR images ($n = 260$ patients) were retrospectively evaluated, graded for central canal stenosis as normal (no stenosis), mild, moderate, or severe from L1/L2 through L5/S1 with 1 grade per spinal level and annotated to measure the DDRCA and DDRDIA. Thresholds were obtained using a decision tree classifier on a subset of patients ($n = 130$) and evaluated on the remaining patients ($n = 130$) for accuracy and consistency across demographics, anatomic variation, and clinical outcomes.

RESULTS: DDRCA and DDRDIA had areas under the receiver operating characteristic curve of 98.6 (97.4–99.3) and 98.0 (96.7–98.9) compared with dural sac cross-sectional area at 96.5 (95.0–97.7) for binary classification. DDRDIA and DDRCA had κ scores of 0.75 (0.71–0.79) and 0.80 (0.75–0.83) compared with dural sac cross-sectional area at 0.62 (0.57–0.66) for multigrade classification. No significant differences ($P > .1$) in the area under the receiver operating characteristic curve were observed for the DDRDIA across variations in the body mass index. The DDRDIA also had the highest area under the receiver operating characteristic curve among symptomatic patients (visual analog scale ≥ 7) or patients who underwent surgery.

CONCLUSIONS: Ratio-based metrics (DDRDIA and DDRCA) are accurate and robust to anatomic and demographic variability compared with quantitative metrics of the dural sac and better correlated with symptomatology and surgical outcomes.

ABBREVIATIONS: AUROC = area under the receiver operating characteristic curve; BMI = body mass index; DDRCA = ratio between dural sac and disc cross-sectional areas; DDRDIA = ratio between dural sac and disc anterior-posterior diameters; DSCA = dural sac cross-sectional area; DSDIA = dural sac anterior-posterior diameter; LSS = lumbar spinal stenosis; VAS = visual analog scale

Lumbar spinal stenosis (LSS) is one of the most common causes for lumbar spinal surgery in patients older than 65 years of age.[1] The etiology is multifactorial but predominantly attributed to degenerative changes. Degenerative canal narrowing can be secondary to changes that include disc protrusion, extrusion; ligamentum flavum hypertrophy; or facet joint arthropathy.[2] Historically, radiographic LSS has been described using morphologic categories ranging from any narrowing of the spinal canal[3] to more detailed descriptors evaluating CSF space obliteration and neural element separation;[4] nevertheless, classification of LSS is highly variable, with a number of grading systems, none of which are widely accepted.[5]

Accurate classification of LSS, however, is essential for subsequent patient management.[6] Clinical symptoms and examination and radiologic findings are all integral and contribute to the diagnosis of symptomatic LSS. There are no physical examination findings or clinical history that is both highly sensitive and specific for diagnosing LSS;[7] imaging can, therefore, confirm the structural diagnosis and clarify the anatomy if therapeutic management such as injections or surgery is contemplated. When imaging is indicated,

Received January 30, 2022; accepted after revision July 25.

From the Departments of Radiology and Biomedical Imaging (U.U.B., V.P., S.M., T.M.L., C.T.C.) and Neurological Surgery (A.R.B.-N., J.H., D.C.), University of California San Francisco, San Francisco, California.

A.R. Ben-Natan and J. Huang contributed equally to this work.

This work was funded by the National Institute of Arthritis and Musculoskeletal and Skin Diseases, grant/award No: UH2AR076724-01.

Please address correspondence to Upasana Upadhyay Bharadwaj, MD, Department of Radiology and Biomedical Imaging, University of California San Francisco, 185 Berry St, Suite 350, San Francisco, CA 94107; e-mail: Upasana.Bharadwaj@ucsf.edu; @UUBharad1

http://dx.doi.org/10.3174/ajnr.A7638

MR imaging is widely accepted as the preferred technique owing to its superior soft-tissue contrast[8,9] and various qualitative, morphologic features; quantitative metrics have been proposed for LSS on MR imaging.[4,10,11]

To optimize the effects of variability, poor agreement, and suboptimal outcomes associated with qualitative features,[12] articles in the literature have proposed quantitative measures for diagnosing and grading LSS.[13,14] The anterior-posterior diameter of the dural sac (DSDIA) and the dural sac cross-sectional area (DSCA) have been evaluated extensively in prior studies with limited success in establishing clinical utility;[15-19] moreover, various thresholds have been proposed for each measure.[14,20] A DSCA of <100 mm^2 at more than 2 of 3 intervertebral levels (L2/L3, L3/L4, L4/L5) was shown to be highly associated with the presence of intermittent claudication;[17] and pronounced stenosis of the canal (DSDIA of <6 mm on myelography) predicted less postoperative pain in a 5-year follow-up study.[21] The increasing number of quantitative measures and potential correlations with outcomes can lead to confusion in the clinical routine because even specialized radiologists apply each measure differently[22-24] according to the results of a recent Delphi survey.[25]

Furthermore, a weakness of commonly used nonratio metrics such as DSCA and DSDIA is that they are not anatomically normalized and incorporate only the absolute distance or area, possibly explaining the high variability and susceptibility to demographic changes.

Given the wide variability of the quantitative measurements and correlation with symptoms and outcomes, a reproducible quantitative grading system for LSS is essential for subsequent management. In this study, we propose to calculate ratios measured at the disc level, the most stenotic level, relative to the dural sac: the dural sac-to-disc ratio of the respective anterior-posterior diameters (DDRDIA) and the dural sac-to-disc ratio of the respective cross-sectional areas (DDRCA) as normalized quantitative metrics for classifying stenosis. We hypothesize that these ratios incorporating the disc level may be better correlated with symptomatology and surgical outcomes compared with quantitative metrics of the dural sac.

MATERIALS AND METHODS

Study Design

In this institutional review board–approved retrospective cross-sectional study, lumbar spine MRIs along with clinical data were evaluated to assess our proposed quantitative metrics, DDRDIA and DDRCA, for grading LSS and comparing it with other more commonly used nonratio metrics such as the DSCA (standard of reference) as well as DSDIA.

Patient Cohort

Patients who underwent lumbar spine MR imaging for clinical indications between 2008 and 2019 were included after applying the following exclusion criteria: Those with age younger than 19 years, transitional anatomy, fractures, postoperative changes, extensive hardware, infection, primary tumors, and widespread metastatic disease to the spine were excluded. Studies with the absence of a T2-weighted axial sequence or poor image quality were also excluded. A total of 30,619 patients were identified, of whom a subset of patients ($n = 260$) were selected at random, with uniform sampling to be included in the study.

Clinical Data

We collected the following clinical data: presenting symptoms, low back pain, and the radicular pain score on a visual analog scale (VAS),[26] ranging from 0 to 10; demographics including age, sex, and body mass index (BMI) from the electronic health record; as well as clinical management spanning noninvasive treatment to surgical procedures.

Image Acquisition

All T2-weighted axial MRIs used in this study were FSE sequences acquired in our institution as part of routine clinical lumbar spine MR imaging studies using a 3T MR imaging scanner (Discovery MR750; GE Healthcare) with a section thickness of 4.0 mm, section spacing of 1.0 mm, FOV of 18.0 cm, TE of 85.0 ms, TR of 4202.0 ms, flip angle of 115°, and a matrix of 512 × 512 pixels. Axial sequences were acquired in the contiguous axial plane as per the imaging protocols at our institution, with no disc-specific adjustments such as disc space–targeted angled axial images.

Grading LSS

A board-certified neuroradiologist (R1) with 25 years of experience qualitatively graded MRIs from the study cohort ($n = 260$) for central canal stenosis as normal (absence of stenosis), mild, moderate, or severe with 1 grade per spinal level (L1/L2, L2/L3, L3/L4, L4/L5, L5/S1). Grading was based on a published qualitative grading system (Schizas system) as follows:[11] Normal indicated absence of LSS based on qualitative criteria on MR imaging: homogeneous distribution of the CSF and individual rootlets visualized in the dorsal aspect of the dural sac; mild, some CSF present and the rootlets still individualized; moderate, the rootlets occupying the entire dural sac with minimal-to-no CSF, epidural fat visualized dorsally; and severe, thecal sac obliterated and no epidural fat, CSF, or individual rootlets visualized.

Quantitative Metrics

This study evaluates the proposed metrics: DDRDIA, which measures the ratio between the anterior-posterior diameters of the dural sac and intervertebral disc, and DDRCA, which measures the ratio between the cross-section areas of the dural sac and intervertebral disc as well as standard metrics such as DSCA and DSDIA. Using a research annotation platform (MD.ai; md.ai/), a trained researcher and a radiology trainee (R2) annotated the T2-weighted axial slices with free-form masks of the dural sac and intervertebral disc, as well as lines for measuring their respective anterior-posterior diameters from which the metrics were computed, as shown in Fig 1. Figure 2 provides examples of normal (no stenosis), mild, moderate, and severe stenosis with metric values.

Cutoff Thresholds for Grading Stenosis

The study cohort ($n = 260$) was partitioned randomly into 2 distinct groups: 1) a development cohort ($n = 130$), used to determine thresholds for DDRDIA, DDRCA, DSDIA, and DSCA (standard of reference); and 2) an evaluation cohort ($n = 130$) on which all metrics were evaluated.

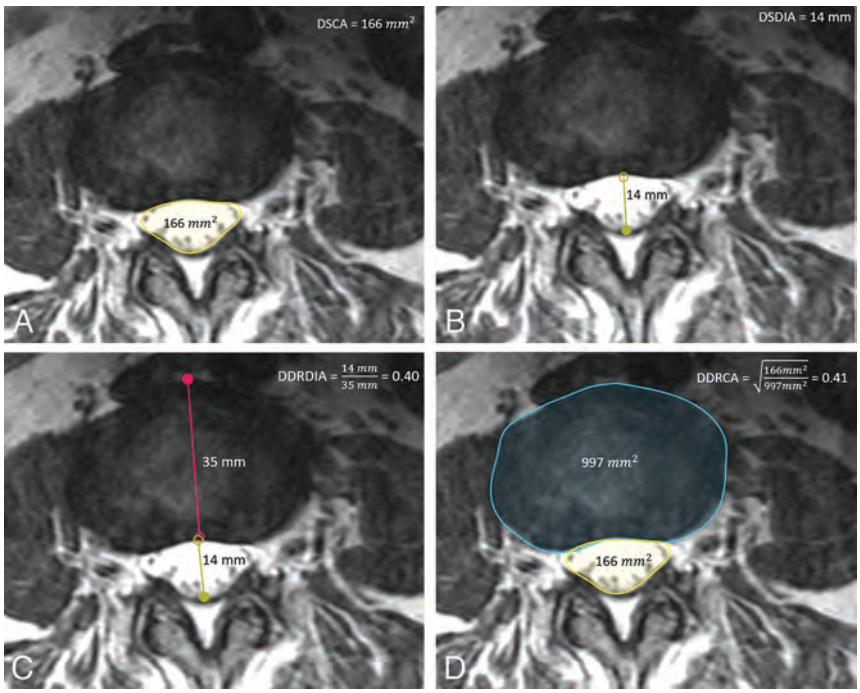

FIG 1. Sample T2-weighted axial section at L2/L3 graded normal with the following: *A*, Free-form annotation around the DSCA of 166 mm^2. *B*, Line annotation with a DSDIA of 14 mm. *C*, Line annotations with a DDRDIA of 0.4. *D*, Free-form annotations with DDRCA of 0.41. The square root is used as a normalization step to account for the quadraticity of area measures.

For each metric, a decision tree classifier was fit on the development cohort ($n = 130$) using R1's grades as ground truth to determine cutoff thresholds for classifying a given T2-weighted axial section as having normal (no stenosis), mild, moderate, or severe stenosis. The decision tree is a statistical modelling technique that automatically creates branches of decisions based on each measurement and its corresponding ground truth grade so that the total classification error is minimized.[27] Decision trees have been previously used to obtain thresholds for LSS and offer the advantage of clinically interpretable rules.[28] The Scikit-learn Python library, Version 0.24.2 DecisionTreeClassifier module (https://scikit-learn.org/stable/index.html) was used with the max_depth parameter set to 3 and max_leaves set to 4 to avoid overfitting.[29]

Statistical Analysis

All analyses were performed on the evaluation cohort ($n = 130$). Statistical power analysis for pair-wise comparison of the quantitative metrics with an assumed effect size of 0.55, α of .05, β of 0.2, and power of 80% resulted in a minimum sample size of 120. The SciPy Version 1.6.0 Python library and its stats module were used for all statistical analyses reported in this article.[30]

Association with Stenosis. The decision tree classifiers fit on the development cohort ($n = 130$) were used to classify 1 section from each disc level of the evaluation cohort ($n = 130$) as normal, mild, moderate, or severe. Association with stenosis for each metric was characterized for both binarized grading of stenosis (normal/mild versus moderate/severe) and multigrade classification.

Binary classification was evaluated using the area under the receiver operation characteristic curve (AUROC). Statistical significance of pair-wise differences in the AUROC corresponding to each quantitative metric was characterized using the DeLong test for comparing AUROCs, with $P < .05$ considered statistically significant.[31] Evaluation was bootstrapped to generate 95% confidence intervals.

Association of each metric with stenosis in the multigrade setting was evaluated using model accuracy, multiclass AUROC with the one-vs-one criterion, and agreement with R1's grades using a linearly-weighted Cohen κ coefficient.

Demographic Variability. The AUROC for binarized grading of stenosis using each metric as a score was used to assess consistency across demographics. AUROC values were computed for sex splits (male versus female), age splits using 45 years as a cutoff (age younger than 45 years versus age 45 years or older),[32] and BMI splits using a mean BMI of 25.0 kg/m^2 as a cutoff (BMI $<$ 25.0 kg/m^2 versus BMI $\geq$ 25.0 kg/m^2).[33]

Symptomatology. The AUROC for binarized grading of stenosis was used to assess the accuracy of each metric across 2 groups: VAS $<$ 7 and VAS $\geq$ 7.

Anatomic Normalization. To evaluate anatomic normalization of each quantitative metric, we clustered spinal levels into 2 groups: 1) upper lumbar levels consisting of L1/L2, L2/L3, and L3/L4, and 2) lower lumbar levels consisting of L4/L5 and L5/S1.

Association with Prognosis. The utility of each metric in association with outcomes was assessed on a subset of the evaluation cohort ($n = 130$), referred to as the "prognostic cohort" ($n = 58$) with patients managed conservatively ($n = 30$) and those who went on to require surgery ($n = 28$). Using each metric as a score, we evaluated the AUROC associated with predicting surgery from the preoperative MR imaging. Only the symptomatic level or the level at which surgery was performed was included in this analysis.

The decision tree classifier was used to grade each spinal level of the prognostic cohort ($n = 58$) as normal, mild, moderate, or severe. Linearly-weighted Cohen κ scores were computed for surgical-versus-conservatively managed cases.

Agreement and Reproducibility. To characterize reliability for the proposed metrics, R2 and R1 annotated another subset of patients ($n = 40$) for lines from the evaluation cohort ($n = 130$).

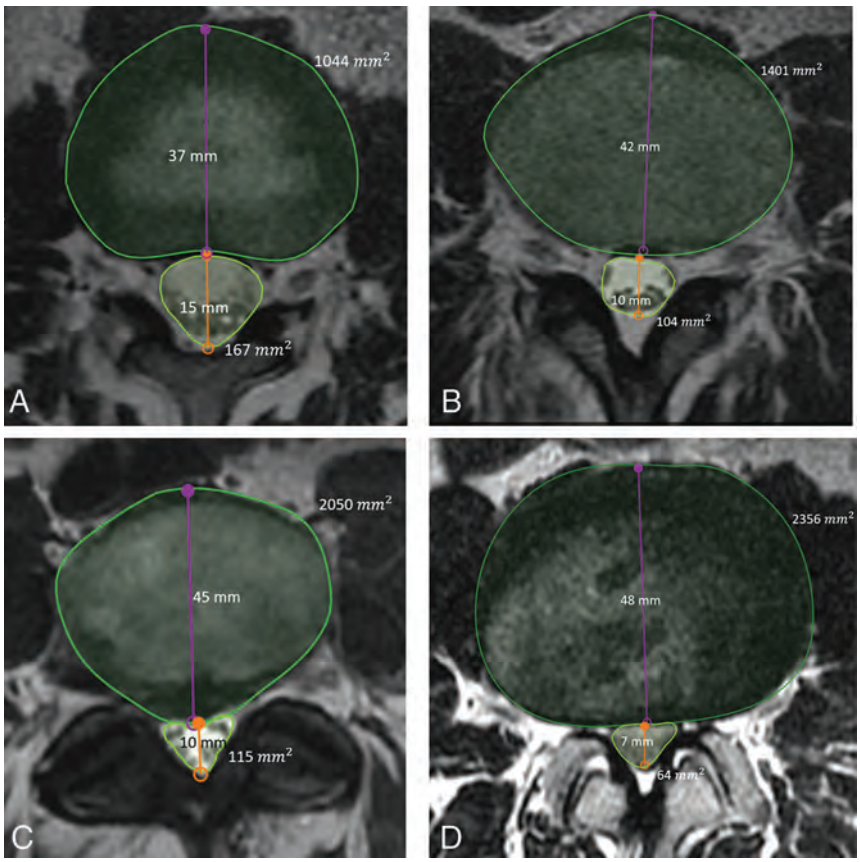

FIG 2. Sample T2-weighted axial MR imaging slices of the lumbar spine for each stenosis grade, determined qualitatively by a neuroradiologist, with the metrics annotated. *A*, Grade: normal; level, L1/L2; DSCA, 167 mm^2; DSDIA, 15 mm; DDRDIA, 0.42; DDRCA, 0.40. *B*, Grade: mild; level, L3/L4; DSCA, 104 mm^2; DSDIA, 10 mm; DDRDIA, 0.24; DDRCA, 0.27. *C*, Grade: moderate; level L4/L5; DSCA, 115 mm^2; DSDIA, 10 mm; DDRDIA, 0.22; DDRCA, 0.24. *D*, Grade: severe; level, L2/L3; DSCA, 64 mm^2; DSDIA, 7 mm; DDRDIA, 0.14; DDRCA, 0.16.

Reproducibility of estimating DDRDIA was computed using the concordance correlation coefficient.

To characterize interrater agreement for the qualitative grading of lumbar spinal stenosis, R1, R2, and a board-certified musculoskeletal radiologist (R3) with 23 years of experience assessed another subset of patients ($n = 32$) from the evaluation cohort ($n = 130$). Interrater agreement among R1, R2, and R3 was evaluated using a linearly-weighted Cohen κ coefficient.

RESULTS

Patient Cohort

The development cohort ($n = 130$) consisted of 65 female and 65 male patients, with a mean age of 57.6 (20.0–96.0) years and a mean BMI of 26.9 (15.3–58.8) kg/m^2. Patients presented with either low back pain ($n = 33$), radicular pain ($n = 14$), or both low back pain and radicular pain ($n = 68$), as well as other symptoms ($n = 15$) including numbness, tingling, weakness, dysesthesia, and tightness. Patients in the development cohort had an average low back pain score of 5.8 (SD, 2.6) and a radicular pain score of 5.9 (SD, 2.7) on an 11-point qualitative numeric pain rating scale.

The evaluation cohort ($n = 130$) consisted of 58 female and 72 male patients with a mean age of 58.3 (19.0–84.0) years and a mean BMI of 26.7 (17.5–41.3) kg/m^2. Patients in this cohort presented with low back pain ($n = 27$), radicular pain ($n = 20$), both ($n = 72$), and other symptoms ($n = 11$) including numbness, weakness, and tightness. Patients in the evaluation cohort had an average low back pain score of 5.8 (SD, 2.4) and a radicular pain score of 6.0 (SD, 2.5) on the numeric rating scale.

LSS Grades

A total of 555 slices were graded in the development cohort with the following distribution: normal ($n = 273$, 49.2%), mild ($n = 200$, 36.0%), moderate ($n = 45$, 8.1%), and severe ($n = 37$, 6.7%) stenosis across lumbar spinal levels L1/L2 ($n = 113$, 20.4%), L2/L3 ($n = 121$, 21.8%), L3/L4 ($n = 122$, 21.9%), L4/L5 ($n = 113$, 20.4%), and L5/S1 ($n = 86$, 15.5%).

A total of 491 slices were graded in the evaluation cohort with the following distribution: normal ($n = 244$, 49.7%), mild ($n = 149$, 30.3%), moderate ($n = 37$, 7.5%), and severe ($n = 61$, 12.5%) stenosis across lumbar spinal levels L1/L2 ($n = 111$, 22.6%), L2/L3 ($n = 113$, 23.0%), L3/L4 ($n = 108$, 22.0%), L4/L5 ($n = 96$, 19.6%), and L5/S1 ($n = 63$, 12.8%).

Cutoff Thresholds for Grading Stenosis

The decision tree for each quantitative metric was of depth 3 as visualized in Fig 3. Cutoff thresholds for grading stenosis using each metric were derived as follows:

DDRDIA: normal, DDRDIA $\geq$ 0.36; mild, 0.24 $\leq$ DDRDIA $<$ 0.36; moderate, 0.15 $\leq$ DDRDIA $<$ 0.24; severe, DDRDIA $<$ 0.15.

DDRCA: normal, DDRCA $\geq$0.31; mild, 0.23 $\leq$ DDRCA $<$ 0.31; moderate, 0.19 $\leq$ DDRCA $<$ 0.23; severe, DDRCA $<$ 0.19.

DSCA: normal, DSCA $\geq$ 189.5 mm^2; mild, 136.0 mm^2 $\leq$ DSCA $<$ 189.5 mm^2; moderate, 91.1 mm^2 $\leq$ DSCA $<$ 136.0 mm^2; severe, DSCA $<$ 91.1 mm^2.

DSDIA: normal, DSDIA $\geq$ 13.4 mm; mild, 10.1 mm $\leq$ DSDIA $<$ 13.4 mm; moderate, 8.5 mm $\leq$ DSDIA $<$ 10.1 mm; severe, DSDIA $<$8 .5 mm.

Statistical Analysis

Association with Stenosis. The proposed metrics, DDRCA and DDRDIA, had the highest AUROC for binarized classification of stenosis at 98.6 (97.4–99.3) and 98.0 (96.7–98.9), respectively, which were significantly higher ($P < .05$) than the standard of reference metrics, DSCA and DSDIA, with an AUROC of 96.5

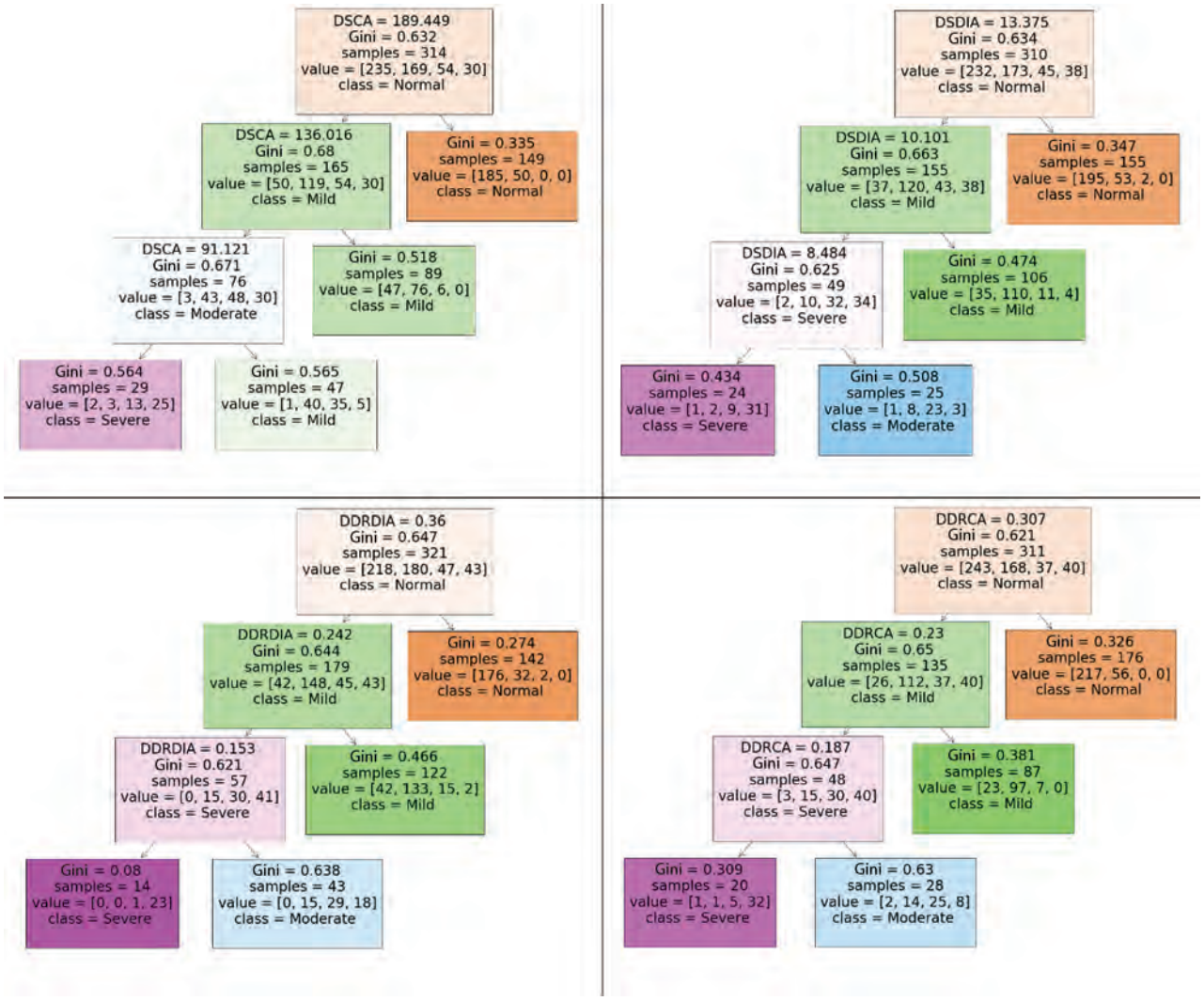

FIG 3. Decision rules and cutoff thresholds generated by a decision the tree classifier (maximum depth = 3, maximum leaves = 4, criterion = Gini impurity) for each quantitative metric.

(95.0–97.7) and DSDIA at 96.6 (95.1–97.8). The results are presented in Table 1 and visualized in Fig 4.

DDRCA and DDRDIA had the highest agreement with R1 for multigrade classification of stenosis with κ values of 0.80 (0.75–0.83) and 0.75 (0.71–0.79), respectively, compared with DSCA at 0.62 (0.57–0.66) and DSDIA at 0.69 (0.64–0.75), respectively. Multiclass accuracy, AUROC, and κ scores for each metric are presented in Table 2.

Demographic Variability. All 4 quantitative metrics had higher AUROC values for men compared with women ($P < .001$). No significant difference ($P < .1$) in the AUROC was observed in the case of the proposed metric DDRDIA across BMI groups. The other 3 metrics (DDRCA, DSDIA, DSCA) all had significant differences in the AUROC among the demographic splits ($P < .001$).

Symptomatology. DDRDIA had a higher AUROC than all other metrics in cases with VAS $\geq$ 7. DDRDIA was also the only metric in which the AUROC for cases with VAS $\geq$ 7 was significantly higher ($P < .001$) than that of cases with VAS $<$ 7. AUROC values are presented in Table 3.

Anatomic Normalization. No significant differences were observed in the values of DDRDIA and DDRCA for stenotic cases (mild, moderate, or severe) across the upper lumbar levels (L1/L2, L2/L3, L3/L4) and the lower lumbar levels (L4/L5 and L5/S1). The standard-of-reference metrics, DSCA and DSDIA. were sensitive to anatomic changes in cases with stenosis ($P < .001$).

Association with Prognosis. The DDRCA had the highest AUROC for predicting surgery at each spinal level from the prognostic cohort ($n = 58$), with a value of 83.5 (76.6–90.1), which was significantly greater than the standard-of-reference DSCA and DSDIA, which had AUROCs of 82.4 (75.5–90.4) and 81.3 (73.2–89.4). DDRDIA had the lowest AUROC for predicting surgery, with a value of 80.8 (73.0–89.5). These results are reported in Table 4.

The DDRDIA had the highest agreement with R1 for multiclass grading of stenosis in surgical cases, with a κ coefficient of 0.77 (0.65–0.90). κ scores for all other metrics across surgical-versus-nonsurgical levels were significantly lower, reported in Table 5.

Table 1: Classification of each spinal level as normal versus stenosed on the evaluation cohort ($n = 130$) using each quantitative metric[a]

Metrics Compared	AUROC: Group 1	AUROC: Group 2	*Z*-Statistic	Significance
DSCA vs DSDIA	96.5 (95.0–97.7)	96.6 (95.1–97.8)	0.19	$P = .85$
DSCA vs DDRDIA	96.5 (95.0–97.7)	98.0 (96.7–98.9)[b]	2.24[b]	$P = .02$[b]
DSCA vs DDRCA	96.5 (95.0–97.7)	98.6 (97.4–99.3)[b]	3.54[b]	$P = .004$[b]
DSDIA vs DDRDIA	96.6 (95.1–97.8)	98.0 (96.7–98.9)[b]	2.56[b]	$P = .01$[b]
DSDIA vs DDRCA	96.6 (95.1–97.8)	98.6 (97.4–99.3)[b]	2.89[b]	$P = .004$[b]
DDRDIA vs DDRCA	98.0 (96.7–98.9)	98.6 (97.4–99.3)	1.57	$P = .12$

[a] Reported are pair-wise comparisons between the quantitative metrics using the DeLong paired test for AUROCs. Data in parentheses represent 95% confidence intervals.
[b] Difference in AUROC is statistically significant ($P < .05$).

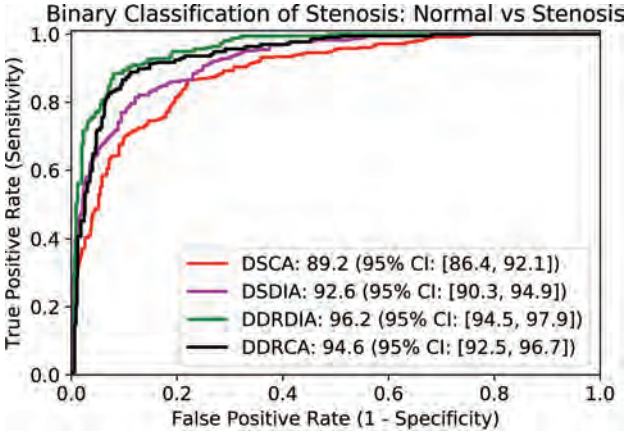

FIG 4. Receiver operator characteristic curve using each quantitative metric as a score for binary classification of stenosis. AUROC values are reported in the legend.

Agreement and Reproducibility. The reproducibility of measuring DDRDIA was substantial, with a concordance correlation coefficient of 0.9 between R1 and R2. Interrater agreement among (R1, R2), (R1, R3), and (R2, R3) was substantial with κ scores of 0.79, 0.72, and 0.65, respectively.

DISCUSSION

In this study, we proposed 2 ratio-based metrics for grading LSS, which, to our knowledge, has heretofore not been investigated in the literature. DDRDIA and DDRCA measured ratios between the dural sac and the intervertebral disc of the anterior-posterior diameters and cross-sectional areas, respectively. Our ratio-based approach naturally lends itself to a normalized metric between 0 and 1, which can be interpreted clinically as a surrogate for the severity of stenosis.

Our results indicate that DDRDIA and DDRCA perform as well or superior to the standard of reference metrics such as DSCA and DSDIA. Prescribed thresholds for DSCA are typically binarized into normal versus stenosed or normal/mild/moderate stenosis versus severe stenosis.[13,14] Our study provides more fine-grained thresholds for grading stenosis using each quantitative metric. The thresholds generated by a decision tree for DSCA and DSDIA, 91.1 mm^2 and 10.1 mm, respectively, are consistent with previously published values for these metrics,[14] further validating our methodology to obtain thresholds using a decision tree classifier.

Our analysis suggests that ratio-based metrics such as DDRDIA and DDRCA are more consistent across demographic variability, anatomically normalized, and better correlated with symptomatology and clinical outcomes compared with nonratio metrics such as DSCA and DSDIA.

DDRCA had a linearly weighted κ score of 0.80 using R1's grades as the ground truth, which is higher (albeit not statistically significant) than the agreement between R1 and R2 as well as between R1 and R3. High accuracy of DDRCA is an encouraging step toward multigrade classification of stenosis using ratio-based quantitative metrics. In comparison, DSCA had a significantly lower κ score of 0.62, lower than all pair-wise interrater agreement scores, confirming our hypothesis that normalized measures may be more effective as a quantitative metric for not only diagnosing stenosis but also classifying it into more granular grades.

Quantitative metrics based on ratios are also inherently robust to measurement, a finding supported by our reproducibility analysis, in which the concordance correlation coefficient between R1 and R2 was 0.9 for estimating DDRDIA. Although not explicitly quantified in this study, DDRDIA may be less prone to errors because it requires the radiologist to draw 2 lines as opposed to segmentation of the dural sac for area measurements, also making it more time-efficient.

A few other quantitative ratios have been proposed in the literature. The stenosis ratio, defined as a ratio between the cross-sectional dural sac area of the motion segment and that of the stable segment, was proposed as a promising alternative to DSCA in controlling for inherent differences in patient demographics.[34,35] The Torg-Pavlov ratio, which measures the ratio between the sagittal diameter of the spinal canal and the sagittal diameter of the vertebral body, is a normalized metric that can be used to assess the presence of spinal cord compression from MR imaging.[36] Neither the stenosis ratio nor the Torg-Pavlov ratio has been widely adopted in clinical practice for grading stenosis. The stenosis ratio requires precise measurements of multiple regions and their respective areas, which can be time-consuming and not consistent.[14] The Torg-Pavlov ratio has been sparsely applied to the cervical spine, with almost no prior studies establishing its effectiveness for the lumbar spine.[37] Moreover, for any given level, the disc level has been reported to be the most stenotic and prone to degenerative changes compared with the vertebral body.[38] Hence, the disc size measured as either the anterior-posterior diameter or the cross-sectional area may be a relevant feature associated with degenerative changes.

Ratios between the dural sac and the vertebral body have been published in the literature for adults as well as children and have been used for evaluation of multiple conditions.[39,40] For degenerative lumbar stenosis, the disc levels are the predominant stenotic

Table 2: Classification of each spinal level as normal, mild, moderate, and severe stenosis on the evaluation cohort ($n = 130$) using decision trees trained on the development cohort ($n = 130$)

	Accuracy		AUROC		Cohen κ	
Metric	Accuracy	95% CI	AUROC	95% CI	κ	95% CI
DSCA	64.9	(60.9–69.0)	76.6	(73.9–79.3)	0.62	(0.57–0.66)
DSDIA	71.4	(67.1–75.7)	80.9	(78.0–83.8)	0.69	(0.64–0.75)
DDRDIA	76.5	(72.6–80.4)[a]	84.3[a]	(81.7–86.9)[a]	0.75[a]	(0.71–0.79)[a]
DDRCA	78.9	(75.0–82.9)[a]	86.0[a]	(83.3–88.5)[a]	0.80[a]	(0.75–0.83)[a]

[a] Ratio-based metrics with higher κ scores ($P < .001$).

Table 3: AUROC for binary classification based on each metric across symptomatic splits (VAS <7 versus VAS ≥7) of low back pain and radicular pain[a]

	Symptomatology Analysis of Low Back Pain				
	VAS < 7		VAS ≥ 7		Significance[a]
Metric	AUROC	95% CI	AUROC	95% CI	*P* Value
Low Back Pain					
DSCA	97.7	(96.7–98.6)	95.1	(92.9–97.3)	$P < .001$
DSDIA	96.6	(95.4–97.8)	96.5	(94.9–98.1)	$P = .43$
DDRDIA	96.8	(95.6–97.9)	97.5	(96.1–98.8)	$P < .001$
DDRCA	98.5	(97.8–99.2)	96.3	(94.8–97.9)	$P < .001$
Radicular back pain					
DSCA	98.4	(97.4–99.4)	96.3	(94.5–98.1)	$P < .001$
DSDIA	98.2	(96.8–99.6)	96.9	(95.5–98.2)	$P < .001$
DDRDIA	98.7	(97.9–99.5)	97.1	(95.6–98.5)	$P < .001$
DDRCA	99.0	(98.4–99.6)	97.1	(95.5–98.7)	$P < .001$

[a] The *P* values represent a comparison of AUROCs among the symptomatic splits.

Table 4: AUROC for predicting surgery using each quantitative metric on the prognostic cohort ($n = 58$)

	Predicting Surgery at Each Spinal Level		
Metric	AUROC	95% CI	Significance[a]
DSCA	82.4	(75.5–90.4)	$P = 1.0$
DSDIA	81.3	(73.2–89.4)	$P < .001$
DDRDIA	80.8	(73.0–89.5)	$P < .001$
DDRCA	83.5[b]	(76.6–90.1)[b]	$P < .001$[b]

[a] The *P* values represent comparison between each metric and AUROC obtained with the baseline metric DSCA.
[b] Quantitative metric with the highest AUROC.

levels, motivating our proposed metrics. Studies calculating a "disc index," a ratio of the disc-to-canal size, have reported that larger disc indexes are associated with more continuous symptoms, and as ratios decreased with time, the symptoms also regressed.[41] An early description of the anterior-posterior length of disc protrusion and the percentage of the canal occupied by the disc protrusion was reported in 1997, and strong predictive effects were found between ratio measurements and patient outcomes.[42] Subsequent studies have also supported the use of disc ratios for predicting patient groups with favorable-versus-unfavorable surgical outcomes.[43] While disc dimension has been previously used in the context of lumbar disc herniation, to our knowledge, it is not commonly incorporated as a potential quantitative feature along with dural sac measurements for grading LSS.

We acknowledge the following limitations of this study: Our results are based on a single expert radiologist grader and do not incorporate consensus grading or any other form of adjudication; while consensus grades are advantageous, prior studies that relied on a single grader have shown meaningful associations.[28] Our approach based on decision trees may be prone to overfitting and brittle decision boundaries, wherein a slight perturbation to the development data can lead to drastically different thresholds.[28] Also, there are numerous statistical and machine learning techniques that can be used to determine a decision rule for each metric. A random forest model, which is a collection of several decision trees, may be more robust; we deliberately selected a decision tree for its interpretable thresholds and decision rules. We limited the depth to 3 and the maximum number of leaves to 4 to address some of the concerns around overfitting, and we observed that the derived thresholds of 91.1 mm^2 for severe stenosis based on DSCA and 10.1 mm for moderate or severe stenosis based on DSDIA are in line with previously published thresholds for the dural sac cross-sectional area and diameter.[14]

Another potential limitation is our reliance on a single outcome measure (VAS) for symptoms and a cutoff threshold of 7 to denote severe pain; other less common measures may be very valuable and the subject of future studies. Last, a potential limitation may be the acquisition of contiguous axial MR images, our institution's routine lumbar spine imaging protocol. A prior study reported that the use of disc space–targeted angled images resulted in a 75% reduction in the detection of migrated or sequestered disc material and a 50% decrease in detected pars defects compared with contiguous axial images.[44]

CONCLUSIONS

We found favorable results for our proposed ratio-based metrics, DDRDIA and DDRCA, which rely on simple measurements of the intervertebral disc and the dural sac, compared with common metrics such as the DSCA. Our results indicate that ratio-based metrics may offer a convenient trade-off between the classification

Table 5: Classification of each spinal level as normal, mild, moderate, and severe stenosis on the prognostic cohort ($n = 58$) using decision trees trained on the development cohort ($n = 130$)

	κ Scores for Grading Stenosis across Surgical vs Nonsurgical Levels				
	Nonsurgical Levels		Surgical Levels		Significance[a]
Metric	κ	95% CI	κ	95% CI	*P* Value
DSCA	0.65	(0.57–0.75)	0.74	(0.63–0.85)	$P < .001$
DSDIA	0.67	(0.58–0.77)	0.68	(0.51–0.85)	$P = .23$
DDRDIA	0.69	(0.61–0.76)[b]	0.77[b]	(0.65–0.90)[b]	$P < .001$[b]
DDRCA	0.71	(0.62–0.79)	0.73	(0.58–0.87)	$P < .001$

[a] The *P* values represent a comparison of κ scores between nonsurgical and surgical levels.
[b] The metric with the highest κ score for surgical levels.

of stenosis, robustness to measurement errors, and normalization across anatomic and demographic variability and stronger associations with LSS symptoms and prognosis. The proposed metrics are also practical in a clinical setting and amenable to automated estimation and can influence the diagnosis and subsequent management of patients with LSS.

ACKNOWLEDGMENTS

We also thank Mirandarae Christine, Steven Li, and Eduarda Vieira for their contributions to image annotations.

Disclosure forms provided by the authors are available with the full text and PDF of this article at www.ajnr.org.

REFERENCES

1. Deyo RA, Gray D, Kreuter W, et al. **United States trends in lumbar fusion surgery for degenerative conditions.** *Spine (Phila Pa 1976)* 2005;30:1441–45 CrossRef Medline
2. Cowley P. **Neuroimaging of spinal canal stenosis.** *Magn Reson Imaging Clin N Am* 2016;24:523–29 CrossRef Medline
3. Arnoldi CC, Brodsky AE, Cauchoix J, et al. **Lumbar spinal stenosis and nerve root entrapment syndromes: definition and classification.** *Clin Orthop Rel Res* 1976;115:4–5 Medline
4. Lee GY, Lee JW, Choi HS, et al. **A new grading system of lumbar central canal stenosis on MRI: an easy and reliable method.** *Skeletal Radiol* 2011;40:1033–39 CrossRef Medline
5. Schroeder GD, Kurd MF, Vaccaro AR. **Lumbar spinal stenosis: how is it classified?** *J Am Acad Orthop Surg* 2016;24:843–52 CrossRef Medline
6. Lurie J, Tomkins-Lane C. **Management of lumbar spinal stenosis.** *BMJ* 2016;352:h6234 CrossRef Medline
7. Katz JN, Zimmerman ZE, Mass H, et al. **Diagnosis and management of lumbar spinal stenosis: a review.** *JAMA* 2022;327:1688–99 CrossRef Medline
8. Morita M, Miyauchi A, Okuda S, et al. **Comparison between MRI and myelography in lumbar spinal canal stenosis for the decision of levels of decompression surgery.** *J Spinal Disord Tech* 2011;24:31–36 CrossRef Medline
9. Alsaleh K, Ho D, Rosas-Arellano MP, et al. **Radiographic assessment of degenerative lumbar spinal stenosis: is MRI superior to CT?** *Eur Spine J* 2017;26:362–67 CrossRef Medline
10. Arana E, Royuela A, Kovacs FM, et al. **Lumbar spine: agreement in the interpretation of 1.5-T MR images by using the Nordic Modic Consensus Group classification form.** *Radiology* 2010;254:809–17 CrossRef Medline
11. Schizas C, Theumann N, Burn A, et al. **Qualitative grading of severity of lumbar spinal stenosis based on the morphology of the dural sac on magnetic resonance images.** *Spine (Phila Pa 1976)* 2010;35:1919–24 CrossRef Medline
12. Khalsa SS, Kim HS, Singh R, et al. **Radiographic outcomes of endoscopic decompression for lumbar spinal stenosis.** *Neurosurg Focus* 2019;46:E10 CrossRef Medline
13. Andreisek G, Imhof M, Wertli M, et al; Lumbar Spinal Stenosis Outcome Study Working Group Zurich. **A systematic review of semiquantitative and qualitative radiologic criteria for the diagnosis of lumbar spinal stenosis.** *AJR Am J Roentgenol* 2013;201:W735–46 CrossRef Medline
14. Steurer J, Roner S, Gnannt R, et al. **Quantitative radiologic criteria for the diagnosis of lumbar spinal stenosis: a systematic literature review.** *BMC Musculoskelet Disord* 2011;12:175 CrossRef Medline
15. Fukusaki M, Kobayashi I, Hara T, et al. **Symptoms of spinal stenosis do not improve after epidural steroid injection.** *Clin J Pain* 1998;14:148–51 CrossRef Medline
16. Koc Z, Ozcakir S, Sivrioglu K, et al. **Effectiveness of physical therapy and epidural steroid injections in lumbar spinal stenosis.** *Spine (Phila Pa 1976)* 2009;34:985–89 CrossRef Medline
17. Hamanishi C, Matukura N, Fujita M, et al. **Cross-sectional area of the stenotic lumbar dural tube measured from the transverse views of magnetic resonance imaging.** *J Spinal Disord* 1994;7:388–93 Medline
18. Mariconda M, Fava R, Gatto A, et al. **Unilateral laminectomy for bilateral decompression of lumbar spinal stenosis: a prospective comparative study with conservatively treated patients.** *J Spinal Disord Tech* 2002;15:39–46 CrossRef Medline
19. Jönsson B, Annertz M, Sjöberg C, et al. **A prospective and consecutive study of surgically treated lumbar spinal stenosis, Part I: clinical features related to radiographic findings.** *Spine* 1997;22:2932–37 CrossRef Medline
20. Dora C, Wälchli B, Elfering A, et al. **The significance of spinal canal dimensions in discriminating symptomatic from asymptomatic disc herniations.** *Eur Spine J* 2002;11:575–81 CrossRef Medline
21. Aalto TJ, Malmivaara A, Kovacs F, et al. **Preoperative predictors for postoperative clinical outcome in lumbar spinal stenosis: systematic review.** *Spine (Phila Pa 1976)* 2006;31:E648–63 CrossRef Medline
22. Andreisek G, Hodler J, Steurer J. **Uncertainties in the diagnosis of lumbar spinal stenosis.** *Radiology* 2011;261:681–84 CrossRef Medline
23. Friedly JL, Jarvik JG. **Agreeing (or not) on how to describe spinal stenosis: expanding a narrow mindset.** *Radiology* 2012;264:3–4 CrossRef Medline
24. Miskin N, Gaviola GC, Huang RY, et al. **Intra- and intersubspecialty variability in lumbar spine MRI interpretation: a multireader study comparing musculoskeletal radiologists and neuroradiologists.** *Curr Probl Diagn Radiol* 2020;49:182–87 CrossRef Medline
25. Mamisch N, Brumann M, Hodler J, et al. **Radiologic criteria for the diagnosis of spinal stenosis: results of a Delphi survey.** *Radiology* 2012;264:174–79 CrossRef Medline
26. Downie WW, Leatham PA, Rhind VM, et al. **Studies with pain rating scales.** *Ann Rheum Dis* 1978;37:378–81 CrossRef Medline
27. Breiman L, Friedman JH, Olshen RA, et al. *Classification and Regression Trees*. Routledge; 1984:368
28. Huber FA, Stutz S, Martini IVd, et al. **Qualitative versus quantitative lumbar spinal stenosis grading by machine learning supported texture analysis: experience from the LSOS study cohort.** *Eur J Radiol* 2019;114:45–50 CrossRef Medline
29. Pedregosa F, Varoquaux G, Gramfort A, et al. **Scikit-learn: machine learning in Python.** *J Mach Learn Res* 2011;12:2825–30

30. Virtanen P, Gommers R, Oliphant TE, et al; SciPy 1.0 Contributors. **SciPy 1.0: fundamental algorithms for scientific computing in Python.** *Nat Methods* 2020;17:261–72 CrossRef Medline
31. DeLong ER, DeLong DM, Clarke-Pearson DL. **Comparing the areas under two or more correlated receiver operating characteristic curves: a nonparametric approach.** *Biometrics* 1988;44:837–45 CrossRef Medline
32. Buser Z, Ortega B, D'Oro A, et al. **Spine degenerative conditions and their treatments: national trends in the United States of America.** *Global Spine J* 2018;8:57–67 CrossRef Medline
33. Nuttall FQ. **Body mass index obesity, BMI, and health: a critical review.** *Nutr Today* 2015;50:117–28 CrossRef Medline
34. Laurencin CT, Lipson SJ, Senatus P, et al. **The stenosis ratio: a new tool for the diagnosis of degenerative spinal stenosis.** *Int J Surg Investig* 1999;1:127–31 Medline
35. Kitab S, Lee BS, Benzel EC. **Redefining lumbar spinal stenosis as a developmental syndrome: an MRI-based multivariate analysis of findings in 709 patients throughout the 16- to 82-year age spectrum.** *J Neurosurg Spine* 2018;29:654–60 CrossRef Medline
36. Pavlov H, Torg JS, Robie B, et al. **Cervical spinal stenosis: determination with vertebral body ratio method.** *Radiology* 1987;164:771–75 CrossRef Medline
37. Bajwa NS, Toy JO, Ahn NU. **Application of a correlation between the lumbar Torg ratio and the area of the spinal canal to predict lumbar stenosis: a study of 420 postmortem subjects.** *J Orthopaed Traumatol* 2013;14:207–12 CrossRef Medline
38. Thomé C, Börm W, Meyer F. **Degenerative lumbar spinal stenosis: current strategies in diagnosis and treatment.** *Dtsch Arztebl Int* 2008;105:373–79 CrossRef Medline
39. Knirsch W, Kurtz C, Häffner N, et al. **Normal values of the sagittal diameter of the lumbar spine (vertebral body and dural sac) in children measured by MRI.** *Pediatr Radiol* 2005;35:419–24 CrossRef Medline
40. Pierro A, Cilla S, Maselli G, et al. **Sagittal normal limits of lumbosacral spine in a large adult population: a quantitative magnetic resonance imaging analysis.** *J Clin Imaging Sci* 2017;7:35 CrossRef Medline
41. Fagerlund MK, Thelander U, Friberg S. **Size of lumbar disc hernias measured using computed tomography and related to sciatic symptoms.** *Acta Radiol* 1990;31:555–58 CrossRef Medline
42. Carragee EJ, Kim DH. **A prospective analysis of magnetic resonance imaging findings in patients with sciatica and lumbar disc herniation: correlation of outcomes with disc fragment and canal morphology.** *Spine* 1997;22:1650–60 CrossRef Medline
43. Varlotta CG, Manning JH, Ayres EW, et al. **Preoperative MRI predictors of health-related quality of life improvement after microscopic lumbar discectomy.** *Spine J* 2020;20:391–98 CrossRef Medline
44. Singh K, Helms CA, Fiorella D, et al. **Disc space-targeted angled axial MR images of the lumbar spine: a potential source of diagnostic error.** *Skeletal Radiol* 2007;36:1147–53 CrossRef Medline

Utility of Dual-Energy CT to Improve Diagnosis of CSF Leaks on CT Myelography following Lateral Decubitus Digital Subtraction Myelography with Negative Findings

S.J. Huls, D.P. Shlapak, D.K. Kim, S. Leng, and C.M. Carr

ABSTRACT

SUMMARY: CSF leaks, including CSF-venous fistulas, which cause spontaneous intracranial hypotension, remain difficult to diagnose, even on digital subtraction myelography and CT myelography. Dual-energy CT technology has been used to improve diagnostic utility within multiple organ systems. The capability of dual-energy CT to create virtual monoenergetic images can be leveraged to increase conspicuity of contrast in CSF-venous fistulas and direct epidural CSF leakage to improve the diagnostic utility of CT myelography. Six cases (in 5 patients) are shown in which virtual monoenergetic images demonstrate a leak location that was either occult or poorly visible on high- or low-kilovolt series. This clinical report describes the novel application of dual-energy CT for the detection of subtle CSF leaks including CSF-venous fistulas.

ABBREVIATIONS: $CTDI_{vol}$ = volume CT dose index; CTM = CT myelography; CVF = CSF-venous fistula; DECT = dual-energy CT; DSM = digital subtraction myelography; LDDSM = lateral decubitus digital subtraction myelography; SIH = spontaneous intracranial hypotension; VMI = virtual monoenergetic images

Spontaneous intracranial hypotension (SIH) is caused by a CSF leak, commonly occurring in the thoracic spine.[1] CSF leaks can be classified into 4 types as shown by Farb et al:[2] ventral dural tears (type 1), proximal nerve root sleeve tears (type 2), CSF-venous fistulas (CVFs, type 3), and distal nerve root sleeve tears (type 4). A variety of techniques using prone or lateral digital subtraction myelography (DSM) and CT myelography (CTM) have been used to identify leaks, with institutions often preferring techniques that are familiar, developed locally, or based on access to equipment.[3] Despite improvements in the lateral decubitus digital subtraction myelography (LDDSM) technique, some patients with intracranial SIH findings on brain MR imaging do not have an identifiable leak on LDDSM or conventional CTM. Conventional CTM may show CVFs as hyperdense paraspinal veins or opacification of the vertebral venous plexus.[3-6] Even after thorough imaging investigation, some studies report a 50% detection rate, while others report detection rates as high as 87%.[2,7] In small or subtle CVFs, insufficient contrast resolution associated with a CSF leak compared with background remains a challenge.

Dual-energy CT (DECT) has numerous applications and is being increasingly used in multiple organ systems.[8] In neuroradiology, DECT has been shown to aid in differentiation of hemorrhage versus contrast, visualization of intracranial aneurysms, diagnosis of malignant sinonasal lesions, and metal artifact reduction.[9] In CTM, DECT has been studied as a mechanism to decrease metal artifacts and radiation exposure.[10] A major benefit of DECT is to reconstruct virtual monoenergetic images (VMI), which mimic images acquired with a monochromatic beam. VMI can be reconstructed at various kiloelectron volt energies (keV) that present different CT density values and image contrast due to the energy dependence of attenuation. For example, iodinated contrast has higher CT attenuation values, due to increased photoelectric effect, as keV levels approach the k-edge of iodine 33.2 keV.[11] Prior studies have demonstrated that 50–60 keV is the optimal energy level for higher attenuation of iodine-based contrast with minimally increased noise levels.[8] This is particularly beneficial for evaluation of CSF leaks in which contrast leakage is subtle. A recent case series by Houk et al[12] described the use of DECT for improved visualization of CSF leaks and CVFs. In this retrospective study, we present several additional cases illustrating the utility of DECT 50-keV VMI to diagnose CSF leaks on CTMs following negative findings on DSMs.

MATERIALS AND METHODS

Patient Selection

This was an institutional review board–approved, Health Insurance Portability and Accountability Act–compliant retrospective study. Informed consent was waived. From April 2019 to March 2021, diagnostic reports of LDDSMs with subsequent lateral decubitus CTMs performed at our institution were consecutively reviewed. Cases with questionable, possible, or equivocal CTM findings were

Received May 23, 2022; accepted after revision July 12.

From the Department of Radiology, Mayo Clinic, Ringgold Standard Institution, Rochester, Minnesota.

Please address correspondence to Sean Huls, MD, Mayo Clinic, 200 First St SW, Rochester, MN 55905; e-mail: huls.sean@mayo.edu

http://dx.doi.org/10.3174/ajnr.A7628

excluded. Cases in which LDDSM findings were negative and subsequent same-day CTM findings were positive were further reviewed, including imaging and patient history. The cases were reviewed separately by 3 board-certified neuroradiologists with 2, 4, and 8 years of experience and a first-year radiology resident; discordant findings were discussed; and a consensus decision was reached. Evaluation of each case was performed at the same window and level settings (W:1000 C:100; Visage Imaging). Cases in which DECT 50-keV VMI aided the diagnosis of subtle CSF leaks on CTM (after negative LDDSM findings) were included. At the site of extradural contrast, maximum and mean Hounsfield units were measured using an ROI of 5 mm for cases 1, 2, 3, and 4. A smaller ROI of 3 mm for case 5 to minimize overlap with osseous structures was used.

Imaging Technique

LDDSM was performed using the technique described by Kim et al.[13] Following the completion of each LDDSM with 11 mL of Omnipaque 300 (GE Healthcare), patients were immediately transferred to CT in the same decubitus position. A lateral decubitus CTM of the entire spine was performed with DECT. LDDSM and subsequent CTM were then repeated on the following day with the patient in the opposite lateral decubitus position, irrespective of whether a CVF was found on the first day. Our institution performs CTM on second- or third-generation dual-source DECT scanners (Somatom Definition Flash and Force; Siemens) (Table 1). CT acquisitions were performed with a 100/Sn 140-kV scanner (Somatom Definition Flash; Sn indicates a tin filter added to the high-kilovolt beam) or 100/Sn 150-kV scanner (Somatom Force). Routine axial, coronal, and sagittal bone and soft-tissue windows were reformatted, and 50-keV VMI were reconstructed with all source images reviewed in multi-planar reformat views.

Table 1: Parameters for CT cervical, thoracic, and lumbar spine myelogram (Siemens dual-source, dual-energy CT models)

DECT Model	Somatom Definition Flash	Somatom Force
Description	128-Section dual-source, dual-energy CT	192-Section dual-source, dual-energy CT
kV(p)	A: 100 B: Sn 140	A: 100 B: Sn 150
Quality reference mAs	A: 230 B: 178	A: 260 B: 130
Scan FOV (mm)	A: 500 B: 332	A: 500 B: 356
Rotation time (sec)	1.0	1.0
Pitch	0.9	0.9
Collimation (mm)	32 × 0.6	128 × .06

RESULTS

Ten patients were identified with initial negative lateral decubitus DSM findings and subsequent positive CTM findings of CSF leak. Six examples in 5 patients were identified in which 50-keV VMI reformats were found to both qualitatively and quantitatively (increased Hounsfield units) improve the diagnosis of a CSF leak. Table 2 summarizes demographic data, symptoms, prior imaging findings, and treatment outcomes for each patient. Table 2 also contains CTM findings, including the presence of renal contrast in the renal collecting system, which is one of the features we use in our

Table 2: Patient demographics, imaging findings, symptoms, treatment, and outcomes

Patient	Age	Sex	Other Imaging Findings	CTM Findings	Symptoms	Treatment	Outcome
1	28	F	High-probability brain MR imaging	T12-L1 CVF on left; T11-12 on right; contrast in the renal collecting system	Orthostatic headache, multifocal pain	T11 nerve root ligation	Initial relief with subsequent recurrence of symptoms in the setting of Marfan syndrome
2	50	M	Intermediate-probability brain MR imaging	CVF at left L2-3 and contrast in the renal collecting system	Orthostatic headache	Blood patch, transvenous embolization of the left L2 paraspinal vein	Dramatic symptom improvement following embolization
3	52	M	High-probability brain MR imaging, positive cisternogram findings	Right T10 distal nerve root sleeve tear with extradural contrast first detected at L2-3	Orthostatic headache, vision changes, pulsatile tinnitus	Hemi-laminectomy right T10-11, repair of CSF leak	Complete symptom resolution sustained for at least 1 year
4	34	F	Intermediate-probability brain MR imaging	Focus of CSF leak arising from the right lateral thecal sac at T7-8 thought to represent dural tear; contrast in the renal collecting system	Orthostatic headache, facial and hand paresthesia	Three targeted blood patches	Improvement after 3 targeted blood patches with recurrence of symptoms
5	50	F	Multiple nerve root diverticula on spine MR imaging	Faint linear hyperattenuation extending from a right T11-12 nerve sleeve diverticulum thought to represent CVF	Orthostatic headache, vision changes	Two targeted and 1 multifocal blood patch	Transient improvement after 2 targeted and 1 multifocal blood patch

Note:—M indicates male; F, female.

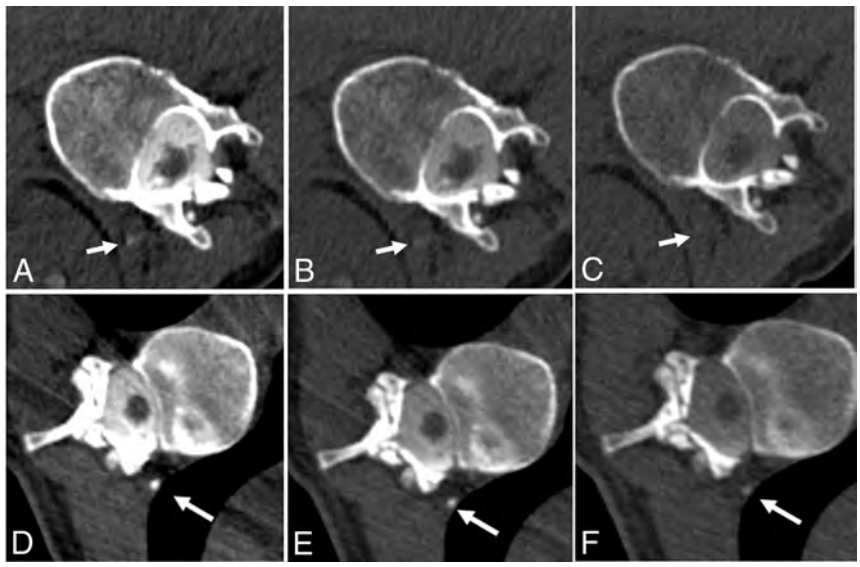

FIG 1. *A*, 50-keV VMI. *B*, 100 kV. *C*, 140 kV. Case 1: Left-side-down CTM with linear contrast at the left T12–L1 neural foramen, thought to reflect a CVF (*arrows*). Contrast is also noted in the renal collecting system. ROI Hounsfield units: *A*, 50-keV VMI Hounsfield unit maximum (max): 283 HU; mean, 76 HU. *B*, 100 -kV Hounsfield unit max: 147 HU; mean, 68 HU. *C*, 140-kV Hounsfield unit max: 116 HU; mean, 46 HU. *D*, 50-keV VMI. *E*, 100 kV. *F*, 140 kV. Case 1: Right-side-down CTM with paraspinal contrast at the level of T11–12, representing a second CVF (*arrows*). ROI Hounsfield units: *D*, 50-keV VMI Hounsfield unit max: 981 HU; mean, 693 HU. *E*, 100-kV Hounsfield unit max: 542 HU; mean, 369 HU. *F*, 140-kV Hounsfield unit max: 233 HU; mean, 107 HU.

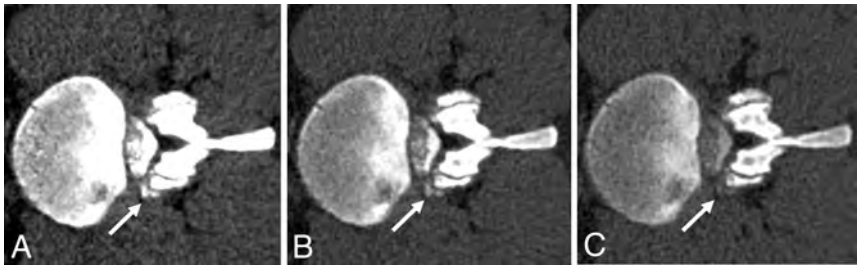

FIG 2. *A*, 50-keV VMI. *B*, 100 kV. *C*, 140 kV. Case 2: Left-side-down CTM with a suspected distal nerve root sleeve tear at the left L2–3 (*arrows*). The patient also had contrast in the renal collecting system (not shown). ROI Hounsfield units: *A*, 50-keV VMI Hounsfield unit maximum (max): 806 HU; mean, 271 HU. *B*, 100-kV Hounsfield unit max: 435 HU; mean, 133 HU. *C*, 140-kV Hounsfield unit max: 210 HU; mean, 68 HU.

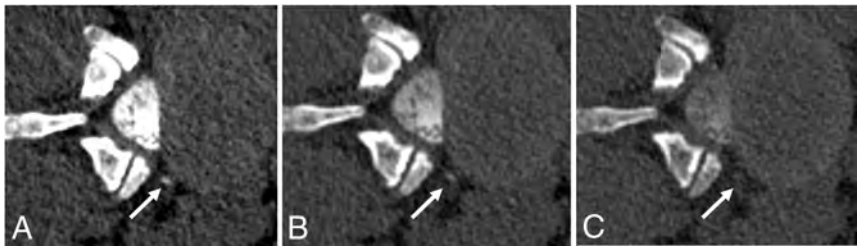

FIG 3. *A*, 50 -keV VMI. *B*, 100 kV. *C*, 150 kV. Case 3: Right-side-down CTM with linear contrast at the right L2–3 neuroforamen (*arrows*), extending into the paraspinal soft tissues, thought to reflect a vessel associated with contrast leakage at a higher right-T10 distal nerve root sleeve tear (not shown). ROI Hounsfield units: *A*, 50-keV VMI Hounsfield unit maximum (max): 485 HU; mean, 118 HU. *B*, 100-kV Hounsfield unit max: 271 HU; mean, 51 HU. *C*, 150-kV Hounsfield unit max: 151 HU; mean, 16 HU.

practice to increase our confidence in subtle or equivocal findings. These cases are illustrated in Figs 1–5, with 140-/150-kV, 100 -kV, and 50-keV VMI. Maximum and mean CT attenuation values (Hounsfield units) over the CSF leak ROIs are reported in the figure legends and Table 3 for each kilovolt peak level and 50-keV VMI reconstructions. For the 5 patients included in this study, the mean volume CT dose index ($CTDI_{vol}$) was 14.5 mGy (range, 13.2–15.6 mGy), the mean dose-length product was 1047.8 mGy × cm (range, 950.6–1150.5 mGy × cm), and the corresponding effective dose (using a K factor of 0.015 mSv/mGy × cm) was 15.7 mSv (range, 14.3–17.3 mSv).

Case 1

A 28-year-old woman with a history of Marfan syndrome developed symptoms of orthostatic headache and multifocal pain 6 years before presentation. MR imaging of the brain showed effacement of the suprasellar and prepontine cisterns, decreased mamillopontine distance, and diffuse dural enhancement and thickening, all indicating SIH (high-probability Bern Score = 6). A high-probability score is a Bern score of >5, based on MR imaging findings of SIH as described in Dobrocky et al.[14] She subsequently underwent LDDSM followed by CTM, which showed a left T12-L1 hyperdense paraspinal vein. Next-day right-side-down LDDSM followed by CTM showed a right hyperdense paraspinal vein at T11-12. Preoperative-planning CTA identified the artery of Adamkiewicz on the left at T12-L1, which prevents nerve root ligation. She underwent packing with venous obliteration of the veins on the left at T12-L1 and nerve root ligation on the right at T11-12. She had transient improvement, but due to her Marfan syndrome, she developed recurrent symptoms and intracranial stigmata of SIH indicating a new leak.

Case 2

A 50-year-old man had a 6-year history of consistently orthostatic symptoms of which headaches were the predominant symptom. At an outside institution, he was initially thought to have a Chiari I deformity related to his low-lying

FIG 4. *A*, 50-keV VMI. *B*, 100 kV. *C*, 140 kV. Case 4: Right-side-down CTM with a small focus of extradural contrast at the right aspect of the thecal sac at T7–8 (*arrows*). ROI Hounsfield units: *A*, 50-keV VMI Hounsfield unit maximum (max): 441 HU; mean, 275 HU). *B*, 100-kV Hounsfield unit max: 277 HU; mean, 165 HU. *C*, 140-kV Hounsfield unit max: 163 HU; mean, 102 HU.

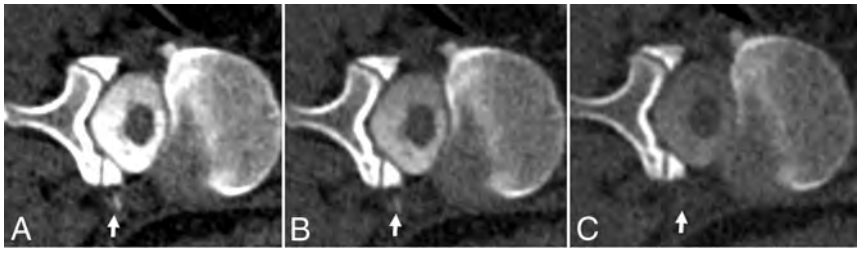

FIG 5. *A*, 50-keV VMI. *B*, 100 kV. *C*, 140 kV. Case 5: CTM right-side-down at the level of T11–12 shows linear focus most consistent with a CSF venous fistula (*arrows*). ROI Hounsfield units: *A*, 50-keV Hounsfield unit maximum (max): 436 HU; mean, 154 HU. *B*, 100-kV Hounsfield unit max: 251 HU; mean, 88 HU. *C*, 140-kV Hounsfield unit max: 125 HU; mean, 33 HU.

cerebellar tonsils, leading to a posterior fossa decompression, C2 laminectomy, and C3-4 laminoplasties 1 year before presentation. Nuclear medicine indium-111 (^{111}In) dethylenetriaminepentaacetic acid cisternogram obtained at our institution was positive for the presence of a CSF leak. MR imaging of the brain showed effacement of the suprasellar and prepontine cisterns and decreased mamillopontine distance (intermediate-probability Bern Score = 4).[14] His left lateral decubitus CTM following negative findings on LDDSM showed irregular contrast within the left L2-3 neural foramen. The patient underwent 2 targeted blood patches resulting in 2–4 weeks of symptom improvement. This was followed by transvenous Onyx (Medtronic) embolization with near-complete resolution of symptoms.

Case 3

A 52-year-old man had a 5-month history of orthostatic headache and pulsatile tinnitus after having his back "cracked" (physical manipulation) at home. He underwent 2 blood patches for presumed CSF leak with transient 2 weeks of partial symptomatic improvement. MR imaging of the brain showed pachymeningeal enhancement, venous sinus engorgement, and effacement of the suprasellar and prepontine cisterns (high-probability Bern score = 7).[14] An ^{111}In-DTPA cisternogram showed delayed radionuclide activity ascent supporting SIH. Right LDDSM had negative findings while subsequent same-side-down CTM showed subtle contrast extravasation along the right at L2–3. Subsequent dedicated lateral decubitus dynamic CTM, for localization, demonstrated that the leak originated at T10. A hemilaminectomy and right T10–11 nerve root ligation resulted in durable and sustained complete symptom relief for more than a year.

Case 4

A 34-year-old woman had postural orthostatic tachycardia syndrome and a 1-year history orthostatic headache and facial and hand paresthesias. Opening pressure with the patient in the prone position was low, measuring 8 cm of water (normal range, 10–25cm);[15] however, opening pressure is variable and not necessarily low in patients with definite CSF leaks. Head MR imaging demonstrated effacement of the suprasellar and prepontine cisterns (intermediate-probability Bern score = 3).[14] Initial right-side-down LDDSM had negative findings, but subsequent CTM showed subtle extradural contrast along the right aspect of the T7–8 neural foramen. Targeted CT-guided epidural blood patches resulted in dramatic reduction in headaches for approximately 8 months. Follow-up CTM after LDDSM again showed extradural contrast on the right at T7–8. The patient underwent Onyx embolization and had improved near-resolution of symptoms, compared with the blood patch.

Case 5

A 50-year-old woman had a 2-year history of orthostatic headache. She had 2 prior targeted blood patches. No recent brain MR imaging was available. Full-spine MR imaging showed multiple nerve root diverticula. CTM after negative DSM findings showed multiple nerve root diverticula with faint linear hyperdensity extending from a right T11–12 nerve sleeve diverticulum, suspicious for a CVF. She underwent a T11–12 targeted blood patch without changes in symptoms.

DISCUSSION

DECT has been commercially available with various technical implementations by different vendors.[16] With measurements from 2 different spectra, DECT enables material characterization and quantification, which has been used in many clinical areas, such as detection of gout, differentiation of renal stones, bone and plaque removal, iodine maps, and virtual noncontrast images.[16] Another major application of DECT is to generate VMI, which mimic the appearance of those images acquired with a monoenergetic beam. VMI at different energies (keV) have different image contrast, with lower kiloelectron volt VMI having higher iodine contrast due to increased photoelectric effect near the K-edge of iodine. These low-kiloelectron volt VMI (eg, 50 keV) have been found to be beneficial to improve image quality, decrease necessary iodinated contrast volume, and reduce the radiation dose. In this study, we aimed for a special application using low-kiloelectron volt VMI for improved detection of subtle differences in attenuation. As evidenced by the findings, 50-keV VMI have the highest CT attenuation value, followed by 100-kV single-energy images, and the lowest CT attenuation value at 140–150 kV.

Table 3: Hounsfield measurements at the site of contrast leak or CVF

Case	50 keV VMI Mean	50 keV VMI Max	100 kV Mean	100 kV Max	140/150 kV Mean	140/150 kV Max
Case 1L	76	283	68	147	46	116
Case 1R	693	981	369	542	107	233
Case 2	271	806	133	435	68	210
Case 3	118	485	51	271	16	150
Case 4	275	441	165	277	102	163
Case 5	154	436	88	251	33	125

Note:—1L indicates left side down CTM; 1R, right side down CTM

A potential downside of DECT, compared with single-energy CT, is an increased ionizing radiation dose. There is a paucity of literature comparing single-energy CTM with dual-energy CTM; however, one study comparing radiation exposures showed dual-energy CTM to have 1.6–1.9 times higher dose-length product and $CTDI_{vol}$ levels in comparison with single-energy CT in the cervical and thoracic spine. In the same study, whole-spine CTM performed with a strictly single-energy CT–capable scanner (Somatom Definition AS+; Siemens) showed a whole-spine mean $CTDI_{vol}$ of 13.99 mGy (range, 10.13–16.15 mGy) and a dose-length product of 837.8 (range, 530.5–1033.0).[17] As expected, these data suggest that DECT results in modest-to-moderate increased radiation exposure.

It is increasingly recognized that there is a subset of patients with intermediate or high-probability Bern scores on head MR imaging and a clinical diagnosis of SIH in whom a radiographically visible leak cannot be found despite multiple myelographic techniques. Given this difficulty of diagnosing apparently radiographically occult CSF leaks, any technique that can improve the diagnostic yield and visualization of subtle findings is critical. The provided examples in this case series demonstrate subtle areas of extradural contrast on CTM that are either best seen or only seen on the 50-keV VMI. DECT improves diagnostic accuracy by increasing the conspicuity of extradural contrast against the background. Correlating the appearance of a suspected CSF leak at different energy levels allows delineation of extradural iodine from other hyperattenuating structures such as osteophytes, heterotopic calcifications, and artifactual volume averaging. Our results are concordant with those of a recent smaller case series by Houk et al[12] showing improved visualization of subtle CSF leaks on CTM using VMI reformats.

CONCLUSIONS

This retrospective series is limited by the small number of cases. However, it adds to the existing literature showing that this novel use of DECT can aid in the radiographic evaluation of SIH. Given the intrinsic challenges of finding subtle CSF leaks, neuroradiologists need to have many tools in their arsenal. This case series would support further investigation for the applications of DECT in the setting of SIH. In addition, if available, routine use of dual-energy technology with virtual monoenergetic images reconstructed at 50 keV for detection of subtle CSF leaks has the potential of diagnosing a leak that would otherwise be missed with conventional imaging.

Disclosure forms provided by the authors are available with the full text and PDF of this article at www.ajnr.org

REFERENCES

1. Schievink WI, Meyer FB, Atkinson JL, et al. **Spontaneous spinal cerebrospinal fluid leaks and intracranial hypotension.** *J Neurosurg* 1996;84:598–605 CrossRef Medline
2. Farb RI, Nicholson PJ, Peng PW, et al. **Spontaneous intracranial hypotension: a systematic imaging approach for CSF leak localization and management based on MRI and digital subtraction myelography.** *AJNR Am J Neuroradiol* 2019;40:745–53 CrossRef Medline
3. Mamlouk MD, Ochi RP, Jun P, et al. **Decubitus CT myelography for CSF-venous fistulas: a procedural approach.** *AJNR Am J Neuroradiol* 2021;42:32–36 CrossRef Medline
4. Kim DK, Carr CM, Benson JC, et al. **Diagnostic yield of lateral decubitus digital subtraction myelogram stratified by brain MRI findings.** *Neurology* 2021;96:e1312–18 CrossRef Medline
5. Kranz PG, Gray L, Malinzak MD, et al. **CSF-venous fistulas: anatomy and diagnostic imaging.** *AJR Am J Roentgenol* 2021;217:1418–29 CrossRef Medline
6. Clark MS, Diehn FE, Verdoorn JT, et al. **Prevalence of hyperdense paraspinal vein sign in patients with spontaneous intracranial hypotension without dural CSF leak on standard CT myelography.** *Diagn Interv Radiol* 2018;24:54–59 CrossRef Medline
7. Kranz PG, Luetmer PH, Diehn FE, et al. **Myelographic techniques for the detection of spinal CSF leaks in spontaneous intracranial hypotension.** *AJR Am J Roentgenol* 2016;206:8–19 CrossRef Medline
8. Albrecht MH, Vogl TJ, Martin SS, et al. **Review of clinical applications for virtual monoenergetic dual-energy CT.** *Radiology* 2019;293:260–71 CrossRef Medline
9. Postma AA, Das M, Stadler AA, et al. **Dual-energy CT: what the neuroradiologist should know.** *Curr Radiol Rep* 2015;3:16 CrossRef Medline
10. Grams AE, Sender J, Moritz R, et al. **Dual energy CT myelography after lumbar osteosynthesis.** *Rofo* 2014;186:670–74 CrossRef Medline
11. De Cecco CN, Boll DT, Bolus DN, et al. **White paper of the Society of Computed Body Tomography and Magnetic Resonance on dual-energy CT, Part 4: abdominal and pelvic applications.** *J Comput Assist Tomogr* 2017;41:8–14 CrossRef Medline
12. Houk JL, Marin DM, Malinzak MD, et al. **Dual energy CT for the identification of CSF-venous fistulas and CSF leaks in spontaneous intracranial hypotension: report of four cases.** *Radiol Case Rep* 2022;17:1824–29 CrossRef Medline
13. Kim DK, Brinjikji W, Morris PP, et al. **Lateral decubitus digital subtraction myelography: tips, tricks, and pitfalls.** *AJNR Am J Neuroradiol* 2020;41:21–28 CrossRef Medline
14. Dobrocky T, Grunder L, Breiding PS, et al. **Assessing spinal cerebrospinal fluid leaks in spontaneous intracranial hypotension with a scoring system based on brain magnetic resonance imaging findings.** *JAMA Neurol* 2019;76:580–87 CrossRef Medline
15. Whiteley W, Al-Shahi R, Warlow CP, et al. **CSF opening pressure: reference interval and the effect of body mass index.** *Neurology* 2006;67:1690–91 CrossRef Medline
16. McCollough CH, Leng S, Yu L, et al. **Dual- and multi-energy CT: principles, technical approaches, and clinical applications.** *Radiology* 2015;276:637–53 CrossRef Medline
17. Zensen S, Bos D, Opitz M, et al. **Single- and dual-source CT myelography: comparison of radiation exposure and establishment of diagnostic reference levels.** *Diagnostics (Basel)* 2021;11:1809 CrossRef Medline

Resisted Inspiration: A New Technique to Aid in the Detection of CSF-Venous Fistulas

I.T. Mark, M.R. Amans, V.N. Shah, K.H. Narsinh, M.T. Caton, S. Teixeira, and W.P. Dillon

ABSTRACT

SUMMARY: We describe a technique termed "resisted inspiration" that could be used during myelography to decrease superior vena cava venous pressure and increase lumbar CSF pressure, potentially aiding in the detection of CSF-venous fistulas.

ABBREVIATIONS: CVF = CSF-venous fistula; IIH = idiopathic intracranial hypertension; LP = lumbar puncture; SIH = spontaneous intracranial hypotension; SVC = superior vena cava

Spontaneous intracranial hypotension (SIH) can be a debilitating disease that often manifests as orthostatic headaches. One cause of SIH is a CSF-venous fistula (CVF).[1] Unfortunately, traditional cross-sectional imaging with CT and MR imaging is unable to detect a CVF.[2,3] Therefore, the diagnosis of a CVF is made by myelography under CT (CT myelography), MR imaging (MR myelography), or fluoroscopy (digital subtraction myelography).[4-6] All 3 of these techniques are contingent on visualizing contrast that is placed into the subarachnoid space via lumbar puncture (LP) and subsequent passage of contrast from the CSF to a radicular vein. The passage of contrast is driven by the CSF-to-venous pressure gradient. The purpose of our article was to demonstrate a new technique of resisted inspiration that decreases superior vena cava (SVC) pressure while increasing lumbar CSF pressure (thereby maximizing the pressure gradient), a potential adjunct to myelography to improve diagnostic evaluation for a CVF.

MATERIALS AND METHODS

Consecutive patients presenting for venous manometry or LP between April and May of 2022 were included under institutional review board approval. Venous and CSF manometry were performed during a series of breathing maneuvers at a single tertiary medical center (University of California, San Francisco). Pertinent patient demographic variables were also collected for all patients.

Breathing Technique

Changes in SVC venous and lumbar CSF pressures were measured at rest to serve as a baseline. Measurements were also obtained during normal (nonresisted) inspiration and a Valsalva maneuver. Resisted inspiration was performed by inspiring through a 5-mL slip tip syringe (BD Medical). Pressure was measured at mid-resisted inspiration (measured as the half-way point between start and end inspiration) and end-resisted inspiration.

Venous Manometry

Venous pressures were prospectively recorded in 4 patients undergoing a catheter cerebral venography and manometry procedure for a separate clinical indication. All venous manometry was performed in the SVC, which is the drainage pathway of the azygos system, the common venous outflow system of a CVF.[7] The manometry zero point was set 1.5 inches anterior to the external auditory canal in accordance with our institution's standard for cerebral venous manometry. We collected details of the procedure, including access site, catheter type, and venous manometry with the 5 breathing techniques.

CSF Manometry

Lumbar CSF pressures were prospectively recorded in 4 separate patients undergoing a clinically indicated CT-guided LP. Pressure was measured with the patient in the lateral decubitus position with a Compass for Lumbar Puncture disposable pressure transducer (Centurion). Details of the procedure including the patient position, access level, and needle size, length, and type were recorded. CSF manometry was recorded with the same breathing technique used for venous manometry.

Received June 17, 2022; accepted after revision July 21.

From the Department of Radiology and Biomedical Imaging (I.T.M., M.R.A., V.N.S., K.H.N., M.T.C., S.T., W.P.D.), University of California, San Francisco, San Francisco, California; and Department of Radiology (I.T.M.), Mayo Clinic, Rochester, Minnesota.

Each of the authors (I.T.M., V.N.S., M.R.A., K.H.N., M.T.C., S.T., W.P.D.) contributed to all categories established by the International Committee of Medical Journal Editors, including conception and design, or acquisition of data, or analysis and interpretation of data, drafting the article or revising it critically for important intellectual content, final approval of the version to be published, and agreement to be accountable for all aspects of the work in ensuring that questions related to the accuracy or integrity of any part of the work are appropriately investigated and resolved.

Please address correspondence to Ian Mark, MD, Department of Radiology, Mayo Building, 3-72W, Rochester, MN 55905; e-mail: Mark.Ian@mayo.edu; @iantmark

http://dx.doi.org/10.3174/ajnr.A7636

Table 1: Individual patient demographics and SVC manometry readings in 4 patients who underwent a catheter venogram

Patient	Age (yr)/ Sex	Indication	BMI	Venous Pressure (mm Hg)				
				Rest Pressure	Valsalva	Normal Inspiration	Mid-Resisted Inspiration	End-Resisted Inspiration
1	57/F	IIH	34.5	3	11	–1	–8	–16
2	63/M	Pulsatile tinnitus	24.8	1	27	–1	–15	–26
3	69/F	Pulsatile tinnitus	31.6	2	25	–6	–15	–31
4	52/F	IIH	42.6	10	25	8	–2	–11

Note:—F indicates female; M, male; BMI, body mass index.

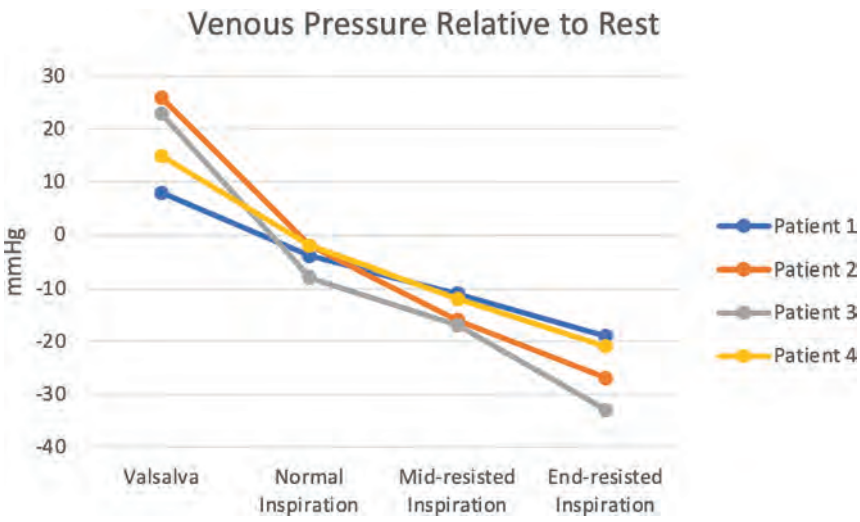

FIG 1. SVC venous pressure changes with 4 different techniques relative to the SVC venous pressure while breathing at rest. End-resisted inspiration leads to the greatest drop in pressure, which is far greater than with normal inspiration.

RESULTS

Venous Manometry Patients

All 4 patients underwent a clinically indicated catheter venogram with manometry. Patient demographics and details of each procedure are listed in Table 1. Venous access was obtained in all 4 patients through the right common femoral vein. Venous pressure was measured with a 6F Benchmark 0.071-inch (Penumbra) guide catheter in patients 1–3 and a 5F UCSF-2/Berenstein III catheter (Cordis) in patient 4. The indication for the venograms included the following: idiopathic intracranial hypertension (IIH) work-up in a patient found to have a transverse sinus stenosis that was subsequently stented (patient 1), 2 cases of pulsatile tinnitus work-up without causative findings on venograms (patients 2 and 3), and 1 follow-up diagnostic case of a prior transverse venous stent for IIH (patient 4). On average and relative to resting pressure, the Valsalva maneuver increased (+18 mm Hg) venous pressure, while inspiration (−4 mm Hg), mid-resisted inspiration (−14 mm Hg), and end-resisted inspiration (−25 mm Hg) decreased venous pressure as depicted in Fig 1.

CSF Pressure Patients

Four patients underwent a CT-guided LP with CSF manometry. CT guidance was chosen per our institutional preference. Patient demographics and procedural details are listed in Table 2. All patients who underwent an LP were in the lateral decubitus position (3 in right lateral, 1 in left lateral). A 9-cm 22-ga Quincke tip needle (BD Medical) was used to access the thecal sac at L5–S1 in each patient. On average and relative to rest breathing, the CSF pressure increased with each maneuver including Valsalva (+5.25 cm H_2O), normal inspiration (+2.5 cm H_2O), mid-resisted inspiration (+4.25 cm H_2O), and end-resisted inspiration (+7 cm H_2O) as depicted in Fig 2.

DISCUSSION

In the current study, we found that resisted inspiration can dramatically decrease SVC venous pressure and concurrently increase CSF pressure, which has the effect of increasing the CSF-to-venous pressure gradient. Increasing this gradient will likely improve detection of a CVF using myelography, a notoriously challenging diagnosis. This is the first description of resisted inspiration as an adjunctive maneuver during myelography to potentially help increase the conspicuity of a CVF.

MR myelography, CT myelography, and digital subtraction myelography have been described as different diagnostic techniques to identify a CVF.[4,5] Each of these techniques requires the passage of contrast from the CSF to the venous system, which is driven by the CSF-to-venous pressure gradient. One prior article has described the effects of respiration on CVF detection. Amrhein et al[8] have shown the benefit of end inspiration with the visualization of CVF on a CT myelogram and digital subtraction myelography. We have built on this work by showing that resisted inspiration dramatically decreases the venous pressure and increases the CSF pressure to an even greater extent compared with normal (nonresisted) inspiration.

Deep inspiration leads to negative intrathoracic pressure, increased cardiac return, and subsequent decreased venous pressure.[9,10] If normal inspiration can generate decreased SVC venous pressure, then resisted inspiration that requires greater effort from the muscles of inspiration should further decrease venous pressure. Gutzeit et al[11] showed that resisted inspiration increases the SVC/inferior vena cava blood flow for opacification of the pulmonary arteries and thereby aids in the detection of pulmonary emboli on CT angiography. While this effect was seen with resisted inspiration, they only noted minimal effect with normal inspiration.

Table 2: Individual patient demographics and lumbar CSF manometry readings in 4 patients who underwent a CT-guided LP

Patient	Age (yr)/ Sex	Indication	BMI	CSF Pressure (cm H_20)				
				Rest Pressure	Valsalva	Normal Inspiration	Mid-Resisted Inspiration	End-Resisted Inspiration
1	69/F	Prior idiopathic leptomeningeal enhancement	19.6	13	15	14	15	17
2	45/F	New-onset psychosis	27.9	33	40	38	39	41
3	75/M	Intrathecal chemotherapy	24.2	0	7	1	1	2
4	59/M	Metastatic lung cancer	27.3	2	7	5	10	16

Note:—F indicates female; M, male; BMI, body mass index.

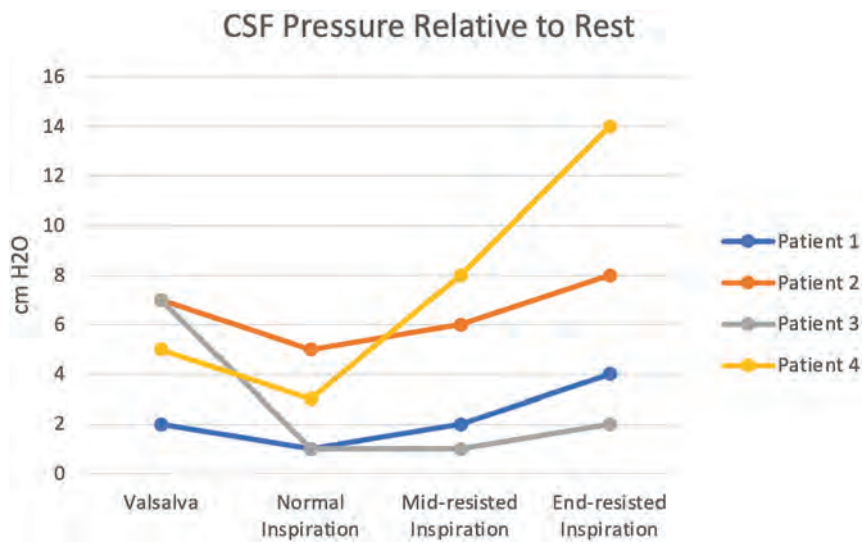

FIG 2. CSF pressure changes with 4 different techniques relative to the CSF pressure while breathing at rest. CSF pressure increased the most with end-resisted inspiration, which was even greater compared with the Valsalva maneuver.

Most interesting and somewhat unexpected, inspiration (both resisted and normal) leads to an increase in CSF pressure. Downward contraction of the diaphragm increases intrabdominal pressure and leads to an influx of blood into the epidural veins and, thus, increases pressure on the thecal sac.[12]

The CSF-to-venous pressure gradient should dictate the flow of CSF and, therefore, intrathecal contrast across a fistula. A 1-way valve between the SVC and azygos vein resists reflux of high pressure from the SVC into the azygos system but would facilitate low pressure in the SVC into the azygos system.[13] This outcome is important as new and effective treatments become available for CVF, which include transvenous endovascular embolization[14] in addition to surgical ligation and percutaneous fibrin glue injection.[15]

There are several limitations to our study. First, we studied a small number of separate patients for venous and CSF manometry. Ideally, we would study the pressure differences in a larger number of patients who would undergo both venous and CSF manometry. However, the venous manometry changes with resisted inspiration were large and consistent across all 4 patients and markedly different from both breathing at rest and normal inspiration. These results have already caused a change in the myelography technique at our institution. Finally, we used SVC pressure as a surrogate for pressure within the azygos system. While this is the most common venous drainage pathway of CVF, there are other venous drainage patterns[7] that may not be affected by pressure changes in the SVC to the same degree.

CONCLUSIONS

We describe a technique termed "resisted inspiration" that could be used during myelography to decrease SVC venous pressure and increase lumbar CSF pressure, which may potentially aid in the detection of CVFs.

Disclosure forms provided by the authors are available with the full text and PDF of this article at www.ajnr.org.

REFERENCES

1. Schievink WI, Moser FG, Maya MM. **CSF-venous fistula in spontaneous intracranial hypotension.** *Neurology* 2014;83:472–73 CrossRef Medline
2. Schievink WI, Maya MM, Jean-Pierre S, et al. **A classification system of spontaneous spinal CSF leaks.** *Neurology* 2016;87:673–79 CrossRef Medline
3. Amrhein TJ, Kranz PG. **Spontaneous intracranial hypotension: imaging in diagnosis and treatment.** *Radiol Clin North Am* 2019;57:439–51 CrossRef Medline
4. Schievink WI, Moser FG, Maya MM, et al. **Digital subtraction myelography for the identification of spontaneous spinal CSF-venous fistulas.** *J Neurosurg Spine* 2016;24:960–64 CrossRef Medline
5. Chazen JL, Robbins MS, Strauss SB, et al. **MR myelography for the detection of CSF-venous fistulas.** *AJNR Am J Neuroradiol* 2020;41:938–40 CrossRef Medline
6. Kim DK, Brinjikji W, Morris PP, et al. **Lateral decubitus digital subtraction myelography: tips, tricks, and pitfalls.** *AJNR Am J Neuroradiol* 2020;41:21–28 CrossRef Medline
7. Kranz PG, Amrhein TJ, Gray L. **CSF venous fistulas in spontaneous intracranial hypotension: imaging characteristics on dynamic and CT myelography.** *AJR Am J Roentgenol* 2017;209:1360–66 CrossRef Medline
8. Amrhein TJ, Gray L, Malinzak MD, et al. **Respiratory phase affects the conspicuity of CSF-venous fistulas in spontaneous intracranial hypotension.** *AJNR Am J Neuroradiol* 2020;41:1754–56 CrossRef Medline
9. Pinsky MR. **Cardiopulmonary interactions: physiologic basis and clinical applications.** *Ann Am Thorac Soc* 2018;15:S45–48 CrossRef Medline

10. Magder S. **Volume and its relationship to cardiac output and venous return.** *Crit Care* 2016;20:271 CrossRef Medline
11. Gutzeit A, Roos JE, Hergan K, et al. **Suction against resistance: a new breathing technique to significantly improve the blood flow ratio of the superior and inferior vena cava.** *Eur Radiol* 2014;24:3034–41 CrossRef Medline
12. Lloyd RA, Butler JE, Gandevia SC, et al. **Respiratory cerebrospinal fluid flow is driven by the thoracic and lumbar spinal pressures.** *J Physiol* 2020;598:5789–805 CrossRef Medline
13. Yeh BM, Coakley FV, Sanchez HC, et al. **Azygos arch valves: prevalence and appearance at contrast-enhanced CT.** *Radiology* 2004;230:111–15 CrossRef Medline
14. Brinjikji W, Savastano LE, Atkinson JL, et al. **A novel endovascular therapy for CSF hypotension secondary to CSF-venous fistulas.** *AJNR Am J Neuroradiol* 2021;42:882–87 CrossRef Medline
15. Mamlouk MD, Shen PY, Sedrak MF, et al. **CT-guided fibrin glue occlusion of cerebrospinal fluid-venous fistulas.** *Radiology* 2021;299:409–18 CrossRef Medline

Zoltan Patay, MD, PhD (1957–2022)

On July 23, 2022, we lost our beloved colleague, master clinician, teacher, scientist, mentor, global citizen, and foremost exceptional friend, Zoltan Patay. He passed away in Hungary, the country where he was born, a country that always remained his home base, his happy place, and a place where he frequently returned to celebrate life with those who meant the most to him: his wife Livia, his son Farkas, his daughter Eszter, and his parents.

Zoltan was born in Hungary, and attended the prestigious Fazekas Mihály High School in Budapest, known for its long tradition of excellence in mathematics and sciences. He graduated from the equally renowned research-oriented Medical School of the Semmelweis University in Budapest in 1982. After graduation, he completed residencies in neurology at the St. Stephen Hospital and Central Military Hospital in Budapest between 1982 and 1987. Zoltan subsequently expanded his formal training into the field of radiology, completing residencies in radiology between 1987 and 1992 at the Departments of Radiology of the Central Military Hospital in Budapest and the Hospital Louis Pasteur in Colmar, France. The combination of both training programs became the foundation of his career in neuroradiology.

In 1992, Zoltan accepted a position as a Specialist Registrar in Neuroradiology in the Department of Radiology of the Erasmus Hospital at the Free University of Brussels in Belgium. He enjoyed 2.5 years of the highest level of academic neuroradiology under the mentorship of Professor Danielle Balériaux. In November 1994, Zoltan returned to Hungary as the newly appointed Chair of the Department of Neuroradiology at the Central Military Hospital in Budapest. During his tenure in Budapest, he completed and successfully defended his PhD dissertation, "Applied MR-Neuroangiography," at the Hungarian Academy of Sciences. By the end of 1997, Zoltan had become recognized for his exceptional expertise in neuroradiology, which, in combination with his interest and flexibility to explore new challenges and opportunities, launched his career outside Europe.

Zoltan first embarked on an academic journey in the Middle East, where he served as Consultant Neuroradiologist and later as head of the Section of Neuroradiology in the Department of Radiology of the King Faisal Specialist Hospital and Research Center in Riyadh of the Kingdom of Saudi Arabia between 1997 and 2007. During his tenure there, he became one of the most reputable experts in the imaging, discovery, and understanding of multiple inborn errors of metabolism that may affect the brain.

Ten years later, Zoltan switched continents and joined the Department of Radiologic Sciences at the St. Jude Children's Research Hospital in Memphis, Tennessee. This move again showed his incredible flexibility and eagerness to be a life-long learner by expanding his expertise in the field of pediatric neuro-oncology. Zoltan was recruited to serve as the head the Section of Neuroradiology, and in 2016, he was selected to be the Chair of the Department of Diagnostic Imaging, a position he held with much virtue until his untimely death. His extensive training, combining a broad clinical-neurologic foundation with a deep understanding of the corresponding neuroimaging patterns, his curiosity and vision to apply advanced imaging techniques for the better understanding of pediatric neurologic diseases, and his tenures in Budapest, Colmar, Brussels, Riyadh, as well as Memphis made him a world-renowned expert in pediatric neuroradiology.

Zoltan collected all the accolades of an exceptional academic career. He published countless articles and book chapters and was recognized for his crystal-clear scientific presentations with more than 300 invited lectures at national and international scientific meetings. Zoltan received honors from multiple prestigious imaging societies, including honorary memberships in the Turkish Society of Neuroradiology, the Hungarian Society of Radiology, and the European Society of Neuroradiology.

He presented many named lectures including the Derek Harwood-Nash Lecture and the Marco Leonardi Plenary Lecture. He was honest and calm, caring and compassionate, eloquent and humble, optimistic and full of humor, a global citizen with an exceptional willingness and energy to embrace any new challenge that lay ahead of him allowing for a broad vision of life. Zoltan was a true friend. He never lost his cool, and he always took the best of what life had to offer. He was an excellent listener, curious and interested in the well-being of his colleagues and friends, always sharing his joys in life with everyone. Words cannot describe enough what a wonderful person he was. Those who had the pleasure of knowing him were truly blessed and will keep him in fond memory.

Last, but not least, Zoltan was a true family man. He deeply loved his wonderful wife Livia and his dear children Farkas and Eszter. He was so proud of his loved ones. Zoltan epitomized what a successful life is about: family and friends, doing good and being humble, and believing in the good of humanity.

Zoltan, we will miss you forever, we will never forget you.

T.A.G.M. Huisman

http://dx.doi.org/10.3174/ajnr.A7641

In the article "Introduction of Ultra-High-Field MR Imaging in Infants: Preparations and Feasibility" (K.V. Annink, N.E. van der Aa, J. Dudink, et al. *AJNR Am J Neuroradiol* 2020;41:1532–37 10.3174/ajnr.A6702) Table 1 and Fig 3 contained errors. The correct table and figure are the following:

	Duke Centered	Ella Centered	Charlie Centered	Charlie –50 mm FH	Charlie +50 mm FH
Global SAR					
Average SAR for 1 W input power (W/kg)	0.066	0.069	0.091	0.075	0.109
Average SAR per $B1^2$ (W/kg/μT2)	0.462	0.465	0.320	0.477	0.484
Average B_1^+ in central section for 1 W input power (μT)[a]	0.379	0.385	0.542	0.397	0.475
Peak SAR					
Peak local SAR (10 g averaged) for 1 W input power (W/kg)	0.435	0.398	0.487	0.345	0.643
Peak local SAR (10 g averaged) per B_1^2 (W/kg/μT2)	3.04	2.63	1.72	2.19	2.85

[a] The power optimization procedure of the MR imaging scanner software calibrates the needed input power to achieve a certain B_1 in the subject. This calibration is based on the average B_1^+ in a central section of the subject (brain in this case).

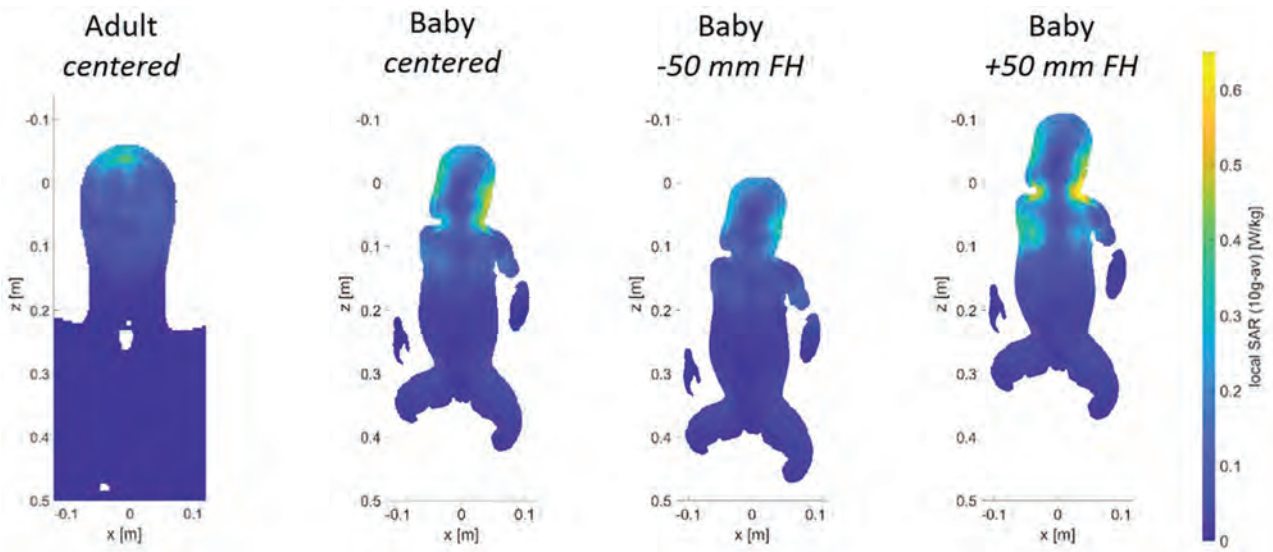

FIG 3. Local SAR levels in adult head (*left*) and Charlie in the different coil positions. Shifts of an infant in the x and y directions are unlikely because of limited space; therefore, the results are not included in the figure. The SAR values when infant Charlie is positioned 50 mm in the x or y direction are comparable with those in the +50-mm FH position.

Textual Changes

ABSTRACT

BACKGROUND AND PURPOSE: Cerebral MR imaging in infants is usually performed with a field strength of up to 3T. In adults, a growing number of studies have shown added diagnostic value of 7T MR imaging. 7T MR imaging might be of additional value in infants with unexplained seizures, for example. The aim of this study was to investigate the feasibility of 7T MR imaging in infants. We provide information about the safety preparations and show the first MR images of infants at 7T.

MATERIALS AND METHODS: Specific absorption rate levels during 7T were simulated in Sim4life by using infant and adult models. A newly developed acoustic hood was used to guarantee hearing protection. Acoustic noise damping of this hood was measured and compared with the 3T Nordell hood and no hood. In this prospective pilot study, clinically stable infants, between term-equivalent age

http://dx.doi.org/10.3174/ajnr.A7660

and the corrected age of 3 months, underwent 7T MR imaging immediately after their standard 3T MR imaging. The 7T scan protocols were developed and optimized while scanning this cohort.

RESULTS: Global and peak specific absorption rate levels in the infant model in the centered position and 50-mm feet direction did not exceed the values used by the scanner to calculate energy deposition. Hearing protection was guaranteed with the new hood. Twelve infants were scanned. No MR imaging-related adverse events occurred. It was feasible to obtain good-quality imaging at 7T for MRA, MRV, SWI, single-shot T2WI, and MR spectroscopy. T1WI had lower quality at 7T.

CONCLUSIONS: 7T MR imaging is feasible in infants, and good-quality scans could be obtained.

RESULTS

Preparation: SAR Simulation

The global SAR and peak local SAR of the virtual infant model did exceed the SAR of the adult models (in the center position by +38% and +12% compared with Duke, respectively) (Table 1). However, the calculated SAR per $B1^2$ values are all below the values used by the scanner to calculate energy deposition (1.83 W/kg/uT^2 for global SAR and 4.96 W/kg/uT^2 for peak local SAR. Numbers as provided by the manufacturer).

Global and peak local SAR levels were highest when the infant model was positioned +50-mm FH. Furthermore, in this position, the local SAR showed hotspots in the neck/shoulder transitions (Fig 3).

The SAR per $B1^2$ was lower in the infant model in the center position than in the adult models, meaning that less power is needed to reach the same B1.

DISCUSSION

We demonstrated that scanning infants in a 7T scanner is feasible and results in good-quality images. While optimization of the sequences is ongoing, we already demonstrated that some sequences showed more details compared with 3T MR imaging.

When the infant's head was further in the coil than isocenter, SAR levels were highest. Thus, the center position of the infant in the coil is essential. Therefore, the position of the infant's head was constrained in the coil, making it mechanically impossible to put the infant's head farther in the coil than center position.

ASNR
American Society of Neuroradiology

Celebrating 60 Years

1962-2022

The American Society of Neuroradiology was formed on April 18, 1962, in New York City. The following purposes of the organization were unanimously adopted by the fourteen founding members:

1. To develop and support standards for the training in the practice of Neuroradiology.
2. To foster independent research in Neuroradiology.
3. To promote a closer fellowship and exchange of ideas among Neuroradiologists.

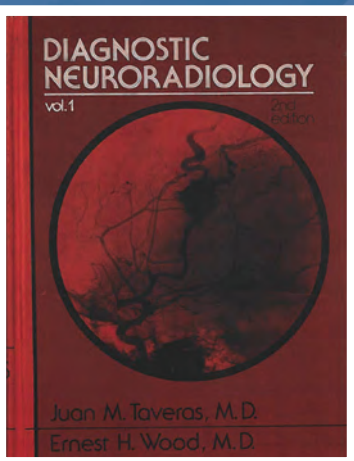

Visit ***www.asnr.org*** for more photos, videos and historical facts and be sure to follow **#ASNR60th** on social media so you don't miss a single thing. We have lots planned for 2022!

In Planning for Brain Metastases Treatment, Imaging may be the Missing Link in Cost Containment[1]

When faced with a patient presenting with metastatic brain cancer, determining whether to use up-front stereotactic radiosurgery (SRS) vs. first treating with whole brain radiotherapy (WBRT) is a significant clinical decision.

WBRT: The whole story on cognitive impairment

While whole brain radiotherapy (WBRT) has been the main treatment option for many years, experts agree that it often results in cognitive deterioration and a negative impact on quality of life. This mental decline has a devastating impact on patients and their families and adds ongoing costs for the healthcare systems managing these symptoms.

Using WBRT instead of SRS in some patients is estimated to decrease the total costs of brain metastasis management, though with increased toxicity.

SRS: Fewer side effects but greater risk of missed tumors

The cost of upfront SRS is the greatest contributor to cost of brain metastasis management.[1] SRS is often more expensive than WBRT. What's more, multiple applications of SRS can increase the cost of treatment greatly.

Stereotactic radiosurgery (SRS) has far fewer side effects, but upfront use of SRS is expensive and can carry the risk of missed tumors, requiring repeat procedures such as salvage SRS.[1]

Number of lesions and lesion size are key factors to be considered when determining the treatment plan for these patients. It follows that increased diagnostic information and accuracy could be beneficial in directing the proper therapy and improving overall long-term patient outcomes and containing costs. Getting the diagnosis right the first time is crucial to ensure proper treatment begins quickly, and high cost/high stakes procedures such as SRS need precise surgical planning.

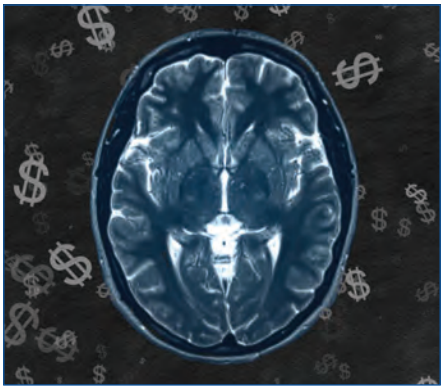

Getting the diagnosis right the first time is crucial to ensure proper treatment begins quickly.

What does optimal visualization mean for outcomes and cost?

For surgical planning with SRS, radiologists need the best visualization achievable to accurately count the number and size of the lesions. These metrics are the key predictors of the need for SRS,[1] WBRT, or a combination of both.

By selecting the ideal contrast agent and equipment protocols, neuroradiologists can identify the proximate numbers of metastases for upfront treatment and reduced salvage treatment occurrences.

The role of radiology

As medical care for oncology patients continues to evolve, it will be increasingly important to assess the cost of various interventions given the often-limited life expectancy of cancer patients, the rising costs of cancer therapy, and the increasing prevalence of cancer in an aging population.

Through seeing all the tumors and tumor borders as clearly as technology allows, radiology can play a part in ensuring that proper treatment can begin quickly, while containing costs through optimized patient care. Efforts to carefully manage treatment approaches require improvements in protocol design, contrast administration in imaging, and utilizing multimodal imaging approaches.

In this era of precision medicine, radiology departments' contribution to this improved standard of care will have significant short and long-term implications by reducing cost of care, providing a more proximate diagnosis, and ensuring optimal patient outcomes. ■

Reference: 1. Shenker, R. F., McTyre, E. R., Taksler, D et al. Analysis of the drivers of cost of management when patients with brain metastases are treated with upfront radiosurgery. *Clin Neurol Neurosurg.* 2019 Jan;176:10-14.

ASNR 61st Annual Meeting and 2023 Foundation of the ASNR Symposium

Call for Abstracts

Join us April 29-May 3, 2023, to present the best scientific research in neuroradiology.

ASNR is looking for abstract submissions on the topics of Adult Brain, Spine, Head and Neck, Pediatrics, Functional/Advanced Imaging, Interventional, Health Policy, and AI/Informatics.

ABSTRACT SUBMISSION DEADLINE

Tuesday, November 1, 2022 (11:59 PM ET)
Submit online at *https://bit.ly/3PsTO19*
Acceptance notifications will be sent on or before January 17, 2023, upon conclusion of peer review.

ABSTRACT SUBMISSION CATEGORIES

Scientific Oral Presentation: *in person presenter attendance required*
Electronic Scientific Poster: *in person OR virtual presenter attendance required*
Electronic Excerpta Poster: *in person OR virtual presenter attendance required*
Electronic Educational Exhibit: *in person OR virtual presenter attendance required*

ABSTRACT SUBMISSION INFORMATION AND CRITERIA

- **By submitting an abstract, you agree that the presenting author will register for the meeting at their own expense.** Oral abstract presenters must register and attend in-person. ePosters/ Educational Exhibits presenters may register for the virtual or in-person meeting format.
- ASNR requires disclosure from all persons in control of content, including all authors on abstracts. When added to an abstract, all co-authors on your submission will be notified to log-in and complete their own disclosure form. Once all co-authors have submitted disclosure, you will be able to finalize your submission. You will not be able to finalize your submission until all authors and co-authors have completed their disclosure forms. If any disclosures cannot be submitted by the deadline, remove authors with missing disclosures and submit the abstract. Authors may be added after submission if disclosure is completed. Email *education@asnr.org* to add authors after the submission deadline.
- Maximum length, not including spaces, title, authors, or image: 2,500 characters (combined from all text fields).
- The submission site allows uploading of a **single JPG file** with each submission. Only one graphic file may be submitted with each abstract. This single JPG can contain multiple images, graphics, and tables.
- At least one reference is required, and up to five references may be included. References should be formatted according to *AJNR* author instructions.
- DO NOT SUBMIT DUPLICATE ABSTRACTS IN MULTIPLE CATEGORIES OR SUBMISSION TYPES.
- Changes can be made to submitted abstracts until the deadline.
- ASNR encourages presenters to submit manuscripts based on their work to the *American Journal of Neuroradiology* or *Neurographics* before considering other journals.
- Available ASNR awards include the David M. Yousem Research Fellow Award, Cornelius Dyke Memorial Award, Outstanding Presentation Awards, and Educational Exhibit Awards.

Questions? Contact the ASNR Education Department at *education@asnr.org*.

ASNR23: TRANSFORMING THE FUTURE OF NEURORADIOLOGY